A mesoscopic spectrometer based on the Josephson effect

Joël Griesmar

To cite this version:

Joël Griesmar. A mesoscopic spectrometer based on the Josephson effect. Physics [physics]. Université Paris sciences et lettres, 2018. English. NNT : 2018PSLET037 . tel-02345684

THÈSE DE DOCTORAT

de l'Université de recherche Paris Sciences et Lettres
PSL Research University

Préparée au Collège de France

Un spectromètre mésoscopique reposant sur l'effet Josephson

A mesoscopic spectrometer based on the Josephson effect

Ecole doctorale n°564

ECOLE DOCTORALE PHYSIQUE EN ÎLE-DE-FRANCE

Spécialité PHYSIQUE

COMPOSITION DU JURY :

M. URBINA Cristián
SPEC CEA, Président du jury

M. HAKONEN Pertti
Aalto University, Rapporteur

M. HOFHEINZ Max
Université de Sherbrooke, Rapporteur

Mme MEYER Julia
Université Grenoble Alpes, Membre du jury

Mme GUERON Sophie
Université Paris-Sud, Membre du jury

M. GIRIT Çağlar
Collège de France, Membre du jury

M. PORTIER Fabien
SPEC CEA, Membre invité

M. DEBLOCK Richard
Université Paris-Sud, Membre invité

Soutenue par Joël GRIESMAR
le 10 décembre 2018

Dirigée par **Çağlar GIRIT**

COLLÈGE DE FRANCE
1530

PSL
RESEARCH UNIVERSITY PARIS

A mesoscopic spectrometer based on the Josephson effect

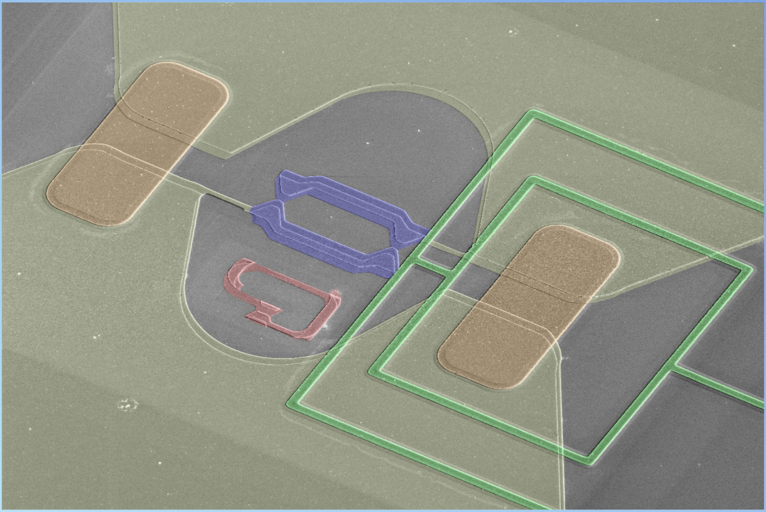

Joël Griesmar
Φ_0 lab
Collège de France, Paris

This thesis discusses the realization of a new device for mesoscopic physics: the Josephson spectrometer. It consists of two Josephson junctions and relies on the Josephson effect to convert a DC voltage to microwave oscillations at frequencies up to 180 GHz. Absorption of the emitted photons is directly measured in the current-voltage characteristic of the spectrometer.

The spectrometer is carefully designed in order to avoid exciting parasitic electromagnetic modes and to optimize the coupling to the device under test.

The Josephson spectrometer is used to measure the spectra of four simple systems over a wide frequency range: a LC resonator mode around 150 GHz, the excitation of quasiparticles in a superconductor above 90 GHz, the plasma frequency of a Josephson junction around 15 GHz and the plasma frequency of a RF-SQUID around 80 GHz.

Finally, some more complex and challenging targets for the spectrometer are presented, as well as improvements to be implemented to the current version of the device.

Cette thèse décrit la réalisation d'un nouveau dispositif pour la physique mésoscopique : le spectromètre Josephson. Il est composé de deux jonctions Josephson et repose sur l'effet Josephson pour convertir une tension continue en oscillations micro-ondes de fréquence pouvant atteindre 180 GHz. L'absorption de ces photons est directement mesurée sur la caractéristique courant-tension du spectromètre.

Le spectromètre est soigneusement dessiné pour éviter qu'il n'excite des modes électromagnétiques parasites et pour optimiser le couplage au système d'intérêt.

Le spectromètre Josephson est utilisé pour mesurer le spectre de quatre systèmes simples dans une large gamme de fréquences : un mode de résonateur LC autour de 150 GHz, l'excitation de quasiparticules dans un supraconducteur au-dessus de 90 GHz, la fréquence plasma d'une jonction Josephson autour de 15 GHz et la fréquence plasma d'un RF-SQUID autour de 80 GHz.

Finalement, quelques systèmes plus complexes et stimulants pouvant être sondés avec le spectromètre sont présentés, ainsi que quelques améliorations à apporter à la version actuelle du spectromètre.

Remerciements

Cette thèse ne s'est pas écrite toute seule, et il y a beaucoup de personnes qui m'ont aidé plus ou moins directement à la faire et j'aimerais les remercier ici très chaleureusement.

Merci tout d'abord à mon directeur de thèse, Çağlar, qui a été présent pour moi pendant ces trois années au Collège de France. Tu as su me faire découvrir le monde de la recherche d'une très belle manière. Toujours prêt à creuser plus profond au tableau, que ce soit pour éclaircir un passage obscur de Likharev ou pour choisir l'eau pour faire un bon espresso.

Merci à Jean-Loup qui était la seule personne présente dans le groupe Phi0 avec Çağlar quand j'ai commencé ma thèse. Grâce à toi, j'ai pu non seulement apprendre les joies de la fabrication en salle blanche, mais aussi découvrir qu'on peut (presque) tout faire en Python. Ça a été un réel plaisir de travailler avec toi.

Pendant ma thèse, j'ai aussi eu la chance et le plaisir d'être encadré par Jean-Damien. Merci à toi pour ta sérénité, tes excellents conseils et ta très bonne humeur ! Malheureusement, tu as rapidement été appelé à partir pour Polytechnique pour y exercer tes talents !

Merci aussi à Vincent, qui, à défaut d'avoir été le premier thésard du groupe, en aura été le premier étudiant de master. Ça a été un plaisir de partager le bureau et tes connaissances sur le café et les machines à espresso avec toi pendant ces trois années.

Merci aussi Fabien pour tes multiples conseils et astuces sur la physique expérimentale, mais aussi sur la vie dans une coloc qui tombe en ruine, le café et l'entretien des vélos !

Merci également à Léo, arrivé quand je commençais à finir ma thèse. J'espère que tu auras bientôt l'occasion de mesurer le bien-nommé Peace-and-lovium pendant ta thèse !

Merci aussi à Teresa et Ramiro, arrivés tout à la fin de mon séjour à Phi0.

En plus du groupe Phi0, je tiens aussi à remercier la deuxième jeune équipe du Collège qui occupe le bureau juste à côté de nous, que j'ai maintenant envahi avec Fabien ! Merci Benoît, Mathieu et Clément pour ces repas, cafés et bières que nous avons pu partager !

Merci aussi à Carmen et aux deux Françoises pour leur aide dans les démarches administratives, leur gentillesse et leur bonne humeur. Je voudrais aussi remercier Pascal et tout l'atelier mécanique pour leur expertise dans la fabrication des porte-échantillons utilisés pour les mesures présentées dans cette thèse.

Merci également aux doctorants de l'étage d'en-dessous, en particulier à Valentin et Rodrigo, que j'ai plaisir à croiser de temps à autre dans les couloirs.

Merci aussi aux équipes MUSI et Vivant de la Cité des Sciences où j'ai eu la chance et le plaisir de découvrir les bases de la médiation scientifique dans une équipe très vivante et sympathique ! Merci notamment aux doctorants avec qui j'ai partagé de très bons moments entre deux médiations : Mathieu, Louis, Justin, Hélène et Jan.

Merci également à tous les scientifiques que j'ai pu rencontrer et avec qui j'ai pu interagir. Merci à tout le groupe Quantronique (et à tous ses anciens membres), avec qui c'est toujours

Le groupe Φ_0 en mai 2019. De gauche à droite : Joël Griesmar, Léo Peyruchat, Ramiro Rodriguez, Teresa Stefani, Vincent Benzoni, Fabien Lafont, Jean-Loup Smirr et Çağlar Girit.

très enrichissant de discuter et de collaborer. Merci Zaki, ça a été un plaisir d'enseigner la mécanique quantique avec toi.

Thank you Benjamín, it was really fun and instructive to work with you when you came visiting us. I hope this manuscript respects the SUCCESS principle!

I would also like to thank all the members of my thesis commitee: Cristián Urbina, Pertti Hakonen, Max Hofheinz, Julia Meyer, Sophie Guéron, Fabien Portier and Richard Deblock.

Merci aussi à tous mes amis qui ont toujours été là pendant ces trois années et depuis bien plus longtemps. Merci Pierre, Vincent, Quentin, Guillaume et Emilie, grâce à qui la vie est plus belle. Merci Léo, Vivien, Clément, Elise et Adrien pour ces parties de coinche endiablées et ces nombreuses dégustations de kebabs. Muchas gracias à la mafia plus ou moins espagnole de Berlin : Pablo, Sergio, Adrià, Laëtitia et Max. El abedul es muy blanco! Un grand poët aussi à tout le Platypus Braxx Band, de loin la meilleure fanfare de France ! Merci aussi à tous les thûrists de HX3 et à tous mes potes de l'X ! Merci également à tous les autres doctorants rencontrés en conf ou en école d'été : David, Pierre, Ambroise, Remko, Lavi, Santiago, Alvaro, Philipp, Andreas, ...

Pour finir, merci à toute ma famille qui m'a toujours soutenu dans tout ce que j'ai fait. Et enfin, merci à Leslie, dont la présence dans ma vie me remplit de joie au quotidien.

Contents

Résumé en français

L'effet Josephson, prédit en 1962 par Brian Josephson [1], et observé expérimentalement seulement un an plus tard par Anderson et Rowell [2], est au cœur de beaucoup d'appareils utilisés aujourd'hui en biologie [3–5], métrologie [6], mesures à bas bruit [7, 8], information quantique [9–16] et même astronomie [17,18]. Ce travail de thèse se concentre sur la réalisation d'un nouvel outil pour la physique mésoscopique reposant sur cet effet, le spectromètre Josephson, conçu pour opérer à des fréquences pouvant atteindre la gamme des térahertz. Il n'y a actuellement pas d'équipement micro-ondes commercial pour étudier des systèmes mésoscopiques au-delà de $50 - 80\,\mathrm{GHz}$. En outre, une calibration est nécessaire pour tenir compte de possibles résonances due aux lignes de mesures. Le spectromètre Josephson proposé ici est un appareil fabriqué sur une puce, qui peut être placé proche du système à sonder (à moins d'une longueur d'onde, de l'ordre du mm à 100 GHz) et supprime ainsi la nécessité de calibrer les lignes de mesure micro-ondes.

Il consiste en une boucle supraconductrice interrompue par deux jonctions Josephson et repose sur l'effet Josephson pour convertir une tension continue V en des oscillations micro-ondes à une fréquence proportionnelle à V. La constante de proportionnalité entre les deux est une constante fondamentale, la constante Josephson K_J, définie comme l'inverse du quantum de flux magnétique, $K_J = 1/\Phi_0 = 483.6\,\mathrm{MHz}\,\mathrm{\mu V}^{-1}$. L'absorption des micro-ondes émises est directement mesurée comme un pic de courant dans la caractéristique courant-voltage du spectromètre.

Utiliser une jonction Josephson pour effectuer la spectroscopie d'un autre système n'est pas une idée totalement nouvelle. Rapidement après la prédiction de Josephson, un courant alternatif à haute fréquence a été observé dans des jonctions tunnel [19], et des contacts ponctuels ont été utilisés pour détecter des radiations millimétriques et submillimétriques [20]. L'idée de combiner à la fois l'émission et l'absorption pour faire un spectromètre a été mise en œuvre pour la première fois en 1967 par Silver et Zimmerman dans une expérience [21] où ils ont mesuré la résonance magnétique nucléaire du Co^{59} à 218 MHz en utilisant des contacts ponctuels de niobium.

Cependant, ce premier spectromètre n'a pas été suivi d'un grand développement de la technique. Dans les années 1970 et 1980, ces processus d'émission et de réabsorption de photons par des jonctions Josephson ont principalement été utilisés pour expliquer des pics de courant dans des caractéristiques courant-voltage de dispositifs supraconducteurs à interférences quantiques (Superconducting QUantum Interference Device ou SQUID en anglais) [22–25]. Il y a eu quelques applications à la spectroscopie de systèmes mésoscopiques : des modes résonants de micro-résonateurs [26, 27] et de lignes de transmission [28] ont été mesurés. Des jonctions Josephson ont aussi été utilisées pour mesurer des transitions entre les niveaux d'énergie d'une autre jonction [29], d'un SQUID [30] ou d'un transistor à paires de Cooper uniques [31].

Plus récemment, le groupe Quantronique à Saclay a réalisé la spectroscopie par absorption d'états liés d'Andreev (Andreev Bound States ou ABS en anglais) dans un contact atomique supraconducteur en utilisant une jonction Josephson [32, 33]. Ce spectromètre a cependant quelques inconvénients :

- Présence de résonances additionnelles dues à des modes dans l'environnement non contrôlé du spectromètre.
- Couplage non-uniforme au système à sonder sur toute la plage de fréquence considérée.

Cette thèse cherche à résoudre ces problèmes en améliorant la conception du spectromètre déjà existant.

Tout d'abord, les propriétés générales des jonctions Josephson nécessaires à la compréhension du fonctionnement du spectromètre sont exposées. En particulier, l'effet Josephson est redérivé et la caractéristique courant-tension idéale d'une jonction est présentée. La dynamique d'un système à deux jonctions (le SQUID) à la base du spectromètre est aussi détaillée.

Ces propriétés sont ensuite utilisées pour expliquer le principe de fonctionnement du spectromètre, notamment la modification de la caractéristique courant-tension en présence d'un mode résonnant dans l'environnement de la jonction. Plusieurs moyens de coupler le spectromètre au système à sonder sont présentés, tels que l'utilisation d'un condensateur (comme dans le cas de la spectroscopie des états d'Andreev [32]), de l'inductance mutuelle entre le SQUID et le système, ou encore la connexion galvanique au système.

La troisième partie présente un modèle plus complet d'une jonction Josephson. Cela permet de comprendre l'origine des modes résonants parasitiques ainsi que les éléments indésirables pouvant apparaître dans la caractéristique courant-tension d'une jonction.

Partant de ces considérations, plusieurs circuits pour le spectromètre sont testés et analysés. Le circuit d'alimentation semble notamment avoir un rôle considérable dans la forme de la caractéristique courant-tension. L'ajout de résistances, d'inductances et de condensateurs sur la puce est tout particulièrement considéré.

Plusieurs spectromètres sont ainsi fabriqués et utilisés pour mesurer le spectre de quatre systèmes simples sur une large gamme de fréquence : un mode LC autour de 150 GHz, l'excitation de quasiparticules dans un supraconducteur au-dessus de 90 GHz, la fréquence plasma d'une jonction Josephson à 15 GHz et la fréquence plasma d'un RF-SQUID proche de 80 GHz.

Finalement des cibles plus complexes et stimulantes pour le spectromètre sont présentées. Les projets les plus avancés consistent à sonder les états d'Andreev dans deux jonctions proches où ils peuvent s'hybrider ou dans des liens faibles à base de nanofils en InAs ou de l'isolant topologique HgTe dans lesquels le spectre d'Andreev est modifié à cause du couplage spin-orbite. Une autre direction prometteuse serait d'observer des croisements de niveaux non-évités dus à la topologie de certains circuits quantiques supraconducteurs.

Introduction aux jonctions Josephson

L'effet Josephson a lieu à tout contact électrique faible entre deux supraconducteurs. Ils peuvent être séparés par un isolant, un métal normal, un semi-conducteur ou n'importe quel autre type de matériel. Dans ce cas, un courant non-dissipatif de paires de Cooper I_S (appelé super-courant) peut circuler à travers la jonction. Il traduit la présence d'une cohérence de

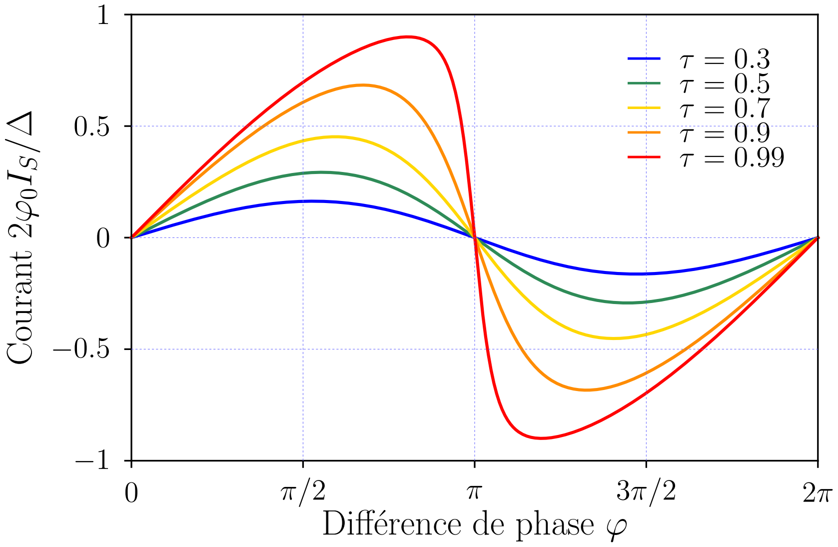

Figure (i).1.: Super-courant porté par un canal de conduction pour différentes transmissions.

phase entre les deux supraconducteurs et il est, dans le cas le plus général, une fonction $2\pi-$périodique de la différence de phase,

$$\varphi = \varphi_2 - \varphi_1.$$

De plus, la symétrie par renversement du temps impose $I_S(-\varphi) = -I_S(\varphi)$ [34]. Combiner ce résultat avec la $2\pi-$périodicité donne $I_S(n\pi) = 0$, $n \in \mathbb{Z}$. Le super-courant d'un lien faible peut donc être écrit sous la forme

$$I_S(\varphi) = \sum_{n=1}^{\infty} I_n \sin n\varphi. \tag{i}$$

Une telle relation courant-phase est toujours limitée par une valeur maximale I_0, appelée courant critique. Il s'agit du courant non-dissipatif maximal que la jonction peut supporter. Il est en général proportionnel à l'aire de la jonction et décroît quand l'épaisseur augmente. Dans une description mésoscopique de l'effet Josephson, un lien faible court (plus petit que la longueur de cohérence supraconductrice) est modélisé par des canaux de conduction de transmission τ_i, accueillant chacun une paire d'états d'Andreev (Andreev Bound States ou ABS en anglais) [35]. Les énergies $E_\pm$ de ces états $|\pm\rangle$ sont données par

$$E_\pm(\varphi) = \pm\Delta\sqrt{1 - \tau \sin^2\frac{\varphi}{2}}.$$

Le super-courant est alors porté par l'état fondamental, $|-\rangle$. Il peut être exprimé comme la dérivée de l'énergie de l'état par rapport à la différence de phase parce que la phase et la charge sont conjuguées. À température nulle, cela s'écrit

$$I_S(\varphi) = \frac{1}{\varphi_0}\frac{\partial E_-}{\partial \varphi} = \frac{\Delta}{4\varphi_0}\frac{\tau \sin\varphi}{\sqrt{1 - \tau \sin^2\frac{\varphi}{2}}}.$$

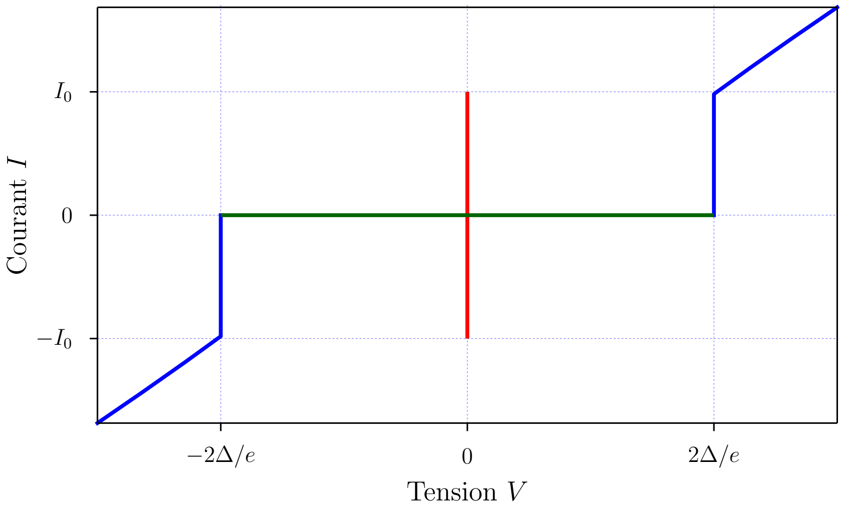

Figure (i).2.: Caractéristique courant-tension idéale pour une jonction Josephson tunnel.

En remarquant que $\sin^2 \varphi/2$ est $2\pi-$périodique, il est possible de développer cette expression en série de Fourier et d'obtenir une forme similaire à celle de l'équation (i), faisant ainsi un lien entre les deux théories.

La Figure (i).1 montre la forme du super-courant pour plusieurs transmissions. Comme attendu, il est nul à $\varphi = 0$, π et 2π et il est plus grand pour des transmissions plus importantes. Pour des faibles transmissions, le super-courant est proche d'une forme sinusoïdale.

Par la suite, nous nous intéresserons principalement à des jonctions avec de faibles transmissions, appelées jonctions Josephson tunnels. Elles ont une relation courant-phase simple,

$$I_S(\varphi) = I_0 \sin \varphi. \tag{ii}$$

La loi de Faraday pour l'induction nous fournit aussi une relation entre la tension et la différence de phase aux bornes de la jonction. Habituellement, on l'écrit $V = \dot{\Phi}$, où V est la tension aux bornes d'une bobine et Φ le flux magnétique la traversant. Pour une inductance supraconductrice ou une jonction Josephson, le flux est proportionnel à la différence de phase, $\Phi = \varphi_0 \varphi$. La tension induite s'écrit alors

$$V = \varphi_0 \dot{\varphi}. \tag{iii}$$

Les équations (ii) et (iii) sont souvent appelées les relations Josephson DC et AC. En les combinant avec les densités d'états des deux supraconducteurs, on peut obtenir la forme de la caractéristique courant-tension (représentée sur la Figure (i).2) d'une jonction tunnel :

- à tension nulle (en rouge), la différence de phase est constante et un super-courant (plus petit que le courant critique) traverse la jonction.

- à une tension V telle que $0 < |V| < 2\Delta/e$ (en vert), la différence de phase croît à un taux $\omega_J = |V|/\varphi_0$, ce qui se traduit par des oscillations de courant à une fréquence de l'ordre de 100 GHz (à $V = \Delta/e$ dans l'aluminium). En moyenne, ce processus résulte en un courant nul.

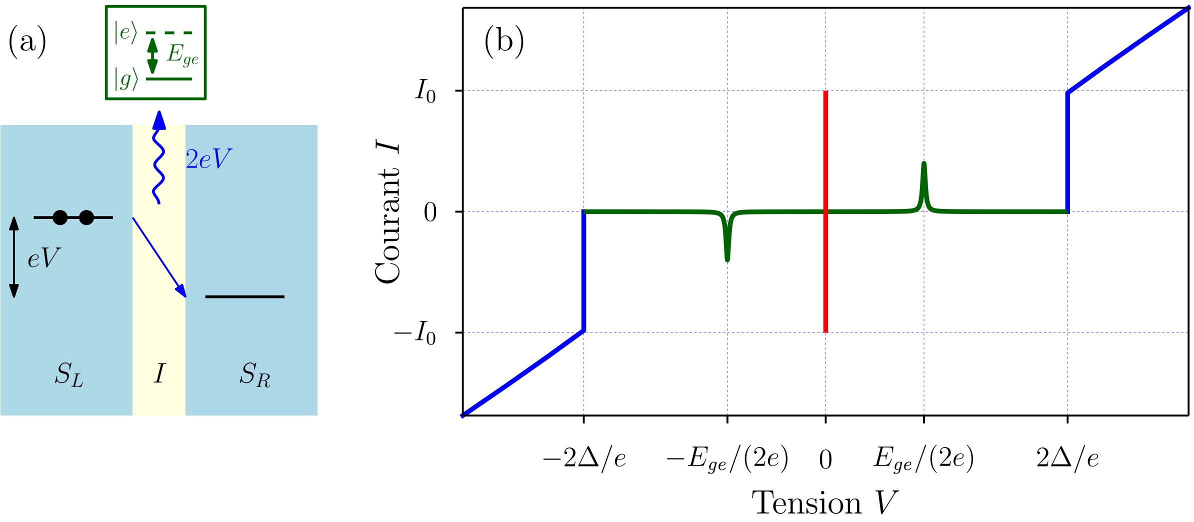

Figure (i).3.: (a) Tunneling inélastique de paires de Cooper ; (b) Caractéristique courant-tension idéale d'une jonction tunnel couplée à un système à deux niveaux.

- Pour une tension plus grande que $2\Delta/e$ (en bleu), des quasiparticules d'un supraconducteur peuvent franchir la barrière tunnel et rejoindre le second supraconducteur. à cause de la singularité BCS à énergie Δ, il y a une marche de courant à tension $2\Delta/e$.

Principe du spectromètre Josephson

En présence d'un mode électromagnétique dans l'environnement d'une jonction Josephson, sa caractéristique courant-tension est fortement modifiée. Pour expliquer ce phénomène, considérons le cas d'un système à deux niveaux $|g\rangle$ et $|e\rangle$ séparés par une énergie E_{ge}. Les oscillations de courant dans la région sous le gap ($0 < |V| < 2\Delta/e$) peuvent être comprises en termes d'émission et de réabsorption par la jonction de photons d'énergie $2e\,|V| = \hbar\omega_J$: une paire de Cooper du supraconducteur de gauche S_L dans la Figure (i).3(a) doit émettre une énergie $2e\,|V|$ pour pouvoir traverser la barrière par effet tunnel. Si le photon émis n'est pas résonnant avec le mode, il est réabsorbé par la paire de Cooper qui revient ainsi en S_L. Cependant, si $2e\,|V| = E_{ge}$, le photon peut aussi être absorbée par le mode électromagnétique, empêchant ainsi la paire de Cooper de revenir en S_L. Cela se traduit par un courant continu fini à travers la jonction, représenté sur le graphe (b) de la Figure (i).3. La hauteur du pic de courant est reliée à la dissipation dans le mode et peut donc être exprimée en fonction de la partie réelle R_e de l'impédance vue par la jonction, ou de façon équivalente par le taux d'absorption Γ,

$$I\left(V\right) = \frac{R_e\left(\omega_J\right) I_0^2}{2V} = 2e\Gamma\left(\omega_J\right).$$

Quand $|V| > 2\Delta/e$, ces pics sont moins visibles car la contribution au courant des quasiparticules domine devant celle des paires de Cooper. Pour de l'aluminium, cela fait une limite supérieure de 180 GHz.

Ce principe a déjà été démontré par le groupe Quantronique à Saclay [32, 33]. Cependant leur spectromètre était trop efficace ! Dans cette expérience, il a non seulement permis de sonder le spectre des états d'Andreev dans un contact atomique (ce qui était leur objectif), mais il a aussi révélé de nombreuses résonances dues à l'environnement électromagnétique et en particulier au circuit de polarisation.

Afin de limiter le couplage à ces modes, un SQUID polarisé en flux à un demi quantum de flux est utilisé à la place d'une seule jonction Josephson, comme montré sur la Figure (i).4. Les deux jonctions sont symbolisées par des croix dans des boîtes carrées et les inductances l modèlent l'inductance de la boucle du SQUID. Les lignes en pointillés partant du spectromètre sont connectées au circuit de polarisation qui ferme le circuit.

Appliquer un champ magnétique génère un flux Φ_e dans la boucle du SQUID qui est relié aux différences de phase φ_1 et φ_2 des jonctions par $\Phi_e/\varphi_0 = \varphi_2 - \varphi_1$. Quand il n'y a pas de flux dans la boucle (image du haut), les deux jonctions ont la même différence de phase, ce qui correspond à des courants micro-ondes circulant dans la même direction, représentés par des flèches rouges sur le schéma. Ils ne peuvent exciter que des modes hors de la boucle. Cette situation est donc équivalente au spectromètre à simple jonction Josephson de Réf. [32, 33].

Quand le SQUID est polarisé à un demi quantum de flux (image du bas), les deux courants micro-ondes sont déphasés de π et, dans le cas où les deux jonctions ont le même courant critique, ils sont confinés dans la boucle. Les modes électromagnétiques en dehors de la boucle ne sont donc pas excités. Cependant, il y a un inconvénient à cette configuration. Il y a un mode LC intrinsèque à la boucle, dû à la capacité électrique des jonctions et à l'inductance de la boucle. Pour le SQUID symétrique représenté en Figure (i).4, ce mode LC est à la fréquence $1/(2\pi\sqrt{lC_J})$, où C_J est la capacité de chaque jonction du SQUID. Pour des valeurs typiques de $l = 50\,\mathrm{pH}$ et $C_J = 50\,\mathrm{fF}$, cette fréquence est de l'ordre de 100 GHz, ce qui se trouve au milieu de la gamme de fréquences où le spectromètre peut être utilisé. En faisant des jonctions ou des boucles plus petites, cette fréquence peut être déplacée en dehors de la bande passante du spectromètre.

Dans cette situation, le système à sonder (Device Under Test ou DUT en anglais) doit être situé dans la boucle, où le courant micro-onde est maximal. Le DUT peut aussi être dans une seconde boucle, couplée inductivement à celle du SQUID.

Conception du spectromètre

En pratique, il n'est pas facile de fabriquer deux jonctions avec un rapport de courants critiques plus grand que 99% avec l'appareil de lithographie optique disponible au Collège de France. Cela permet déjà de bien se découpler des modes parasites de l'environnement. La petite quantité de courant micro-onde qui peut circuler hors de la boucle du SQUID à demi quantum de flux peut néanmoins exciter ces modes et faire une différence assez importante dans la caractéristique courant-tension. Il est donc crucial de concevoir un environnement électromagnétique pour le SQUID permettant de déplacer les modes résonants non désirés hors de la bande passante du spectromètre ou de les amortir pour qu'ils n'apparaissent pas dans le spectre. Plusieurs géométries ont été implémentées, jusqu'à ce qu'un spectre sans résonance soit mesuré. Cela est résumé dans la Figure (i).5.

La première géométrie (ligne supérieure du tableau) consiste à connecter directement le spec-

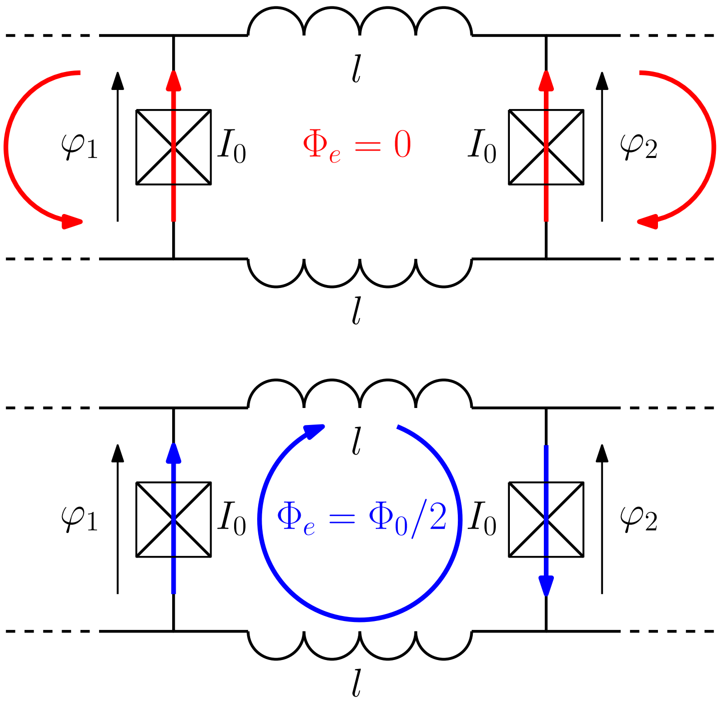

Figure (i).4.: Schéma électrique d'un spectromètre constitué d'un SQUID symétrique à $\Phi_e = 0$ et $\Phi_0/2$.

tromètre à des fils supraconducteurs pour utiliser leur inductance qui a une haute impédance à hautes fréquences pour découpler le spectromètre du circuit de polarisation. La caractéristique courant-tension obtenue contient plusieurs résonances à basse fréquence à $\Phi_e = 0$ (en rouge) qui sont partiellement supprimées à demi quantum de flux (courbe bleue). Elles ont à présent été identifiées comme des modes de la ligne de transmission formée par les wirebonds utilisés pour connecter la puce sur laquelle le spectromètre est fabriqué au circuit de polarisation.

Grâce à l'ajout d'un condensateur (ligne centrale du tableau), ces modes sont court-circuités. Mais une nouvelle résonance apparaît, à la pulsation $1/\sqrt{LC}$, typiquement de l'ordre de $20 - 50\,\text{GHz}$. À demi quantum de flux, il y a encore quatre pics présents dans le spectre, mais celui-ci est déjà bien plus propre, notamment à basse fréquence. L'augmentation du courant à haute tension à $\Phi_e = \Phi_0/2$ correspond à l'excitation du mode LC de la boucle du SQUID.

Des résistances sont finalement ajoutées sur la puce pour amortir les modes présents mais aussi pour faire office de filtre passe-bas en dessous de $1/(RC)$. Cette fréquence de coupure peut facilement être plus petite que $500\,\text{MHz}$, garantissant peu de modes basse-fréquence. La caractéristique courant-tension obtenue à $\Phi_e = 0$ ne contient plus que deux pics. Le plus large à $275\,\mu\text{V}$, est à présent identifié comme un mode dû à des trop grands plans d'aluminium présents dans le dessin du spectromètre. Le second, autour de $150\,\text{GHz}$, correspond à la fréquence $1/(2\pi\sqrt{LC})$. Même avec un faible rapport de symétrie[1] $\alpha \sim 0.75$, la caractéristique courant-tension est quasiment vierge à demi quantum de flux. Il ne reste plus que le pic à

---

[1] Le rapport de symétrie d'un SQUID est défini comme le rapport entre les courants critiques de ces deux jonctions. Un rapport égal à un correspond à un SQUID parfaitement symétrique.

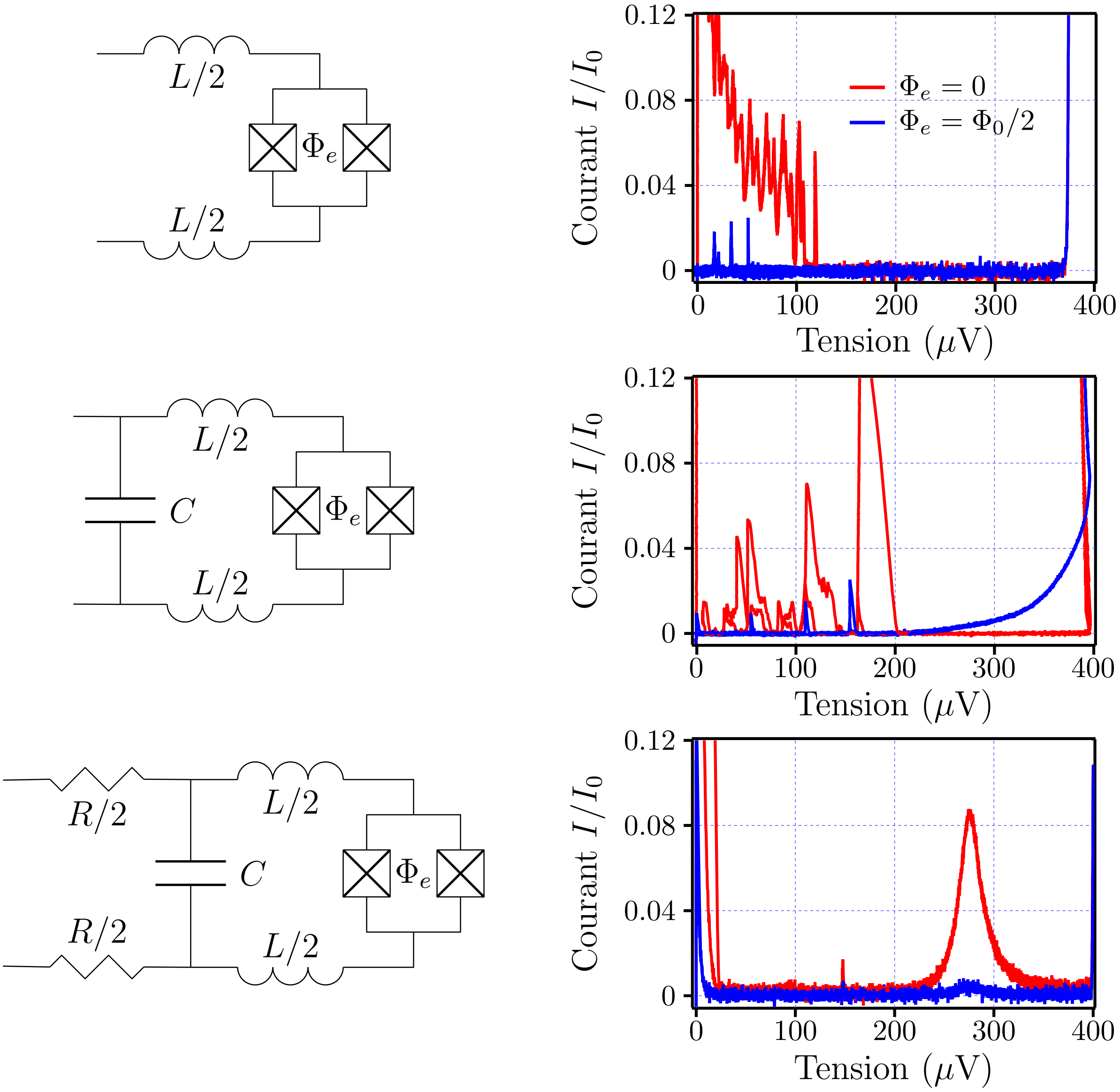

Figure (i).5.: Tableau récapitulant les géométries testées.

275 µV qui culmine à 400 pA.

Spectroscopie Josephson de quatre systèmes test

Afin de vérifier que le spectromètre fonctionne comme prévu, ce dernier a tout d'abord été testé sur quatre systèmes simples couvrant une grande partie de sa bande passante ($2-180$ GHz) : le mode d'un résonateur LC autour de 150 GHz, l'excitation de quasiparticules dans un supraconducteur au-dessus de 90 GHz, la fréquence plasma d'une jonction Josephson vers 15 GHz, ainsi que celle d'un RF-SQUID autour de 80 GHz.

Ces quatre systèmes ont aussi permis de montrer le fonctionnement du spectromètre dans différentes situations. Les trois premiers ont été mesurés avec un couplage galvanique dans la boucle du SQUID. Cette configuration est facile à mettre en place, mais seulement si le système à sonder peut être fabriqué dans la boucle du spectromètre, ce qui n'est pas le cas de la plupart des systèmes qui pourraient être mesurés. Le spectre du RF-SQUID a été mesuré en couplant le spectromètre inductivement à la boucle du RF-SQUID. Cela prouve la possibilité d'utiliser un tel mode de couplage ainsi que de contrôler indépendamment deux flux magnétiques : celui dans la boucle du SQUID et celui dans la boucle du RF-SQUID. Dans cette expérience, une largeur de raie de 550 MHz a été obtenue.

Cibles proposées pour le spectromètre

Cette thèse va plus loin que cette preuve de fonctionnement et présente des cibles plus complexes et stimulantes pour le spectromètre, pour lesquelles la fabrication a déjà commencé. Les projets les plus avancés consistent à sonder les états d'Andreev dans des liens faibles non conventionnels :

- Rapprocher deux jonctions Josephson plus proche que la longueur de cohérence supraconductrice permet d'hybrider leurs états d'Andreev et de former ainsi une molécule artificielle dans laquelle des super-courants non locaux devraient être observés [36].
- Le fort couplage spin-orbite dans des longs nanofils lève la dégénérescence de spin des états d'Andreev même en l'absence de champ Zeeman et peut donner lieu à des croisements non-évités de niveaux d'énergie, similaires à des points de Weyl [37, 38].
- Des jonctions Josephson à base d'isolants topologiques voient la $2\pi-$périodicité habituelle du spectre transformée en une $4\pi-$périodicité anomale due à des invariants topologiques non-triviaux. [39].

La forme de ces états d'Andreev modifiés est présentée, ainsi que des estimations du courant que l'on mesurerait si l'on sondait ces états avec un spectromètre Josephson.

D'autres systèmes qui pourraient être sondés avec un spectromètre Josephson sont les circuits quantiques supraconducteurs topologiques. Ce sont des circuits électroniques comportant des composants linéaires habituels tels que des condensateurs et des bobines, mais aussi les composants non-linéaires que sont les jonctions Josephson. Ces dispositifs non-dissipatifs peuvent

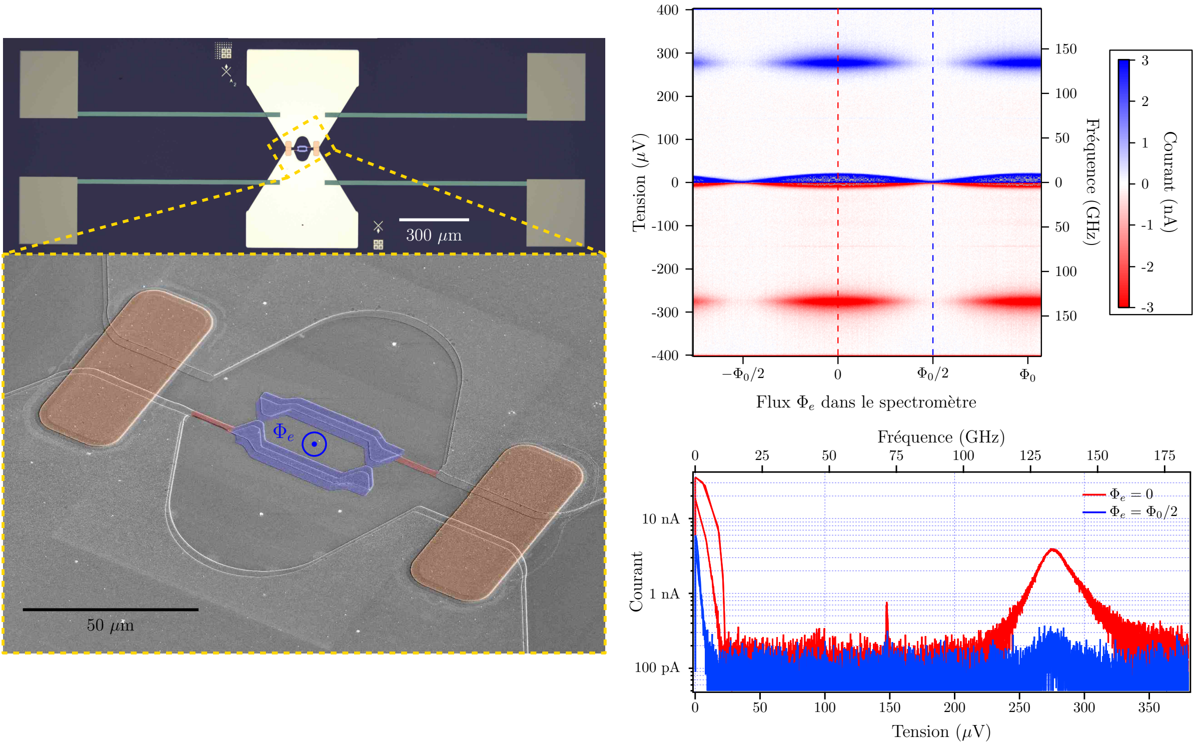

Figure (i).6.: Photographies au microscope et au MEB (Microscope Électronique à Balayage) et caractéristique courant-tension de la dernière version du spectromètre.

dans certains cas donner lieu à des croisements entre niveaux d'énergie protégés topologiquement, à la base de propriétés de transport quantifiées. Fabriquer de tels circuits quantiques permet de créer un Hamiltonien avec autant de paramètres que souhaités et peut avoir des applications potentielles à la simulation quantique de systèmes plus complexes.

Conclusion

Partant d'une réalisation expérimentale d'un spectromètre reposant sur l'effet Josephson [32], nous avons compris ses défauts et implémenté un nouveau dispositif (visible dans la partie gauche de la Figure (i).6) pour y remédier. Les principaux désavantages de la première génération de spectromètre étaient la présence de plusieurs modes résonants parasites dus à l'environnement électromagnétique de la jonction ainsi qu'un couplage non-uniforme au système d'intérêt.

Utiliser un SQUID symétrique (colorisé en bleu) polarisé à un demi quantum de flux permet de découpler de manière significative la jonction de son environnement. Ce dernier est aussi conçu soigneusement afin de supprimer les modes restants. La haute impédance d'inductances (en rouge) placées proche des jonctions contribue à un bon découplage. Une grande partie des micro-ondes émises, ainsi que le bruit venant de l'extérieur, sont court-circuités par deux condensateurs (en orange) à l'autre bout des inductances. Les modes résonants toujours présents sont ensuite amortis par de grandes résistances (en vert) fabriquées sur la puce.

Le couplage au système d'intérêt peut se faire en utilisant l'inductance de la boucle du SQUID au lieu d'un condensateur, comme dans la première version du spectromètre. Cela garantit une excitation de phase uniforme aux bornes de l'inductance, alors que dans le cas d'un couplage capacitif, cette dépendance était proportionnelle à l'inverse du carré de la fréquence.

Toutes ces améliorations ont permis de mesurer un spectre quasiment vierge lorsque le spectromètre n'est couplé à aucun système. La partie droite de la Figure (i).6 montre de telles caractéristiques courant-tension. La carte couleur du haut montre l'évolution des caractéristiques IV par rapport au flux Φ_e dans la boucle du SQUID et les courbes du bas sont des coupes (en échelle logarithmique) suivant les lignes pointillées rouge et bleue à $\Phi_e = 0$ et $\Phi_0/2$. Le courant restant à $\Phi_e = \Phi_0/2$ en dessous du gap est de l'ordre de 200 pA pour des jonctions avec un courant critique de 100 nA. Cela correspond à une puissance équivalente de bruit (Noise Equivalent Power en anglais) intrinsèque de 10^{-17} W/$\sqrt{\text{Hz}}$ sur une bande passante de 180 GHz. Les quelques modes résiduels à 150 et 275 µV ont maintenant été identifiés comme dus aux larges plans d'écrantage visible en jaune pâle sur la photographie microscope. Ils peuvent donc être déplacés hors de la bande-passante du spectromètre dans la prochaine version.

Le spectre de quatre systèmes de test a été mesuré sur une large gamme de fréquence : le mode d'un résonateur LC à 150 GHz, l'excitation de quasiparticules dans un supraconducteur au-dessus de 90 GHz, la fréquence plasma d'une jonction Josephson à 15 GHz, ainsi que celle d'un RF-SQUID à 80 GHz. Les spectres mesurés coïncident avec la théorie et permettent de prouver que le spectromètre peut être utilisés dans des situations variées. La spectroscopie du RF-SQUID a notamment été faite par un couplage mutuel à une inductance en parallèle avec le spectromètre, prouvant ainsi la faisabilité d'un tel couplage sans contact. Puisque le couplage à la boucle est resté assez faible dans ce cas, les prochains spectromètres à SQUID contiendront les systèmes à sonder directement dans leur boucle.

Finalement, quelques systèmes particulièrement adaptés à être sondés par spectroscopie Josephson ont été présentés, tels que des états d'Andreev hybridés dans deux jonctions proches, des états d'Andreev modifiés par le couplage spin-orbite dans des nanofils d'InAs et des liens faibles à base de l'isolant topologique HgTe, ainsi que des circuits quantiques supraconducteurs topologiques dans lesquels les niveaux d'énergie plasma peuvent subir des croisements non-évités dus à la topologie des systèmes.

Perspectives

Le dispositif obtenu dans cette thèse peut encore être amélioré. Une des directions possibles consiste en le fabriquer sur un substrat transparent en saphir. Avec une telle puce-spectromètre, il serait possible de sonder tout type de système en les approchant l'un de l'autre. Cela permettrait d'éviter des étapes de fabrication sur le système d'intérêt qui peut être fragile et ne pas supporter les étapes de chauffage nécessaires à la fabrication du spectromètre. Avec une boucle de SQUID de rayon 50 µm, le couplage reste conséquent jusqu'à une distance de l'ordre de 100 µm entre le spectromètre et le système d'intérêt, facilement atteignable avec des techniques d'alignement simples. Le groupe Φ_0 est actuellement en train de travailler à la conception d'un nouveau dispositif pour l'alignement dans lequel la puce contenant le système à sonder peut être déplacé avec des vis micrométriques et ainsi être bien aligné sur le spectromètre. Le premier essai d'alignement a résulté en une distance verticale entre les deux puces de 10 µm et une erreur horizontale de l'ordre de 20 µm. La fabrication et la caractérisation de spectromètres sur des substrats de saphir ont déjà commencé et donnent des caractéristiques courant-tension comparables à celles obtenues sur des substrats de silicium.

Une autre amélioration possible serait d'utiliser un matériau supraconducteur avec un gap plus grand pour atteindre des fréquences plus élevées. Avec des jonctions en niobium, 1.4 THz pourrait être atteint, contre 180 GHz avec des jonctions en aluminium. Cependant la fabrication est plus délicate car il faut former un sandwich Nb/Al/AlOx/Al/Nb pour avoir un bon oxyde. Ceci requiert un système à pulvérisation, plutôt qu'un évaporateur, à cause du caractère réfractaire du niobium. Cependant, des expériences sont en cours dans le groupe pour essayer d'obtenir des jonctions tunnels avec du niobium évaporé. Des jonctions Al/AlOx/Al/Nb ont ainsi déjà été fabriquées avec un gap supraconducteur plus grand que celui de l'aluminium mais plus petit que celui du niobium. La tension à laquelle la branche de quasiparticules commence ($2\Delta/e$) est de l'ordre de 800 µV, correspondant à une fréquence de 400 GHz.

Le groupe Φ_0 est aussi en train de travailler sur un autre dispositif capable de délivrer une tension continue précise à un milliardième près. Il repose sur la stabilité des pas de Shapiro apparaissant lors d'une irradiation par des micro-ondes. Brancher cette source haute-précision sur le spectromètre permettrait théoriquement une largeur de raie de l'ordre du kHz.

Le plus grand inconvénient du spectromètre développé dans cette thèse est que le signal mesuré dépend de la dissipation dans le système que l'on sonde. Être capable de détecter l'amplitude et surtout la phase du signal micro-onde réfléchi vers la jonction permettrait de sonder des systèmes dissipant moins et augmenterait donc la sensibilité du spectromètre. La possibilité de verrouiller la phase de jonctions Josephson à celle d'une source micro-onde cohérente pourrait contribuer au développement d'un tel analyseur de réseau vectoriel sur puce et large-bande.

Introduction

The Josephson effect, predicted in 1962 by Brian Josephson [1] and observed experimentally only one year later by Anderson and Rowell [2], is at the heart of various devices used today in biology [3–5], metrology [6], low noise measurements [7, 8], quantum information [9–16] and even astronomy [17, 18]. This thesis work focuses on the realization of a new tool for mesoscopic physics based on this effect, the Josephson spectrometer, designed for operating at frequencies up to the terahertz range. Commercial microwave equipment for the study of mesoscopic systems is not available above $50 - 80\,\mathrm{GHz}$. In addition, a calibration is needed to account for possible resonances in the measurements lines when using conventional spectrum or network analyzers. The proposed Josephson spectrometer is an on-chip device which can be located within a wavelength (some millimeters in the $100\,\mathrm{GHz}$ range) of the device under test and thus suppresses the need for calibration of the measurement lines.

It consists of a superconducting loop interrupted by two Josephson junctions and relies on the Josephson effect to convert a DC voltage V to microwave oscillations at a frequency proportional to V. The proportionality constant between both is a fundamental constant, the Josephson constant K_J, defined as the inverse of the magnetic flux quantum, $K_J = 1/\Phi_0 = 483.6\,\mathrm{MHz}\,\mu\mathrm{V}^{-1}$. Absorption of the emitted microwaves can be directly measured in the current-voltage characteristic of the Josephson junction as a current peak.

Using a Josephson junction to perform the spectroscopy of another system is not a totally new idea. Rapidly after the prediction of Josephson, an alternative high-frequency current was observed in tunnel junctions [19] and point contacts were used to detect millimeter and sub-millimeter radiations [20]. The idea of combining both emission and absorption to make a spectrometer was first implemented in 1967 by Silver and Zimmerman in an experiment [21] where they measured the nuclear magnetic resonance of Co^{59} at $218\,\mathrm{MHz}$ using niobium point-contacts.

This early spectrometer was however not followed by a large development of the technique. In the 1970s and the 1980s, this phenomenon of emission and re-absorption of photons by Josephson junctions was mainly used to explain current peaks in current-voltage characteristics of SQUIDs [22–25]. Some applications to the spectroscopy of mesoscopic systems were found: resonant modes of microresonators [26, 27] and transmission lines [28] were measured. Josephson junctions were also used to measure transitions between energy levels of another junction [29], a SQUID [30] or a single-Cooper-pair transistor [31].

More recently, absorption spectroscopy of Andreev Bound States in a superconducting atomic contact using a Josephson junction was demonstrated by the Quantronics group at Saclay [32, 33], paving the way for the development of a ready-to-use spectrometer. This device suffers however several drawbacks:

- Presence of spurious resonance peaks due to electromagnetic modes in the uncontrolled environment of the spectrometer

- Non-uniform coupling to the device under test over the frequency range of interest

This thesis aims at resolving these issues by improving the design of the existing spectrometer.

First, the general properties of Josephson junctions needed to understand the operation of the spectrometer are discussed. This includes a derivation of the Josephson effect and the ideal shape of the current-voltage characteristic of a junction. The dynamics of the two-junction device, the SQUID, used in the spectrometer is also described.

These properties are then applied to understand the principle of the spectrometer and the modification of the current-voltage characteristic in presence of a resonant mode. Different coupling schemes are presented, such as using a capacitor (as in Ref. [32]), coupling via two mutual inductors or directly connecting to the system of interest.

In a third part, a more comprehensive model of a Josephson junction is exhibited. It allows understanding the origin of most spurious resonance peaks as well as all undesired features which can be encountered when designing a Josephson junction.

Using these results, different designs for the spectrometer are experimentally implemented and discussed. The role of the biasing circuit appears to be of preponderate importance: the effect of adding on-chip resistors, inductors and capacitors is analyzed in details.

Consequently, fabricated spectrometers are used to measure the spectra of four simple systems over a wide frequency range: an LC resonator mode around 150 GHz, the excitation of quasiparticles in a superconductor above 90 GHz, the plasma frequency of a Josephson junction around 15 GHz and the plasma frequency of a RF-SQUID around 80 GHz.

Finally, some more complex and challenging targets for the spectrometer are presented. The most developed projects consist of probing Andreev Bound States in two close junctions, where they can hybridize, or in weak links based on InAs nanowires and on the topological insulator HgTe, in which the ABS spectrum is considerably modified by spin-orbit coupling. Another exciting direction is measuring non-avoided energy crossings in topological superconducting quantum circuits.

Introduction to Josephson junctions

The Josephson effect occurs at any weak electrical contact between two superconductors. They can be separated by an insulator, a normal metal, a semiconductor, or any other type of material. In that case, a non-dissipative current of Cooper pairs I_S (called supercurrent) can flow through the junction. It is the sign of the presence of phase coherence between the two superconductors and it is, in the most general case, a $2\pi-$periodic function of the phase difference,

$$\varphi = \varphi_2 - \varphi_1.$$

Furthermore, time-reversal symmetry imposes $I_S(-\varphi) = -I_S(\varphi)$ [34]. Combined with the $2\pi-$periodicity argument, this gives $I_S(n\pi) = 0$, $n \in \mathbb{Z}$. The supercurrent of a weak link can thus be written in the form

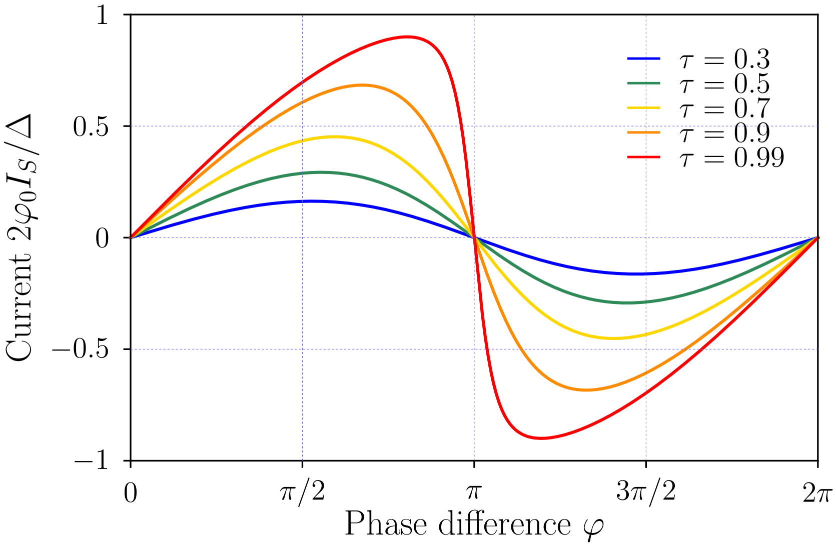

Figure (ii).1.: Supercurrent carried by a conduction channel for several transmission amplitudes.

$$I_S(\varphi) = \sum_{n=1}^{\infty} I_n \sin n\varphi. \tag{i'}$$

Such a current-phase relation is always limited by a maximal value I_0. It is the maximal non-dissipative current that the junction can withstand and is called the critical current. It is in general proportional to the surface area of the junction and decreases when its thickness is increased. In a mesoscopic theory of the Josephson effect, a short weak link (smaller than the superconducting coherence length) is modeled by a set of conduction channels of transmission τ_i, each hosting a pair of Andreev Bound States (ABS) [35]. The energies $E_\pm$ of these $|\pm\rangle$ states are given by

$$E_\pm(\varphi) = \pm\Delta\sqrt{1-\tau\sin^2\frac{\varphi}{2}}.$$

The supercurrent is then carried by the ground state, $|-\rangle$. It can be expressed as the derivative of the energy with respect to the phase, because phase and charge are conjugate. At zero temperature, this gives

$$I_S(\varphi) = \frac{1}{\varphi_0}\frac{\partial E_-}{\partial\varphi} = \frac{\Delta}{4\varphi_0}\frac{\tau\sin\varphi}{\sqrt{1-\tau\sin^2\frac{\varphi}{2}}}.$$

Noticing that $\sin^2\varphi/2$ is $2\pi-$periodic, it is possible to develop this expression in the form of Equation (i'), making a link between both theories.

Figure (ii).1 shows the shape of the supercurrent for several transmission amplitudes. As expected, it is zero at $\varphi = 0$, π and 2π and it is larger for larger transmissions. For low transmission, the supercurrent is close to a simple $\sin\varphi$ shape.

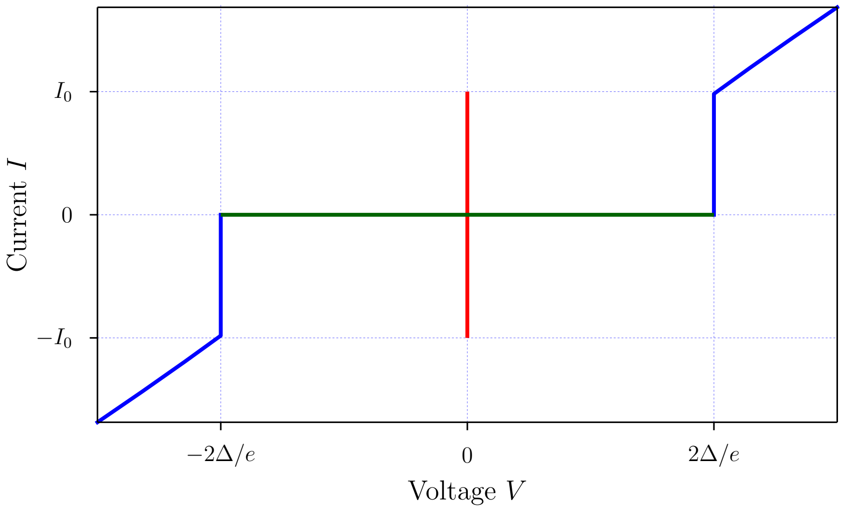

Figure (ii).2.: Ideal current-voltage characteristic of a tunnel Josephson junction.

In the following, we will mostly deal with low transmission junctions, called tunnel Josephson junctions. They have a simple current-phase relation,

$$I_S(\varphi) = I_0 \sin\varphi. \tag{ii'}$$

The Faraday's law of induction also provides a relation between the voltage across the junction and its phase difference. Its usual formulation is $V = \dot{\Phi}$, where V is the voltage across an inductor and Φ the magnetic flux threading it. For a superconducting inductance or a Josephson junction, the flux is proportional to the phase difference, $\Phi = \varphi_0\varphi$, such that the induced voltage is

$$V = \varphi_0\dot{\varphi}. \tag{iii'}$$

Equations (ii') and (iii') are often referred to as the DC and AC Josephson relations. Combined with the densities of states of the two superconductors, they allow calculating the shape of the current-voltage characteristic (shown in Figure (ii).2) of a tunnel Josephson junction:

- At zero voltage (in red), the phase difference is constant and a supercurrent (smaller than the critical current) flows.
- At a voltage $0 < |V| < 2\Delta/e$ (in green), the phase increases at a rate $\omega_J = |V|/\varphi_0$, resulting in current oscillations at a frequency of the order of 100 GHz (for $V = \Delta/e$ in the case of aluminum). In average, this makes a net zero current.
- At a voltage larger than $2\Delta/e$ (in blue), single quasiparticles of one superconductor can tunnel to the other one. The BCS singularity at the gap predicts a current step at $2\Delta/e$.

Principle of the Josephson spectrometer

In presence of an electromagnetic mode in the environment of the Josephson junction, its current-voltage characteristic is strongly modified. To explain this phenomenon, consider a

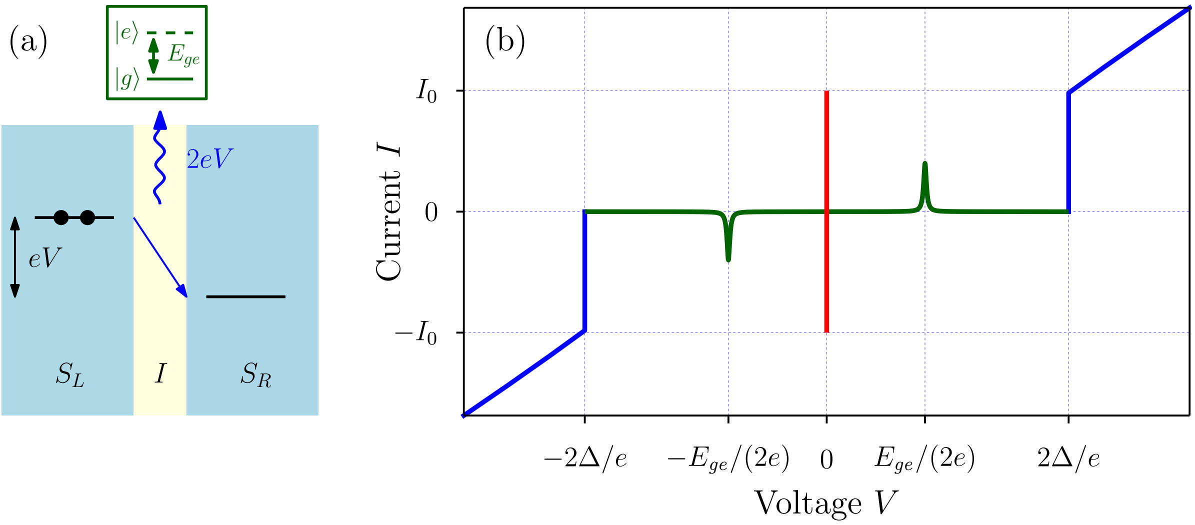

Figure (ii).3.: (a) Inelastic Cooper pair tunneling ; (b) Ideal current-voltage characteristic of a tunnel Josephson junction coupled to a two-level system.

simple two-level system with energy spacing E_{ge}. The current oscillations in the subgap region ($0 < |V| < 2\Delta/e$) can be understood in terms of the emission and re-absorption by the junction of virtual photons of energy $2e\,|V| = \hbar\omega_J$: a Cooper pair on the left-hand side superconductor S_L of Figure (ii).3(a) needs to emit an energy $2e\,|V|$ to tunnel to S_R. If the emitted photon is not resonant with the mode, it is reabsorbed by the Cooper pair which tunnels back to S_L. However, if $2e\,|V| = E_{ge}$, the photon can be absorbed by the electromagnetic mode, thus preventing the Cooper pair from tunneling back to S_L. This gives rise to a finite current through the junction, shown in panel (b) of Figure (ii).3. The height of the current peak is related to the dissipation in the mode and can thus be expressed in terms of the real part R_e of the impedance seen by the junction or equivalently of the rate of absorption Γ,

$$I\left(V\right) = \frac{R_e\left(\omega_J\right) I_0^2}{2V} = 2e\Gamma\left(\omega_J\right).$$

When $|V| > 2\Delta/e$, such peaks are less visible, as the contribution of the quasiparticles dominates over that of the Cooper pairs. For aluminum, this yields an upper limit of 180 GHz.

The principle of absorption spectroscopy using a Josephson junction was already demonstrated by the Quantronics group at Saclay [32,33]. But the spectrometer was too effective! In this experiment, it allowed not only probing the desired Andreev Bound States spectrum, but it also revealed many spurious resonances due to the uncontrolled electromagnetic environment and in particular to the biasing circuit.

In order to limit the coupling to these modes, a Superconducting QUantum Interference Device (SQUID) biased at half a flux quantum is used in place of a single Josephson junction as depicted in Figure (ii).4. The two junctions are symbolized by cross symbols in boxes and the inductors l model the inductance of the loop of the SQUID. The dashed lines leaving from the spectrometer are connected to the biasing circuit which closes the circuit.

In the SQUID loop, the applied flux is linked to the phase differences φ_1 and φ_2 of the

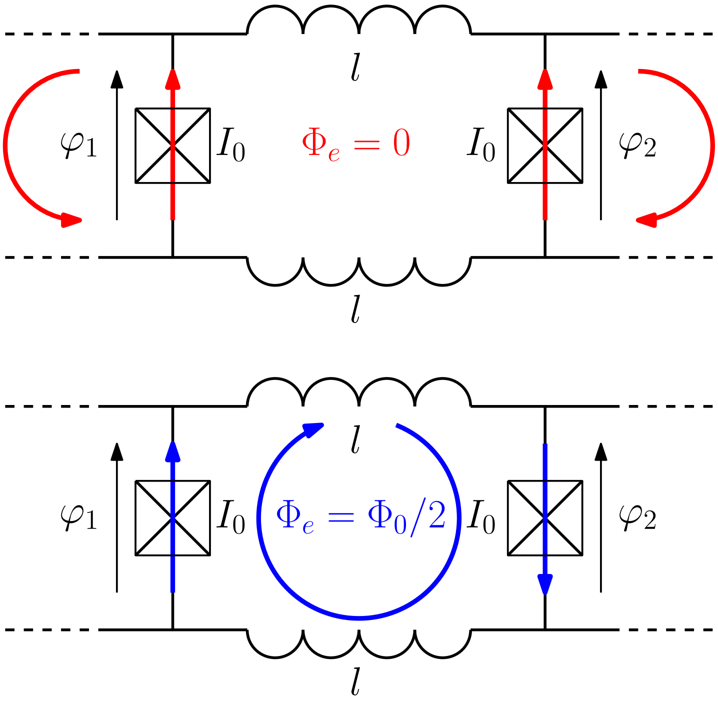

Figure (ii).4.: Electric diagram of a spectrometer based on a symmetrical SQUID at $\Phi_e = 0$ and $\Phi_0/2$.

junctions by $\Phi_e/\varphi_0 = \varphi_2 - \varphi_1$. When no flux is applied to the SQUID (top panel), the two junctions have the same phase difference, corresponding to microwave currents flowing in the same direction (represented by red arrows). They can only excite modes outside the loop. This device is in that sense equivalent to the single junction spectrometer of Ref. [32, 33].

When the SQUID is biased at half a flux quantum (bottom panel), the two microwave currents are dephased by π and, if the two junctions are identical, they cannot leave the loop. The undesired electromagnetic modes are thus not excited. However, there is a drawback to this configuration. There is an intrinsic LC mode due to the capacitance of the junctions and the inductance of the loop. For the symmetrical SQUID shown in Figure (ii).4, the LC mode is at the frequency $1/(2\pi\sqrt{lC_J})$, where C_J is the capacitance of each junction of the SQUID. For typical values of $l = 50\,\mathrm{pH}$ and $C_J = 50\,\mathrm{fF}$, this makes a frequency of 100 GHz which is in the operating range of the spectrometer. Using smaller junctions or smaller loops allows pushing this frequency out of the bandwidth of the spectrometer.

In this situation, the device under test (DUT) must be placed in the loop, where the probing current is maximal. Another possible location for the DUT is in a second loop, inductively coupled to the SQUID loop.

Design of the spectrometer

In practice, it is difficult to fabricate two junctions with a ratio of critical currents larger than 99% with the optical lithography setup available at Collège de France. This already allows for a large decoupling from the undesired environmental modes but the small amount of microwave current leaving the SQUID at half a flux quantum can excite them and make a noticeable difference in the current-voltage characteristic. It is thus crucial to carefully design the electromagnetic environment of the SQUID to shift the undesired resonance frequencies out of the bandwidth of the spectrometer or to damp these modes so that they do not appear in the spectrum. Several designs were implemented until a flat spectrum was measured, as summarized in Figure (ii).5.

The first design (top line of the table) consists of directly connecting the spectrometer to superconducting wires in order to take advantage of their high impedance at high frequency to decouple the spectrometer from the biasing circuit. The measured current-voltage characteristic exhibits several low-frequency resonances at $\Phi_e = 0$ (in red), which are partially suppressed at half a flux quantum (blue curve). They have now been identified as resonant modes of the microwave transmission line formed by the wire-bonds used to connect to the circuit.

Adding a large capacitor (central line of the table) allows shunting these modes but introduces resonances at higher frequencies, in particular one at $1/\sqrt{LC}$, typically of the order of $20-50\,\text{GHz}$. At half a flux quantum, some of them are still excited but the spectrum is already cleaner. The rise of the IV characteristic at $\Phi_e = \Phi_0/2$ at high frequencies corresponds to the excitation of the LC mode of the loop of the SQUID.

On-chip resistors are finally added to the design to damp the existing modes but also to cut all frequencies higher than $1/(RC)$. This cut-off frequency can easily be smaller than 500 MHz. The resulting current-voltage characteristic at $\Phi_e = 0$ only exhibits one large peak at 275 µV, now understood to be due to a too large design of the spectrometer, as well as a smaller and narrower peak around 150 GHz, possibly at a frequency $1/\sqrt{LC}$. Even with a low symmetry ratio[1] for the SQUID of only 0.75, the current-voltage characteristic is almost flat at $\Phi_e = \Phi_0/2$ and consists of only one single peak which culminates at 400 pA.

Josephson spectroscopy of four mesoscopic test systems

In order to verify that the spectrometer operates as expected, it was first tested on four simple benchmark systems covering a large part of its bandwidth ($2-180\,\text{GHz}$): an LC resonator mode around 150 GHz, the excitation of quasiparticles in a superconductor above 90 GHz, the plasma frequency of a Josephson junction around 15 GHz and the plasma frequency of a RF-SQUID around 80 GHz.

These four systems also allowed showing the operation of the spectrometer in different situations. The LC resonator mode, the excitation of quasiparticles and the plasma frequency of a Josephson junction were measured using a galvanic in-loop coupling scheme which is quite easy to implement but only if the system to probe can be fabricated in the loop of the spectrometer. The RF-SQUID was probed in a mutual coupling to an inductance shunting the junctions of the spectrometer. It proved the possibility of using such a coupling scheme, as well as independently controlling two magnetic fluxes. In this experiment, a linewidth of 550 MHz was measured.

---

[1] The symmetry ratio α of a SQUID is defined as the ratio between the critical currents of its two junctions. It is one for two identical junctions.

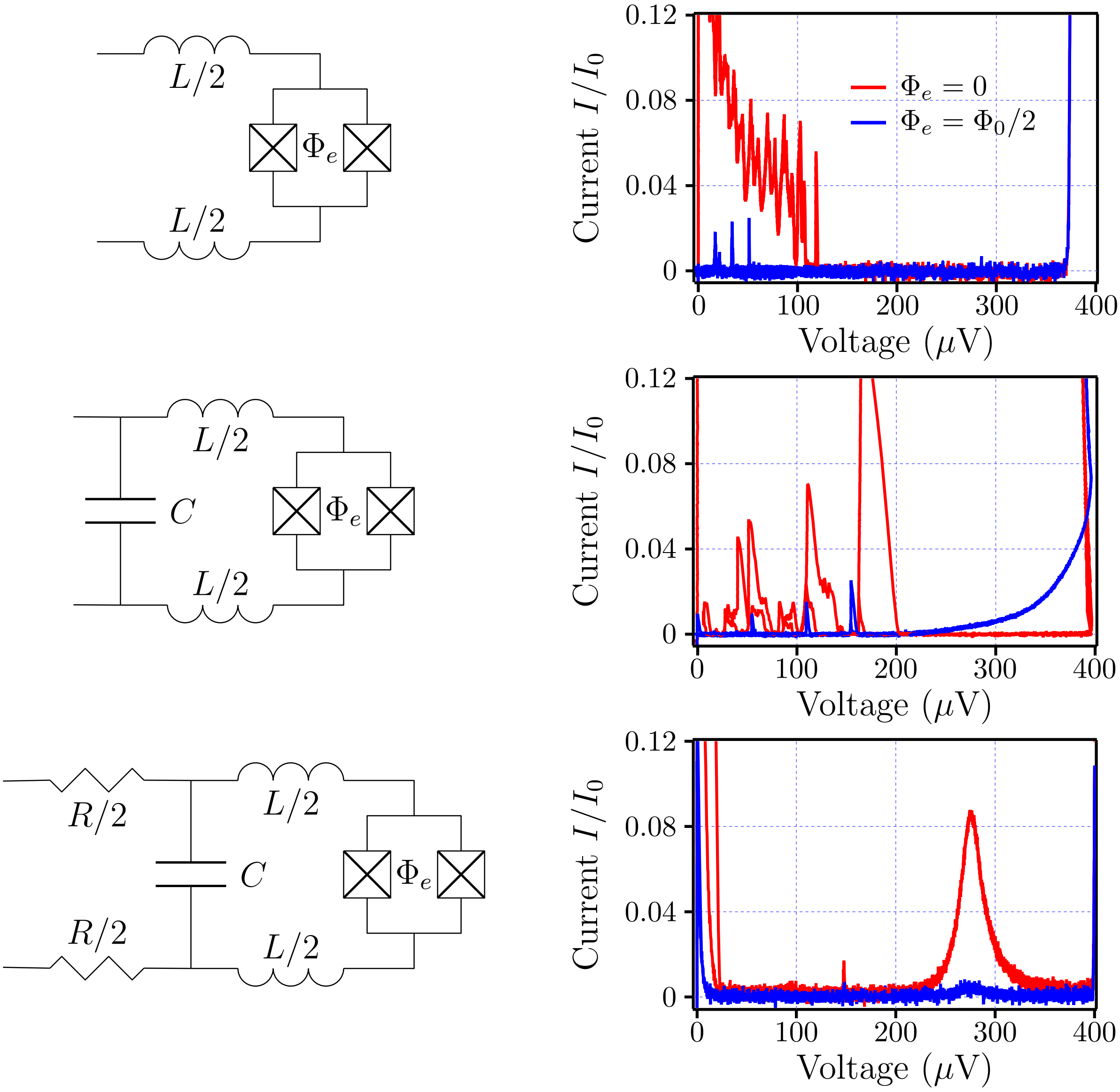

Figure (ii).5.: Table summarizing the tested designs.

Proposed targets for the spectrometer

This thesis goes beyond this proof of operation and presents more challenging targets for the spectrometer, on which experimental work is currently under progress. The most advanced projects are focused on probing the Andreev Bound States (ABS) in non-conventional types of weak links:

- Bringing two Josephson junctions close (closer than the superconducting coherence length) allows hybridizing their ABS and form an artificial molecule in which non-local supercurrents should be observed [36].
- The strong spin-orbit coupling in long semiconducting InAs nanowires lifts the spin degeneracy of the ABS even without applied magnetic field and can reveal interesting non-avoided energy crossings, similar to Weyl points [37, 38].
- Making Josephson junctions based on topological insulators permits to transform the usual $2\pi-$periodicity of the spectrum in an anomalous $4\pi-$periodicity due to non-trivial topological invariants [39].

The form of these modified ABS is presented, as well as estimates of the current that we would measure if we were to probe them with a Josephson spectrometer.

Other pertinent systems to be probed via Josephson spectroscopy are topological superconducting quantum circuits. They consist of electronic circuits including usual linear components such as capacitors and inductors, but also non-linear Josephson junctions. These non-dissipative devices can, in some cases, exhibit topologically protected crossings of energy levels, at the basis of quantized transport properties. Building such quantum circuits allows completely designing a Hamiltonian with as many parameters as wanted and have potential applications to quantum simulation of more complicated systems.

1. General properties of Josephson junctions

A Josephson tunnel junction consists of two superconductors weakly coupled by a thin insulating layer. The phenomenon of tunneling of Cooper pairs from one side to the other that occurs in such a junction was first predicted by Josephson in 1962 [1] and observed one year later by Anderson and Rowell [2].

In this chapter we will first derive the equations governing the dynamics of Josephson junctions using two quite different approaches: a macroscopic one in which the junction is seen as a barrier between two Cooper pair condensates and a microscopic one in which the junction is a scattering element for quasiparticles.

Next we will consider the junction as a non-linear circuit element and derive its ideal current-voltage characteristic in the limit of zero temperature.

Then we will turn to the interference effects occurring when two junctions are brought together in a superconducting loop, called a Superconducting QUantum Interference Device (SQUID).

Finally, we will describe the applications of Josephson junctions in physics and other scientific fields and show how challenging it can be to fully capture their complex behavior.

1.1. Derivation of the Josephson effect

1.1.1. Macroscopic approach

Consider two superconductors S_L and S_R separated by an insulating layer I as sketched in Figure 1.1. Both superconductors can be described by their macroscopic Ginzburg-Landau wavefunctions [40]

$$\psi_{L,R}(\vec{r},t) = \sqrt{n_{L,R}(\vec{r},t)}\mathrm{e}^{i\varphi_{L,R}(\vec{r},t)}. \tag{1.1}$$

They describe the fact that each superconductor is a condensate of Cooper pairs of density $n_{L,R}$ and phase $\varphi_{L,R}$.

If the insulating layer is thick (compared to the superconducting coherence length ξ), the two superconductors are completely decoupled and there is no leakage from one side to the other. If it is thinner, tunneling can occur between the two superconductors through the insulating barrier [41]. The Schrödinger equation for this system can be written

$$\begin{cases} i\hbar\dfrac{\partial\psi_L}{\partial t} = \mathcal{E}_L\psi_L - \mathcal{T}\psi_R, \\ i\hbar\dfrac{\partial\psi_R}{\partial t} = \mathcal{E}_R\psi_R - \mathcal{T}\psi_L, \end{cases} \tag{1.2}$$

where $\mathcal{T}$ is the tunneling amplitude of the junction which depends mainly on the thickness of the insulator. $\mathcal{E}_L$ and $\mathcal{E}_R$ are respectively the chemical potentials of the left and right

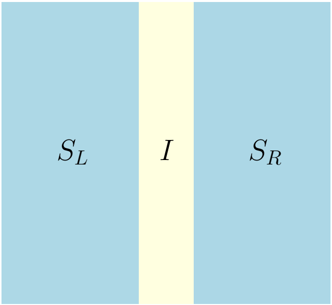

Figure 1.1.: A junction between two superconductors S_L and S_R.

superconductors. Applying a voltage V between the two superconductors allows tuning the difference $\mathcal{E}_L - \mathcal{E}_R = 2eV$[1]. Choosing the 0 of energy, such that $\mathcal{E}_L = eV$ and $\mathcal{E}_R = -eV$ allows rewriting Equations (1.2) as

$$\begin{cases} i\hbar\dfrac{\partial\psi_L}{\partial t} = eV\psi_L - \mathcal{T}\psi_R \\ i\hbar\dfrac{\partial\psi_R}{\partial t} = -eV\psi_R - \mathcal{T}\psi_L \end{cases} \tag{1.3}$$

Writing the wavefunctions in terms of density and phase, as in Equation (1.1) gives

$$\begin{cases} i\hbar\dfrac{\partial\sqrt{n_L}}{\partial t} - \hbar\sqrt{n_L}\dot{\varphi}_L - eV\sqrt{n_L} = -\mathcal{T}\sqrt{n_R}\mathrm{e}^{-i\varphi}, \\ i\hbar\dfrac{\partial\sqrt{n_R}}{\partial t} - \hbar\sqrt{n_R}\dot{\varphi}_R + eV\sqrt{n_R} = -\mathcal{T}\sqrt{n_L}\mathrm{e}^{i\varphi}, \end{cases} \tag{1.4}$$

where $\varphi = \varphi_L - \varphi_R$ is the phase difference across the junction. By taking the real and imaginary part of equations (1.4), we get four equations:

$$\begin{cases} \dot{\varphi}_L = \dfrac{eV}{\hbar} + \dfrac{\mathcal{T}}{\hbar}\sqrt{\dfrac{n_R}{n_L}}\cos\varphi, \\ \dot{\varphi}_R = -\dfrac{eV}{\hbar} + \dfrac{\mathcal{T}}{\hbar}\sqrt{\dfrac{n_L}{n_R}}\cos\varphi, \\ \dot{n}_L = 2\dfrac{\mathcal{T}}{\hbar}\sqrt{n_L n_R}\sin\varphi, \\ \dot{n}_R = -2\dfrac{\mathcal{T}}{\hbar}\sqrt{n_L n_R}\sin\varphi. \end{cases} \tag{1.5}$$

The last two equations show that $\dot{n}_L + \dot{n}_R = 0$. When Cooper pairs leave the L superconductor, they enter the R superconductor at the same rate and reciprocally. This can be understood as a current of amplitude $I = 2e\dot{n}_L$. It has for direct consequence that $n_L \to 0$ or $n_R \to 0$. In fact, due to the battery connected to L and R, n_L and n_R are kept constant at the same value n_0. By calling $I_0 = 4e\frac{\mathcal{T}}{\hbar}\sqrt{n_L n_R}$, we obtain the DC Josephson relation:

$$\boxed{I = I_0 \sin\varphi.} \tag{1.6}$$

---

[1] The factor 2 is here because the charge of a Cooper pair is $2e$.

The two other lines of Equation (1.5) show that

$$\dot{\varphi} = \frac{2e}{\hbar}V + \frac{\mathcal{T}}{\hbar}\frac{n_R - n_L}{\sqrt{n_L n_R}}\cos\varphi. \tag{1.7}$$

Because $n_L = n_R = n_0$, equation (1.7) can be written

$$\boxed{V = \varphi_0 \dot{\varphi}.} \tag{1.8}$$

This last equation is the AC Josephson relation and relates the phase difference to the voltage across the junction. The proportionality constant φ_0 is the reduced magnetic flux quantum and yields $\varphi_0 = 3.291059 \times 10^{-16}$ Wb.

The combination of the two Josephson relations show that there can be a current flowing between the two superconductors, even when no voltage is applied to the junction. Such a non-dissipative current is called a supercurrent and is the sign of the phase coherence between the two superconductors. A constant voltage V leads to oscillations of the current at frequency $\nu_J = 2eV/h$. The proportionality constant between frequency and voltage is $483.6\,\mathrm{MHz\,\mu V^{-1}}$.

1.1.2. Microscopic theory: Andreev Bound States

Another way of understanding the Josephson effect is with a mesoscopic point of view. The junction is considered as an assembly of independent conduction channels [42,43] of transmission τ_i. The total current flowing through the junction can then be expressed as the sum of the contribution of each channel:

$$I = \sum_i I(\tau_i).$$

The number of conduction channels in a tunnel junction can be estimated by the ratio of the surface of the junction to the area of a channel: $(\lambda_F/2)^2$, λ_F being the Fermi wavelength of the electrons. In a junction of $\sim 1\ \mu\mathrm{m}^2$ (which is the typical size of the junctions we will consider), there are $\sim 5 \times 10^6$ channels (considering a Fermi wavelength of 1 nm). In reality, the roughness of the surface reduces this figure by a factor of ~ 10.

To get the current flowing through the junction, we can calculate the current for each channel independently and then sum these individual channel currents. For each channel, we will consider the situation sketched in Figure 1.2. The junction is modeled by a δ function potential of amplitude V_0 at $x = 0$. The zero width of this model is enough as long as the barrier is thin compared to the superconducting coherence length. To the left and right are the superconductors S_L and S_R forming the junction.

Normal state scattering

Consider first the case where the two superconductors are normal metals and assume an electron is coming from the left-hand side of Figure 1.2 (in blue). The wavefunction of the electron is

$$\Psi(x) = \begin{cases} A\mathrm{e}^{ikx} + B\mathrm{e}^{-ikx} & \text{if} x < 0, \\ C\mathrm{e}^{ikx} & \text{if} x > 0, \end{cases} \tag{1.9}$$

where A, B and C are respectively the incident, reflected and transmitted amplitudes. At the interface, the continuity of the wavefunction and its derivative yield:

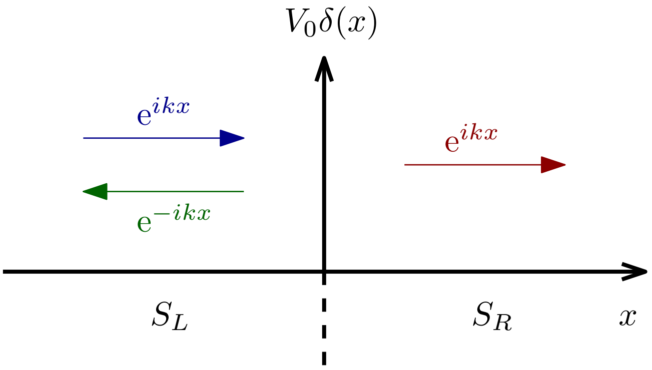

Figure 1.2.: A junction between two superconductors S_L and S_R with incoming plane wave on the left in blue, reflected wave in green and transmitted wave in red.

$$\begin{cases} \Psi(x=0^-) = \Psi(x=0^+), \\ -\frac{\hbar^2}{2m}\frac{d\Psi}{dx}(x=0^-) = -\frac{\hbar^2}{2m}\frac{d\Psi}{dx}(x=0^+) + V_0\Psi(x=0). \end{cases}$$

This gives two equations linking A, B and C

$$\begin{cases} A + B = C, \\ A - B = (1+2i\eta)C, \end{cases}$$

where $\eta = mV_0/(\hbar^2 k)$ describes the barrier. What we called earlier the transmission probability τ of the conducting channel is the absolute square of the ratio of the transmitted amplitude to the incoming amplitude and can be expressed as

$$\tau = \left|\frac{C}{A}\right|^2 = \frac{1}{1+\eta^2} \tag{1.10}$$

Superconducting case

For superconductors, another formalism is required to describe the scattering processes. In the BCS mean-field approximation [44], a complex coupling term $\Delta(x)$ at position x is introduced between spin-up annihilation operators $c_\uparrow(x)$ and spin-down creation operators $c_\downarrow^\dagger(x)$ in second quantization formalism. An adequate object to describe the situation is a spinor operator

$$\Psi(x) = \begin{pmatrix} c_\uparrow(x) \\ c_\downarrow^\dagger(x) \end{pmatrix}.$$

It can be understood as the annihilation field of a quasiparticle composed of a spin-up electron annihilation field and a spin-down hole annihilation field. This spinor obeys the Bogolioubov-de Gennes (BdG) Equation [44] linking the Schrödinger equations for electron-like and hole-like part of the wavefunction:

$$\begin{pmatrix} \mathcal{H}(x) & \Delta(x) \\ \Delta^*(x) & -\mathcal{H}^*(x) \end{pmatrix} \Psi(x) = E(x)\Psi(x) \tag{1.11}$$

where $\mathcal{H}(x) = -\frac{\hbar^2}{2m}\nabla^2 + V(x) - E_F$ is the single-particle Hamiltonian with a potential $V(x) = V_0\delta(x)$. E_F is the Fermi energy and $\Delta(x)$ is the pairing potential. If we consider S_L and S_R to be made of the same material, $\Delta(x)$ can be written as $\Delta(x) = \Delta \mathrm{e}^{i\varphi(x)}$ everywhere, except in the insulating barrier ($x = 0$) where it is 0. The order parameter phase φ is taken constant in each superconducting electrode. Call it φ_L in the left superconductor and φ_R in the right superconductor.

To solve the BdG equation in the case of a Josephson junction, we first must solve it independently in the left and the right superconductors and look for a solution $\Psi_k(x)$ as a plane wave as we did for normal metals:

$$\Psi_k(x) = \begin{pmatrix} a_k \\ b_k \end{pmatrix} \mathrm{e}^{ikx}.$$

For $x < 0$ or $x > 0$, the BdG Equation (1.11) can be rewritten

$$\begin{cases} \left(\dfrac{\hbar^2 k^2}{2m} - E_F\right) a_k + \Delta \mathrm{e}^{i\varphi(x)} b_k = E_k(x) a_k, \\ -\left(\dfrac{\hbar^2 k^2}{2m} - E_F\right) b_k + \Delta \mathrm{e}^{-i\varphi(x)} a_k = E_k(x) b_k. \end{cases}$$

This gives two sets of solution:

$$\begin{cases} E_k^+(x) = \sqrt{\xi_k^2 + \Delta^2}, \\ \Psi_k^+(x) = \begin{pmatrix} u_k \\ v_k \mathrm{e}^{-i\varphi(x)} \end{pmatrix} \mathrm{e}^{ikx}, \end{cases} \quad \text{or} \quad \begin{cases} E_k^-(x) = -\sqrt{\xi_k^2 + \Delta^2}, \\ \Psi_k^-(x) = \begin{pmatrix} v_k \mathrm{e}^{i\varphi(x)} \\ u_k \end{pmatrix} \mathrm{e}^{ikx}, \end{cases} \tag{1.12}$$

where $\xi_k = \frac{\hbar^2 k^2}{2m} - E_F$ is the kinetic energy referred to the Fermi energy and

$$\begin{cases} u_k = \sqrt{\dfrac{1}{2}\left(1 + \dfrac{\xi_k}{E_k}\right)}, \\ v_k = \sqrt{\dfrac{1}{2}\left(1 - \dfrac{\xi_k}{E_k}\right)}. \end{cases} \tag{1.13}$$

For a given energy E, the wavevector k can be expressed as

$$\frac{\hbar^2 k^2}{2m} = E_F \pm \sqrt{E^2 - \Delta^2},$$

$$k = \pm k_F \sqrt{1 \pm \frac{\sqrt{E^2 - \Delta^2}}{E_F}},$$

where k_F is the wavevector at the Fermi energy.

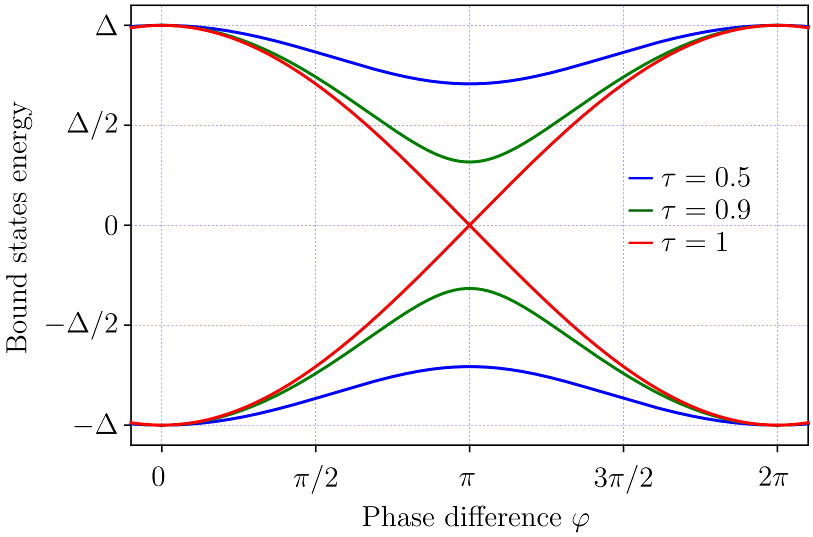

Figure 1.3.: Spectrum of the Andreev Bounds States for $\tau = 0.5$, $\tau = 0.9$ and $\tau = 1$.

If $E \geq \Delta$, $k \in \mathbb{R}$ and the states are purely propagating as was the case for normal metals.

When $E < \Delta$, $k \notin \mathbb{R}$ and another type of states is possible: evanescent waves. In that case, and when $\Delta \ll E_F$, k can be expressed as

$$k = k_F \pm i\kappa(E).$$

This Taylor expansion is called the Andreev approximation and

$$\kappa(E) = k_F \frac{\sqrt{\Delta^2 - E^2}}{2E_F} \ll k_F.$$

These states are bound to the junction and decay exponentially over a length $1/\kappa(E)$. It is possible to find the admissible energies $E_\pm$ for a given phase difference $\varphi = \varphi_L - \varphi_R$. This calculation is done in Appendix A and yields

$$E_\pm = \pm\Delta\sqrt{1 - \tau \sin^2 \frac{\varphi}{2}},$$

where τ is the transmission amplitude given by Equation (1.10). These energies are plotted in Figure 1.3 for several transmission probability values. When the transmission is small, the energy of the bound states stays close to the superconducting gap. The larger the transmission, the larger the modulation of the energy with the phase difference. For a transmission of 1, the energy even reaches 0 at a phase difference of π.

In the case of a tunnel junction, all $\tau_i \ll 1$, so the expression for the bound state energy reduces to $E_\pm \sim \pm\Delta\left(1 - \frac{\tau}{2}\sin^2\frac{\varphi}{2}\right)$

According to the derivation made in Appendix B, the current carried by an Andreev bound state $|\pm\rangle$ is

$$I_\pm = \frac{1}{\varphi_0}\frac{\partial E_\pm}{\partial \varphi}.$$

In the case of a low transmission channel, this gives

$$I_\pm = \mp\frac{1}{\varphi_0}\frac{\Delta}{4}\tau \sin\varphi.$$

The contribution of the channel i to the current through the junction is the sum of the positive and negative bound states currents weighted by the Fermi population of the states: $I_i = I_-\left(f_- - f_+\right)$.

$$I_i = \frac{1}{\varphi_0}\frac{\Delta}{4}\tau_i \sin\varphi \tanh\left(\frac{\Delta}{2k_BT}\right).$$

The total current flowing through the junction is then $I_J = \sum I_i$,

$$I_J = \frac{1}{\varphi_0}\frac{\Delta}{4}\sin\varphi \tanh\left(\frac{\Delta}{2k_BT}\right)\sum_i \tau_i.$$

Using Landauer's fundamental relation [42] for the conductance G of a channel of transmission τ, $G = \frac{2e^2}{h}\tau$, the total normal state resistance of the junction R_N can be expressed as $R_N = \left(2e^2/h\sum\tau_i\right)^{-1}$.

Using this relation, the Josephson current is given by

$$I_J = \frac{\pi\Delta}{2eR_N}\tanh\left(\frac{\Delta}{2k_BT}\right)\sin\varphi.$$

In the zero-temperature limit, we retrieve the DC Josephson relation derived earlier in Equation (1.6), $I = I_0\sin\varphi$, where I_0 is the critical current of the junction given by the Ambegaokar-Baratoff relation [45]:

$$\boxed{I_0 = \frac{\pi\Delta}{2eR_N}.} \tag{1.14}$$

Considering a uniform distribution of transmissions on the surface, the normal conductance $G_N = 1/R_N$ of the junction is proportional to its surface S. This results in the critical current I_0 also being proportional to S,

$$I_0 \propto S. \tag{1.15}$$

1.1.3. The Josephson potential energy

Intrinsic potential energy

Now that we derived the Josephson relations, consider the Josephson junction from an energetic point of view. The DC relation $I_J = I_0\sin\varphi$ describes the tunneling of Cooper pairs across the junction without any applied voltage. There is thus no dissipation in the junction. However, there can be energy stored in a junction. To calculate it, consider changing the phase difference from φ_1 at time t_1 to φ_2 at time t_2. The change in potential energy W during this process is:

$$W = \int_{t_1}^{t_2} I_J V dt. \tag{1.16}$$

Using the Josephson relations (1.6) and (1.8), we get

$$W = \varphi_0 I_0 \int_{\varphi_1}^{\varphi_2} \sin\varphi d\varphi = \varphi_0 I_0 \left(\cos\varphi_1 - \cos\varphi_2\right). \tag{1.17}$$

This energy W only depends on the initial and final states of the junction and therefore derives from a potential U. The potential which is 0 at zero phase difference is

$$\boxed{U\left(\varphi\right) = E_J\left(1 - \cos\varphi\right),} \tag{1.18}$$

where $E_J = \varphi_0 I_0$ is the Josephson energy of the junction.

Current-biased Josephson junction

When the junction is biased with an external current I_b, the total energy of the system consists of the potential energy (1.18) of the junction and the potential energy of the current source:

$$-\int_0^t I_b V dt = -\varphi_0 \int_0^{\varphi} I_b d\phi = -\varphi_0 \varphi I_b. \tag{1.19}$$

Introducing the reduced current $i_b = I_b/I_0$, the total potential energy of the circuit is thus

$$\boxed{U\left(\varphi\right) = E_J\left(1 - \cos\varphi - i_b\varphi\right).} \tag{1.20}$$

This potential energy (1.20) is often called the titled washboard potential due to its shape shown in Figure 1.4 for different bias currents.

The evolution of the current and voltage across the junction is equivalent to the classical movement of a fictitious "phase" particle (represented as a circle mark in Figure 1.4) in the tilted washboard potential. In the absence of fluctuations, if the bias current is smaller than I_0 (blue and green curves), the system will stay at a local minimum of the potential. The phase being constant, there is no voltage across the junction ($V = \varphi_0\dot{\varphi} = 0$). When I_b becomes larger than I_0 there is no local minimum in the potential and the particle will slide down acquiring a phase velocity and a voltage will develop across the junction.

In practice, a Josephson junction always has a parallel capacitance C. The junction consists of two metallic planes separated by an insulating layer of thickness t. If the junction has a surface S, its capacitance is approximately $C = \varepsilon S/l$, with ε the permittivity of the insulator.

The effect of the capacitance C has to be added to the total energy of the junction to better understand its behavior. When there is a voltage V across the junction, the capacitor stores an energy

$$K = \frac{CV^2}{2} = \frac{C\varphi_0^2}{2}\dot{\varphi}^2 = \frac{1}{2}E_J\omega_p^{-2}\dot{\varphi}^2, \tag{1.21}$$

where $\omega_p = \sqrt{\frac{I_0}{\varphi_0 C}}$ is the "plasma frequency" of the Josephson junction, the importance of which is emphasized later. One remarkable property of ω_p is that, as $I_0 \propto S$ and $C \propto S$, it

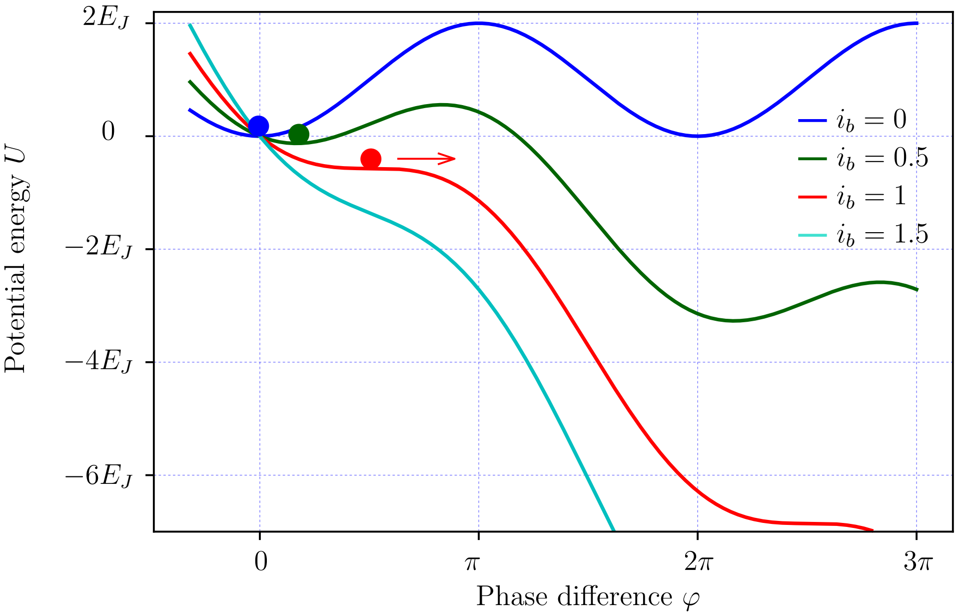

Figure 1.4.: The tilted washboard potential for bias currents from 0 to $1.5 I_0$.

pendulum	**Josephson junction**
angle θ	phase difference φ
mass m	capacitance C
applied torque T	bias current I_b
critical gravitational torque mgl	critical current I_0

Table 1.1.: Analogy between a pendulum and a Josephson junction.

is independent of the area of the junction. It only depends on the insulator permittivity and thickness. For the junctions we consider later, ω_p is typically around 15 GHz.

In the tilted washboard potential, the capacitive energy can be seen as a kinetic energy, as it is proportional to $\dot{\varphi}^2$. Adding a capacitance is analogous to adding inertia to the fictitious phase particle.

The total energy E of the circuit can be written as $E = U + K$.

$$E\left(\varphi, \dot{\varphi}\right) = E_J\left(1 - \cos\varphi - i_b\varphi\right) + \frac{1}{2}E_J\omega_p^{-2}\dot{\varphi}^2. \tag{1.22}$$

Note that the Equation (1.22) with $i_b = 0$ is the same as for a simple mechanical pendulum (sketched in Figure 1.5). The potential energy of such a pendulum of mass m and length l forming an angle θ with the vertical axis is $E_p = mgl\left(1 - \cos\theta\right)$ and its kinetic energy is given by $E_k = \frac{1}{2}ml^2\dot{\theta}^2$. The total energy is thus $mgl\left(1 - \cos\theta\right) + \frac{1}{2}ml^2\dot{\theta}^2$. The $i_b\varphi$ term can be seen as the work W of a constant torque T applied to the pendulum $W = T\theta$. The analogous terms are summarized in Table 1.1.

Consider now the behavior of the junction around an equilibrium phase φ_{eq} when the bias

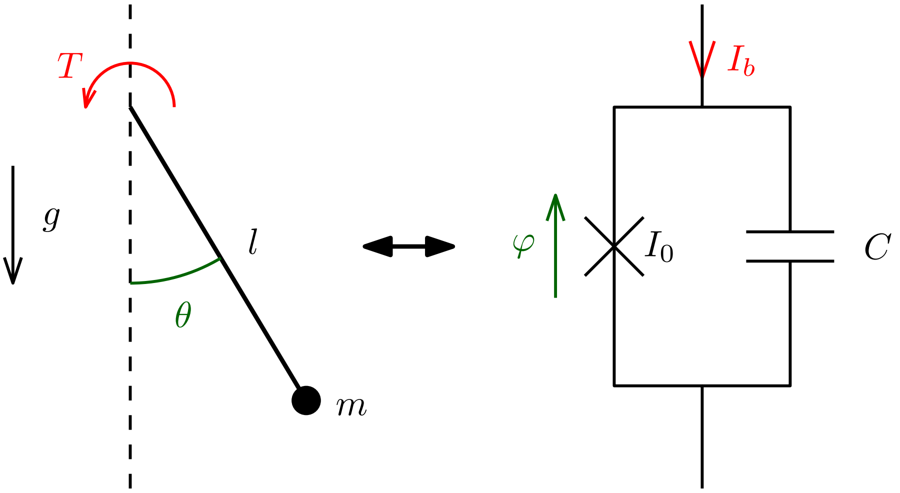

Figure 1.5.: The pendulum, a mechanical analogue of the Josephson junction.

current is smaller than the critical current of the junction (minimum of the potential in Figure 1.4). φ_{eq} is defined as $\frac{\partial E}{\partial \varphi}\left(\varphi_{eq}, \dot{\varphi}\right) = 0$, i.e. $\sin \varphi_{eq} = i_b$. Around $\varphi = \varphi_{eq}$, the energy can be written as:

$$E\left(\varphi_{eq} + \delta\varphi, \dot{\varphi}\right) - E\left(\varphi_{eq}, 0\right) = \frac{\mu}{2}\dot{\varphi}^2 + \frac{k}{2}\left(\delta\varphi\right)^2, \tag{1.23}$$

where $\mu = E_J \omega_p^{-2}$ and $k = E_J \cos \varphi_{eq}$. Equation (1.23) is the energy of a harmonic oscillator of mass μ and spring constant k. The frequency of the oscillations around an equilibrium position is $\omega_0 = \sqrt{\frac{k}{\mu}}$.

$$\omega_0 = \omega_p \left(1 - i_b^2\right)^{1/4}. \tag{1.24}$$

When $i_b = 0$, the frequency of the oscillations is the plasma frequency ω_p of the junction. These oscillations are therefore called plasma oscillations and can be understood as oscillations of the charge from one side of the junction to the other as is the case in plasma oscillations of a bulk metal.

1.1.4. Tunneling Hamiltonian of a Josephson junction

The Josephson junction is intrinsically a quantum object, as the DC and AC Josephson effects consist of tunneling of particles through a barrier. However, we can ignore quantum fluctuations and describe the dynamics classically, considering that the phase φ across the junction and the current I flowing through it are classical variable, as we did in Section 1.1.3. But when the temperature is sufficiently low compared to the zero-point energy of quantum fluctuations ($k_B T < \hbar\omega_0$, where $\hbar\omega_0$ is the zero-point energy), we cannot neglect the quantum nature of these variables.

To derive a Hamiltonian for a junction, we need first to calculate the Lagrangian $\mathcal{L}$, following the method of Ref. [46] to quantize electromagnetic circuits. The potential energy of a

Josephson junction is $U = -E_J \cos\varphi$ (as derived in Equation (1.18)[2]) and its kinetic energy is $K = CV^2/2$. Using the AC Josephson relation (1.8), the Lagrangian $\mathcal{L}$ is

$$\mathcal{L}(\varphi, \dot{\varphi}) = K(\varphi, \dot{\varphi}) - U(\varphi, \dot{\varphi}) = \frac{C\varphi_0^2}{2}\dot{\varphi}^2 + E_J \cos\varphi. \tag{1.25}$$

The momentum conjugate to the phase difference φ can be expressed as $q_\varphi = \frac{\partial \mathcal{L}}{\partial \dot{\varphi}}$. This gives

$$q_\varphi = C\varphi_0^2 \dot{\varphi}. \tag{1.26}$$

Using again the AC Josephson Equation (1.8), it becomes

$$q_\varphi = \varphi_0 CV = \varphi_0 Q, \tag{1.27}$$

where Q is the charge accumulated across the capacitance. The classical Hamiltonian $\mathcal{H}$ of the Josephson junction is thus

$$\mathcal{H}(\varphi, Q) = K + U = \frac{Q^2}{2C} - E_J \cos\varphi. \tag{1.28}$$

In this Hamiltonian framework, the quantization is easily performed, just by replacing the classical variables φ and Q by quantum operators $\hat{\varphi}$ and $\hat{Q}$. The fact that φ and Q are Lagrangian conjugate gives the commutation relation $\left[\hat{\varphi}, \hat{Q}\right] = i\hbar\{\varphi, Q\} = i\hbar\varphi_0 = 2ie$, where $\{\ ,\ \}$ denotes the classical Poisson bracket. The quantum Hamiltonian $\hat{\mathcal{H}}$ of the junction is therefore

$$\hat{\mathcal{H}}\left(\hat{\varphi}, \hat{Q}\right) = \frac{\hat{Q}^2}{2C} - E_J \cos\hat{\varphi}. \tag{1.29}$$

To work with dimensionless variables, we introduce the charge energy $E_C = \frac{2e^2}{C}$ and the Cooper pairs number operator $\hat{N}$ defined as $\hat{Q} = 2e\hat{N}$. It corresponds to the number of transferred Cooper pairs. The Hamiltonian now becomes

$$\boxed{\hat{\mathcal{H}}\left(\hat{\varphi}, \hat{N}\right) = E_C \hat{N}^2 - E_J \cos\hat{\varphi},} \tag{1.30}$$

with commutation relation $\left[\hat{\varphi}, \hat{N}\right] = i$.

It is possible to find the eigenstates and eigenenergies of this Hamiltonian in the general case using Mathieu functions [47] but it is more instructive to start looking at the two particular limits of large Josephson energy $E_J \gg E_C$ and large Coulomb energy $E_C \gg E_J$.

Large Josephson energy

In the case where $E_J \gg E_C$, tunneling through the barrier occurs easily and $\hat{N}$ is not a good quantum operator to describe the situation, as $\left|\left\langle \hat{N}^2 \right\rangle - \left\langle \hat{N} \right\rangle^2\right| \gg 1$. On the contrary,

---

[2] The origin of energy is here chosen differently as in Equation (1.18). This is the reason for the absence of the constant E_J term.

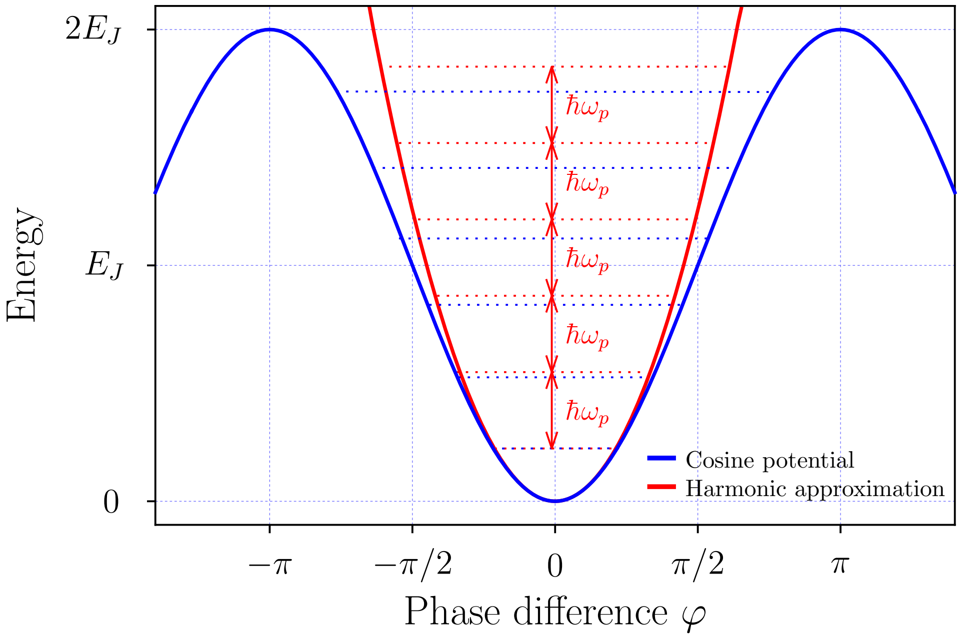

Figure 1.6.: Schematic of the energy levels for a Josephson junction in the limit $E_J \gg E_C$.

the phase operator satisfies $\left\langle\hat{\varphi}^2\right\rangle \ll 1$. So, $\cos\hat{\varphi}$ can be approximated by $1-\frac{\hat{\varphi}^2}{2}$ and the Hamiltonian of Equation (1.30) is reduced to that of a harmonic oscillator,

$$\hat{\mathcal{H}}\left(\hat{\varphi},\hat{N}\right) = E_C\hat{N}^2 + E_J\frac{\hat{\varphi}^2}{2}. \tag{1.31}$$

Its eigenvalues are just $E_n = \hbar\omega_p\left(n+\frac{1}{2}\right)$ where n is a positive integer and $\hbar\omega_p = \sqrt{2E_CE_J}$ is the plasma frequency of the Josephson junction.

Figure 1.6 shows the cosine potential of a Josephson junction in thick blue lines, as well as the harmonic approximation in red. The energy levels of both are also plotted in dashed lines. At low energies, the approximation is good. But at higher energies, the actual cosine potential is wider than the parabolic one, resulting in closer energy levels.

Large Coulomb energy

In that case, operator $\hat{N}$ is best suited to express the Hamiltonian. Recalling that $\left[\hat{\varphi},\hat{N}\right] = i$, it is possible to express $\mathrm{e}^{i\hat{\varphi}}$ and thus $\cos\hat{\varphi} = \frac{1}{2}\left(\mathrm{e}^{i\hat{\varphi}} + \mathrm{e}^{-i\hat{\varphi}}\right)$ in the charge $\left(|M\rangle\langle N|\right)_{(M,N)}$ basis.

The operator $\mathrm{e}^{i\hat{\varphi}}$ can be explained as an operator transforming $|N\rangle$ in $|N+1\rangle$. To understand this, consider the case of the usual position $\hat{x}$ and impulsion $\hat{p}$ operators. The operator $\mathrm{e}^{i\hat{p}a/\hbar}$, where a is a distance, is the translation operator $\hat{T}_a$, such that $\hat{T}_a|x\rangle = |x+a\rangle$. Here, the commutator $[\hat{x},\hat{p}] = i\hbar$ is replaced by $\left[\hat{\varphi},\hat{N}\right] = i$. Thus, $\mathrm{e}^{i\hat{\varphi}}|N\rangle = |N+1\rangle$ and

$$\mathrm{e}^{\pm i\hat{\varphi}} = \sum_{N=-\infty}^{+\infty} |N \pm 1\rangle \langle N|.$$

The Hamiltonian (1.30) can therefore be written

$$\hat{\mathcal{H}}\left(\hat{\varphi}, \hat{N}\right) = \sum_{N=-\infty}^{+\infty} E_C N^2 |N\rangle \langle N| - \frac{E_J}{2} \left(|N+1\rangle \langle N| + |N-1\rangle \langle N|\right). \tag{1.32}$$

This gives in matrix form, with N from $-\infty$ to $+\infty$,

$$\hat{\mathcal{H}} = \begin{pmatrix} \ddots & \ddots & 0 & 0 & 0 \\ \ddots & E_C(N-1)^2 & -E_J/2 & 0 & 0 \\ 0 & -E_J/2 & E_C N^2 & -E_J/2 & 0 \\ 0 & 0 & -E_J/2 & E_C(N+1)^2 & \ddots \\ 0 & 0 & 0 & \ddots & \ddots \end{pmatrix}. \tag{1.33}$$

The lowest energy levels are close to $|-1\rangle$, $|0\rangle$ and $|1\rangle$ as the tunneling terms $-E_J/2$ are much smaller than the diagonal matrix elements of the order of E_C and the Hamiltonian can reduce to

$$\hat{\mathcal{H}} = \begin{pmatrix} E_C & -E_J/2 & 0 \\ -E_J/2 & 0 & -E_J/2 \\ 0 & -E_J/2 & E_C \end{pmatrix}. \tag{1.34}$$

It is easy to find the eigenstates and eigenenergies of this Hamiltonian as it is a 3×3 matrix. The eigenenergies are $-E_J^2/(2E_C)$, E_C and $E_C + E_J^2/(2E_C)$, which tend to 0 and E_C when E_J goes to 0.

General case

Recalling that $\hat{N}$ and $\hat{\varphi}$ are conjugate quantum variables, the operator $\hat{N}$ acts in phase space as a derivative:

$$\hat{N} = \frac{1}{i}\frac{\partial}{\partial\varphi}.$$

The time-independent Schrödinger equation for the Hamiltonian of the junction can thus be written (in phase space)

$$-E_C \Psi''(\varphi) + \left(-E_J \cos\varphi - E\right)\Psi(\varphi) = 0, \tag{1.35}$$

where $\Psi(\varphi)$ is the wavefunction in phase space of the eigenstate with eigenenergy E. This differential equation is the Mathieu Equation [47]: $y'' + (a - 2q\cos x)\, y = 0$ with $a = 4E/E_C$, $q = -2E_J/E_C$ and $x = \varphi/2$.

The solutions of the Mathieu equation are the Mathieu cosines (C subscript) and sines (S subscript) $M_{C,S}(a, q, x)$ which are tabulated functions. Because the wavefunction $\Psi(\varphi)$ has to be $2\pi-$periodic, we are only interested in the periodic Mathieu functions. Only those for which

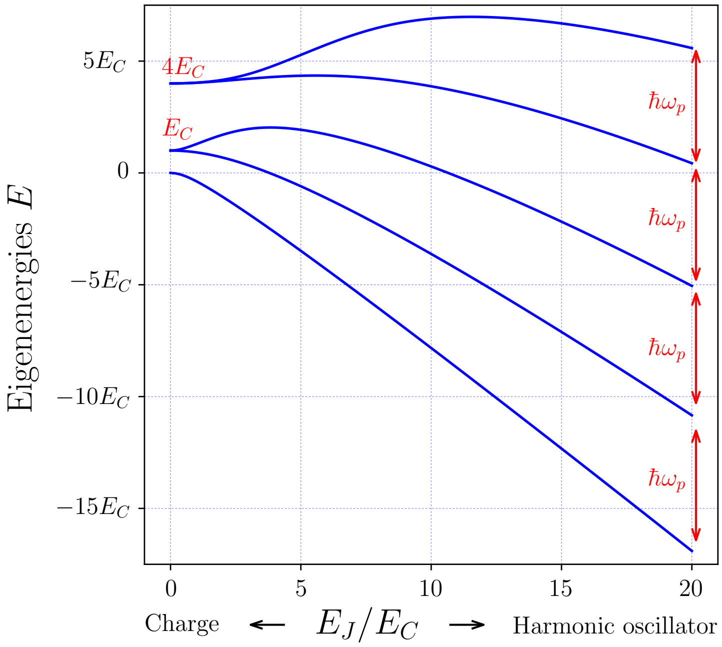

Figure 1.7.: The 5 first energy levels for a Josephson junction with arbitrary E_J/E_C ratio.

the parameter a is a Mathieu characteristic value are periodic. Half of them are $\pi-$periodic and the other half is $2\pi-$periodic in the variable $x = \varphi/2$. So, we need only consider the π-periodic Mathieu functions.

Figure 1.7 shows the first allowed energies with appropriate periodicity. The limits of large Coulomb and large Josephson energy can be seen for $E_J/E_C \to 0$ and $E_J/E_C \to \infty$. In the limit $E_J \ll E_C$, the eigenenergies tend to $E_C n^2$ with n integer, as seen just above. In this limit, the levels are degenerate because the $|-n\rangle$ and $|n\rangle$ states have the same energy. In the opposite limit $E_J \gg E_C$, the eigenenergies tend to be uniformly spaced as in the case of the harmonic oscillator.

1.2. The current-voltage characteristic

Now that we have derived the basic equations governing the dynamics of a Josephson junction, let us focus on the shape of the ideal current-voltage characteristic of a Josephson junction of critical current I_0 and consider it as a circuit element.

The electric schematic of a Josephson junction is represented in Figure 1.8. The cross symbol in the left-hand side part symbolizes a junction without capacitance, where the current I, voltage V and phase difference φ obey

$$\begin{cases} I = I_0 \sin\varphi, \\ V = \varphi_0 \dot{\varphi}. \end{cases} \tag{1.36}$$

The box with a cross inside in the right-hand part of the figure symbolizes a Josephson

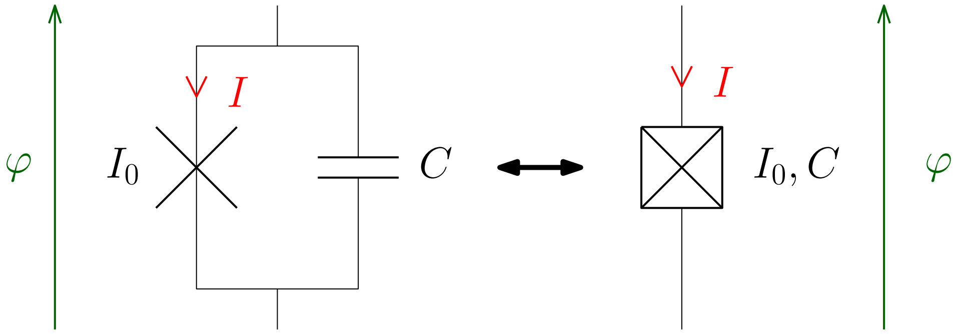

Figure 1.8.: Electric schematic for a single Josephson junction of critical current I_0 and intrinsic capacitance C.

junction, taking its intrinsic capacitance into account. Equation (1.36) is modified to

$$\begin{cases} I = I_0 \sin\varphi + C\varphi_0\ddot{\varphi}, \\ V = \varphi_0\dot{\varphi}. \end{cases} \tag{1.37}$$

This model is often called the CSJ (Capacitively Shunted Junction) model. A more refined model also contains a shunt resistance R in parallel with the junction and the capacitance: the RCSJ (Resistively and Capacitively Shunted Junction) model. The R in this model accounts for losses in the conduction channels at finite voltage and is usually high in tunnel junctions.

1.2.1. The zero-voltage state

For a Josephson junction biased at a current I_b, in the tilted washboard model plotted in Figure 1.4, as long as $|I_b| < I_0$, there is no voltage drop across the junction. This part of the current-voltage characteristic is called the supercurrent peak, as the current flowing through the junction is dissipationless. In the RCSJ model, as the voltage drop is constant and equals 0, there is no current flowing in the shunt resistance nor in the shunt capacitance.

On this branch, the DC Josephson relation, $I_J = I_0 \sin\varphi$, is reminiscent of the current-flux relation for an inductance L: $I_L = \varphi_0\varphi/L$, except that it is not linear. To better understand this, consider the Taylor expansion about I,

$$I + \delta I = I_0 \sin\left(\varphi + \delta\varphi\right).$$

The change in current is

$$\delta I = I_0 \delta\varphi \cos\varphi. \tag{1.38}$$

Comparing Equation (1.38) to the similar expression for a standard inductance ($I = \varphi_0\varphi/L$) gives an expression for the non-linear Josephson inductance L_S,

$$L_S = \frac{\varphi_0}{I_0\cos\varphi} = \frac{L_J}{\cos\varphi}, \tag{1.39}$$

where $L_J = \varphi_0/I_0$ is the Josephson inductance. The inductance L_S of a Josephson junction differs from a standard linear inductance as it diverges when $\varphi \to \pi/2$ and can even be negative

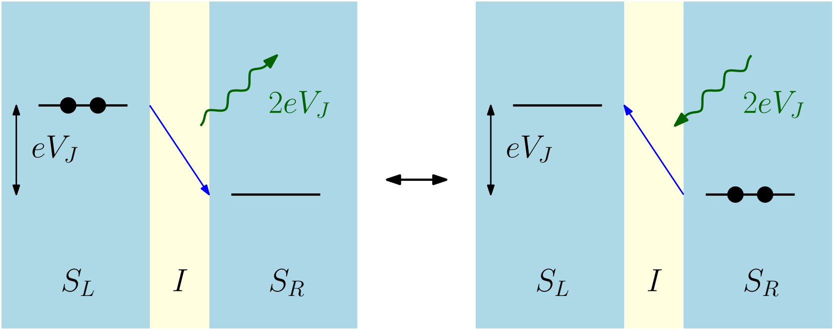

Figure 1.9.: Energy levels of the Cooper pairs condensates of two superconductors forming a Josephson junction when the applied voltage is below $2\Delta/e$.

for $\pi/2 < \varphi < 3\pi/2$. Physically, however, the junction is not equivalent to an inductor. When a supercurrent flows, no magnetic field is generated.

Note that with this definition of L_J, it is possible to write the plasma frequency of a Josephson junction as $\omega_p = (L_J C)^{-1/2}$ and understand the plasma oscillations as occurring in a LC resonator circuit made of the Josephson inductance and the capacitance of the junction. The characteristic impedance Z_J of this circuit, called the Josephson impedance, is

$$Z_J = \sqrt{\frac{L_J}{C}} = \sqrt{\frac{\varphi_0}{I_0 C}}.$$

1.2.2. The subgap region

Consider a Josephson junction biased at a voltage V_J. As represented in Figure 1.9, no Cooper pair can tunnel from one side to the other since there are no states available at the same energy level. The only way for a Cooper pair to tunnel through the junction is to emit the energy $2e\,|V_J|$, as there are two electrons in a Cooper pair. If a photon is emitted this way, it is reflected by the capacitance of the junction and is absorbed again. The Cooper pair that tunneled from one side to the other tunnels back to its original side. This corresponds to an average zero DC current flowing through the junction.

Implicitly, the electromagnetic environment is limited to the junction capacitance. In reality, the situation is more complicated. For instance, if we include a simple bias circuit, such as the one shown in Figure 1.10, the voltage across the junction is not V but $V_J = V - R_b I_J$.

Using the Norton equivalent of the right-hand side of the figure, it appears that the parallel R_s resistance of the RCSJ model can be taken into account by changing the bias resistance R_b in the parallel combination of R_b and R_s, called R in the following. A Josephson junction biased with a current source of amplitude I is also described by this circuit, with $R = R_s$.

Using the Josephson relations, the Kirchhoff's law can be rewritten

$$\frac{V}{R_b I_0} = \sin\varphi + \frac{\varphi_0}{R I_0}\dot{\varphi} + \frac{C\varphi_0}{I_0}\ddot{\varphi}. \tag{1.40}$$

To have a better understanding of this equation, we introduce the time constant $\tau = \varphi_0/(R I_0)$,

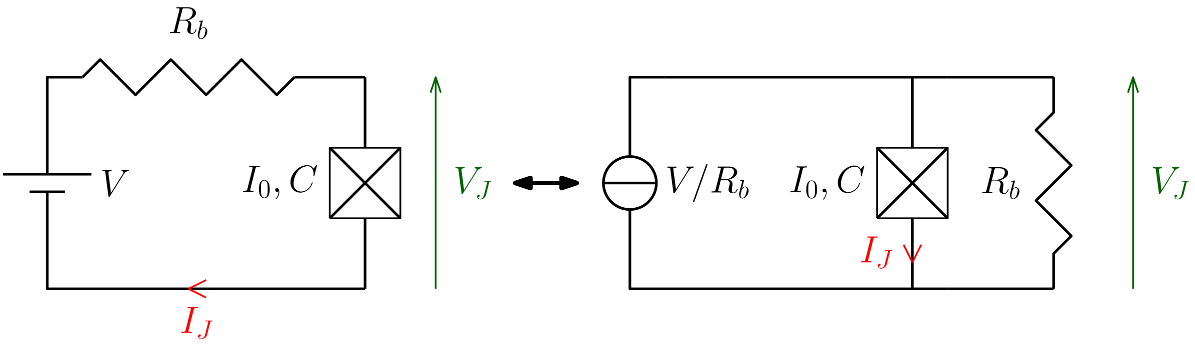

Figure 1.10.: Electric schematic of a Josephson junction biased via a resistance.

the reduced voltage $v = V/(R_b I_0)$ and the plasma frequency $\omega_p = \sqrt{I_0/(\varphi_0 C)}$. With these notations, Equation (1.40) can be written

$$v = \sin\varphi + \tau\dot{\varphi} + \omega_p^{-2}\ddot{\varphi}. \tag{1.41}$$

This non-linear second order differential equation cannot be solved analytically. It is the same problem as in Section 1.1.3 of a particle in the tilted washboard potential of Equation (1.22) with a viscous force $\tau\dot{\varphi}$ accounting for dissipation. In order to understand the behavior of the junction, it is instructive to rewrite this equation as a function of the reduced time $\tilde{t} = t/\tau$. Differentiation with respect to $\tilde{t}$ is denoted by a prime symbol,

$$v = \sin\varphi + \varphi' + \beta_C\varphi'', \tag{1.42}$$

where β_C is the Stewart-McCumber parameter introduced by W.C. Stewart [48] and D.E. McCumber [49] in 1968,

$$\beta_C = \frac{R^2 I_0 C}{\varphi_0} = (\omega_p\tau)^2 = \frac{R^2}{Z_J^2}. \tag{1.43}$$

This parameter quantifies the damping of the junction by the resistance R. It is the square of the quality factor of the RLC resonator circuit made of the Josephson inductance, the capacitance of the junction and the resistance R. A large β_C parameter corresponds to a high quality factor and thus a low damping. It is therefore called the underdamped limit. In this case, the phase particle slides down the potential with almost no friction. The opposite overdamped limit ($\beta_C \ll 1$) corresponds to a particle slowed down effectively in the potential and easily trapped in potential wells.

To find conditions under which Equation (1.41) can be solved, we write the phase difference $\varphi(t)$ in the form

$$\varphi(t) = \varphi^{(0)} + \omega_J t + \sum_{n>0} a_n \sin(n\omega_J t + \varphi_n), \tag{1.44}$$

where $\omega_J = V/\varphi_0$. This form comes from the fact that a voltage across the junction induces a linear phase increase and thus current oscillations. They can in turn induce voltage oscillations due to the capacitance of the junction and the biasing circuit acting as a linear impedance. Substituting this expression for φ in Equation (1.41) gives

$$\begin{aligned} v = {} & \sin\left(\varphi^{(0)} + \omega_J t + \sum_{n>0} a_n \sin\left(n\omega_J t + \varphi_n\right)\right) \\ & + \tau\omega_J + \sum_{n>0} a_n n\omega_J \tau \cos\left(n\omega_J t + \varphi_n\right) - \sum_{n>0} a_n \left(n\frac{\omega_J}{\omega_p}\right)^2 \sin\left(n\omega_J t + \varphi_n\right). \end{aligned} \tag{1.45}$$

The first term can be expanded in Fourier series to give components at all harmonics of ω_J:

$$\sin\left(\varphi^{(0)} + \omega_J t + \sum_{n>0} a_n \sin\left(n\omega_J t + \varphi_n\right)\right) = \tilde{a}_0 + \sum_{n>0} \tilde{a}_n \sin\left(n\omega_J t + \tilde{\varphi}_n\right).$$

The exact derivation of the $\tilde{a}_n$ and $\tilde{\varphi}_n$ coefficients involves products of sums of Bessel functions and is not performed here. One important remark on these coefficients is that the $\tilde{a}_n$ are of order 1 or smaller because the sine function in the left-hand side of the above equation is smaller than 1 (in absolute value).

In Equation (1.45), the term oscillating at frequency $n\omega_J$ satisfies

$$\tilde{a}_n \sin\left(n\omega_J t + \tilde{\varphi}_n\right) + a_n n\omega_J \tau \cos\left(n\omega_J t + \varphi_n\right) - a_n \left(n\frac{\omega_J}{\omega_p}\right)^2 \sin\left(n\omega_J t + \varphi_n\right) = 0.$$

If there is a n_0 for which $n_0\omega_J \gg \omega_p$ or $n_0\omega_J \gg 1/\tau$, the first term can be neglected. This results in all the a_n coefficients with $n \geq n_0$ being 0. If in addition $n_0 = 1$, all a_n are 0 and the phase difference is just given by

$$\varphi = \varphi^{(0)} + \omega_J t.$$

This limit is called the high-frequency limit and can be expressed

$$\omega_J \gg \min\left(\omega_p, 1/\tau\right). \tag{1.46}$$

As $\beta_C = \left(\omega_p \tau\right)^{-2}$, this condition is different for underdamped and overdamped junctions. In underdamped junctions, it is $\omega_J \gg \omega_p$, while in overdamped junctions, it is $\omega_J \gg 1/\tau$.

Underdamped junction

In the case of a tunnel junction, the underdamped limit is almost always achieved as the shunt resistance of the junction is large for good tunnel junctions. Typical shunt resistance values are $10\,\mathrm{M\Omega}$ for junctions with $I_0 = 100\,\mathrm{nA}$ and $C = 150\,\mathrm{fF}$. This gives $\beta_C \sim 5 \times 10^7 \gg 1$. The high-frequency limit of Equation 1.46 is reached as soon as $\omega_J \gg \omega_p \sim 15\,\mathrm{GHz}$. φ is thus given by

$$\varphi = \varphi^{(0)} + \omega_J t.$$

The resulting current is purely sinusoidal at frequency ω_J and results in an averaged current of 0.

A more physical interpretation of this averaged zero current is that the capacitance has a low impedance at frequencies higher than ω_p and shunts effectively the oscillating part of the junction current: $\sin\varphi + \omega_p^{-2}\ddot{\varphi} \sim 0$. This results in an almost constant voltage across the junction and thus a phase increasing linearly with time: $\varphi = \varphi^{(0)} + \omega_J t$.

Overdamped junction

In the case of a junction with a small bias resistance, the quality factor is low and Equation (1.42) reduces to

$$v = \sin\varphi + \varphi'. \tag{1.47}$$

This differential equation has an analytical solution (calculated by integration in Appendix C) for bias current larger than the critical current ($v > 1$):

$$\varphi = 2\arctan\left(\sqrt{1-\frac{1}{v^2}}\tan\left(\frac{\sqrt{v^2-1}}{2}\tilde{t} - \arctan\left(\frac{1}{\sqrt{v^2-1}}\right)\right) + \frac{1}{v}\right) + 2n\pi.$$

The $2n\pi$ in this expression accounts for the fact that the phase of the junction is continuous and does not jump from π to $-\pi$ when the argument of the arctan function reaches ∞, that is to say when the argument of the tan reaches $(2k+1)\,\pi/2$. n is the integer such that:

$$n = \left\lfloor \frac{\frac{\sqrt{v^2-1}}{2}\tilde{t} - \arctan\left(\frac{1}{\sqrt{v^2-1}}\right) + \frac{\pi}{2}}{\pi} \right\rfloor.$$

From this expression for the phase, the current flowing through the junction and the voltage across it can readily be calculated using the Josephson relations: $I_J = I_0 \sin\varphi$ and $V_J = \varphi_0\dot{\varphi} = RI_0\varphi'$.

φ, I_J and V_J are plotted in the top panel of Figure 1.11 for bias voltages $1.1RI_0$, $2RI_0$ and $10RI_0$. The bias resistance R is $0.1R_N$. For small bias voltage (blue curves), the current and voltage oscillations are highly non-sinusoidal, resulting in a finite average current. When the bias gets larger, the phase tends to a linear shape and the current becomes sinusoidal with an average value of zero. The average values of current and voltage are plotted in dashed lines in the figure.

The frequency $\omega = 2\pi/T$ of the current and voltage oscillations depends on the voltage as $\omega = \sqrt{v^2-1}/\tau$. This frequency can be expressed as a function of the Josephson frequency $\omega_J = V/\varphi_0$,

$$\omega = \omega_J\sqrt{1-\frac{1}{(\omega_J\tau)^2}} = \omega_J\sqrt{1-\left(\frac{RI_0}{V}\right)^2}.$$

At large voltage, this oscillation frequency tends to the Josephson frequency. This behavior was expected, as this corresponds to the high-frequency limit expressed in Equation (1.46).

Using the Josephson relation linking voltage and phase, it is straightforward to compute the average voltage:

$$\begin{aligned}
\langle V_J\rangle &= \frac{1}{T}\int_0^T \varphi_0\dot{\varphi}dt,\\
\langle V_J\rangle &= \frac{RI_0\sqrt{v^2-1}}{2\pi}\varphi(T),\\
\langle V_J\rangle &= \sqrt{V^2-(RI_0)^2}.
\end{aligned}$$

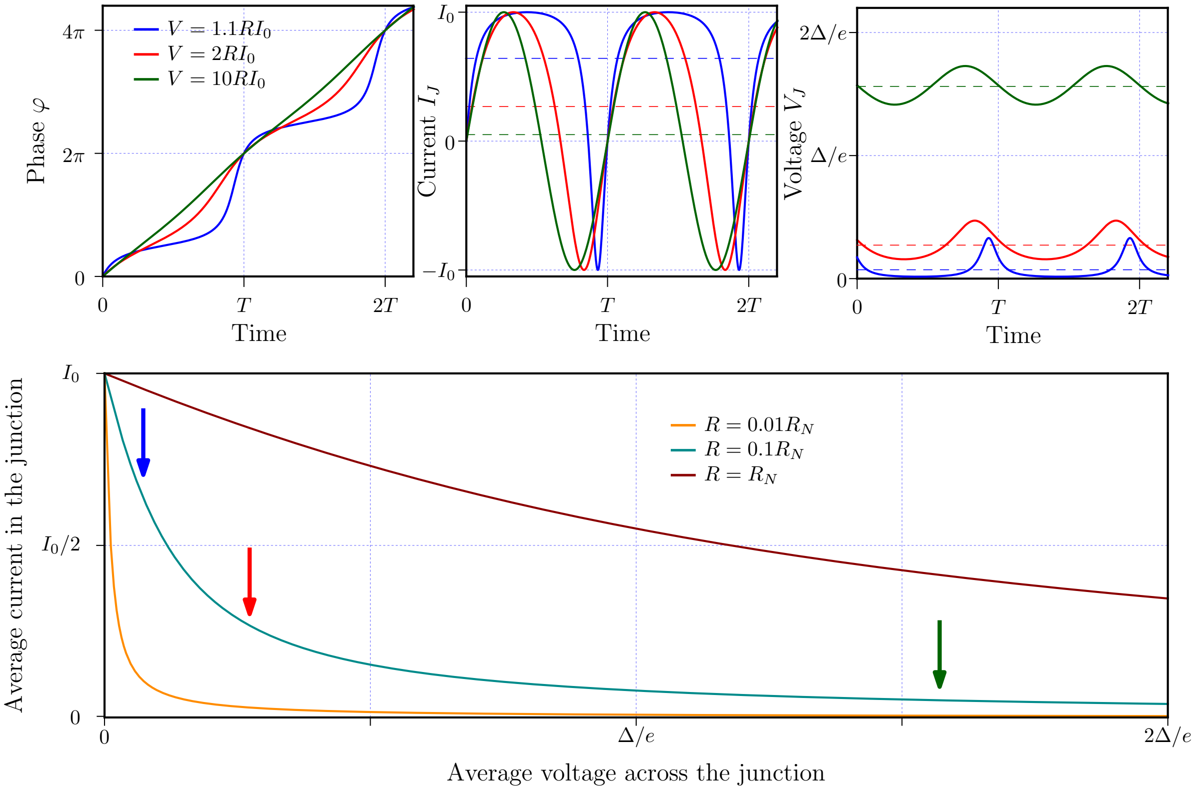

Figure 1.11.: Top graphs: evolution of the phase, current and voltage of a Josephson junction biased in series with a resistance $R = 0.1R_N$. For the current and voltage, the dashed lines correspond to the average value. Bottom graph: averaged current-voltage of a junction for three different bias resistances.

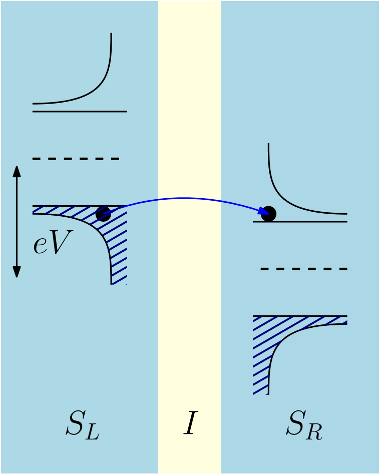

Figure 1.12.: The density of states for the two superconductors forming a Josephson junction when applied voltage is above $2\Delta/e$.

The average current is then obtained from the Kirchhoff law, $V = R\langle I_J\rangle + \langle V_J\rangle$,

$$\frac{\langle I_J\rangle}{I_0} = \sqrt{1 + \left(\frac{\langle V_J\rangle}{RI_0}\right)^2} - \frac{\langle V_J\rangle}{RI_0}. \tag{1.48}$$

This expression shows a universal shape for the averaged current-voltage characteristic when the voltage is normalized to RI_0. However, in the bottom panel of Figure 1.11, the voltage is not expressed in terms of RI_0 but in terms of Δ/e, resulting in different curves.

1.2.3. The quasiparticle branch

When the bias voltage becomes larger than $2\Delta/e$ there is also a possibility for quasiparticles to tunnel through the insulating barrier as shown in Figure 1.12. For $V \gg 2\Delta/e$, the density of states is the same as for a normal metal and the junction acts as a normal resistance, $I_J = V_J/R_N$, where R_N is the normal state resistance of the junction, which is related to the supercurrent via Equation (1.14).

For $V \gtrsim 2\Delta/e$, the exact shape of the current-voltage characteristic can be calculated using Fermi's golden rule for the tunneling rate, $I_{qp}(V) = e\Gamma$, where

$$\begin{aligned}\Gamma = \frac{2\pi}{\hbar}\bigg(&\int_{-\infty}^{+\infty} n_S(E+eV)\, n_S(E)\, f(E)\,(1-f(E+eV))\,dE \\ &- \int_{-\infty}^{+\infty} n_S(E)\, n_S(E+eV)\, f(E+eV)\,(1-f(E))\,dE\bigg),\end{aligned} \tag{1.49}$$

$$\Gamma = \frac{2\pi}{\hbar}\int_{-\infty}^{+\infty} n_S(E+eV)\, n_S(E)\,(f(E) - f(E+eV))\,dE, \tag{1.50}$$

and $n_S(E)$ is the superconducting density of states and $f(E)$ is the Fermi function describing the thermal occupation of the levels. In the BCS theory, $n_S(E) = n_N \frac{|E|}{\sqrt{E^2-\Delta^2}}$ for $|E| > \Delta$ with n_N the normal state density of states. n_N is related to the normal resistance R_N via the same integral as (1.50) but for normal densities of states:

$$I_N = e\frac{2\pi}{\hbar}\int_0^{eV} n_N^2 dE = \frac{2\pi}{\hbar}e^2 n_N^2 V = \frac{V}{R_N} \tag{1.51}$$

In the limit of $T = 0$, Equation (1.50) gives

$$\Gamma = \frac{1}{e^2 R_N}\int_{\Delta-eV}^{-\Delta} \frac{|E|}{\sqrt{E^2-\Delta^2}} \frac{|E+eV|}{\sqrt{(E+eV)^2-\Delta^2}} dE. \tag{1.52}$$

The integral (1.52) can be written in terms of elliptic integrals [50],

$$I_N(V) = \begin{cases} 0 & \text{if } |eV| \leq 2\Delta, \\ \dfrac{V}{R_N}\left(E(x) - 2\left|\dfrac{\Delta}{eV}\right|^2 K(x)\right) & \text{if } |eV| > 2\Delta, \end{cases} \tag{1.53}$$

where functions K and E are complete elliptic integrals of the first and second kind of argument $x = \sqrt{1 - \left|\frac{2\Delta}{eV}\right|^2}$,

$$\begin{cases} K(x) = \displaystyle\int_0^{\frac{\pi}{2}} \frac{1}{\sqrt{1-x^2\sin^2\theta}} d\theta, \\ E(x) = \displaystyle\int_0^{\frac{\pi}{2}} \sqrt{1-x^2\sin^2\theta} d\theta. \end{cases}$$

The shape of $I_N(V)$ is plotted in Figure 1.13a in blue.

1.2.4. Ideal zero-temperature current-voltage characteristic

The calculations made in Sections 1.2.1, 1.2.2 and 1.2.3 give the shape plotted in Figure 1.13a for the ideal current-voltage characteristic of an underdamped (for which the high-frequency condition is always satisfied) Josephson junction of critical current I_0 at zero temperature. The red branch corresponds to the supercurrent discussed in Section 1.2.1, the green branch is the subgap region explained in Section 1.2.2 and the blue branch is the quasiparticle branch of Section 1.2.3. At high voltage, the I-V characteristic tends to the straight line of equation $I = V/R_N$ plotted in dashed line.

Figure 1.13b shows an experimental current-voltage characteristic. It is similar to the theoretical one except for some details:

- The region for $|V| < 50\,\mu\text{V}$ does not have $I = 0$. This is due to an unstable biasing circuit as discussed in Chapter 3.

- There is a feature around ±300 µV which will be explained in Chapter 2 and is the core of the spectrometer operation.

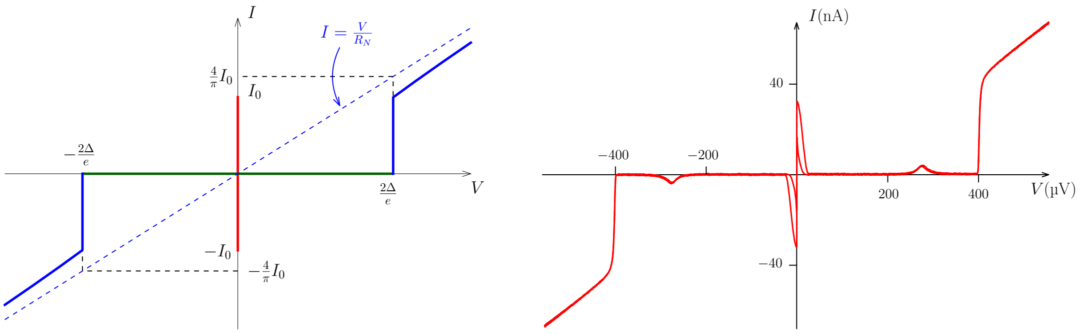

(a) Theoretical IV characteristic.

(b) Experimental IV characteristic.

Figure 1.13.: The ideal current-voltage characteristic for a Josephson junction and an experimental characteristic.

- The rounding of the quasiparticle branch at $2\Delta/e$ is due to the density of states not being exactly the BCS one.

1.3. The Superconducting QUantum Interference Device (SQUID)

As seen with the DC Josephson Equation (1.6), the current flowing through a junction depends on the phase difference across the junction. A good way of controlling the phase difference across a Josephson junction is to make a superconducting loop. In addition, if we want to apply a voltage, we need a loop with two junctions.

1.3.1. Critical current and loop current

Consider a superconducting loop interrupted by two Josephson junctions JJ_1 and JJ_2 of critical current I_{01} and I_{02} as sketched in Figure 1.14 and consider injecting a current I_b. The phase difference across junction 1 is φ_1 and the phase difference across 2 is φ_2. The superconductor forming the loop can be modeled as an inductor and divided into two parts L_1 and L_2 corresponding to the metal of the side of junction 1 and 2 respectively. A perpendicular magnetic field $\vec{B}_e = \vec{\nabla} \times \vec{A}_e$ can be applied to the loop.

The phase difference acquired around the loop is

$$\delta = \varphi_1 + \frac{1}{\varphi_0} L_1 I_1 - \frac{1}{\varphi_0} L_2 I_2 - \varphi_2 + \frac{1}{\varphi_0} \int_{loop} \vec{A}_e \cdot \vec{dl}. \tag{1.54}$$

The integral $\int_{loop} \vec{A}_e \cdot \vec{dl}$ is the magnetic flux $\Phi_e = B_e S$ threading the loop of surface S. It can be decomposed in two parts:

$$\int_{loop} \vec{A}_e \cdot \vec{dl} = \int_{left} \vec{A}_e \cdot \vec{dl} + \int_{right} \vec{A}_e \cdot \vec{dl} \tag{1.55}$$

If we consider the trajectory of a Cooper pair injected from the top of Figure 1.14, the first integral (labeled *left*) corresponds to the phase acquired after the traveling through the left

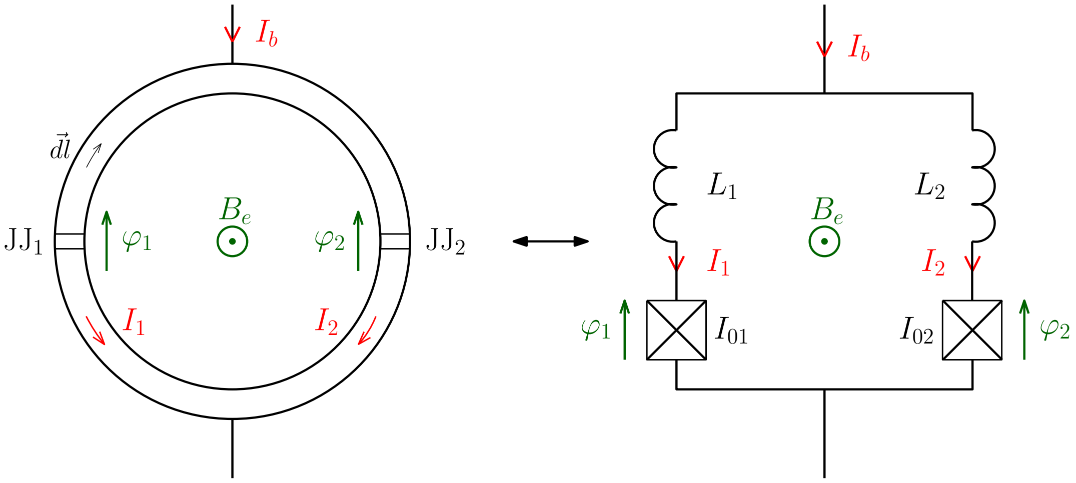

Figure 1.14.: Schematics of a superconducting loop interrupted by two Josephson junctions.

branch of the loop and the second integral is the phase acquired through the right branch. The sum of both can therefore be considered as an interference term between these two paths. This is the reason why this superconducting loop interrupted by two Josephson junctions is called a Superconducting QUantum Interference Device (SQUID).

The total phase difference δ of Equation (1.54) must be equal to 0 (or to a multiple of 2π) to satisfy the uniqueness of the wavefunction in the superconductor,

$$\varphi_2 - \varphi_1 = \frac{L_1}{\varphi_0} I_1 - \frac{L_2}{\varphi_0} I_2 + \frac{\Phi_e}{\varphi_0} \quad (2\pi) \tag{1.56}$$

Negligible loop inductance

If we neglect the inductance of the loop, $L_1 I_{01}, L_2 I_{02} \ll \varphi_0$. For typical junctions of critical current $I_0 \sim 500\,\mathrm{nA}$, this gives $L_{1,2} \ll 650\,\mathrm{pH}$. Because $\mu_0 \sim 1\,\mathrm{pH\,\mu m^{-1}}$, such an inductance corresponds to a loop perimeter of 650 µm which is quite large compared to typical perimeters of 50 µm considered in this thesis.

In this limit, Equation (1.56) can be rewritten

$$\varphi_2 - \varphi_1 = \frac{\Phi_e}{\varphi_0} \quad (2\pi). \tag{1.57}$$

This shows that the external magnetic flux directly gives the difference in phase drops across the junctions.

The total current I_b flowing through the SQUID is $I_b = I_1 + I_2 = I_{01} \sin \varphi_1 + I_{02} \sin \varphi_2$. If we denote φ_e the reduced flux such that $\varphi_e = \Phi_e / \varphi_0 \; (2\pi)$ with $0 \leq \varphi_e < 2\pi$, we obtain $I_b = I_{01} \sin \varphi_1 + I_{02} \sin(\varphi_1 + \varphi_e)$. Using a trigonometric identity,

$$I_b = I_0 \sin(\varphi_1 + \varphi), \tag{1.58}$$

where I_0 and φ are defined by:

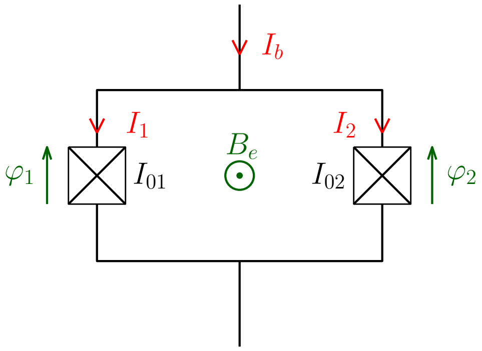

Figure 1.15.: Schematics of a SQUID with no inductance.

$$\begin{cases} I_0^2 = I_{01}^2 + I_{02}^2 + 2I_{01}I_{02}\cos\varphi_e, \\ \tan\varphi = \dfrac{I_{02}\sin\varphi_e}{I_{01} + I_{02}\cos\varphi_e}. \end{cases} \tag{1.59}$$

Equation (1.58) shows that a SQUID acts as a Josephson junction with tunable critical current. Its maximal value is $I_{01} + I_{02}$ and is reached for an external flux of $\Phi_e = 0\ (\Phi_0)$. The minimal critical current is $|I_{01} - I_{02}|$ and is reached for $\Phi_e = \Phi_0/2\ (\Phi_0)$. When the SQUID is biased at $\Phi_e = \Phi_0/2\ (\Phi_0)$, there is also a current circulating in the loop of maximal magnitude $I_{01} + I_{02}$ to impose the phase equality of Equation (1.57).

The amplitude of the maximal current I_0 is directly given by Equation (1.59). To get the maximal amplitude of the loop current I_L, we have to do the same reasoning as with I_b. The current flowing in the loop is $|I_1 - I_2| = |I_{01}\sin\varphi_1 - I_{02}\sin(\varphi_1 + \varphi_e)|$. Noticing that $-I_{02}\sin(\varphi_1 + \varphi_e) = I_{02}\sin(\varphi_1 + \varphi_e + \pi)$, we can see that $I_L(\varphi_e)$ is just $I_0(\varphi_e + \pi)$.

The critical current and maximal loop current are plotted in Figure 1.16 for three ratios of $\alpha = I_{02}/I_{01}$. It is possible to cancel the critical current only when the two junctions are exactly identical ($\alpha = 1$, blue curves in the figure).

In practice, it is impossible to make two identical junctions and obtain $\alpha = 1$. Typical values are of the order of 98%.

Larger loop inductance

When the inductance of the loop is not negligible, the phase drops across the inductance, so the phase difference of the junctions is not directly proportional to the external magnetic flux and it is not possible to derive the dependence of $I_0(\varphi_e)$ in the same way as before. If we introduce two parameters $\beta_1 = L_1 I_{01}/\varphi_0$ and $\beta_2 = L_2 I_{02}/\varphi_0$, the ratios of the loop inductance to the Josephson inductance, Equation (1.56) can be rewritten,

$$\varphi_2 - \varphi_1 = \beta_1 \sin\varphi_1 - \beta_2 \sin\varphi_2 + \varphi_e, \tag{1.60}$$

where φ_e is again the reduced flux taken between 0 and 2π.

The total potential energy U of the SQUID is made of three terms:

- the Josephson potential: $-\varphi_0 I_{0i}\cos\varphi_i$ for junctions $i = 1$ and 2,

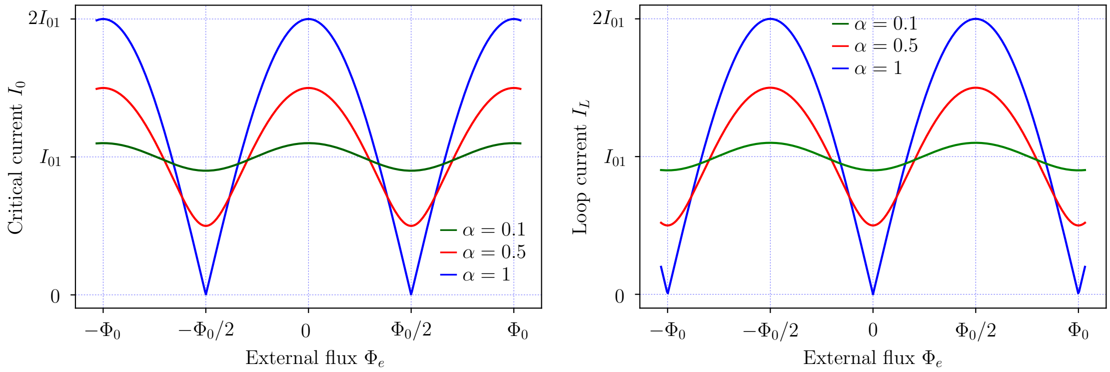

(a) Critical current of the SQUID.

(b) Maximal loop current.

Figure 1.16.: Critical current and maximal loop current in a SQUID for $\alpha = I_{02}/I_{01}$ ratios of $0.1, 0.5$ and 1.

- the inductive energy: $\frac{1}{2}L_iI_i^2 = \frac{1}{2}L_iI_{0i}^2\sin^2\varphi_i = \frac{\varphi_0}{2}\beta_iI_{0i}\sin^2\varphi_i$,
- the work of the external current: $-\int_0^t I_eV\,dt = -\frac{\varphi_0}{2}I_e\left(\int_0^{\varphi_1}d\phi + \int_0^{\varphi_2}d\phi\right)$.

$$\frac{U}{\varphi_0} = -I_{01}\cos\varphi_1 - I_{02}\cos\varphi_2 + \frac{1}{2}\left(\beta_1I_{01}\sin^2\varphi_1 + \beta_2I_{02}\sin^2\varphi_2\right) - I_e\frac{\varphi_1+\varphi_2}{2}. \tag{1.61}$$

To get the values of φ_1 and φ_2 for every applied flux Φ_e and extract the $I_0(\Phi_e)$ dependence, one way is to solve numerically for φ_2 as a function of φ_1 in Equation (1.60), inject this value in the potential U and find a stable minimum of $U(\varphi_1)$.

For a symmetrical SQUID ($L_1 = L_2 \equiv L$ and $I_{01} = I_{02} \equiv I_c$), the $I_0(\Phi_e)$ dependence is plotted in Figure 1.17. The β_L parameter is $\beta_L = \beta_1 = \beta_2$. The effect of the inductance is to reduce the accessible values of the phase differences of the junctions. The larger the inductance, the larger the phase drop across the inductance and the smaller the phase difference across the junctions. The inductance also makes the system bistable: for $\beta_L \neq 0$, there are flux values for which two critical currents are possible for the SQUID.

As for the SQUID with negligible inductance, the reduction of the critical current corresponds to the creation of a current circulating in the loop.

More details about the critical current of a SQUID with non-negligible loop inductance and different critical currents can be found in Ref. [51] and Ref. [52].

1.3.2. Plasma frequency control

In a SQUID, not only can the critical current and loop current be controlled by an external magnetic field, but also the plasma frequency. To derive an expression for $\omega_p(\varphi_e)$, consider the case of negligible loop inductance which can be analytically solved. Setting $\beta_1 = \beta_2 = 0$ in Equation (1.61), the total potential energy of the SQUID is:

$$U(\varphi_1,\varphi_2) = -\varphi_0I_{01}\cos\varphi_1 - \varphi_0I_{02}\cos(\varphi_2). \tag{1.62}$$

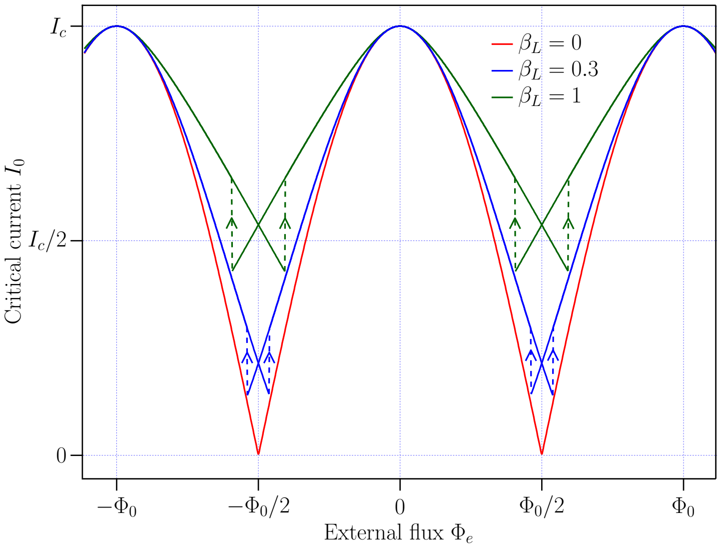

Figure 1.17.: Critical current of a symmetrical SQUID for $\beta_L = 0, 0.3$ and 1.

Recalling that $\varphi_2 = \varphi_1 - \varphi_e$, this expression can be rewritten

$$U(\varphi_1, \varphi_e) = -\varphi_0 I_0 \cos(\varphi_1 - \varphi), \tag{1.63}$$

where I_0 and φ are defined as in Equation (1.59) by

$$\begin{cases} I_0^2 = I_{01}^2 + I_{02}^2 + 2I_{01}I_{02}\cos\varphi_e, \\ \tan\varphi = \dfrac{I_{02}\sin\varphi_e}{I_{01} + I_{02}\cos\varphi_e}. \end{cases} \tag{1.64}$$

The kinetic energy of the SQUID, due to the capacitances C_1 and C_2 of the junctions has the form

$$K(\dot{\varphi}_1, \dot{\varphi}_2) = \frac{C_1}{2}\varphi_0^2\dot{\varphi_1}^2 + \frac{C_2}{2}\varphi_0^2\dot{\varphi_2}^2 = \frac{1}{2}(C_1 + C_2)\varphi_0^2\dot{\varphi_1}^2. \tag{1.65}$$

So, the total energy of the SQUID is

$$E(\varphi_1, \dot{\varphi}_1) = -\varphi_0 I_0 \cos(\varphi_1 - \varphi) + \frac{1}{2}(C_1 + C_2)\varphi_0^2\dot{\varphi_1}^2. \tag{1.66}$$

This energy is minimal when $\varphi_1 = \varphi$. Around this equilibrium position, the energy can be estimated with the harmonic approximation,

$$E(\varphi_1, \dot{\varphi}_1) \sim -\varphi_0 I_0 \left(1 - \frac{1}{2}(\varphi_1 - \varphi)^2\right) + \frac{1}{2}(C_1 + C_2)\varphi_0^2\dot{\varphi_1}^2. \tag{1.67}$$

The plasma oscillations around this equilibrium position occur at the plasma frequency ω_p, such that

$$\omega_p^2(\varphi_e) = \frac{I_0}{\varphi_0(C_1 + C_2)} = \frac{\sqrt{I_{01}^2 + I_{02}^2 + 2I_{01}I_{02}\cos\varphi_e}}{\varphi_0(C_1 + C_2)}, \tag{1.68}$$

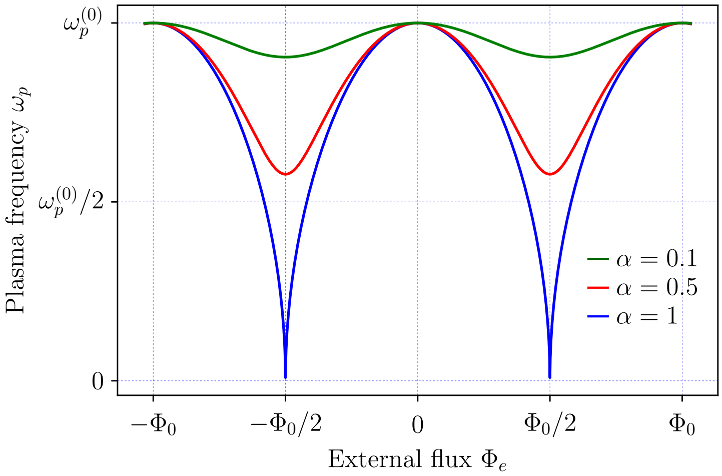

Figure 1.18.: Plasma frequency ω_p for a SQUID with negligible loop inductance for $\alpha = 0.1, 0.5$ and 1.

where $C_1 + C_2$ is the total capacitance of the SQUID, corresponding to C_1 and C_2 in parallel. Recalling that both I_{0i} and C_i are proportional to the area S_i of the junctions, the plasma frequency of the SQUID can be expressed as

$$\omega_p\left(\varphi_e\right) = \omega_p^{(0)} \left(\frac{\sqrt{S_1^2 + S_2^2 + 2S_1S_2 \cos\varphi_e}}{S_1 + S_2} \right)^{\frac{1}{2}}, \tag{1.69}$$

where $\omega_p^{(0)}$ is the plasma frequency of a single Josephson junction. The plasma frequency of the SQUID is maximal when no magnetic field is applied and takes the value of the single junction plasma frequency $\omega_p^{(0)}$. When the SQUID is biased at half a flux quantum, the plasma frequency is minimal and goes to 0 for a symmetric SQUID. This dependence is plotted in Figure 1.18 for some ratios $\alpha = S_2/S_1$.

In the case of a symmetrical SQUID, the plasma frequency is simply

$$\omega_p\left(\varphi_e\right) = \omega_p^{(0)} \left| \cos\frac{\varphi_e}{2} \right|. \tag{1.70}$$

When the inductance of the loop is larger, the effect is the same as for the critical current: a large β_L reduces the variations in ω_p and makes it multi-valued. This appears more clearly when writing the plasma frequency as

$$\omega_p = \sqrt{\frac{I_0}{\varphi_0\left(C_1 + C_2\right)}}.$$

1.3.3. Flux quantization in a SQUID

Consider a symmetrical SQUID with negligible loop inductance to which we apply a magnetic flux starting from $\Phi_e = 0$. The potential energy of such a SQUID is plotted in Figure 1.19a for

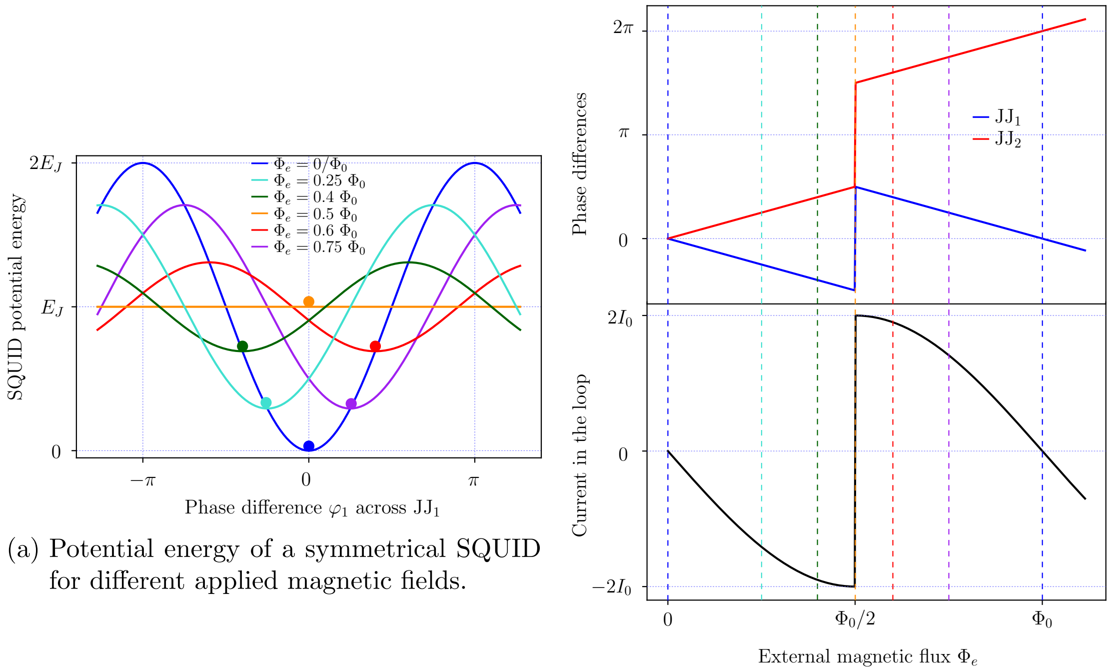

(a) Potential energy of a symmetrical SQUID for different applied magnetic fields.

(b) Phase differences and current circulating in the loop.

Figure 1.19.: Potential energy of a symmetrical SQUID and corresponding current in the loop.

different magnetic flux values. When $\Phi_e = 0$ (blue curve in the figure), the minimum energy is obtained for $\varphi_1 = \varphi_2 = 0\ (2\pi)$.

When the magnetic flux Φ_e is increased from 0 to Φ_0, φ_1 decreases and φ_2 increases until Φ_e reaches $\Phi_0/2$. This phase difference modification is plotted in Figure 1.19b and corresponds to interferences between the two arms of the loop, generating a current in the loop. It is also plotted in the figure. The colored vertical dashed lines correspond to the colored marks in Figure 1.19a.

When the applied flux reaches $\Phi_0/2$, (φ_1, φ_2) reaches $(-\pi/2, \pi/2)$ and the potential becomes flat. For a magnetic flux slightly larger than $\Phi_0/2$, both phase differences undergo a π kink and the current in the loop switches direction. This corresponds to one magnetic flux quantum entering the loop through the Josephson junctions.

When the flux is increased further, φ_1 keeps on decreasing and φ_2 keeps on increasing, to reach $(\varphi_1, \varphi_2) = (0, 2\pi)$ for $\Phi_e = \Phi_0$ which is the same situation as when no flux was present, except that one flux quantum has entered the loop, making $\varphi_2 - \varphi_1 = 2\pi$.

If we keep increasing the flux, the same process will take place: at $\Phi_e = (2n+1)\,\Phi_0/2$ with n an integer, a flux quantum enters the loop, φ_1 and φ_2 undergo a π kink and the current switches direction. At $\Phi_e = n\Phi_0$, $\varphi_2 - \varphi_1 = 2n\pi$ and n flux quanta are in the loop.

This process was explained in the case of a symmetrical SQUID with negligible loop inductance, but the same happens for a non-negligible inductance and for junctions with different critical currents.

1.4. Applications of Josephson junctions

Josephson junctions are widely used today due to their strong dependence in the magnetic field, their non-linearity and their quantum nature. Various applications exist, not only in mesoscopic physics, but also in biology, metrology, quantum information and even astronomy.

1.4.1. A sensitive magnetometer

The SQUID introduced in Section 1.3 has a current-voltage characteristic which depends sensitively on the magnetic flux. Biasing a SQUID with a current and measuring the voltage across it is a common method used to measure magnetic fields precisely. To keep the ratio of the Josephson inductance to the inductance of the loop small, these SQUIDs have necessarily small loop area and thus collect little flux. To increase the signal, larger superconductive pick-up loops as often added to the device, coupled via a mutual inductance to the loop of the SQUID. The resolution of such magnetometers can then be as low as a few $\mathrm{fT}/\sqrt{\mathrm{Hz}}$ [3,53].

A simpler device based on a Josephson junction is also commonly used to measure low magnetic fields, the RF-SQUID. It consists of a superconducting loop interrupted by one single junction. The flux threading it imposes a phase difference across the junction and a supercurrent in the loop to satisfy flux quantization. If the RF-SQUID is inductively coupled to a resonator circuit, a change in the magnetic field induces a change of the impedance of the junction (because of its non-linearity) and thus a change of the resonance frequency of the resonator. This response is Φ_0-periodic in the flux threading the RF-SQUID, allowing determining the magnetic field. However, RF-SQUIDs are less sensitive than SQUIDs with a typical resolution of $10\,\mathrm{fT}/\sqrt{\mathrm{Hz}}$ [3] but cheaper and easier to fabricate.

Using two SQUIDs located close to each other and subtracting their signals also allows for measurement of the gradient of the magnetic field, providing efficient spatial filtering. Because the field from a dipole decays with distance r from the source as $1/r^3$, the first-derivative decays even faster, as $1/r^4$. Noise sources located far away from the gradiometer thus produce significantly less signal than a source close to it. Another common method to measure the gradient of the magnetic field is to add two pick-up loops of the same area S at positions $\vec{r}$ and $\vec{r}+\delta\vec{r}$ wound in opposition. They are threaded respectively by fluxes $\vec{B}\left(\vec{r}\right)\cdot\vec{S}$ and $-\vec{B}\left(\vec{r}+\delta\vec{r}\right)\cdot\vec{S}$. The total measured flux is thus proportional to the gradient of the magnetic field, $\delta\vec{r}\cdot\vec{\nabla}\left(\vec{B}\left(\vec{r}\right)\cdot\vec{S}\right)$.

Since the measurement of the magnetic activity of the heart in 1970 by Cohen [54], SQUID-based magnetometers and gradiometers have been widely used in biology to study the activity of the heart and the brain [3–5]. The SQUIDs can detect the magnetic fields generated by neuronal electrical currents in the brain of order $1-10\,\mathrm{fT}$ [3,55]. They are also a good asset for this purpose, as they have a good spatial resolution. Using an array of ~ 300 SQUIDs is now a common method to make functional maps of the brain [3].

1.4.2. Detectors for astronomy

Josephson junctions are also commonly used as detectors in radio astronomy [17,18]. They exploit the process of photo-assisted tunneling (described in more detail in Chapter 4), the tunneling of quasiparticles through the junction with the help of an incident photon. If the

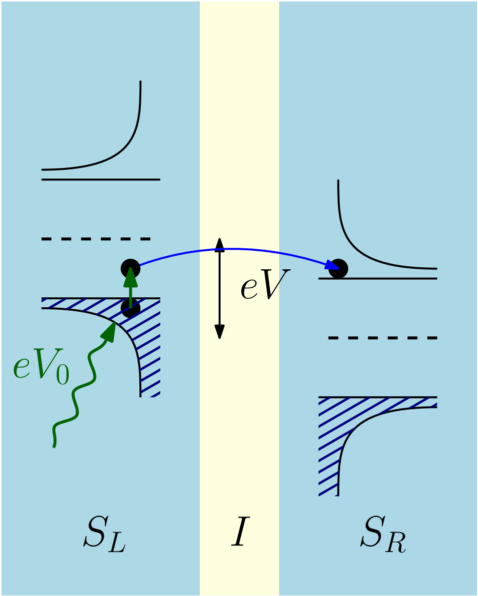

Figure 1.20.: Photo-assisted tunneling: a photon of energy eV_0 excites a quasiparticle which can tunnel through the junction.

junction is voltage-biased at $V = 2\Delta/e - V_0$, a photon of energy eV_0 can increase the energy of a quasiparticle and make it tunnel to the other side of the junctions where energy levels are available, as sketched in Figure 1.20.

The energy of the detected incoming photons has to be smaller than twice the gap. This threshold is $\sim 180\,\mathrm{GHz}$ for aluminum and can reach 1.4 THz for niobium. There are few detectors available in this energy range of hundreds of GHz which is rich for astronomy. For instance, the cosmic microwave background has its maximal spectral radiance around 280 GHz [56].

1.4.3. The voltage standard

The Josephson effect introduced in this chapter states that a constant voltage V applied to a Josephson junction induces an oscillating supercurrent at the Josephson frequency $\omega_J = V/\varphi_0$. The opposite is also possible: applying an oscillating signal at frequency ω develops a constant voltage $V_\omega = \varphi_0\omega$ across the junction. This effect, predicted by Josephson [1], was observed by Shapiro one year later [57].

Because commercial microwave sources can achieve extremely narrow linewidth (below the hertz for gigahertz signals), the voltage on a Shapiro step is stable and is at the basis of the voltage standard. In the 1980s, different Josephson junctions were tested and a reproducibility of 10^{-16} was found for the V_ω to ω ratio [58]. The volt is nowadays defined using arrays of ~ 8000 Josephson junctions and the relative uncertainty is below 10^{-9} [6].

Figure 1.21 shows the evolution of the uncertainty on the volt between 1930 and 2000. Between 1930 and 1970, Weston cells (stable mercury cadmium chemical batteries) were used to realize the volt. Around 1970, single Josephson junctions (single Junction JVS in the figure) replaced the Weston cells and helped reduce the uncertainty by two orders of magnitude. In

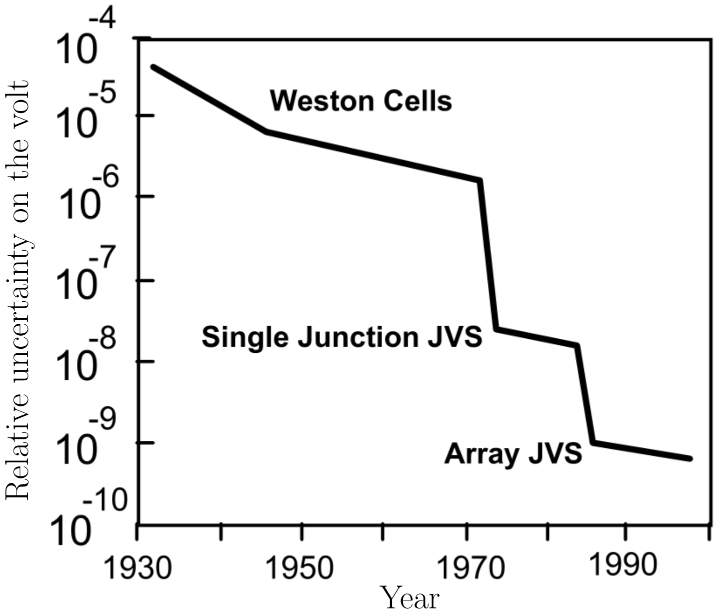

Figure 1.21.: Evolution of the uncertainty on the volt between 1930 and 2000, adapted from reference [6].

the 1980s, array of Josephson junctions (Array JVS in the figure) were introduced and another order of magnitude was gained.

1.4.4. A building block for superconducting qubits

As seen in Section 1.1.4, the Josephson junction energy levels are not uniformly spaced as opposed to the levels of a harmonic oscillator. This allows working with only the two lowest states: exciting the ground state $|g\rangle$ with energy $\hbar\omega_p$ will excite the Josephson junction to the first excited state $|e\rangle$. Exciting the state $|e\rangle$ with the same energy won't make a transition to a higher level, as the energy spacing is not the same. Being able to restrict the dynamics to two levels is a prerequisite for qubits, making Josephson junctions good candidates.

Another prerequisite for qubits is long decoherence times, allowing performing error correction and operations on the qubits before they lose coherence. Josephson junctions are non-dissipative as they are superconducting and should therefore grant long coherence times.

As of today, Josephson junctions are used to make qubits with coherence times larger than 10 µs [9]. Using microwave pulses, single qubit as well as two qubits quantum gates have also been implemented, such as the controlled-NOT (or cNOT) gate [10].

Josephson junctions are not used on their own but in various superconducting circuits using also capacitors and inductors, such as

- the phase qubit [11]: a large Josephson junction ($E_J \gg E_C$) biased with a current slightly smaller than the critical current,

pendulum	**Josephson junction**
angle θ	phase difference φ
mass m	capacitance C
applied torque T	bias current I_b
damping constant b	bias conductance $1/R$
critical gravitational torque mgl	critical current I_0

Table 1.2.: Extended analogy between a pendulum and a Josephson junction.

- the Cooper pair box [12]: a small Josephson junction ($E_C \gg E_J$) on which it is possible to add charges via a local gate,
- the quantronium [13]: a variant of the Cooper pair box where the junction is replaced by a SQUID,
- the flux qubit [14]: a large Josephson junction ($E_J \gg E_C$) shunted with a large inductance (made of an array of larger Josephson junctions),
- the transmon [15]: a Cooper pair box shunted by a large capacitance to decrease E_C so that $E_J \gg E_C$,
- the fluxonium [16]: a small junction shunted by the high inductance of an array of large-capacitance junctions ($E_J \sim E_C$).

1.4.5. Quantum limited amplifiers

The non-linearity of the Josephson junction has also been used to make amplifiers for microwave photons adding little noise to the signal. The first implementations were using a large junction in a microwave resonator [59,60]. Now, more sophisticated circuits consisting of a Wheatstone-like structure with four Josephson junctions [7,8] can almost reach the quantum limit of adding half a photon of noise [61].

Such amplifiers have promising applications, in particular in circuit QED and quantum information where quantum states are manipulated, and the signals are weak and need to be amplified without adding noise.

1.5. Rich phenomena and chaos in a quantum non-linear system

The fact that the Josephson equations are non-linear can lead to a lot of interesting physics which need the tools of non-linear physics to be understood. Some situations can even lead to chaotic behavior as we will see in this section.

As introduced in Section 1.1.3, the current biased Josephson junction is analogous to a pendulum driven by a torque T. This analogy (summarized in Table 1.2) can be extended by adding the bias resistance R which is analogous to a viscous damping torque $b\dot{\theta}$. The two analogous differential equations are

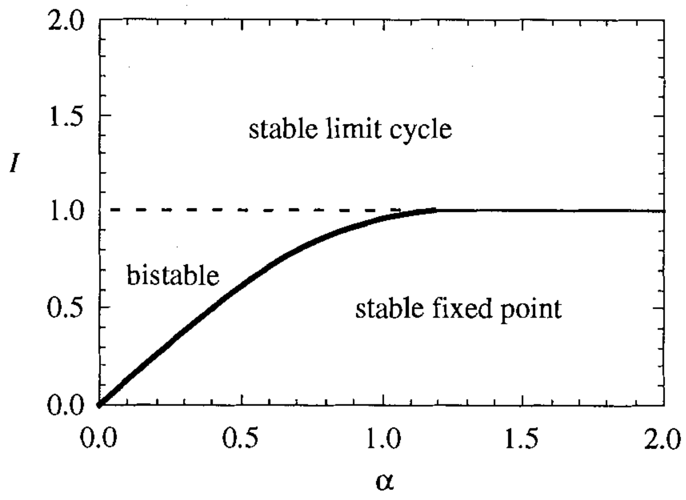

Figure 1.22.: Homoclinic bifurcation between a stable point and a stable limit cycle, taken from reference [62].

$$\begin{cases} I_b = C\varphi_0\ddot{\varphi} + \frac{1}{R}\varphi_0\dot{\varphi} + I_0 \sin\varphi, \\ T = ml^2\ddot{\theta} + b\dot{\theta} + mgl\sin\theta. \end{cases}$$

These differential equations are highly non-linear and can thus exhibit curious behaviors. Considering the pendulum, when the applied torque is not too strong (smaller than mgl), there can be two distinct stable limits: it can either come to a stable rest angle compensating for the applied torque or to a periodic evolution in which it rotates over the top of the pendulum. In non-linear physics, these two states are respectively labeled a stable fixed point and a stable limit cycle [62]. For the Josephson junction, the stable fixed point corresponds to having a finite phase difference and thus a current flowing through the junction and no voltage drop across the junction (supercurrent peak). The stable limit cycle corresponds to an oscillating current and a voltage across the junction (subgap region).

The transition between these two stable limits is called a homoclinic bifurcation. Considering the pendulum, this bifurcation occurs when the applied torque becomes smaller than a critical value and cannot overcome gravity and damping. The phase diagram for this bifurcation is shown in Figure 1.22, where I and α are respectively the normalized bias and damping.

For the Josephson junction, $I = I_b/I_0$ and $\alpha = \sqrt{\varphi_0/(CI_0)}/R$.

For the pendulum, $I = T/(mgl)$ and $\alpha = b/\sqrt{m^2gl^3}$.

This situation corresponds to one of the simplest bias circuit to work with a Josephson junction and is already quite complicated to understand. Adding an inductance in the bias circuit, as shown in Figure 1.23 can lead to even more sophisticated non-linear dynamics. This inductance is always present in experiments, as every wire generates a magnetic field when a current flows through it. When dealing with usual resistive electronic circuits, this inductance is often neglected compared to the resistance of the wires, but at high frequencies (above $\omega_L = R/L$), it must be considered.

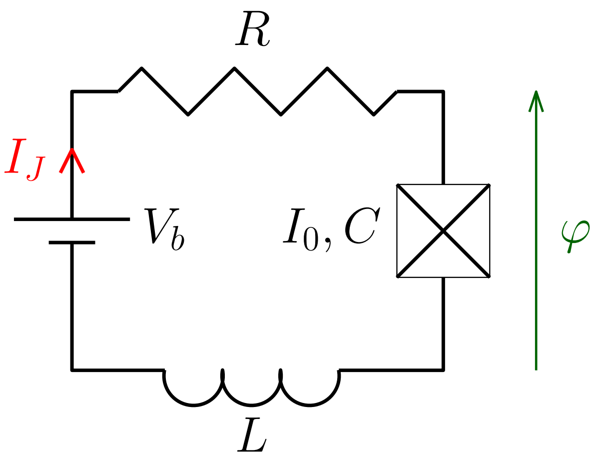

Figure 1.23.: Electric schematic of a Josephson junction biased via a resistance and an inductance.

The Kirchhoff's laws for this circuit give $V_b = RI_J + V_J + L\dot{I}_J$, that is to say

$$\frac{V_b}{R} = \frac{LC}{R}\varphi_0\dddot{\varphi} + C\varphi_0\ddot{\varphi} + \frac{\varphi_0}{R}\dot{\varphi}\left(1 + \frac{LI_0}{\varphi_0}\cos\varphi\right) + I_0\sin\varphi. \tag{1.71}$$

To make this equation dimensionless, we introduce the reduced time $\tau = RI_0t/\varphi_0$. Differentiation with respect to τ is noted with a prime symbol. $I = V_b/(RI_0)$ is the dimensionless bias. $\beta_L = LI_0/\varphi_0$ and $\beta_C = R^2CI_0/\varphi_0$ are the dimensionless inductance and capacitance. Equation (1.71) can be rewritten in a dimensionless form,

$$I = \beta_L\beta_C\varphi''' + \beta_C\varphi'' + \varphi'\left(1 + \beta_L\cos\varphi\right) + \sin\varphi. \tag{1.72}$$

The equation governing the evolution of the junction is now a third-order non-linear differential equation. Such equations cannot be solved numerically using standard computational methods as they lead to chaotic solutions [63, 64]. Figure 1.24 shows the numerical simulation of the bifurcation diagram for a Josephson junction shunted by an inductance, with $I = 1.2$ and $\beta_C = 0.707$. The horizontal axis is the reduced inductance β_L and the vertical axis V_{max} show the local maxima of the reduced voltage $v = V_J/(RI_0)$ with V_J the voltage across the junction. For a value of β_L, if there is one point in the diagram (as for $\beta_L = 0$ corresponding to the limit considered above), the evolution is periodic with one maximum. If there are two points, the evolution is still periodic, but with two maxima in a period and so on. If the diagram is denser, as for $\beta_L \sim 2.4$, the system is chaotic.

For values of β_L between 0 and 10, the system undergoes several transitions from periodic to chaotic evolutions. If I and β_C were also to change, this diagram would be even richer. Totally predicting the dynamics of one single Josephson junction thus requires tools from several fields of physics and mathematics and is beyond the scope of this thesis. We will thus concentrate only on the details of the dynamics of junctions which are relevant to the Josephson spectrometer.

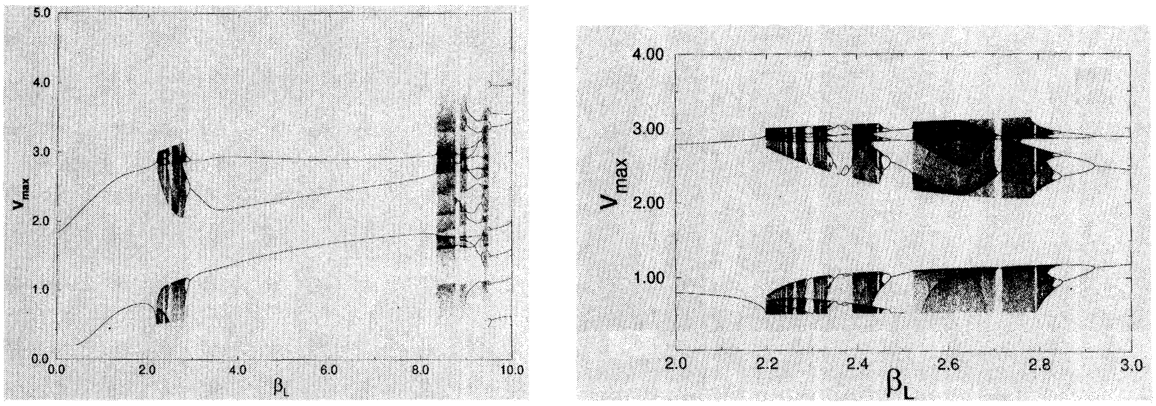

(a) β_L from 0 to 10.

(b) Detail of (a).

Figure 1.24.: Bifurcation diagram for $I = 1.2$ and $\beta_C = 0.707$, taken from reference [63].

1.6. Conclusion

In this first chapter, we have shown that a junction between two superconductors acts as a non-linear circuit element in which the current I, the voltage V and the phase difference φ are related by two simple fundamental equations:

$$
\begin{aligned}
I &= I_0 \sin \varphi, \\
V &= \varphi_0 \dot{\varphi}.
\end{aligned}
$$

These equations were then used to derive the dynamics and the current-voltage characteristic of a Josephson junction in the case of a simple biasing circuit. The characteristic consists of a non-dissipative current at zero voltage, an open-circuit like situation for voltages below twice the gap and an approximately resistive behavior for larger voltages.

Bringing two junctions together in a loop introduces interference effects, allowing modulating and even suppressing in some cases the zero-voltage supercurrent with an applied magnetic field.

Even in simple situations, predicting the behavior of a Josephson junction can be complex due to their non-linear character. This behavior can even be chaotic.

The physics of the Josephson effect is rich and numerous applications exist in magnetometry, astronomy, metrology, quantum information and low-noise measurement. The application which is the focus of this thesis and the topic of the next chapter is the realization a spectrometer in the terahertz range.

2. The Josephson spectrometer

In the previous chapter, we derived some essential equations to describe a Josephson junction. We will now use them to explain the principle of the Josephson spectrometer.

For that purpose, we will first come back to the AC Josephson effect and see how it is modified in the presence of dissipative modes in the electromagnetic environment. This will lead us to a recent implementation of the spectrometer [32, 33] which will be commented. Some limitations will be discussed and we will describe how they can be overcome by using a two-junction device instead of a single Josephson junction.

Then we will discuss the coupling schemes to the systems of interest and detail the modifications of the current-voltage characteristic due to dissipative modes.

Finally, the limitations of the Josephson spectrometer and a brief comparison to other conventional spectrometers will be presented.

2.1. Principle of the single junction spectrometer

2.1.1. Inelastic Cooper pair tunneling

As described in Section 1.2.2, the AC Josephson effect can be understood in terms of tunneling of Cooper pairs from one side to the other of a Josephson junction by emitting and re-absorbing photons of energy $2e\left|V\right|$, where V is the voltage applied between the two superconductors forming the junction.

In this case, photons are reflected because the impedance of the junction is purely imaginary (it consists of its intrinsic capacitance). They are then re-absorbed by the Cooper pairs which tunnel back to their original side. If the impedance had a real part, some emitted photons could have been dissipated. This would result in a net DC current as some Cooper pairs that have tunneled cannot tunnel back because of missing photons.

Consider the situation depicted in Figure 2.1 where a Josephson junction is coupled to a two-level system with energy spacing E_{ge}. When the energy of the photon emitted by the junction $2eV$ is resonant with the two-level system, it is absorbed. It may then relax by emitting another photon, or some other process. If this photon is not emitted in the direction of the junction, the Cooper pair which tunneled does not tunnel back.

This creates a current (called inelastic Cooper pair tunneling) from the left electrode to the right electrode of magnitude $I\left(V\right) = 2e\Gamma\left(2eV\right)$, where $\Gamma\left(E\right)$ is the rate at which Cooper pairs tunnel and is proportional to the probability that the two-level system absorbs photons at energy E. In the limit where this rate stays small compared to the difference between the energy levels of the junction (of the order of the plasma frequency), inelastic Cooper pair tunneling can be seen as a perturbation of the Hamiltonian and Γ can be expressed using

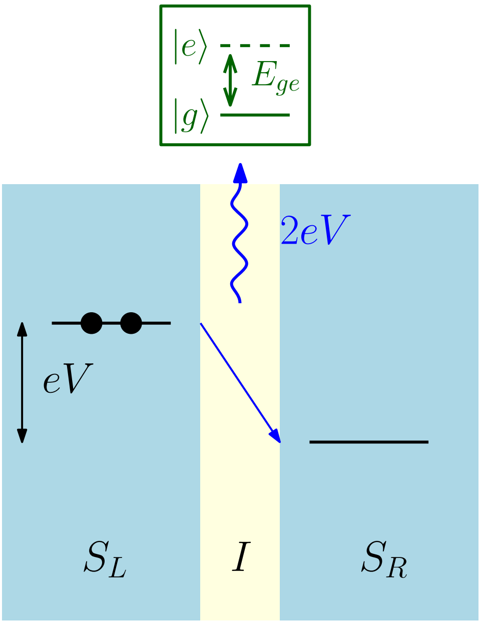

Figure 2.1.: Josephson junction biased with voltage V coupled to a two-level system with energy spacing E_{ge}.

Fermi's golden rule [65, 66]

$$\Gamma(E) = \frac{2\pi}{\hbar} \left| \left\langle Q - 2e \middle| \hat{\mathcal{H}} \middle| Q \right\rangle \right|^2 P(E).$$

Here, $|Q\rangle$ is the initial state with charge Q on the left electrode of the junction and $|Q-2e\rangle$ is the state where the charge is $Q-2e$ because a Cooper pair (of charge $2e$) has tunneled. $\hat{\mathcal{H}}$ is the Hamiltonian of the junction and $P(E)$ is the probability density to absorb photons of energy E in the two-level system. The matrix element $\left\langle Q - 2e \middle| \hat{\mathcal{H}} \middle| Q \right\rangle$ is simply given by $-E_J/2 = -\varphi_0 I_0/2$. This gives an expression for the current flowing through the junction:

$$\boxed{I\left(V\right) = \frac{\pi}{2}\varphi_0 I_0^2 P(2eV).} \tag{2.1}$$

Measuring the current flowing through the junction as a function of the voltage V across it gives the spectrum of the system(s) coupled to the junction: when the current is zero, no photon is absorbed at energy $2eV$ and when the current is different from zero, photons are absorbed and the current is proportional to the absorption probability of the system(s).

With this inelastic Cooper pair tunneling, it is possible to use a Josephson junction as a spectrometer. However, at voltages higher than $2\Delta/e$ (where Δ is the superconducting gap), quasiparticles can tunnel through the junction, resulting in a large background current of the order of the critical current of the junction. This reduces greatly the sensitivity of the device. For aluminum, this gives an upper limit of $\sim 180\,\mathrm{GHz}$.

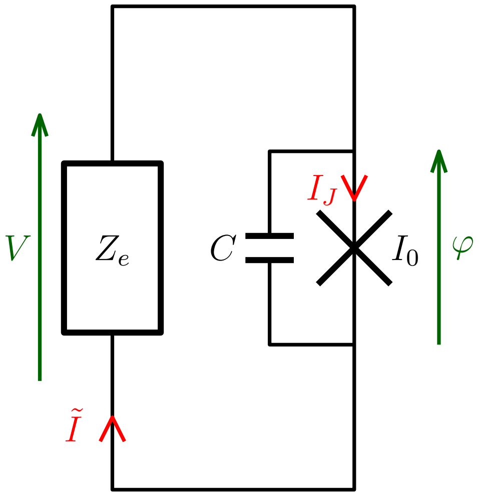

Figure 2.2.: Josephson junction connected to an impedance Z_e.

2.1.2. Energy conservation

The DC current flowing through the junction in the case of the inelastic Cooper pair tunneling is dissipative, as the voltage across the junction is non-zero. The DC power $\mathcal{P}_{DC} = I_{DC}V_{DC}$ which is provided by the DC power supply is converted in an AC power radiated by the junction, $\mathcal{P}_r$. Considering the external system which can absorb photons as an impedance Z_e, the radiated power is $\mathcal{P}_r = \frac{1}{2}\left|I_{\omega_J}\right|^2 \Re\left(Z_e(\omega_J)\right)$, if we assume that the AC current is sinusoidal with amplitude I_{ω_J} at the Josephson frequency $\omega_J = V/\varphi_0$.

The DC voltage V implies, via the Josephson relations, the flow of an alternative current at frequency ω_J and of amplitude I_0. But if the junction is connected to an impedance Z_e, this current creates an alternative voltage at frequency ω_J and of amplitude $V_{\omega_J} = Z_e\left(\omega_J\right) I_0$. Substituting this voltage in the AC Josephson relation gives an oscillating phase at frequency ω_J which generates currents at all frequencies which are multiple of ω_J. The assumption that the alternative current is purely sinusoidal appears to be quite illusory! We will see later that this assumption can be a good approximation in many situations.

Energy conservation implies that $\mathcal{P}_{DC} = \mathcal{P}_r$. But there is no simple expression for $\mathcal{P}_r$ in the general case where the current is not purely a sine wave. This equality allows calculating the DC current flowing through the junction at finite voltage according to $I_{DC} = \mathcal{P}_r/V_{DC}$.

2.1.3. Detailed operation

Consider a Josephson junction of critical current I_0 and intrinsic capacitance C connected to an impedance Z_e (including the DC biasing circuit) as sketched in Figure 2.2.

From the Kirchhoff's laws and the Josephson relations, it is possible to write the differential equation governing the dynamics of this circuit,

$$I_0 \sin\varphi + \mathcal{Y}_e\left[\varphi_0\dot{\varphi}\right] + C\varphi_0\ddot{\varphi} = 0, \tag{2.2}$$

where $\mathcal{Y}_e$ is a linear operator with its Fourier transform being the admittance $Y_e(\omega) = 1/Z_e(\omega)$.

Such an operator is introduced because φ is *a priori* non-sinusoidal. However, if the junction is biased at a constant voltage V_{DC}, the oscillating phase at frequency $\omega_J = V_{DC}/\varphi_0$ generates current at all harmonics $\omega_n = n\omega_J$, such that the phase can be written in the form

$$\varphi = \theta_0 + \omega_J t + \sum_{n=1}^{+\infty} a_n \sin\left(\omega_n t + \theta_n\right), \tag{2.3}$$

where θ_n and a_n are real constants. The current flowing through the junction is thus

$$I_J = I_0 \sin\left(\theta_0 + \omega_J t + \sum_{n=1}^{+\infty} a_n \sin\left(\omega_n t + \theta_n\right)\right). \tag{2.4}$$

It can also be expanded in Fourier series,

$$I_J = I_0 \sum_{n=0}^{+\infty} \tilde{a}_n \sin\left(n\omega_J t + \tilde{\theta}_n\right),$$

such that Equation 2.2 writes, at frequency ω_n,

$$I_0 \mathrm{e}^{i\left(\tilde{\theta}_n - \theta_n\right)} \tilde{a}_n + \left(iY_e\left(\omega_n\right)\varphi_0\omega_n - C\varphi_0\omega_n^2\right) a_n = 0. \tag{2.5}$$

The coefficients $\tilde{a}_n$ can be calculated by writing

$$I_J = I_0 \Im\left(\mathrm{e}^{i(\theta_0 + \omega_J t)} \prod_{n=1}^{+\infty} \mathrm{e}^{ia_n \sin(n\omega_J t + \theta_n)}\right),$$

$$I_J = I_0 \Im\left(\mathrm{e}^{i(\theta_0 + \omega_J t)} \mathrm{e}^{ia_1 \sin(\omega_J t + \theta_1)} \prod_{n=2}^{+\infty} \mathrm{e}^{ia_n \sin(n\omega_J t + \theta_n)}\right).$$

Using the Jacobi-Anger expansion [67], this gives

$$I_J = I_0 \Im\left(\mathrm{e}^{i(\theta_0 + \omega_J t)} \sum_{n_1=-\infty}^{+\infty} J_{n_1}\left(a_1\right) \mathrm{e}^{in_1(\omega_J t + \theta_1)} \prod_{n=2}^{+\infty} \mathrm{e}^{ia_n \sin(n\omega_J t + \theta_n)}\right),$$

$$I_J = I_0 \sum_{n_1=-\infty}^{+\infty} \Im\left(J_{n_1}\left(a_1\right) \mathrm{e}^{i(\theta_0 + n_1\theta_1)} \mathrm{e}^{i(1+n_1)\omega_J t} \prod_{n=2}^{+\infty} \mathrm{e}^{ia_n \sin(n\omega_J t + \theta_n)}\right),$$

where J_{n_1} is the first Bessel function of the n_1-th order. Using the same identity for all n gives

$$I_J = I_0 \sum_{n_1=-\infty}^{+\infty} \cdots \sum_{n_\infty=-\infty}^{+\infty} \Im\left(J_{n_1}\left(a_1\right) \cdots J_{n_\infty}\left(a_\infty\right) \mathrm{e}^{i(\theta_0 + n_1\theta_1 + \ldots + n_\infty\theta_\infty)} \mathrm{e}^{i(1+n_1+\ldots+n_\infty)\omega_J t}\right),$$

$$I_J = I_0 \sum_{n_1=-\infty}^{+\infty} \cdots \sum_{n_\infty=-\infty}^{+\infty} \prod_{i=1}^{+\infty} \left(J_{n_i}\left(a_i\right)\right) \sin\left(\sum_{i=0}^{+\infty} n_i\omega_J t + \sum_{i=0}^{+\infty} n_i\theta_i\right) \tag{2.6}$$

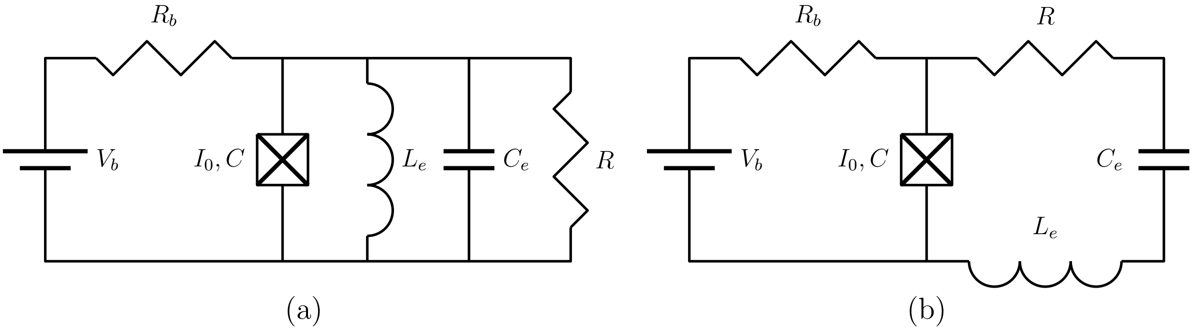

(a) (b)

Figure 2.3.: A LC resonator with a dissipative part R. (a) Parallel configuration ; (b) Series configuration.

By convention, $n_0 = 1$. This expression allows extracting the component oscillating at $n\omega_J$. It is the sum of all terms such that

$$1 + n_1 + \ldots + n_\infty = \pm n.$$

With this expression for $\tilde{a}_n$, Equation (2.5) seems quite complicated to solve. At frequency $n\omega_J$, the coefficient a_n is coupled to a non-linear combination of Bessel functions of all other $a_{n'}$.

To simplify it, we write the modulus of Equation (2.5) as

$$\left|\frac{a_n}{\tilde{a}_n}\right|^2 = \frac{1}{\frac{1}{z^2} + \left(\frac{\varphi_0\omega_n}{I_0}\right)^2 \left(\Im(Y_e) + i\omega_n C\right)^2}, \tag{2.7}$$

where $z = I_0/(\varphi_0\omega_n\Re(Y_e))$ is the coupling parameter to the impedance. Using the Ambegaokar-Baratoff relation (Equation (1.14)), z can be expressed as

$$z = \frac{\pi}{4}\frac{R_e}{R_N}\frac{V_g}{V_0},$$

where $R_e = 1/\Re(Y_e)$, R_N is the normal state resistance of the junction, $V_0 = \varphi_0\omega_n$ and $V_g = 2\Delta/e$ is the gap voltage. For instance, in the middle of the gap, a R_e resistance of $R_N/2$ makes $z \sim 0.8$.

In the general case of an arbitrary Z_e, the situation is quite complex to describe, but it is always possible to approximate an impedance Z_e by a different RLC model (parallel or series) around each frequency. For instance, a transmission line has alternate series and parallel types of resonances [68]. Each series type resonance (diverging impedance) can be modeled by a series RLC resonator and each parallel type resonance (diverging admittance) by a parallel RLC resonator. We focus therefore on the study of both types of RLC resonators, sketched in Figure 2.3. In both cases, a simple biasing circuit consisting of a voltage source V_b and a bias resistor R_b is added.

- The parallel RLC resonator (Figure 2.3(a)). At low frequencies, the admittance Y_e is dominated by the inductance, $Y_e \sim 1/(iL_e\omega)$, such that the amplitude of the a_n

coefficients in Equation (2.7) is small. At high frequencies, the admittance is dominated by the capacitance $Y_e \sim iC_e\omega$ and the a_n coefficients tend to zero. Around the frequencies ω_0 such that

$$\Im\left(Y_e\right) + i\omega_0 C = 0,$$

the amplitude of the a_n depends on the real part $1/R + 1/R_b$ of the admittance, that is to say on the value of the z coefficient. If z is small (in the case of a low quality factor resonator), the a_n coefficients can stay small. On the other hand, large z values result in large a_n coefficients. The limit of small z parallel resonator is discussed in Section 2.1.4.

- The series RLC resonator (Figure 2.3(b)). At low frequencies, the admittance Y_e tends to $1/R_b$ and the situation is the same as the one discussed in Section 1.2.2 for the biasing of a junction via a resistor. The current-voltage characteristic has thus the universal shape of Equation 1.48,

$$\frac{\langle I_J\rangle}{I_0} = \sqrt{1 + \left(\frac{\langle V_J\rangle}{RI_0}\right)^2} - \frac{\langle V_J\rangle}{RI_0},$$

  where $\langle V_J\rangle$ and $\langle I_J\rangle$ are the average values of the voltage and current of the junction. At high frequencies, the junction capacitance contribution makes that $a_n \sim 0$. Between these two limits, the admittance of the RLC resonator is small and increases close to the resonance frequency ω_0. If it overcomes the admittance of the bias resistor and the junction capacitance, a drop in the current-voltage characteristic can be seen. The series resonator is presented in Section 2.1.5.

2.1.4. The parallel resonator

For the parallel resonator, the total admittance Y_e (including the biasing circuit) is

$$Y_e = \frac{1}{R_b} + \frac{1}{R} + i\omega C_e - \frac{i}{\omega L_e},$$

such that the effect of the bias resistor is to increase the real part of the admittance. In the following, R is the parallel combination of R and R_b.

Two limits are discussed for the parallel resonator:

- The zeroth order approximation, corresponding to small z: all a_n are zero. In that case, the phase is linear, $\varphi = \theta_0 + \omega_J t$.
- The first order approximation, corresponding to larger z: all a_n but a_1 are zero. The phase has a sinusoidal component, $\varphi = \theta_0 + \omega_J t + a_1 \sin\left(\omega_J t + \theta_1\right)$.

Zeroth order approximation

In the case of the coupling to a low z system, φ can be approximated by a linear expression,

$$\varphi = \theta_0 + \omega_J t, \tag{2.8}$$

resulting in sinusoidal oscillations of the supercurrent.

In that case, the current $\tilde{I}$ flowing through the impedance is also sinusoidal, of amplitude

$$\tilde{I} = I_J \frac{Y_e(\omega_J)}{Y_e(\omega_J) + i\omega_J C}.$$

The power dissipated in the external system is

$$\mathcal{P}_r = \frac{1}{2}\left|\tilde{I}\right|^2 \Re(Z_e(\omega_J)) = \frac{I_0^2}{2} \frac{\Re(Y_e(\omega_J))}{\left|Y_e(\omega_J) + i\omega_J C\right|^2}. \tag{2.9}$$

For a dissipative external system (for which $\Re(Z_e) > 0$), the dissipated power $\mathcal{P}_r$ is positive. As the DC current flowing through the spectrometer is proportional to it ($\mathcal{P}_r = VI_{DC}$), this expression allows calculating the current-voltage characteristic of the junction.

A peak in the current-voltage characteristic is thus equivalent to a maximum of $\mathcal{P}_r$. This is achieved when the denominator of Equation (2.9) is minimal, which is at the frequency ω_0, such that

$$\boxed{\Im(Y_e(\omega_0)) = -\omega_0 C.} \tag{2.10}$$

Such a frequency always exists if the external system has an inductive part (for which $\Im(Y_e) < 0$), which is the case for a parallel resonator. For the resonator of Figure 2.3(a) of intrinsic resonance frequency $\omega_e = 1/\sqrt{L_e C_e}$, ω_0 is different from ω_e,

$$\omega_0 = \omega_e \left(1 + \frac{C}{C_e}\right)^{-\frac{1}{2}}.$$

This value is smaller than ω_e. Having a resonator with a large capacitance allows keeping $\omega_0 \sim \omega_e$. At frequency ω_0, the dissipated power is

$$\mathcal{P}_{r,max} = \frac{1}{2} I_0^2 \frac{1}{\Re(Y_e(\omega_0))}. \tag{2.11}$$

Energy conservation imposes this power to be equal to the power supplied by the DC bias: $\mathcal{P}_r = I_{DC}V$. At the resonance voltage $V_0 = \omega_0 \varphi_0$, the DC current can thus be written $I_{DC} = \mathcal{P}_{r,max}/V_0$. With the formalism introduced in Section 2.1.1, it is also possible to write $I_{DC}(V) = \frac{\pi}{2}\varphi_0 I_0^2 P(2eV)$. So, the photon absorption probability density P is linked to the impedance of the environment by

$$\boxed{\hbar\omega_0 P(\hbar\omega_0) = \frac{G_0}{G_e},} \tag{2.12}$$

where $G_e = \Re\left(Y_e(\omega_0)\right)$ and $G_0 = 4e^2/h = 155\,\mu\mathrm{S}$ is the superconducting quantum of conductance. Equation (2.12) is a fundamental relation showing that the probability to absorb a photon of energy $\hbar\omega_0$ in an admittance Y_e is simply given by the ratio of the conductance quantum to the real part of the admittance.

It is also possible to find the shape of the current-voltage characteristic around the resonance value ω_0. In that case, we write, close to the resonance frequency ω_0,

$$Y_e(\omega_J) + iC\omega_J = G_e\left(1 + i\xi\right),$$

where

$$\xi = \frac{\omega_J - \omega_0}{G_e}\frac{d}{d\omega_J}\left(\Im\left(Y_e(\omega_J)\right) + C\omega_J\right).$$

For a parallel RLC resonator of resonance frequency ω_0 and quality factor Q, ξ can be expressed as

$$\xi = 2Q\frac{\omega_J - \omega_0}{\omega_0}.$$

With these notations, Equation (2.9) can be transformed to a Lorentzian,

$$I(V) = I_0\frac{z/2}{1+\xi^2}.$$

First order approximation

When the z parameter is larger, the next order approximation consists of adding a sinusoidal term to φ, such that,

$$\varphi = \theta_0 + \omega_J t + \delta\sin\left(\omega_J t + \theta_1\right).$$

By changing the origin of time, it is possible to choose $\theta_1 = 0$ without loss of generality. δ is the amplitude of the oscillations of the phase and is to be determined.

Equation (2.6) for the current can be written in that case

$$I = I_0\sum_{n=-\infty}^{+\infty} J_n(\delta)\sin\left(\theta_0 + (n+1)\,\omega_J t\right). \tag{2.13}$$

The DC component I_{DC} can be extracted of this expression, obtained when $n = -1$:

$$I_{DC} = -I_0 J_1(\delta)\sin\left(\theta_0\right). \tag{2.14}$$

The negative sign in this expression does not necessarily imply a negative current. We will see later that $\sin\theta_0 < 0$, resulting in a positive value for the current. The complex [1] amplitude of the first harmonic of I at frequency ω_J is

$$I_{\omega_J} = I_0\left(-iJ_0(\delta)\mathrm{e}^{i\theta_0} + iJ_2(\delta)\mathrm{e}^{-i\theta_0}\right). \tag{2.15}$$

With this expression, it is possible to rewrite Equation (2.5) as

$$\begin{cases} \varphi_0\delta\omega_J\Re\left(Y_e(\omega_J)\right) = -2I_0\dfrac{J_1(\delta)}{\delta}\sin\theta_0 \\ \varphi_0\delta\omega_J\left(\Im\left(Y_e(\omega_J)\right) + C\omega_J\right) = I_0\left(J_0(\delta) - J_2(\delta)\right)\cos\theta_0 \end{cases}. \tag{2.16}$$

The first line of (2.16) is similar to Equation (2.14) for the DC current and combining them gives the following expression for the DC current at voltage V,

---

[1] The real and imaginary axis are chosen such that $\cos\left(\omega_J t\right)$ is the real part of the phasor I_{ω_J}.

$$I_{DC}(V) = \frac{1}{2} V \delta^2 \Re \left(Y_e \left(\frac{V}{\varphi_0} \right) \right). \tag{2.17}$$

The fundamental Harmonic-Balance [23, 69] equation relating the amplitude δ of the phase oscillations to the admittance of the external system at the Josephson frequency can be found by summing the squares of the two lines of Equation (2.16).

$$\left(\frac{\Re \left(Y_e(\omega_J) \right)}{J_0(\delta) + J_2(\delta)} \right)^2 + \left(\frac{\Im \left(Y_e(\omega_J) \right) + C\omega_J}{J_0(\delta) - J_2(\delta)} \right)^2 = \left(\frac{I_0}{\varphi_0 \delta \omega_J} \right)^2. \tag{2.18}$$

Solving this equation for δ allows getting the DC current and thus predict the current-voltage characteristic of the spectrometer coupled to an external system. But this equation is highly non-linear and cannot be solved analytically.

Section 2.1.3 predicts a non-zero DC current at frequencies ω_0, such that $\Im \left(Y_e(\omega_0) \right) + C\omega_0 = 0$. At these frequencies, Equation (2.18) takes the form

$$\frac{\delta}{J_0(\delta) + J_2(\delta)} = \frac{I_0}{V_0 G_e} = z, \tag{2.19}$$

where $V_0 = \varphi_0 \omega_0$. The coupling parameter z can also be written

$$z = \frac{I_0^2}{G_e} \frac{1}{V_0 I_0}.$$

With this expression, it appears as the ratio of power dissipated in the impedance to the available power at voltage V_0. It is also possible to express z as a function of the photon absorption probability density $P(E)$ using Equation (2.12),

$$z = E_J P(\hbar \omega_0).$$

With these notations, the maximal DC current at ω_0 can be expressed as

$$I_{max} = \frac{1}{2} I_0 \frac{\delta^2}{z}.$$

Numerically solving Equation (2.19) gives δ at the resonance frequencies and thus the DC current. Figure 2.4 shows the dependence of this maximal current on the coupling parameter z. For low z values, the maximal current first increases with z until it reaches a maximum for $z \sim 2.92$. The maximal value reached is $I_{max} \sim 0.58 I_0$, which is smaller than I_0. For larger coupling constants, the height of the resonance peak decreases slowly. To understand what happens when $z > 2.92$, it is instructive to focus on the shape of the current-voltage characteristic in the vicinity of a resonance.

Around a resonance frequency ω_0, we can develop $Y_e(\omega_J) + iC\omega_J$ and write

$$Y_e(\omega_J) + iC\omega_J = G_e \left(1 + i\xi \right),$$

with

$$\xi = \frac{\omega_J - \omega_0}{G_e} \frac{d}{d\omega_J} \left(\Im \left(Y_e(\omega_J) \right) + C\omega_J \right).$$

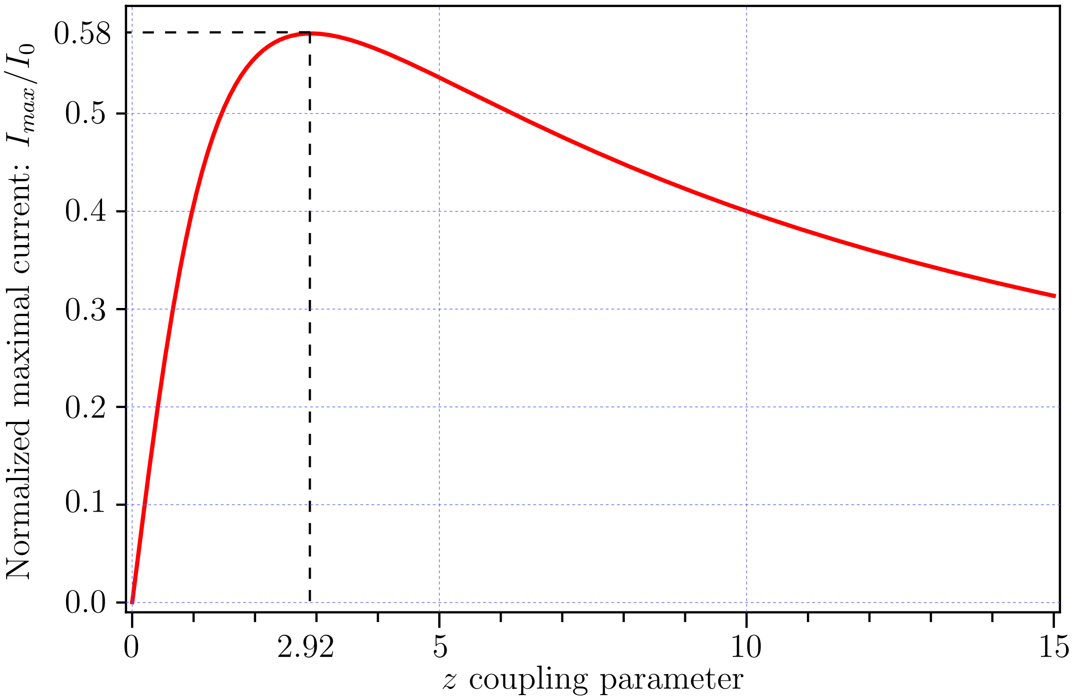

Figure 2.4.: Maximal DC current as a function of the coupling parameter z.

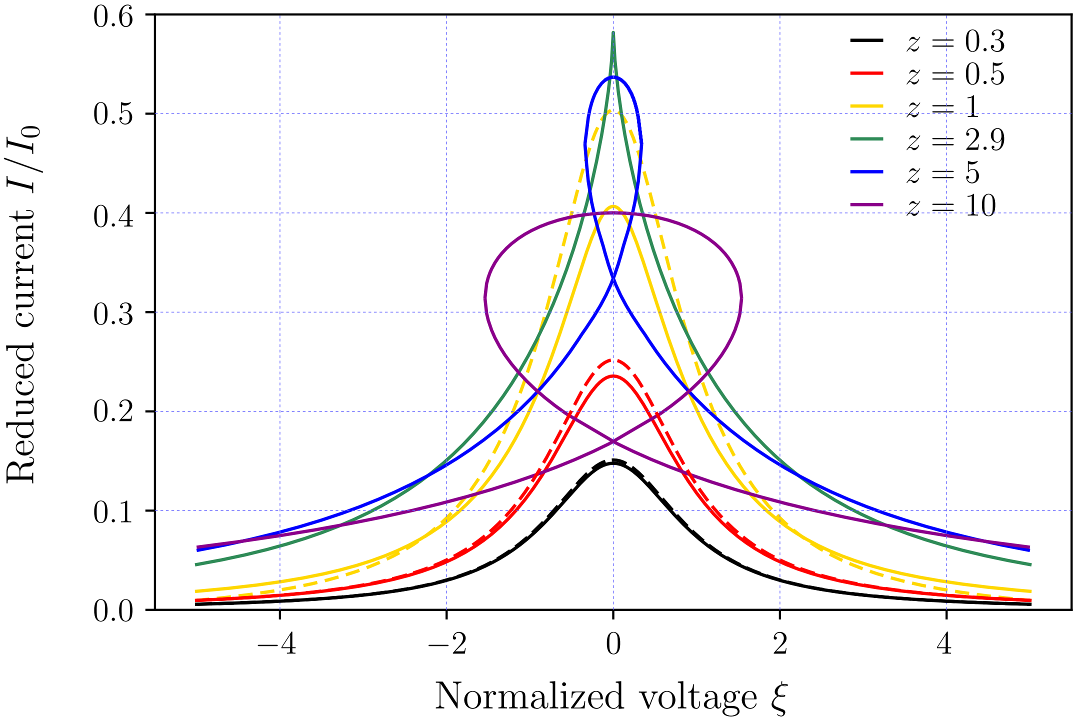

Figure 2.5.: Shape of the resonance peak for coupling parameter z from 0.3 to 10.

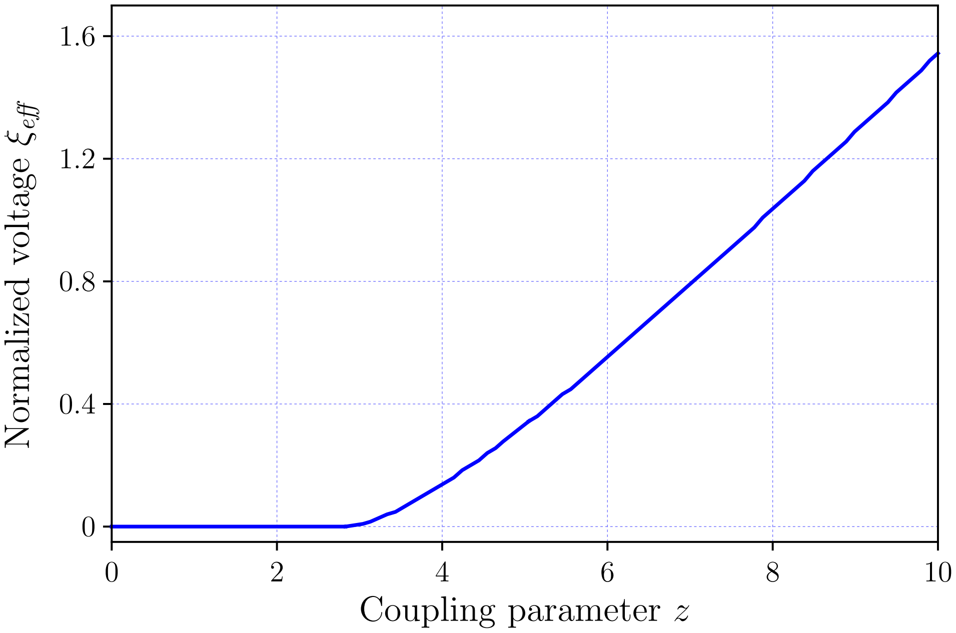

Figure 2.6.: Effective peak position ξ_{eff}.

With these notations, Equation (2.18) can be rewritten

$$\left(\frac{1}{J_0(\delta)+J_2(\delta)}\right)^2+\left(\frac{\xi}{J_0(\delta)-J_2(\delta)}\right)^2=\left(\frac{z}{\delta}\right)^2. \tag{2.20}$$

This equation can be solved numerically to give the amplitude of the phase oscillations δ for an admittance Y_e at a voltage ξ. Figure 2.5 shows the DC current obtained by solving Equation 2.20 for z between 0.3 and 10. The dashed lines are obtained with the Lorentzian approximation of Section 2.1.4. When z is small, resonance peaks have a smooth shape ($z = 0.3$, 0.5 and 1 in the picture) and are close to the Lorentzian approximation. For $z < 0.5$, the relative error made with the approximation is below 5%. When z approaches the critical 2.92 value of Figure 2.4 (green curve), the peak becomes sharper and forms a cusp at the resonance frequency ($\xi = 0$). For larger z, a loop appears above the cusp and the height of the peak reduces. The loop also gets wider when z increases. For even higher z (above ~ 38), the loop is disconnected from the bottom branch and when $z > 130$, a third manifold is also possible [69].

In the loops, there is a voltage for which $dI/d\xi \to \infty$. The biasing for the part of the loop above this current becomes unstable, such that the measured voltage at the maximum of current is not the resonance voltage. Figure 2.6 shows the position of the effective peak maximum ξ_{eff} as a function of the parameter z from 0 to 10. $\xi_{eff} = 1$ corresponds to an effective frequency $\omega_{eff} = \omega_0\,(1 + 1/(2Q))$, which is displaced from the true resonance frequency ω_0 by half the width of the peak. This can make quite noticeable changes in the spectrum.

Figure 2.7 emphasizes the different peak shapes with the same maximal value. The curves with $z = 5$ and 10 from Figure 2.5 are plotted in full lines and peaks with the same I_{max} and smaller z are plotted in dashed lines. The width of the peak is larger for the large z parameters.

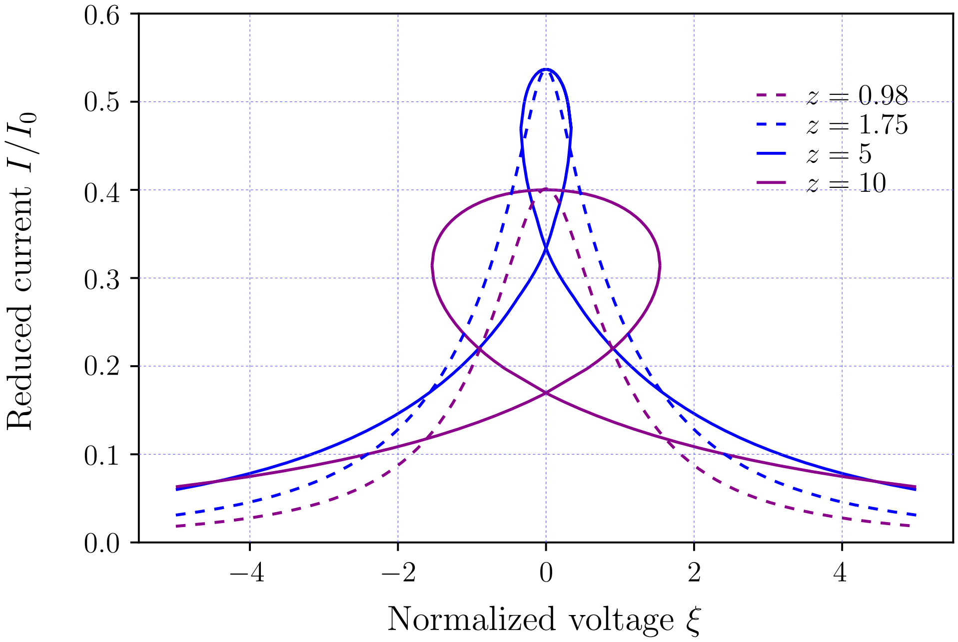

Figure 2.7.: Shape of the resonance peak for the same maximal value but different z.

2.1.5. The series resonator

For the series resonator, the total admittance Y_e (including the biasing circuit) is

$$Y_e = \frac{1}{R_b} + \frac{1}{R + i\omega L_e + \frac{1}{i\omega C_e}}.$$

The situation is thus quite different from the parallel resonator.

For low frequencies, $\omega \ll \min\left(1/(RC_e), 1/(R_b C)\right)$, all capacitors can be considered as open circuits, such that the junction only sees the bias resistance and the shape of the current-voltage characteristic is described by the universal shape of Section 1.2.2.

For barely larger frequencies, the capacitors have to be considered, such that the total admittance seen by the junction is

$$Y_e \sim \frac{1}{R_b} + iC_e\omega.$$

The equivalent circuit (including the junction capacitance) is thus that of Figure 2.8.

When applying a bias current I to that circuit, the Kirchhoff's laws give

$$I = \frac{V}{R_b} + I_0 \sin\varphi + (C + C_e)\,\dot{V}.$$

The Josephson relation between voltage and phase yields

$$\frac{I}{I_0} = \frac{\varphi_0\dot{\varphi}}{R_b I_0} + \sin\varphi + \varphi_0\frac{C + C_e}{I_0}\ddot{\varphi}.$$

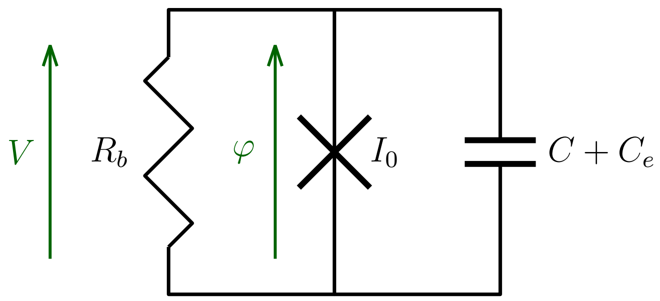

Figure 2.8.: Equivalent circuit of a Josephson junction coupled to a series resonator at low frequency.

Introducing the time constant $\tau = \varphi_0/(R_b I_0)$ and the reduced time $\tilde{t} = t/\tau$, this gives

$$\frac{I}{I_0} = \varphi' + \sin\varphi + \frac{R_b^2\,(C + C_e)\,I_0}{\varphi_0}\varphi'', \tag{2.21}$$

where the prime symbol denotes differentiation with respect to $\tilde{t}$. The solutions $\varphi(\tau)$ of this equation depend only on the parameter

$$\beta_C = \frac{R_b^2\,(C + C_e)\,I_0}{\varphi_0},$$

which is a generalization of the Stewart-McCumber parameter of Equation (1.43). A small β_C corresponds to a small capacitance and thus to a situation close to Equation (1.48) where only a bias resistor is present. Equation (2.21) is not analytically solvable. Applying usual numerical methods to solve it is difficult as the period of the solution depends greatly on the bias current (as for the resistive case for which some solutions are plotted in Figure 1.11). The period can be large for small bias, resulting in a tedious numerical integration. Nevertheless, this equation was numerically analyzed with AUTO [70], a software for continuation and bifurcation problems in ordinary differential equations. This software finds the period of the solutions and is thus able to compute the solutions. Figure 2.9 shows the resulting averaged current-voltage characteristic for various β_C parameters. For small β_C, the solutions are close to the shape calculated in Section 1.2.2. For larger β_C, the current decreases faster to its zero limit at high voltages.

At high frequencies, the junction capacitance dominates the admittance, such that the a_n coefficients are quite small, and the average current is zero.

For intermediate frequencies, the total admittance of the system is

$$Y_e + i\omega C = \frac{1}{R_b} + i\omega C + \frac{1}{R + i\omega L_e + \frac{1}{i\omega C_e}}.$$

It is possible to observe noticeable deviations from the resistive and capacitive behaviors when the admittance of the resonator becomes of the order of $1/R_b + i\omega C$. The maximal admittance for the resonator is achieved when $\omega = \omega_e = 1/\sqrt{L_e C_e}$. At this frequency, it is $1/R$. If R is larger than R_b, the resulting change in the admittance is small. On the other hand, if $R < R_b$,

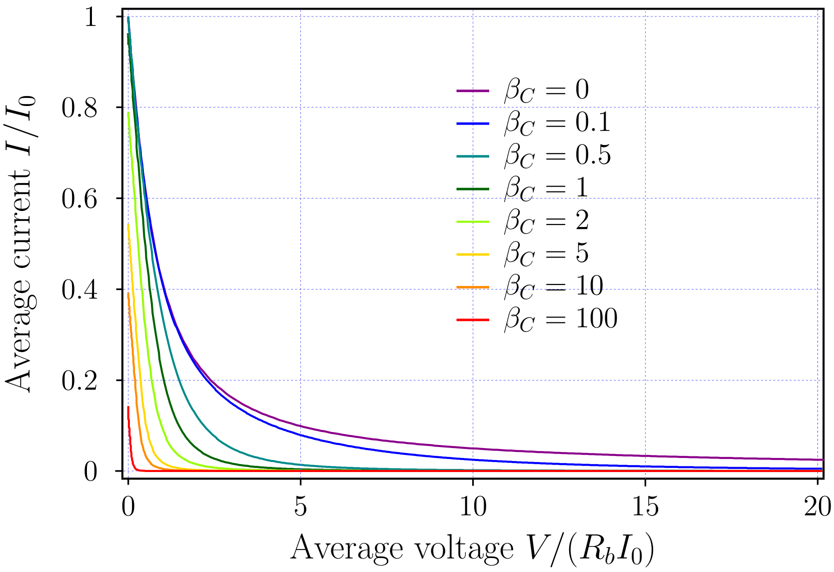

Figure 2.9.: Current voltage characteristic of a resistively and capacitively shunted Josephson junction.

there is a peak in $\Re(Y_e)$ at ω_e, as well as a peak in $\Re(1/(Y_e + i\omega C))$ at the frequency ω_0, such that,

$$\Im\left(Y_e\right) + i\omega_0 C = 0,$$

which can here be rewritten as

$$\omega_0 = \omega_e \left(1 + \frac{C_e}{C}\right)^{\frac{1}{2}}.$$

The peak in $\Re(Y_e)$ leads to a current drop at ω_e and the peak in the real part of the impedance leads to a current peak at ω_0.

The resonance frequency ω_0 appears as the resonant frequency of an LC resonator with inductance L_e and capacitance the series combination of C and C_e, $CC_e/(C + C_e)$. The frequency shift is in the other direction as for the parallel resonator, such that the measured peak frequency is always larger than the true resonator frequency.

For small C/C_e ratios, the peak at ω_0 can be at high frequency, where the resonator capacitor can be considered as a short-circuit. For large C/C_e ratios, $\omega_0 \sim \omega_e$. In that case, the junction capacitance shunts most of the microwave current, resulting in a smaller peak.

The current peak at frequency ω_0 can be described independently of the current dip at frequency ω_e if $\omega_0 \gg \omega_e$. In that case, the calculations of Section 2.1.4 for the parallel resonator hold true. However, when $\omega_0 \sim \omega_e$, the description below is more adapted (in the limit of large C/C_e ratio).

As the current is quite small already (for tunnel junctions), the current drop is almost invisible, except at low frequencies where the current can be higher. For voltages above $2\Delta/e$, there is also a large quasiparticle current, on which the current drop can also be observed. If junctions with less opaque transmission channels are used, the current in absence of resonator is higher, such that the current dip is noticeable.

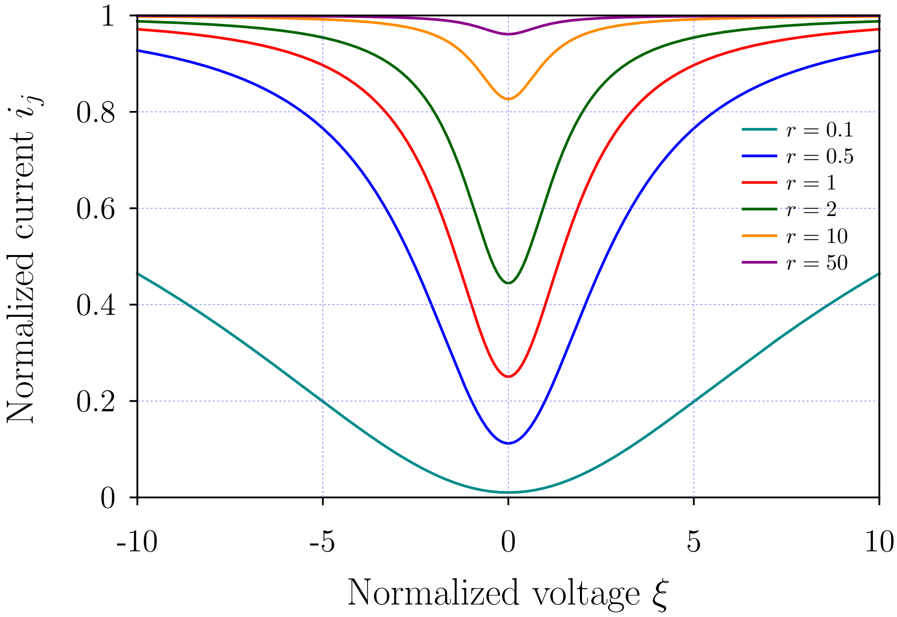

Figure 2.10.: Reduced current-voltage characteristic of a junction coupled to a series resonator with $C/(QC_e) = 0$, $z = 0.1$.

To estimate its depth, we write the phase difference as

$$\varphi = \theta_0 + \omega_J t + \delta \sin \omega_J t. \tag{2.22}$$

This leads to the same Harmonic-Balance equation as for the parallel resonator. Around the resonance frequency ω_e, the impedance Z_r of the resonator can be expanded in Taylor series, such that

$$Z_r = R\left(1 + i\xi\right),$$

with

$$\xi = \frac{\omega_J - \omega_0}{R} \frac{d}{d\omega_J} \Im\left(Z_r(\omega_J)\right).$$

The total admittance seen by the junction (including the bias resistor and the junction capacitance) is thus

$$Y_e\left(\omega_J\right) + i\omega_J C = \frac{1}{R_b} + i\omega_J C + \frac{1}{R}\frac{1}{1+i\xi},$$

Substituting this expression in the Harmonic-Balance Equation (2.18) leads to

$$\left(\frac{\frac{1}{R_b} + \frac{1}{R}\frac{1}{1+\xi^2}}{J_0\left(\delta\right) + J_2\left(\delta\right)}\right)^2 + \left(\frac{\omega_J C - \frac{1}{R}\frac{\xi}{1+\xi^2}}{J_0\left(\delta\right) - J_2\left(\delta\right)}\right)^2 = \left(\frac{I_0}{\delta\varphi_0\omega_J}\right)^2.$$

Multiplying this expression by R^2 gives

$$\left(\frac{r + \frac{1}{1+\xi^2}}{J_0\left(\delta\right) + J_2\left(\delta\right)}\right)^2 + \left(\frac{\frac{1}{Q}\frac{C}{C_e}\frac{\omega_J}{\omega_e} - \frac{\xi}{1+\xi^2}}{J_0\left(\delta\right) - J_2\left(\delta\right)}\right)^2 = \left(\frac{z}{\delta}\right)^2,$$

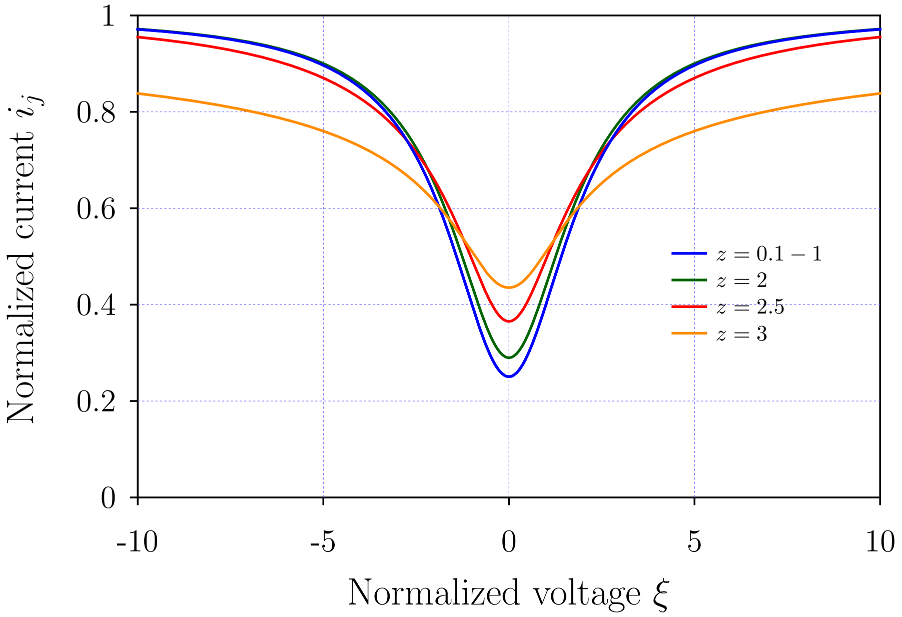

Figure 2.11.: Reduced current-voltage characteristic of a junction coupled to a series resonator with $C/(QC_e) = 0$, $r = 1$.

where $r = R/R_b$ is the ratio of the resonator resistance to the bias resistance, $Q = 1/R\sqrt{L_e/C_e}$ is the quality factor of the series resonator and $z = RI_0/\omega_e$ is the coupling parameter. Figures 2.10, 2.11 and 2.12 show the effects of the different parameters z, r and $C/(QC_e)$ on the resulting current dip. The normalized current i_j is the DC current divided by its value without the resonator, which is quite small for tunnel junctions and depend on the bias resistor R_b.

First, the ratio $C/(QC_e)$ was taken equal to zero, which is a good approximation if the quality factor of the resonator is large, and the ratio of capacitances C/C_e is not too small. In that case, the current dip is more significant for smaller R/R_b ratios, as shown in Figure 2.10. This behavior was expected, as, at resonance, the impedance of the resonator is R. A large R/R_b ratio implies that the alternative current mainly flows through the bias resistor R_b and thus makes only a small change in the DC current.

Keeping $C/(QC_e) = 0$, the effect of the coupling parameter z was then investigated. The resulting current-voltage characteristics are plotted in Figure 2.11. For small z values, the shape of the dip is not affected. Only for $z > 1$ does it change. It gets wider and less deep for larger z.

Finally, the $C/(QC_e)$ ratio is changed with a constant $r = 1$ and $z = 1$. When it increases, the dip first becomes less deep and moves to lower voltages. For large enough ratio, a peak appears at a larger voltage than the dip voltage, getting higher and higher for larger ratios. For large ratio, the peak height decreases, and the current becomes flat. This peak is at the frequency ω_0 and cancels the dip when $\omega_0 \to \omega_e$.

For tunnel junctions, in the limit of small $C/(QC_e)$ ratio, the current dip at ω_e is not observable, as the background current is quite small. However, it can have visible effects when probing a system exhibiting a parallel type resonance at a frequency ω_r close to ω_e in

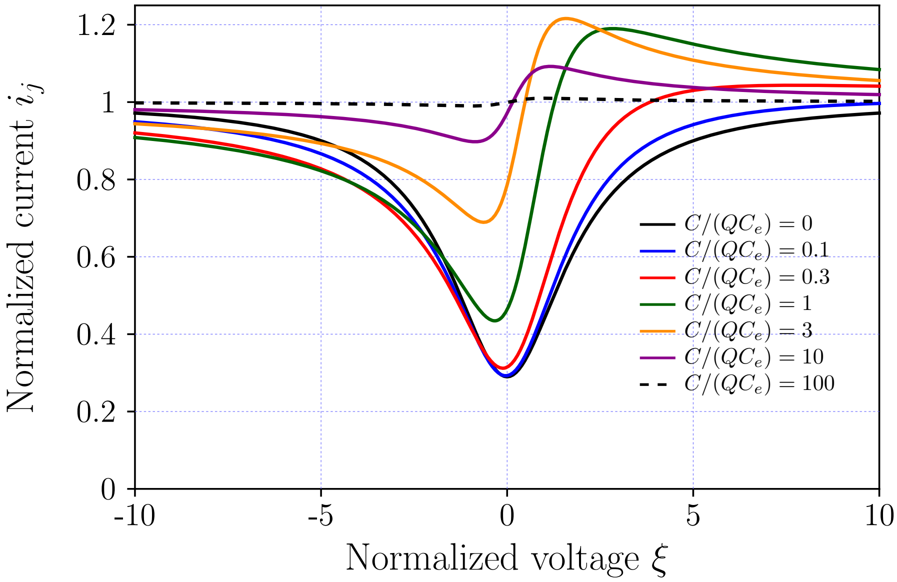

Figure 2.12.: Reduced current-voltage characteristic of a junction coupled to a series resonator with $r = 1$, $z = 1$.

presence of a series mode at ω_e. The expected peak at ω_r is readily reduced due to the peak of admittance of the series resonator.

When considering the coupling to a series resonator, it is possible to transform the resonances into parallel type resonances and therefore get a larger signal in the current-voltage characteristic. To do so, an inductance can be added in parallel of the resonator, such that the impedance is zero at low frequencies. For instance, for the spectroscopy of the Andreev Bound States [32] in an atomic contact, a large Josephson junction (equivalent to an inductor) was added in parallel because the admittance of the ABS in a weak link with high transmission diverges at the transition frequency between the two levels [71], such that the weak link can be represented by a series resonator.

2.1.6. Implementations and limits of the single junction spectrometer

Already in 1966, Josephson junctions were proposed as microwave generators for frequencies up to 1 THz [72]. One year later, the principle of absorption spectroscopy was demonstrated by Silver and Zimmerman in 1967 when they measured the nuclear magnetic resonance of Co^{59} at 218 MHz [21]. The inelastic Cooper pair tunneling was afterwards extensively used to explain current peaks in current-voltage characteristics of SQUIDs in the 1970s and 1980s [22–25].

Resonant modes of microresonators [26, 27] and transmission lines [28] were measured using the same principle. Josephson junctions have also been used to measure transitions between energy levels of another junction [29], a SQUID [30] or a single-Cooper-pair transistor [31].

More recently, absorption spectroscopy of a mesoscopic system using a Josephson junction was demonstrated by the Quantronics group at Saclay [32, 33]. Figure 2.13 shows the electric schematic of this spectrometer as well as the measured spectrum for the Andreev Bound States in an atomic contact. The spectrometer is the yellow Josephson junction in Figure 2.13a and

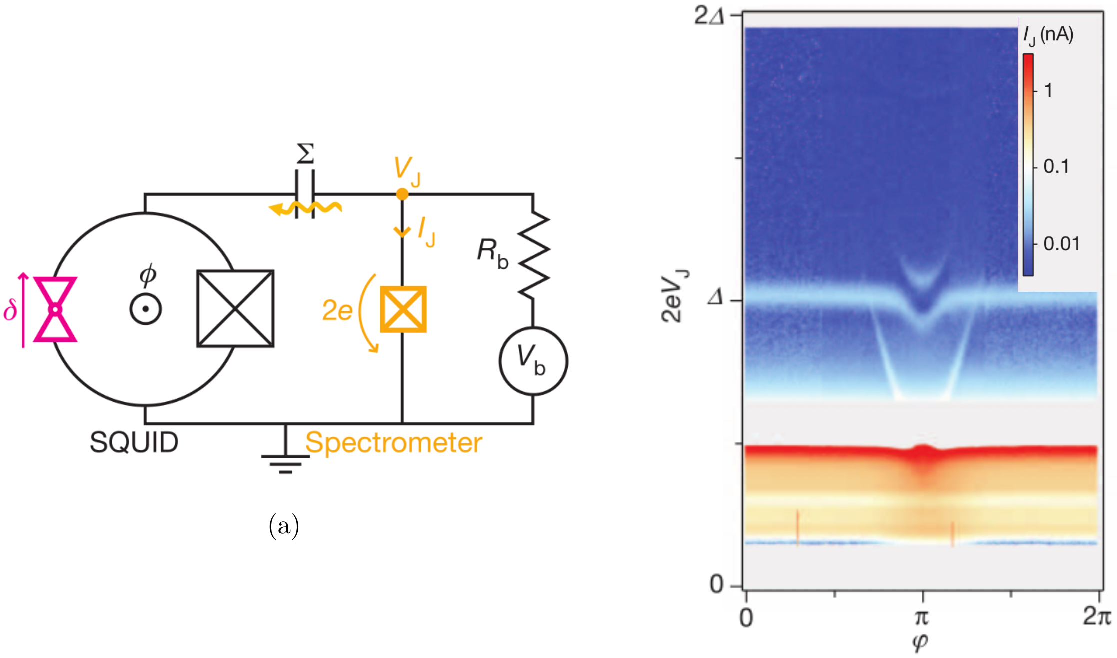

(a)

(b)

Figure 2.13.: The Quantronics spectrometer, taken from [32]: (a) Schematic of the Quantronics spectrometer, capacitively coupled to an atomic contact SQUID and (b) Spectrum of the ABS in an atomic contact with two channels of transmission 0.942 and 0.26 as a function of the reduced flux in the SQUID loop. The colors represent the current in the junction according to the color scale and grey means no data because the bias is unstable.

the pink superconducting atomic contact is a mechanical break junction between two aluminum electrodes: it is only a few atoms wide. The Josephson junction spectrometer is coupled to the atomic contact via the large capacitor Σ, allowing microwave photons to access the contact and blocking the DC bias. The atomic contact together with a larger Josephson junction makes a SQUID, allowing for control of the phase difference φ by applying a magnetic flux in the SQUID. Figure 2.13b shows the measured spectrum for an atomic contact with two conduction channels of transmissions 0.942 and 0.26 (these transmissions were measured independently).

The most prominent feature in the spectrum is the plasma frequency of the SQUID (the almost flat red line around $\Delta/2$) and its harmonic around Δ. Along these two lines, two white lines showing a larger modulation with respect to the reduced flux φ can be seen. The one with the lowest energy corresponds to the excitation of a negative Andreev bound state $|-\rangle$ to the corresponding positive bound state $|+\rangle$. The energy difference is $2\Delta\sqrt{1-\tau\sin^2\varphi/2}$, as shown in Section 1.1.2. The second line corresponds to a two-photon process: the excitation of the Andreev transition with one photon and the excitation of the SQUID plasma frequency with another.

This spectrum is quite promising as the Andreev transition can easily be seen, but there are three main drawbacks:

1. low energies cannot be reached because of the supercurrent peak,
2. there are a lot of spurious resonances (in particular at low energy) due to an uncontrolled electromagnetic environment. They were subtracted in the data shown here but are visible in the Supplementary Information of Ref. [32],
3. the signal becomes weaker at higher energy. This is due to the intrinsic capacitance of the junction shunting efficiently the microwave signal at high frequency.

These three issues can efficiently be addressed by using a SQUID instead of a single junction.

2.2. The SQUID-based spectrometer

As introduced in Section 1.3, applying a magnetic field through the loop of a SQUID can modify its critical current and create a current circulating around the loop. Biasing the SQUID at half a flux quantum allows for a smaller critical current which can reach 0 with a symmetrical interferometer. This fully removes the inaccessible low energy range of the single junction spectrometer.

Biasing a SQUID at half a flux quantum also allows for a better isolation from the biasing circuit and thus reduces the amount of spurious resonances. At $\Phi_e = \Phi_0/2$, the phases of the two Josephson junctions of the SQUID are opposite. This corresponds to AC currents of the same magnitude but opposite signs (in the case of a symmetrical device). This situation is represented in Figure 2.14b. The dashed lines are connected to the biasing and measurement circuits which close the circuits. Figure 2.14a correspond to having a flux bias of 0 in the loop and is the same excitation as with a single junction. In that case, the AC Josephson current can circulate everywhere, including in the bias circuit, whereas when $\Phi_e = \Phi_0/2$, it is confined in the loop.

In the rest of this section, these two excitation modes are described in more details.

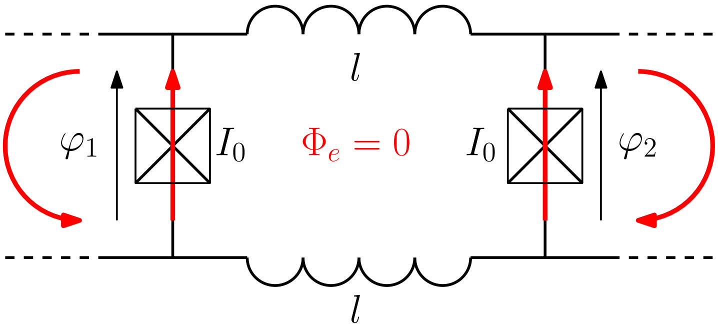

(a) The off-loop mode

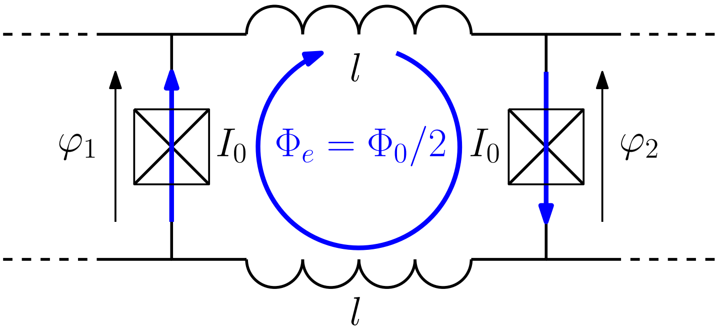

(b) The in-loop mode

Figure 2.14.: Electric diagram of a spectrometer based on a symmetrical SQUID. The l inductors model the SQUID loop inductance. $\Phi_e = 0$ or $\Phi_0/2$ is the flux threading the loop.

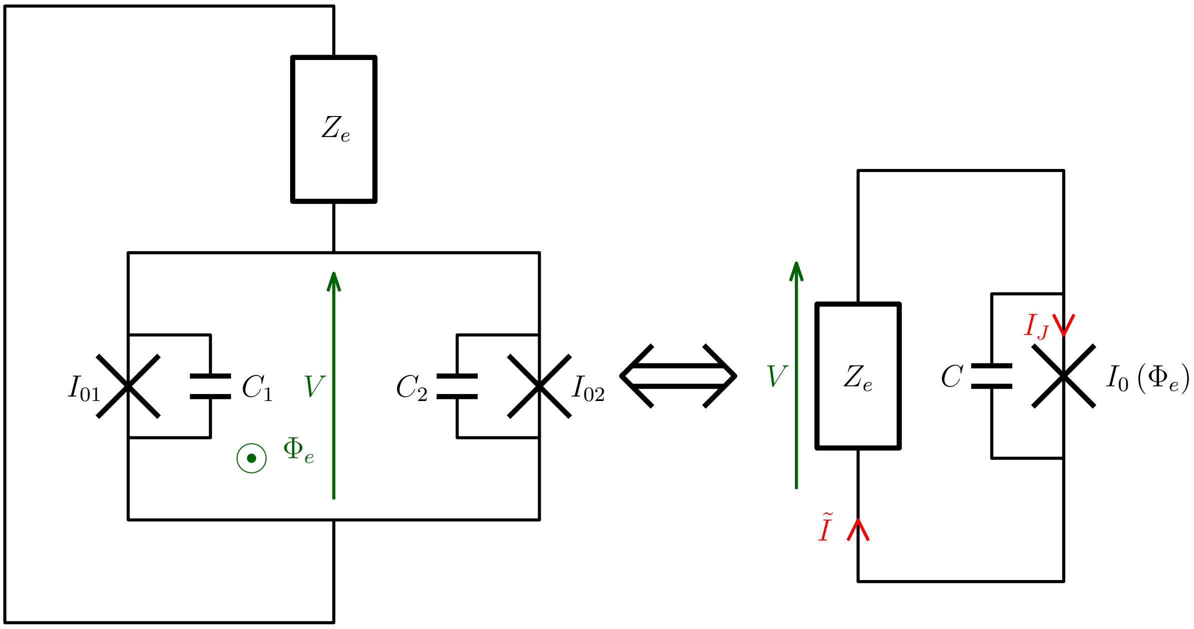

Figure 2.15.: SQUID connected to an impedance Z_e out of the loop. I_{01} and I_{02} are the critical currents of the junctions and C_1 and C_2 their intrinsic capacitances. Φ_e is the external magnetic flux. The two representations are equivalent if $C = C_1 + C_2$ is the association of C_1 and C_2 in parallel and $I_0(\Phi_e)$ is the critical current of the SQUID calculated in Section 1.3.

2.2.1. Off-loop mode

Consider the off-loop mode in the circuit shown in Figure 2.15 where a SQUID is connected to an external impedance Z_e. Because Z_e is out of the loop, the SQUID can be considered as a Josephson junction with tunable critical current $I_0(\Phi_e)$ and a capacitance $C = C_1 + C_2$. An expression for $I_0(\Phi_e)$ can be found in Section 1.3. It is always maximal at $\Phi_e = 0$ and minimal at $\Phi_e = \Phi_0/2$. This makes the measured signal maximal when there is no flux in the loop.

2.2.2. In-loop mode

If the device under test is located in the loop, as shown in Figure 2.16, the situation is different. As the current in the loop is maximal at half a flux quantum, we should expect the signal to also be maximal at the same flux bias. Only parallel resonators are considered in this configuration because a series resonator has an infinite impedance at zero frequency and forbids flux biasing.

In a first time, the biasing circuit is not included in the calculations as it is out of the loop. Its role will be described in Section 2.2.3. In that case, the current $\tilde{I}$ flowing through the impedance is given by

$$\tilde{I} = I_{02}\sin\varphi_2 + C_2\varphi_0\ddot{\varphi}_2 - I_{01}\sin\varphi_1 - C_1\varphi_0\ddot{\varphi}_1,$$

where φ_1 and φ_2 are the phase differences across the junctions. In average, their difference is

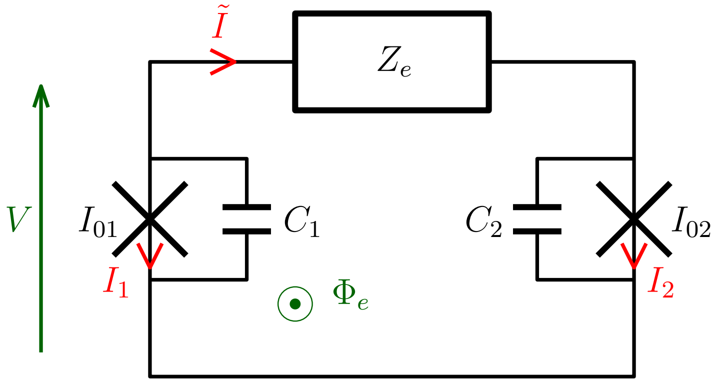

Figure 2.16.: SQUID connected to an impedance Z_e in the loop. I_{01} and I_{02} are the critical currents of the junctions and C_1 and C_2 their intrinsic capacitances. Φ_e is the external magnetic flux.

given by the flux Φ_e,

$$\overline{\varphi_2 - \varphi_1} = \frac{\Phi_e}{\varphi_0}.$$

In addition to these equations, the voltage drop across the impedance follows

$$\mathcal{Y}_e \left[\varphi_0 \left(\dot{\varphi}_1 - \dot{\varphi}_2\right)\right] = \tilde{I},$$

where $\mathcal{Y}_e$ is a linear operator with its Fourier transform being the admittance Y_e. The differential equation governing this circuit is thus

$$\mathcal{Y}_e \left[\varphi_0 \left(\dot{\varphi}_1 - \dot{\varphi}_2\right)\right] = I_{02} \sin \varphi_2 + C_2 \varphi_0 \ddot{\varphi}_2 - I_{01} \sin \varphi_1 - C_1 \varphi_0 \ddot{\varphi}_1. \tag{2.23}$$

As for the single junction spectrometer, it is possible to expand φ_1 and φ_2 in Fourier series to re-express Equation (2.23) in terms of the Fourier coefficients of φ_1 and φ_2. This gives the same type of equation as Equation (2.7) which we can solve in the same limits.

The zeroth order approximation

In the zeroth order approximation (and thus in the high-frequency limit), when the two Josephson junctions are biased at the same voltage V, the phase difference across them have the form $\varphi_i = \theta_{0i} + \omega_J t$ where $\omega_J = V/\varphi_0$ is the Josephson frequency and θ_{0i} are integration constants. This will generate alternative currents in each junction $I_i = I_{0i} \sin\left(\theta_{0i} + \omega_J t\right)$. They have the same frequency but are dephased because of the magnetic flux in the loop: $\varphi_2 - \varphi_1 = \theta_{02} - \theta_{01} = \varphi_e$ (in the case of negligible loop inductance).

The current flowing through the external system of impedance Z_e is

$$\tilde{I} = I_2 \frac{Y_{e2}}{Y_{\Sigma 2}} - I_1 \frac{Y_{e1}}{Y_{\Sigma 1}},$$

where Y_{ei} is the admittance seen by junction $i = 1, 2$ in parallel of its own capacitance and $Y_{\Sigma i}$ is the total admittance seen by junction i including its own capacitance. Each junction sees the other junction as a current source and therefore as an open circuit, implying

$$\begin{cases} Y_{ei}^{-1}(\omega) = Z_e(\omega) + \dfrac{1}{i\omega C_j}, \\ Y_{\Sigma i}(\omega) = Y_{ei}(\omega) + i\omega C_i. \end{cases}$$

In these definitions, when subscript i stands for junction 1, subscript j denotes junction 2 and vice versa. These expressions are only valid in the high-frequency limit ($\omega \gg \omega_p$). At low frequency (below the plasma frequency), $\tilde{I}$ is simply $I_2 - I_1$.

Because the intrinsic capacitance and the critical current of a Josephson junction are both proportional to the surface of the junction, $I_{02}/I_{01} = C_2/C_1$. If we call this ratio α and define I_C and C_0 such that $I_{01} = I_C$, $I_{02} = \alpha I_C$, we get $C_1 = C_0$ and $C_2 = \alpha C_0$. With these notations,

$$\begin{cases} Y_{e1}^{-1}(\omega) = Z_e(\omega) + \dfrac{1}{i\omega\alpha C_0} \\ Y_{\Sigma 1}(\omega) = \dfrac{1}{Z_e(\omega) + \frac{1}{i\omega\alpha C_0}} + i\omega C_0 \end{cases} \text{and} \begin{cases} Y_{e2}^{-1}(\omega) = Z_e(\omega) + \dfrac{1}{i\omega C_0} \\ Y_{\Sigma 2}(\omega) = \dfrac{1}{Z_e(\omega) + \frac{1}{i\omega C_0}} + i\omega\alpha C_0 \end{cases}.$$

$\tilde{I}$ can be expressed as

$$\tilde{I} = I_C \left(\frac{\alpha e^{i\varphi_2}}{1 + \alpha + i\omega_J \alpha C_0 Z_e(\omega_J)} - \frac{e^{i\varphi_1}}{1 + \frac{1}{\alpha} + i\omega_J C_0 Z_e(\omega_J)} \right).$$

The complex amplitude of $\tilde{I}$ is therefore

$$\tilde{I}_{\omega_J} = 2I_C \frac{1}{1 + \frac{1}{\alpha} + i\omega_J C_0 Z_e(\omega_J)} \sin\frac{\varphi_e}{2}. \tag{2.24}$$

The dissipated power is given by $\mathcal{P}_r = \frac{1}{2}\left|\tilde{I}_{\omega_J}\right|^2 \Re(Z_e(\omega_J)) = \frac{1}{2}\left|\tilde{I}_{\omega_J} Z_e(\omega_J)\right|^2 \Re(Y_e(\omega_J))$. With Equation (2.24) for $\tilde{I}$, the power can be expressed as:

$$\mathcal{P}_r = 2I_C^2 \left(\sin\frac{\varphi_e}{2}\right)^2 \frac{\Re(Y_e(\omega_J))}{\left|\left(1 + \frac{1}{\alpha}\right) Y_e(\omega_J) + i\omega_J C_0\right|^2}.$$

Again, it is a positive quantity for a dissipative system. It is maximal at ω_0 such that

$$\boxed{\Im(Y_e(\omega_0)) = -\frac{\alpha}{1+\alpha} C_0 \omega_0 = -C_s \omega_0,} \tag{2.25}$$

where C_s is the series combination of C_0 and αC_0. Such a frequency exists, providing that the external system has an inductive part ($\Im(Y_e) < 0$).

The maximal dissipated power at frequency ω_0 can be expressed as

$$\mathcal{P}_{r,max} = \frac{1}{2}\left(\frac{2\alpha}{1+\alpha}\right)^2 I_C^2 \left(\sin\frac{\varphi_e}{2}\right)^2 \frac{1}{\Re(Y_e(\omega_0))}. \tag{2.26}$$

Both Equations (2.25) and (2.26) show that the in-loop mode is formally equivalent to the off-loop mode of a junction with capacitance $C_s = C_0\alpha/(1+\alpha)$ and critical current I_0',

$$I_0' = \frac{2\alpha}{1+\alpha} I_C \sin\frac{\varphi_e}{2}.$$

Putting an external system inside the loop of a SQUID appears to be a promising direction, as the dissipated power in an in-loop mode is maximal at half a flux quantum, that is to say when the coupling to the off-loop mode (and therefore the bias circuit) is minimal. However, there is a drawback to this which is described below.

If we consider a SQUID with no external system in the loop, $Y_e(\omega)$ is simply $-i(\omega L)^{-1}$ with L the inductance of the superconducting loop. There is an intrinsic resonance frequency ω_S of the SQUID, such that $\omega_S = 1/\sqrt{LC_s}$. This intrinsic resonance appears as the LC mode formed of the total inductance of the loop and the series combination of the capacitances of the junctions.

It is possible to go around this intrinsic SQUID loop mode by carefully designing the spectrometer in order to have this mode out of the working range of the spectrometer. For instance, if the loop length is of the order of 10 µm, the corresponding inductance is roughly $L \sim 10\,\mathrm{pH}$. With typical junction capacitance of 50 fF, this makes a resonance frequency around 225 GHz which is above $4\Delta/h$ for aluminum ($\sim 180\,\mathrm{GHz}$).

When working with superconductors with larger superconducting gaps, this mode stays in the middle of the operating range of the spectrometer. Using smaller junctions with higher supercurrent density, it is possible to decrease the capacitance while keeping the critical current almost constant. This allows pushing the resonant SQUID loop mode to higher frequencies without decreasing the signal. However, this has some limitations. A too high supercurrent density can degrade the oxide, giving rise to larger subgap currents.

In-loop mode in the first order approximation

As for the single junction case, we add sine terms to the expression of the phase differences φ_1 and φ_2,

$$\begin{cases} \varphi_1 = \theta_1 + \omega_J t + \delta_1 \sin\omega_J t, \\ \varphi_2 = \theta_2 + \omega_J t + \delta_2 \sin\omega_J t. \end{cases}$$

The applied flux Φ_e imposes

$$\varphi_e = \overline{\varphi_2 - \varphi_1} = \theta_2 - \theta_1,$$

where the horizontal bar symbol denotes temporal averaging. The current circulating in the loop obeys

$$\mathcal{Z}_e\left[\tilde{I}\right] = \varphi_0(\dot\varphi_1 - \dot\varphi_2) = \varphi_0(\delta_1 - \delta_2)\omega_J \cos\omega_J t.$$

The current $\tilde{I}$ is also related to I_1 and I_2 by

$$\tilde{I} = I_2^{(\omega_J)} \frac{1}{1+\alpha+i\alpha C_0\omega_J Z_e} - I_1^{(\omega_J)} \frac{1}{1+\frac{1}{\alpha}+iC_0\omega_J Z_e},$$

$$\tilde{I} = \frac{1}{1+\alpha+i\alpha C_0\omega_J Z_e}\left(I_2^{(\omega_J)} - \alpha I_1^{(\omega_J)}\right),$$

where $I_{1,2}^{(\omega_J)}$ are the components at frequency ω_J of I_1 and I_2. In the bottom branch of the SQUID, Kirchhoff's laws impose

$$I_1^{(\omega_J)} + I_2^{(\omega_J)} + I_{C1}^{(\omega_J)} + I_{C2}^{(\omega_J)} = 0,$$

where $I_{C1(2)}$ is the current flowing through the capacitor of junction 1(2). It is given by

$$\begin{cases} I_{C1}^{(\omega_J)} &= -C_0\omega_J^2\varphi_0\delta_1, \\ I_{C2}^{(\omega_J)} &= -\alpha C_0\omega_J^2\varphi_0\delta_2. \end{cases}$$

Substituting these expressions in Kirchhoff's law gives

$$I_1^{(\omega_J)} + I_2^{(\omega_J)} = C_0\omega_J^2\varphi_0\left(\delta_1 + \alpha\delta_2\right).$$

So, we have two equations:

$$\begin{cases} i\varphi_0\omega_J(\delta_1-\delta_2) = \dfrac{1}{(1+\alpha)Y_e + i\alpha C_0\omega_J}\left(I_2^{(\omega_J)} - \alpha I_1^{(\omega_J)}\right), \\ C_0\omega_J^2\varphi_0\left(\delta_1+\alpha\delta_2\right) = \left(I_1^{(\omega_J)} + I_2^{(\omega_J)}\right). \end{cases} \tag{2.27}$$

Using Bessel functions to develop $I_{1(2)}^{(\omega_J)}$, we get

$$\begin{cases} I_1^{(\omega_J)} &= -iI_C\left(J_0(\delta_1)\mathrm{e}^{i\theta_1} - J_2(\delta_1)\mathrm{e}^{-i\theta_1}\right), \\ I_2^{(\omega_J)} &= -i\alpha I_C\left(J_0(\delta_2)\mathrm{e}^{i\theta_2} - J_2(\delta_2)\mathrm{e}^{-i\theta_2}\right). \end{cases}$$

Substituting these expressions in Equations (2.27) give two complex equations to get four real variables (θ_1, θ_2, δ_1 and δ_2). Once these equations have been solved numerically, it is possible to get the DC current flowing out of the SQUID by taking the DC component of $I_1 + I_2$,

$$I_{DC} = I_C\left(J_1(\delta_1)\sin\theta_1 + \alpha J_1(\delta_2)\sin\theta_2\right).$$

In the case of a symmetrical SQUID ($\alpha = 1$), the situation is much simpler, as we can assume $\delta_1 + \delta_2 = 0$ following Ref. [23]. This gives expressions for the sum and differences of phases:

$$\begin{cases} \dfrac{\varphi_2+\varphi_1}{2} = \theta_0 + \omega_J t, \\ \dfrac{\varphi_2-\varphi_1}{2} = \dfrac{\varphi_e}{2} + \delta\sin\omega_J t. \end{cases}$$

The first line of Equation (2.27) can be rewritten

$$i\varphi_0\omega_J(\delta_1-\delta_2) = \frac{1}{2Y_e + iC_0\omega_J}\left(I_2^{(\omega_J)} - I_1^{(\omega_J)}\right). \tag{2.28}$$

This gives

$$\begin{aligned}
\frac{I_1 - I_2}{I_C} &= \sin\left(\theta_2 + \omega_J t + \delta_2 \sin \omega_J t\right) - \sin\left(\theta_1 + \omega_J t + \delta_1 \sin \omega_J t\right) \\
&= 2\cos\left(\theta_0 + \omega_J t\right) \sin\left(\frac{\varphi_e}{2} + \delta \sin \omega_J t\right) \\
&= 2 \sum_{k=-\infty}^{+\infty} J_k(\delta) \sin\left(k\omega_J t + \frac{\varphi_e}{2}\right) \cos\left(\theta_0 + \omega_J t\right) \\
&= \sum_{k=-\infty}^{+\infty} J_k(\delta) \left(\sin\left((k+1)\omega_J t + \frac{\varphi_e}{2} + \theta_0\right) + \sin\left((k-1)\omega_J t + \frac{\varphi_e}{2} - \theta_0\right)\right).
\end{aligned}$$

The component at frequency ω_J is thus

$$\left(\frac{I_2 - I_1}{\alpha I_C}\right)^{(\omega_J)} = 2\left(J_0(\delta)\mathrm{e}^{i\theta_0} + J_2(\delta)\mathrm{e}^{-i\theta_0}\right) \sin\left(\varphi_e/2\right).$$

So, Equation (2.28) gives

$$I_C \sin\left(\varphi_e/2\right) \left(J_0(\delta)\mathrm{e}^{i\theta_0} + J_2(\delta)\mathrm{e}^{-i\theta_0}\right) = -\varphi_0 \delta \omega_J \left(2Y_e + i\omega_J C_0\right).$$

Taking the real and imaginary parts of this equation gives two equations similar to Equation (2.16):

$$\begin{cases} \varphi_0 \delta \omega_J \Re(Y_e) = -\dfrac{J_1(\delta)}{\delta} \cos\theta_0 I_C \sin\left(\varphi_e/2\right), \\ \varphi_0 \delta \omega_J \left(2\Im(Y_e) + C_0\omega_J\right) = -\left(J_0(\delta) - J_2(\delta)\right) \sin\theta_0 I_C \sin\left(\varphi_e/2\right). \end{cases} \tag{2.29}$$

It is also possible to get the Harmonic balance equation to solve to get δ:

$$\left(\frac{2\Re\left(Y_e(\omega_J)\right)}{J_0(\delta) + J_2(\delta)}\right)^2 + \left(\frac{2\Im\left(Y_e(\omega_J)\right) + C_0\omega_J}{J_0(\delta) - J_2(\delta)}\right)^2 = \left(\frac{I_C \sin\left(\varphi_e/2\right)}{\varphi_0 \delta \omega_J}\right)^2. \tag{2.30}$$

When $2\Im\left(Y_e(\omega_0)\right) + C_0\omega_0 = 0$, the phase oscillation amplitude is maximal and $\sin\theta_0 = 0$. The equation to solve to get the maximal phase oscillation amplitude δ is

$$\frac{\delta}{J_0(\delta) + J_2(\delta)} = \tilde{z}.$$

This equation is the same as for the off-loop mode (2.19) with a coupling parameter $\tilde{z}$ slightly different,

$$\tilde{z} = \frac{I_C \left|\sin\left(\varphi_e/2\right)\right|}{2VG_e}.$$

The DC current flowing out of the SQUID can be calculated by taking the DC component of $I_1 + I_2 = I_C\left(\sin\varphi_1 + \sin\varphi_2\right)$. Calling $\varphi_\pm = \left(\varphi_2 \pm \varphi_1\right)/2$, we get

$$\begin{aligned}\frac{I_1+I_2}{I_C} &= 2\sin\varphi_+\cos\varphi_- - \\ &= 2\sum_{k=-\infty}^{+\infty} J_k(\delta)\cos\left(k\omega_J t+\varphi_e/2\right)\sin\left(\theta_0+\omega_J t\right) \\ &= \sum_{k=-\infty}^{+\infty} J_k(\delta)\sin\left((1-k)\omega_J+\theta_0-\varphi_e/2\right)+\sum_{k=-\infty}^{+\infty} J_k(\delta)\sin\left((1+k)\omega_J+\theta_0+\varphi_e/2\right).\end{aligned}$$

The DC component is:

$$\begin{aligned}I_{DC} &= \frac{J_1(\delta)I_C}{2}\left(\sin\left(\theta_0-\varphi_e/2\right)-\sin\left(\theta_0+\varphi_e/2\right)\right) \\ &= -J_1(\delta)I_C\sin\left(\frac{\varphi_e}{2}\right)\cos\theta_0.\end{aligned}$$

At a resonance frequency, $\sin\theta_0=0$, so $\cos\theta_0=\pm1$ and

$$I_{max}=-\cos\theta_0 J_1(\delta)I_C\sin\left(\varphi_e/2\right).$$

This expression can be substituted in Equation (2.29) to give

$$I_{max}=\varphi_0\omega_0\delta^2\Re(Y_e(\omega_0)).$$

Using the definition of $\tilde{z}$, this gives

$$I_{max}=I_C\left|\sin\left(\varphi_e/2\right)\right|\frac{\delta^2}{2\tilde{z}}.$$

As seen in Section 2.1.4, the maximum of $\delta^2/(2z)$ is 0.58. This means that for an optimal coupling, the maximal current for an in-loop mode is also $0.58 I_C\left|\sin\left(\varphi_e/2\right)\right|$.

2.2.3. Comparison between in and off-loop modes

LC resonator

To emphasize on the differences between in-loop and off-loop modes, consider the case of a simple external system: a parallel LC resonator with losses as shown in Figure 2.3(a). A resistance R was added in order to account for losses and quantify dissipation. R is chosen such that the coupling parameter z stays small and the zeroth order approximation is valid. The admittance at frequency ω is $Y_e(\omega)=1/R+iC_e\omega-i/(L_e\omega)$.

If the LC resonator is out of the loop, according to the calculations of Section 2.2.1, the resonance occurs at $\omega_0^{(o)}$ such that $\Im(Y_e(\omega_0^{(o)}))=-\omega_0^{(o)}\left(1+\alpha\right)C_0$. In that case,

$$\begin{cases}\omega_0^{(o)}=\omega_e\left(1+\left(1+\alpha\right)\dfrac{C_0}{C_e}\right)^{-\frac{1}{2}}, \\ \mathcal{P}_{max}^{(o)}=\dfrac{R}{2}I_C^2\left(1+\alpha^2+2\alpha\cos\varphi_e\right).\end{cases} \tag{2.31}$$

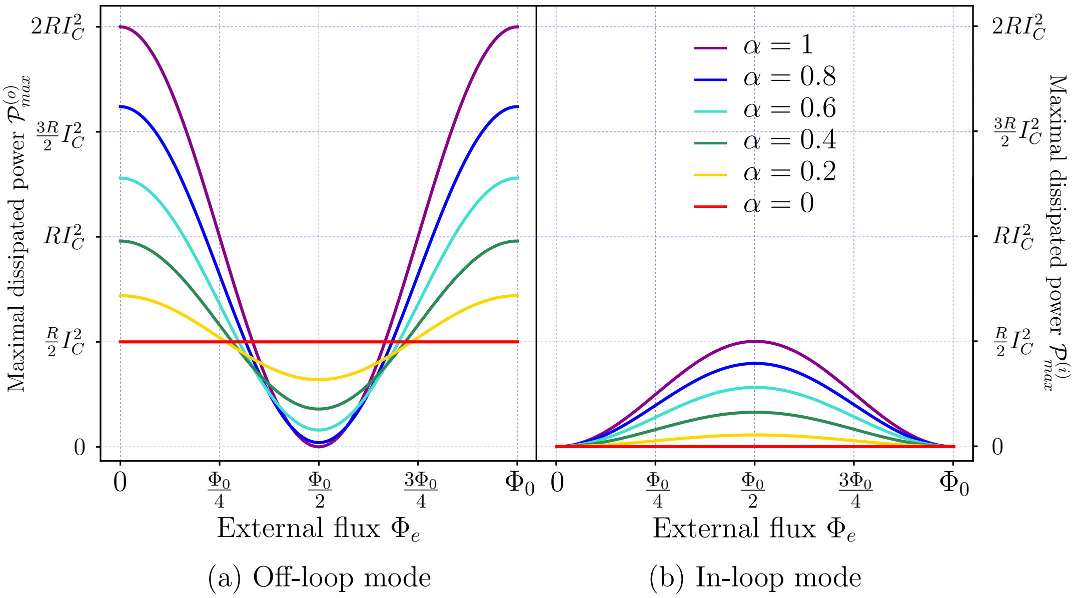

(a) Off-loop mode (b) In-loop mode

Figure 2.17.: Maximal dissipated power in the (a) off-loop mode and (b) in-loop mode as a function of applied magnetic flux for symmetry ratios from 0 to 1.

If the LC resonator is in the loop, the calculations from Section 2.2.2 show that the resonance occurs at $\omega_0^{(i)}$ such that $\Im(Y_e(\omega_0^{(i)})) = -\frac{\alpha}{1+\alpha} C_0 \omega_0^{(i)}$. This gives

$$\begin{cases} \omega_0^{(i)} = \omega_e \left(1 + \dfrac{\alpha}{1+\alpha} \dfrac{C_0}{C_e}\right)^{-\frac{1}{2}}, \\ \mathcal{P}_{max}^{(i)} = \dfrac{R}{2} I_C^2 \left(\dfrac{2\alpha}{1+\alpha} \sin \dfrac{\varphi_e}{2}\right)^2. \end{cases} \tag{2.32}$$

In both cases, the resonance frequency is displaced from its bare value $\omega_e = 1/\sqrt{L_e C_e}$ towards lower frequencies. The resonant frequency is different in the in-loop and in the off-loop modes and depends on the intrinsic capacitances of the junctions. In the off-loop mode, the parallel combination of the two junctions capacitances ($(1+\alpha)\, C_0$) is relevant and in the in-loop mode, it is the series combination ($\alpha C_0/(1+\alpha)$).

Figure 2.17 shows the maximal dissipated power in an RLC resonator located out of the loop (a) and in the loop (b) as a function of the applied magnetic flux Φ_e. The off-loop mode is maximally excited when the flux is a multiple of Φ_0 while the in-loop mode is maximal at $\Phi_0/2$ (Φ_0). This was expected as the loop current is maximal at half a flux quantum and minimal at 0 flux bias.

For the off-loop mode, the maximal dissipation occurs at multiples of Φ_0. With this flux, the dissipated power can reach $2RI_C^2$ for $\alpha = 1$. For an asymmetrical SQUID, the dissipation is less and is proportional to $(1+\alpha)^2$ so it is always non-zero. At half a flux quantum, the dissipation is minimal and goes as $(1-\alpha)^2$. In the case of a symmetrical SQUID, there is no dissipation at all as all the current circulates in the loop. But in an asymmetrical situation, there is always dissipation because there is always some current proportional to $(1-\alpha)\, I_C$

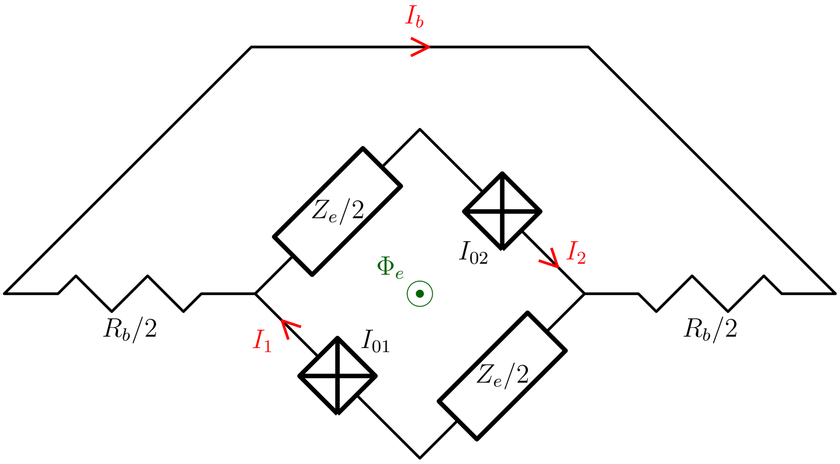

Figure 2.18.: Equivalent circuit of an in-loop mode with a bias resistor R_b.

leaking out of the loop.

For the in-loop mode, the maximal dissipation occurs at half a flux quantum. It is always smaller than $RI_C^2/2$, the maximal value achieved with a symmetrical SQUID. At zero flux, the dissipation is always 0 as no current at all circulates in the loop.

At $\Phi_e = \Phi_0/2$, if the junctions are not identical, there is a small amount of microwaves I_b which can circulate in the bias circuit. To estimate its effect on the resonance peak, we consider the circuit shown in Figure 2.18 where the bias circuit is represented by a bias resistor R_b. In the limit of small z, the current is sinusoidal at frequency ω_J and

$$I_b = I_C \mathrm{e}^{i(\omega_J t + \theta_1)} \left(1 + \alpha \mathrm{e}^{i\varphi_e}\right).$$

The amplitude of this quantity is

$$|I_b|^2 = I_C^2 \left(1 + \alpha^2 + 2\alpha \cos\varphi_e\right).$$

This makes a dissipated power in the bias resistance of $R_b I_C^2/2 \left(1 + \alpha^2 + 2\alpha\cos\varphi_e\right)$, maximal at $\varphi_e = 0$ and minimal at $\varphi_e = \pi$. This additional dissipation has for effect to decrease the quality factor of the resonator. In the loop of the SQUID, the dissipated power is $R/4\left(|I_1|^2 + |I_2|^2\right)$, which makes $R\left(1+\alpha^2\right) I_C^2/4$.

At $\varphi_e = \pi$, the ratio of power dissipated in the bias circuit to the power dissipated in the resonator is thus

$$\gamma = \frac{2R_b}{R} \frac{(1-\alpha)^2}{1+\alpha^2}.$$

For $\alpha \sim 1$, we can write $\alpha = 1 - \tilde{\alpha}$, with $\tilde{\alpha} \ll 1$. This gives $\gamma \propto \tilde{\alpha}^2$. This square dependence shows that the quality factor of the resonance stays quite close to the intrinsic quality factor in a large range of α close to 1.

Example

Figure 2.19 (a) shows an experimental current-voltage characteristic of a SQUID with $I_c = 88\,\mathrm{nA}$ and $\alpha = 0.84$. The red curve corresponds to zero flux bias and the blue one to half a

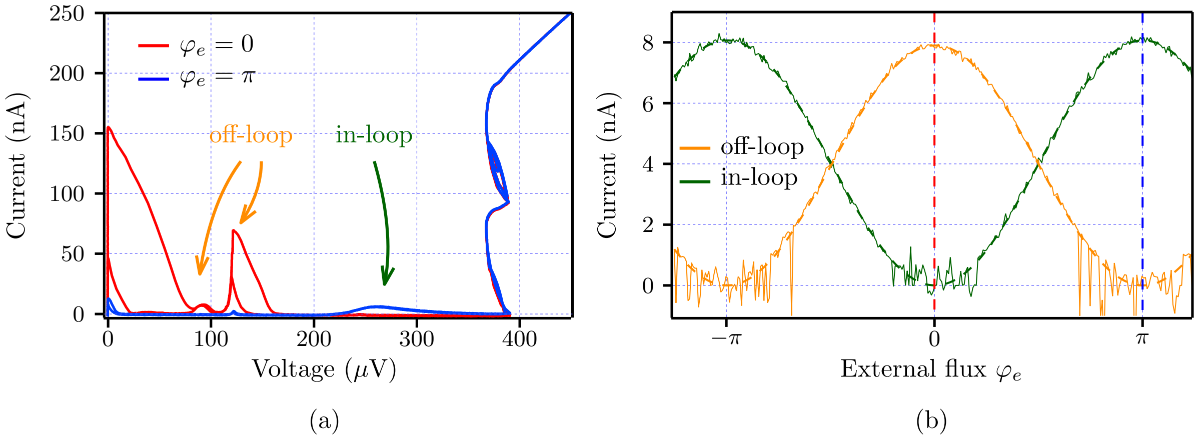

(a) (b)

Figure 2.19.: (a) Experimental current-voltage characteristic of a SQUID with $\alpha = 0.84$ showing a few resonance peaks at zero and π flux bias. (b) Evolution of the height of the two smallest peaks with respect to the applied flux. The dashed lines are fits using equations (2.31) and (2.32). The red and blue dashed lines correspond to the red and blue curves in (a).

flux quantum. The shape of the quasiparticle branch will be explained later in Section 3.6. Three resonant peaks can be seen in the spectrum. The two around 100 µV are due to filtering capacitances and inductances and are thus located out of the loop and maximally excited at zero flux bias. The last one is maximal at π reduced flux bias and corresponds to the LC mode of the loop briefly introduced in Section 2.2.2.

Figure (b) shows the evolution of the height of these peaks with respect to the reduced flux $\varphi_e = \Phi_e/\varphi_0$. Only the first off-loop mode and the in-loop mode are plotted because the largest off-loop mode is too strongly coupled to the spectrometer to be described by the zeroth order approximation. As the maximal current on top of the peak is proportional to the power $I_{max} = \mathcal{P}_{max}/V_0$ (where V_0 is the voltage at the peak maximum), Equations (2.31) and (2.32) can be used to obtain the dependence of I_{max} on the flux. The dashed lines are fits to the experiment data using these formulas. From the fits, we obtain $R_o = 46\,\Omega$ (respectively $R_i = 542\,\Omega$) for the real part of the impedance at the resonance in the case of the off-loop mode (resp. the in-loop mode).

2.2.4. Power tunability

Both in and off-loop modes have coupling parameters z depending on the flux Φ_e. For the off-loop mode, z is proportional to the critical current of the SQUID and for the in-loop mode, $\tilde{z}$ is proportional to $I_C\,|\sin(\varphi_e/2)|$. This allows tuning the power radiated to the system and thus the coupling parameter z. If it is too large, the current is not sinusoidal, giving rise to peaks with cusps or loops. In that case, the measured resonance frequency is not the true one as explained in Section 2.1.4. Changing the flux allows bringing z to the sinusoidal phase region, where the position of the peak is the true resonance frequency. It is thus possible to observe peaks moving to lower frequencies when the flux is changed to reduce z.

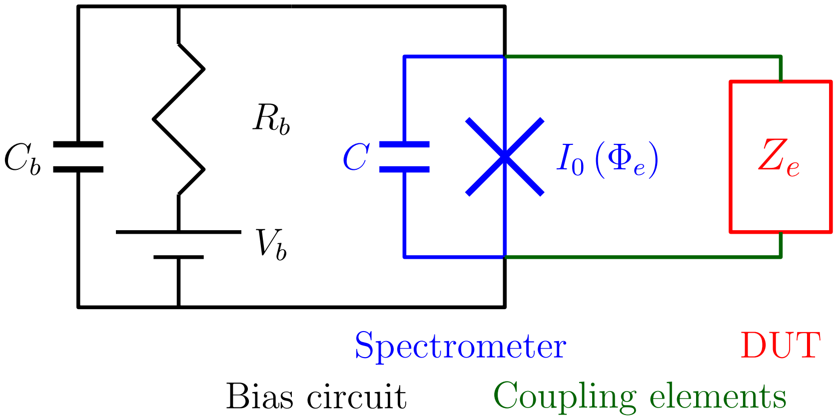

Figure 2.20.: Galvanic coupling of the spectrometer to a device of impedance Z_e out of the SQUID loop.

2.3. Coupling to an external system

In the previous sections, only galvanic coupling was considered, that is to say the device under test (DUT) is directly connected to the spectrometer with wires. But it is also possible to consider different coupling schemes, such as a capacitive one (as was the case in the Quantronics spectrometer [32, 33]) or an inductive one using the inductance of the superconducting loop.

2.3.1. Galvanic coupling

A galvanic coupling is the easiest scheme to imagine as it consists of connecting the DUT to the spectrometer with DC wires. This situation is represented in Figure 2.20 in the case of off-loop spectroscopy. The large capacitor C_b is here to filter out noise and has no important role in this discussion. Because the DUT is out of the loop, the SQUID is represented as a simple Josephson junction with tunable critical current. The spectrometer is colored in blue and the DUT in red.

The main advantage of this coupling scheme resides in that the coupling is the same for every frequency. However, if the admittance of DUT at zero frequency is not zero, such as in a parallel resonator, the DC bias current is divided between the spectrometer and the DUT. This results in a non-zero background for the current-voltage characteristic if the current is measured across the bias resistance R_b.

The galvanic coupling is thus well adapted for systems with zero admittance at zero frequency, such as series resonator, which prevents the DC bias current from reaching the DUT.

Also, if we want to couple the spectrometer to other mesoscopic systems, it is not always possible to make good electric contacts between the spectrometer and the DUT.

2.3.2. Capacitive coupling

Adding a large capacitance C_c between the spectrometer and the DUT is a good way to decouple the DC currents from the radiated microwaves, in particular if the system has a finite admittance at zero frequency. This was the solution chosen in Ref. [32]. The capacitance acts as an open circuit for the DC bias and forbids DC current to flow through it and through the DUT. On the other hand, for the microwaves radiated by the junction, the capacitance has a low impedance $1/(iC_c\omega)$ which allows for a good coupling.

Capacitive coupling is only possible when considering off-loop modes. As a matter of fact, adding a capacitance in the SQUID loop in series with the DUT opens the superconducting loop (at least for DC magnetic fields) and forbids flux biasing.

The phase excitation provided by a capacitive coupling is not uniform over the spectrometer frequency range. According to Josephson relations, the AC voltage across the junction is $\sim \left(Z_e + \frac{1}{iC_c\omega_J}\right) I_0 \mathrm{e}^{i\omega_J t}$. The phase thus oscillates with an amplitude $\sim \frac{1}{\varphi_0\omega_J}\left(Z_e + \frac{1}{iC_c\omega_J}\right) I_0 \mathrm{e}^{i\omega_J t}$. Away from divergences of Z_e (such as resonances in parallel resonators with high quality factor) or series resonator (where Z_e is large at all frequencies except at resonance), Z_e is usually smaller than the impedance of the coupling capacitance, such that the amplitude of the phase oscillations decreases as $1/\omega_J^2$ with frequency. This reduces the coupling to the DUT at high frequencies.

The coupling capacitance C_c also changes the impedance of the DUT. From the junction, the impedance is now

$$\tilde{Z}_e = Z_e - \frac{i}{C_c\omega}.$$

For a simple parallel LC resonator circuit (with inductance L_e and capacitance C_e), this added capacitance will change the resonance frequency to

$$\frac{1}{\sqrt{L_e\left(C_e + \frac{CC_c}{C+C_c}\right)}}.$$

A large coupling capacitance C_c is thus required to keep this frequency close to $1/\sqrt{L_eC_e}$, which is the resonance frequency of the LC circuit.

If C is of the order of 50 fF, C_c must be at least some pF in order to be much larger than C. For instance a capacitor made of two squares of side $d = 100\,\mu\mathrm{m}$ separated by a layer of $t = 50\,\mathrm{nm}$ of alumina (with $\varepsilon_r \sim 10$) gives $C_c \sim 20\,\mathrm{pF}$.

Making a large capacitance can introduce other resonant modes due to the physical extension of the capacitor planes. For two metallic planes with longest dimension d and separated by a thickness t of insulator with permittivity ε and permeability μ, the speed of light is reduced to $c = 1/\sqrt{\varepsilon\mu}$. This results in a planar resonator mode at frequency $f = c/(2d)$ [68]. If the metallic planes are superconducting, the speed of light will be further reduced due to the kinetic inductance of the superconductor, resulting in lower resonant frequencies. This resonant modes will be discussed in more details in Section 4.3.2. The square capacitor considered just above has for instance a self-resonance around $f \sim 70\,\mathrm{GHz}$ which is in the middle of the frequency range of a spectrometer made of aluminum. Care must be taken in order to avoid such resonances when capacitive coupling is envisaged.

2.3.3. Inductive coupling

Another possibility to couple the spectrometer to a DUT is using mutual inductances. If the microwave current generated by the junction encounters an inductance, an oscillating magnetic

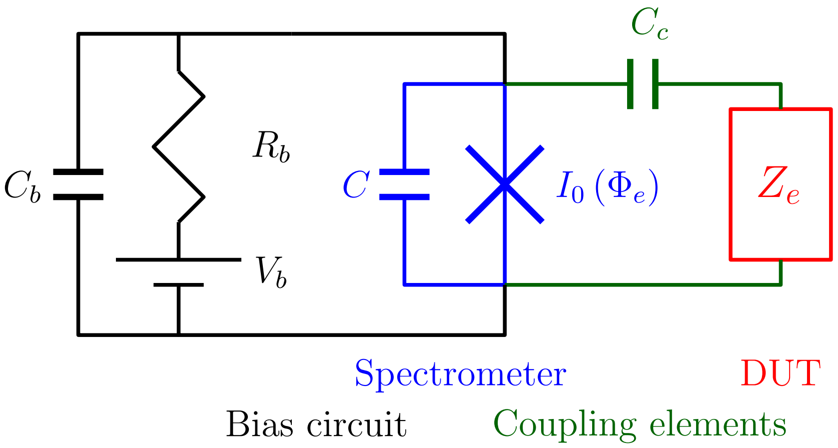

Figure 2.21.: Capacitive coupling of a spectrometer to a device of impedance Z_e out of the SQUID loop, with coupling capacitance C_c.

field is produced which can generate a current in another inductance coupled to the first one. But placing an inductor l in parallel with a Josephson junction prevents from imposing a voltage across it. Using a SQUID allows for inductive coupling and the ability of applying a voltage to the junctions. The schematic for such a coupling scheme is shown in Figure 2.22. As the coupling inductance is in the SQUID loop, the coupling is maximal when the applied flux is half a flux quantum.

When there is an alternative current I_L in the SQUID loop, there is also a current I_Z flowing in the loop of the DUT due to the mutual coupling of the two loops. The voltages V_L and V_Z and currents I_L and I_Z in the two loops are related by

$$\begin{cases} V_L = il\omega I_L + iM\omega I_Z, \\ V_Z = il_c\omega I_Z + iM\omega I_L. \end{cases}$$

The mutual inductance M is often expressed as a function of the coupling constant k:

$$M = k\sqrt{ll_c}.$$

It is a number between -1 and 1 quantifying the coupling between two systems: $k = 0$ means that a current flowing in one system does not influence the second one. $k = \pm 1$ means that all the magnetic flux generated by one loop threads the other. The sign of k indicates the direction of the induced current.

In the loop of the DUT, the current is also related to the voltage by $V_Z = -Z_e I_Z$. This gives the following relation between I_L and I_Z:

$$I_Z = -\frac{ik\sqrt{ll_c}\omega}{Z_e + il_c\omega} I_L.$$

In the SQUID loop, this gives

$$V_L = \left(il\omega + \frac{k^2 ll_c\omega^2}{Z_e + il_c\omega}\right) I_L.$$

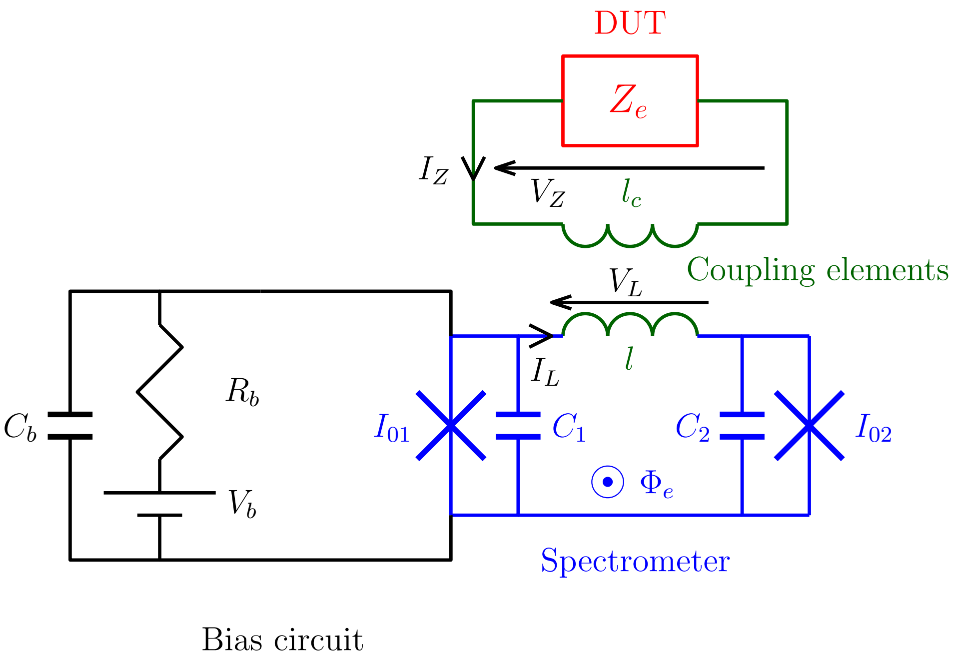

Figure 2.22.: Inductive coupling of a SQUID spectrometer to a device of impedance Z_e with coupling inductances l and l_c.

This equation shows that the mutual coupling to another loop is equivalent to having an impedance $\tilde{Z}_e$ in the loop, such that

$$\tilde{Z}_e = il\omega \left(1 - k^2 \frac{l_c\omega}{l_c\omega - iZ_e}\right). \tag{2.33}$$

The corresponding admittance $\tilde{Y}_e$ is

$$\tilde{Y}_e = \frac{-i}{l\omega}\left(1 - k^2 \frac{l_c\omega}{l_c\omega - iZ_e}\right)^{-1}.$$

It is therefore possible to use Equation (2.25) with $\tilde{Y}_e$ to find the resonance frequency of this circuit: $\Im(\tilde{Y}_e) = -C_s\omega$.

Using the SQUID loop frequency $\omega_s = 1/\sqrt{lC_s}$, this condition can be written

$$\Re\left(\left(1 - \frac{k^2 l_c\omega}{l_c\omega - iZ_e}\right)^{-1}\right) = \left(\frac{\omega_s}{\omega}\right)^2.$$

In the limit where there is no coupling between the two loops ($k = 0$), we recover ω_s as the resonance frequency of the system. The simplest case we can consider is when the spectrometer is just coupled to an LC circuit formed of the coupling inductance l_c and a capacitance C_e with eigenfrequency $\omega_e = 1/\sqrt{l_c C_e}$. The impedance Z_e is in that case $Z_e(\omega_J) = 1/(iC_e\omega_J)$. The resonance condition (2.25) becomes

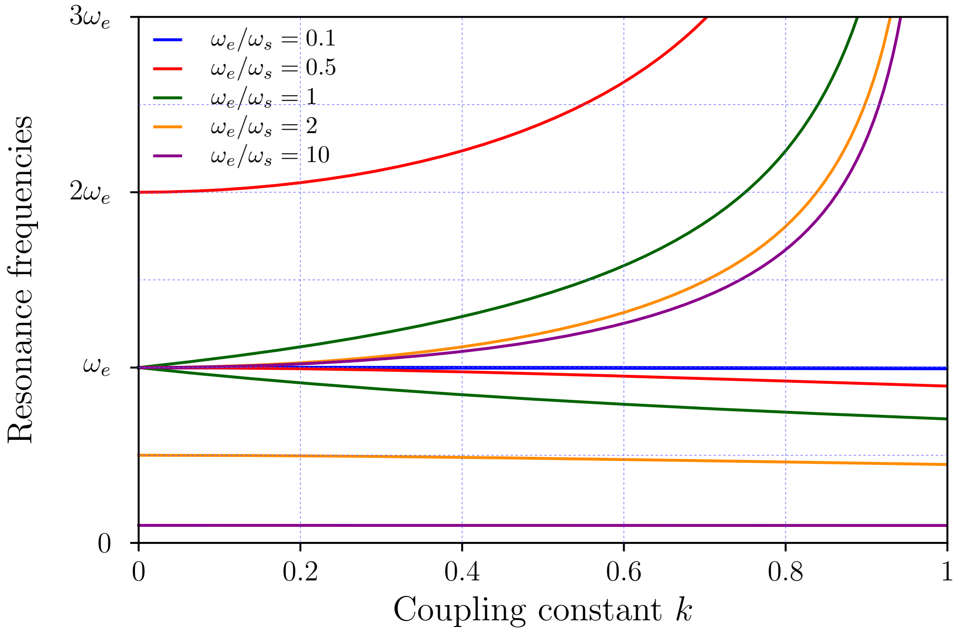

Figure 2.23.: Resonance frequencies for a LC circuit coupled inductively to the spectrometer.

$$\left(\frac{\omega_0}{\omega_s}\right)^2\left(\left(1-k^2\right)\left(\frac{\omega_0}{\omega_e}\right)^2-1\right)=\left(\frac{\omega_0}{\omega_e}\right)^2-1. \tag{2.34}$$

Figure 2.23 shows the two solutions of this equation for different ω_e/ω_s ratios. For low coupling constant k, the two resonant frequencies are just ω_e and ω_s, as expected because the two loops are not coupled in that case. When k increases and tends to maximal coupling, only one solution stays finite, at

$$\omega_0=\frac{\omega_e\omega_s}{\sqrt{\omega_e^2+\omega_s^2}}.$$

To have the resonance frequency at the desired value ω_e, it is best to work in one of these two conditions:

$$\begin{cases} k \ll 1, \\ \omega_e \ll \omega_s. \end{cases} \tag{2.35}$$

If we want to quantify the dissipated power, we add a resistance R in parallel to C_e. According to Equation (2.26), the dissipated power is proportional to $\Re\left(1/(Y_e+i\omega C_s)\right)$. Introducing the quality factor of the resonator, $Q=R\sqrt{C_e/l_c}$, this real part can be expressed as the real part of

$$\frac{1}{i\omega C_s}\left(1-\left(\frac{\omega_s}{\omega}\right)^2\frac{\left(\frac{\omega}{\omega_e}\right)^2-\frac{iQ\frac{\omega}{\omega_e}}{1+iQ\frac{\omega}{\omega_e}}}{\left(\frac{\omega}{\omega_e}\right)^2(1-k^2)-\frac{iQ\frac{\omega}{\omega_e}}{1+iQ\frac{\omega}{\omega_e}}}\right)^{-1}.$$

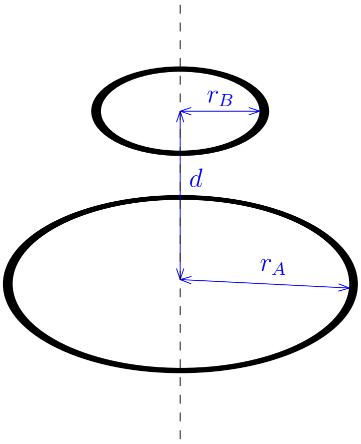

Figure 2.24.: Two concentric circular loops.

After some calculations, this gives at the resonance frequency ω_0 (if $\omega_e < \omega_s$),

$$\frac{1}{\omega_0 C_s} \frac{Q \frac{\omega_0}{\omega_e} \left(1 - \left(\frac{\omega_0}{\omega_e}\right)^2 (1 - k^2)\right)}{\left(\frac{\omega_s}{\omega_0}\right)^2 - 1}.$$

If we consider that $\omega_0 \sim \omega_e$ in one of the limits of Equation 2.35, this expression is

$$\frac{Q}{\omega_e C_s} \frac{k^2}{\left(\frac{\omega_s}{\omega_0}\right)^2 - 1}.$$

As this expression is proportional to k^2, the second condition of Equation 2.35 ($\omega_e \ll \omega_s$) is more favorable to get a large signal. It permits working with large k while the other possible condition implies a weak signal.

The mutual inductance (and thus the coupling constant k) between two loops of zero thickness can be expressed using the Neumann formula (derived in Appendix D)

$$M = \frac{\mu_0}{4\pi} \oint_{\mathcal{C}_Z} \oint_{\mathcal{C}_L} \frac{\vec{dl}_L \cdot \vec{dl}_Z}{r}. \tag{2.36}$$

It is possible to derive an analytic expression for M (and thus k) in the case of two concentric circular loops, as sketched in Figure 2.24. This situation is quite close to the actual spectrometer design: the SQUID and the probe system loops can be modeled by circular loops placed on top of one another as described in Chapters 4 and 5. If we call r_A the radius of the SQUID loop, r_B the radius of the loop of the DUT and d the distance between their centers, the double integral in the Neumann formula can be expressed in terms of the complete elliptic integrals K and E (the derivation is presented in Appendix E):

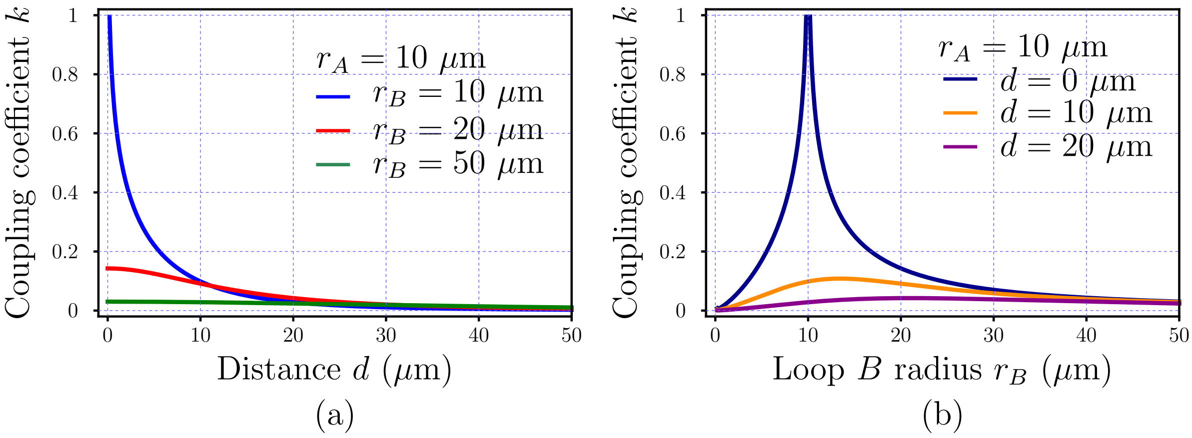

Figure 2.25.: Coupling coefficient between two circular loops with wire radius $a = 200$ nm as a function of (a) the distance d between the loops and (b) the radius r_B of loop B.

$$\begin{aligned} k &= \frac{1}{\gamma}\sqrt{\frac{\left(r_A+r_B\right)^2+d^2}{r_A r_B}}\left(\frac{r_A^2+r_B^2+d^2}{\left(r_A+r_B\right)^2+d^2}K\left(\beta\right)-E\left(\beta\right)\right), \\ \text{with } \beta &= 2\sqrt{\frac{r_A r_B}{\left(r_A+r_B\right)^2+d^2}}. \end{aligned} \tag{2.37}$$

The coefficient γ accounts for the radius a of the wires forming the loops in the evaluation of the loop inductances,

$$\gamma^2 = \left(\ln\frac{8r_A}{a}-2\right)\left(\ln\frac{8r_B}{a}-2\right).$$

Figure 2.25 shows the coupling coefficient for different values of r_A, r_B and d, with a fixed wire radius of 200 nm.

In panel (a), the two loops have fixed radii and the distance between them is changed. The coefficient k decreases when the distance between the loops increases. The decrease rate is larger when the loop is smaller.

In panel (b), the distance between the loops is fixed, as well as the radius of one loop, and the radius of the probe loop is changed. For each distance d, there is an optimum probe loop radius for which the coupling is maximal, but the highest value is for $d = 0$.

However, this analytic calculation of the coupling coefficient is not fully realistic: several parameters were not considered, such as the superconducting character of the conductors, the width of the wires or the real shape of the loops.

To make an adequate calculation, the correct procedure would be to

- combine Maxwell and London equations to get $\nabla^2\vec{B} = \vec{B}/\lambda^2$ in the superconductors and $\nabla^2\vec{B} = \vec{0}$ outside
- solve this differential equation for $\vec{B}$ with boundary conditions modeling the junctions by current sources and imposing fluxoid quantization in superconducting loops

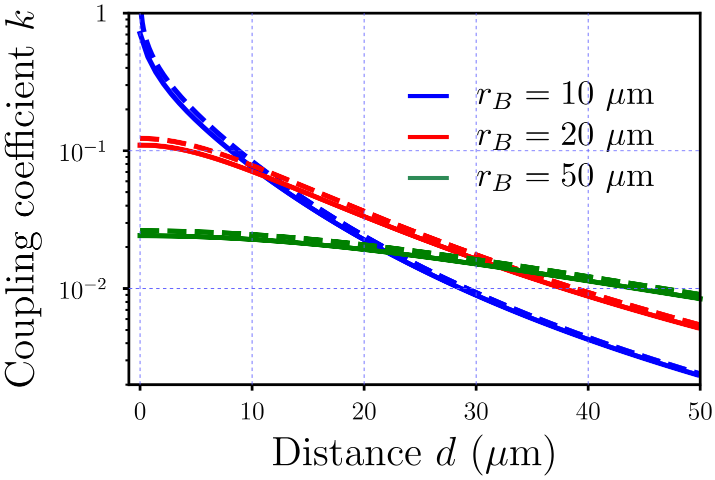

Figure 2.26.: Coupling coefficient k as a function of the distance d between the loops for $r_A = 10\,\mu\text{m}$. The dashed lines are calculated using Equation 2.37 and the full lines are simulated with 3D-MLSI.

- calculate the total energy of the system and extract the inductance matrix

For the systems considered in this thesis, two other assumptions can be made on the conductors: the thickness of the films t is small compared to their width and t is of the order of the London penetration λ. Typically, $t \sim 100\,\text{nm}$ and $\lambda \sim 100\,\text{nm}$ for aluminum.

The 3D-MLSI simulator, developed by M. Khapaev [73], assumes these considerations and allows for calculation of current density, magnetic fields and inductance matrices using a finite element method.

Figure 2.26 shows results of simulation of two circular loops (of radii $r_A = 10\,\mu\text{m}$ and $r_B = r_A$, $r_B = 2r_A$ or $r_B = 5r_A$) on top of one another with 3D-MLSI. The wires are 400 nm thick. The full lines are obtained with 3D-MLSI and the dashed lines are calculations using Equation 2.37 for thin wires of radius 200 nm. Both calculations yield close values for the coupling parameter k showing that the effect of the penetration of the magnetic field in aluminum is negligible.

In conclusion, the best coupling parameter is obtained for loops with similar radius, located as close as possible.

2.4. Limitations of the Josephson spectrometer

The Josephson spectrometer as presented in this chapter seems to be a powerful tool, as it can easily couple to mesoscopic systems and cover a frequency range which is not easily accessible with conventional microwaves techniques. However, it has some limitations.

2.4.1. Frequency limitation

First, the inelastic Cooper pair tunneling at the basis of the spectrometer principle of operation is the dominant tunneling process only below $2\Delta/e$. Above this voltage, the tunneling of quasiparticles add a contribution of the order of V/R_N to the current, reducing the sensitivity of the device. This corresponds to a high frequency limitation of $4\Delta/h$. In the case of aluminum (which is the material used throughout this thesis), the maximal frequency is $f_{Al} \sim 180\,\mathrm{GHz}$. It is possible to reach higher frequencies by using other superconductors with higher critical temperature such as tin ($f_{Sn} \sim 500\,\mathrm{GHz}$), lead ($f_{Pb} \sim 1.1\,\mathrm{THz}$) or niobium ($f_{Nb} \sim 1.4\,\mathrm{THz}$) but the fabrication processes are less advanced for these materials.

There is also a low frequency limitation due to dissipation in the junction and its environment. At small voltage, the phase particle (introduced in the previous chapter) can be trapped in a potential well because of losses which can decrease its kinetic energy. This results in a switching towards the zero-voltage state. This retrapping phenomenon is described in more details in Section 3.2. Usually in experiments, it is possible to reduce the voltage to a value of $\sim 2\,\mu\mathrm{V}$, corresponding to a frequency of $\sim 1\,\mathrm{GHz}$.

2.4.2. Magnetic field effect

For a SQUID-shaped spectrometer, applying a magnetic field to the device allows controlling the phase difference across the junctions. The typical magnetic fields used in experiments correspond to one flux quantum. For a $10 \times 10\,\mu\mathrm{m}^2$ SQUID loop, it makes a value of $20\,\mu\mathrm{T}$. Such fields have no visible effect on one junction, but when they are stronger they can have unpleasant consequences.

Vanishing critical current

First, when the magnetic field inside a Josephson junction becomes large, the phase difference starts being inhomogeneous and the critical current can vanish. To understand this effect, consider the junction sketched in Figure 2.27a. The insulating barrier is the yellow region labeled I and the superconductors are the blue regions labeled S_1 and S_2. The junction has an extension in the z direction of width W and a magnetic field is applied along this direction.

The magnetic field is expelled by the Meissner effect in the superconductors. It is thus confined in a region of thickness of order $t = a + 2\lambda$ where λ is the London penetration length and is typically 15 nm in bulk aluminum and 100 nm in more realistic aluminum. So, if the contour $\mathcal{C}$ goes deep inside the superconductors, such that at $y_0 \gg \lambda$, there is no magnetic field at $y = \pm y_0$.

Inside the junction, the magnetic field is not exactly $\vec{B}_e$. The Josephson current along $\vec{y}$ generates a field $\vec{B}_i$. The total field $\vec{B} = \vec{B}_e + \vec{B}_i$ satisfies Maxwell's equation: $\vec{\nabla} \times \vec{B} = \mu_0 \vec{j}$ in the static limit, with $\vec{j}$ the density of current. $\vec{B}_i$ can be taken in the form $\vec{B}_i = B_i(x)\vec{z}$ if we consider the length a of the junction small and the current being oriented along $\vec{y}$. B_i then follows $\frac{dB_i}{dx}(x) = \mu_0 j(x)$.

If we integrate the gradient of the superconducting phase ϕ along the contour $\mathcal{C}$, we get

$$\frac{1}{\varphi_0}\oint_{\mathcal{C}} \vec{A}\cdot\vec{dl} + \oint_{\mathcal{C}} \vec{\nabla}\phi\cdot\vec{dl} = 0 \quad (2\pi),$$

where $\vec{A}$ is the potential vector from which derives $\vec{B}$. If we note $\varphi_{1(2)}$ the superconducting phase in superconductor 1 (2), we get

$$\frac{1}{\varphi_0}\iint_{\mathcal{S}} \vec{B}\cdot\vec{dS} + \varphi_1(x+dx) - \varphi_1(x) - \varphi_2(x+dx) + \varphi_2(x) = 0 \quad (2\pi).$$

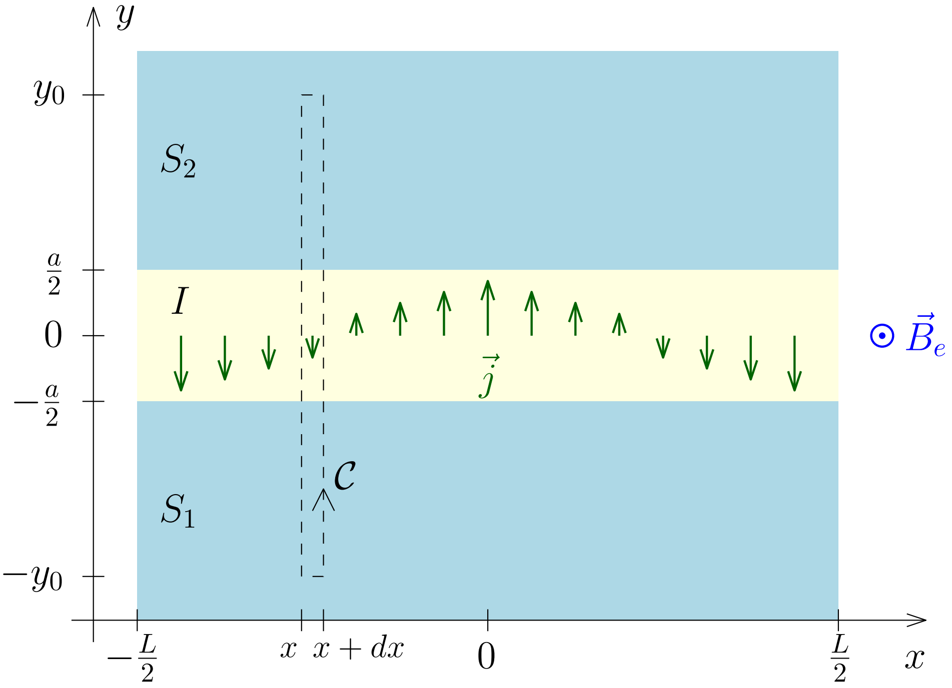

(a) Schematic of a Josephson junction with applied magnetic field $\vec{B}$. The green arrows represent the supercurrent density in the case of $\Phi = \Phi_0$.

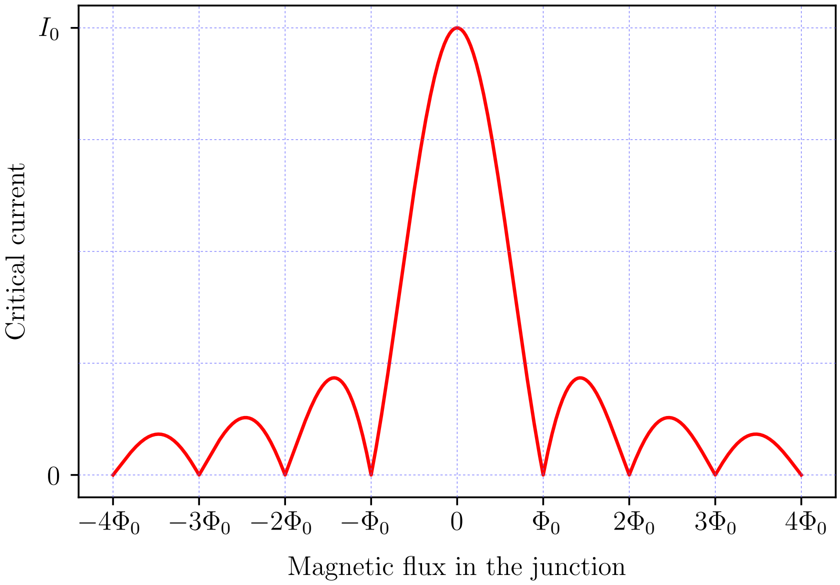

(b) Critical current of a Josephson junction as a function of the magnetic field.

Figure 2.27.: Effect of the magnetic field on a Josephson junction.

Calling $\varphi(x) = \varphi_2(x) - \varphi_1(x)$ the phase difference across the junction, the last equation gives

$$\frac{1}{\varphi_0} B(x) t dx - \frac{d\varphi}{dx}(x) dx = 0,$$

where $t = a + 2\lambda$ is the effective thickness of the insulating layer. Differentiating this equation with respect to x gives

$$\varphi_0 \frac{d^2\varphi}{dx^2}(x) = t \frac{dB}{dx}(x) = \mu_0 t j(x).$$

The Josephson relation for $j(x)$ is $j(x) = j_0 \sin\varphi(x)$, where j_0 is the supercurrent density, such that $I_0 = j_0 W L$ in a homogeneous junction of supercurrent I_0 and widths W and L. This leads to a Sine-Gordon equation for the phase

$$\sin\varphi(x) = \lambda_J^2 \frac{d^2\varphi}{dx^2}(x),$$

where $\lambda_J = \sqrt{\frac{\varphi_0}{\mu_0 t j_0}}$ is the so-called Josephson length and is usually much larger than the London penetration length: $\lambda_J \sim 50\,\mu\text{m}$ for a typical aluminum Josephson junction. If the width L of the junction is much smaller than the Josephson length (this is always the case in this thesis as the junctions we consider have a size $\sim 2\,\mu\text{m} \times 500\,\text{nm}$), it is possible to neglect the contribution of the induced field $\vec{B}_i$ and get a linear expression for the phase difference:

$$\varphi(x) = \frac{\Phi}{\varphi_0} \frac{x}{L} + \varphi^{(0)},$$

where Φ is the magnetic flux of the applied field $\vec{B}_e$ through the entire junction. The supercurrent of the junction is given by the integral of $j_0 \sin\varphi(x)$ over the whole junction: $I = W \int_{-L/2}^{L/2} j(x) dx$.

$$I = I_0 \frac{\sin\frac{\Phi}{2\varphi_0}}{\frac{\Phi}{2\varphi_0}} \sin\left(\varphi^{(0)}\right).$$

The critical current in a uniform junction with applied magnetic field is proportional to $\left|\text{sinc}\left(\frac{\Phi}{2\varphi_0}\right)\right|$. This shape (shown in Figure 2.27b) is the same Fraunhofer dependence as for diffraction of light through a slit. As in diffraction, it describes interferences between different phases. When Φ is a multiple of Φ_0, there is no supercurrent. In the case where $\Phi = \Phi_0$, the phase φ is linearly increased by 2π along the junction width L. This wrapping of the phase corresponds to having one flux quantum inside the Josephson junction and results in the supercurrent density plotted in Figure 2.27a with green arrows.

In the case of a spectrometer, having a zero critical current means that no spectrum can be measured. The current response to a resonance is indeed proportional to the square of the critical current as discussed in this chapter. For a typical size of junction of $2\,\mu\text{m} \times 1\,\text{nm}$, one flux quantum corresponds to $\sim 100\,\text{mT}$. Due to magnetic field focusing (more details in Appendix F) by the superconducting electrodes, having $100\,\text{mT}$ inside the junction can be reached with much lower fields, of order $1 - 10\,\text{mT}$.

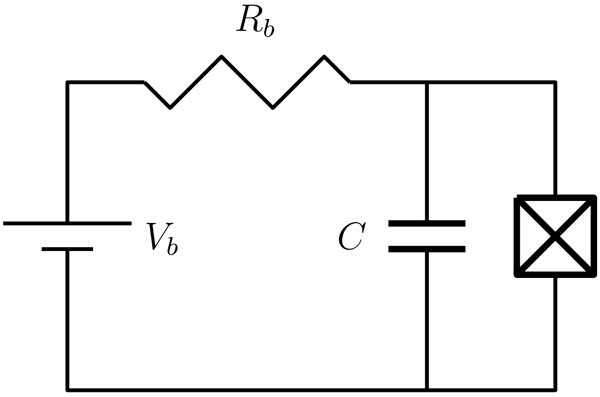

Figure 2.28.: Typical bias circuit with bias resistor R_b and filtering capacitor C.

Superconductivity loss

When the applied field becomes larger than the superconducting critical field, the junctions lose their superconducting character and the spectrometer cannot operate. For aluminum, the critical field is of the order of 100 mT. Using lead or niobium would allow for a gain of one order of magnitude.

2.4.3. Emission linewidth

As the frequency of the emitted photons is proportional to the voltage across the junction, the emission frequency linewidth of the spectrometer depends on the voltage noise.

For an RC low-pass filter as sketched in Figure 2.28, the thermal noise spectral density of the resistance is given by $V_R^2 = 4k_BTR_b$. In order to get the spectral density of noise across the capacitor, V_R^2 must be multiplied by the square of the gain of the filter: $|H(\omega)|^2 = 1/(1 + R_b^2C^2\omega^2)$. The total integrated noise is then

$$\begin{aligned} V_{rms}^2 &= \frac{1}{2\pi}\int_0^\infty \frac{4k_BTR_b}{1+R_b^2C^2\omega^2}d\omega, \\ V_{rms} &= \sqrt{\frac{k_BT}{C}}. \end{aligned}$$

Interestingly, this noise doesn't depend on the resistance in the circuit before the filtering capacitor. For 100 nF capacitors, this gives at 100 mK a voltage noise of 4 nV, corresponding to a frequency linewidth of 2 MHz.

In practice, commercial capacitors have parasitic components dominating their impedance at high frequencies: an Equivalent Series Resistance (ESR) and an Equivalent Series Inductance (ESL). The capacitors we use (Murata ULSC and ULEC series) are designed for operation at high-frequency, such that their ESR and ESL are quite low. They have $ESR \sim 500\,\mathrm{m}\Omega$, resulting in a voltage noise of the order of 25 pV at 100 mK in a 1 kHz bandwidth, smaller than the noise due to the capacitance.

This emission linewidth has to be compared to that of conventional microwave sources. It is common to have commercial devices providing a linewidth of the order of 1 Hz up to a frequency of the order of $\sim 80\,\mathrm{GHz}$, which is a better resolution than that of the Josephson spectrometer. However, one possible improvement of the spectrometer discussed in the conclusion consists of using the narrow linewidth of such sources to generate a precise voltage across the junction and thus reduce the emission linewidth to a value comparable to that of conventional microwave sources.

2.4.4. Absorption linewidth

Broadening due to the bias circuit

A resonance peak can get wider because of dissipation in the biasing circuit: the probe system is connected to the bias circuit and its impedance is modified by the bias resistance R_b. In other words, losses in the bias resistance are added to the losses in the probe system. To estimate the effect of the biasing circuit, we consider both parallel and series resonator of quality factor Q_e.

For a parallel resonator out of the SQUID loop, the bias resistance is in parallel of the resonator resistance R, such that the total resistance is $RR_b/(R+R_b)$, reducing the quality factor to

$$Q = \left(\frac{1}{Q_e} + \frac{1}{Q_b}\right)^{-1},$$

where Q_b is the quality factor due to the bias circuit. Here $Q_b = R_b\sqrt{C_e/L_e}$. For instance, for a circuit with $L_e = 100\,\mathrm{pH}$ and $C_e = 100\,\mathrm{fF}$ and a large Q_e factor of order 1000, a bias resistance of $1\,\mathrm{k\Omega}$ reduces Q to 30.

For a series resonator out of the SQUID loop, the situation was already treated in Section 2.1.5. Figure 2.10 shows the effect of the bias resistor on the depth of the resonance. A small bias resistance leads to a smaller current dip than a larger resistance. At resonance, the two resistors are in parallel, such that the quality factor is increased to

$$Q = Q_e + Q_b.$$

Here $Q_b = R_b^{-1}\sqrt{L_e}C_e$.

If the resonator is in the loop of a perfectly symmetric SQUID, no microwave current can leave the loop, such that no power is dissipated in the bias resistor. For a SQUID with $\alpha \neq 1$, the ratio of power dissipated in the bias resistor to the power dissipated power in the resonator is

$$\gamma = \frac{2R_b}{R}\frac{(1-\alpha)^2}{1+\alpha^2},$$

as seen in Section 2.2.3.

The spectrometer is thus not well adapted to measure off-loop parallel resonances because their width is extensively increased by the bias circuit. On the contrary, in-loop spectroscopy is almost not affected by the bias circuit and leaves the width of the peaks close to their actual one. This result is comparable to usual microwave spectroscopy setups, where the width of the measured peak is limited by the quality factor of the used resonator. But the Josephson spectrometer guarantees this linewidth over a broader bandwidth: up to $180\,\mathrm{GHz}$, compared to a limit of the order of $40\,\mathrm{GHz}$ for conventional setups.

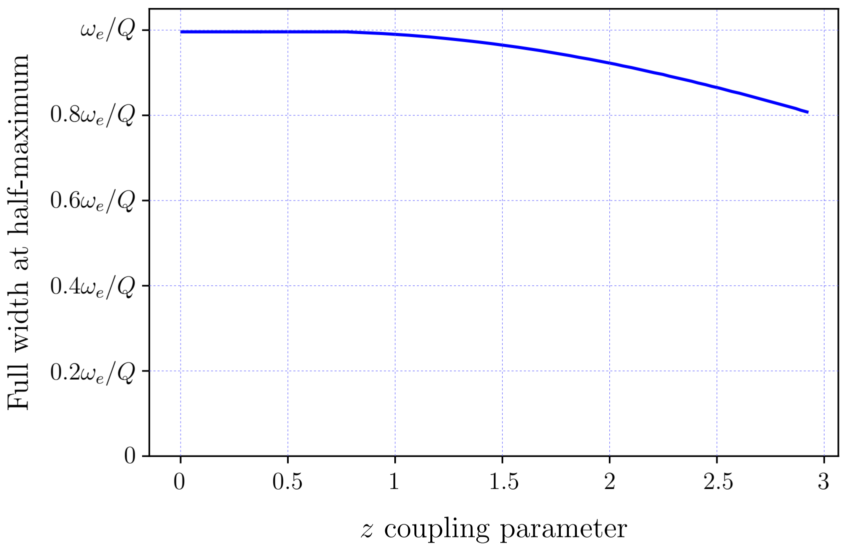

Figure 2.29.: Full width at half-maximum of a resonance detected by the spectrometer as a function of the coupling parameter z.

Broadening due to the shape of the peak

But dissipation in the bias circuit is not the only element that can broaden a peak. As seen in Section 2.1.4, at high coupling parameter z, parallel resonance peaks can take unusual shapes and get broadened. In order to quantify the width of the peaks, we can calculate the full width at half-maximum for different couplings z.

For low z, the shape of resonance peaks is simply a Lorentzian:

$$I_{DC} = I_0 \frac{z/2}{1+\xi^2}.$$

I_{DC} is half of its maximum when $\xi = \pm 1$. For an RLC resonator with resonance frequency ω_e and quality factor Q, this gives $\omega_\pm = \omega_e\,(1 \pm 1/(2Q))$. The full width at half-maximum is thus ω_e/Q. This is the same width as the bare resonator and can be of order 500 kHz for a resonator with high quality factor ($Q \sim 10^5$) and $\nu_e \sim 50\,\text{GHz}$.

When the coupling z increases (and stays below the critical value 2.92), the peak gets sharper. Using the Harmonic balance equation, it is possible to numerically calculate the full width at half-maximum of a peak for arbitrary coupling $z < 2.92$. This dependence is shown in Figure 2.29. It is possible to reduce the width of a peak down to $\sim 0.8\omega/Q$ with optimal coupling. However, when z is larger than the critical value, the peak gets wider because of the formation of a loop.

2.4.5. Sensitivity

To estimate the sensitivity of the spectrometer, we consider the bias circuit presented in the left-hand side panel of Figure 2.30. It consists of a voltage source V_b, a bias resistor R_b and a Josephson junction (of critical current I_0 and capacitance C). The signal of the spectrometer

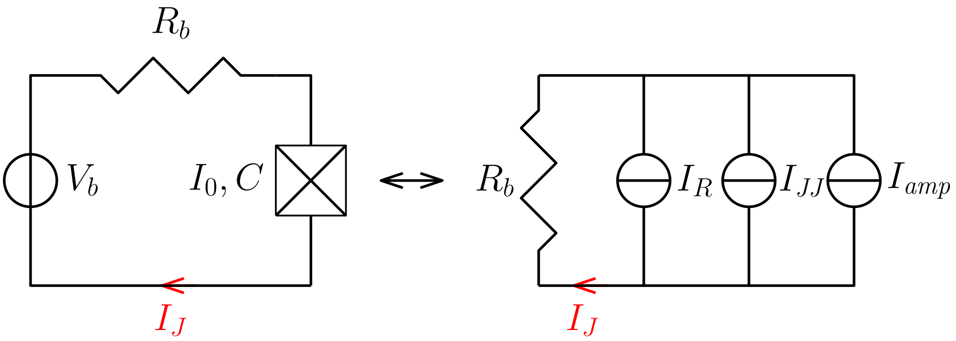

Figure 2.30.: Simplified bias circuit and equivalent noise circuit.

is the DC current of the junction I_J. We measure it across the resistor R_b, such that the signal voltage is $V_S = R_b I_J$. The noise sources in this circuit are

- The resistor R_b. It generates a Johnson noise of current spectral density $S_{I_R} = \sqrt{4k_BT/R_b}$. We model it by a current source I_R.
- The spectrometer. It generates a shot noise of spectral density $S_{I_{JJ}} = \sqrt{2eI_{bg}}$, where I_{bg} is the background current in the subgap region. A typical value if $I_{bg} = 10\,\mathrm{pA}$ for junctions with $I_0 \sim 100\,\mathrm{nA}$. We model it by a current source I_{JJ}.
- The amplifier used to measure the voltage across R_b. It has a voltage noise density e_n and a current noise density e_i. We model it by a current source I_{amp} of spectral density $S_{I_{amp}} = \sqrt{e_n^2/R_b^2 + e_i^2}$.

These three noise sources are independent, such that the total spectral density of the current noise is

$$S_I = \sqrt{S_{I_R}^2 + S_{I_{JJ}}^2 + S_{I_{amp}}}.$$

$$S_I = \sqrt{\frac{4k_BT}{R_b} + 2eI_{bg} + \frac{e_n^2}{R_b^2} + e_i^2}.$$

The corresponding voltage spectral density across the resistor is $S_V = R_b S_I$. The signal-to-noise ratio in a 1 Hz bandwidth of the spectrometer can thus be written as

$$SNR = \frac{I_J}{\sqrt{\frac{4k_BT}{R_b} + 2eI_{bg} + \frac{e_n^2}{R_b^2} + e_i^2}}.$$

The first two terms of the denominator are dominated by $4R_bk_BT$ as long as the bias resistor is smaller than $R_{cr} = 2k_BT/(eI_{bg})$. At 100 mK with a subgap current of 10 pA, this crossover resistance is $2\,\mathrm{M\Omega}$, much larger than the typical resistances we use, of order $1\,\mathrm{k\Omega}$ and below. For such a resistance, $\sqrt{4k_BT/R_b}$ is of the order of $100\,\mathrm{fA}/\sqrt{\mathrm{Hz}}$. The amplifiers we use at the moment (NF, LI-75A) have $e_n \sim 1\,\mathrm{nV}/\sqrt{\mathrm{Hz}}$ and $e_i \sim 10\,\mathrm{fA}/\sqrt{\mathrm{Hz}}$. With $R_b = 1\,\mathrm{k\Omega}$, $e_n/R_b = 1\,\mathrm{pA}/\sqrt{\mathrm{Hz}}$, which is then the dominant noise source.

Using amplifiers based on high electron mobility transistors (HEMT) operating at cryogenic temperatures, it is possible to reach a noise level of the order of 100 pV/$\sqrt{\mathrm{Hz}}$ at frequencies of the order of 1 kHz [74]. With such amplifiers, the sensitivity would be limited by the Johnson noise of the resistance, such that the signal-to-noise ratio becomes

$$SNR = \frac{R_b I_J}{\sqrt{4k_B T}}.$$

The minimal current that the spectrometer can detect (in a δf bandwidth) corresponds to $SNR = 1$. This corresponds to $I_J^2 = 4k_B T\Delta f/R_b$. If we consider using the spectrometer in its linear regime where $z = R_e I_0/V_0 \ll 1$ (where R_e is the real part of the probed impedance and V_0 the resonance voltage), $I_J = zI_0/2$ at the current peak. Using the amplifiers described above, the minimal detectable R_e is thus given by

$$\frac{R_{e,min}}{V_0} = \frac{4}{I_0^2}\sqrt{\frac{k_B T\delta f}{R_b}}.$$

For a better sensitivity, the temperature must stay low, and the bias resistance and critical current must be as large as possible. In practice, to correctly voltage bias the junction, R_b cannot be much larger than R_N, the normal resistance of the junction. If we impose $R_b \sim R_N$, the minimal R_e can be expressed, using the Ambegaokar-Baratoff relation derived in Chapter 1, as

$$\frac{R_{e,min}}{V_0} = \frac{4}{I_0^{3/2}}\sqrt{\frac{2ek_B T\delta f}{\pi\Delta}}.$$

For instance, at $V_0 = 200\,\mu\mathrm{V}$, the minimal measurable resistance in a 1 Hz bandwidth is $R_{e,min} = 2\,\mathrm{m}\Omega$ with $I_0 = 100\,\mathrm{nA}$. With a junction ten times larger ($I_0 = 1\,\mu\mathrm{A}$), $R_{e,min} = 50\,\mu\Omega$. In comparison, these values become respectively $3\,\mathrm{m}\Omega$ and $300\,\mu\Omega$ when using NF amplifiers.

A common figure of merit used to quantify the sensitivity of a spectrometer is the noise equivalent power (NEP) corresponding to the emitted power giving a signal-to-noise ratio of one in a bandwidth of 1 Hz. For the spectrometer, it can be expressed as

$$NEP = I_{J,min}V_0 = 2V_0\sqrt{\frac{2ek_B T I_0}{\pi\Delta}}.$$

This expression is proportional to the square root of the critical current. Small junctions are therefore favorable to obtain a small NEP. For a junction with $I_0 = 100\,\mathrm{nA}$, $NEP = 10^{-17}$ W/$\sqrt{\mathrm{Hz}}$ at $V_0 = 200\,\mu\mathrm{V}$. This value is low compared to other conventional terahertz spectrometers reaching values of the order of 10^{-16} W/$\sqrt{\mathrm{Hz}}$ with a larger linewidth or 10^{-14} W/$\sqrt{\mathrm{Hz}}$ with a comparable linewidth of the order of 1 MHz [75]. When using NF amplifiers, the NEP becomes

$$NEP = \frac{2eI_0V_0}{\pi\Delta}e_n,$$

which gives $NEP = 7 \times 10^{-17}$ W/$\sqrt{\mathrm{Hz}}$ for the same junction.

A more common quantity in mesoscopic physics is the minimal absorption rate Γ_{min}, also proportional to $\sqrt{I_0}$ for the spectrometer. It is of the order of $\Gamma_{min} \sim 100$ kHz for a 100 nA critical current Josephson spectrometer in the middle of the subgap region, which is much less than typical rates of the order of 1 MHz for usual mesoscopic systems.

2.5. Conclusion

Using the essential equations governing Josephson junctions derived in the previous chapter, we have shown that a single Josephson junction can be used as a spectrometer to detect photon absorption for frequency below $4\Delta/h$. However, such a spectrometer has some drawbacks: an inaccessible low frequency region, a too high coupling to an uncontrolled electromagnetic environment and a bad coupling to the system of interest at high frequencies.

One simple way to palliate these weaknesses is to use a SQUID instead of a single Josephson junction. This allows reducing the inaccessible low frequency region by decreasing the zero-voltage current at half a flux quantum bias, an efficient decoupling from the electromagnetic environment by taking advantage of currents in the SQUID loop and a more constant coupling to the probe system by using the SQUID loop inductance as a coupling element.

This coupling scheme is then discussed and compared to galvanic and capacitive couplings, showing that they can all be adapted to different situations and result in a modified impedance for the probe system.

Regardless of the coupling scheme, the microwave interaction of the spectrometer with a resonant mode is explained, leading to a modified current-voltage characteristic exhibiting current peaks at the resonant frequencies. The shape of these peaks is also described, revealing that the peaks can become flat when the coupling is too high.

The limitations of the spectrometer are finally exposed. They show that the Josephson spectrometer can reach a linewidth of 2 MHz with a minimal measurable absorption rate of 100 kHz in its 180 GHz operating frequency range. It is also shown that there is a tradeoff for the size of the junction. A larger junction gives a better sensitivity and a smaller junction gives a lower Noise Equivalent Power.

The next chapter explains the shape of a realistic current-voltage characteristic and the possible solutions to limit these features in order to make a Josephson spectrometer.

3. Comprehensive model of a Josephson junction

In practice, the current-voltage characteristic of a Josephson junction (or a SQUID) is not as simple as presented in Chapters 1 and 2. Multiple parameters can alter its shape such as temperature, noise, the biasing circuit… Figure 3.1 shows a more realistic IV characteristic for positive voltage. The thick black line is the ideal zero-temperature form described in Chapter 1. The colored features will be described separately throughout this chapter. In order to have an optimal spectrometer, these features need to be suppressed.

Briefly, the switching current I_s *is the bias current at which the junction leaves the zero-voltage state. When decreasing the bias voltage, there is a finite voltage at which the junction is trapped in a potential well. This phenomenon is called retrapping. The bias circuit can have several effects on the I-V characteristic, such as adding low frequency resonances or relaxation oscillations. Applying microwaves to a Josephson junction leads to Shapiro steps and photo-assisted tunneling (not shown in the figure). For* $V < 2\Delta/e$*, there is a finite subgap current due to temperature and possibly to high transmission channels in the junction. The temperature is not zero, resulting in rounding of the quasiparticle branch. This branch can also exhibit surprising back-bending behaviors due to quasiparticle heating.*

3.1. The switching current

When we first introduced the ideal current-voltage characteristic of a junction, the tilted washboard potential approach showed that for a bias current $I_b < I_0$, the junction stays in the zero-voltage state. However, it is possible for the junction to leave the potential minimum, even with $I_b < I_0$ because of thermal noise, quantum fluctuations or microwave oscillations. The current value at which the junction switches out of the potential well is called switching current and is denoted I_s in this section.

To have an estimate of I_s, consider the tilted washboard potential shown in Figure 3.2 in the case of $I_b < I_0$. φ_n is the phase difference in the n-th minimum of the potential and φ_n' the phase difference at the n-th maximum. For the junction to escape the n-th potential well and acquire a finite voltage, it has to go over a potential barrier of height ΔU_0. This can be done in several ways: thermal noise can give energy $k_B T$ to the junction, resulting in oscillations of the phase and the junction can tunnel across the potential barrier.

Calling $i_b = I_b/I_0$, the potential U of the junction is $U(\varphi) = E_J(1 - \cos\varphi - i_b\varphi)$. φ_n and φ_n' can be expressed as $\varphi_n = \arcsin i_b + 2n\pi$ and $\varphi_n' = (2n+1)\pi - \arcsin i_b$. This gives an expression for ΔU_0,

$$\Delta U_0 = E_J \left(2\sqrt{1 - i_b^2} - 2 i_b \arccos i_b \right).$$

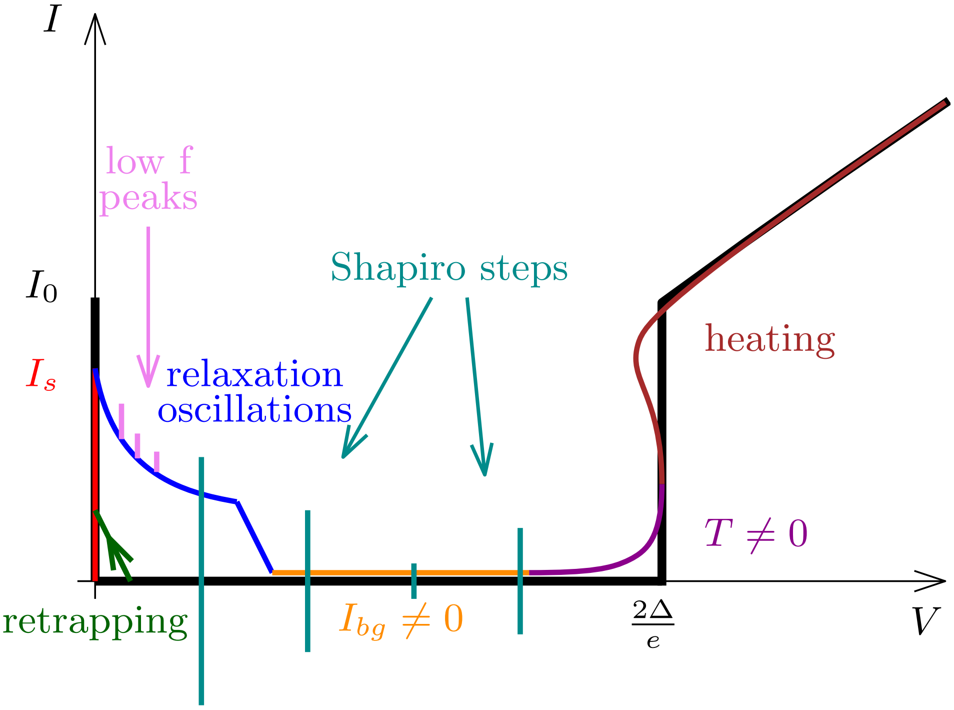

Figure 3.1.: Realistic shape of a Josephson junction current-voltage characteristic.

3.1.1. Thermal fluctuations

Consider a Josephson junction biased via a bias resistor R_b at temperature T. This resistance generates a noise voltage V_N across it (and thus a noise current I_N) of spectral density $S_{V_N} = 4k_BTR_b$, where k_B is the Boltzmann constant. This thermal noise provides energy to the junction and can make it overcome the barrier ΔU_0. The probability for the junction to escape the well in one attempt is thus $\mathrm{e}^{-\Delta U_0/(k_BT)}$, using standard Boltzmann statistics. At the bottom of the well, the phase particle oscillates at a frequency $\omega_0 = \omega_p\left(1 - i_b^2\right)^{\frac{1}{4}}$ (as seen in Chapter 1). It has thus a probability Γ (called escape rate) to escape the potential well per unit of time, where

$$\Gamma = \frac{\omega_0}{2\pi}\mathrm{e}^{-\Delta U_0/(k_BT)}.$$

Büttiker *et al.* [76] and Devoret *et al.* [77] give an expression close to this approximation by considering damping by a parallel resistance R,

$$\Gamma = a\frac{\omega_0}{2\pi}\exp\left(-\frac{\Delta U_0}{k_BT}\right),$$

where the prefactor a depends weakly on the ratio $k_BT/\Delta U_0$,

$$a = \frac{4\alpha}{\left(1 + \sqrt{1 + \frac{\alpha Q k_B T}{1.8\Delta U_0}}\right)^2}.$$

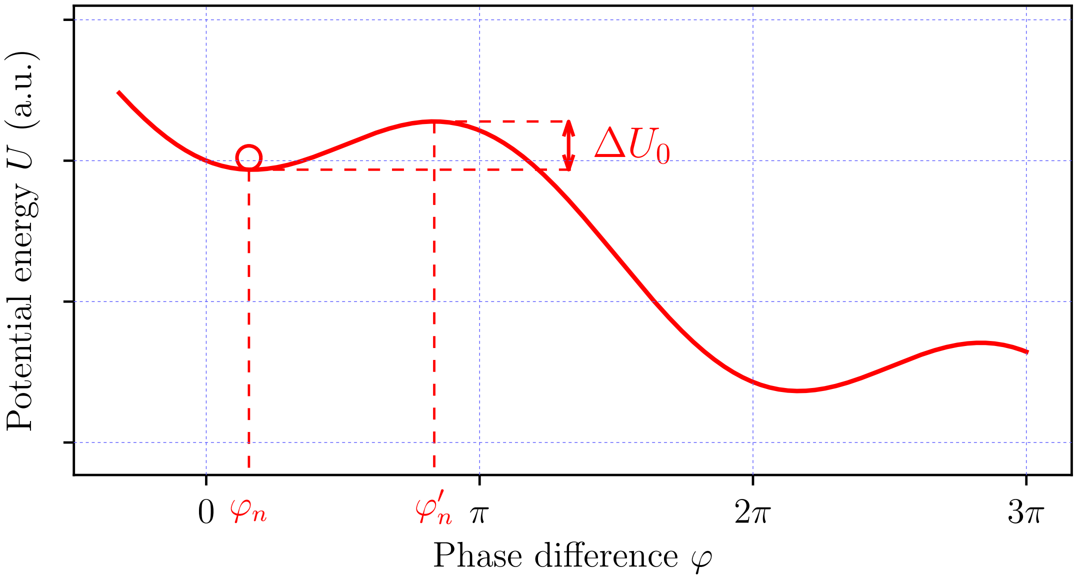

Figure 3.2.: The tilted washboard potential for $I_b < I_0$.

In this expression, α is a numerical constant of order 1 and Q is a quality factor describing dissipation in the junction. Q is linked to the Stewart-McCumber parameter β_C introduced in Chapter 1, $Q = 1/\sqrt{\beta_C}$. A high Q corresponds to low dissipation. In Ref. [77] and in more recent simulations [78], a is considered constant and of the order of 1, giving a simple expression for Γ,

$$\Gamma = \frac{\omega_0}{2\pi}\exp\left(-\frac{\Delta U_0}{k_B T}\right). \tag{3.1}$$

This expression is the same as the one given by simple physical arguments and was proposed by Kramers in 1940 [79] to describe the escape of a particle over a smooth potential barrier.

In spectroscopy measurements, the junction (or SQUID) is biased via a bias resistor and the voltage across it is swept slowly (compared to the plasma frequency), such that all voltages between 0 and $2\Delta/e$ are reached. To estimate the switching current in such a situation, we consider a Josephson junction with no bias current at time $t = 0$ and increase the bias current at a constant rate $\dot{I} = I_0/\tau$ (with $1/\tau \ll \omega_0$). The barrier height gradually decreases, resulting in a higher escape rate for the junction.

Between t and $t + dt$, there is a probability $\Gamma(t)dt$ that the junction has escaped over the barrier. If we call $p(t)$ the probability that the junction is still in the well at time t,

$$\begin{aligned} p(t+dt) &= p(t)\left(1 - \Gamma(t)dt\right), \\ \frac{dp}{p} &= -\Gamma(t)dt, \\ \frac{dp}{p} &= -\tau\Gamma(i_b)di_b. \end{aligned}$$

This differential equation cannot be analytically integrated as $\Gamma(i_b)$ is a quite complex expres-

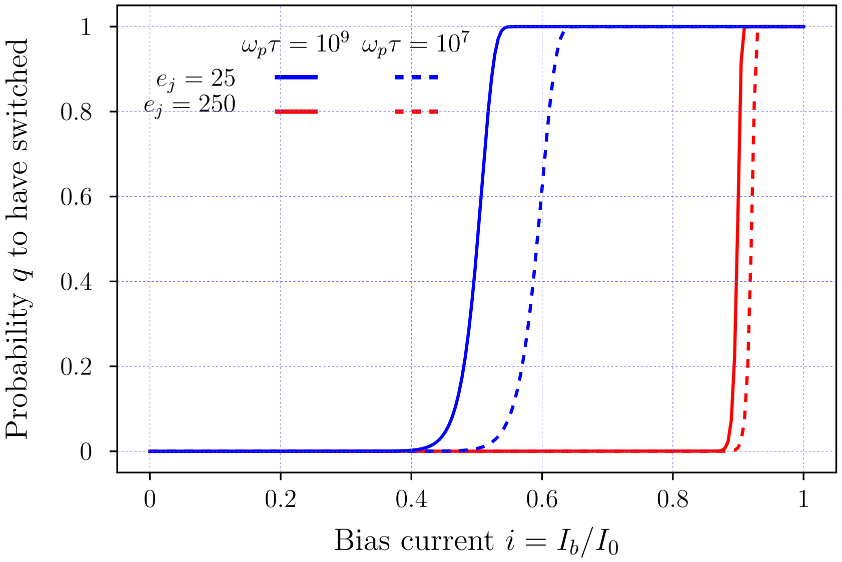

Figure 3.3.: Switching probability as a function of the bias current for a rate $\dot{I}$ such that $\omega_p I_0/\dot{I} = 10^9$.

sion. However, it is possible to integrate it numerically to get $p(i_b)$ for a given $\dot{I}/I_0$ rate. The probability that the junction has switched $q(i_b) = 1-p(i_b)$ is plotted in Figure 3.3 for $\omega_p\tau = 10^9$ and 10^7, for two Josephson energies: $e_j = I_0\varphi_0/(k_BT) = 25$ (in blue) and 250 (in red). The slower rate ($\omega_p\tau = 10^9$) is plotted in full lines and the faster in dashed lines. At a temperature of 50 mK, $e_j = 25$ corresponds to a critical current of 50 nA and $e_j = 250$ to a junction with $I_0 = 500$ nA. Small junctions are much more sensitive to thermal fluctuations and it can be difficult to reach $I_s \sim I_0$. Sweeping the bias current faster allows increasing I_s, the shorter it takes to increase I_b, the less time the junction has to switch out of the zero-voltage state. This is the solution we commonly use to measure the dependence of the critical current of a SQUID on the flux threading it. A more refined method consists of sending short ($\tau_b \sim 1\,\mu$s) current pulses of intensity $I_b < I_0$ as in Ref. [80]. For each pulse, the rate $\Gamma(I_b)$ is constant, and the differential equation for p can be integrated, yielding

$$q(t) = 1 - \mathrm{e}^{-\Gamma(I_b)t}.$$

At the end of the pulse, the probability that the junction has switched is $q(\tau_b) = 1 - \mathrm{e}^{-\Gamma(I_b)\tau_b}$. Averaging over numerous pulses allows extracting Γ.

3.1.2. Noise around the plasma frequency

To get a better insight of the reason why the plasma frequency is the relevant frequency to use in the escape rate of Equation (3.1), it is instructive to look at the spectral density of the phase $S_\varphi(\omega)$ in presence of thermal noise and see what is its behavior around ω_0.

As Likharev [69], we consider small oscillations of the phase around the potential minimum φ_n and write $\varphi = \varphi_n + \delta\varphi$, with $|\delta\varphi| \ll 1$. φ is linearly related to the voltage V by $V = \varphi_0\dot{\varphi}$. So, the Fourier transform of $\delta\varphi$ and V, $\tilde{\varphi}(\omega)$ and $\tilde{V}(\omega)$ follow $\tilde{V}(\omega) = i\omega\varphi_0\tilde{\varphi}(\omega)$. This gives the following relation between the spectral densities,

$$S_\varphi(\omega) = \left(\frac{1}{\varphi_0 \omega}\right)^2 S_V(\omega).$$

The spectral density of the junction voltage is related to the spectral density of the current by $S_V(\omega) = |Z_J(\omega)|^2 S_I(\omega)$, where $Z_J(\omega)$ is the impedance of the junction. The admittance $Y_J(\omega) = 1/Z_J(\omega)$ is formed by the capacitance C of the junction and the non-linear inductance $L_J = \varphi_0/I_0$ for small oscillations around φ_n. $Y_J(\omega) = iC\omega - i\cos\varphi_n/(L_J\omega)$. This gives for the spectral density of the phase,

$$S_\varphi(\omega) = \left(\frac{1}{\varphi_0 \omega}\right)^2 \left(C\omega - \frac{\sqrt{1-i_b^2}}{L_J \omega}\right)^{-2} S_I(\omega).$$

Using the plasma frequency of the junction $\omega_0 = \omega_p \left(1 - i_b^2\right)^{1/4}$, this expression can be rewritten as

$$S_\varphi(\omega) = \frac{1}{I_0^2}\frac{1}{1-i_b^2}\left(\frac{1}{\frac{\omega^2}{\omega_0^2} - 1}\right)^2 S_I(\omega). \tag{3.2}$$

For a white source of noise such as a resistance, $S_I(\omega) = 4k_BT/R$ is independent of the frequency. Equation (3.2) shows that the noise is maximal at the plasma frequency ω_0 of the junction. With this expression, there should be infinite phase fluctuations at ω_0 bringing the junction out of the considered limit of $|\delta\varphi| \ll 1$. In practice, the admittance Y_J always has a small real part G_J, resulting in a finite value of $S_\varphi(\omega_0) = (\varphi_0\omega_0 G_J)^{-2} S_I(\omega_0)$. Equation (3.2) also explains why small junction are more sensitive to noise than larger junctions. $S_\varphi(\omega)$ is proportional to $1/I_0^2$ which is smaller for large junctions.

3.1.3. Macroscopic Quantum Tunneling

As briefly mentioned earlier in the introduction of this section, it is also possible that the junction tunnels out of the potential well. This tunneling effect is different from the tunneling of Cooper pairs across the junction at the basis of all Josephson physics: it consists indeed of the tunneling of the whole junction state and is thus called Macroscopic Quantum Tunneling (MQT). As introduced in Section 1.1.4, the quantum state of a Josephson junction is a combination of phase and charge states and the wavefunction has a certain extension in the phase space as shown in Figure 3.4. The potential of the junction is plotted in red and a symbolic shape of the square of the wavefunction of the junction corresponding to $\langle\hat{\varphi}\rangle = \varphi_n$ is plotted in blue. It is possible that the wavefunction is not zero for $\varphi > \varphi_n'$ where the maximum of the potential is located. In that case, the junction can tunnel out of the well and is not in a localized state (in the phase space) anymore.

For this phenomenon to occur, the width of the junction wavefunction has to be of the order of $\varphi_n' - \varphi_n = \pi - 2\arcsin i$. In order to get an order of magnitude of this width, consider the case of a Josephson junction with a large Josephson energy ($E_J > E_C$). In this case, the junction potential can be approximated around the minimum of potential by

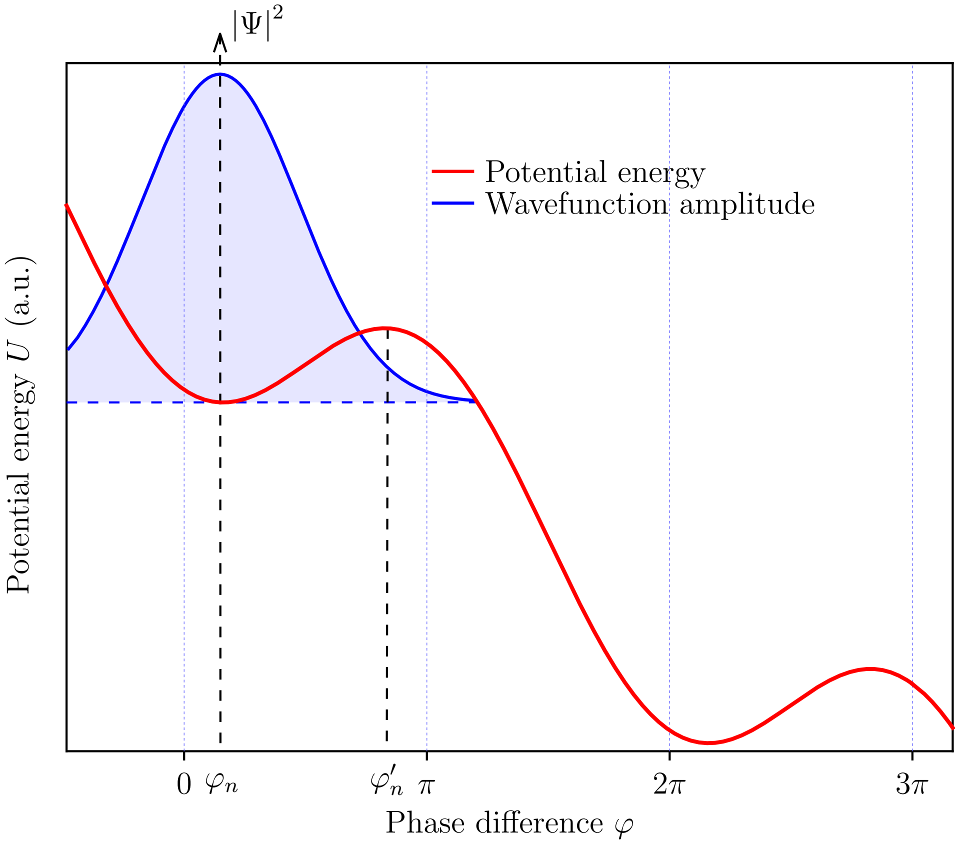

Figure 3.4.: Tilted washboard potential for $I_b < I_0$ and schematics of the junction wavefunction.

$U = E_C N^2 + E_J\sqrt{1-i_b^2}\,(\delta\varphi)^2/2$ according to the calculations of Section 1.1.3. This gives a Hamiltonian

$$\hat{\mathcal{H}}\left(\hat{\varphi},\hat{N}\right) = E_C\hat{N}^2 + \frac{E_J}{2}\sqrt{1-i_b^2}\hat{\varphi}^2,$$
$$\hat{\mathcal{H}}\left(\hat{\varphi},\hat{N}\right) = \frac{\hbar\omega_0}{2}\left(\frac{\hbar}{\mu\omega_0}\hat{N}^2 + \frac{\mu\omega_0}{\hbar}\hat{\varphi}^2\right).$$

This Hamiltonian is that of a harmonic oscillator with frequency $\omega_0 = \omega_p\left(1-i_b^2\right)^{1/4}$ and effective mass $\mu = \hbar^2/(2E_C)$. The extension of the phase is thus of order

$$\Delta\varphi = \sqrt{\frac{\hbar}{\mu\omega_0}} = \left(\frac{2E_C}{E_J\sqrt{1-i_b^2}}\right)^{\frac{1}{4}}.$$

For typical junctions with critical current $I_0 = 500\,\mathrm{nA}$ and intrinsic capacitance 50 fF, the E_C/E_J ratio is of the order of 5×10^{-3}. This gives $\Delta\varphi \sim 0.4\,\mathrm{rad}$ at $0.9I_0$ current bias which stays smaller than $\varphi_n' - \varphi_n = 0.9\,\mathrm{rad}$. For junctions 10 times smaller, E_C/E_J is 100 times larger and $\Delta\varphi \sim 1.3\,\mathrm{rad}$ which indicates a phase extension larger than the width of the potential well and thus a larger tunneling probability.

This probability can be crudely estimated by considering the potential barrier as an infinitely thin barrier of height ΔU_0. The tunneling probability for a particle with energy E is then $p = \mathrm{e}^{-\Delta U_0/E}$. To get an estimate of the macroscopic quantum tunneling rate out of the junction potential well, we can use this formula with $\Delta U_0 = E_J\left(2\sqrt{1-i_b^2} - 2i_b\arccos i_b\right)$ and $E = \hbar\omega_0/2$ the energy of the junction at the fundamental level of the well. This gives an escape rate of

$$\Gamma_{MQT} = \frac{\omega_0}{2\pi}\exp\left(-\frac{2\Delta U_0}{\hbar\omega_0}\right).$$

It is possible to get a more exact result by using the harmonic oscillator approximation in the vicinity of the potential minimum and the quasi-classical WKB approximation for the shape of the wavefunction around φ_n'. This gives a slightly different expression for the escape rate [69],

$$\Gamma_{MQT} = \frac{\omega_0}{2\pi}\sqrt{\frac{864\pi\Delta U_0}{\hbar\omega_0}}\exp\left(-\frac{36\Delta U_0}{5\hbar\omega_0}\right).$$

This tunneling has globally the same effect as thermal fluctuations to reduce the switching current. As long as k_BT is much larger than $\hbar\omega_0$, the thermal effects are dominant and macroscopic quantum tunneling barely happens. In the opposite limit $\hbar\omega_0 \gg k_BT$, switching due to thermal fluctuations is almost non-existent. The crossover temperature between both regimes if commonly [81, 82] expressed as

$$k_BT_{cr} = \frac{\hbar}{2\pi}\omega_0.$$

The 2π factor accounts for the $36/5 = 7.2$ in the exponential and the prefactor before the exponential. For junctions with $\omega_p = 2\pi\times15\,\mathrm{GHz}$, the crossover temperature is of the order of

100 mK. In practice, it can be hard to achieve electronic temperatures in junctions of 100 mK and below.

3.1.4. Phase diffusion

In an ideal junction, as soon as the junction moves out of a potential well, it runs down the potential and acquires a constant voltage V such that $V = \varphi_0 \dot{\varphi}$. But in realistic junctions, due to dissipation in the dielectric or in the environment, it is possible that the junction stops in the next potential well. This results in another zero-voltage state with a phase difference increased by 2π. Due to fluctuations, it is also possible for the junction to jump from potential minimum φ_n to the previous one φ_{n-1}. This leads to a random walk between the potential minima. Because of the tilt of the potential, in the case of a positive bias current, jumps to larger phase differences are more favorable than jumps to smaller phase difference. This diffusion process leads to an average positive drift: $\langle \dot{\varphi} \rangle > 0$, resulting in turn in a finite voltage $\langle V \rangle = \varphi_0 \langle \dot{\varphi} \rangle$.

It is rather straightforward to estimate this voltage for small bias currents in the case of infinite damping where the junction always stops in the next or previous potential well after one jump as shown in Ref. [83]. Starting from the n-th minimum φ_n, the junction can jump over the next or previous potential maximum φ'_n or φ'_{n-1}. The potential height for the next maximum is $\Delta U_+ = E_J \left(2\sqrt{1-i_b^2} - 2 i_b \arccos i_b\right)$ calculated just above. For the previous maximum, the potential difference is $\Delta U_- = E_J \left(2\sqrt{1-i_b^2} + 2 i_b \pi - 2 i_b \arccos i_b\right) = \Delta U_+ + 2 i_b \pi E_J$. Using the same expression for the probability rate as in Section 3.1.1, we get

$$\Gamma_\pm = \frac{\omega_0}{2\pi} \exp\left(-\frac{\Delta U_\pm}{k_B T}\right).$$

With these definitions, the junction has a probability $\Gamma_+ dt$ to jump to φ_{n+1} and a probability $\Gamma_- dt$ to jump to φ_{n-1} in a time dt. Calling $p_n(t)$, the probability for the junction to be in the n-th minimum at time t, we get the following equation for the evolution of $p_n(t)$,

$$\begin{aligned} p_n(t+dt) &= p_{n-1}(t)\Gamma_+ dt + p_{n+1}(t)\Gamma_- dt + p_n(t)\left(1 - \Gamma_+ dt - \Gamma_- dt\right), \\ \dot{p}_n(t) &= \Gamma_+ \left(p_{n-1}(t) - p_n(t)\right) + \Gamma_- \left(p_{n+1}(t) - p_n(t)\right). \end{aligned}$$

Let $p(\varphi, t)$ the probability for the junction to be at phase φ at time t. If we assume that the jumps occur instantly, $p(\varphi, t) = 0$ except at the potential minima, where $p(\varphi_n, t) = p_n(t)$. With these notations,

$$p_{n+1}(t) - p_n(t) = 2\pi \frac{\partial p}{\partial \varphi}(\varphi_n, t).$$

This gives the following partial differential equation for $p(\varphi, t)$,

$$\frac{\partial p}{\partial t}(\varphi, t) + 2\pi \left(\Gamma_+ - \Gamma_-\right) \frac{\partial p}{\partial \varphi}(\varphi, t) = 0.$$

The solutions of this equation are functions of the variable $\varphi - 2\pi\left(\Gamma_+ - \Gamma_-\right) t$ which propagates towards higher φ if the bias current is positive (resulting in $\Delta U_+ < \Delta U_-$ and thus $\Gamma_+ > \Gamma_-$). This gives an average phase velocity $\langle \dot{\varphi} \rangle = 2\pi \left(\Gamma_+ - \Gamma_-\right)$ and a voltage $\langle V \rangle = \varphi_0 \langle \dot{\varphi} \rangle$,

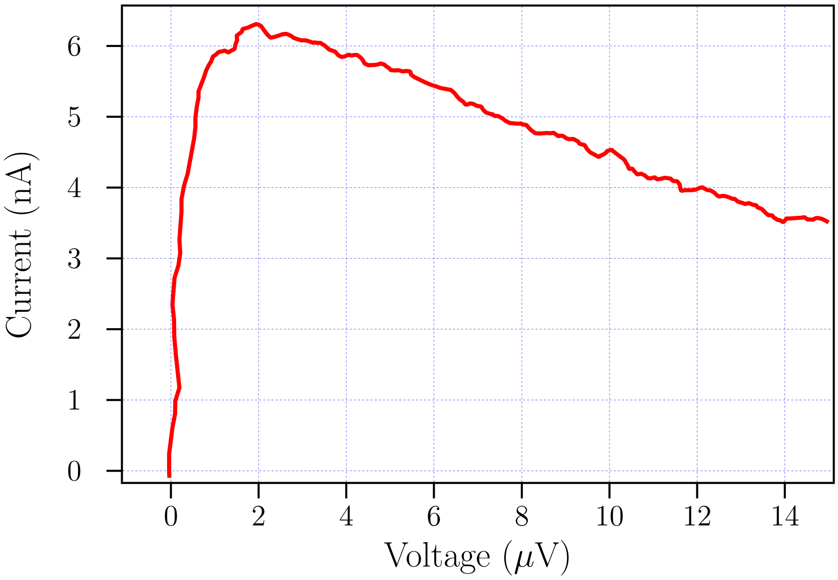

Figure 3.5.: Experimental current-voltage characteristic of a small Josephson junction exhibiting phase diffusion.

$$\langle V\rangle = \omega_0\varphi_0\left(\exp\left(-\frac{\Delta U_+}{k_BT}\right) - \exp\left(-\frac{\Delta U_-}{k_BT}\right)\right).$$

Noticing that $\Delta U_- = \Delta U_+ + 2i_b\pi E_J$, the voltage can be written as

$$\langle V\rangle = \omega_0\varphi_0\exp\left(-\frac{\Delta U_+}{k_BT}\right)(1-\exp(-2i_b\pi E_J)).$$

When $i_b \ll 1$, $\Delta U_+ \sim 2E_J$, such that

$$\langle V\rangle \sim \omega_0\varphi_0 \mathrm{e}^{-\frac{2E_J}{k_BT}}\frac{2i_b\pi E_J}{k_BT}.$$

This gives an effective resistance R_{pd} at low voltage,

$$R_{pd} = \frac{\omega_0}{2\pi}\frac{h^2}{4e^2k_BT}\mathrm{e}^{-\frac{2E_J}{k_BT}}.$$

For junctions with plasma frequency 15 GHz at a temperature of 50 mK, a critical current of 100 nA gives $R_{pd} \sim 10^{-39}\ \Omega$. Smaller junctions with $I_0 = 10\,\mathrm{nA}$ have $R_{pd} \sim 4\,\Omega$ making a noticeable deviation from the vertical supercurrent peak. Figure 3.5 shows an experimental current-voltage characteristic of a junction with $I_0 \sim 10\,\mathrm{nA}$. The non vertical slope at the origin does not appear quite clearly, but the effect of phase diffusion is more visible close to the switching current where the I-V characteristic is bent. Simulations and a more accurate theory, taking into account a finite damping and valid at larger bias currents, can be found for example in Ref. [84, 85].

To make a spectrometer, large junctions are thus favorable as they are less sensitive to noise and have a current-voltage characteristic close to the ideal one. With smaller junctions, the deviation from the vertical supercurrent peak makes it difficult to operate the spectrometer in the low voltage region.

3.2. The retrapping phenomenon

Starting from the subgap region and decreasing the bias voltage, there is a finite voltage below which the phase particle can stay trapped in a potential well. In the tilted washboard potential, the subgap region corresponds to the phase particle sliding down the potential with a finite $\dot{\varphi}$. For small tilts (with $I_b < I_0$), the profile of the potential consists of several hills that the particle has to climb. If there is no dissipation, it is always possible to overcome them. But, in presence of a parallel resistance, the energy of the phase particle decreases and the junction can be trapped in a potential well. This phenomenon is called retrapping and the bias current at which the junction switches back to the zero-voltage state the retrapping current I_r.

To model the dissipation in the junction, we use the RCSJ (Resistively and Capacitively Shunted Junction) model in which the Josephson junction is modeled by an ideal junction in parallel to a capacitance C and a resistance R as done for instance in Ref. [86,87]. The damping parameter $\beta_C = (\omega_p RC)^2$ is supposed large in this reasoning, leading to little dissipation.

When biased at a voltage V, the junction slides down the tilted potential and its phase oscillates at frequency $\omega_J = V/\varphi_0$. Per cycle, the junction dissipates (with I_R the current flowing through the resistance)

$$W = \int_0^{2\pi/\omega_J} I_R V dt = \varphi_0 \int_0^{2\pi} I_R d\varphi.$$

The current I_R is linked to the phase difference via Josephson relation and Ohm's law: $I_R = \varphi_0\dot{\varphi}/R$. This gives

$$W = \frac{\varphi_0^2}{R}\int_0^{2\pi} \dot{\varphi} d\varphi.$$

For small bias currents, $I \ll I_0$, the energy of the junction can be approximated by $E(\varphi) = E_J\left(1 - \cos\varphi + \omega_p^{-2}\dot{\varphi}^2/2\right)$ as derived in Chapter 1. For small dissipation, $E(\varphi)$ is essentially constant. This allows expressing $\dot{\varphi}$ as a function of E and φ,

$$\dot{\varphi} = \omega_p\sqrt{2\left(\frac{E}{E_J} - 1 + \cos\varphi\right)}.$$

The retrapping current is the current for which the kinetic energy cancels at the maximum of the potential well, i.e. $E = 2E_J$. This allows to calculate the dissipation integral W,

$$W = 8\frac{\varphi_0^2\omega_p}{R}.$$

This dissipated energy is equal to the energy supplied by the current source W_s

$$W_s = \int_0^{2\pi/\omega_J} IV dt = \Phi_0 I_r.$$

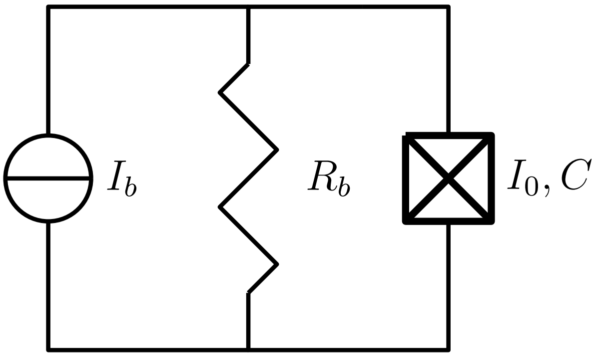

Figure 3.6.: Bias circuit with a resistance in parallel to the junction.

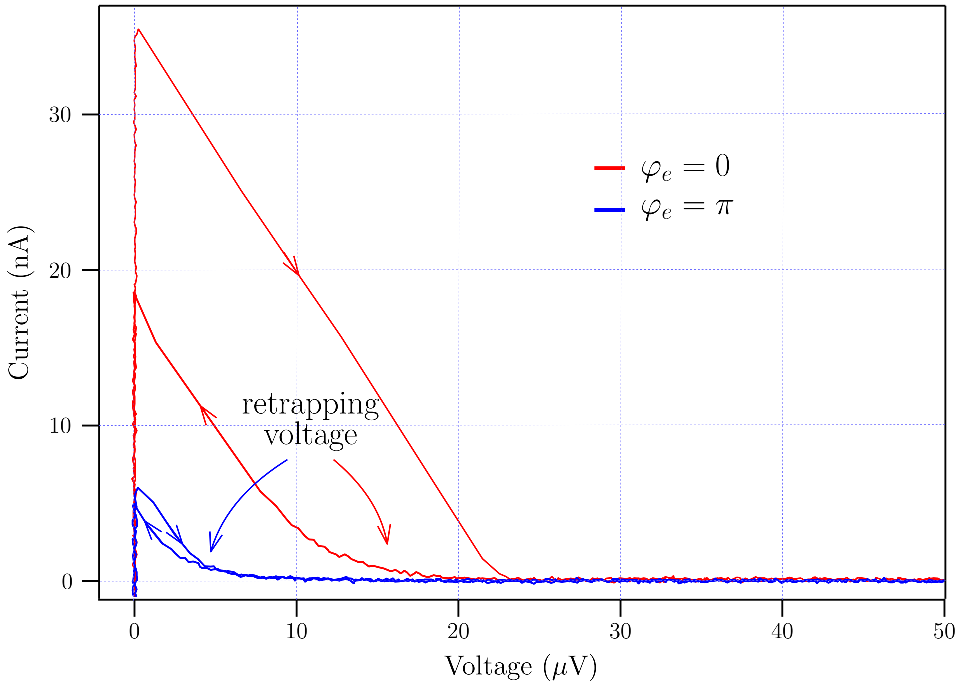

Figure 3.7.: Current-voltage characteristic of an asymmetric SQUID at 0 and π flux biasing.

This gives an expression for the retrapping current,

$$I_r = \frac{8\varphi_0^2\omega_p}{R\Phi_0} = \frac{4}{\pi}\frac{I_0}{\sqrt{\beta_C}}.$$

When the bias resistance is R_b, the retrapping voltage is thus

$$V_r = \frac{4}{\pi}\frac{R_b I_0}{\sqrt{\beta_C}}. \tag{3.3}$$

The R and the C in this expression are the junction intrinsic capacitance and resistance. But if there are additional capacitances in the circuit in parallel to the junction, they increase the total capacitance, leading to a higher β_C parameter and thus a lower retrapping voltage. On the contrary, adding a resistance in parallel to the junction reduces the β_C parameter and increase the retrapping voltage.

For junctions with the bias resistor in parallel to them as in Figure 3.6, $V_r = 4\varphi_0\omega_p/\pi$. This gives $V_r \sim 40\,\mu\text{V}$ for a typical plasma frequency of $\omega_p = 2\pi \times 15\,\text{GHz}$. For SQUIDs, this retrapping voltage is reduced when the flux threading the loop is non-zero as the plasma frequency is changed. With a capacitance C_s in parallel to the junction, V_r becomes

$$V_r = \frac{4}{\pi}\varphi_0\omega_p\frac{C}{C+C_s}.$$

It is rather easy to fabricate on-chip capacitors of order 1 pF, reducing the retrapping voltage to $V_r \sim 5\,\mu\text{V}$ for junctions with critical current around 500 nA.

Figure 3.7 shows the low-voltage region of an experimental current-voltage characteristic of an asymmetric SQUID shunted by a ~ 1 pF capacitance. The arrows on the characteristic denote the biasing direction. Retrapping occurs when the bias voltage is decreased (arrow to the left). Changing the flux in the SQUID allows to change the plasma frequency of the device. At 0 flux bias, the retrapping voltage is maximal and is of order 15 µV. At half a flux quantum, the retrapping voltage is reduced to 5 µV. The discrepancy between the calculated value of 5 µV and the actual 15 µV can be due to the fact that the actual resistance at high frequencies is not R_b. Because of a parasitic capacitance to the ground, this resistance is decreased, resulting in a smaller β_C parameter and thus in a larger retrapping voltage.

For the Josephson spectrometer to operate at low frequencies, a small retrapping voltage is necessary. Adding a large shunt capacitance in parallel to the junction is thus favorable.

3.3. Influence of the biasing circuit

We have already seen that the bias circuit can influence the behavior of the junctions in many ways: changing the spectrometer absorption and emission linewidth (Section 2.4), altering the switching current because of the induced current noise (Section 3.1), modifying the retrapping voltage with parallel resistors and capacitors (Section 3.2). But there are other features due to the biasing circuit which can occur, in particular because of too high inductors.

3.3.1. Low frequency resonances

The principle of the Josephson spectrometer is to detect the absorption of emitted photons by the environment. In the most ideal situation, the only resonant modes are the one we want to study but it is highly probable that there are other modes due to the biasing circuit as already briefly introduced in Section 2.2.1 when the bias circuit consists of a shunt capacitance and a decoupling inductance. If the inductor has a large inductance value, the corresponding frequency is quite low. For instance, if there are aluminum wirebonds directly connected to the spectrometer and a filtering capacitance at the other end, the corresponding LC mode has a low frequency resonance: the inductance of a 1 mm long wirebond is $\sim 1\,\text{nH}$ and a typical capacitance used to filter out noise of 100 pF gives a resonance frequency of $\sim 500\,\text{MHz}$. Because the length of the wirebonds is comparable to the wavelength of the microwaves (6 mm at 50 GHz in vacuum), they have to be considered as transmission lines with several resonance frequencies.

In addition, a Josephson junction biased at half a resonance frequency ω_0 generates an oscillating supercurrent at frequency $\omega_0/2$. Because of the non-linear character of the junction, there will also be harmonics at ω_0, $3\omega_0/2$, $2\omega_0$, … and the harmonic at ω_0 is resonant. This generation of harmonics can add several spurious peaks in the spectrum, at $\omega_0/2$, $\omega_0/3$, …

If the junction is biased at $2\omega_0$, the revers process can occur. The emitted photon at $2\omega_0$ can be converted in two photons at the resonant frequency ω_0. The same can happen at $3\omega_0$, $4\omega_0$, … If there are several resonant modes, for instance at ω_0 and ω_1, biasing the junction at $n_0\omega_0 + n_1\omega_1$ (with n_0 and n_1 positive integers) can generate photons resonant with both modes.

The IV characteristic quickly becomes quite complicated. The processes leading to the generation of such harmonics and sub-harmonics is explained in more details in Section 3.3.3.

An experimental current-voltage characteristic of a Josephson junction with a resonant mode close to 2.5 GHz is shown in Figure 3.8. There are current peaks for every multiple of the resonance frequency. It is not straightforward to deduce the spectrum of the system of interest from such an IV characteristic.

3.3.2. Relaxation oscillations

Another interesting feature due to large inductors connected to a Josephson junction is the appearance of relaxation oscillations. To understand this phenomenon, we follow the work of Ref. [88] and consider the bias circuit sketched in Figure 3.9a with a bias resistance R_b and a bias inductance L_b. Depending on the bias current $I_b = V_b/R_b$, there are three different situations (represented in Figure 3.9b) for a junction with critical current I_0 and intrinsic capacitance C:

(1) The zero-voltage state: the Josephson junction acts as a wire with no resistance,

(2) The subgap region: the junction is equivalent to its intrinsic capacitance C,

(3) The quasiparticle branch: the junction can be modeled by a voltage source of voltage $2\Delta/e$.

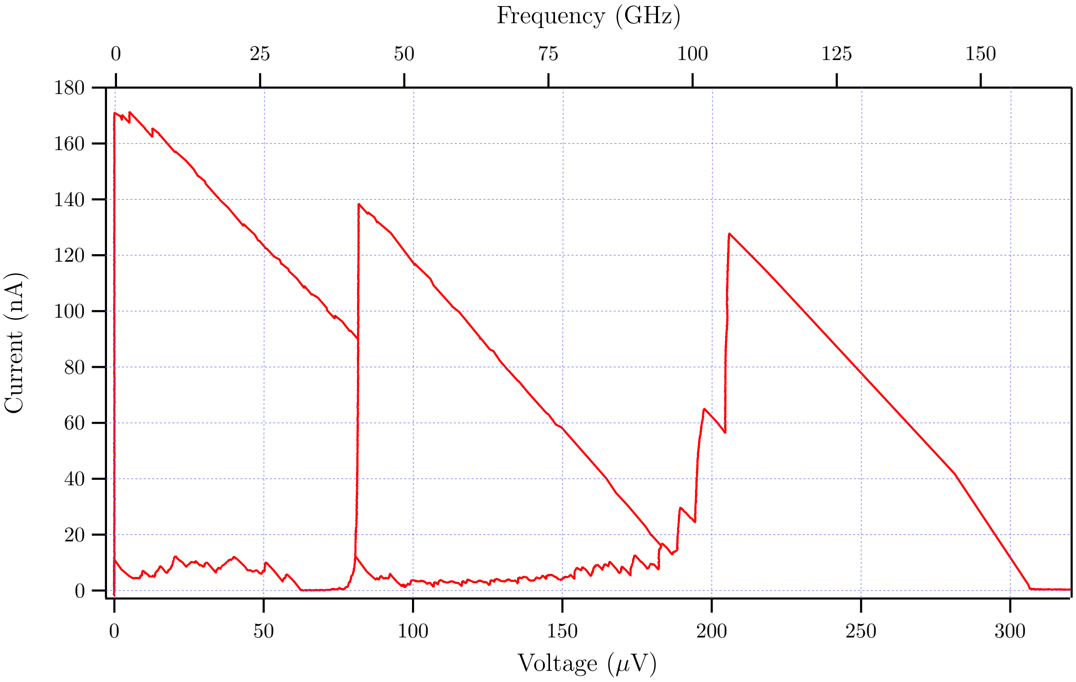

Figure 3.8.: Current-voltage characteristic of a Josephson junction with a mode close to 2.5 GHz.

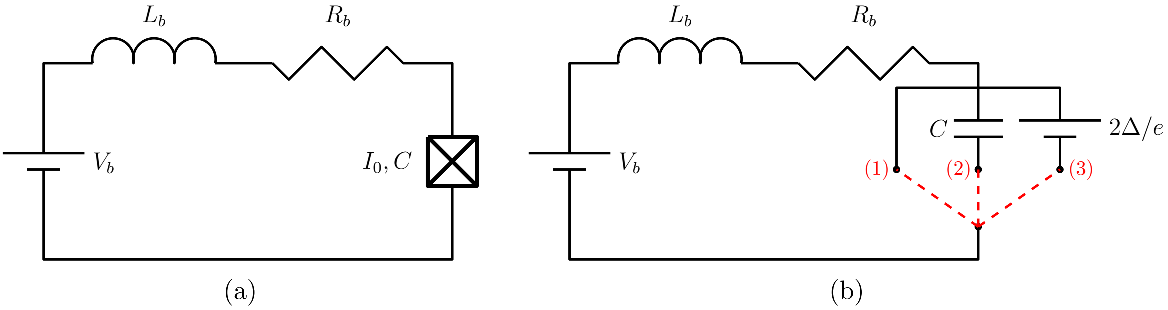

Figure 3.9.: (a) Bias circuit for a Josephson junction containing an inductance and a resistance. (b) Equivalent circuit in the CSJ model.

Figure 3.10 shows a simulation of these oscillations for a bias voltage of $V_b = 0.6\Delta/e$ with a bias resistance $R_b = 0.3R_N$, resulting in a current bias $I_b = 4I_0/\pi > I_0$. The quality factor $Q = 1/R_b\sqrt{L_b/C}$ of the series RLC circuit is 5. The different colors correspond to the three different situations described above: in phase (1) the junction is a superconducting wire, in phase (2) and (2′) it is equivalent to a capacitor and in phase (3) to a voltage source. Figure (a) and (b) show the voltage V across the junction and the current I flowing through the junction as a function of time t with $\overline{V}$ and $\overline{I}$ the average values. Figure (c) represents the current against the voltage during one oscillation cycle with the average value $\left(\overline{V}, \overline{I}\right)$ marked with a cross. (d) is the average current-voltage characteristic for values of bias voltage ranging from 0 to above the gap. The cross corresponds to the bias voltage of panels (a), (b) and (c).

When $I_b \gtrsim I_0$, without the inductance, after a short time $\sim \tau_C = R_bC$, the junction voltage would simply go to R_bI_b and the current would reach 0. But with the inductance L_b, when I_b reaches I_0, a voltage $2\Delta/e$ rapidly (in a time $\sim \tau_C$) develops across the capacitance C since current cannot change instantaneously. In the same time, the current almost stays I_0 because of the inductance. At this point, the junction acts as a voltage source and the current decreases slowly (in some $\tau_L = L/R$) until it reaches 0 and the junction switches rapidly back to the zero-voltage state (in $\sim \tau_C$) because of the overshoot of the voltage in the RLC circuit. This leads to oscillations of the junction voltage and current. The measured current-voltage characteristic is the average value of these so-called relaxation oscillations. They stop as soon as the energy stored in the inductance is not sufficient to charge the capacitance up to the voltage $2\Delta/e$ in phase (2) and charge it to 0 in (2′). At this bias voltage, the amplitude of the oscillations decreases with time and the current tends to zero.

Figure 3.11 shows two experimental current-voltage characteristics of a Josephson junction with a large bias inductance L_b of about 5 nH as well as the biasing circuit. The shunt capacitance C_S was evaporated on the sample (following the method described in Chapter 4) and is of the order of 1 pF. The bias resistance is 200 Ω. The red capacitance C_f was added in the red curve of the left-hand side graph. It is a high-frequency capacitor of 100 nF. The quality factors of both circuits estimated with these values are $Q \sim 0.4$ without C_f and $\sim 10^{-3}$ with C_f. In the red curve, the relaxation oscillations have almost disappeared and it is possible to see peaks which were hidden in the blue curve. These peaks are due to a non-controlled electromagnetic environment and will not be discussed here.

Low bias inductances and large shunt capacitances are thus a good solution to limit the relaxation oscillations and have an appreciable sensitivity at low frequencies for the spectrometer.

3.3.3. Generation of harmonics and sub-harmonics

Consider the same biasing circuit as in Figure 3.9a with V_b such that the junction is not in the zero-voltage state. Kirchhoff's law gives $V_b = V + R_bI + L_b\dot{I}$. Combining with the AC Josephson relation, this gives an expression for $\dot{\varphi}$,

$$\dot{\varphi}\varphi_0 = V_b - R_bI - L_b\dot{I}. \tag{3.4}$$

If we consider a large bias voltage, such that $V_b \gg R_bI_0$, we can neglect R_bI in Equation (3.4) and integrate it to get

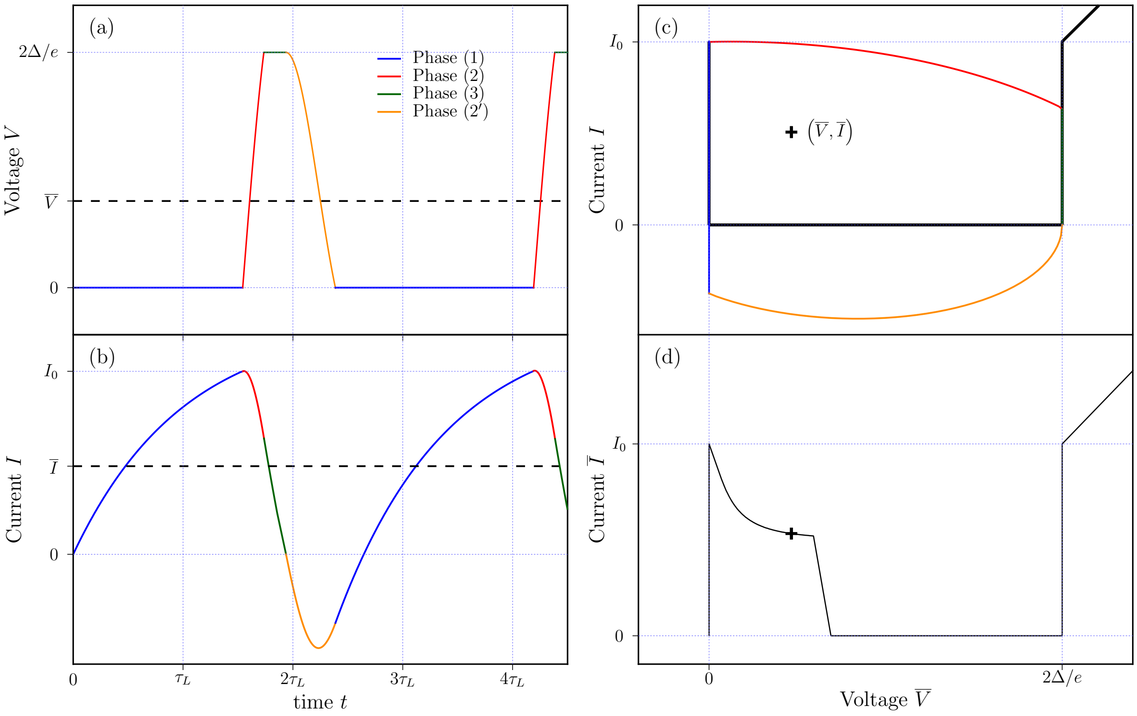

Figure 3.10.: Evolution of voltage (a), current (b) when the current bias is larger than the critical current. (c) Resulting current-voltage characteristic for one bias voltage V_b. (d) Current-voltage characteristic for V_b varying from 0 to above the gap.

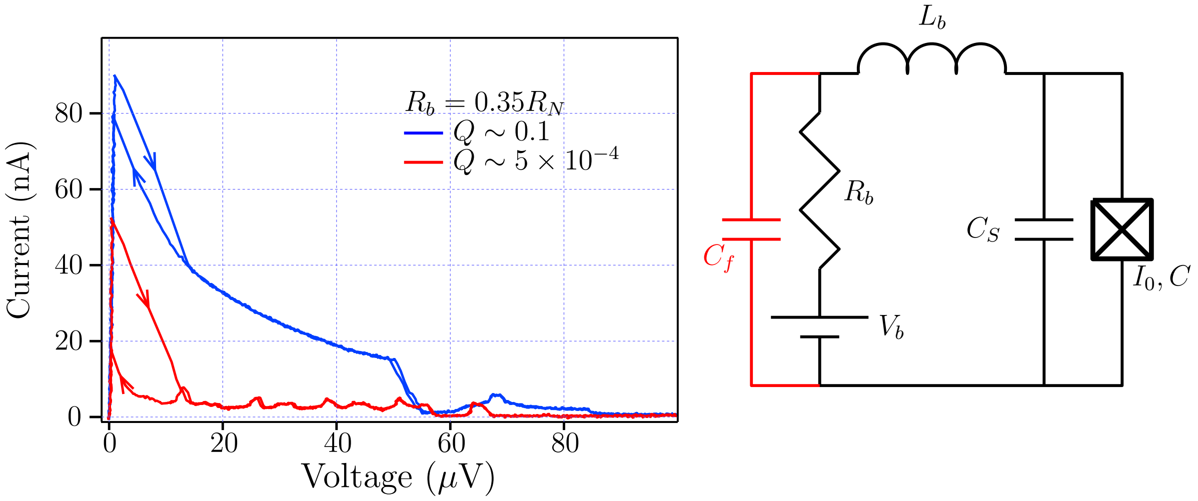

(a) (b)

Figure 3.11.: (a) Experimental current-voltage characteristic of a Josephson junction exhibiting relaxation oscillations ; (b) Biasing circuit.

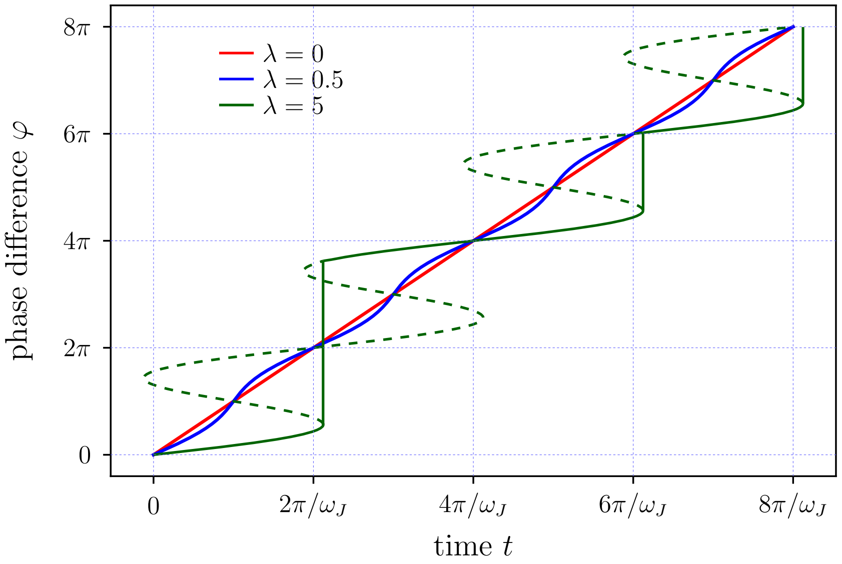

Figure 3.12.: Phase difference as a function of time for $\lambda = 0$, 0.5 and 5.

$$\varphi = \omega_J t - \lambda \sin\varphi,$$

where $\omega_J = V/\varphi_0$ is the Josephson frequency and $\lambda = L_b I_0/\varphi_0 = L_b/L_J$ is the ratio of the bias inductance to the Josephson inductance.

If there is no bias inductance or if it is negligible ($\lambda \ll 1$), $\varphi = \omega_J t$ and we get usual Josephson oscillations at the Josephson frequency. If $\lambda > 1$, $\varphi(t)$ is not continuous and $\sim 2\pi$ jumps are possible or even $\sim 2n\pi$ jumps as shown in Figure 3.12. The time interval between a phase jump of n phase quanta and n' phase quanta is $\Delta t = 2n\pi/\omega_J$. During this time, the phase increases by $\Delta\varphi = 2n'\pi$. This results in a phase oscillation frequency $\omega = \Delta\varphi/\Delta t = \omega_J n'/n$. There are of course oscillations at the Josephson frequency ω_J but also at harmonics and sub-harmonics of this frequency!

When $\lambda \gg 1$, it is easy to estimate the number of solutions of $\varphi + \lambda \sin\varphi = 0$. There is always 1 evident solution of this equation ($\varphi = 0$) plus 2 other solutions per 2π period, until $|\varphi| > \lambda$. This gives $4N + 1$ solutions where $N \sim \lfloor \lambda/(2\pi) \rfloor$ is the largest integer smaller than or equal to $\lambda/(2\pi)$. Only half of them are stable. Starting from one value, it is thus possible to make a maximal phase jump of $2N$, resulting in a greatest harmonic of $2N\omega_J$ and a lowest sub-harmonic of $\omega_J/(2N)$

As the generated frequencies are $\omega_J n'/n$ with n and n' integers smaller than $2N$, there are in total a bit less than $4N^2$ frequencies! These frequencies are plotted in the case of $N = 0$, $N = 1$ and $N = 2$ in Figure 3.13 with the fundamental Josephson frequency ω_J in red. If $N \geq 1$, the measured spectrum can be quite complicated to read.

A biasing circuit such that $\lambda \ll 1$ is thus favorable for the spectrometer. As $\lambda = L_b I_0/\varphi_0$, decreasing L_b is a good solution. I_0 can also be decreased but has to stay large enough to limit the sensitivity to noise.

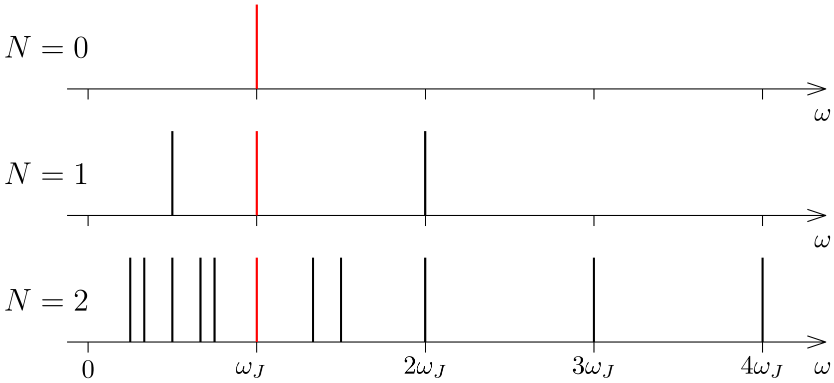

Figure 3.13.: Frequencies generated by a Josephson junction with a series inductance and resistance.

3.4. External microwave effects

Josephson junctions are quite sensitive to their microwave environment. This is the basis of the operation of the Josephson spectrometer. A resonant mode is indeed translated in a peak in the current-voltage characteristic. It appears therefore quite logical that an external microwave source can influence the behavior of a junction. The two main phenomena resulting from external microwaves are the appearance of so-called Shapiro steps or peaks in the current-voltage characteristic and photo-assisted tunneling of quasiparticles through the junction.

3.4.1. The Shapiro steps

Applying a DC voltage V_{DC} to a junction results in a fast oscillating current through the junction at the Josephson frequency $\omega_J = V_{DC}/\varphi_0$. Similarly, applying microwaves at a frequency ω_{RF} to a Josephson junction results in a DC voltage $V_{RF} = \varphi_0 \omega_{RF}$. This effect was first observed in 1963 by S. Shapiro [57] and is at the heart of the Josephson voltage standard as already mentioned in Section 1.4.3. Due to the non-linearity of Josephson junctions, there are also peaks at multiples of this voltage, nV_{RF}.

Applying microwaves at frequency ω_{RF} creates a voltage at the same frequency across the junction and its capacitance (and also the bias circuit or any other impedance in parallel to the junction). This gives

$$V = V_1 \cos \omega_{RF} t,$$

where V_1 is the amplitude of the microwaves. In presence of an additional DC voltage V_{DC}, the phase difference φ can be written as

$$\varphi = \theta_0 + \omega_J t + \frac{V_1}{V_{RF}} \sin \omega_{RF} t. \tag{3.5}$$

The total current through the junction is thus (using the Jacobi-Anger expansion introduced in Chapter 2)

$$I = I_0 \sin \varphi = I_0 \sum_{n=-\infty}^{+\infty} J_n \left(\frac{V_1}{V_{RF}} \right) \sin \left(\theta_0 + \omega_J t + n\omega_{RF} t \right),$$

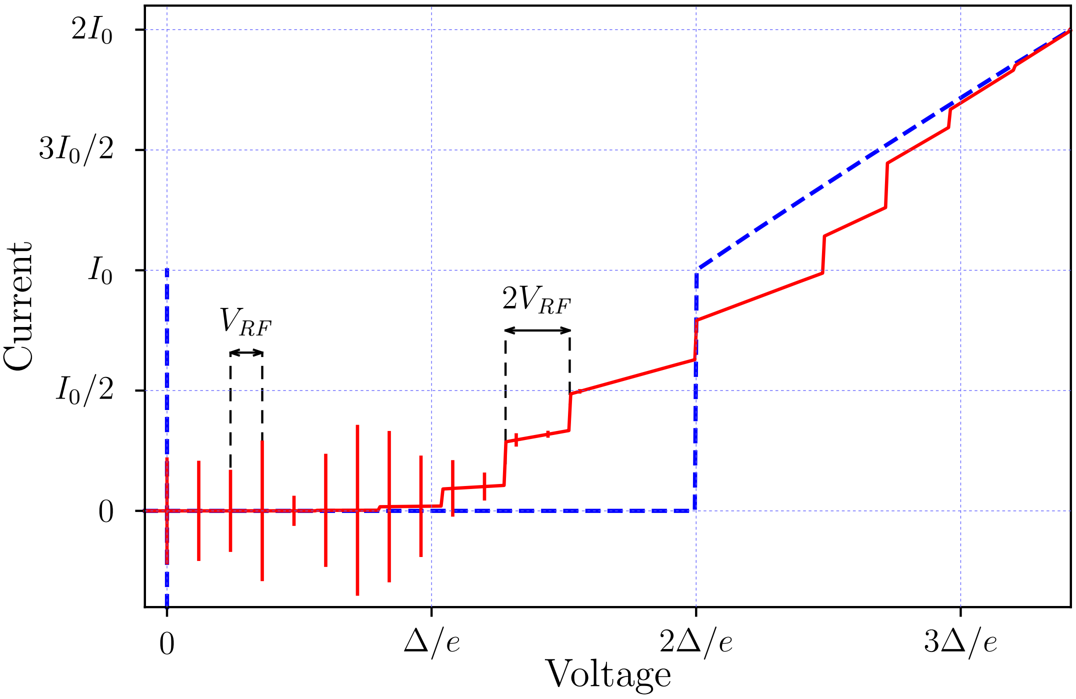

Figure 3.14.: Ideal current-voltage characteristic of a Josephson junction irradiated by microwaves at frequency ω_{RF} with $V_1/V_{RF} = 8$.

where $J_n(\delta)$ is the n-th Bessel function of the first kind of argument δ. The average value of this current is 0 except when the DC voltage is such that $\omega_J = n\omega_{RF}$. At these voltages, the current is

$$I_n = I_0 J_{-n}\left(\frac{V_1}{V_{RF}}\right)\sin\theta_0.$$

The current-voltage characteristic consists of current peaks at voltages nV_{RF}, called the Shapiro peaks, as shown in Figure 3.14. The steps around $2\Delta/e$ are due to photo-assisted tunneling and are described in the next section. The dashed blue line is the ideal characteristic without applied microwaves. The red curve has $V_1/V_{RF} = 8$. Due to the properties of the Bessel functions, it is possible to have several peaks of non-negligible amplitude.

The supercurrent of the junction is also modulated by the microwaves. For $V = 0$, the $n = 0$ term of the sum gives $I_0 J_0(V_1/V_{RF})\sin\theta_0$ which is smaller in amplitude than the ordinary supercurrent I_0.

As shown in the figure, it is possible to have $I < 0$ and $V > 0$. This means that the junction provides a positive power $\mathcal{P} = -IV$ to the DC power supply and acts as an active element! This is only possible because this power is supplied by the microwave source. The junction here converts microwave power to DC power. These Shapiro peaks are thus different in nature from the peaks due to a resonance in the environment which can never have $IV < 0$ as they correspond to absorption of energy by the resonant system.

According to the calculations made just above, the linewidth of the Shapiro peaks is zero.

In practice, the measured width is limited by the linewidth of the microwaves irradiating the junction. Commercial sources allow for a linewidth of the order of 1 Hz, resulting in a voltage linewidth of the order of 1 fV. This precise DC voltage could be used to bias the spectrometer and thus provide a narrow emission linewidth. This is also one of the projects of the Φ_0 group and is one of the perspective presented in the conclusion of this work.

3.4.2. Photo-assisted tunneling

Microwave signals can also provide energy to quasiparticles in the superconductors and help them tunnel. If the junction is voltage biased at a voltage $V = 2\Delta/e - V_0$ (or higher), a photon of energy eV_0 can raise the energy of quasiparticles on one side of the junction to the level of free levels on the other side. This leads to an increased current between $2\Delta/e - V_0$ and $2\Delta/2$. When the junction is biased at $2\Delta/e - nV_0$, n photons of energy eV_0 can also produce the same phenomenon. On the contrary, when the junction is biased at $2\Delta/e + V_0$, the quasiparticle current is reduced because the tunneling of a quasiparticle is accompanied by the emission of a photon of energy eV_0. The resulting current-voltage characteristic is thus modified around the gap voltage and consists of steps at $V_n = 2\Delta/e - nV_0$ and downwards steps at $\tilde{V}_n = 2\Delta/e + nV_0$. The amplitude of these steps can be calculated by a method introduced by Tien and Gordon [89]. In presence of a DC voltage V_{DC} and microwaves at frequency ω_{RF}, we write the phase difference as in Equation (3.5) giving the following expression for the voltage

$$V = V_{DC} + V_1 \cos \omega_{RF} t.$$

The energy of a quasiparticle in the junction is thus $E = eV$, such that the quantum phase factor $\exp(-iEt/\hbar)$ writes

$$\exp\left(-\frac{i}{\hbar}\left(eV_{DC}t + \frac{eV_1}{\omega_{RF}} \sin \omega_{RF} t\right)\right).$$

Using the Jacobi-Anger expansion, this phase factor is

$$\sum_{n=-\infty}^{+\infty} J_n\left(\frac{V_1}{2V_{RF}}\right) \mathrm{e}^{-\frac{i}{\hbar}(eV_{DC}+n\hbar\omega_{RF})t}.$$

This can be understood as the quasiparticles being divided between the energy levels at $eV_{DC} + n\hbar\omega_{RF}$ with amplitudes the Bessel coefficients. The density of states is thus modified from $\rho(eV_{DC})$ without microwaves to

$$\rho_{RF}(eV_{DC}) = \sum_{n=-\infty}^{+\infty} \rho\left(eV_{DC} + n\hbar\omega_{RF}\right) J_n\left(\frac{V_1}{2V_{RF}}\right)^2.$$

The quasiparticle current calculated in Section 1.2.3 without microwaves now becomes

$$I_N\left(V_{DC}\right) = \sum_{n=-\infty}^{+\infty} J_n\left(\frac{V_1}{2V_{RF}}\right)^2 I_N^0\left(V_{DC} + 2n\varphi_0\omega_{RF}\right),$$

where $I_N^0(V)$ is the current calculated without microwaves. The steps visible in Figure 3.14 were calculated with this formula for $V_1/V_{RF} = 8$.

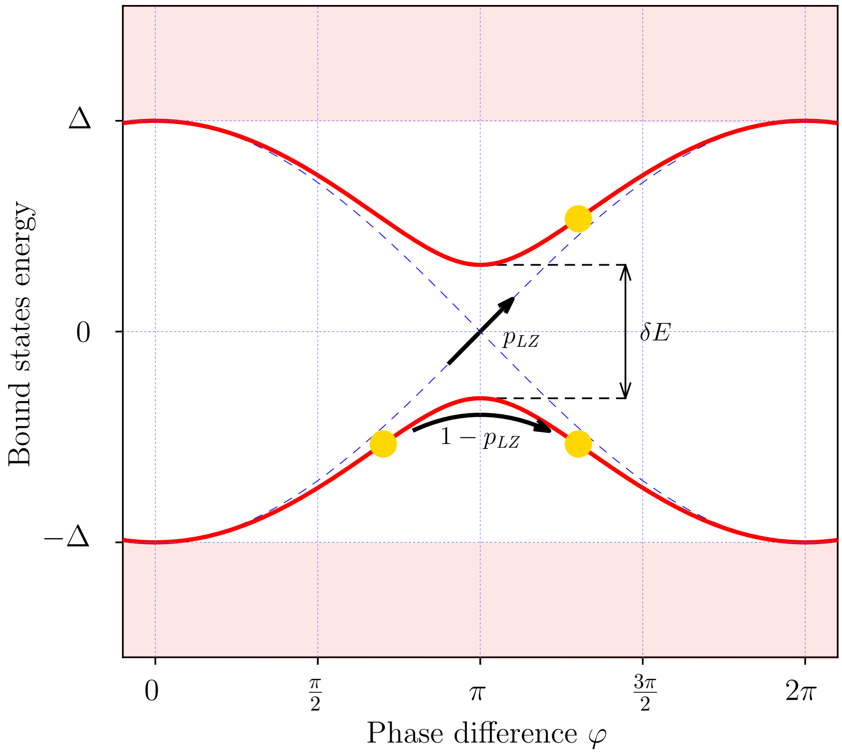

Figure 3.15.: Landau-Zener transition for a quasiparticle in a Josephson junction.

3.5. Background in the subgap region

3.5.1. Dissipative current carried by Andreev Bound States

When the current-voltage characteristic was first introduced in Chapter 1, the current at finite voltage was assumed to be zero because no Cooper pairs or quasiparticles can tunnel since there are no available states at the same energy. In the microscopic description of Josephson junctions, the current at zero voltage is carried by Andreev bound states (ABS) in the junction. However, at a finite voltage, some quasiparticles can tunnel through the junction via Landau-Zener transitions [90, 91] between two ABS. To estimate the magnitude of these processes, we follow the work of Ref. [92].

At finite voltage V, the phase of the junction changes with a rate $\dot{\varphi} = V/\varphi_0$. As shown in Figure 3.15 a quasiparticle starting from the ground state (the lower ABS) at $\varphi = 0$, will stay in this state as the phase is swept to 2π and there is no current through the junction. There is also a finite probability p_{LZ} to induce a Landau-Zener transition to the upper ABS. When such a transition occurs, the quasiparticle which was in the lower band of the continuum at $\varphi = 0$ ends up in the upper band of the continuum at $\varphi = 2\pi$. At this point, it can tunnel to the other electrode and generate a current through the junction.

The Landau-Zener probability p_{LZ} to have a transition between the two levels is given by the following relation [90, 91],

$$p_{LZ} = \exp\left(-\frac{\pi}{2\hbar}\frac{(\delta E)^2}{\left|\frac{d}{dt}\varepsilon\right|_{\varphi=\pi}}\right), \tag{3.6}$$

where δE is the energy difference between the states $|+\rangle$ and $|-\rangle$ at $\varphi = \pi$ where they are the closest in energy. ε is the energy difference of the states if they were to cross. In the case of Andreev bound states, it is the energy of $|\pm\rangle$ with a transmission of 1. They are plotted in Figure 3.15 in thin dashed blue lines. The Landau-Zener probability of Equation (3.6) holds true as long as the sweeping is adiabatic which is when the sweeping rate is small compared to the difference between the energy levels where they are the closest ($\hbar\dot{\varphi} \ll \delta E$). For a conduction channel with transmission τ,

$$\delta E = 2\Delta\sqrt{1-\tau}.$$

So, the condition to stay adiabatic is $eV \ll \Delta\sqrt{1-\tau}$. For junctions with $\tau < 10^{-2}$, $\Delta\sqrt{1-\tau}/e$ is of the order of 200 µV.

$$\begin{aligned}\left|\frac{d}{dt}\varepsilon\right|_{\varphi=\pi} &= -2\Delta \lim_{\varphi\to\pi^-}\frac{d}{dt}\left|\cos\frac{\varphi}{2}\right| \\ &= \frac{\Delta\,|V|}{\varphi_0}.\end{aligned}$$

This gives an expression for p_{LZ},

$$p_{LZ} = \exp\left(-\frac{\pi\Delta}{e\,|V|}(1-\tau)\right).$$

This probability is higher for larger transmissions and reaches 1 for a transparent barrier. In the case of a tunnel junction where $\tau \ll 1$, this probability is low. For instance, at $V = \Delta/(10e)$, $p_{LZ} \sim 10^{-14}$ for $\tau = 10^{-3}$.

Considering independent channels, the total current associated with this process is $I_{ABS} = Q\nu_J p_{LZ}$ where Q is the charge transferred in one cycle and $\nu_J = |V|/\Phi_0$ is the Josephson frequency. This transition transfers as many charges as one single channel of transmission one. The current carried by such a channel is $\Delta/(2\varphi_0)\sin\varphi/2$, using the formula derived in the first chapter. The charge Q is then

$$Q = \frac{\Delta}{2\varphi_0}\int_0^{\nu_J^{-1}} \sin\frac{\varphi}{2}dt = \frac{2\Delta}{|V|}.$$

This gives the following expression for the current carried by one conduction channel of transmission τ,

$$I_{ABS} = \operatorname{sgn}(V)\frac{\Delta}{\pi\varphi_0}\exp\left(-\frac{\pi\Delta}{e\,|V|}(1-\tau)\right). \tag{3.7}$$

In the case of tunnel junctions, this current is negligible: with the gap of aluminum and $\tau = 10^{-3}$, the current is below 10^{-21} A at $V = \Delta/(10e)$ which is much smaller than the typical noise of 10 pA. Only transmissions above 0.75 result in a current above this noise background.

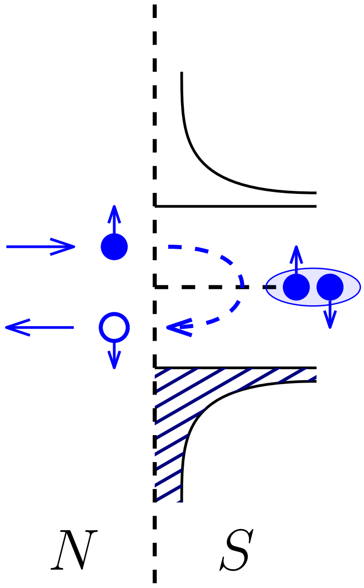

Figure 3.16.: Andreev reflection: an electron arriving at the interface between a normal metal and a superconductor is reflected as a hole.

For a junction with several independent channels, the total current is the contribution of all channels. So, only one channel with a high transmission can give rise to a large current.

Equation (3.7) is only valid for small voltages where the ABS slowly vary in time. At larger voltages, the ABS are largely out of equilibrium and another formalism is needed to quantify the resulting dissipative current, the multiple Andreev reflections (MAR).

3.5.2. Multiple Andreev Reflections

This process consists of tunneling of quasiparticles between the two superconducting electrodes of a Josephson junction to which a finite voltage V is applied. It was first introduced in the 1980s [93] and further investigated in the 1990s [94, 95]. To explain it, we first need to understand the Andreev reflection mechanism occurring at the interface between superconducting and normal regions.

Consider an electron with spin up arriving from a normal metal to a superconductor with energy below the gap as shown in Figure 3.16. The incoming electron is sketched as a full blue circle with an arrow (representing its spin) pointing up. The simplest process that can happen is a simple back-scattering as a spin-up electron (not depicted in the figure). Because its energy is below the gap energy of the superconductor, it cannot go into the superconductor as it is. The only possible way for the electron to enter the superconductor is to be coupled to an electron with spin down going to the left via the superconducting pairing interaction (represented as a light blue ellipse). This process implies that a hole with spin down comes out of the superconductor (empty blue circle). It is called Andreev reflection. As it is elastic, all electrons and holes have the same energy.

In Josephson junctions, Andreev reflections are the process giving rise to the Andreev Bound

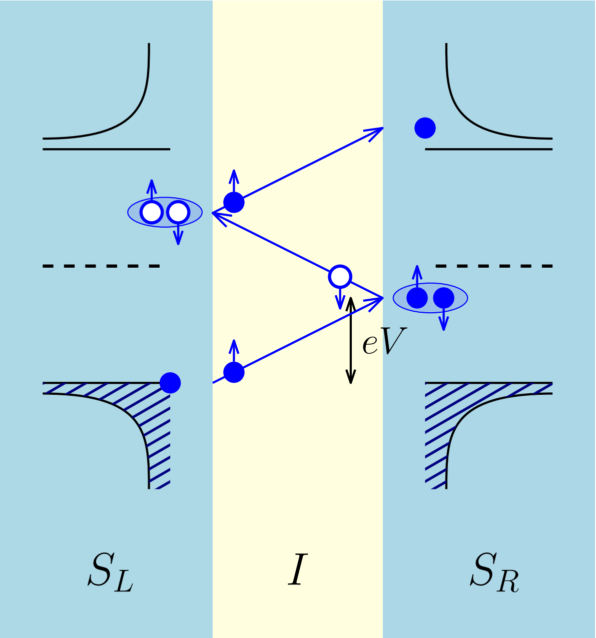

Figure 3.17.: Multiple Andreev reflection: an electron arriving at the interface between a normal metal and a superconductor is reflected as a hole.

States: the reflected hole then arrives at the left-hand side superconducting electrode and is Andreev-reflected as an electron, forming a bound state in the junction.

If a voltage is applied across a Josephson junction, multiple Andreev reflections can occur in the junction as sketched in Figure 3.17 for one conduction channel of transmission τ. The two electrodes of the junction S_L and S_R are plotted at the same chemical potential and the voltage V across the junction is represented as kinetic energy for the electrons and holes. A quasiparticle from the left electrode crosses the insulating barrier and acquires an energy eV. There is only a probability τ that the electron crosses the barrier and a probability $1-\tau$ that it is reflected directly by the insulator as an electron. When it arrives at the right electrode, the electron is Andreev reflected as a hole and a Cooper pair is created in the right electrode. The reflected hole crosses in turn the barrier (with probability τ) and loses energy $-eV$ (or gain eV). It can also be Andreev reflected when it arrives at the left electrode resulting in the destruction of a Cooper pair in the left electrode. After a certain even number of reflections (2 in the figure), an electron reaches the right upper continuum. It is also possible that a hole reaches the left upper continuum after an odd number of reflections.

A MAR process involving n reflections is called the MAR of order $n+1$ and involves the transfer of a charge $(n+1)\,e$ across the junction.

- When n is even, $n/2$ Cooper pairs are created in the right-hand electrode and $n/2$ Cooper pairs are annihilated in the left-hand electrode. This makes a charge ne. To this charge, e is added accounting for the quasiparticle ending in the upper continuum.
- When n is odd, $(n+1)/2$ Cooper pairs are created in the right-hand electrode and $(n-1)/2$ are annihilated in the left-hand electrode. On top of that, a quasiparticle is

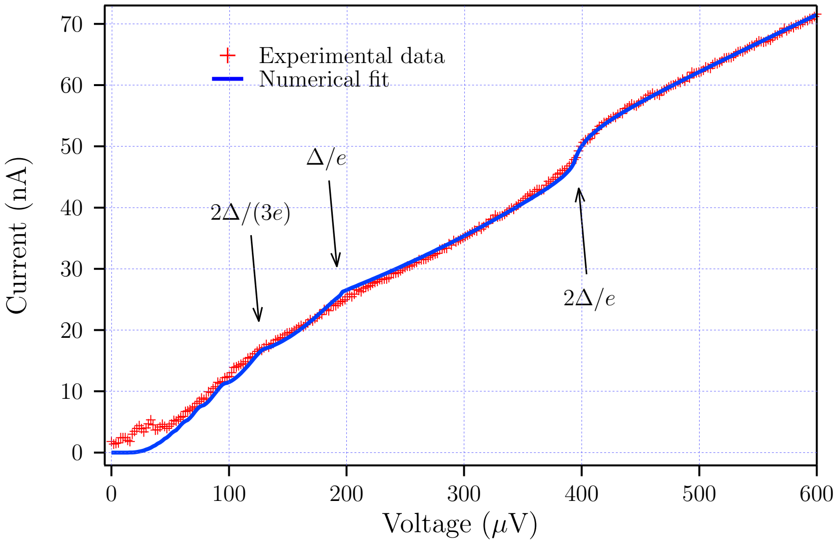

Figure 3.18.: Experimental current-voltage characteristic of a Josephson junction with high transmission channels and numerical fit using the technique of Ref. [96].

excited to the left upper continuum, equivalent to the breaking of one Cooper pair. It makes a total of $(n+1)\,e$ transferred to the right.

For a given voltage V, the minimum number of reflections n is

$$n(V) = \left\lceil \frac{2\Delta}{eV} \right\rceil - 1.$$

This corresponds to a transferred charge

$$Q(V) = \left\lceil \frac{2\Delta}{eV} \right\rceil e.$$

For the MAR of order n, the barrier is crossed n times, resulting in a current proportional to τ^n. As $\tau < 1$, the MAR of the lowest order $n(V)$ is dominant.

The resulting current-voltage characteristic consists of steps at voltages V_n such that $V_n = 2\Delta/(ne)$: when $V_{n+1} < V < V_n$, the n-th order MAR is dominant and the current scales as τ^n. The exact shape of $I(V)$ is calculated for example in Ref. [97]. For a junction with several conduction channels of transmission i, these MAR processes occur independently in all the channels, so that the current is the sum over every channels

$$I(V) = \sum_i \kappa_i \tau_i^{n(V)},$$

where κ_i is the proportionality constant between τ_i^n and the resulting current. Figure 3.18 shows an experimental current-voltage characteristic of a Josephson junction with high transmission channels. This junction was made small and with a thin oxide layer to allow for pinholes, channels with high transmission. The numerical fit was performed using the technique developed in Ref. [96] to find the transmission of the conduction channels with a non-negligible

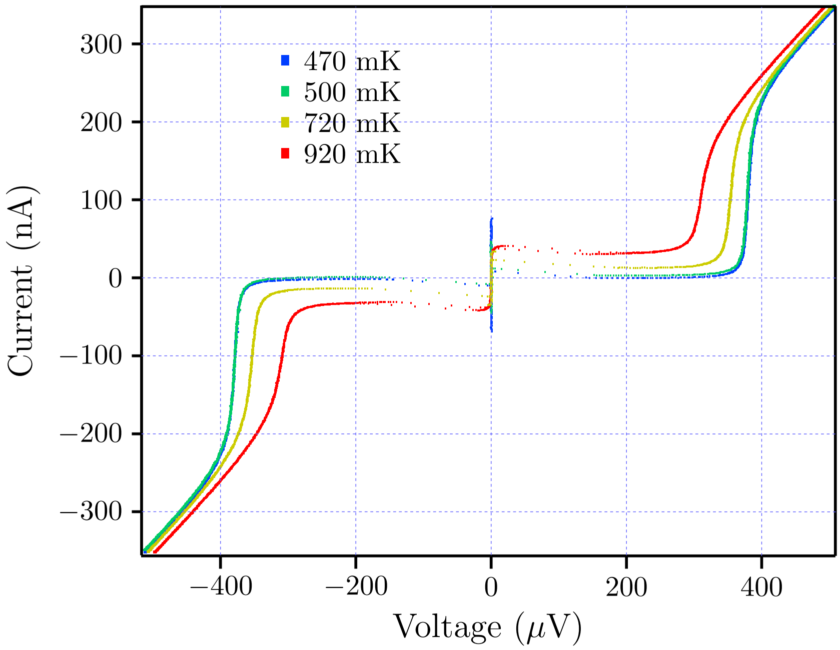

Figure 3.19.: Experimental current-voltage characteristics of a Josephson junction at different temperatures.

contribution to the current. In this case, the channels with a transmission larger than 1% have $\tau = 0.81$, $\tau = 0.12$, $\tau = 0.098$, $\tau = 0.07$ and $\tau = 0.026$.

To make a spectrometer, a current-voltage characteristic such as the one shown in Figure 3.18 is not acceptable, as the background current is quite large and rapidly of the order of 10 nA. This greatly reduces the sensitivity of detection, proportional to the square root of the subgap current. Junctions with low transmissions are thus needed for a sensitive spectrometer.

3.6. The quasiparticle branch

3.6.1. Temperature effect

At a finite temperature, it is possible for quasiparticles to tunnel through the junction due to thermal activation. The effect of temperature on the current-voltage characteristic is shown in Figure 3.19 where a Josephson junction of critical current of the order of 200 nA was measured at different temperatures[1] with a large bias resistance of the order of 20 kΩ, approximately ten times the normal resistance of the junction. There are two main features visible in the figure.

- The superconducting gap decreases when the temperature increases. This effect is well described by the BCS theory and gives a dependence of the gap Δ as $\Delta(T) = \Delta_0\sqrt{1-(T/T_C)^2}$ with Δ_0 the gap at zero temperature.

---

[1] The temperatures printed in the graph were obtained by fitting the IV characteristic with Equation (3.8).

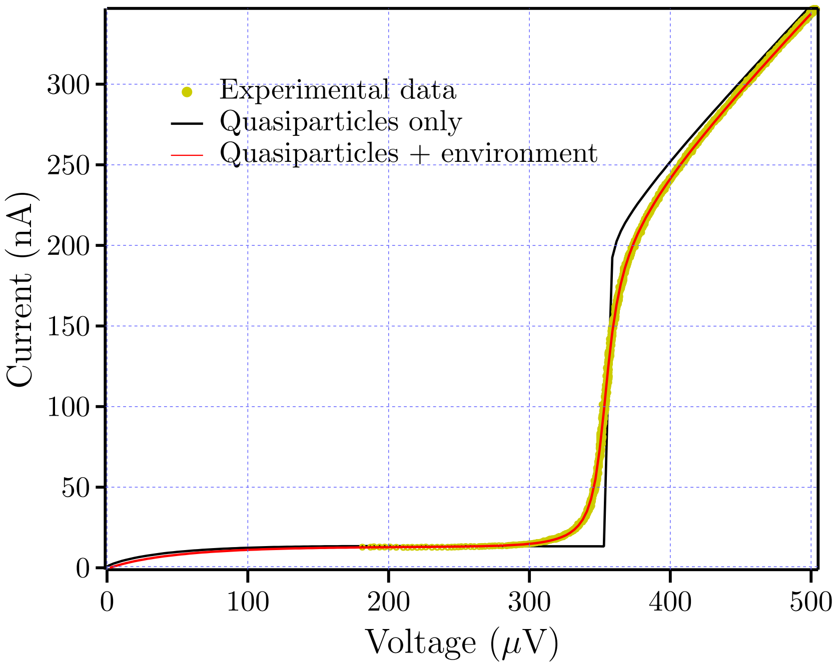

Figure 3.20.: Experimental current-voltage characteristic of a Josephson junction at 720 mK and fit with and without the influence of the electromagnetic environment.

- The background current below the gap increases with temperature. This effect is explained in the following.

As explained in Section 1.2.3, the current due to quasiparticles is

$$I_N(V) = \frac{2e\pi}{\hbar} \int_{-\infty}^{+\infty} n_S\,(E + eV)\, n_S\,(E)\,(f\,(E) - f\,(E + eV))\, dE, \tag{3.8}$$

where the temperature T appears in the Fermi function f and in the superconducting gap: $\Delta(T) = \Delta_0\sqrt{1-(T/T_c)^2}$. At zero temperature this expression is exactly 0 for $V < 2\Delta/e$, increases rapidly at $2\Delta/e$ and tends to V/R_N at large voltages.

For a finite temperature, a current of quasiparticles can flow for $V < 2\Delta/e$ because some quasiparticles are thermally excited. This leaves empty levels for other quasiparticles to tunnel in through the junction.

Figure 3.20 shows one of the current-voltage characteristics of Figure 3.19 in yellow and the result of the integral (3.8) at 720 mK in black. The current far below the gap ($V < 300\,\mu\text{V}$) and far above the gap, as well as the gap value are in good agreement with the experiment but the shape around the gap is not well described by this integral. The discrepancy between both comes from the electromagnetic environment of the junction.

3.6.2. Role of the electromagnetic environment

The presence of an electromagnetic environment can help quasiparticles tunnel through the junction because they can exchange energy with it. Without environment, the quasiparticle current is given by Equation (3.8), which can be decomposed in tunneling rates towards both directions, $\overrightarrow{\Gamma}_0(V)$ and $\overleftarrow{\Gamma}_0(V)$,

$$I_N(V) = e\left(\overrightarrow{\Gamma}_0(V) - \overleftarrow{\Gamma}_0(V)\right).$$

Both tunneling rates are linked by $\overleftarrow{\Gamma}_0(V) = \overrightarrow{\Gamma}_0(-V)$, and

$$\overrightarrow{\Gamma}_0(V) = \frac{1}{e^2 R_N} \int_{-\infty}^{+\infty} \frac{n_S\left(E+eV\right) n_S\left(E\right)}{n_N^2} f\left(E\right)\left(1 - f\left(E+eV\right)\right) dE.$$

This integral can be rewritten as

$$\overrightarrow{\Gamma}_0(V) = \frac{1}{e^2 R_N} \iint_{-\infty}^{+\infty} \frac{n_S\left(E\right) n_S\left(E'+eV\right)}{n_N^2} f\left(E\right)\left(1 - f\left(E'+eV\right)\right) \delta(E-E') dE dE'.$$

The Dirac function in this expression can be understood as the probability for a system with energy E to change its energy to E'. This probability is 0 as soon as $E \neq E'$. Adding the possibility for the quasiparticle to exchange energy with the electromagnetic environment changes this probability to $P(E-E')$ [66, 98]. For positive energy E, $P(E)$ is the probability for the environment to absorb E. For negative E, it is the probability for the environment to emit E. At zero temperature, $P(E)$ vanishes for negative energy as no energy is emitted. The tunneling rate is now

$$\overrightarrow{\Gamma}(V) = \frac{1}{e^2 R_N} \iint_{-\infty}^{+\infty} \frac{n_S\left(E\right) n_S\left(E'+eV\right)}{n_N^2} f\left(E\right)\left(1 - f\left(E'+eV\right)\right) P(E-E') dE dE'.$$

A little algebra (done in Appendix G) allows finding an expression for the current in presence of an electromagnetic environment,

$$I_N^{(e)}(V) = \int_{-\infty}^{+\infty} \frac{1 - \mathrm{e}^{-\beta eV}}{1 - \mathrm{e}^{-\beta E}} P(eV - E) I_N\left(\frac{E}{e}\right) dE, \tag{3.9}$$

where $\beta = 1/(k_B T)$ is the inverse temperature and $I_N(V)$ is the current without environment calculated using Equation (3.8). Figure 3.20 shows in red the result of this calculation for the same Josephson junction as before. The environment seen by the junction is modeled in this case by the junction intrinsic capacitance (15 fF) in parallel to a bias resistance of 450 Ω. The model is now close to the experimental data.

Temperature decreases the gap and increases the background current. These two effects are prejudicial to the sensitivity of the spectrometer. Working at a temperature well below the critical temperature of the superconductor is thus a prerequisite for a sensitive spectrometer. Dilution cryostats allow for an electronic temperature of the order of 100 mK, where the quasiparticle current is negligible.

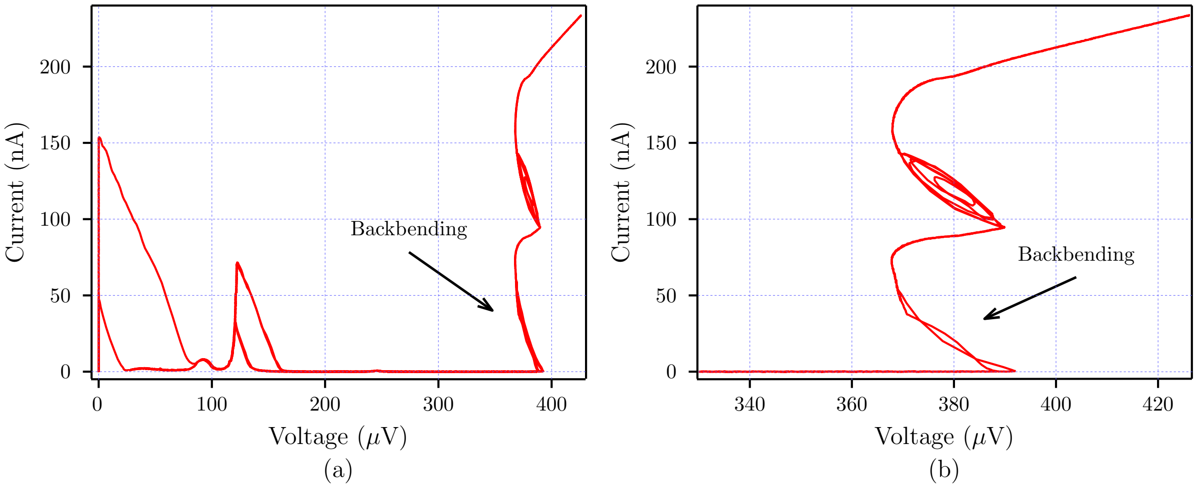

(a)

(b)

Figure 3.21.: (a) Experimental current-voltage characteristic of a SQUID at 10 mK exhibiting a backbending behavior and (b) detail around the gap voltage.

3.6.3. Backbending and oscillations

At low temperatures (< 100 mK), the quasiparticle current below the gap calculated in the previous section is negligible. However, the current of the quasiparticle branch is not fully described by Equation (3.8) as can be seen in Figure 3.21.

For a bias voltage slightly larger than $2\Delta/e$, a dissipative current develops in the junction, generating quasiparticles in the superconductors close to the junction. As they have a long lifetime compared to the time it takes them to thermalize with the lattice [99, 100], they have a non-equilibrium distribution which can decrease the superconducting gap. An exact calculation of the gap in the BCS theory as a function of the generated quasiparticle density can be found in Ref. [101]. The result of this calculation gives a quasiparticle branch bent to lower voltages in the current-voltage characteristic and is often called backbending.

The IV characteristic shown in Figure 3.21 has this typical shape for low currents. For currents slightly smaller than 100 nA, $I(V)$ has a linear shape before entering a second backbending zone for higher currents. The reason for this is that this is not the IV characteristic of a single Josephson junction but of a SQUID. If the gap is slightly different for the two junctions of the SQUID, the current first flow through one junction where $V > 2\Delta_1/e$ while the second stays at zero current because the voltage is smaller than $2\Delta_2/e$.

For current larger than 100 nA, there is a region with large current and voltage oscillations. This is possibly due to an inhomogeneous gap in the electrodes due to the non-equilibrium quasiparticle distribution [102]. To explain them, we consider a model in which the superconducting electrodes consist of two distinct regions a and b with gaps Δ_a and Δ_b ($\Delta_a < \Delta_b$). The current-voltage characteristics for region a is sketched in Figure 3.22 with a simple backbending modeling consisting of a negative differential resistance region. The two regions are biased in parallel, such that both regions are at the same voltage. Starting form a bias voltage below $2\Delta_a/e$, both a and b are in the subgap region (mark (1) in the figure). Region a is much smaller than region b because the quasiparticle density is close to the equilibrium one.

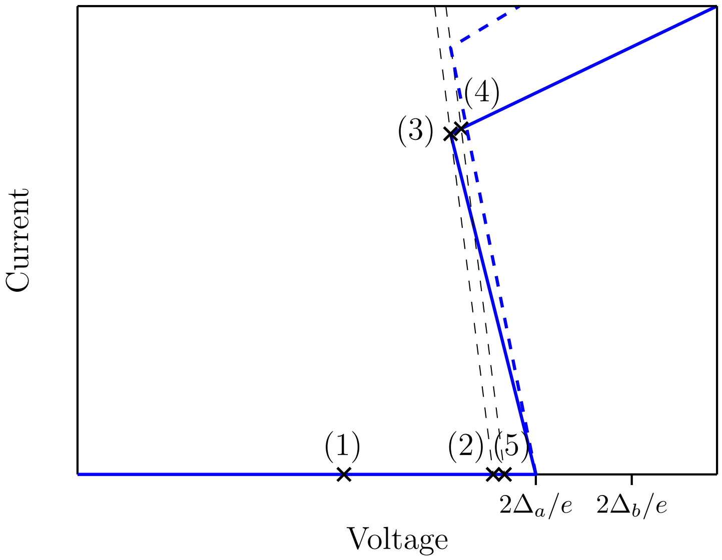

Figure 3.22.: Quasiparticle oscillations process.

The current in region b between $2\Delta_a/e$ and $2\Delta_b/e$ is essentially zero, such that the total current is dominated by the tunneling of quasiparticles of region a. As this current is small, the negative differential resistance modeling the backbending is quite large. If it is higher than the bias resistance (as in the figure), when the bias is increased from mark (1) to mark (2), the current rapidly increases to reach mark (3) in the upper part of the IV characteristic of region a. When the bias is further increased to mark (4), more and more out of equilibrium quasiparticles are generated. This has for effect to increase the size of region a and thus rescale the IV characteristic (the dashed blue line in the figure). At some point, the bias point comes back to the lower branch of the IV characteristic at mark (5), at a voltage larger than mark (2). Some out of equilibrium quasiparticles have had time to recombine, reducing the effective size of region a. This process is then repeated until the bias current is large enough to be on the resistive branch of the IV characteristic of both junctions.

3.7. Conclusion

In this chapter, we have seen that, if no special care is taken, the measured current-voltage characteristic of a Josephson junction (or a SQUID) is not as simple as the ideal one presented in the first chapter.

The critical current is reduced due to thermal noise and quantum fluctuations. These effects are smaller for larger junctions and low temperatures. For small junctions, the supercurrent peak deviates from a true zero-voltage state and has a resistive behavior, limiting the sensitivity of the spectrometer at low voltages.

The low voltage region is inaccessible due to the retrapping phenomenon. Adding a shunt capacitance in parallel to the junction allows decreasing the retrapping voltage and thus increasing the low frequency bandwidth of the spectrometer.

A too inductive biasing circuit can generate several parasitic features to the IV characteristic:

a current plateau below a voltage as large as 50 µV in some cases, harmonics and sub-harmonics of the Josephson frequency. Reducing the inductance of the leads and shunting them at high frequencies with a capacitance allows reducing these effects.

Applying microwaves to a Josephson junction changes greatly its IV characteristic and can be useful to generate a precise voltage to bias the spectrometer.

For voltages below $2\Delta/e$, a current can flow through the junction if the transmission of at least one of its conduction channels becomes large. The spectrometer must therefore be realized with a tunnel junction with low transmission.

The effect of temperature on the IV characteristic was also studied, showing that quasiparticles can be thermally excited, giving rise to a current at voltages below $2\Delta/e$ as soon as the temperature becomes comparable to the critical temperature of the superconductor.

The next chapter explains how the spectrometer is designed in practice to suppress these undesired features.

4. Design of the Josephson spectrometer

The previous chapter described all the undesired features which can be encountered when making a Josephson junction or a SQUID. We will now see how they are avoided in practice with a well-thought design. To test a design, the current-voltage characteristic of the device is taken at half a flux quantum. The desired IV characteristic consists of zero current at every voltage between 0 *and* $2\Delta/e$*. The ideal design will be exposed starting from the spectrometer core and continuing with elements located farther and farther away.*

The essential elements of the spectrometer are the two Josephson junctions acting as emitter and receiver of photons. Their design will be discussed in the first place.

These two junctions are put in a superconducting loop forming a SQUID to improve the spectrometer as discussed in Section 2.2. This loop is also crucial to the good operation of the spectrometer and will be described subsequently.

Then we will turn to the on-chip electromagnetic environment of the SQUID which need to be designed carefully as seen in Chapter 3.

Finally the off-chip measuring setup, also of paramount importance, will be exposed.

4.1. Design of Josephson junctions

4.1.1. Superconductor material

In order to have the largest bandwidth for the spectrometer, the material with the largest superconducting gap Δ should be used as the sensitivity is greatly reduced for frequencies above $4\Delta/h$. The most promising candidates compatible with usual nanofabrication techniques are niobium ($\Delta \sim 1.5\,\mathrm{meV}$), lead ($\Delta \sim 1.1\,\mathrm{meV}$), tin ($\Delta \sim 520\,\mu\mathrm{eV}$) and aluminum ($\Delta \sim 190\,\mu\mathrm{eV}$).

4.1.2. Thickness of the junctions

In order to have a good sensitivity, the background current I_{bg} at voltage below $2\Delta/e$ needs to be small enough so that the shot noise in the junction is smaller than the Johnson noise of the bias resistor R_b, $2eI_{bg} < 4k_BT/R_b$, as seen in Section 2.4.5. For a typical bias resistance of $1\,\mathrm{k\Omega}$, this makes an upper limit for the background current of $15\,\mathrm{nA}$ at $100\,\mathrm{mK}$. The calculations of Section 3.5 show that the transmission of the conduction channels forming the junction has to be quite low for that purpose. This is achieved by making a thick insulating barrier. The simplest way to make such a barrier is to let the superconductor oxidize in an oxygen environment, creating a native oxide layer, usually insulating. Unfortunately, niobium native oxide creates strain at the interface between niobium and niobium oxide resulting in bad Josephson junctions [103]. However, it is possible to make hybrid niobium (Nb)/aluminum (Al) junctions, with a Nb/Al/AlOx/Al/Nb structure, taking advantage the high quality of aluminum oxide (AlOx). But this is a more complicated process which requires niobium layers

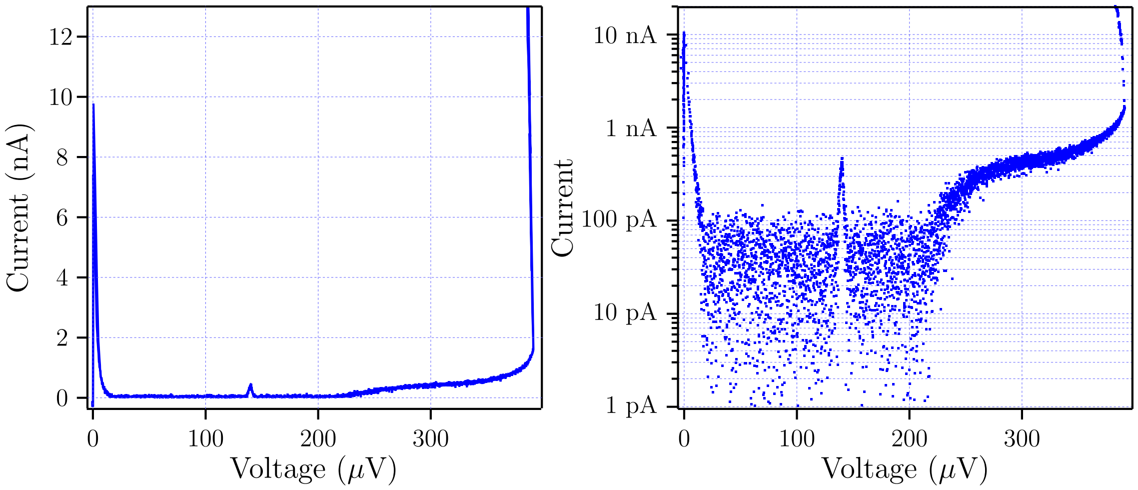

Figure 4.1.: Experimental current-voltage characteristic of a Josephson junction with low subgap current.

with a small roughness obtained by sputtering. At Collège de France, we do not have a sputtering system and therefore do not use niobium for tunnel junctions. One of the projects of the group, mentioned in the Conclusion, is to develop good niobium based junctions to increase the bandwidth of the spectrometer. Lead and tin are not used either because they do not make good tunnel barriers. However, aluminum is quite easy to process with a simple electron beam evaporator.

This is the reason why all junctions described subsequently are made of aluminum. The insulating layer is grown in a 200 mbar pressure of pure oxygen during 10 min. This results in a ~ 1 nm thick barrier.

With such barriers the measured current in the subgap region is lower than 100 pA as shown in Figure 4.1 for a junction of critical current of the order of 100 nA. The left panel is the current-voltage characteristic and the right panel is the same curve with a logarithmic scale to highlight the current amplitude. The measured device is a SQUID biased at half a flux quantum so that there are as few features as possible. The current rise after 200 µV $\sim \Delta/e$ is due to excitation of the quasiparticle by photons of energy 2Δ. This feature is described in more details in Section 5.2.

The thickness t of the barrier also determines the supercurrent density as well as the surface capacitance:

- According to the Ambegaokar-Baratoff relation (Equation (1.14)), the supercurrent of a Josephson junction is proportional to its normal conductance G_N. As the phenomenon responsible for this normal conductance is tunneling, G_N is exponential in the thickness of the barrier. The fabricated junctions are highly inhomogeneous in thickness due to the roughness of the aluminum surfaces. Only the regions with the smallest thickness actually contribute to the supercurrent density. In general, this represents $\sim 10\%$ of the surface. The distribution of thicknesses is independent of the surface of the junction, such that the normal conductance is nevertheless proportional to the surface. For the oxidation described just above, the measured supercurrent density j_0 is of the order of $80\,\mathrm{nA\,\mu m^{-2}}$.

- The capacitance can crudely be estimated by $C = \varepsilon_0 \varepsilon_r S/t$ where ε_r is the dielectric constant of the barrier, S the surface of the junction and t the average thickness of the insulating barrier. For an alumina ($\varepsilon_r \sim 10$) barrier of 1 nm thick, the estimated surface capacitance is $C_\Sigma = 80\,\mathrm{fF\,\mu m^{-2}}$. This value was not directly measured experimentally.

If the supercurrent density and the surface capacitance are fixed, the plasma frequency of the junctions is also fixed by

$$\omega_p = \sqrt{\frac{j_0}{\varphi_0 C_\Sigma}}.$$

This plasma frequency was directly measured using Josephson spectroscopy. The experimental setup and spectrum are described in Section 5.3. These measurements give $\omega_p = 2\pi \times 16.0\,\mathrm{GHz}$.

Using the measured values of supercurrent density and plasma frequency, it is possible to get a value for the surface capacitance: $C_\Sigma = 25\,\mathrm{fF\,\mu m^{-2}}$. This value is quite different from the estimated value of $80\,\mathrm{fF\,\mu m^{-2}}$. The discrepancy mainly comes from the junction not being made of two infinite parallel plates. Their finite size allows for large fringing fields increasing the capacitance.

The intrinsic Stewart-McCumber parameter (Equation (1.43)) of the junctions is also fixed by their thickness. In the RCSJ model, the quasiparticle leakage resistance of the junction R is inversely proportional to the surface and only depends on the oxide quality,

$$\beta_C = \frac{R^2 I_0 C}{\varphi_0} = \frac{R_\Sigma^2 j_0 C_\Sigma}{\varphi_0}.$$

With the above values of j_0 and C_Σ, a β_C of 1 corresponds to a resistance of $R_\Sigma = 400\,\Omega\,\mathrm{\mu m^2}$. The typical measured values of leakage resistance are larger than $1\,\mathrm{M\Omega}$ for junctions of area $\sim 1\,\mathrm{\mu m^2}$. The junctions are thus well in the underdamped limit. When put in an electrical circuit, β_C is largely decreased. For instance when a bias resistance $R_b \ll R$ is in parallel to the junction, β_C becomes

$$\beta_C^{(b)} = \frac{R_b^2 I_0 C}{\varphi_0} \ll \beta_C.$$

4.1.3. Area of the junctions

The area of the junctions determine the critical current and the capacitance of the junction. The larger the junctions, the larger the critical current and capacitance. As seen in Chapter 2, the minimal detectable absorption rate is proportional to the square root of the critical current. Small junctions are thus needed in order to have a good sensitivity.

In order for the spectrometer to operate in the linear regime where the resonant peaks have a Lorentzian shape, the z parameter introduced in Chapter 2 ($z = I_0/(V_0 G_e)$ with G_e the real part of the admittance at the resonance voltage V_0) has to stay small. Small junctions are thus favorable for that purpose.

In practice, because we use an optical lithography setup (see details in Appendix H), the resolution of the designs is limited by the size of the laser spot of the order of $1\,\mathrm{\mu m}$. With the two-angle evaporation technique, the overlap between the two superconducting electrodes in the junctions is not limited by the resolution of the lithography but by the precision on the angle in the evaporator, resulting in an overlap of $\sim 100\,\text{nm}$. The minimal size for a junction is thus of the order of $0.1\,\mu\text{m}^2$.

The spectrometer is not made of one junction, but of two junctions which have to be as similar as possible. As seen in Section 2.2.3, to have a good decoupling from the bias circuit and the external electromagnetic environment, the ratio α between the two critical current has to be as close to one as possible. Experimentally, the minimal reproducible width of the junction obtained is of the order of $1.5\,\mu\text{m}$ and the minimal reproducible overlap of the order of $300\,\text{nm}$. This makes junctions of area $0.5\,\mu\text{m}^2$ which have a critical current of the order of $40\,\text{nA}$.

4.2. Design of the SQUID loop

When the SQUID-shaped spectrometer was introduced in Section 2.2.2, an intrinsic LC mode appeared, due to the junctions capacitances and the loop inductance. Its resonance frequency $1/\sqrt{LC_s}$, where L is the loop inductance and C_s the series combination of the two junctions capacitances, can be in the operating frequency range of the spectrometer and hide features which are close to this frequency. It is thus necessary to make this frequency larger than $4\Delta/\hbar$, the upper limit of the operating range of the spectrometer. For two aluminum junctions of $0.5\,\mu\text{m}^2$, with a surface capacitance of $25\,\text{fF}\,\mu\text{m}^{-2}$, a loop inductance smaller than $130\,\text{pH}$ is required to have the resonance frequency above $4\Delta/h = 180\,\text{GHz}$.

The inductance of the loop also needs to be smaller than the Josephson inductance of the junctions, such that the phase drop induced by an applied magnetic flux mainly occur across the junctions and not across the loop inductance as explained in Section 1.3. This allows being able to have the phase differences of the junctions separated by π, where the decoupling is maximal. For junctions of $0.5\,\mu\text{m}^2$, $I_0 = 40\,\text{nA}$ and the Josephson inductance is $L_J = 16\,\text{nH}$. If the condition to have the SQUID intrinsic LC mode at a frequency larger than $180\,\text{GHz}$ ($L < 130\,\text{pH}$) is satisfied, $\beta_L = L/L_J \ll 1$, which allows good flux biasing.

Following this reasoning, the loop should be as small as possible, but if the coupling is made using the loop inductance, it should not be zero! The best compromise is thus to have the largest inductance L satisfying both $1/\sqrt{LC_s} > 2\pi \times 180\,\text{GHz}$ and $\beta_L \ll 1$. This gives a value of $130\,\text{pH}$ for two junctions of $0.5\,\mu\text{m}^2$.

To get the size of the loop needed to have $L = 130\,\text{pH}$, two contributions to the inductance have to be taken into account: the geometrical inductance L_{geo} due to the magnetic field generated by the current flowing in the wire and the kinetic inductance L_K due to the inertial mass of charge carriers.

4.2.1. Geometric inductance

In first order approximation, the SQUID loop is made of two parallel wires as sketched in Figure 4.2. The thickness of the wires t is considered much smaller than their width a. The length of the wires l is considered much larger than the distance d between them.

If the two wires are sufficiently far away, the inductance of the loop is just the sum of the contribution of the wires [104],

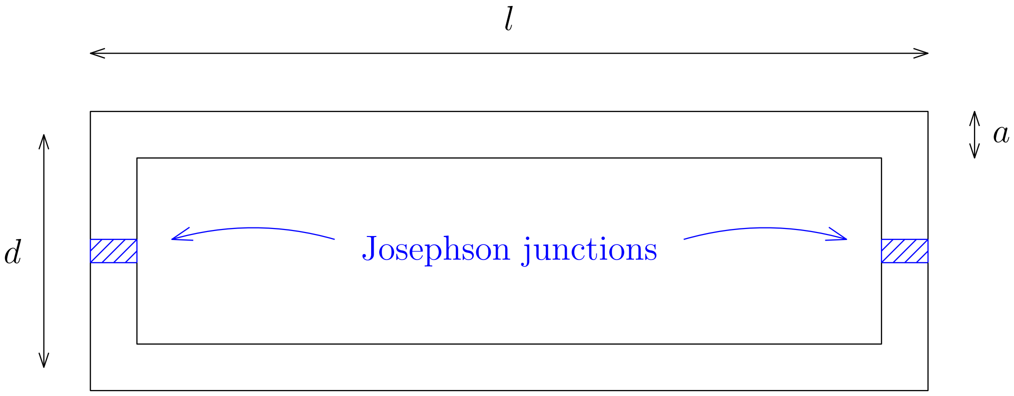

Figure 4.2.: Sketch of a SQUID.

$$L_g = \frac{\mu_0 l}{\pi} \ln\left(\frac{d}{a}\right),$$

where μ_0 is the vacuum permittivity. If the wires are closer, a current flowing in one arm can induce current in the other and the correct value for L_{geo} is $L_g - M$ where M is the mutual inductance between the two wires. Exact expressions for M can be found for instance in Ref. [104]. There are also simulators available on the internet to estimate the value of L_{geo} for a given circuit. For example, two parallel wires of section $t \times a = 100\,\mathrm{nm} \times 5\,\mu\mathrm{m}$ and length $l = 100\,\mu\mathrm{m}$ separated by a distance $d = 25\,\mu\mathrm{m}$ give an inductance of $L_{geo} \sim 120\,\mathrm{pH}$.

4.2.2. Kinetic inductance

When a DC current flows through a superconducting wire, there is no resistance. But if the current is not DC and varies with time, the charge carriers (the Cooper pairs) will not react instantly due to their mass. This delay is similar to an inductive behavior. To prove it and estimate the kinetic inductance L_K of a superconducting wire, we calculate the kinetic energy of the Cooper pairs traveling at a speed v. For a wire of length l and surface S, this energy is

$$E_K = \frac{1}{2}\left(2m_e\right)\left(n_s l S\right) v^2,$$

where $2m_e$ is the mass of a Cooper pair and n_s is the density of Cooper pairs. If an AC current I is flowing through this wire, the speed v is related to the current by: $I = 2evn_sS$. Injecting this expression in the kinetic energy gives

$$E_K = \frac{1}{2}\frac{m_e l}{2e^2 n_s S} I^2.$$

This expression is the same as the magnetic energy of an inductance L_K through which a current I flows, with

$$L_K = \frac{m_e}{2e^2 n_s}\frac{l}{S}. \tag{4.1}$$

It is possible to find a relationship between L_K and R_N the normal state resistance of the same superconducting wire if we consider a piece of wire of length ξ, the superconducting coherence length. A current I flowing through it induces a phase drop $\varphi = L_K I/\varphi_0$. If this phase drop becomes of the order of 2π, superconductivity is lost because coherence in a Cooper pair is broken. The current such that $\varphi = 2\pi$ is thus the critical current of the wire I_0. This gives

$$L_K I_0 = \Phi_0.$$

We have seen in Chapter 1 that the critical current of a tunnel junction is linked to its normal state resistance via the Ambegaokar-Baratoff relation $R_N I_0 = \pi\Delta/e$. For a weak link with a higher transmission this relation is not true but the $R_N I_0$ product stays proportional to Δ/e, at least in the short limit where the length of the weak link is of the order or smaller than ξ [41]. This can be applied to our short superconducting wire, comparable to a weak link in the short limit to give

$$L_K \propto \frac{h}{\Delta} R_N.$$

A more exact derivation of L_K within the BCS theory is performed in Appendix J, based on [41], yielding

$$L_K = \frac{\hbar}{\pi\Delta} R_N.$$

For aluminum, this impedance is quite low. Considering the same two wires as before (of cross section $t \times a = 100\,\mathrm{nm} \times 5\,\mu\mathrm{m}$ and length $100\,\mu\mathrm{m}$), this kinetic inductance is close to 5 pH which is much lower than the geometric inductance of 120 pH.

For metals with smaller gap such as titanium ($\Delta \sim 50\,\mu\mathrm{eV}$) or hafnium ($\Delta \sim 20\,\mu\mathrm{eV}$), this kinetic inductance can be much higher. For the same wires, it reaches 300 pH for titanium and 800 pH for hafnium.

The SQUID in Figure 4.3 is a typical design of a spectrometer. The blue and red zones are aluminum electrodes forming the SQUID. Purple zones are overlap regions. The two Josephson junctions of the SQUID are denoted JJ and indicated by black arrows.

The total inductance of the loop is of the order of $L = 45\,\mathrm{pH}$ and the critical current of the SQUID is $I_0 = 40\,\mathrm{nA}$. This makes a capacitance of 35 fF per junction and thus a resonant frequency of 182 GHz, just above the gap voltage. The β_L ratio is quite small: $\beta_L = 0.05 \ll 1$.

4.3. On-chip electromagnetic environment

As discussed in Chapters 2 and 3, the bias circuit is crucial for the good operation of the spectrometer. It can broaden the probe system absorption linewidth, influence the noise seen by the Josephson junctions, increase the retrapping voltage, add spurious resonances, modify the low-voltage part of the current-voltage characteristic or contribute to the generation of sub-harmonics and harmonics of the Josephson frequency.

The main constraints we have on the design is that it has to let the DC bias current flow and stop all high-frequencies signal (noise and Josephson oscillations). There should also be an inductive element through which the oscillating Josephson current flows to allow coupling to a system of interest, as well as a bias resistor to apply a current.

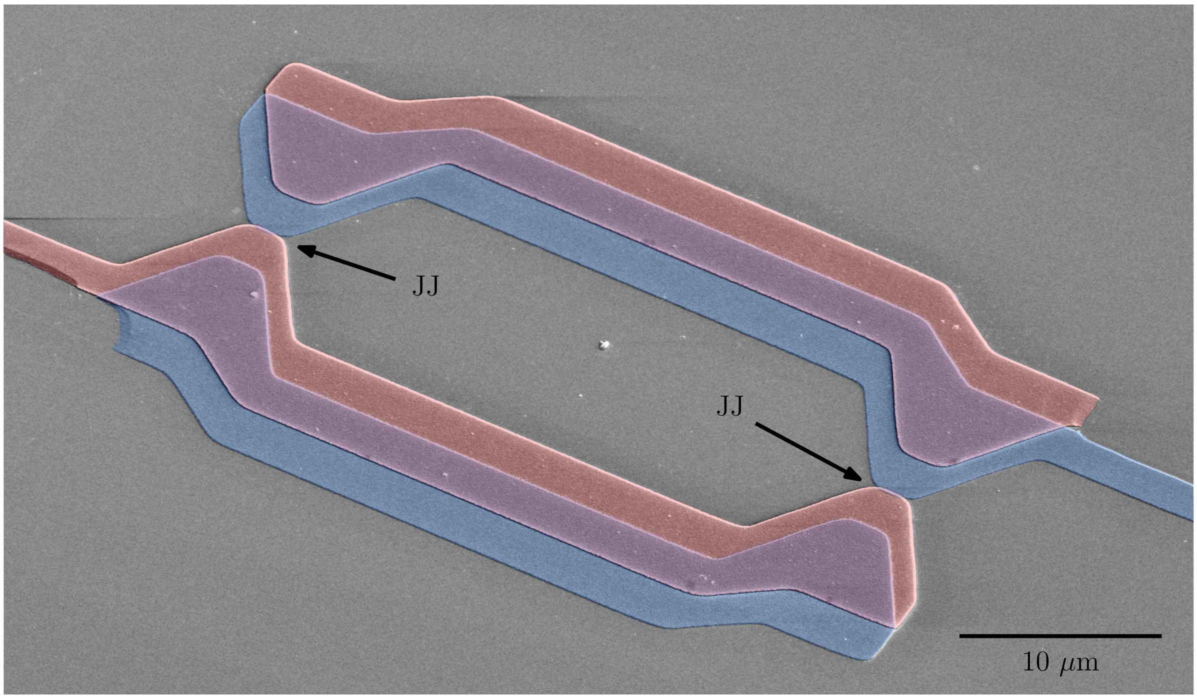

Figure 4.3.: False colors SEM picture of a SQUID.

4.3.1. Highly inductive leads

Preliminary considerations

The simplest bias circuit satisfying these constraints is shown in Figure 4.4, where the spectrometer is the SQUID colored in blue. The inductance of its loop allows coupling to a system of interest and is not represented in the figure. The black inductors of the diagram are unavoidable. They represent the aluminum wirebonds used to connect the sample to the biasing circuit, consisting here of a voltage source V_b, a bias resistor R_b across which the current can be measured and a filtering capacitor C_f to filter out high-frequency noise. The element realizing the decoupling of the spectrometer from the electromagnetic environment is the inductance L_b (in red). It has a negligible impedance at low frequencies and thus allows current biasing and a high impedance at high frequencies. It can be fabricated in a superconductor with a high kinetic inductance (such as titanium or hafnium) to grant a higher inductance, $\sim 10\,\mathrm{pH\,\mu m^{-1}}$ for a titanium wire with section $100\,\mathrm{nm} \times 1\,\mathrm{\mu m}$. This value is to be compared to the geometric inductance of a wire close to $\mu_0 \sim 1.3\,\mathrm{pH\,\mu m^{-1}}$.

This bias circuit is an RLC series resonator for which the calculations made in Chapter 2 predict a series type resonance (dip in the current) at

$$\omega_e = \frac{1}{\sqrt{(L_b + L_w)\,C_f}},$$

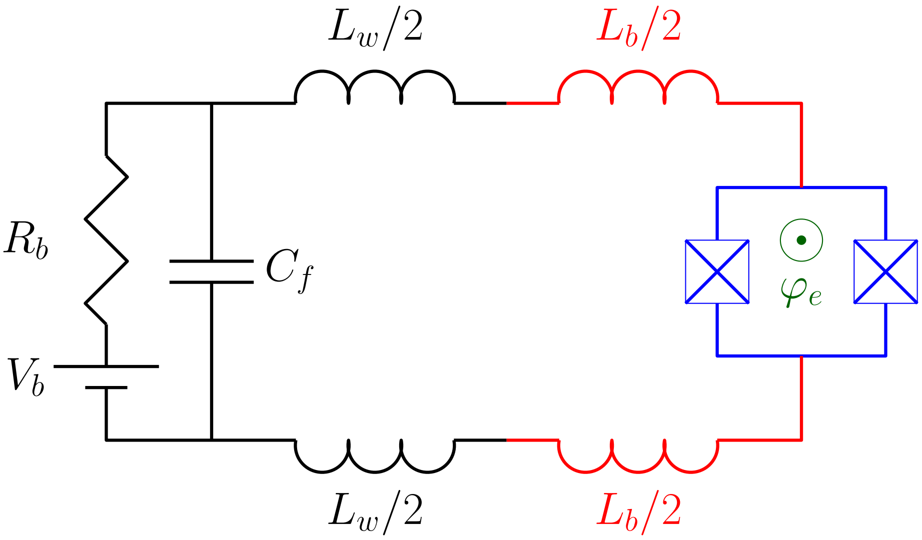

Figure 4.4.: Schematic of the spectrometer with inductive leads.

as well as a parallel type resonance (current peak) at

$$\omega_0 = \omega_e \sqrt{1 + \frac{C_f}{C}},$$

where C is the sum of the capacitances of the junctions. For 50 µm long titanium leads ($L_b = 1\,\mathrm{nH}$), 5 mm long wirebonds ($L_w \sim 10\,\mathrm{nH}$) and $C_f = 1\,\mathrm{nF}$, ω_e is of the order of $2\pi \times 50\,\mathrm{MHz}$. With C of the order of 100 fF, $\omega_0 = 2\pi \times 5\,\mathrm{GHz}$.

However, such a schematic is a simplified vision of the situation. A more refined model of the situation consists of replacing the inductances (both on-chip and wirebonds) by lossless transmission lines as they can be quite long (some mm for the wirebonds) and their length can reach the wavelength (∼ 6 mm at 50 GHz in vacuum).

The inductive leads form microstrip lines [68], represented in Figure 4.5 in red. Estimating the effective permeability and permittivity allows obtaining the speed of light and thus the resonant frequencies. They are the electromagnetic parameters of an equivalent homogeneous medium replacing the substrate and the air around the microstrip line.

The effective permittivity of a microstrip line is calculated in Ref. [68],

$$\varepsilon_e = \frac{\varepsilon_r + 1}{2} + \frac{\varepsilon_r - 1}{2} \frac{1}{\sqrt{1 + 12\frac{d}{W}}},$$

with the notations of Figure 4.5. In our case, $d = 350\,\mu\mathrm{m}$ and $W = 1\,\mu\mathrm{m}$, such that this expression reduces to

$$\varepsilon_e = \frac{\varepsilon_r + 1}{2}.$$

This gives for a silicon substrate with $\varepsilon_r = 12$, $\varepsilon_e = 6.5$.

As the wire is superconducting, the magnetic field can penetrate in a depth of the order of the London length λ. Swihart [105] gives a value for the effective permeability in the case

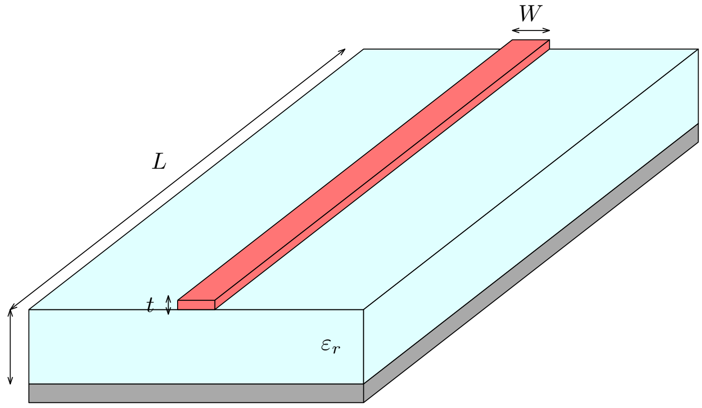

Figure 4.5.: Microstrip line.

where the width of the line is of the order or larger than the thickness of the substrate,

$$\mu_e = 1 + \frac{\lambda \coth\left(\frac{t}{\lambda}\right)}{d}.$$

For titanium, λ is of the order of 1 µm, such that μ_e for a $t = 100\,\mathrm{nm}$ thick wire can be expressed as

$$\mu_e \sim 1 + \frac{\lambda^2}{dt}.$$

However, the limit $W > d$ considered by Swihart is not achieved in our case. Belitsky *et al.* [106] analyzed the case of arbitrary W/d ratio and found that the λ/d factor calculated by Swihart has to be multiplied by a factor of order 10. In our case, μ_e stays close to 1, as $\lambda \ll d, t$.

This gives a speed of light $v = c/\sqrt{\varepsilon_e \mu_e} \sim c/2.5$ which can give rise to resonant modes at low frequencies. The characteristic impedance of the microstrip lines made of titanium is $Z_{ms} = Z_0\sqrt{\mu_e/\varepsilon_e} \sim 150\,\Omega$, where $Z_0 = \sqrt{\mu_0/\varepsilon_0} = 377\,\Omega$ is the impedance of vacuum.

The aluminum wirebonds connected to the chip also form a transmission line. They can be considered as two parallel wires of radius $r \sim 50\,\mu\mathrm{m}$ separated by a distance $d \sim 1\,\mathrm{mm}$ in vacuum. In that case, the speed of light is close to c because $r \ll d$ and the kinetic inductance of aluminum is smaller than the geometric inductance of the wires. The characteristic impedance Z_{wb} is also close to that of vacuum.

Due to the change of impedance between the on-chip titanium microstrip lines and the aluminum wirebonds, there can be resonant modes in the microstrip lines. Because $Z_{ms} > Z_{wb}$, the wirebonds can be approximated by a short circuit. At the other end, they are connected to the junctions, acting as a microwave current source which can therefore be considered as an open circuit. Resonant modes in the microstrip lines thus satisfy $(n+1)\,\lambda/4 = L$, where λ is the wavelength of the wave, L is the length of the lines and n is an integer. This gives the resonant frequencies

$$\nu_n = (n+1)\,\frac{v}{4L}.$$

These modes are at frequencies larger than 180 GHz, as soon as the length of the leads is smaller than 170 µm. In practice, it is easy to design leads smaller than this value.

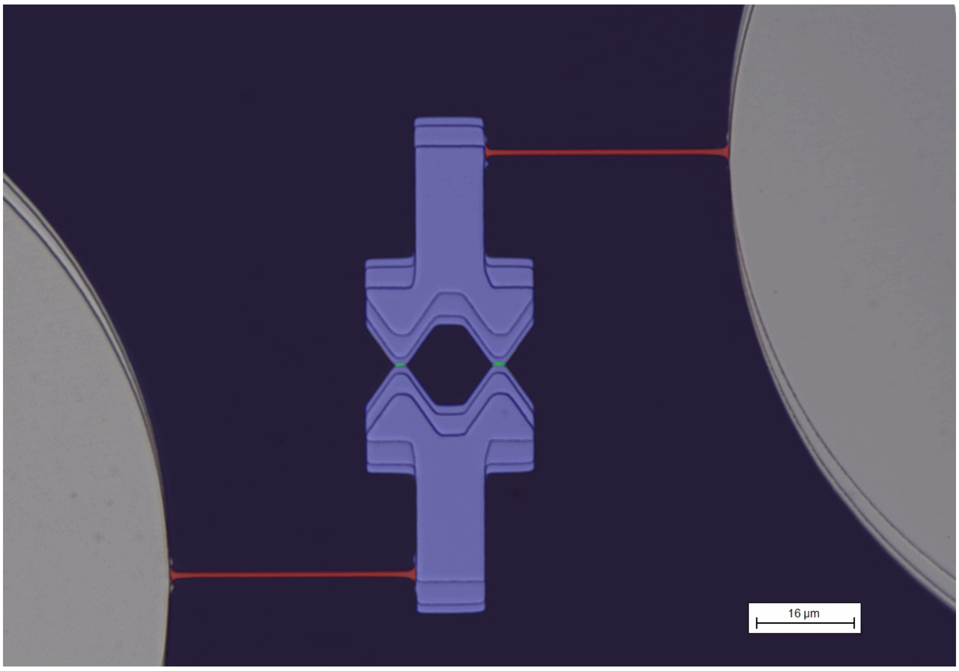

Figure 4.6.: False colors microscope picture of a SQUID with high inductive leads (in red).

For the wirebonds, the filtering capacitance C_f acts as a short-circuit for high-frequency microwaves. The other side of the line is an open circuit as $Z_{ms} > Z_{wb}$, leading to resonant modes such that $(2n+1)\,\lambda/4 = L'$, where λ is the wavelength of the wave, L' is the length of the wirebonds and n is an integer. This gives the resonant frequencies

$$\nu'_n = (2n+1)\,\frac{c}{4L'}.$$

The first one, ν'_0, is at 15 GHz for 5 mm long wirebonds. To have this mode above 180 GHz, the maximal length L' is 400 µm, which is quite hard to manage in practice.

Experimental realization: sample SSQ05

Figure 4.6 shows a microscope picture of sample SSQ05, a SQUID with inductive leads, highlighted in red in the figure. They are made of titanium and have a section 100 nm × 1 µm. Each lead is 50 µm long, granting the microstrip modes ν_n to be above 180 GHz. Using the same notations as above, $L_b = 1\,\mathrm{nH}$. The SQUID loop (in blue) was made quite small in order to have the SQUID LC resonance out of the frequency range.

Figure 4.7 shows the current-voltage characteristic of this SQUID at reduced flux 0 and π. The maximal switching current is quite low: $\sim 20\%$ of the critical current. This is mainly due to the fact that the junctions are small and thus more sensitive to noise. The filtering circuit was also not optimal at the time of these measurements, resulting in a high noise density. At $\varphi_e = 0$, the IV characteristic consists of a typical relaxation oscillation shape, explained in Section 3.3.2 and represented in dashed green line in panel (b). On top of it, several narrow peaks are superimposed. The shape of the IV characteristic after one of such peak is also due

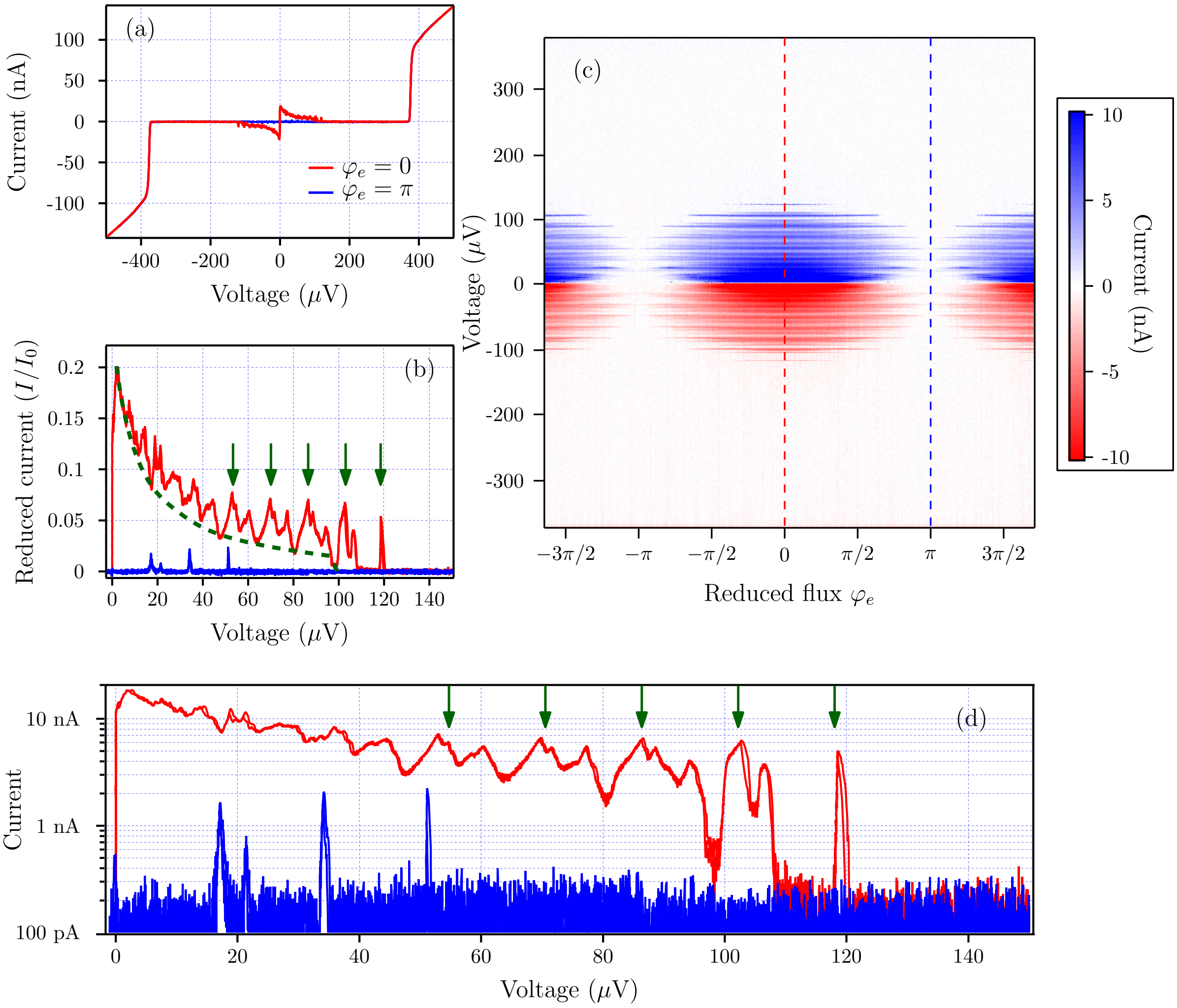

Figure 4.7.: (a) Current-voltage characteristic of a spectrometer with inductive bias, at reduced flux $\varphi_e = 0$ and π ; (b) Zoom on the low voltage region ; (c) Map of current-voltage characteristics ; (d) Current-voltage characteristic in log scale.

to relaxation oscillations. One pattern seems to be repeated in the characteristic: one peak followed by two smaller peaks (the first peak is indicated with green arrows in (b) and (d)). At lower voltage, the structure is less clear, probably because of the relaxation oscillations. Two following patterns are separated by $\sim 16\,\mu\mathrm{V}$, corresponding to a frequency of $\sim 8\,\mathrm{GHz}$. 2 cm long wirebonds could be responsible for such a spacing. The resonant modes at the origin of these peaks are located out of the loop because their amplitude is maximal at $\varphi_e = 0$ and decreases when $\varphi_e \to \pi$.

The SQUID has an excellent symmetry ratio: the remaining supercurrent at $\varphi_e = \pi$ is only 500 pA, compared to a theoretical value of 92 nA at zero flux bias. This gives a ratio between the area of the two junctions of $\alpha = 0.989$. This allows for a good decoupling from most of the off-loop modes at $\varphi_e = \pi$. Only four peaks remain at $V_1 = 17\,\mu\mathrm{V}$, $V_{1'} = 34\,\mu\mathrm{V}$, $V_{1''} = 51\,\mu\mathrm{V}$ and $V_2 = 21\,\mu\mathrm{V}$ as can be seen in the blue curves. The three first are most likely harmonics of the same resonance or correspond to multiple photon processes, as $V_{1'} = 2V_1$ and $V_{1''} = 3V_1$.

Advantages: High inductive leads allow for good quality factors as they do not add dissipation.

Drawbacks: They lead to relaxation oscillation phenomena and do not decouple efficiently from off-loop resonances.

4.3.2. Inductive leads and shunting capacitance

Preliminary considerations

To limit the relaxation oscillations, the leads can be made less inductive and a shunt capacitance can be added just after the inductive leads as depicted in Figure 4.8. This capacitance adds to the capacitance of the junction in the RLC circuit responsible for relaxation oscillations. Another beneficial effect is to shunt all emitted microwaves with frequencies higher than $1/(\sqrt{L_w C_S})$, with L_w the inductance of the wirebonds and C_S the shunt capacitance. Above this frequency, which can be of the order of $2\pi \times 5\,\mathrm{GHz}$ with $C_S = 1\,\mathrm{pF}$ and $L_w = 1\,\mathrm{nH}$, the capacitance has a low impedance compared to that of the wirebonds. It also forms a low-pass filter with the inductance of the leads L_b for high-frequency noise coming from the voltage source and the "hot" part of the circuit.

However, there are several resonant frequencies in this circuit. The impedance seen by the junction is

$$Z_e = iL_b\omega + \frac{1}{iC_S\omega + \frac{iC_f\omega}{1-L_wC_f\omega^2}}.$$

As $1/\sqrt{L_w C_f}$ is of the order of 15 MHz for $C_f = 100\,\mathrm{nF}$ and $L_w = 1\,\mathrm{nH}$, the admittance can be expressed as (at frequencies higher than 15 MHz)

$$Y_e = \frac{1}{i\,(L_b + L_w)\,\omega}\frac{1 - L_wC_S\omega^2}{1 - \frac{L_bL_w}{L_b+L_w}C_S\omega^2}. \tag{4.2}$$

In the limit where $L_b \ll L_w$, the condition for parallel resonances, $\Im(Y_e) = -iC\omega$, with C the capacitance of the SQUID, can be written

$$CL_w\omega^2 = \frac{1 - L_wC_S\omega^2}{1 - L_bC_S\omega^2}.$$

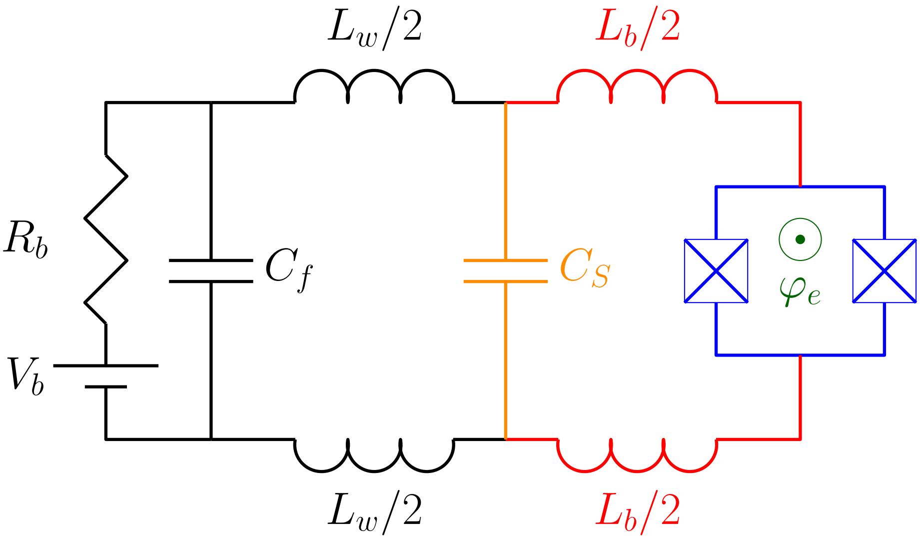

Figure 4.8.: Schematic of the spectrometer with inductive leads and a shunt capacitance.

This equation has two solutions which are (when the capacitance of the junctions is smaller than the shunt capacitance)

$$\omega_1 = \frac{1}{\sqrt{L_w C_S}},$$
$$\omega_2 = \frac{1}{\sqrt{L_b C}}.$$

Typical values are $L_w = 1\,\mathrm{nH}$, $C_S = 1\,\mathrm{pF}$, $L_b = 100\,\mathrm{pH}$ and $C = 100\,\mathrm{fF}$. This gives $\omega_1 \sim 2\pi \times 5\,\mathrm{GHz}$ and $\omega_2 \sim 2\pi \times 50\,\mathrm{GHz}$.

The admittance of Equation (4.2) also has a pole at

$$\omega_3 = \sqrt{\frac{L_b + L_w}{L_b L_w C_S}} \sim \frac{1}{\sqrt{L_b C_S}} \sim 2\pi \times 15\,\mathrm{GHz},$$

where a series type resonance occurs.

In addition to resonances at ω_1, ω_2 and ω_3, the microstrip line and the wirebonds also contribute to the spectrum, with modes at the same ν_n and ν_n' as before.

Figure 4.9 shows a simulation of the response of the junctions to the circuit shown in Figure 4.8 where the wirebonds are modeled by a transmission line of fundamental frequency 15 GHz, corresponding to $\sim$ 5 mm long wirebonds. The inductive lines are assumed small enough for ν_n to be above 180 GHz. The junctions are replaced by a capacitance $C = 100\,\mathrm{fF}$ in parallel with an alternative current source of amplitude $I_0 = 100\,\mathrm{nA}$, the frequency of which is swept from 1 to 100 GHz. This current creates an alternative voltage of complex amplitude V_ω across the SQUID. The vertical axis of the graph is the real part of V_ω divided by the equivalent DC voltage $V_{DC} = \varphi_0 \omega$. This quantity z_e is related to the real part of the impedance Z_e of the circuit seen by the SQUID and thus to the losses in the circuit corresponding to peaks in the IV characteristic:

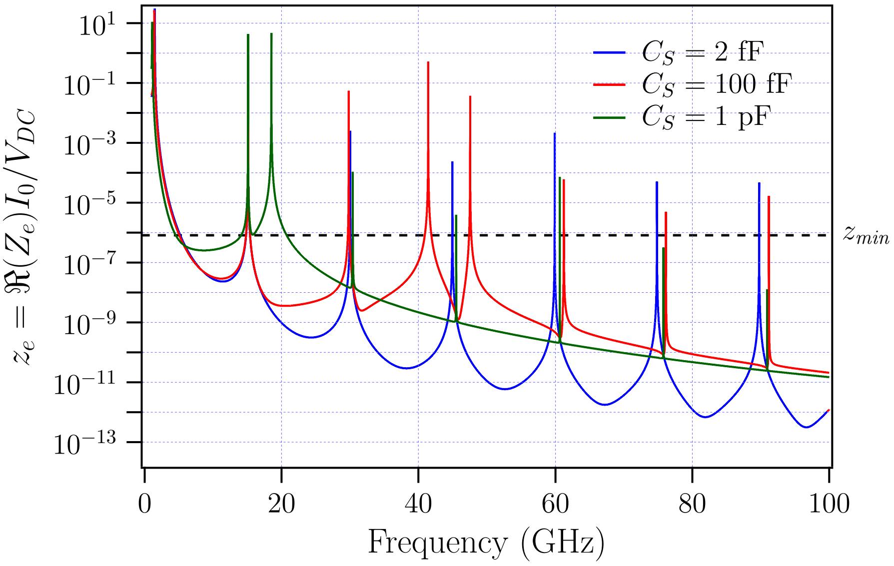

Figure 4.9.: Reduced real part of the impedance of circuit 4.8 seen by the SQUID.

$$z_e = \frac{\Re(Z_e)I_0}{V_{DC}}.$$

According to the calculations of Chapter 2, the minimal detectable z in a δf bandwidth is

$$z_{min} = 4\sqrt{\frac{2ek_BT\delta f}{\pi\Delta I_0}}.$$

In a 1 Hz bandwidth, a junction with 100 nA can detect at 100 mK a value of $z_{min} \sim 10^{-6}$. This is represented by a black dashed horizontal line in the graph. The blue curve with $C_S = 2\,\mathrm{fF}$ corresponds to the situation where there is no shunt capacitance. This value is an estimate of the capacitance between the two pads, through the ground plane. The curve exhibits wide peaks close to the resonance frequencies of the transmission line. When a shunt capacitance is added, these peaks are slightly displaced and get sharper. The peak at frequency f_1 also appears (close to 40 GHz for $C_S = 100\,\mathrm{fF}$ and close to 20 GHz for $C_S = 1\,\mathrm{pF}$). A capacitance as large as possible is thus advantageous to have a simple IV characteristic.

The simplest way to make a large capacitance is to use two metallic plates separated by a layer of dielectric. The resulting capacitance is then given by $C_S = \varepsilon_r\varepsilon_0 S/s$ where S is the area of the plates and s is the thickness of dielectric of relative permittivity ε_r. To get $C_S > 1\,\mathrm{pF}$, two $25 \times 25\,\mu\mathrm{m}^2$ plates separated by 50 nm of alumina are sufficient.

But there are possible resonant modes in such a structure. If we consider two metallic plates of dimensions $L \times l$ separated by a thickness s of a dielectric of permittivity $\varepsilon = \varepsilon_r\varepsilon_0$ and permeability μ_0, microwaves can propagate at a speed $v = c/\sqrt{\varepsilon_r}$ in the dielectric. If the structure is closed (or open) at both sides, there are resonance modes at frequencies f such that $\lambda/2 = \left(m^2/l^2 + n^2/L^2\right)^{-1/2}$, where $\lambda = v/f$ is the wavelength of the wave and m and n are two integers with $mn \neq 0$ [68]. This gives resonant frequencies

$$f_{m,n} = \frac{c}{2\sqrt{\varepsilon_r}}\sqrt{\left(\frac{m}{l}\right)^2 + \left(\frac{n}{L}\right)^2}.$$

For the spectrometer, these resonant modes are undesired. Fortunately they can easily be pushed to frequencies higher than 180 GHz. The lowest resonant frequency is $f_{0,1}$ if $L > l$. $f_{0,1} > 180\,\mathrm{GHz}$ corresponds to $L < 260\,\mu\mathrm{m}$ with alumina as dielectric ($\varepsilon_r \sim 10$).

However, when using superconductors, this rationale is not sufficient. The magnetic field of the light traveling in the transmission line penetrates in the superconductor on a thickness close to the London penetration length. This has for effect to reduce the speed of light in the dielectric [105]. An effective relative permeability can be derived for two superconductors of thickness t_1 and t_2 and London length λ_1 and λ_2,

$$\mu_{\mathit{eff}} = 1 + \frac{\lambda_1}{s}\coth\frac{t_1}{\lambda_1} + \frac{\lambda_2}{s}\coth\frac{t_2}{\lambda_2}.$$

To minimize this effect, the dielectric and aluminum thicknesses have to be as large as possible. The characteristic thickness is the London length which is close to 100 nm in aluminum. With a thickness of 150 nm for the two aluminum planes, the two coth functions give a value of 1.1 close enough to 1. However, increasing the dielectric thickness decreases the capacitance value. A thickness of 125 nm for the dielectric is a good compromise, giving $\mu_{\mathit{eff}} \sim 2.8$. This decreases the maximal dimension admissible for the design by a factor $\sqrt{\mu_{\mathit{eff}}} \sim 1.7$. The condition $L < 260\,\mu\mathrm{m}$ is transformed in $L < 155\,\mu\mathrm{m}$ imposing a more restrictive design. But a $40 \times 40\,\mu\mathrm{m}^2$ square is sufficient to get $C_S > 1\,\mathrm{pF}$. It is even possible to reach $C_S = 7\,\mathrm{pF}$ with a $100 \times 100\,\mu\mathrm{m}^2$ square.

Experimental realization: sample SSQ14

Figure 4.10 shows sample SSQ14, a sample with inductive leads (in red) and two shunt capacitors (in orange). Using two capacitors instead of one not only allows for a capacitance value twice as big, but also reduces high-frequency magnetic noise: in the design, there appears to be two loops (each delimited by one capacitor and the inductive leads) which are closed at high-frequency and can thus only be threaded by quantized values of high-frequency flux. The high-frequency magnetic field generated by the alternative current in the SQUID loop is also contained in these loops due to the Meissner effect forbidding the magnetic field to cross the superconductors.

The inductive leads (in red) are made in aluminum. They are 65 µm long, 1 µm wide and 100 nm thick, resulting in an inductance of ∼ 70 pH per lead. Each orange plane in the figure is a $100 \times 250\,\mu\mathrm{m}^2$ rectangle of 150 nm thick aluminum, separated by a thickness $t = 125\,\mathrm{nm}$ of alumina from the large aluminum planes (in light yellow in the picture). This results in two series capacitors C_{sq} of section $S = 100 \times 100\,\mu\mathrm{m}^2$. The total capacitance per orange plane is thus $C_o = C_{sq}/2$. The total shunt capacitance is $C_S = 2C_o = C_{sq} = 7\,\mathrm{pF}$.

Figure 4.11 shows the current-voltage characteristic of this SQUID at reduced flux 0 and π. The maximal switching current is almost equal to the critical current of the SQUID, showing good noise filtering. At φ_e, the switching current is reduced to 2.5 nA, showing a good symmetry ratio of $\alpha = 0.98$.

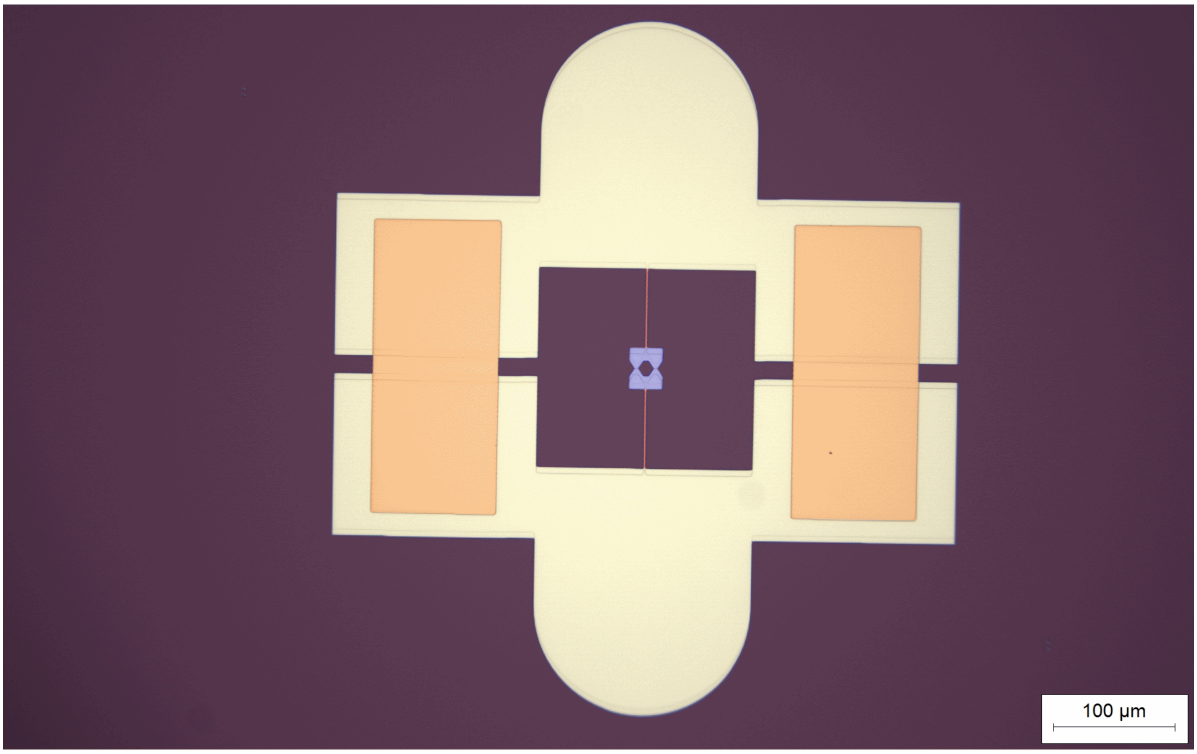

Figure 4.10.: False colors microscope picture of a SQUID with inductive leads (in red) and two shunt capacitors (in orange).

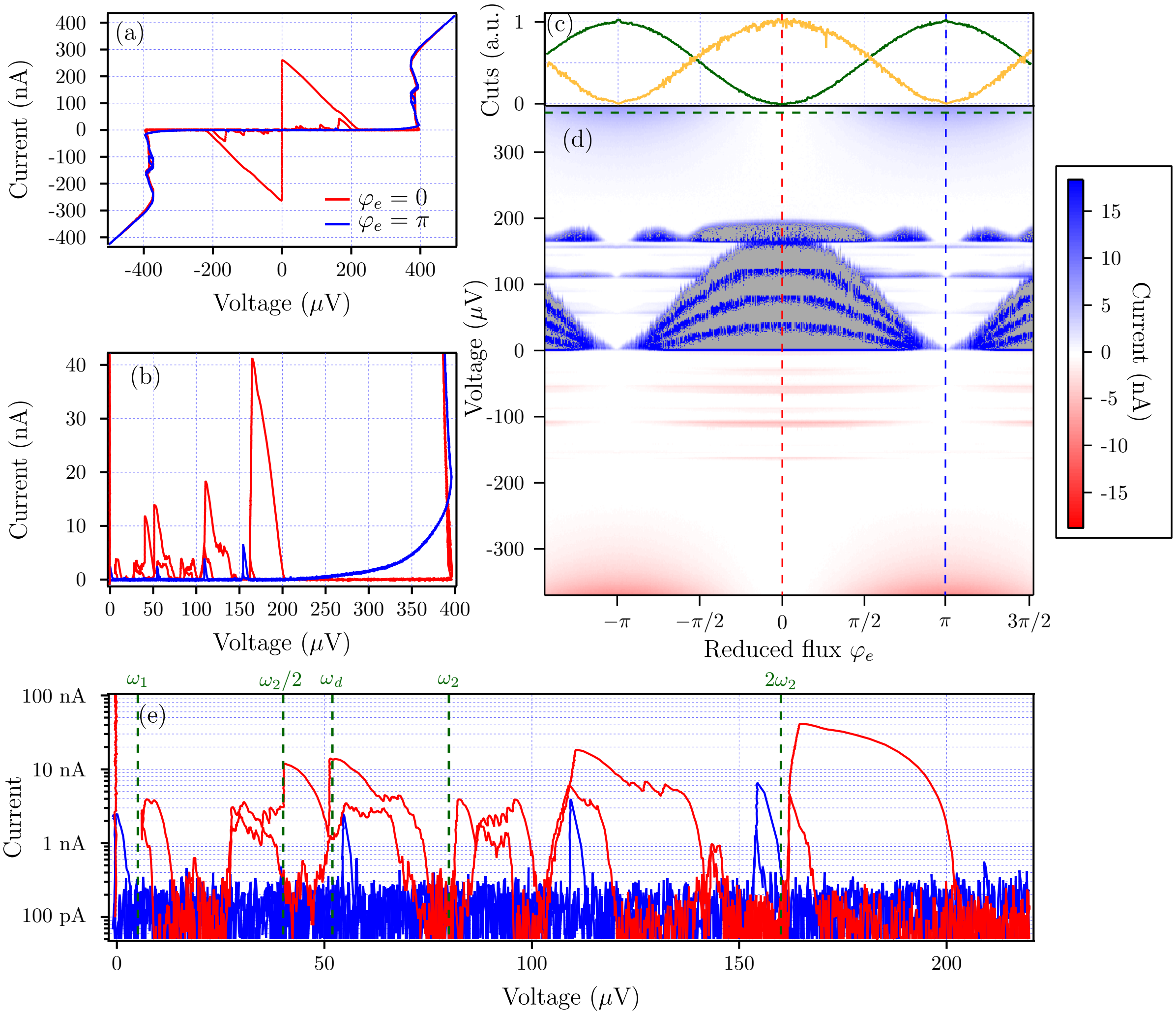

Figure 4.11.: (a) Current-voltage characteristic of a spectrometer with inductive bias and a shunt capacitance, at reduced flux $\varphi_e = 0$ and π ; (b) Zoom on the low voltage region ; (c) Switching current (orange) and current at 360 µV (green) plotted against the reduced flux ; (d) Map of current-voltage characteristics ; (e) Current-voltage characteristic in log scale.

The backbending shape of the quasiparticle branch at $2\Delta/e$ is due to heating caused by the quasiparticles, as explained in Section 3.6.3. The rise of the current at φ_e when $V \to 2\Delta/e$ is believed to originate from the LC resonance of the SQUID loop. The inductance of the loop is estimated to $\sim 25\,\mathrm{pH}$ and the capacitance of each junction to $50\,\mathrm{fF}$, leading to a resonant voltage of $415\,\mathrm{\mu V}$. Because this corresponds to a frequency of $200\,\mathrm{GHz}$ above $2\Delta/h \sim 90\,\mathrm{GHz}$, the real part of the impedance of the loop is not zero. Quasiparticles can be excited at such frequencies, as explained in Section 5.2. This decreases the quality factor of the LC resonance and increases its width, making it visible far from the resonance frequency. The green curve in graph (c) shows the intensity at a voltage $V = 360\,\mathrm{\mu V}$ (represented by a green dashed line in (d)) plotted against the flux, in the rising part of the IV characteristic. This evolution is out of phase with the orange curve, which is the switching current of the SQUID. All of this is consistent with this peak being the SQUID loop LC mode.

For this sample, the capacitance C of the SQUID can be estimated with the critical current of the SQUID, $C \sim 100\,\mathrm{fF}$. The inductance of the bias lead is geometrically estimated at $L_b \sim 150\,\mathrm{pH}$. $C_S = 7\,\mathrm{pF}$ and $L_w \sim 1\,\mathrm{nH}$. This gives $\omega_1 \sim 2\pi \times 2\,\mathrm{GHz}$ and $\omega_2 \sim 2\pi \times 41\,\mathrm{GHz}$. The position of the estimated ω_1 and ω_2 are indicated in panel (e) by vertical green lines, as well as $\omega_2/2$ and $2\omega_2$. They are quite close to peaks in the IV characteristic.

To understand the origin of the remaining modes, the device was simulated using a high frequency electromagnetic software for planar circuit analysis: Sonnet. Details on this simulation are given in Appendix K.1. It predicts one resonant mode at $\omega_d = 2\pi \times 24\,\mathrm{GHz}$, corresponding to current circulating around the central loop of the design, similar to an electric dipole.

Most of these peaks disappear at $\varphi_e = \pi$, where only three peaks remain, two of them have resonant voltages multiple of one another.

Advantages: The inductance of the leads allows for good quality factors. The shunt capacitance helps to reduce the relaxation oscillations and decoupling from off-loop resonances.

Drawbacks: Some off-loop resonances are still present.

4.3.3. Inductive leads, shunting capacitance and series resistance

Preliminary considerations

Adding a resistance in series with the previous circuit can damp the remaining off-loop modes, so that they do not appear in the spectrum. Figure 4.12 shows the schematic of such a circuit. With the shunt capacitance, the series resistance form a low pass filter allowing only microwaves with frequency lower than $1/(R_s C_S)$ to leave the SQUID. With a shunt capacitance of $7\,\mathrm{pF}$, a resistance of $100\,\Omega$ makes a cut-off frequency of $200\,\mathrm{MHz}$, filtering out most of the frequencies of interest.

Figure 4.13 shows how the resistance damps the modes of the transmission line formed by the wirebonds. The horizontal line at z_{min} is the detection threshold of the spectrometer. The larger the resistance, the broader the resonance peaks. For $R_s = 1000\,\Omega$, only the peak due to the bias inductance and the shunt capacitance remains.

At $\varphi_e = \pi$ for a symmetric SQUID, this resistance does not affect the width of the resonance peaks as no microwave current can leave the loop in principle. However, if the SQUID is asymmetric, there can be an alternative current flowing through the resistance whose effect

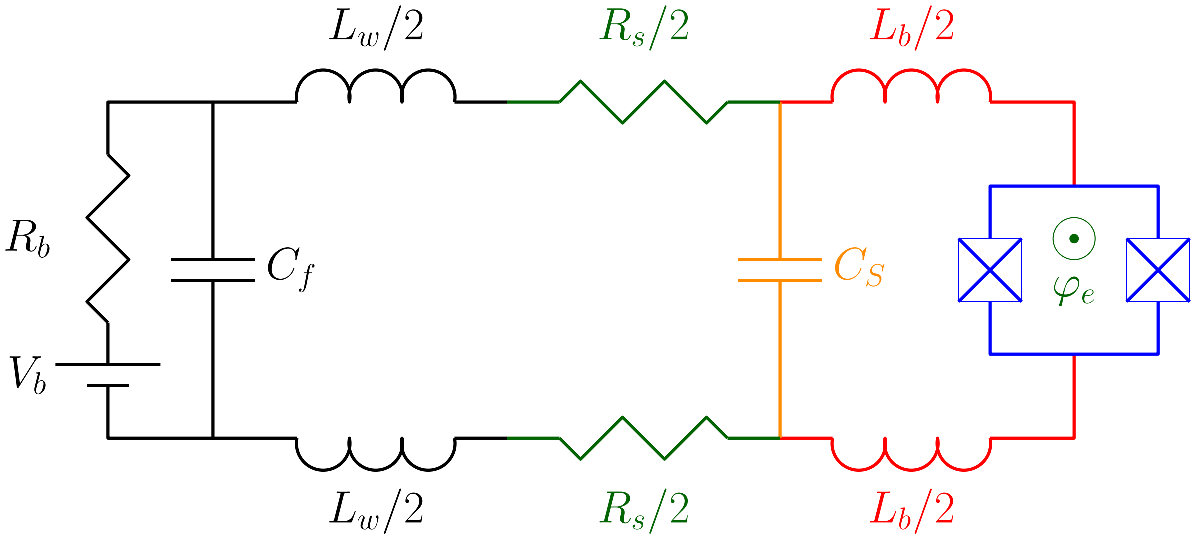

Figure 4.12.: Schematic of the spectrometer with inductive leads, a shunt capacitance and resistive leads.

is to reduce the quality factor of the resonances. For a SQUID with symmetry ratio α, the current out of the loop is $(1-\alpha)\,I_C$ and the current in the loop is $(1+\alpha)\,I_C$ at $\varphi_e=\pi$. If we call Y_{out} the admittance seen by the SQUID in its loop and Y_{in} the admittance out of the loop, the total admittance seen by the SQUID is

$$Y = (1-\alpha)\,Y_{out} + (1+\alpha)\,Y_{in}.$$

At a parallel resonance in the loop, $\Re(Y_{in}) = 1/R_{in}$ and $\Re(Y_{out}) = 1/R_{out}$. If no current flows out of the loop, the quality factor of the resonance is given by $Q_{in} = Y_e R_{in}/(1+\alpha)$, where Y_e is the characteristic admittance of the mode. In presence of current out of the loop, it is modified to $Q = Y_e/\Re(Y)$, such that

$$Q = Q_{in}\left(1+\frac{1-\alpha}{1+\alpha}\frac{R_{in}}{R_{out}}\right)^{-1}.$$

R_{out} is dominated by the resistance of the leads, $R_{out}\sim R_s$. A large resistance is thus desirable to keep this modified quality factor as large as possible, as well as two identical junctions in the SQUID.

The bias current flows through this series resistance, which can cause heating of the substrate and thus heating of the superconductors. This is an unwanted effect which can dramatically affect the shape of the current-voltage characteristic. To estimate the temperature increase, consider the current flowing through the spectrometer at a resonance peak of $I\sim I_0/10$. With $I_0 = 100\,\mathrm{nA}$, this current generates $10\,\mathrm{fW}$ when flowing in a $100\,\Omega$ resistor. This power heats the electrons to a temperature T_e. They can then cool by exchanging energy with the phonons (at a temperature T_p). The rate at which this energy transfer occurs is given by $\mathcal{P}_{e\to p} = \Sigma\Omega\left(T_e^5 - T_p^5\right)$ where Ω is the volume of the resistance and Σ the electron-phonon coupling constant depending on the material and of the order $1\,\mathrm{nW\,\mu m^{-3}\,K^{-5}}$ [107]. When

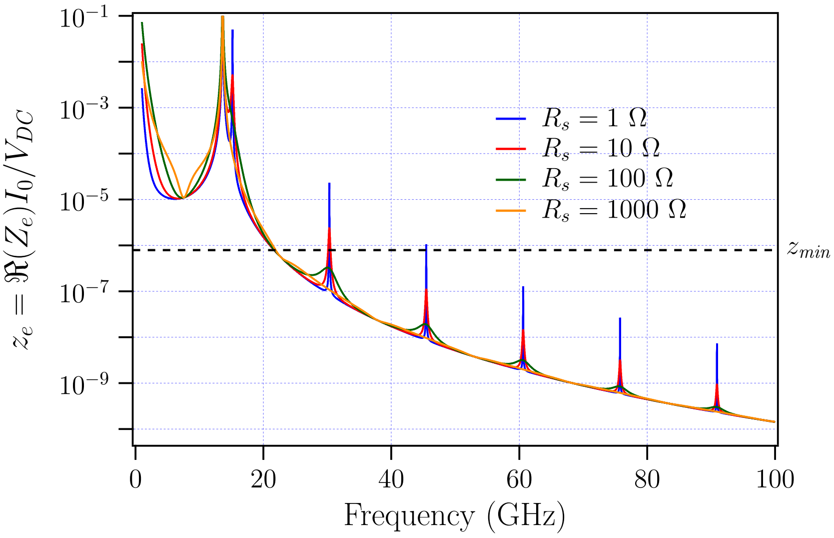

Figure 4.13.: Reduced real part of the impedance of circuit 4.12 seen by the SQUID.

the phonons are totally cooled to the substrate temperature T_0 (assumed much lower than T_p and T_e) the electrons can only cool down to $(\mathcal{P}_J/(\Sigma\Omega))^{1/5}$ because of the power $\mathcal{P}_J$. For $\mathcal{P}_J = 10\,\mathrm{fW}$, a volume larger than $1\,\mu\mathrm{m}^3$ is needed to ensure $T < 100\,\mathrm{mK}$. For instance, a metal of thickness 100 nm and width 1 µm has to be at least 10 µm long to keep the electrons cooler than 100 mK.

If this resistance is made too long, microwaves can propagate in it but will be attenuated because of dissipation. Considering a transmission line along the x axis. The power of a wave injected at $x = 0$ propagates as $\mathrm{e}^{-2\gamma x}$ towards the positive x direction. In the case of a transmission line with inductance per length $\mathcal{L}$, capacitance per length $\mathcal{C}$ and resistance per length $\mathcal{R}$, the propagation constant γ is given [68], at a frequency ω, by

$$\gamma = \sqrt{(i\mathcal{L}\omega + \mathcal{R})\, i\mathcal{C}\omega},$$

$$\gamma = i\omega\sqrt{\mathcal{LC}}\sqrt{1 - i\frac{\mathcal{R}}{\mathcal{L}\omega}}.$$

If we assume for the moment a transmission line with low losses, $\mathcal{R} \ll \mathcal{L}\omega$, γ can be expressed as

$$\gamma \sim i\omega\sqrt{\mathcal{LC}} + \frac{\mathcal{R}}{2Z_0},$$

where $Z_0 = \sqrt{\mathcal{L}/\mathcal{C}}$ is the characteristic impedance of the transmission line. The amplitude of a wave injected at $x = 0$ is thus reduced after a length L by a factor $\exp(-\mathcal{R}L/Z_0) = \exp(-R/Z_0)$ where $R = \mathcal{R}L$ is the total resistance of the line. As soon as R is larger than some Z_0, the amplitude of the wave is almost zero. For a transmission with higher losses, where the Taylor expansion is not possible, the damping is even faster. As mentioned in Section 4.3.1, the typical impedance of microstrip lines is 100 Ω, such that the total resistance of the line has to be of the order of some hundreds of Ohms.

In summary, the resistance has to be larger than 100 Ω to damp the transmission line modes and voluminous enough to allow good thermalization.The solution we choose is to use a stack of 25 nm of palladium and 45 nm of hafnium. Hafnium is a metal with high resistivity but is superconducting under $T_C \sim 170\,\mathrm{mK}$. Fortunately, the inverse proximity effect due to the layer of palladium weakens the superconductivity in the hafnium layer and even brings the hafnium back to its normal state. The resulting resistance at low temperature is $4\,\Omega/\square$. With this value and a width of 20 µm, a total length of 1.5 mm is needed to reach 300 Ω. This geometry guarantees a temperature below 30 mK when a current of 10 nA flows through the resistor. The temperature starts to overcome 100 mK for currents of 300 nA.

Experimental realization: sample HS04

Sample HS04 shown in Figure 4.14 has four resistive leads (in green): two for measuring the voltage and two for biasing the sample. The leads are each 20 µm wide and 900 µm long, yielding a resistance of 180 Ω at low temperature. The 1.5 mm length obtained above is the minimal value for a pair of leads, here measuring 1.8 mm long.

The size of the capacitance was reduced in this sample, as compared to the previous one. C_S in this sample is estimated to 440 fF. The red bias inductance was also made smaller to yield $L_b \sim 30\,\mathrm{pH}$.

The current-voltage characteristic of this sample is shown in Figure 4.15. The maximal switching current is only 80% of the critical current of 45 nA, but the junctions are quite small, making them more sensitive to thermal activation as discussed in Section 3.1. At $\varphi_e = \pi$, the remaining switching current is 6 nA, that is 15% percent of the critical current, showing a symmetry ratio of only $\alpha = 0.75$ because of the difficulty to make small and identical junctions with the optical lithography setup used, as discussed in Appendix H.1.

At $\varphi_e = 0$, there are only two visible peaks: a narrow one at 148 µV and a second one, much wider, centered around 275 µV. At $\varphi_e = \pi$, the first one completely disappears and the second one is much reduced. This is compatible with these modes being off-loop. In order to understand the origin of these modes, the device was simulated using Sonnet. Details on this simulation are given in Appendix K.2. It predicts resonances at 38.5 GHz (80 µV), 72.5 GHz (150 µV), 112 GHz (230 µV) and 126 GHz (260 µV) which are damped in presence of a resistive environment. The predicted resonance frequencies are indicated by green dashed vertical lines in panel (d) of Figure 4.15. The first mode is due to the inductance of the leads (in red in Figure 4.14) and of the large aluminum planes and the capacitance of the junctions. It is not clearly observed experimentally but there is a small hump just below 100 µV which could be the mode damped by the resistors. The second mode (a "drumhead" mode) is close to the observed peak at 148 µV. The large resonance experimentally measured at 275 µV is close to the predicted mode at 260 µV. Its large width can be explained by damping due to the resistive leads, but also by the fact that above a frequency $2\Delta/h$ (90 GHz or 190 µV for aluminum), superconductors acquire a resistance due to the excitation of quasiparticles (as discussed in Section 5.2). Both these phenomena make the observed resonance quite large and can hide the expected mode at 230 µV in the tail of the higher frequency mode.

Advantages: Inductive leads (with $\beta_L < 1$) allow for good quality factors and no relaxation oscillations. The shunt capacitance helps further reducing the relaxation oscillations and decoupling from some off-loop resonant modes. The series resistance damps all remaining off-loop modes on the other side of the resistance.

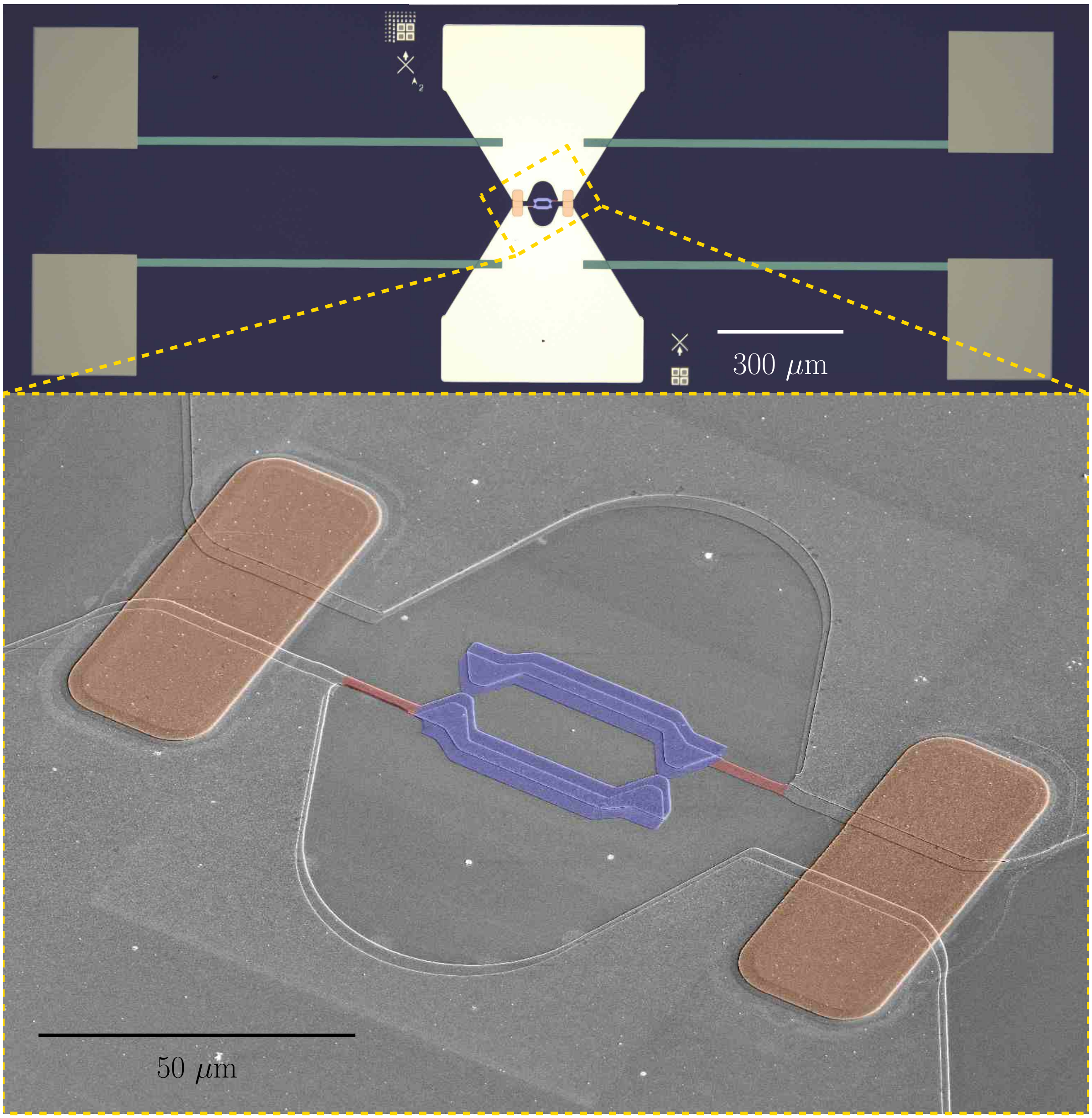

Figure 4.14.: Top picture: false colors microscope picture of a SQUID (in blue) with inductive leads (in red), two shunt capacitors (in orange) and resistive leads (in green). Bottom picture: false picture scanning electron micrograph of the yellow rectangle in the top picture.

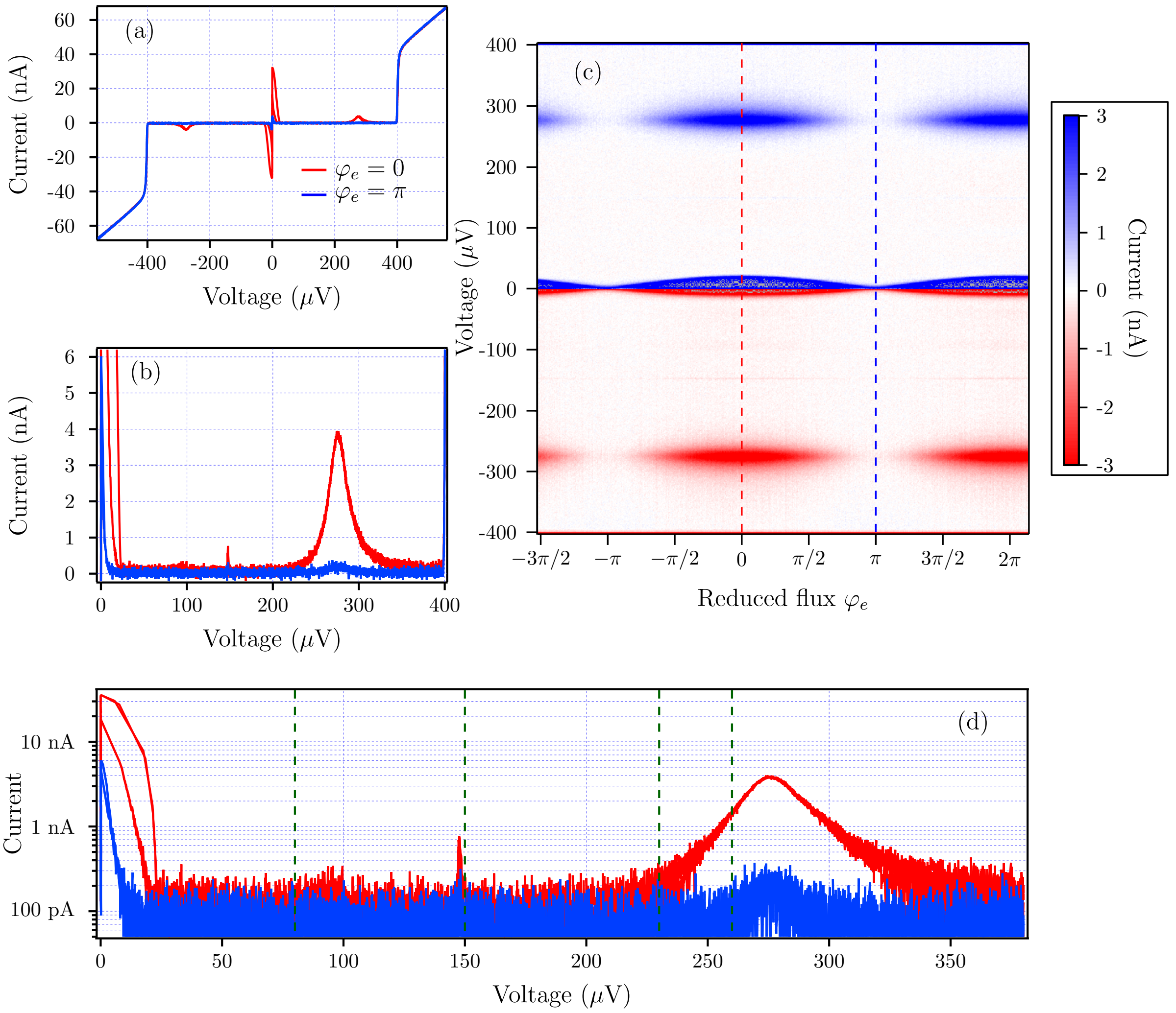

Figure 4.15.: (a) Current-voltage characteristic of a spectrometer with inductive bias, a shunt capacitance and resistive leads, at reduced flux $\varphi_e = 0$ and π ; (b) Zoom on the low voltage region ; (c) Map of current-voltage characteristics ; (d) Current-voltage characteristic in log scale.

4.4. Experimental measurement scheme

Not only the on-chip filtering circuit is important to get low noise and a flat background, but also the off-chip environment. To understand the solution implemented in this work, consider first a simple circuit composed of a bias source and a load Z_L which is our spectrometer. There can be various sources of noise, but they can be classified in two categories depending on the position of the noise source: differential noise and common noise. Panels (a) and (b) of Figure 4.16 show these two situations. Noise is here represented by a voltage source V_N either in the circuit (a) or out of the circuit (b). The red and blue arrows represent respectively differential and common noise currents circulating in the circuit and the capacitor C_g symbolizes the stray capacitance between the load and the ground. Situation (a) is commonly referred to as differential noise since the noise current is opposite in the upper and lower branches of the circuit. Situation (b) is called common noise as the noise is the same in both branches.

To reduce high-frequency differential noise, shunt capacitors (such as C_d in panel (c) of Figure 4.16) can be added between the two lines. They have a low impedance at high frequencies, such that differential noise is shunted. A better solution consists of using low-pass filters made of a shunt capacitor and a resistor in series (R in the figure) with the line. However, this solution does not work for common noise as the capacitor is not in parallel to the noise current path. To decrease common noise, capacitors to the ground (C_c in the figure) can be added, such that their low impedance at high frequency shunts the common noise current to the ground. Both these solutions are implemented in the experimental setup shown in Figure 4.17.

This diagram represents only the circuit contained in the sample box, visible in Figure 4.18. The off-chip circuit is only shown for the voltage measurement line $V_\pm$. It is the same for the current measurement lines ($I_\pm$), represented by dotted lines on the right-hand side of the figure. In the bias lines ($B_\pm$), there are additional shunt resistors to divide the voltage from the source (RIGOL DG 1032). The colors in the on-chip region corresponds to the colors used throughout this chapter.

Large filtering capacitors (C_f in Figure 4.17) of 100 nF are added close to the sample in order to shunt high-frequency differential noise. These capacitors (Murata ULSC and ULEC series) are components designed specially for microwave use. Their construction and their small size (1 mm × 0.5 mm × 0.4 mm) minimize their equivalent series resonance ($ESR \sim 500\,\mathrm{m\Omega}$) and maximize their self-resonance frequency above which their behavior deviates from an ideal capacitor. This guarantees a good operation up to 20 GHz.

To further decouple the spectrometer from the upstream circuit, microwave resistors (Vishay FC series) are placed close to the capacitors (R_f in the diagram). They are designed to have a high self-resonance frequency (SRF) larger 10 GHz for 100 Ω resistors. For typical non-microwave resistors, this SRF is of the order of several hundreds of MHz. For frequencies above SRF, the resistors acquire a capacitive behavior.

The lid and the bottom of the sample box shown in Figure 4.18 are covered with a layer of a magnetically loaded material (Ecosorb MFS series) which has a high permeability and magnetic losses. Its high permeability allows to concentrate the magnetic field which is then damped due to the high magnetic losses. This should help reduce the resonant modes originating from the finite size of the sample box.

The bonding pads on the sample holder are connected to larger metal planes on both side of a 25 µm thick polyimide film, creating an additional capacitance (of several hundreds of

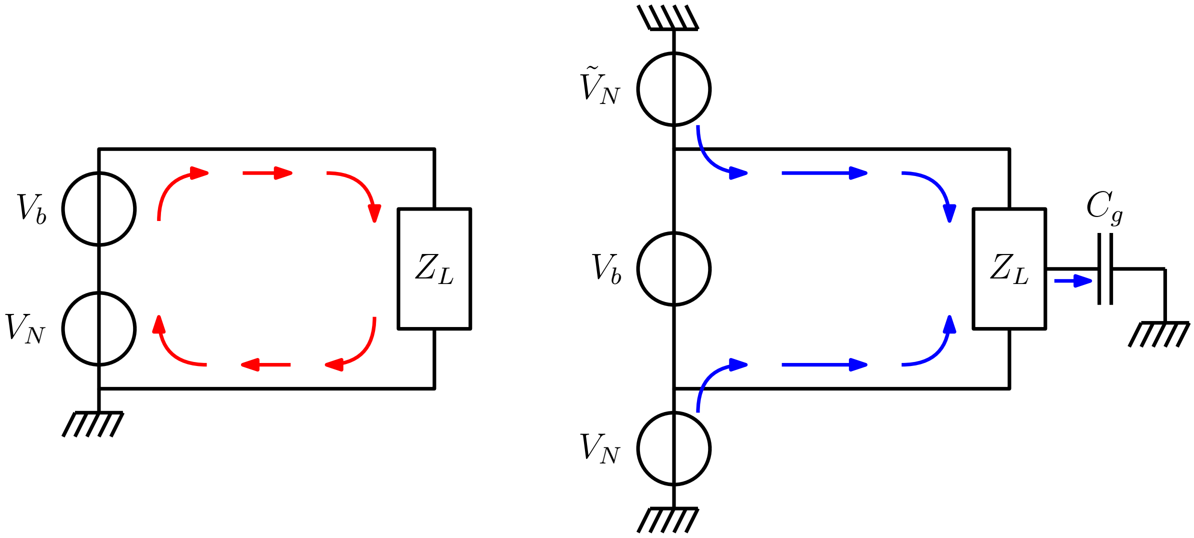

(a) Differential noise (b) Common noise

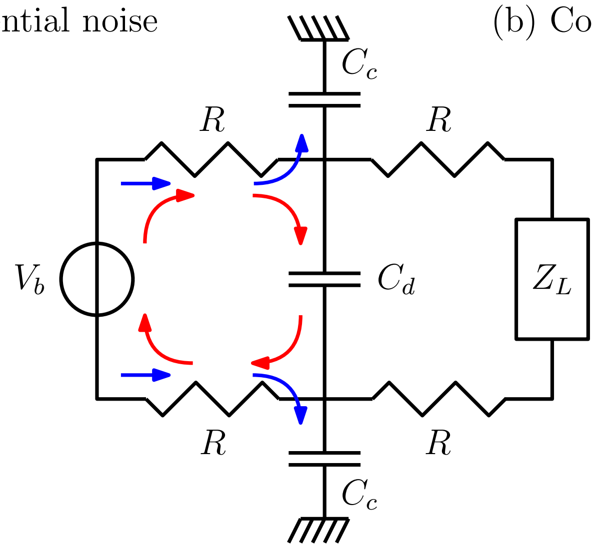

(c) Filtering scheme

Figure 4.16.: Common and differential noise and a solution to filter them out.

pF) between + and − lines. The tracks on the printed circuit board (PCB) visible in picture (c) of Figure 4.18 are long meandering lines stacked between the polyimide film and a layer of magnetically loaded material. This absorbs microwaves possibly propagating through the wires. Inside the sample box are located several standard resistors of the order of $100\,\Omega$ (R in the diagram) and capacitors of $100\,\text{nF}$ (C and C_g), realizing low-pass filters with a cut-off frequency below $100\,\text{kHz}$ to reduce the high-frequency noise coming from the outside of the cryostat and to prevent microwaves generated by the junctions to leave the region of interest.

When cooled down, the sample box is wrapped in aluminum foil, making an impervious screen for outside magnetic fields, due to the Meissner effect.

Outside of the sample box, commercial twisted pairs, thermally connected to each stage of the cryostat, are used. Resistive (with a total resistance of the order of $20\,\Omega$) phosphor-bronze wires, adding a distributed low-pass filtering, were chosen for voltage measurements lines and superconducting niobium-titanium wires for bias and coil lines.

All measurements presented in this thesis were performed in a Bluefors LD cryostat reaching a base temperature below $10\,\text{mK}$. It encloses a mu-metal shield preventing the external magnetic field from entering the cryostat.

Such a cryostat uses a pulsed tube to cool down to $4\,\text{K}$. This generates mechanical friction between the wires and thus tribo-electric noise. To reduce it, homemade cables printed on a PCB are currently being developed in the group. They are visible in Figure 4.18 (b) as a large gray sheet. Each pair consists of two continuous meandering tracks printed on both sides of the PCB made in polyimide. As this film is thin, there is a large distributed capacitance ($2.8\,\text{nF}$ along the whole line) between both conductors and little magnetic noise can thread between them. The fact that the tracks are continuous along the whole PCB helps to reduce friction between the cables. The resistance of such a copper wire is of the order of $60\,\Omega$ at room temperature and $4\,\Omega$ when the cryostat is at base temperature. This PCB is wrapped in a material with high permeability and magnetic losses in order to damp all high frequency signals. A metallic shielding is finally added to provide protection from high-frequency electromagnetic noise and a distributed capacitance (of order $2\,\text{nF}$) to the ground.

4.5. Conclusion

In this chapter, we have seen that, via a careful design of the SQUID and the on-chip electromagnetic environment, it is possible to get a quasi-featureless current-voltage characteristic at half a flux quantum.

The use of opaque Josephson junctions allows for a quite low background current for voltages below $2\Delta/e$. Typical values are of the order of $100\,\text{pA}$. Making them small increases the sensitivity and junctions with a critical current of $100\,\text{nA}$ can reach a Noise Equivalent Power of $10^{-17}\ \text{W}/\sqrt{\text{Hz}}$.

It is feasible to make SQUIDs which do not add resonances to the spectrum with a symmetry such that the switching current is almost zero at half a flux quantum. This grants access to the low frequency range (as low as $1\,\text{GHz}$ in some cases).

Adding inductors close to the junctions contributes to a good decoupling from the environment. This inductance is made small enough to reduce relaxation oscillations and low frequency resonances. A capacitance fabricated near the junctions is used to shunt a large

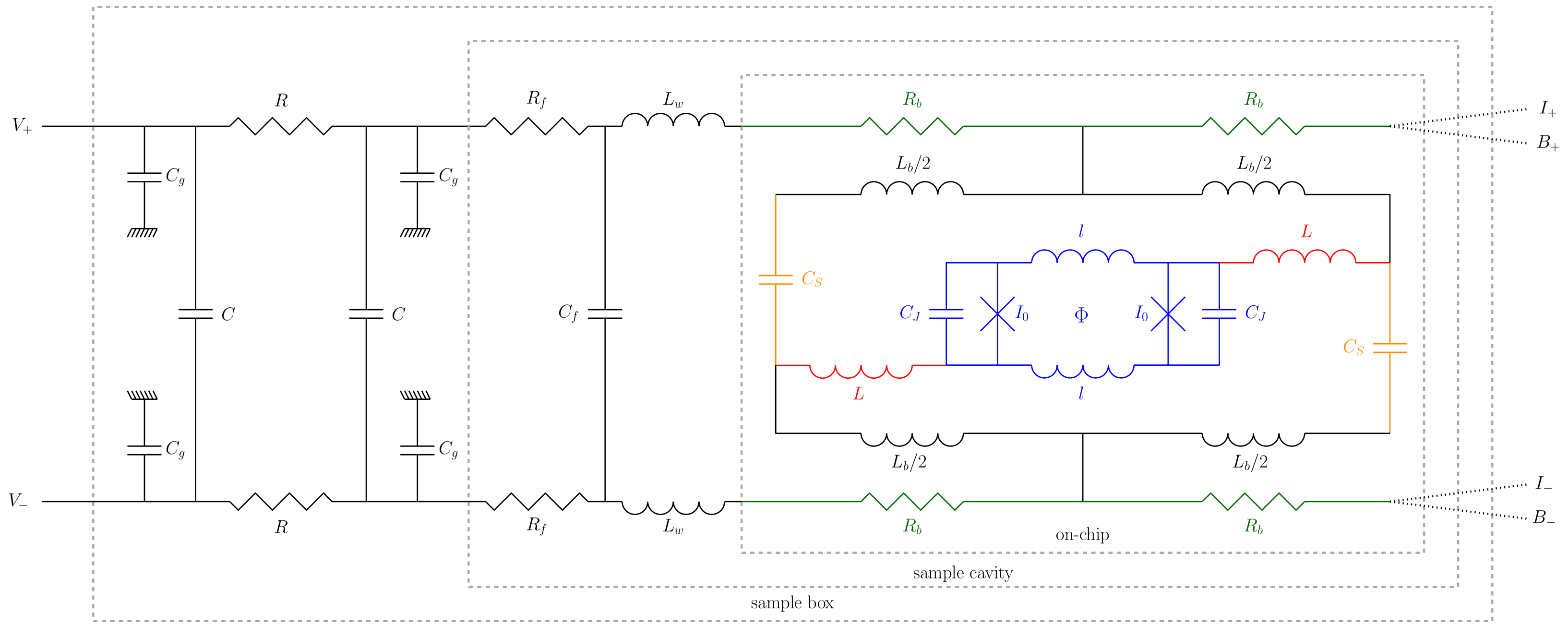

Figure 4.17.: Electric diagram of the full circuit.

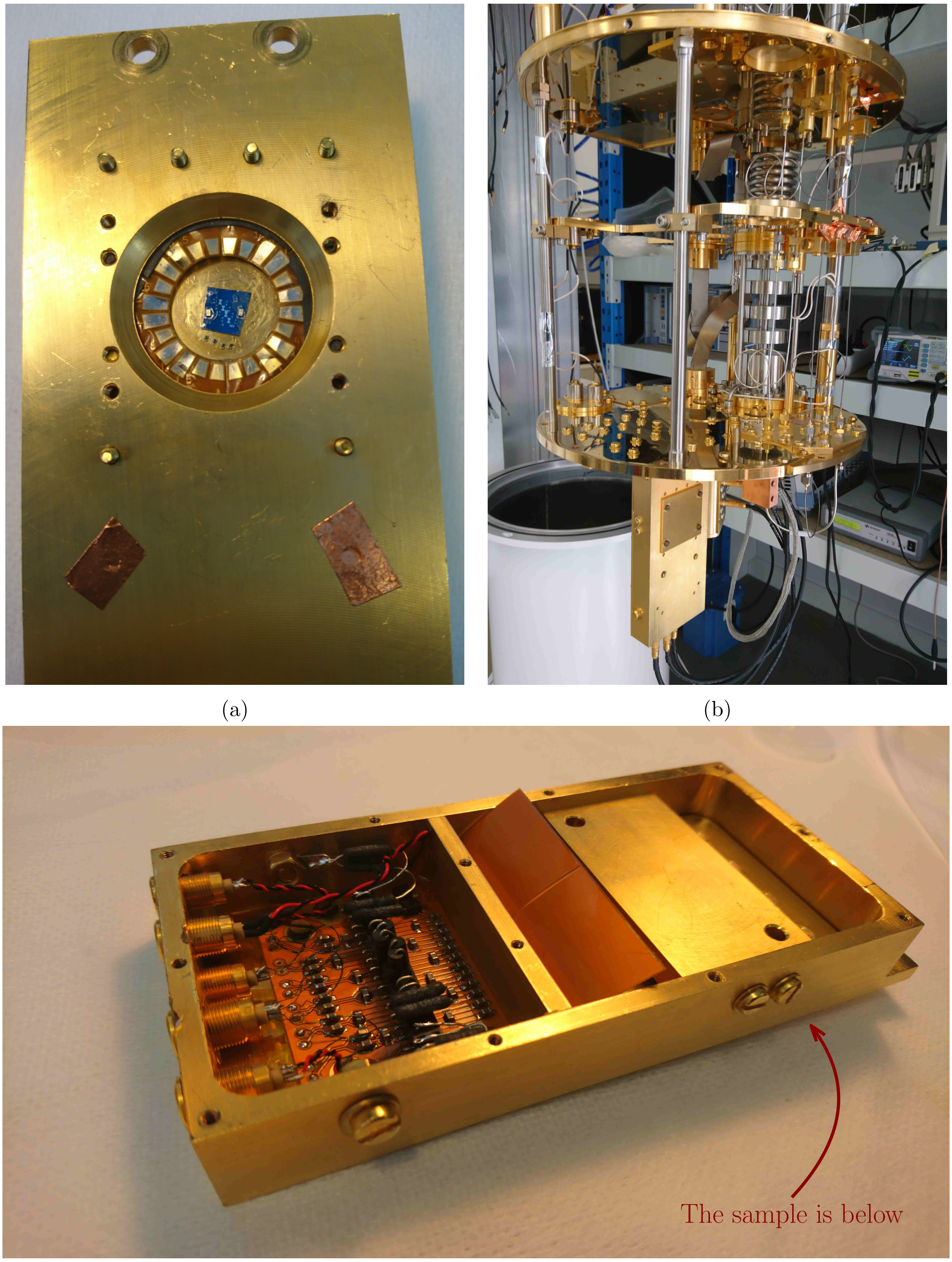

(a) (b)

(c)

Figure 4.18.: (a) Recto of sample box opened with one sample inside ; (b) Sample box closed and mounted in the cryostat ; (c) Verso of sample box opened to show filtering resistors and capacitors.

amount of the microwaves emitted by the spectrometer, as well as the high frequency noise coming from the external environment. Several features are already removed with this capacitance. The remaining resonant modes are then damped by on-chip resistors, large enough to prevent heating.

The off-chip filtering circuit, including several both distributed and lumped low-pass filters permits efficient high-frequency noise rejection.

The last measured IV characteristic at half a flux quantum consists of only a broad peak around 275 µV, the height of which is smaller than 400 pA. This paves the way for using the spectrometer to analyze other systems.

5. Josephson spectroscopy of four mesoscopic test systems

While Chapter 2 presented the principle of operation of the Josephson spectrometer, Chapter 3 introduced the obstacles which can be encountered when making such a device. Chapter 4 explained how to overcome these difficulties by carefully designing the spectrometer. With such a design, it is now possible to investigate some simple systems.

The simplest resonant mode to examine is the mode due to the inductance of the loop and the capacitance of the junctions of the SQUID forming the spectrometer. This mode is naturally present when making a loop large enough and can be used to estimate the inductance of the loop and the losses in the spectrometer.

Another interesting and simple spectroscopy to perform is to study the losses in the superconductor forming the junction: at a voltage larger than Δ/e*, the energy of the generated photons is larger than* 2Δ *which allows the excitation of quasiparticles.*

A Josephson junction itself has an intrinsic resonance frequency: the plasma frequency ω_p*. It is possible to use the Josephson spectrometer to measure the plasma frequency of another Josephson junction.*

Shunting a Josephson junction with an inductor to form a loop allows significantly increasing the plasma frequency up to some 100 GHz*. Conventional microwave techniques cannot reach frequencies as high as this but a Josephson spectrometer can measure this resonant frequency.*

5.1. LC loop mode of a SQUID

In order to verify the proper operation of the spectrometer, the simplest spectroscopy to perform is to examine the LC loop mode of a SQUID. For that purpose, the total inductance L of the loop of the SQUID must be large enough, such that the resonant frequency $1/(2\pi\sqrt{LC_s})$ is below 180 GHz, where C_s is the series combination of the capacitance of the two junctions. For a SQUID with two junctions with critical current around 100 nA, $C_s \sim 15\,\mathrm{fF}$. The inductance L must be larger than 50 pH in order to have $1/(2\pi\sqrt{LC_s}) < 180\,\mathrm{GHz}$.

The loop of the sample shown in Figure 5.1 can be approximated by a rectangular loop of $50 \times 50\,\mu\mathrm{m}^2$ with a cross section of $100\,\mathrm{nm} \times 5\,\mu\mathrm{m}$. This gives an inductance of $L \sim 60\,\mathrm{pH}$, using an analytical formula from Ref. [104]. A more exact estimation can be obtained by using the 3D-MLSI simulator (introduced in Chapter 2) which takes into account the actual geometry of the sample, as well as the kinetic inductance of aluminum. It gives $L = 62\,\mathrm{pH}$.

The current-voltage characteristic of this device is plotted in Figure 5.2. Graph (a) shows a large scale IV characteristic at $\varphi_e = 0$ and π. The shape of the quasiparticle branch with two visible backbends is believed to originate from different gaps in the junctions, as explained in Section 3.6.3. The low-voltage region exhibits the typical relaxation oscillations shape

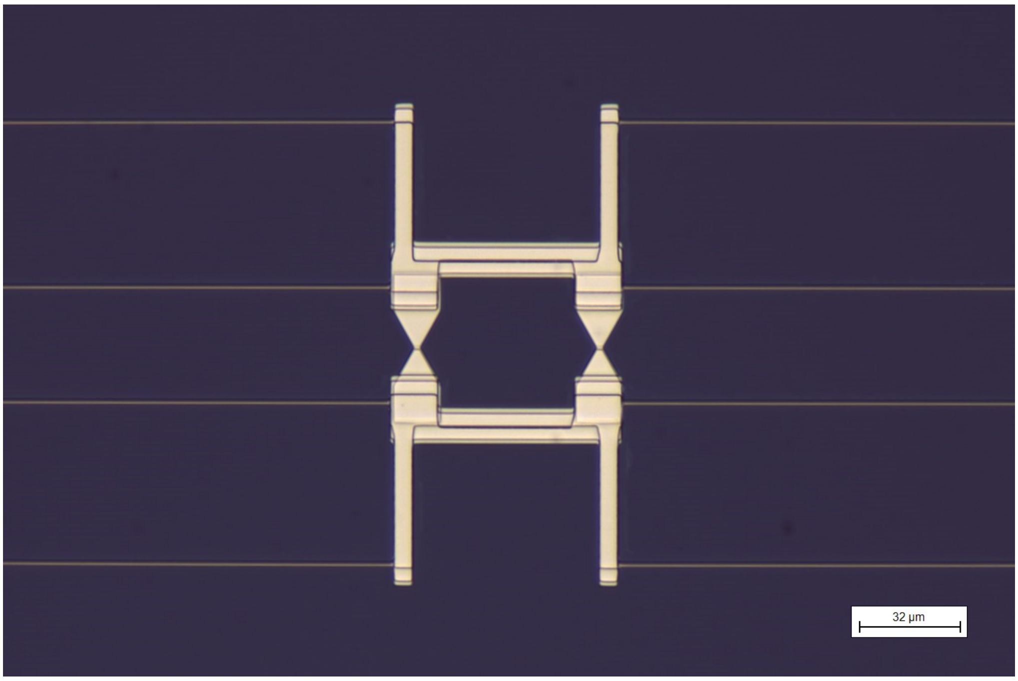

Figure 5.1.: Microscope picture of a SQUID with a loop large enough to have the LC mode below 180 GHz.

described in Section 3.3.2. This is due to the absence of shunt capacitance and a large bias inductance ($\sim 5\,\mathrm{nH}$) and does not affect the considered LC resonance at higher voltages[1].

Measured at the bend of the quasiparticle branch, an estimate of the critical current of the SQUID is 245 nA. Taking a plasma frequency of $\sim 15\,\mathrm{GHz}$[2] for the two junctions, it is possible to estimate the capacitance C_s: $C_s \sim 20\,\mathrm{fF}$ and thus the expected resonance frequency: $\omega_0 \sim 2\pi \times 145\,\mathrm{GHz}$.

At $\varphi_e = 0$, the IV characteristic is featureless, except for the relaxation oscillation region. When a magnetic flux $\varphi_e = \pi$ threads the loop, a peak appears around $300\,\mu\mathrm{V}$ (or 150 GHz). Graph (b) shows this peak in more detail for several values of flux between 0 and π. The peak develops a shoulder on the right side ($V > 300\,\mu\mathrm{V}$) as $\varphi_e \to \pi$ due to relaxation oscillations of the circuit similar to the relaxation oscillations observed after the supercurrent branch presented in Section 3.3.2. At a bias voltage larger than the peak voltage, the bias circuit can impose underdamped oscillations which are larger when the peak current is higher. This results in more prominent oscillations at $\varphi_e = \pi$ for the in-loop mode. The reduced current i_b on the right-hand scale is defined as $i_b = 4I/I_0$ where I_0 is the critical current of the SQUID, such that i_b corresponds to the coupling parameter $\tilde{z}$ of a symmetric SQUID (as defined in Chapter 2).

Because i_b (and therefore $\tilde{z}$) is small, the resonance peak can reasonably be approximated by a Lorentzian, as discussed in Chapter 2. For $z < 0.5$, the error made with this approximation

---

[1] This sample was made before the considerations of Chapter 4 on the relaxation oscillations, in order to test the operation of the spectrometer.

[2] The plasma frequency of the Josephson junctions was measured at 16.0 GHz in a setup presented in Section 5.3.

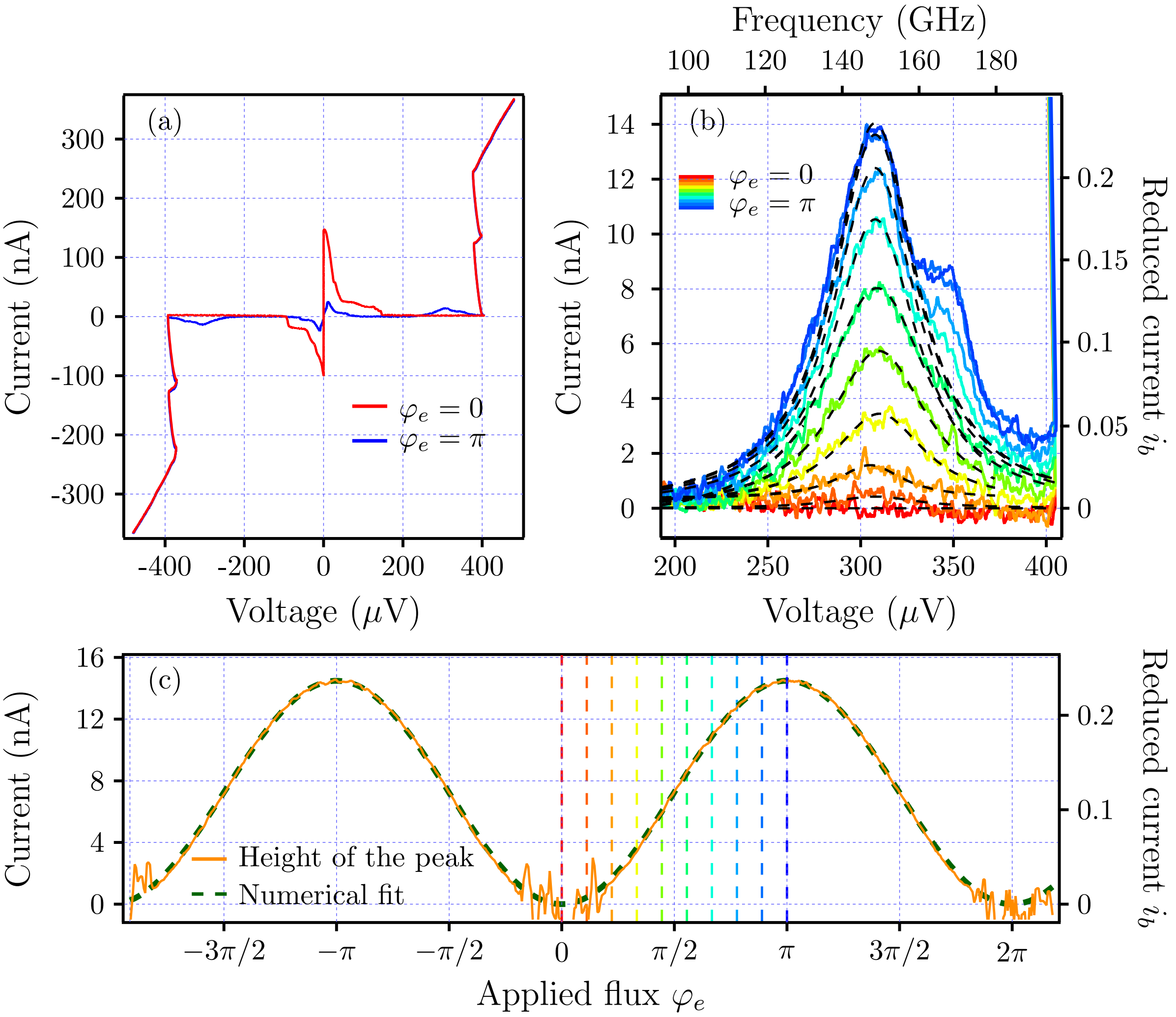

Figure 5.2.: (a) Large scale current-voltage characteristic of the sample of Figure 5.1 ; (b) Detail of the resonance peak for several fluxes with fit to a Lorentzian ; (c) Evolution of the height of the peak with respect to applied flux.

is smaller than 5%. The dashed black lines in (b) are numerical fits to Lorentzians for each flux value. Only the left-hand part of the peak is fitted for the blue curves because of the shoulder around 350 µV. This fit also gives a value for the voltage (or frequency) position of the resonance. Averaging over fluxes from $\pi/2$ to $3\pi/2$ and $-3\pi/2$ to $-\pi/2$ (where the signal is the largest), the resonance is found at

$$\boxed{\begin{aligned}&V_0 = 308\,\mu\mathrm{V},\\ &\omega_0 = 2\pi \times 149\,\mathrm{GHz}.\end{aligned}}$$

This value is in good agreement with the estimated value of $2\pi \times 145\,\mathrm{GHz}$.

Graph (c) of the figure displays in orange the height of the peak resulting from the fit. The dependence of the height of the peak on the applied flux is also verified: the dashed green line in (c) is a fit of the height of the peak with Equation (2.32),

$$I_{max} = \frac{RI_0^2}{8V_0} \sin\left(\frac{\varphi_e}{2}\right)^2.$$

The resistance R in this expression quantifies the dissipation in the resonator. It is the inverse of the real part of the admittance seen by the spectrometer. The fit gives

$$\boxed{R = 595\,\Omega.}$$

Because this mode is in the loop, this value of R has to be compared to the losses in the loop. As 149 GHz is above twice the gap of aluminum ($\sim 90\,\mathrm{GHz}$), quasiparticles can be excited in the loop (as explained in Section 5.2). The resulting resistance is of the order of the normal resistance of the SQUID loop, which is of the order of the Ohm. This is two orders of magnitude smaller than the observed value of $595\,\Omega$. There should therefore be another mechanism responsible for the losses in this mode.

In Figure 5.1, four leads are visible on each side of the SQUID. They are made in titanium and were designed to be highly inductive by taking advantage of the high inductance of titanium. In order to be sure to apply the same voltage across both junctions, the titanium leads at the top and bottom of the sample were connected together by wirebonds as shown in Figure 5.3, where the wirebonds are represented by curved red lines. This creates an impedance in parallel to the inductance of the loop. Titanium has a much lower gap than aluminum, of the order of 10 GHz, such that the contribution of the quasiparticles dominates the impedance at 149 GHz and the resistance is close to the normal state resistance. The long leads visible in the picture as twice as long as the short leads, such that the total admittance in parallel to the SQUID (both upper and lower arms) can be estimated by

$$Y_p \sim 2\left(\frac{1}{R_{Ti} + Z_{wb}} + \frac{1}{2R_{Ti} + Z_{wb}}\right) + \frac{1}{R_n + iL\omega}, \tag{5.1}$$

where R_{Ti} is the normal state resistance of one short lead, Z_{wb} the impedance of the wirebonds connecting the ends of the leads, L the inductance of the SQUID loop and R_n the normal state resistance of the SQUID loop. The simplest model for a wirebond is an inductance of the order of $1\,\mathrm{pH}\,\mu\mathrm{m}^{-1}$. At room temperature, we measured $R_{Ti} \sim 2\,\mathrm{k}\Omega$. At low temperature, it is reduced to $R_{Ti} \sim 1\,\mathrm{k}\Omega$. The inductance of the loop was evaluated earlier at $L = 62\,\mathrm{pH}$. The

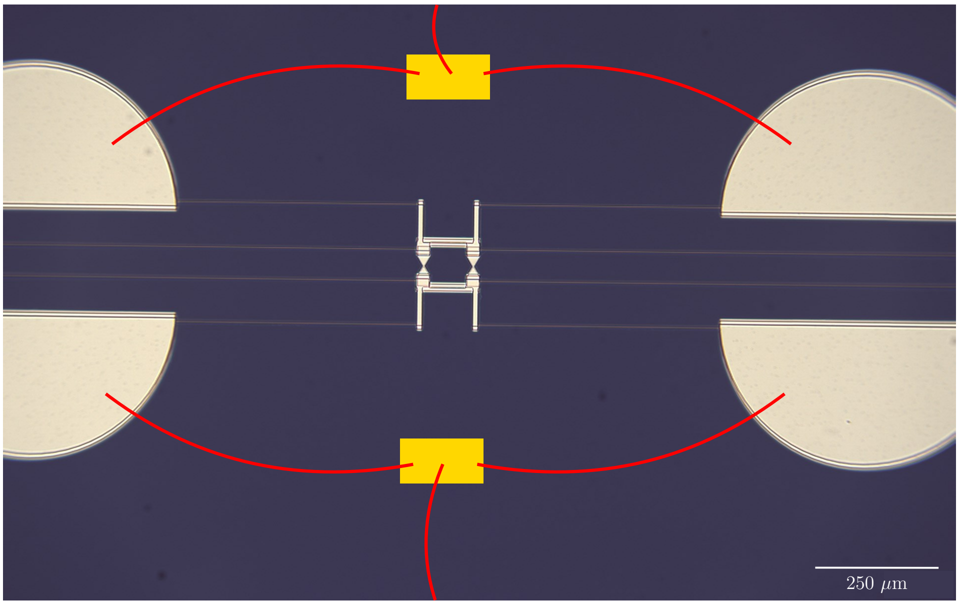

Figure 5.3.: Larger scale micrograph of the sample considered in this section.

normal state resistance of the loop R_n can be estimated by considering the sheet resistance of aluminum of $93\,\mathrm{m}\Omega/\square$ measured in another sample just above the critical temperature. The loop contains approximately 20 squares, such that $R_n \sim 2\,\Omega$. The length of the wirebonds is of the order of 5 mm, such that their inductance L_{wb} is close to 5 nH. Because they are close to each other, this value can be decreased due to the mutual coupling of two wirebonds carrying currents in opposite directions. With $L_{wb} = 2\,\mathrm{nH}$, we obtain $R \sim 700\,\Omega$ at 149 GHz which is of the order of the measured $R \sim 595\,\Omega$.

However, at such a high frequency, the wavelength in vacuum is small, 2 mm at 149 GHz. The wirebonds cannot be modeled by simple inductors but have to be described as transmission lines. Their exact length is difficult to extract and thus their impedance as well. This could be a reason for the small discrepancy between the estimated and measured values of R.

5.2. Quasiparticle excitation

5.2.1. Theoretical considerations

When a superconductor is irradiated with photons of energy lower than 2Δ, quasiparticles cannot be excited. However, for larger energies, quasiparticles can be excited, resulting in absorption of photons and thus dissipation. This absorption A is related to the real part of the conductivity σ_1 of the superconductor [41, 108]: for a field of amplitude E penetrating inside the superconductor, the dissipation per unit volume is $\sigma_1 E^2$. This dissipation is also equal to the absorbed energy which is proportional to AE^2. Mattis and Bardeen [108] give expressions for the conductivity $\sigma = \sigma_1 - i\sigma_2$, considering the applied microwaves as a perturbation of the BCS Hamiltonian. At zero temperature, they find

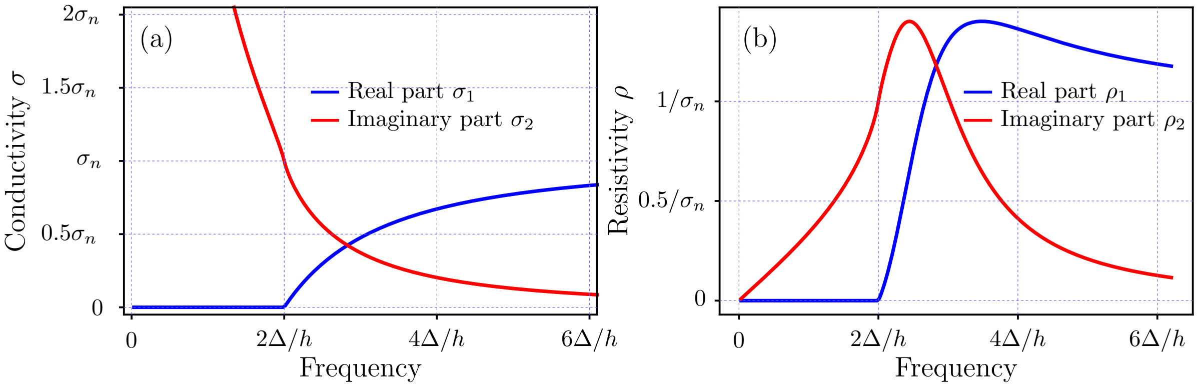

Figure 5.4.: Conductivity (a) and resistivity (b) of a superconductor with the BCS density of states.

$$\frac{\sigma_1}{\sigma_n}(\omega) = \begin{cases} 0 \text{ if } \hbar\omega < 2\Delta, \\ \left(1+\frac{2\Delta}{\hbar\omega}\right)E(k) - \frac{4\Delta}{\hbar\omega}K(k) \text{ if } \hbar\omega \geq 2\Delta, \end{cases}$$
$$\frac{\sigma_2}{\sigma_n}(\omega) = \left(\frac{2\Delta}{\hbar\omega}+1\right)\frac{E(k')}{2} + \left(\frac{2\Delta}{\hbar\omega}-1\right)\frac{K(k')}{2}, \tag{5.2}$$

where K and E are the complete elliptic integrals of first and second kind. Their arguments k and k' are

$$k = \frac{\hbar\omega - 2\Delta}{\hbar\omega + 2\Delta},$$
$$k' = \sqrt{1-k^2}.$$

Figure 5.4 (a) shows the real and imaginary parts of the conductivity, calculated with Equation 5.2. The real part (in blue) is exactly zero for frequencies below $2\Delta/h$ and rises for greater energies. It tends to the normal conductivity σ_n for large frequencies. The imaginary part is large for low frequencies and vanishes at large frequencies. At $2\Delta/h$, there is an abrupt change of slope for σ_2 corresponding to the rise of σ_1 at the same frequency.

The resistivity $\rho = 1/\sigma = \rho_1 + i\rho_2$ (plotted in (b)) gives a better insight on the behavior of the superconductor: at low frequency, the real part of the resistivity is zero, as expected for a superconductor, and the imaginary part rises linearly, as for an inductance. The slope of ρ_2 corresponds to the kinetic inductance calculated in Chapter 2. At $2\Delta/h$, the superconductor acquires a resistance and the slope of ρ_2 diverges. Close to $3\Delta/h$, the real part reaches a maximum which is larger than the normal state resistivity $1/\sigma_n$. For larger frequencies, the real part decreases and tends to the normal state resistivity while the imaginary part tends to zero.

It is possible to measure the absorption spectrum of a superconductor using the Josephson spectrometer. At a voltage V, the junctions generate an alternative current at the Josephson frequency $\omega_J = V/\varphi_0$ of magnitude I_0. At $\varphi_e = \pi$, this current circulating in the SQUID is dissipated by the real part of the conductivity. Writing the power balance allows relating the measured dc current I to the real part of the impedance Z of the superconductor,

$$VI = \frac{1}{2} I_0^2 \Re \left(Z \left(\omega_J \right) \right).$$

The impedance Z of the superconductor is proportional to its resistivity

$$Z \left(\omega \right) = \frac{L}{S} \rho \left(\omega \right),$$

Where S and L are the surface area and the length of the superconductor. The real part of the impedance Z is thus given by

$$\Re \left(Z \left(\omega \right) \right) = \frac{L}{S} \rho_1 \left(\omega \right) = \frac{L}{S} \frac{\sigma_1 \left(\omega \right)}{\sigma_1^2 \left(\omega \right) + \sigma_2^2 \left(\omega \right)}.$$

Using the notations $\tilde{\sigma}_{1,2} = \sigma_{1,2} / \sigma_n$, the dc current at voltage V is

$$I \left(V \right) = \frac{R_n I_0^2}{2V} \frac{\tilde{\sigma}_1 \left(\omega_J \right)}{\tilde{\sigma}_1^2 \left(\omega_J \right) + \tilde{\sigma}_2^2 \left(\omega_J \right)}, \tag{5.3}$$

where R_n is the normal resistance of the piece of superconductor of surface area S and length L.

5.2.2. Experimental results

Figure 5.5 shows a microscope picture of sample HS02 for which the quasiparticle spectrum was measured. Its current-voltage characteristic is shown in Figure 5.6. Panel (a) shows a large scale IV characteristic at zero flux and half a flux quantum threading the SQUID. In the (b) panel, a detail of the spectrum at half a flux quantum is exhibited. Two resonance peaks are visible. One at 30 µV and a second one close to 200 µV. The former is the plasma frequency of two parasitic RF-SQUIDs formed by the small inductive leads ((α) and (β) in the microscope picture) and large Josephson junctions (labeled PJJ in the figure) between the two layers of aluminum. More details about these parasitic RF-SQUIDs can be found in Appendix I. The second peak below 200 µV is due to the large size of the design and is an LC resonance with the capacitance of the junctions and the inductance of the leads, similar to the ones simulated in Appendix K. For voltages larger than ~ 200 µV, the current starts to rise, possibly corresponding to the excitation of quasiparticles discussed above. The dashed red line is a fit of the experimental data with expressions (5.2) and (5.3). The fit agrees well with the experimental data up to 300 µV. Above this voltage, the data increases faster. This is due to the LC loop mode of the SQUID. With this geometry, the inductance of the loop is estimated at 32 pH (according to a simulation with the 3D-MLSI software) and the capacitance of each junction of the order of 40 fF. With these two values, the LC resonance is expected around 410 µV (or 200 GHz). The orange dashed line is a numerical fit including both the quasiparticle excitations and the LC mode. It reproduces quite well the experimental data.

There are four fitting parameters for the orange curve, the superconducting gap Δ and the normal state resistance of the loop R_n for the quasiparticle excitation and the LC frequency ω_{LC} and its corresponding resistance R_{LC}. The best fit is obtained with

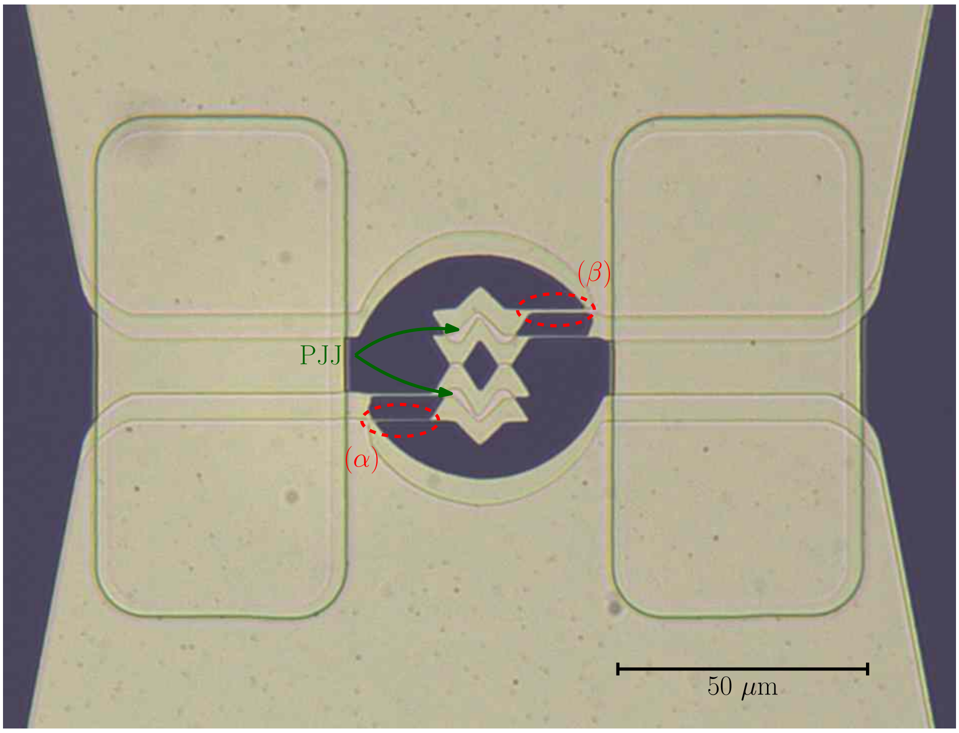

Figure 5.5.: Microscope picture of sample HS02, for which the quasiparticle spectrum was measured.

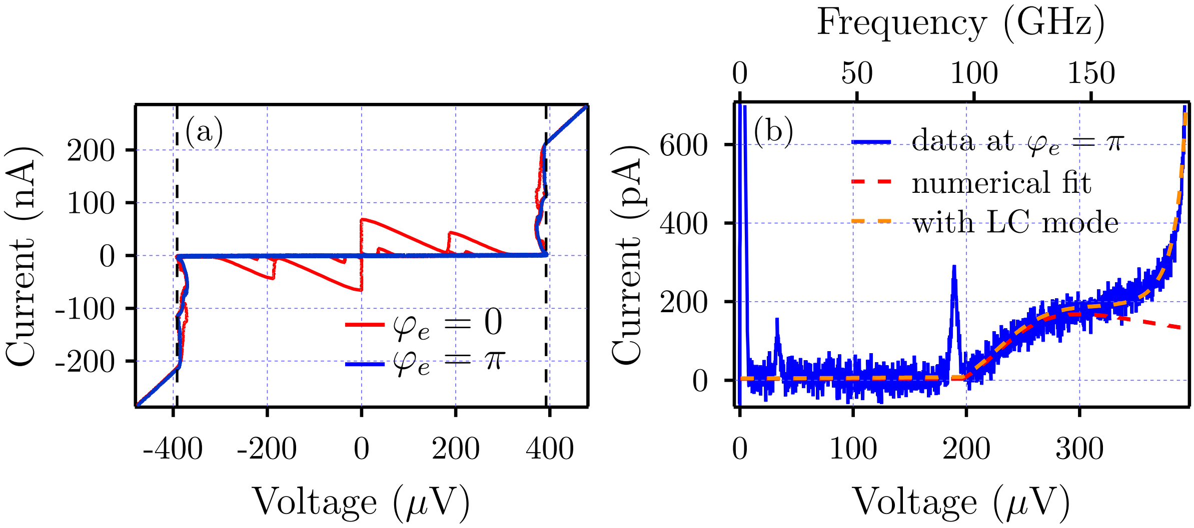

Figure 5.6.: (a) Current-voltage characteristic of a SQUID at $\varphi_e = 0$ and π ; (b) Zoom on the current-voltage characteristic at $\varphi = \pi$ and fit using formulae (5.2) and (5.3).

$$\boxed{\begin{aligned}\Delta &= 196\,\mu\text{eV},\\ R_n &= 1.5\,\Omega,\\ \omega_{LC} &= 2\pi\times 199\,\text{GHz},\\ R_{LC} &= 909\,\Omega.\end{aligned}}$$

The dashed black lines in (a) were drawn at voltage $\pm 2\Delta/e$, with the value of Δ obtained from the fit. They correspond quite well to the experimental rise of the quasiparticle branch.

The value of R_n is also consistent with the geometry of the sample. The SQUID loop contains approximately 10 squares. Using a value of $93\,\text{m}\Omega/\Box$ for the sheet resistivity of aluminum[3], we obtain a crude estimate for R_n of $930\,\text{m}\Omega$, not too far from the value of $1.5\,\Omega$ obtained from the fit.

The resonance frequency of the LC loop mode is close to the estimated value of 200 GHz. The resistance R_{LC} is the inverse of the real part of the loop admittance at the resonance frequency $Y_l = 1/(R_n + iL\omega_{LC})$, such that

$$R_{LC} = R_n\left(1 + \left(\frac{L\omega_{LC}}{R_n}\right)^2\right).$$

Using the estimated value of 32 pH for L and the value obtained from the fit for $R_n = 1.5\,\Omega$, this expression gives $R_{LC} = 1050\,\Omega$, not so far from the value of $909\,\Omega$. The difference between these values can be explained by the fact that the fit of the LC mode is not accurate because only the left-hand side part of the peak is visible and not the top of the peak.

5.3. Spectrum of a Josephson junction

5.3.1. Plasma frequency of a Josephson junction

As introduced in Chapters 1 and 4, the frequency of small oscillations at the bottom of the potential of a Josephson junction is independent of its area and depends only on the oxidation parameters. This plasma frequency ω_p can also be understood as the frequency separating the two lowest energy levels of a Josephson junction and can thus be measured by absorption spectroscopy. For a junction with critical current I_C and capacitance C_J, it is

$$\omega_p = \sqrt{\frac{I_C}{\varphi_0 C_J}}.$$

When a magnetic field threads the junction, the critical current is reduced, following

$$\tilde{I}_C = I_C\left|\text{sinc}\frac{\Phi_{JJ}}{2\varphi_0}\right|,$$

where Φ_{JJ} is the magnetic flux threading the junction. This results in a modified plasma frequency,

---

[3] This value was measured just above the critical temperature in another sample.

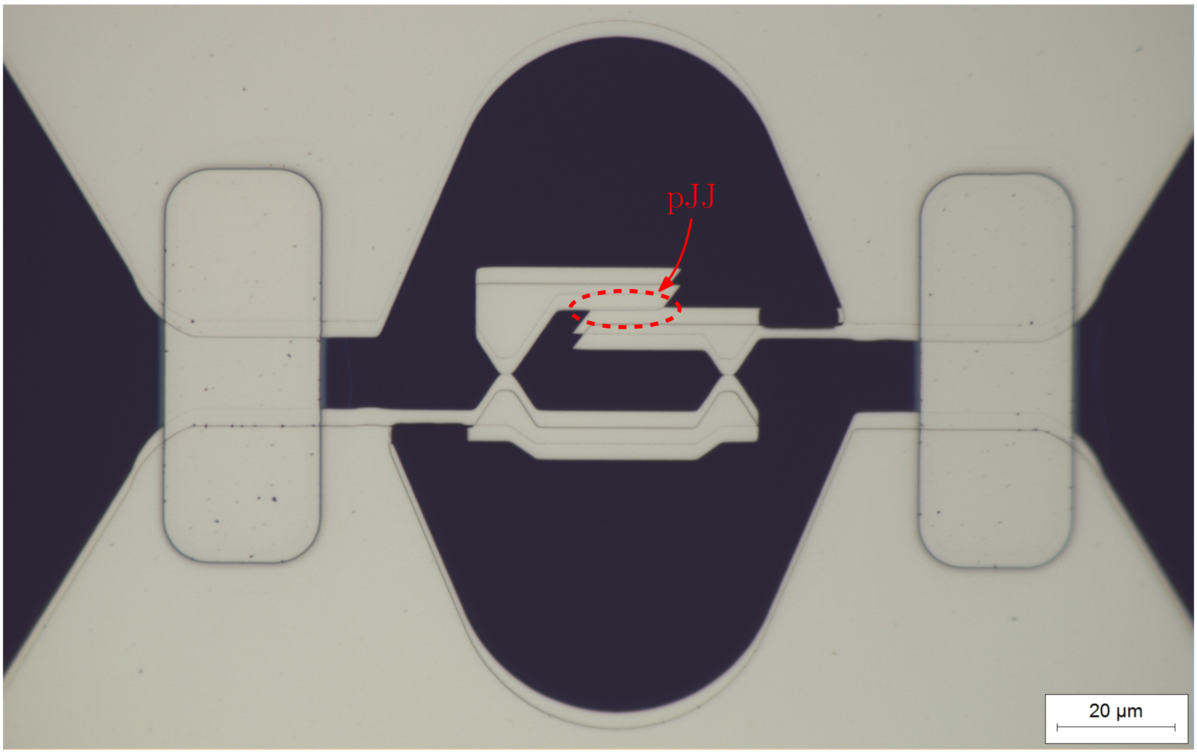

Figure 5.7.: Microscope picture of a SQUID with a large Josephson junction (pJJ) in the loop.

$$\tilde{\omega}_p = \omega_p \sqrt{\left| \operatorname{sinc} \frac{\Phi_{JJ}}{2\varphi_0} \right|}. \tag{5.4}$$

5.3.2. Design used to perform the spectroscopy

In order to measure the plasma frequency of our junctions, a large junction was made in the loop of the SQUID, as can be seen in Figure 5.7. This junction (labeled pJJ in the figure) was made large enough so that its critical current I_C is larger than the critical current of the junctions of the SQUID I_0. This ensures that pJJ is always kept in the zero-voltage state. In practice, its area is $\sim 12\,\mu\text{m} \times 500\,\text{nm}$ whereas the two smaller junctions of the SQUID each measure $\sim 1\,\mu\text{m} \times 200\,\text{nm}$. This makes a I_C/I_0 ratio of the order of 15.

With such a design, pJJ can be modeled by an inductor of inductance $L_J = \varphi_0/I_C$ in parallel with a capacitor of capacitance C_J. At $\varphi_e = \pi$, there should be a resonant peak in the current-voltage characteristic at the frequency ω_0 calculated using formula (2.25) for an in-loop mode,

$$\omega_0 = \frac{1}{\sqrt{L_J \left(C_J + \frac{C_0}{2}\right)}}, \tag{5.5}$$

where C_0 is the capacitance of one junction of the SQUID, such that $C_0/2$ is the series combination of both junctions capacitances. Because $I_C/I_0 = 15$, $C_J/C_0 = 15$. This allows expanding Equation (5.5) in

$$\omega_0 \sim \omega_p \left(1 - \frac{C_0}{4C_J}\right) \sim \omega_p. \tag{5.6}$$

The measured frequency is thus close to the plasma frequency.

5.3.3. Spectroscopy

Figure 5.8 shows the current-voltage characteristic measured for the sample shown in Figure 5.7 containing a large Josephson junction in the SQUID loop. The curves in (a) were taken at $\varphi_e = 0$ (red) and π (blue). They are asymmetric with respect to the voltage axis because the voltage is swept from the negative values to the positive values only. The minimal negative value of the supercurrent peak corresponds to the retrapping current and the maximal positive value to the switching current. The maximal switching current is 85% of the critical current, showing good noise rejection. The remaining switching current at $\varphi_e = \pi$ is 4 nA, corresponding to 11% of the critical current and thus to a symmetry ratio of $\alpha = 0.79$.

The blue curve in (b) shows more detail on the structure of the IV characteristic at $\varphi_e = \pi$. There are three visible peaks:

> ***(i)*** $V_i = 33.5\,\mu\text{V}$, corresponding to a frequency of 16.2 GHz. This frequency is close to the estimated value for the plasma frequency of 15 GHz.
>
> ***(i')*** $V_{i'} = 67\,\mu\text{V}$. $V_{i'}$ is close to $2V_i$. This could be the transition between the ground state and the second energy level of pJJ. If $I_C \sim 500\,\text{nA}$, $E_J/E_C \sim 500$, such that the energy levels of pJJ are almost those of a harmonic oscillator (as discussed in Section 1.1.4).
>
> ***(ii)*** $V_{ii} = 36.5\,\mu\text{V}$. This peak was not clearly identified but is believed to originate from the lower arm of the SQUID loop acting as a small inductor in parallel with pJJ.

In order to verify that the (i) peak is the plasma resonance of the Josephson junction, it is instructive to increase the magnetic field, so that a magnetic flux threads pJJ. The surface area of pJJ is quite small ($\sim 2\,\text{nm} \times 12\,\mu\text{m}$) and a large field is needed to have one flux quantum threading pJJ. Fortunately, as explained in Appendix F, when a magnetic field is applied perpendicularly to the sample, it cannot cross the superconducting regions and it is deviated and focused towards the non-superconducting regions, including the Josephson junctions. This increases significantly the magnetic field threading pJJ. The orange, green and violet curves were measured at $\varphi_e = 19\pi$, $\varphi_e = 35\pi$ and $\varphi_e = 49\pi$ respectively (vertically shifted for clarity purposes). The last one corresponds to having almost a flux quantum in pJJ.

The (i) peak, as well as the (i') and (ii) peaks are displaced to lower voltages. The (i') peak is less marked in the orange curve and invisible in the green and violet curve.

Panel (c) shows the evolution of the IV characteristic with respect to the applied magnetic field. The horizontal axis is the reduced flux φ_x threading pJJ. The red, blue, orange and green vertical dashed lines correspond to $\varphi_e = 0$, $\varphi_e = \pi$, $\varphi_e = 19\pi$ and $\varphi_e = 35\pi$, the IV characteristics of which are plotted in (a) and (b). The (i), (i') and (ii) peaks are visible in

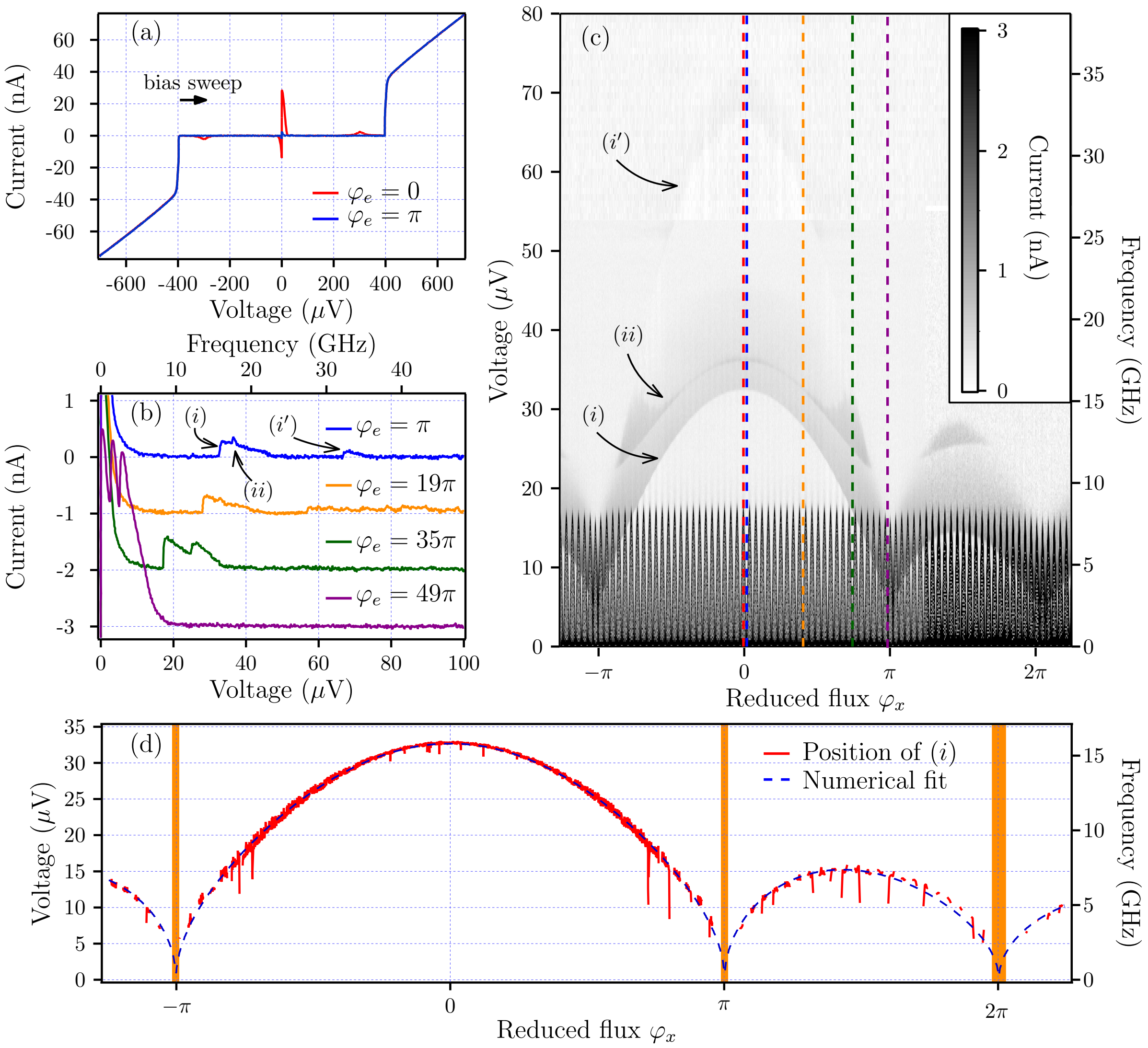

Figure 5.8.: (a) Current-voltage characteristic of the SQUID with a Josephson junction in the loop at $\varphi_e = 0$ and π ; (b) Zoom on the low-voltage region for three different coil currents (the orange, green and violet curves are shifted by 1, 2 and 3 nA respectively) ; (c) Map of current-voltage characteristics with φ_x from $-\pi$ to 2π ; (d) Position of peak (i) and fit with Equation (5.4).

this figure and highlighted with arrows. The (i') peak is hardly visible in the figure and is always at twice the voltage of the (i) peak.

Panel (d) shows the position of peak (i) (in solid red) and a fit (in dashed blue) of this voltage using Equation (5.4). For several values of the current in the coil, the data appears quite erratic or there is even no data point for the position of the peak. This is due to the fact that the (i) peak can be hidden by the supercurrent when φ_e is a multiple of 2π. The fit gives

$$\boxed{\omega_p = 2\pi \times 16.0\,\text{GHz}.}$$

When $\varphi_x \to n\pi$ (with $n \in \mathbb{Z}^*$), the critical current $I_C\left(\varphi_x\right)$ of pJJ is almost zero, such that the alternative current I_0 flowing in the SQUID loop can be larger than the critical current of pJJ. In that case, the description of the device as a SQUID with a parallel LC circuit in the loop is not sufficient. The circuit must be treated as a three-junction device to fully understand its behavior. However, the flux region where the LC approximation is not valid is small. As the plasma frequency is proportional to the square root of the critical current of pJJ, having $I_C\left(\varphi_x\right) < I_0$, *i.e.* $I_C\left(\varphi_x\right) < I_C\left(\varphi_x = 0\right)/15$ corresponds to a plasma frequency below $\omega_p/15^2 \sim 0.07\omega_p$. This limit corresponds to quite narrow regions around $\varphi_x = -\pi$, π and 2π. Even a less strict condition, for instance $I_C\left(\varphi_x\right) < 5I_0$, corresponds to narrow regions, highlighted in orange in Figure 5.8 (d).

All features visible in Figure 5.8 are not totally understood, in particular those concerning the (ii) peak. The reason for its broadening around $\pm 3\pi/4$ and $3\pi/2$ remains unclear, as well as its disappearance close to $-\pi$, π and 2π. A more comprehensive model would certainly require the description of the circuit as a three-junction device.

5.4. Spectrum of a RF-SQUID

The previous spectra were measured using a galvanic coupling scheme, ensuring a large coupling to the system of interest. To assess the performance of the Josephson spectrometer in the inductive coupling scenario, a simple system to couple to was needed. A superconducting loop interrupted by one junction (called RF-SQUID) seems adequate, as it contains an inductance allowing for inductive coupling. In addition, the resonant frequency of a RF-SQUID depends on the magnetic flux threading the loop. In order to control both spectrometer and RF-SQUID fluxes independently, a second flux line is needed. Measuring the plasma frequency of a RF-SQUID thus also allows testing such a configuration.

5.4.1. The plasma frequency of a RF-SQUID

As briefly introduced just above, a RF-SQUID is a superconducting loop interrupted by one Josephson junction as sketched in panel (a) of Figure 5.9. It was first introduced and described by Silver and Zimmerman in 1967 [21]. Having a Josephson junction in an inductive loop allows imposing a phase difference φ across the junction and thus controlling the plasma frequency of the junction. If we call φ_L the phase difference across the inductance L and Φ_x the applied magnetic flux, we get the following equation for the phase differences,

$$\Phi_x/\varphi_0 = \varphi + \varphi_L. \tag{5.7}$$

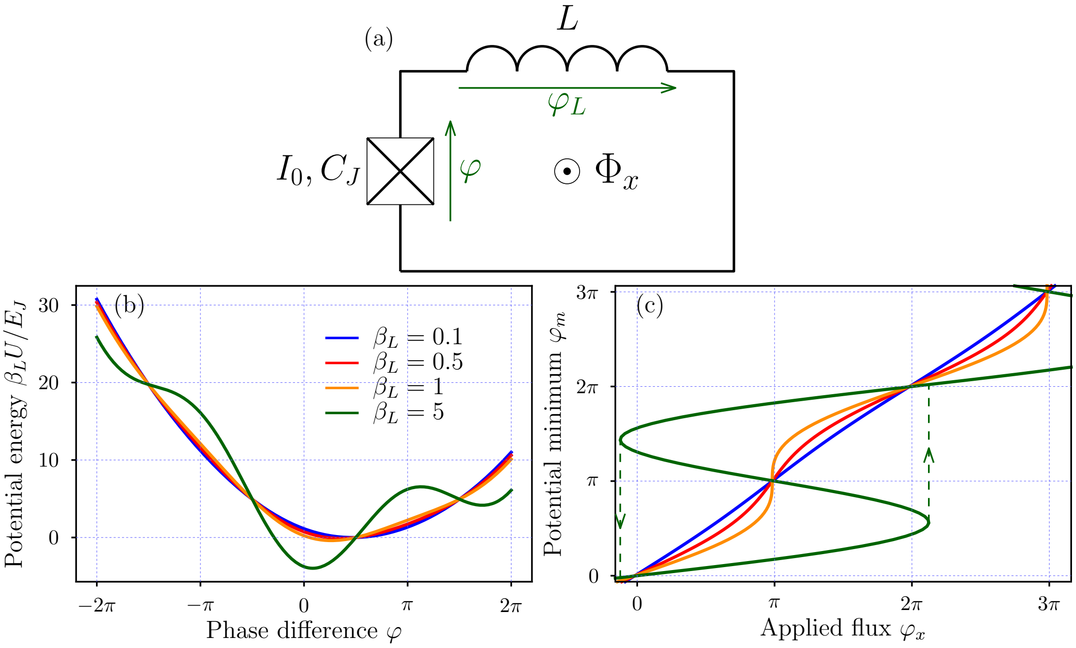

Figure 5.9.: (a) Electric diagram of a RF-SQUID ; (b) Potential energy of a RF-SQUID for several $\beta_L = LI_0/\varphi_0$ ratios and $\varphi_x = \pi/2$; (c) Minimum of the potential energy for several β_L ratios.

For a single Josephson junction, the plasma frequency is defined as the frequency of small oscillations around the minimum of potential. For a RF-SQUID, it is the same. The potential energy for the RF-SQUID sketched in Figure 5.9 can be written

$$U(\varphi) = \frac{(\varphi_0 \varphi_L)^2}{2L} - \varphi_0 I_0 \cos\varphi.$$

Using Equation (5.7) linking the phase differences and writing $\varphi_x = \Phi_x/\varphi_0$, the potential energy can be written

$$U(\varphi) = \frac{\varphi_0^2}{2L}(\varphi - \varphi_x)^2 - \varphi_0 I_0 \cos\varphi.$$

Introducing the ratio β_L between the loop inductance and the Josephson inductance: $\beta_L = LI_0/\varphi_0$, as well as the Josephson energy $E_J = \varphi_0 I_0$, the potential energy can be written

$$\frac{U(\varphi)}{E_J} = \frac{1}{2\beta_L}(\varphi - \varphi_x)^2 - \cos\varphi.$$

Panel (b) of Figure 5.9 shows this potential energy for $\beta_L = 0.1$, 0.5, 1 and 5 in units of E_J/β_L. For small β_L values, the potential energy is close to the parabolic energy of the inductance L. For larger β_L, the energy looks more like the cosine shape of the Josephson junction.

To obtain the plasma frequency, we need to find the minimum φ_m of this potential. This can be done by solving $dU/d\varphi(\varphi_m) = 0$. That is to say

$$\varphi_m + \beta_L \sin \varphi_m = \varphi_x. \tag{5.8}$$

The solution of this non-linear equation is plotted in panel (c) of Figure 5.9 for several values of β_L between 0.1 and 5. For small β_L, most the phase difference occurs across the junction, resulting in an almost linear dependence. For larger β_L, the phase difference imposed by the magnetic field is divided between the junction and the inductance, giving a more complicated dependence. When $\beta_L > 1$, φ_m becomes multi-valued for some applied flux values and jumps in φ can occur when sweeping φ_x, indicated by the dashed lines.

Around φ_m, $U(\varphi)$ can be written

$$U(\varphi) = U(\varphi_m) + \frac{1}{2}\frac{d^2U}{d\varphi^2}(\varphi_m)\,(\varphi - \varphi_m)^2 .$$

The total energy of the RF-SQUID also includes the capacitive energy $K = C_J V^2/2$, where V is the voltage across the junction. Using the Josephson relations, this total energy can be expressed as

$$\frac{E(\varphi, \dot{\varphi})}{E_J} = U(\varphi_m) + \frac{1}{2}\frac{d^2U}{d\varphi^2}(\varphi_m)\,(\varphi - \varphi_m)^2 + \frac{1}{2}\omega_{p0}^{-2}\dot{\varphi}^2,$$

where ω_{p0} is the bare junction plasma frequency. This energy is that of a harmonic oscillator around φ_m with an effective mass $\mu = E_J/\omega_{p0}^2$ and stiffness $k = E_J d^2U/d\varphi^2(\varphi_m)$. The frequency of small oscillations around φ_m (the plasma frequency) is thus

$$\omega_p = \sqrt{\frac{k}{\mu}},$$
$$\omega_p = \omega_{p0}\sqrt{\frac{1}{\beta_L} + \cos \varphi_m}.$$

Note that this expression can be rewritten in terms of the loop inductance L and the Josephson inductance $L_J = \varphi_0/I_0$,

$$\omega_p = \frac{1}{\sqrt{C_J}}\sqrt{\frac{1}{L} + \frac{\cos \varphi_m}{L_J}}. \tag{5.9}$$

This result could have been guessed immediately by noting that the Josephson junction acts as an inductance $L_J/\cos\varphi$ in parallel with a capacitance C_J, such that the circuit shown in Figure 5.9 reduces the parallel combination of C_J, L and $L_J/\cos\varphi$, the resonant frequency of which is given by Equation (5.9).

Figure 5.10 shows the dependence of plasma frequency on the applied flux for $\beta_L = 0.1$, 0.5, 1 and 5. As long as $\beta_L \leq 1$, the plasma frequency is single-valued and reaches its minima at $\varphi_x = -\pi$ or π. When $\beta_L > 1$, the plasma frequency becomes multi-valued, due to the presence of several minima in the potential energy. This translates in a hysteretic behavior around $\varphi_x = 2n\pi$, with $n \in \mathbb{Z}$. The dashed lines correspond to other minima of the potential energy.

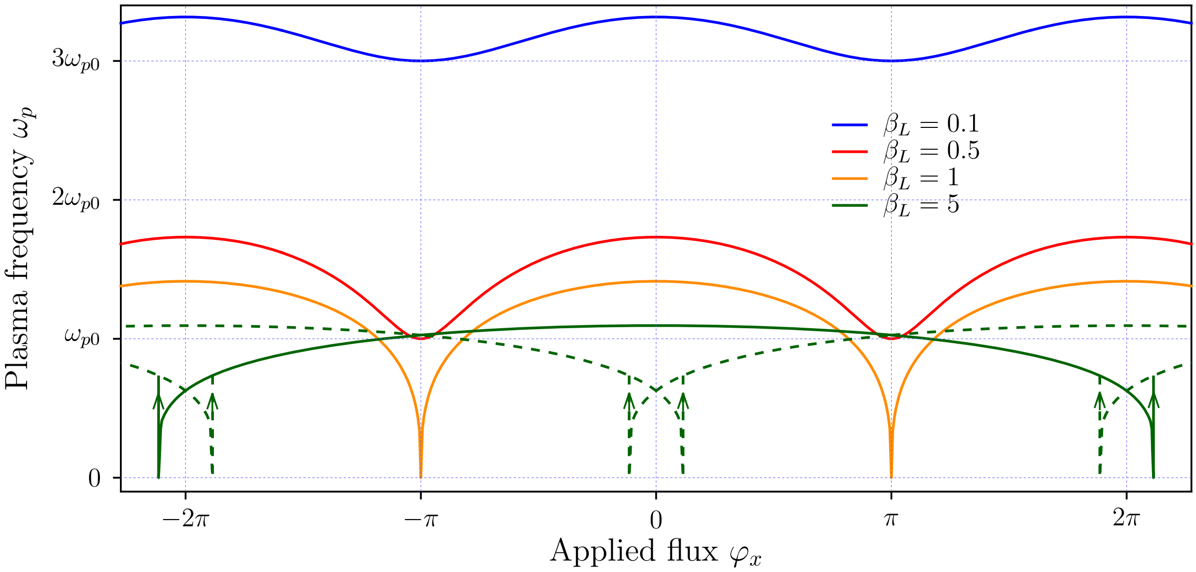

Figure 5.10.: Plasma frequency of a RF-SQUID for several β_L ratios.

5.4.2. Design of the device

In order to have the largest coupling to the RF-SQUID, it should be made on top of the spectrometer SQUID, with the same radius. However, this is not the solution chosen for this device, in particular because this would require more fabrication steps. Furthermore, the design of the spectrometer discussed in the previous chapter (such as the one shown in Figure 4.14) allows for a relatively large space between the SQUID and the large aluminum planes. It is thus possible to fabricate a RF-SQUID quite close to the spectrometer SQUID and keep a reasonable coupling constant.

Figure 5.11 shows a false color scanning electron micrograph of the fabricated device. The SQUID spectrometer is colored in blue and its two junctions are $\sim 0.5\,\mu\text{m}^2$ large. The two orange planes are capacitors made according to the considerations of the previous chapter. They have each a capacitance of $\sim 5\,\text{pF}$. The large yellow aluminum planes act as shield planes possibly screening magnetic flux noise. The RF-SQUID of interest is highlighted in red. In order to control independently the flux φ_e in the SQUID and the flux φ_x in the RF-SQUID, a local gradiometric flux line (green) was evaporated in front of the symmetry axis of the SQUID. A layer of 120 nm of alumina insulates this line from the spectrometer. The flux current follows the green arrows and generates a magnetic flux which is almost zero in the spectrometer, as the contributions of the lower and upper arms cancel out. However, in the RF-SQUID, only the lower arm generates a non-negligible flux in the loop. A larger coil, located on the sample holder and not visible in this picture, allows changing the flux threading the SQUID.

In order to estimate the value of β_L for this RF-SQUID, we need to know the critical current I_0 of the Josephson junction and the inductance L of the loop. The surface area of the Josephson junction is $2.5\,\mu\text{m}^2$, corresponding to a critical current of $\sim 200\,\text{nA}$. The loop can be approximated by a wire of cross section $100\,\text{nm} \times 2.5\,\mu\text{m}$ making a rectangular loop of

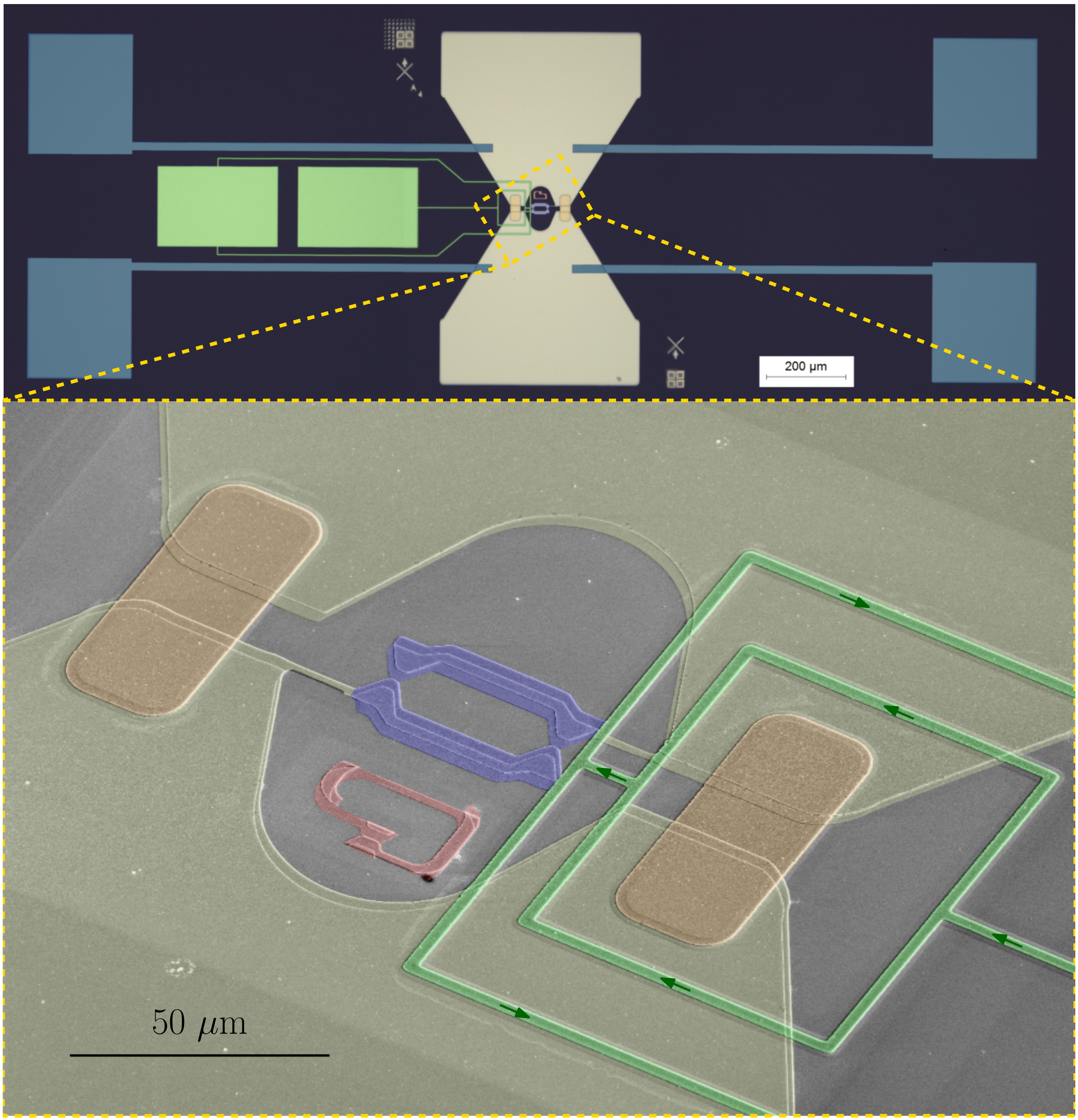

Figure 5.11.: False color scanning electron micrograph of a SQUID spectrometer (in blue) coupled to a RF-SQUID (in red). The green line is a local flux line.

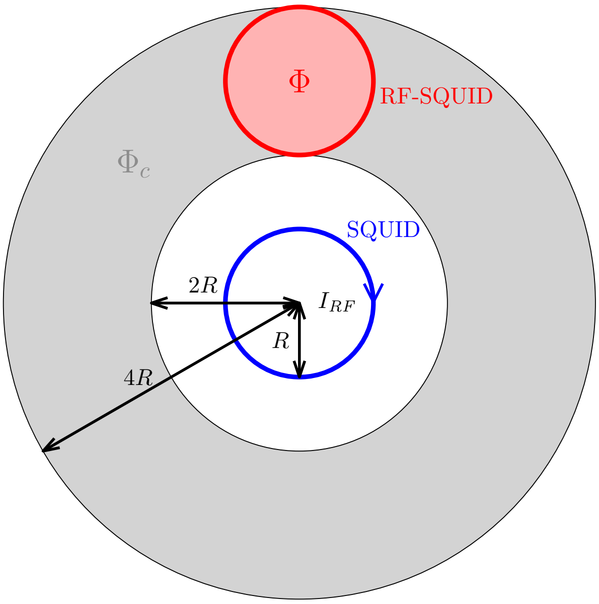

Figure 5.12.: Sketch of the spectrometer (in blue) coupled to a RF-SQUID (in red).

$30 \times 20\,\mu\text{m}^2$. This gives a geometric inductance of $L_g \sim 30\,\text{pH}$, using an analytical formula from Ref. [104]. A better estimate for the inductance of the loop can be obtained with the 3D-MLSI simulator [73] assuming the conductors are superconducting and considering the actual geometry. It yields $L = 57\,\text{pH}$. This gives an estimate for β_L of $\beta_L = 0.035$.

A crude estimate of the coupling constant between the SQUID spectrometer and the RF-SQUID can be obtained by considering the SQUID loop as a magnetic dipole, represented in blue in Figure 5.12. More than a conductor's width away from the loop, the magnetic field decreases as $1/r^3$, where r is the distance from the center of the loop. We write it B_0/r^3. The flux threading the gray circular annulus with a radius between $2R$ and $4R$ can be estimated by

$$\Phi_c = \int_{2R}^{4R} \frac{B_0}{r^3} 2\pi r dr = \frac{2\pi}{3} B_0 \left(\frac{1}{8R^3} - \frac{1}{64R^3} \right).$$

If we consider that the red RF-SQUID occupies $1/10$ of this annulus, the flux threading it is $\Phi = 0.1\Phi_c$. The total flux created by the SQUID is of the order of

$$\Phi_{tot} = \int_{R}^{+\infty} \frac{B_0}{r^3} 2\pi r dr = \frac{2\pi}{3} \frac{B_0}{R^3}.$$

With these estimates, the coupling coefficient k is

$$k = \frac{\Phi}{\Phi_{tot}} = 0.01.$$

A simulation with the 3D-MLSI simulator [73], introduced earlier in Section 2.3.3, taking into account the exact geometry of the sample and assuming that the materials are superconducting, gives $k = 0.0181$.

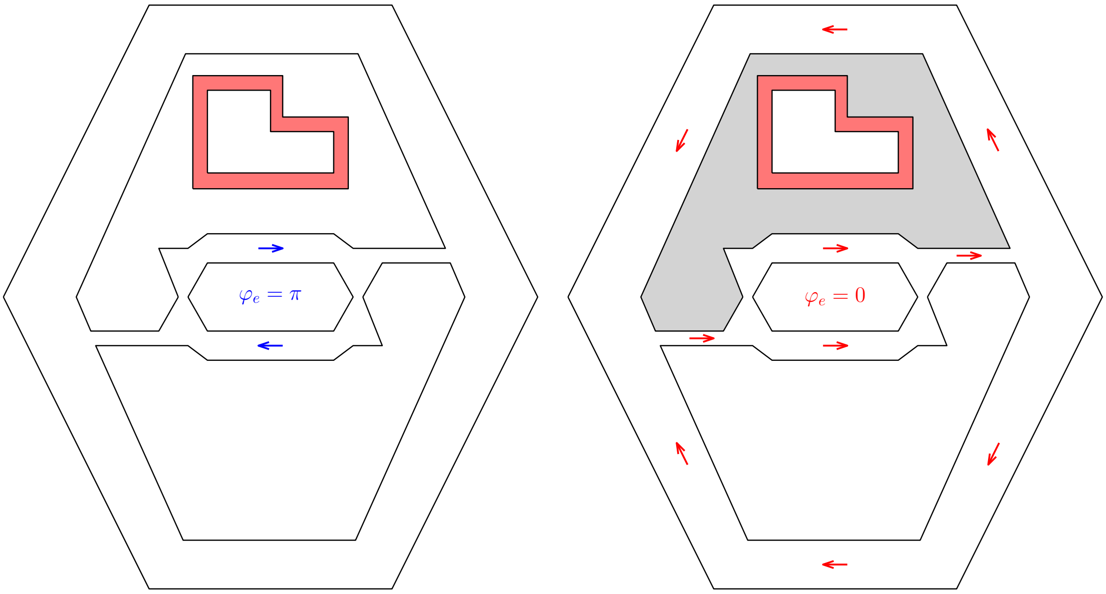

(a) $\varphi_e = \pi$.

(b) $\varphi_e = 0$.

Figure 5.13.: Schematic representation of the spectrometer coupled to the RF-SQUID (in light red) at reduced flux π and 0.

Because of the large aluminum shield planes and the two shunt capacitors around the SQUID and the RF-SQUID, the high-frequency magnetic field generated by the spectrometer at $\varphi_e = \pi$ is confined in the central region, as explained in Appendix F. This can increase the coupling constant between the SQUID and the RF-SQUID. Including this shield plane, the 3D-MLSI simulators gives $k = 0.0184$. The coupling constant is increased by 1.5% but stays quite low.

Fortunately, it is also possible to couple to the RF-SQUID at $\varphi_e = 0$. With this flux biasing, the microwave current circulates around the RF-SQUID, as shown in panel (b) of Figure 5.13. In that case, the coupling constant k is much higher than for $\varphi_e = \pi$ where the microwave current only circulates in the SQUID loop. As the surface area of the RF-SQUID is of the order of 10% of the area in gray in Figure 5.13b, the flux threading it is of the order of 10% of the total flux created by the current, such that $k \sim 0.1$. The 3D-MLSI simulator yields $k = 0.123$ when $\varphi_e = 0$, which is one order of magnitude larger than when $\varphi_e = \pi$.

As the power dissipated in the case of inductive coupling is proportional to k^2 (as seen in Section 2.3.3), the signal is expected to be almost 50 times larger at $\varphi_e = 0$. In that case, the situation is as shown in Figure 5.14. The Josephson junction of the RF-SQUID is equivalent to its capacitance in parallel with the Josephson inductance $L_S(\Phi_x)$, depending on the flux threading the RF-SQUID. For small β_L ratio, $L_S(\Phi_x) \sim L_J/\cos\varphi_x$ with the notations of Section 5.4.1.

According to the calculations of Section 2.3.3, the equivalent impedance seen by the junction is

$$\tilde{Z}_e = il\omega \left(1 - k^2 \frac{l_c\omega}{l_c\omega - iZ_e}\right),$$

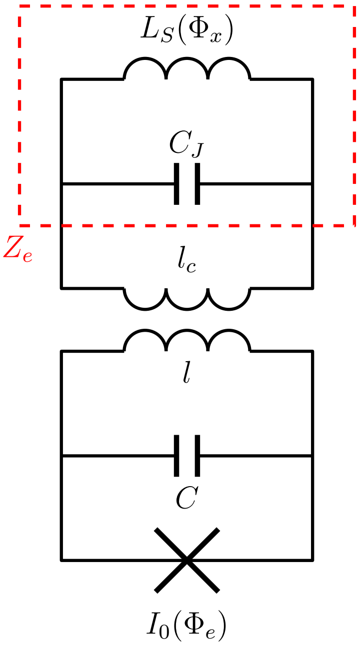

Figure 5.14.: Electric schematic of the spectrometer coupled to a RF-SQUID.

where $Z_e = iL_S\omega/\big(1-(\omega/(L_SC_J)^2\big)$. In the small β_L limit, this gives

$$\tilde{Z}_e = il\omega\left(\frac{\frac{1}{\beta_L\cos\varphi_x}+\left(1-k^2\right)\left(1-\left(\frac{\omega}{\omega_{p0}}\right)^2\cos\varphi_x\right)}{1+\frac{1}{\beta_L\cos\varphi_x}-\left(\frac{\omega}{\omega_{p0}}\right)^2\cos\varphi_x}\right),$$

where ω_{p0} is the bare plasma frequency of the junction in the RF-SQUID, $\omega_{p0} = 1/\sqrt{L_JC_J}$. The resonance condition can thus be written, with $\omega_s = 1/\sqrt{lC}$,

$$\left(\frac{\omega_0}{\omega_s}\right)^2\left(1-k^2+\frac{1}{\beta_L\cos\varphi_x}-\left(1-k^2\right)\left(\frac{\omega_0}{\omega_{p0}}\right)^2\cos\varphi_x\right) = 1+\frac{1}{\beta_L\cos\varphi_x}-\left(\frac{\omega_0}{\omega_{p0}}\right)^2\cos\varphi_x.$$

Written in terms of the plasma frequency ω_p of the RF-SQUID, this gives

$$\left(\frac{\omega_0}{\omega_s}\right)^2\left(1-k^2\frac{\beta_L\cos\varphi_x}{1+\beta_L\cos\varphi_x}-\left(1-k^2\right)\left(\frac{\omega_0}{\omega_p}\right)^2\right) = 1-\left(\frac{\omega_0}{\omega_p}\right)^2. \tag{5.10}$$

The designed β_L value is of the order of 0.035 and $k \sim 0.12$, such that $\beta_L, k \ll 1$. Equation (5.10) thus reduces to

$$\left(\frac{\omega_0}{\omega_s}\right)^2\left(1-\left(\frac{\omega_0}{\omega_p}\right)^2\right) = 1-\left(\frac{\omega_0}{\omega_p}\right)^2, \tag{5.11}$$

which has two solutions, ω_s and ω_p. We are therefore assured to measure the exact plasma frequency of the RF-SQUID, as well as the frequency of the lC circuit.

The measured signal is then proportional to k^2 (as seen in Section 2.3.3). But if k is too large, the resonant frequencies deviate from ω_s and ω_p. For small β_L ratios, Equation (5.11) is the same as Equation (2.34) discussed in Section 2.3.3 for the case where the junction of the RF-SQUID is replaced by a capacitance. The calculated solutions are plotted in Figure 2.23 for several ω_p/ω_s ratios. For the sample considered here, ω_s is of the order of 40 GHz and $\omega_p \sim \omega_{p0}/\sqrt{\beta_L} \sim 70\,\text{GHz}$, such that $\omega_p/\omega_s \sim 2$. With such a ratio, ω_0 stays within 5% of ω_p as long as $k < 0.26$. For the estimated value of $k = 0.12$, $\omega_0 = 1.0097\omega_p$.

5.4.3. Spectroscopy

Figure 5.15 shows the current-voltage characteristic measured for the device of Figure 5.11. The (a) graph is a large-scale IV characteristic at $\varphi_e = 0$ and π. The bias voltage is swept from negative values to positive values, giving an asymmetric shape to the curves. The switching current at $\varphi_e = 0$ is 85% of its nominal value, showing good noise filtering. At $\varphi_e = \pi$, the switching current is around 3 nA, that is 6% of the critical current, corresponding to a good symmetry ratio of $\alpha = 0.88$.

Panels (b) and (c) show the detailed structure of the IV characteristic at $\varphi_e = 0$ and π. The small peaks S_1 at 80 µV and S_2 at 150 µV as well as the large peak S_3 at 270 µV were identified in Section 4.3.3 as corresponding to resonant modes due to the large dimensions of the shield planes. In addition to these peaks, there are three other peaks in the spectrum at $\varphi_e = 0$. The signal of the plasma resonance of the RF-SQUID is expected to be ~ 50 larger at $\varphi_e = 0$ than at $\varphi_e = \pi$. So, if one of these peaks of amplitude ~ 500 pA is the plasma peak, it should be ~ 10 pA at $\varphi_e = \pi$, which is in the noise of the measurement.

In order to understand their origin and confirm that one of them is the plasma resonance of the RF-SQUID, the gradiometric flux line was used to thread the RF-SQUID with a magnetic flux φ_x while keeping the flux in the spectrometer at 0. The effect of this is displayed in (d). The red curve is the same as in (a)-(c). The violet, orange and green curves were all taken at $\varphi_e = 0$ with different φ_x values. They were shifted respectively by 0.5, 1 and 1.5 nA for clarity. The S_1, S_2, G_1 and G_2 peaks do not change when φ_x increases. But the P peak first moves to lower voltages and then comes back to higher voltages.

(e) shows the evolution of the IV characteristic with the applied flux φ_x, while the flux in the SQUID stays at $\varphi_e = 0$. The colored vertical lines correspond to the curves in (d). As seen in (d), only the P peak moves and its position is periodic with respect to the magnetic field, as expected for the plasma frequency of the RF-SQUID.

G_1 and G_2 are suspected to originate from resonant modes introduced by the gradiometric flux line. This hypothesis was confirmed by a simulation made with Sonnet, described in Appendix K.3.

As these peaks are small ($\sim 1\%$ of the critical current of the SQUID), it is possible to fit them with a Lorentzian according to the considerations of Chapter 2 to obtain the resonance frequency at the center of the peak. The result of this fit for the plasma peak is plotted in red below the map. The dashed blue line is a fit of this resonance frequency using the formula derived in Section 5.4.1,

$$\omega_p = \omega_{p0}\sqrt{\frac{1}{\beta_L} + \cos\varphi_m}.$$

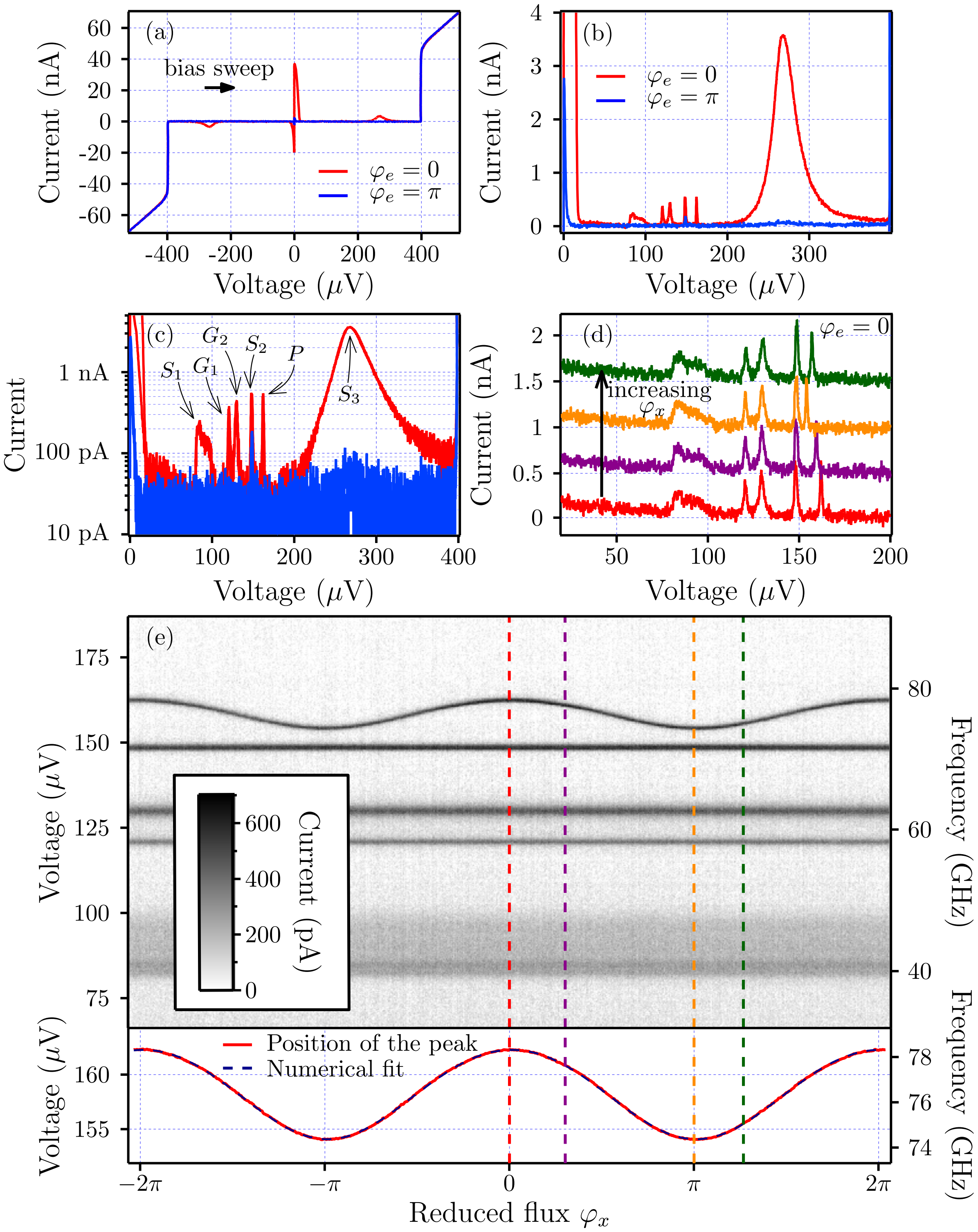

Figure 5.15.: (a) Large scale current-voltage characteristic of the spectrometer coupled to a RF-SQUID for $\varphi_e = 0$ and π ; (b)-(c) Low current region of the IV characteristic in linear and logarithmic scale ; (d) Detail of the five first peaks at $\varphi_e = 0$ and for different values of flux φ_x in the RF-SQUID ; (e) IV characteristics as a function of φ_x and fit of $\omega_p(\varphi_x)$.

The fit gives

$$\boxed{\begin{aligned}\omega_{p0} &= 2\pi \times 17.3\,\text{GHz},\\ \beta_L &= 0.052.\end{aligned}}$$

The value found here for the plasma frequency of the Josephson junction is close to the value of $2\pi \times 16.0\,\text{GHz}$ found in Section 5.3, but a bit higher. The small discrepancy between both measured plasma frequencies can come from differences in the geometry of the junctions. As stated in Chapter 4, the plasma frequency of a Josephson junction does not depend on its surface area S since both capacitance and critical current are proportional to S. This can be considered true if the junction consists only of two parallel plates separated by a thin dielectric layer. In practice there is always a stray capacitance between the two electrodes of a junction which is not necessarily proportional to its surface area and depends on the geometry of the sample. The devices measured in Section 5.3 and here have quite different geometries (visible in Figures 5.7 and 5.11), resulting in different capacitance per surface area.

The value obtained for β_L is larger than the estimated one of 0.035. The value taken for the critical current of the junction to estimate β_L was obtained with its surface area measured in a microscope picture. This value is therefore not precise and can be wrong by a factor of 2. If we take $L = 57\,\text{pH}$ for the inductance of the loop, the critical current of the junction has to be $I_C = 300\,\text{nA}$ to ensure $\beta_L = 0.052$.

The fit also gives the width of the peak. It is almost constant with respect to flux. Averaged over all measured peaks, the full width at half maximum ΔV is found to be $\Delta V = 1.14\,\mu\text{V}$, corresponding to a frequency linewidth of $\Delta\omega = 2\pi \times 550\,\text{MHz}$. The voltage thermal noise across the shunt capacitance C_S is given by $V_{rms} = \sqrt{k_B T / C_S}$ according to the discussion of Section 2.4.3. With C_S of the order of 1 pF, this gives $V_{rms} = 1.2\,\mu\text{V}$, comparable to the measured width of the peaks.

It is also possible to extract the real part G_e of the admittance of the mode via $I_p = I_0^2/(2V_p G_e)$ or $I_p = R I_0^2/(2V_p)$, where V_p and I_p are the voltage and the current at the peak. This gives here

$$\boxed{\begin{aligned}G_e &= 13.2\,\text{mS},\\ R &= 75.8\,\Omega.\end{aligned}}$$

This dissipation is mainly due to the on-chip bias resistors (in blue in Figure 5.11). The bonding pads at the end of the leads are quite large and there can be a non-negligible capacitance C_p between them. In our case, they are squares of $250 \times 250\,\mu\text{m}^2$ separated by a length of $250\,\mu\text{m}$. Using a software available online [109], the capacitance between them is estimated at 40 fF in pure silicon. Writing R_b the resistance of one bias lead, the admittance seen by the junction in parallel with the resonator is

$$Y_p = \frac{2}{2R_b + \frac{1}{iC_p\omega}}.$$

With $R_b = 160\,\Omega$ and $C_p \sim 40\,\text{fF}$ for the capacitance, an estimate for the inverse of the real part of Y_p at 80 GHz is $R \sim 165\,\Omega$, larger than the measured value. In practice, there is also a distributed capacitance between the bias leads which can reduce the effective value of R. A simulation of the actual geometry of the sample with Sonnet gives a resistance seen by the junction of the order of $75\,\Omega$.

5.5. Conclusion

The first spectra measured with the Josephson spectrometer shown in this chapter were taken on simple systems to demonstrate the good operation of the designed device.

The LC mode of a SQUID was measured at 149 GHz, which is a quite high frequency for conventional microwave techniques. For this spectrum, the dependence of the amplitude of the signal on the applied magnetic field was also understood and modeled with the considerations of Chapter 2.

The spectrometer also allows measuring quantities directly related to the density of states of a superconductor as shown in Section 5.2.

It was also used to measure one characteristic properties of the fabricated Josephson junctions: their plasma frequency. The measured spectrum shows $\omega_p = 2\pi \times 16\,\mathrm{GHz}$ and has the expected dependence on the magnetic field.

Finally, the spectrum of a RF-SQUID was taken to verify the ability to use an inductive coupling scheme in which there is no galvanic contact between the spectrometer and the system of interest.

In conclusion, we have implemented a new type of spectrometer able to operate in a large frequency range from 2 GHz up to 180 GHz with a linewidth as small as 550 MHz in some cases. There are only a few parasitic resonances in the spectrum which have now been understood and can thus be suppressed (or at least shifted to other frequencies). The ability of using a local gradiometric flux line to control independently two magnetic fluxes was also demonstrated. All these elements are necessary for using the spectrometer on the systems of interests presented in the next chapter.

6. Future directions

As shown in the previous chapters, the designed spectrometer allows measuring spectra in the $1-180\,\mathrm{GHz}$ *range. There are several other particular systems which seem pertinent for the use of the spectrometer and which were studied in this thesis. The Andreev Bound States hosted in various types of weak links between superconductors can be addressed with the Josephson spectrometer. It can also probe mesoscopic quantum circuits exhibiting interesting topological properties.*

6.1. Spectrum of Andreev Bound States

The Josephson spectrometer is well suited to measure the spectrum of Andreev Bound States as the excitation energies vary between zero[1] and twice the superconducting gap Δ. If they are made in pure aluminum, the frequency range of excitations is $0-90\,\mathrm{GHz}$, which is half the range of the spectrometer. In practice, it is not possible to measure a zero-gap in conventional ABS because this would require a transmission exactly equal to one which is only possible in unconventional situations due to spin-orbit coupling as will be explained in Sections 6.1.3 and 6.1.4. Typically, the smallest gap values obtained with aluminum atomic contacts are $1\,\mathrm{GHz}$.

As derived in Section 1.1.2, a conduction channel of transmission τ between two superconductors hosts two ABS: $|\pm\rangle$ of energies:

$$E_\pm = \pm\Delta\sqrt{1-\tau\sin^2\frac{\varphi}{2}}$$

The spectrometer can only measure transitions between these states. The resulting spectrum is shown in Figure 6.1 for conduction channels ranging from 0 to 1. If the transmission is 0, the excitation energy is always 2Δ, no matter the phase difference φ across the weak link. When the transmission increases, the energy starts to change when φ varies with a minimum at $\varphi = \pi$, leaving an excitation gap opened. For $\tau = 1$, the modulation is maximal and the energy gap is closed.

The ABS spectrum of an atomic contact was already probed by the Quantronics group [32, 33], using a Josephson junction as a spectrometer as detailed earlier in Section 2.1.6.

When some properties of the superconductor forming the weak link are changed, the usual spectrum shown in Figure 6.1 can be modified, resulting in level crossings or gap closings. Before looking at these non-conventional ABS, we first investigate what the ABS spectrum looks like when probed with a Josephson spectrometer.

---

[1] Zero for ABS with transmission $\tau = 1$. For a transmission τ, the minimum excitation energy is $2\Delta\sqrt{1-\tau}$.

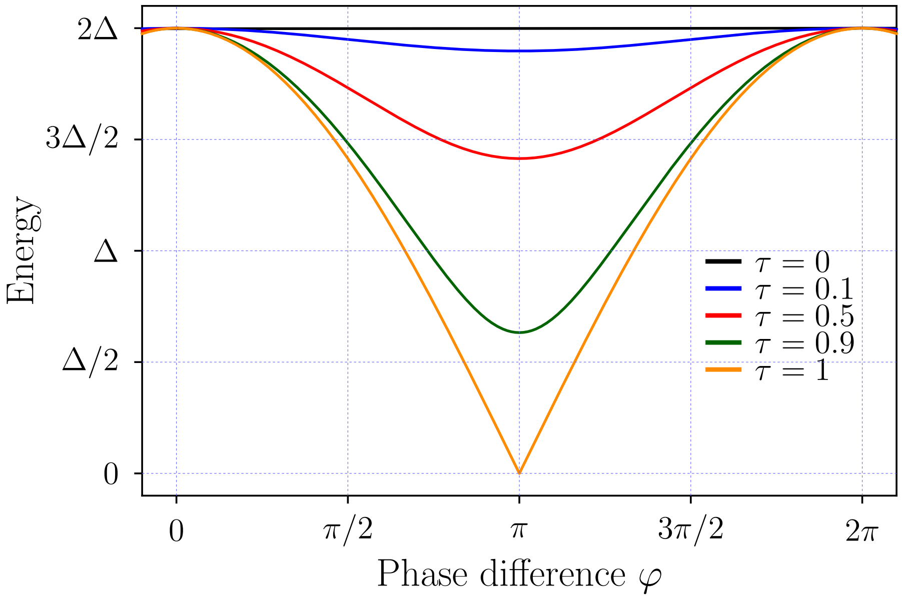

Figure 6.1.: Calculated ABS spectrum for conduction channels with transmissions 0, 0.1, 0.5, 0.9 and 1.

6.1.1. Form of the ABS spectrum probed by a Josephson spectrometer

Due to the presence of inductors and capacitors in the spectrometer circuit, the measured frequency can be different from the actual transition frequency, as in the case of an LC parallel resonator discussed in Chapter 2. To estimate the frequency we will measure with the Josephson spectrometer, we need an expression for the admittance Y_{wl} of the weak link. Kos *et al.* calculate such an expression in the case of a short superconducting weak link [71] by using linear response theory on an alternative voltage applied to the tunneling Hamiltonian describing the weak link. They obtain for a single transmission channel at a frequency ω,

$$Y_{wl}\left(\omega\right) = \frac{1}{iL_J\omega} + \sum_{i=1}^{5} Y_i\left(\omega\right), \tag{6.1}$$

where L_J is the Josephson inductance of the weak link present at low frequencies,

$$\frac{1}{L_J} = \frac{1}{\varphi_0}\frac{\partial I_J}{\partial \varphi} = \sum_j \frac{\Delta\tau_j}{4\varphi_0^2}\frac{\cos\varphi + \tau_j \sin^4\frac{\varphi}{2}}{\left(1-\tau_j\sin^2\frac{\varphi}{2}\right)^{3/2}}, \tag{6.2}$$

with I_J the current flowing through the weak link, φ the phase difference across it and τ_j the transmission of channel j. The five $Y_i\left(\omega\right)$ terms in Equation (6.1) are due to quasiparticles excitations and each have a different origin depicted in Figure 6.2. E_A is the energy of the Andreev Bound State of the transmission channel and Δ the superconducting gap. The five excitation schemes, labeled (1) to (5), correspond respectively to the five Y_i terms in the admittance. (1) is the excitation of a pair of quasiparticles to the continuum, (2) of one quasiparticle to the continuum and one to the ABS, (3) of two quasiparticles to the ABS, (4)

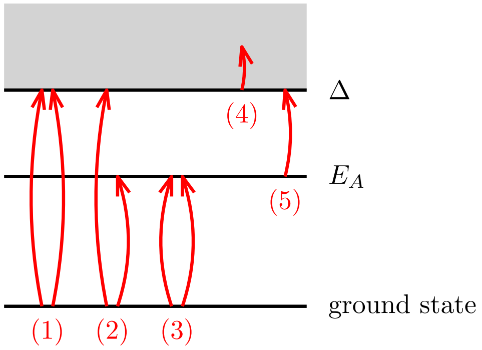

Figure 6.2.: Possible quasiparticles excitation schemes in a superconducting weak link.

of one quasiparticle from the continuum to a higher energy, (5) of one quasiparticle from the ABS to the continuum.

The transitions discussed in Sections 6.1.2 and 6.1.4, as well as the even manifold of Section 6.1.3 correspond to excitations between the ground state and the ABS and are thus of type (3). For such excitations the admittance is given by

$$\begin{cases} \Re(Y_3) = \dfrac{2e^2\tau}{h}\dfrac{\left(\Delta^2 - E_A^2\right)\left(E_A^2 - \Delta^2\cos^2\frac{\varphi}{2}\right)}{2E_A^3}\pi^2\delta\left(\hbar\omega - 2E_A\right), \\ \Im(Y_3) = \dfrac{2e^2\tau}{h}\dfrac{\left(\Delta^2 - E_A^2\right)\left(E_A^2 - \Delta^2\cos^2\frac{\varphi}{2}\right)}{\hbar\omega E_A^2}\pi\left(\dfrac{1}{\hbar\omega - 2E_A} - \dfrac{1}{\hbar\omega + 2E_A} + \dfrac{1}{E_A}\right). \end{cases} \tag{6.3}$$

The imaginary part is plotted in Figure 6.3 at $\varphi = \pi$ for several values of transmission. The real part is only non-zero when $\hbar\omega = 2E_A$ and the reached value corresponds to absorption of photons by the weak link. At this frequency, the imaginary part has a pole. For low frequencies, Y_3 is proportional to $-i\omega$ and tends to zero, as for a capacitance. At high frequencies, Y_3 is proportional to i/ω and tends to zero, as for an inductance.

For $\hbar\omega$ close to $\hbar\omega_A = 2E_A$, the admittance of the weak link of Equation (6.1) is dominated by $\Im\left(Y_3\right)$. $\Im\left(Y_1\right)$ can be large, but close to 2Δ and $\Im\left(Y_2\right)$ at $\Delta + E_A$. $\Im\left(Y_4\right)$ and $\Im\left(Y_5\right)$ are zero when no quasiparticle is present in the weak link. The contribution of L_J is only important at low frequencies.

Writing

$$\tilde{G} = \frac{2e^2\pi\tau}{h}\frac{\left(\Delta^2 - E_A^2\right)\left(E_A^2 - \Delta^2\cos^2\frac{\varphi}{2}\right)}{4E_A^4},$$

Y_3 can be expressed close to $2E_A$,

$$\begin{cases} \Re\left(Y_3\right) \sim \pi\tilde{G}\omega_A\delta\left(\omega - \omega_A\right), \\ \Im\left(Y_3\right) \sim -\tilde{G}\dfrac{\omega_A^2}{\omega^2 - \omega_A^2}. \end{cases}$$

This expression is similar to the admittance of a lossless series LC circuit with resonance

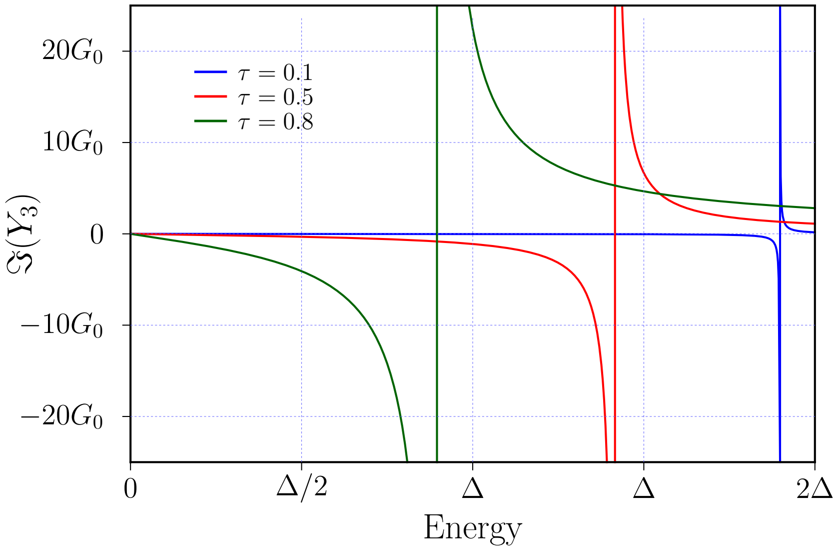

Figure 6.3.: Imaginary part of Y_3 at $\varphi = \pi$ for several values of transmission, in units of $G_0 = 2e^2/h$.

frequency $\omega_0 = 1/\sqrt{LC}$ and characteristic impedance $Z_0 = \sqrt{L/C}$,

$$\begin{cases} \Re\left(Y_{LC}\right) = \dfrac{\pi\omega_0}{Z_0}\delta\left(\omega - \omega_0\right), \\ \Im\left(Y_{LC}\right) = -\dfrac{1}{Z_0}\dfrac{\omega\omega_0}{\omega^2 - \omega_0^2} \sim -\dfrac{1}{Z_0}\dfrac{\omega_0^2}{\omega^2 - \omega_0^2}. \end{cases}$$

Both systems are formally equivalent if we impose $Z_0 = 1/\tilde{G}$ and $\omega_0 = \omega_A$.

In order to quantify dissipation in the equivalent LC circuit, the simplest way is to add a series resistance R. This changes the admittance to

$$\begin{cases} \Re\left(Y_{LC}\right) = \dfrac{Q}{Z_0}\dfrac{1}{1 + Q^2\left(\frac{\omega}{\omega_0} - \frac{\omega_0}{\omega}\right)^2}, \\ \Re\left(Y_{LC}\right) = -\dfrac{Q^2}{Z_0}\dfrac{\frac{\omega}{\omega_0} - \frac{\omega_0}{\omega}}{1 + Q^2\left(\frac{\omega}{\omega_0} - \frac{\omega_0}{\omega}\right)^2}, \end{cases}$$

where $Q = Z_0/R$ is the quality factor of the resonator. The effect of the resistance R is to give a width to the resonance peak in the real part of the admittance. The full width at half maximum due to R is $\Delta\omega = \omega_0/Q$. For weak links, it is possible to measure experimentally the width of the ABS. For instance, in atomic contacts in aluminum, $\Delta\omega$ was found of the order of 20 MHz [110]. A method to model the admittance of a weak link with dissipation is to replace it by an RLC series circuit (as shown in Figure 6.4) in the vicinity of the resonance

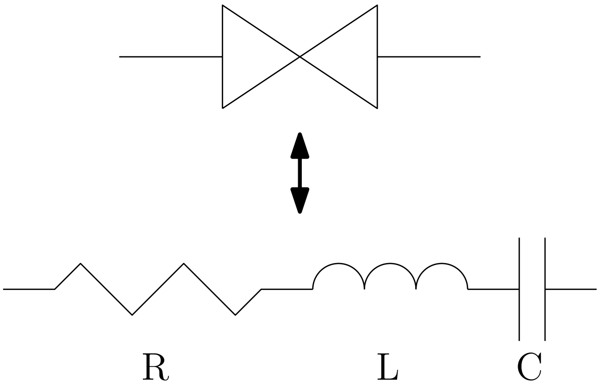

Figure 6.4.: Equivalent circuit of a weak link close to resonance.

$(\omega \sim \omega_A)$ with

$$\begin{cases} \omega_0 = \omega_A, \\ Z_0 = \dfrac{h}{2e^2\pi\tau} \dfrac{4E_A^4}{\left(\Delta^2 - E_A^2\right)\left(E_A^2 - \Delta^2 \cos^2 \frac{\varphi}{2}\right)}, \\ Q = \dfrac{\omega_A}{\Delta\omega}. \end{cases} \tag{6.4}$$

The equivalent R, L and C are then given by

$$R = \frac{Z_0}{Q},\; L = \frac{Z_0}{\omega_0},\; C = \frac{1}{Z_0\omega_0}. \tag{6.5}$$

Galvanic or capacitive coupling

If we consider coupling a weak link to the spectrometer galvanically (or capacitively, using a large capacitance), it has to be in a superconducting loop to allow changing its phase difference. This corresponds to adding an inductance L_p in parallel with the weak link, such that the admittance is $Y_{wl} - i/(L_p\omega)$. The inductance L_p has the same effect as reducing the Josephson inductance L_J in Equation (6.1) to the parallel combination $L_{\|}$ of L_J and L_p. For one conduction channel of transmission τ, according to the expression of Equation (6.2) for L_J, L_J is always larger (in absolute value) than the value reached at $\varphi = \pi$, $L_J(\pi) = 4\varphi_0^2\sqrt{1-\tau}/(\Delta\tau)$. For $\tau = 0.99$ for instance, $|L_J| > 1.5\,\mathrm{nH}$ and reaches larger values for smaller transmissions. The total inductance for a weak link is the parallel combination of all transmission channels, such that for a weak link with a few channels, the inductance can hardly be smaller than $1\,\mathrm{nH}$. The inductances realized experimentally to make loops are typically much smaller than this value, of the order of $100\,\mathrm{pH}$, such that $L_{\|} \sim L_p$. The resonant frequency we will measure ω_m corresponds to having

$$\Im\left(Y_3\right) = \frac{1}{L_p\omega_m} - C_J\omega_m, \tag{6.6}$$

with C_J the capacitance of the spectrometer. The other Y_i terms were not considered here. With the equivalent RLC circuit introduced in Equations (6.4) and (6.5), the resonance condition can be rewritten

$$\frac{Q^2}{Z_0}\frac{\frac{\omega_m}{\omega_0}-\frac{\omega_0}{\omega_m}}{1+Q^2\left(\frac{\omega_m}{\omega_0}-\frac{\omega_0}{\omega_m}\right)^2}=C_J\omega_m-\frac{1}{L_p\omega_m}, \tag{6.7}$$

Equation (6.7) is in general not easy to solve. With a width for the ABS of the order of $\Delta\omega = 20\,\mathrm{MHz}$, $Q = \omega_A/\Delta\omega \sim 1000 \gg 1$. To find the resonance frequency, we can replace Equation (6.7) by

$$\frac{1}{Z_0}\frac{1}{\frac{\omega_m}{\omega_0}-\frac{\omega_0}{\omega_m}}=C_J\omega_m-\frac{1}{L_p\omega_m},$$

This equation can be recast in a biquadratic form

$$\left(\frac{\omega_m}{\omega_0}\right)^4-\left(1+\frac{1}{C_J\omega_0}\left(\frac{1}{Z_0}+\frac{1}{L_p\omega_0}\right)\right)\left(\frac{\omega_m}{\omega_0}\right)^2+\frac{1}{L_pC_J\omega_0^2}=0.$$

The expression for Z_0 in Equation (6.4) diverges at $\varphi = 0$ and is minimal at $\varphi = \pi$. Its minimal value is

$$Z_{0,min}=\frac{1}{G_0}\frac{4}{\pi}\frac{1-\tau}{\tau^2}.$$

For $\tau = 0.99$, this minimal value is $150\,\Omega$. It is larger for smaller transmissions. For typical L_p of the order of $50\,\mathrm{pH}$, $L_p\omega_0$ reaches $30\,\Omega$ at $100\,\mathrm{GHz}$, such that, in the frequency range of interest, $1/Z_0 \ll 1/(L_p\omega_0)$. This simplifies greatly the equation for the resonance frequency which now has two solutions

$$\begin{cases}\omega_1=\omega_0,\\ \omega_2=\dfrac{1}{\sqrt{L_pC_J}}.\end{cases}$$

The measured frequency is thus the actual Andreev frequency $\omega_0 = \omega_A$. The second resonance frequency ω_2 can be problematic if it crosses the Andreev line. To avoid such a crossing, there are two possible solutions, either $\omega_2 > \omega_{A,max}$ or $\omega_2 < \omega_{A,min}$. The former condition is easier to fulfill since $\omega_{A,min}$ can be quite close to 0 if the transmission of the channel is large. $\omega_{A,max} = 2\Delta/\hbar = 2\pi \times 95\,\mathrm{GHz}$ with the bare superconducting gap of aluminum. This value can be reduced due to the proximity effect in long junctions, making an easier condition on ω_2. With a typical value of $L_p = 50\,\mathrm{pH}$, C_J has to be smaller than $50\,\mathrm{fF}$, corresponding to a Josephson junction with critical current $150\,\mathrm{nA}$. Larger junctions are possible if the shunt inductance is smaller.

We can evaluate the height of the peak in the case where $\omega_m \sim \omega_A$ to understand what parameters are favorable to a large signal. At ω_A, the real part of the impedance seen by the spectrometer is

$$R_e=\Re\left(\frac{1}{Y_3\left(\omega_A\right)+iC_J\omega_A-\frac{i}{L_p\omega_A}+\tilde{G}_e}\right),$$

where $\tilde{G}_e$ describes the real part of the admittance of the biasing circuit. $\tilde{G}_e$ is generally of the order of the bias resistance R_b. At the resonance frequency, the imaginary part of the denominator cancels out, such that

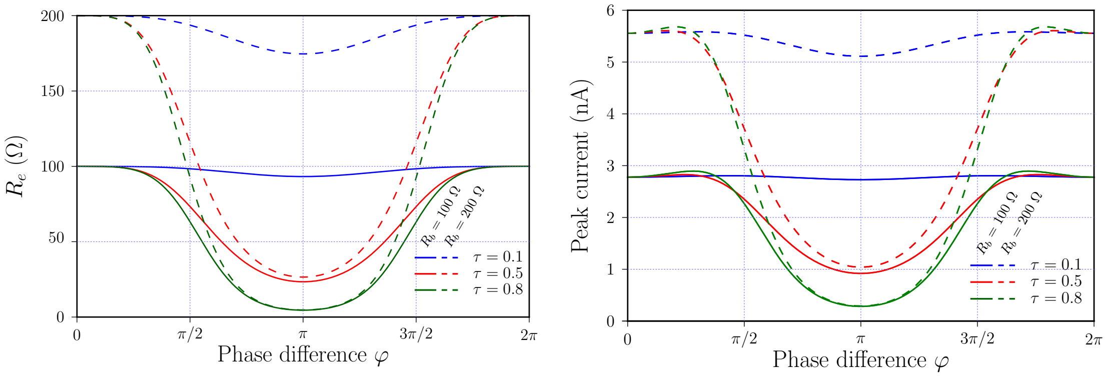

(a) Real part R_e of the impedance.

(b) Peak current in the junction.

Figure 6.5.: Real part of the impedance seen by the spectrometer and peak current in a junction with $I_0 = 100\,\mathrm{nA}$ for conduction channels of transmission 0.1, 0.5 and 0.8 with bias resistances 100 and 200 Ω.

$$R_e = \frac{1}{\tilde{G}_e + \frac{Q}{Z_0}}.$$

R_e is plotted in Figure 6.5a for conduction channels of transmission 0.1, 0.5 and 0.8 with bias resistances 100 and 200 Ω, assuming the width $\Delta\omega$ of the ABS constant at 20 MHz. At $\varphi = 0$, $Z_0 \to \infty$, such that R_e would vanish if there was no real part in the biasing circuit. However, at $\varphi = \pi$, Z_0 is minimal and R_e is the parallel combination of the equivalent resistance of the weak link and the bias resistance. Figure 6.5b shows the resulting peak current flowing through a spectrometer with critical current 100 nA. With $\tilde{G}_e = 0$, the minimal resistance at $\varphi = \pi$ is

$$R_e(\pi) = \frac{\hbar\Delta\omega}{\Delta}\frac{4}{\pi G_0}\frac{\sqrt{1-\tau}}{\tau^2}.$$

With $\tau = 0.9$ for instance, $R_e(\pi) \sim 3\,\Omega$. With a spectrometer of critical current I_0, the current measured at the peak is

$$I_p = 4\frac{\hbar\Delta\omega\varphi_0 I_0^2}{\tau^2\Delta^2}.$$

For $\tau = 0.9$, the peak value is only $I_p = 250\,\mathrm{pA}$ which is small but detectable. A larger signal can be obtained with a larger Josephson junction. However, this increases the junction capacitance C_J and decreases the resonance frequency $\omega_2 = 1/\sqrt{L_p C_J}$ which can become of the order of $2\Delta/\hbar$ and prevent seeing the Andreev peak. Reducing the parallel inductance L_p is a good solution to keep ω_2 larger than $2\Delta/\hbar$ and increase the measured signal.

Inductive coupling

If the coupling is made via a mutual inductance to the loop of the SQUID, the situation is quite different. Consider making a loop with the weak link by adding an inductance l_c in parallel to it. The parallel inductance L_p necessary in the case of galvanic or capacitive coupling to impose a phase difference across the weak link is here not needed as a loop is naturally present. The admittance seen by the spectrometer is

$$\tilde{Y}_e = -\frac{i}{l\omega}\frac{1 + il_c\omega Y_3}{1 + i\left(1-k^2\right) l_c\omega Y_3},$$

where l is the inductance of the loop of the SQUID. To find the resonance condition, we first consider a non-dissipative weak link, *i.e.* with an infinitely narrow ABS width. This gives for Y_3,

$$Y_3 = -\frac{i}{Z_0}\frac{\frac{\omega}{\omega_0}}{\left(\frac{\omega}{\omega_0}\right)^2 - 1},$$

with the expressions for Z_0 and ω_0 given by Equation (6.4). $\tilde{Y}_e$ can thus be expressed

$$\tilde{Y}_e = -\frac{i}{l\omega}\frac{\left(\frac{\omega}{\omega_0}\right)^2\left(1 + \frac{l_c\omega_0}{Z_0}\right) - 1}{\left(\frac{\omega}{\omega_0}\right)^2\left(1 + \left(1-k^2\right)\frac{l_c\omega_0}{Z_0}\right) - 1}. \tag{6.8}$$

The resonance condition writes here $\Im\left(\tilde{Y}_e\right) = -C_s\omega_m$, where C_s is the series combination of the capacitances of the junctions of the SQUID. This gives

$$lC_s\omega_m^2 = \frac{\left(\frac{\omega_m}{\omega_0}\right)^2\left(1 + \frac{l_c\omega_0}{Z_0}\right) - 1}{\left(\frac{\omega_m}{\omega_0}\right)^2\left(1 + \left(1-k^2\right)\frac{l_c\omega_0}{Z_0}\right) - 1}.$$

This can be recast in a biquadratic form

$$lC_s\omega_0^2\left(1 + \left(1-k^2\right)\frac{l_c\omega_0}{Z_0}\right)\left(\frac{\omega_m}{\omega_0}\right)^4 - \left(1 + lC_s\omega_0^2 + \frac{l_c\omega_0}{Z_0}\right)\left(\frac{\omega_m}{\omega_0}\right)^2 + 1 = 0 \tag{6.9}$$

As in the previous situation, Z_0 is much larger than the impedance of the inductance l_c typically of the order of 100 pH, such that Equation (6.9) is simply

$$\left(\frac{\omega_m}{\omega_0}\right)^4 - \left(1 + \frac{1}{lC_s\omega_0^2}\right)\left(\frac{\omega_m}{\omega_0}\right)^2 + \frac{1}{lC_s\omega_0^2} = 0$$

The two positive solutions of this equation are

$$\begin{cases} \omega_1 = \omega_0, \\ \omega_2 = \dfrac{1}{\sqrt{lC_s}}. \end{cases}$$

As in the galvanic (and capacitive) case, there is a second resonance frequency ω_2 which is the loop mode of the SQUID. The spectrometer can be designed to ensure $\omega_2 > 2\Delta/\hbar$, such that the loop mode does not interfere with the Andreev transitions.

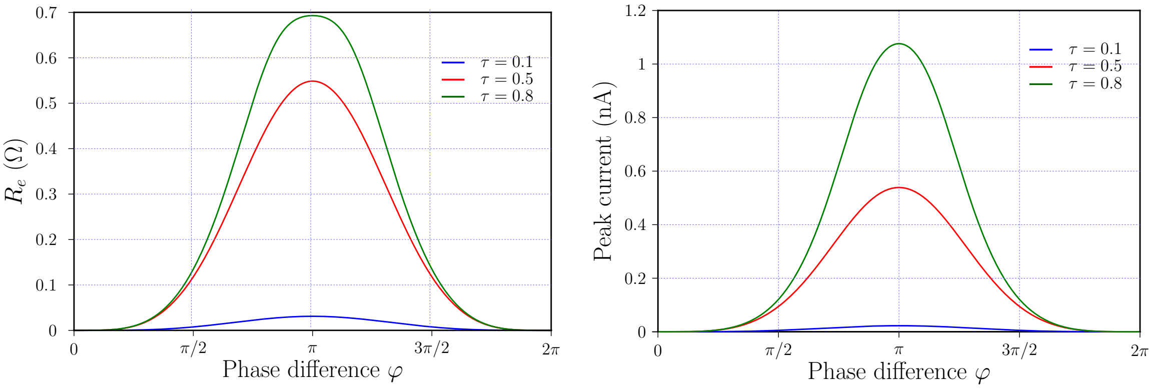

(a) Real part R_e of the impedance.

(b) Peak current in the spectrometer.

Figure 6.6.: Real part of the impedance seen by the spectrometer and peak current in a spectrometer with $I_0 = 500\,\mathrm{nA}$ for conduction channels of transmission 0.1, 0.5 and 0.8 with coupling inductances $l = 50\,\mathrm{pH}$ and $l_c = 50\,\mathrm{pH}$.

To evaluate the height of the current peak, we add a series resistance in the RLC equivalent model presented in Equations (6.4) and (6.5). At the resonance frequency $\omega = \omega_0$, $Y_3 = Q/Z_0$, such that $\tilde{Y}_e$ is

$$\tilde{Y}_e = -\frac{i}{l\omega_0}\frac{1 + i l_c \omega_0 \frac{Q}{Z_0}}{1 + i\left(1 - k^2\right) l_c \omega_0 \frac{Q}{Z_0}}.$$

If the spectrometer is biased at half a flux quantum and if it is perfectly symmetric, the total admittance seen by the spectrometer is $Y_\Sigma = \tilde{Y}_e + iC_s\omega_0$,

$$Y_\Sigma = iC_s\omega - \frac{i}{l\omega}\frac{1 + i l_c \omega \frac{Q}{Z_0}}{1 + i\left(1 - k^2\right) l_c \omega \frac{Q}{Z_0}}.$$

Assuming $lC_s\omega_0^2 \ll 1$, the real part R_e of the impedance Z_Σ seen by the spectrometer is, after a few calculation steps,

$$\Re\left(Z_\Sigma\right) = k^2 \frac{l l_c \omega_0^2 \frac{Q}{Z_0}}{1 + \left(l_c \omega_0 \frac{Q}{Z_0}\right)^2}. \tag{6.10}$$

As expected, this expression is proportional to k^2. Figure 6.6a shows this expression for conduction channels of transmission 0.1, 0.5 and 0.8 as a function of the phase difference. The coupling inductances are $l = 50\,\mathrm{pH}$ and $l_c = 50\,\mathrm{pH}$ and Figure 6.6b shows the current that would be measured at the resonance in a spectrometer with critical current $I_0 = 500\,\mathrm{nA}$. The signal is maximal at $\varphi = \pi$ where it reaches $1\,\mathrm{nA}$ for a conduction channel with transmission 0.8.

These calculations were made assuming that the spectrometer SQUID is perfectly symmetric. In practice, it is not the case, such that the admittance Y_Σ seen at half a flux quantum also contains a small real part G_b due to the biasing circuit. Writing α the symmetry ratio of the SQUID, $G_b = (1 - \alpha)/R_b$, where R_b is the bias resistance. At phase difference $\varphi = 0$, the impedance Z_0 diverges, such that

$$Y_\Sigma\left(\varphi=0\right)=G_b+\frac{1}{il\omega_0}\left(1-lC_s\omega_0^2\right).$$

Assuming $lC_s\omega_0^2 \ll 1$, $Y_\Sigma\left(\varphi=0\right)\sim G_b-i/(l\omega_0)$. This gives for the real part of the impedance,

$$\Re\left(Z_\Sigma\right)=\frac{1}{G_b}\frac{1}{1+\left(\frac{1}{l\omega_0 G_b}\right)^2}\sim\left(l\omega_0\right)^2 G_b=\left(l\omega_0\right)^2\frac{1-\alpha}{R_b}.$$

With typical values of $l = 50\,\mathrm{pH}$ and $R_b = 100\,\Omega$, a symmetry ratio of 0.95 gives $\Re\left(Z_\Sigma\right) = 400\,\mathrm{m}\Omega$, corresponding to a current of the order of 500 pA with a spectrometer of critical current 500 nA. The ABS is thus visible for all phase differences.

Summary

It is thus possible to probe the ABS spectrum with a Josephson spectrometer using the galvanic and inductive coupling schemes, as well as the capacitive coupling scheme, provided that the coupling capacitance is large. In all cases, a second resonance frequency ω_2 is present due to the junction of the spectrometer and the shunt inductance L_p in the galvanic case or the SQUID loop inductance l in the inductive case. This resonance frequency can be tuned to a frequency larger than the maximal frequency of interest $2\Delta/h = 90\,\mathrm{GHz}$, for an aluminum weak link. In hybrid long weak links, such as the ones presented in Sections 6.1.3 and 6.1.4, the gap can be reduced due to the proximity effect, resulting in an easier condition for the parasitic resonance frequency ω_2.

The resulting currents that would be measured with a spectrometer with critical current 500 nA are larger than 500 pA which is measurable with our setup. For instance, in the spectroscopy of a RF-SQUID described Section 5.4, the current at the top of the resonance peak was of the order of 500 pA. A larger junction increases the measured signal but also results in larger capacitances and thus a smaller resonance frequency ω_2 which can become smaller than $2\Delta/h = 90\,\mathrm{GHz}$. The inductance L_p in the galvanic case (or l in the inductive case) can be made smaller to increase ω_2. The inductance of the SQUID loop cannot be decreased too much since this reduces the coupling constant k to the weak link loop and thus the measured signal.

In the most general case, the current measured with the capacitive coupling scheme is larger than the one measured in the inductive coupling scheme, but the spectrometer is much more sensitive to resonances in the environment. To measure a clean spectrum, inductive coupling is thus favorable. However, the signal can be quite small due to the constraint on the parasitic resonance, $\omega_2 > \Delta/\hbar$. For systems with small gaps, as the ones presented in Sections 6.1.3 and 6.1.4, the junctions of the spectrometer can be made larger, allowing for a larger signal. But for systems with the intrinsic aluminum gap, such as the one presented in Section 6.1.2, this constraint is too strong for the height of the peak to be large.

6.1.2. Hybridization of two ABS: the Andreev molecule

Another object of study of the Φ_0 group is the so-called Andreev molecule [36]. It consists of two Josephson junctions brought within a distance of the order of the superconducting coherence

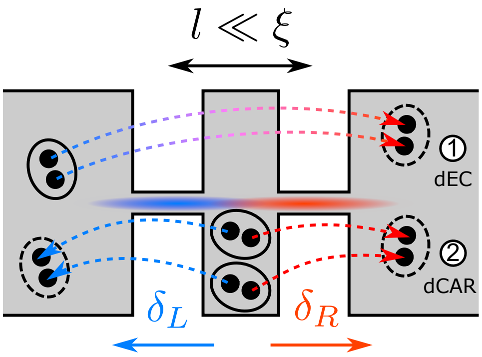

Figure 6.7.: Schematic of the Andreev molecule, adapted from [36].

length ξ_0 of each other. This proximity results in a hybridization of the ABS of the junctions and thus a modified ABS spectrum which can be probed by the Josephson spectrometer.

The ABS of a single Josephson junction (or weak link) are not localized only in the junction. As they are quantum states, they have a spatial extension and decay exponentially away from the junction over a distance $\xi = \xi_0/\sqrt{\tau}\left|\sin\frac{\varphi}{2}\right|$, where τ is the transmission of the channel and φ the phase difference across the junction [92]. If two junctions are brought within a distance ξ, the wavefunctions of their ABS will overlap, leading to hybridized states. This hybridization can be microscopically understood in terms of two different mechanisms: the double elastic cotunneling of Cooper pairs (dEC) and the double crossed-Andreev reflections (dCAR) [111–113]. The former is the direct transfer of Cooper pairs across the two junctions (dEC in Figure 6.7), while the latter is the joint splitting of two Cooper pairs in the center of the device and their recombination in the left and right electrodes (dCAR in Figure 6.7). Due to their different natures, these two phenomena have different phase dependence. With the notations of Figure 6.7, dEC has a $\delta_R - \delta_L$ dependence because the transferred Cooper pair acquires a phase $\delta_R - \delta_L$. In the dCAR process, the quasiparticles going to the left (right) acquire $\delta_{L(R)}$, resulting in a $\delta_L + \delta_R$ dependence in the spectrum.

The resulting spectrum was calculated in Ref. [36] by solving the Bogolioubov-de Gennes equation in which the junctions are modeled by δ functions potential with amplitudes $U_{L,R}$. The transmission of the conduction channel is linked to the scattering potential amplitude via similar equations as in Section 1.1.2, involving the Fermi velocity v_F:

$$\tau_{L,R} = \left|1 + i\frac{U_{L,R}}{\hbar v_F}\right|^{-2}.$$

Figure 6.8 shows the eigenenergies of this Hamiltonian as a function of the phase δ_L with fixed $\delta_R = 3\pi/5$ for different distances l between the junctions. Both junctions have a single conduction channel of transmission ~ 0.94. The blue color corresponds to the left-hand side junction and the red color to the right-hand side junction of Figure 6.7. The pink color in the figure corresponds to a hybridized state. In (a), $l \gg \xi_0$. The energies of both junctions are totally independent and cross each other in the spectrum. When l decreases ((b) to (e)), the crossings are avoided, sign of the hybridization of the two states. These avoided crossings separate the energies, such that one ABS is partially pushed out of the gap ($|E| > \Delta$) and that the gap in the spectrum is reduced. For $l \gg \xi_0$, one ABS is totally in the continuum

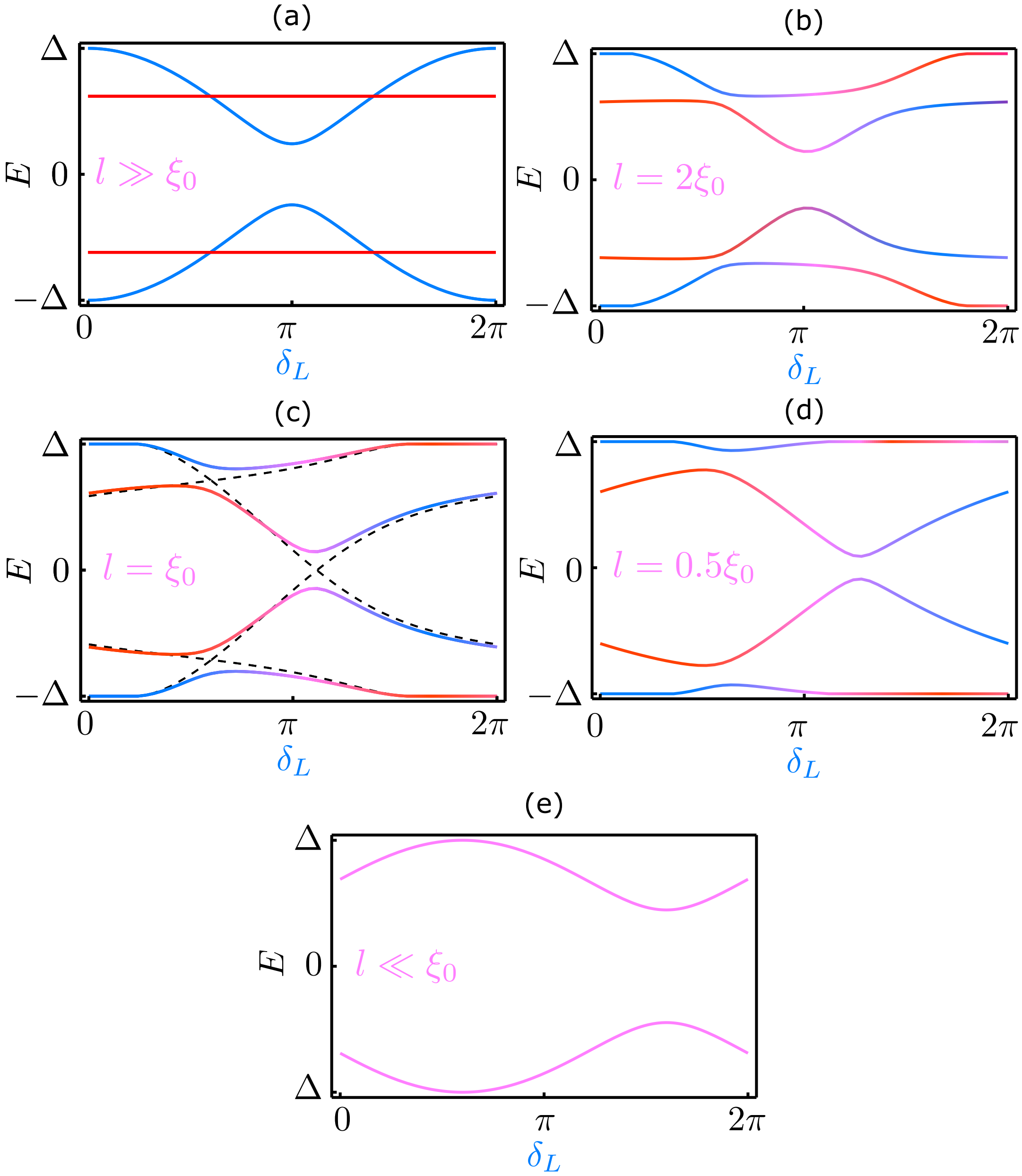

Figure 6.8.: Calculated ABS spectrum for the Andreev molecule made of two junctions with one conduction channel of transmission 0.94 at $\delta_R = 3\pi/5$, adapted from [36].

and only one remains in the gap. This was expected because the two junctions now form one single junction with scattering amplitude $U_L + U_R$. This larger amplitude is equivalent to a smaller transmission, close to 0.8 in the situation of Figure 6.8. In (e), the resulting spectrum is indeed the spectrum of a single ABS with transmission ~ 0.8 shifted by $\delta_R = 3\pi/5$.

The spectrum also loses his symmetry with respect to $\delta_L = \pi$. This is due to the fact that dEC and dCAR respectively depends on $\delta_R - \delta_L$ and $\delta_L + \delta_R$, such that time-reversal symmetry now imposes $E\left(\delta_L, \delta_R\right) = E\left(-\delta_L, -\delta_R\right)$.

Experiments to fabricate Andreev molecules are currently being performed in the Φ_0 group. As the avoided crossings in the spectrum of the Andreev molecule are one strong signature of the hybridization of the states, probing the spectrum is one of the first experiments to perform on the realized devices. The Josephson spectrometer is well adapted for this measurement as the energy scale of the excitations is the superconducting gap of aluminum.

To estimate the expected signal in the case of coupling to a Josephson spectrometer, a derivation similar to the one of Section 6.1.1 would have to be performed. Because there are two junctions, their admittances have to be combined to give an expression for the real part R_e of the impedance seen by the spectrometer. To obtain an estimate of R_e, we can consider only one junction instead of two.

Considering the inductive coupling scheme with inductances of the order of 30 pH and a coupling coefficient $k \sim 0.2$, the condition on the series combination C_s of the two junctions of the SQUID is $C_s < 100\,\mathrm{fF}$, corresponding to a critical junction for the SQUID of $I_0 = 1\,\mu\mathrm{A}$ assuming a plasma frequency of 15 GHz. This gives for a channel of transmission 0.9 at $\varphi = \pi$ a current peak of height 500 pA.

In a capacitive coupling scenario with a shunt inductance of $L_p = 30\,\mathrm{pH}$, the maximal value for the critical current of the spectrometer is $I_0 = 250\,\mathrm{nA}$. This corresponds to a current peak of height 5 nA for the same conduction channel. This current is one order of magnitude larger than the one in the inductive case but the resulting spectrum can also contain peaks due to the environment as the microwave current can circulate out of the SQUID loop.

6.1.3. ABS in InAs nanowires

Shape of the spectrum of ABS in nanowires

The ABS in usual weak links are spin degenerate [32, 110]. However, it is possible to lift this degeneracy by taking advantage of the strong spin-orbit coupling of semiconducting nanowires and using them as weak links between two superconductors, as was recently shown [114–116]. These experiments were performed in the limit of $l \lesssim \xi$ where l is the length of the nanowire and thus of the weak link and ξ is the superconducting coherence length in the weak link. In the case of ballistic propagation, ξ can be estimated as $\xi = \hbar v_F/\Delta$, where v_F is the Fermi velocity in the weak link and Δ the gap of the superconductor. It is typically of the order of 100 nm. In the short limit, a finite Zeeman magnetic field is required to observe effects of the spin-orbit interaction [117]. Using longer nanowires allows lifting the degeneracy with only a phase difference across the junction, in presence of several subbands with different Fermi velocity [37, 38]. However, the spectrum remains degenerate at a phase difference of π where time-reversal symmetry is preserved. This is visible as non-avoided crossings in the spectrum, similar to Weyl points.

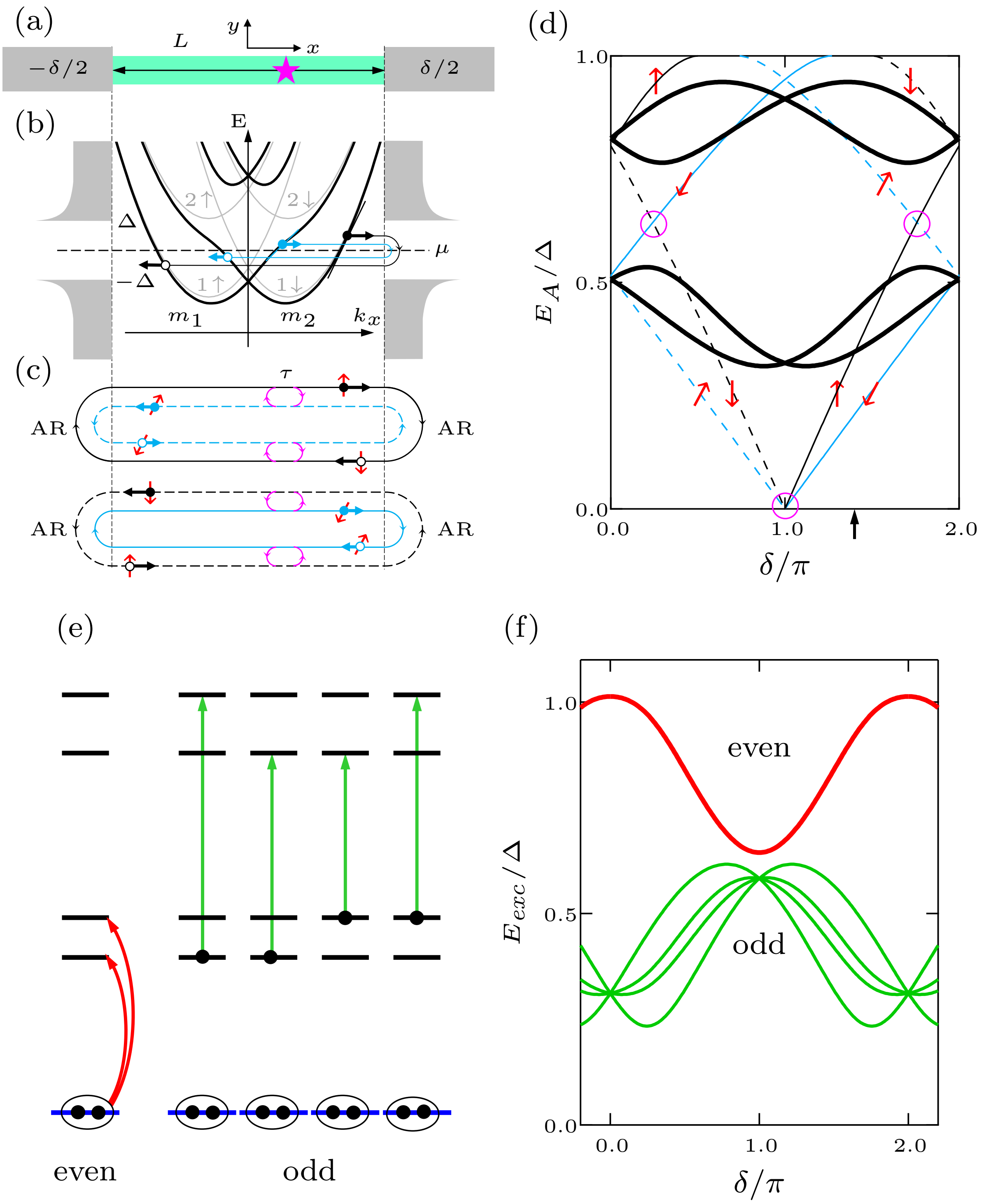

Figure 6.9.: Effect of the spin-orbit effect on the Andreev Bound States, taken from Ref. [118].

Figure 6.9, taken from Ref. [118], explains the shape of the resulting spectrum for the situation sketched in (a). As shown in (b), the Rashba spin-orbit (RSO) coupling spin-splits the parabolic dispersion relation in the nanowire along the k_x axis (thin gray lines). Different subbands (of opposite spin) are also coupled by the spin-orbit interaction, giving rise to avoided crossings as shown in thick black lines. The quasiparticles at the Fermi level (at the chemical potential μ in (b)) have thus different velocities. Calculating the Andreev Bound States resulting from the Andreev reflections shown in (c) (as we did in Section 1.1.2 without RSO coupling) gives the thin black and blue lines of (d), where the horizontal axis δ is the phase difference across the weak link. The presence of impurities and the possible variation of electrostatic potential along the nanowire leads to backscattering and thus coupling of electrons and holes of different energies. The resulting ABS spectrum is shown in thick black lines in (d) and consists of two manifolds of two spin-split bands. (e) shows the possible excitations at the phase highlighted with a black arrow in (d). The even transitions correspond to the excitation of a Cooper pair in two quasiparticles of the lower manifold of (d). The odd excitations correspond to the excitation of a quasiparticle trapped in one of the states of the first manifold to an empty state of the second manifold. As of today, the origin of such quasiparticles is not well understood. However, their presence was experimentally measured, showing quite long lifetimes, typically longer than 100 µs [119]. All these transitions can be induced by microwaves (either with conventional techniques or with the Josephson spectrometer). The resulting absorption spectrum is shown in (f) and consists of two separate manifolds: an even one with no information on the spin structure and an odd one with four subbands due to spin-splitting.

Design of the device

In order to measure the spectrum of the ABS in such nanowires, a collaboration with the Center for Quantum Devices in Copenhagen and the Quantronics group in Saclay has been made. The Center for Quantum Devices in Copenhagen fabricates InAs nanowires with in-situ epitaxially grown aluminum on top [120], allowing for a well-defined superconducting gap in the nanowires [121]. The fabricated nanowires are then processed by the Quantronics group which fabricates weak links in the long limit ($L > \xi$) with them. Their length L is typically 300 nm, while ξ is of the order of 100 nm. In Ref. [118], a fit of the experimental data to the theory described above gives $L \sim 2\xi$. Capacitive side-gates are also added in order to deplete the weak link region and thus modify the transmission of the conduction channels of the weak links, as shown in Ref. [122]. The fabricated junctions have few and good conduction channels: one device has less than four conduction channels with non-negligible transmission and the highest transmission reaches 0.98 with the appropriate gate voltages.

Due to the proximity effect and the length of the weak link, the superconducting gap is reduced in the nanowire, such that $2\Delta/h \sim 30\,\text{GHz}$. This allows measuring the ABS spectrum with a conventional spectroscopy setup. This was performed by the Quantronics group who recently measured the ABS spectrum of one of these devices by using two-tone spectroscopy [118], a usual circuit-QED technique where the weak link is coupled to a microwave cavity resonant at a frequency f_0. The weak link is irradiated with photons at a frequency f_1. If a photon is absorbed, the impedance of the weak link changes, resulting in a shift of the resonant frequency of the cavity. The spectrum they measured is shown in Figure 6.10 where the horizontal axis is the phase difference across the weak link, the vertical axis is the frequency

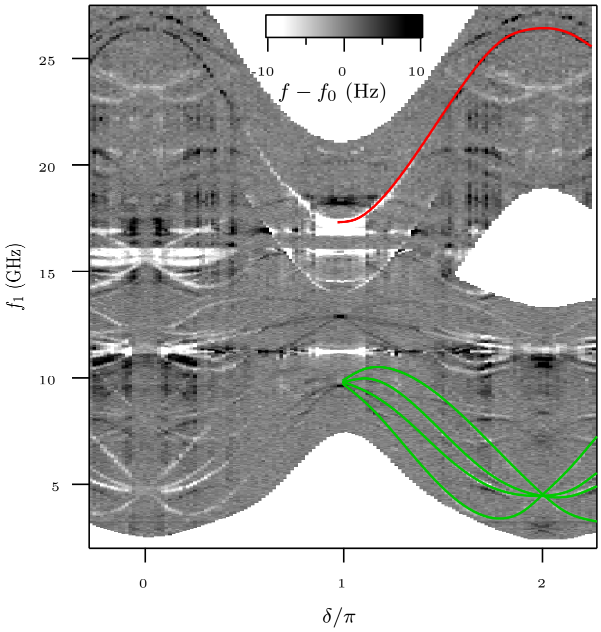

Figure 6.10.: Two-tone spectrum of a weak link based on an InAs nanowire, taken from Ref. [118].

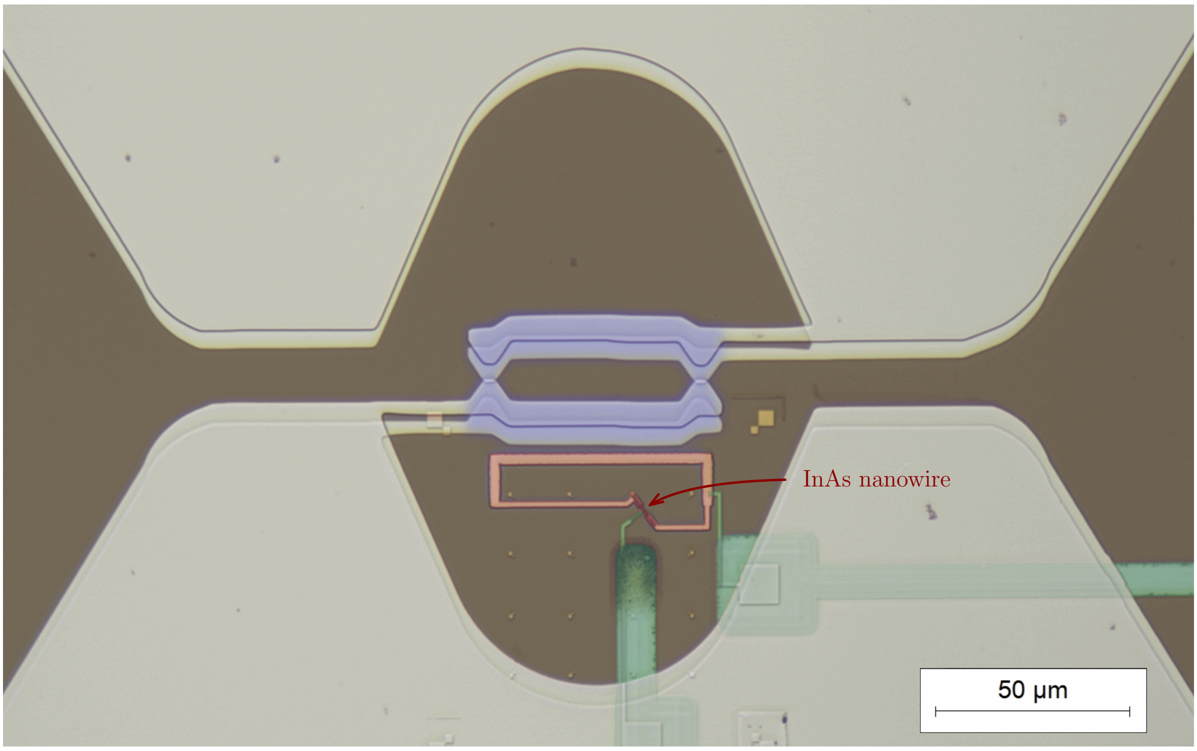

Figure 6.11.: Preliminary microscope picture of a spectrometer coupled to an InAs nanowire.

f_1 of the applied microwaves and the color scale corresponds to the resonance frequency shift from the intrinsic value of $f_0 = 3.26\,\mathrm{GHz}$. Several transitions (black and white lines) are visible in this spectrum including transitions between the Andreev levels. In the right-hand side of the graph, numerical fits to the model described above are added. Green lines correspond to odd transitions and red lines to even transitions. The other observable transitions are replica of the Andreev transitions, shifted by multiples of f_0, and involve the absorption of one (or several) photons of frequency f_0 by the cavity.

Using the Josephson spectrometer would allow measuring this spectrum without the supplementary transitions. We fabricated a device for that purpose based on the design of sample HS04 presented in Section 4.3.3. Figure 6.11 shows the resulting device[2]. The InAs nanowire is indicated by a red arrow and is put in a superconducting loop (in red) fabricated by the Quantronics group. The spectrometer SQUID is colored in blue. The green leads are buried below the pale-yellow aluminum plane and can be used to deplete the weak link region. The top one is galvanically connected to the red loop and the bottom one ends close to the nanowire and acts as a capacitive gate. For this design, the 3D-MLSI simulator gives a coupling constant k of $k_\pi = 0.062$ at $\varphi_e = \pi$ and $k_0 = 0.14$ at $\varphi_e = 0$, where φ_e is the reduced flux in the spectrometer loop. The coupling constant at $\varphi_e = \pi$ is larger than the value simulated for the design used for the spectroscopy of the RF-SQUID in Section 5.4 where $k_\pi = 0.018$. This was made possible by bringing the two loops closer to one another. This increases the measured signal at $\varphi_e = \pi$ by a factor of 10 since the signal is proportional to k^2 and could make the peak visible. The value at $\varphi_e = 0$ is almost the same as for the spectroscopy of the RF-SQUID where k_0 was 0.12. The spectrum at $\varphi_e = 0$ can thus be used to verify the presence of the Andreev transition. At $\varphi_e = 0$ however, the spectrum can contain several resonances due to the biasing circuit and the large geometry of the sample (as described in Sections 4.3.3 and 5.4). The measured peaks can also be broadened due to the biasing circuit. Probing the nanowire at $\varphi_e = \pi$ reduces the height of the parasitic resonances and the width of the peaks of interest. The best spectrum is thus obtained at this flux bias. Having a coupling constant of $k_\pi = 0.062$ could make it possible to measure this spectrum. This sample was cooled down and measured but no Andreev transition was observed at $\varphi_e = \pi$.

A new strategy to further improve the coupling to the nanowire consists of fabricating the spectrometer SQUID around the loop containing the nanowire, as sketched in Figure 6.12. The green gradiometric flux line allows flux biasing the red nanowire loop without changing the flux in the blue spectrometer loop with a current flowing as represented by the green arrows. The Josephson junctions of the SQUID are labeled JJ in the figure. Simulating such a device with the 3D-MLSI simulator gives $k_\pi = 0.2$, comparable to the coupling constants obtained at $\varphi_e = 0$ in the previous designs.

To obtain the largest signal, the quantity $k^2 l l_c I_0^2$ has to be maximized according to Equation (6.10), while keeping $1/(2\pi\sqrt{lC_s}) > 2\Delta/h \sim 30\,\mathrm{GHz}$. The critical current I_0 is proportional to the capacitance C_s, such that we seek to maximize lC_s^2 and keep lC_s constant. C_s has to be made as large as possible and l as small as possible. To keep a reasonable coupling constant and enough place to make a loop inside the SQUID loop, l cannot be too small. $l = 50\,\mathrm{pH}$ is the minimal inductance satisfying these constraints. The maximal admissible C_s

---

[2] This is not the finished device. The shunt capacitors on both sides of the spectrometer and a gradiometric flux line to independently flux bias the nanowire loop are not yet evaporated in the picture.

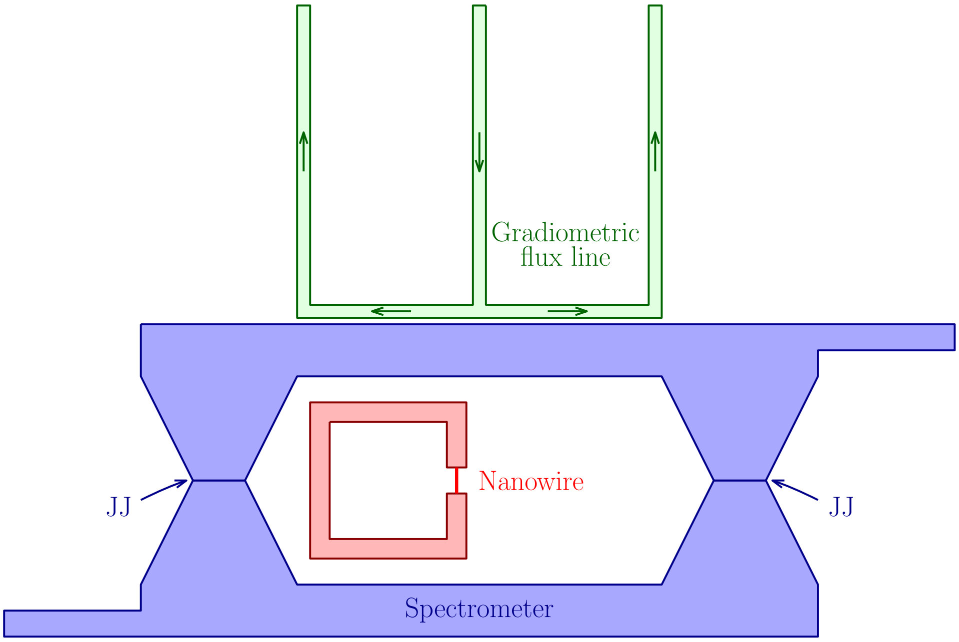

Figure 6.12.: New design proposed to couple the spectrometer to an InAs nanowire.

satisfying $1/(2\pi\sqrt{lC_s}) > 2\Delta/h \sim 30\,\mathrm{GHz}$ is thus $C_s = 500\,\mathrm{fF}$. This is the series combination of the junctions of the loop, such that the capacitance of each junction is $2C_s = 1\,\mathrm{pF}$, corresponding to a critical current of $3\,\mu\mathrm{A}$ per junction and thus $I_0 = 6\,\mu\mathrm{A}$ for the SQUID. With $l_c = 20\,\mathrm{pH}$ for the loop of the weak link, a channel of transmission 0.8 would result in a current peak of height $20\,\mathrm{nA}$ at $\varphi = \pi$ which is easily measurable.

6.1.4. ABS in topological insulator-based Josephson junctions

Shape of the spectrum of ABS in a TI-based Josephson junction

A 3D topological insulator [123] (TI) is an insulating material possessing helical states on its surfaces. For a quasiparticle in such a state, the spin is locked perpendicular to the momentum. This provides a good protection against back-scattering, as the spin of the quasiparticle needs to be flipped in order to be back-scattered.

When a TI is placed in the vicinity of a conventional s-type superconductor, superconductivity is induced in the TI. But, due to the spin structure of the TI, the spin rotation symmetry is broken, giving rise to p-type superconductivity [124–126].

When making a TI-based Josephson junction as depicted in the left panel of Figure 6.13, the conduction channels have perfect transmission due to the absence of back-scattering in the TI [39]. This results in a gapless ABS spectrum such as the one shown in the right panel of Figure 6.13 as a function of the phase difference φ across the junction. Starting at $\varphi = 0$ in the lower blue state and adiabatically increasing φ leads to following the full blue line to reach energy Δ at $\varphi = 2\pi$ and $-\Delta$ at $\varphi = 4\pi$. The supercurrent $I \propto \partial E/\partial\varphi$ is thus now 4π−periodic. No direct observation of a 4π−periodic supercurrent was performed up to this date but some experiments [127, 128] observed an anomalous Shapiro effect: the doubling of

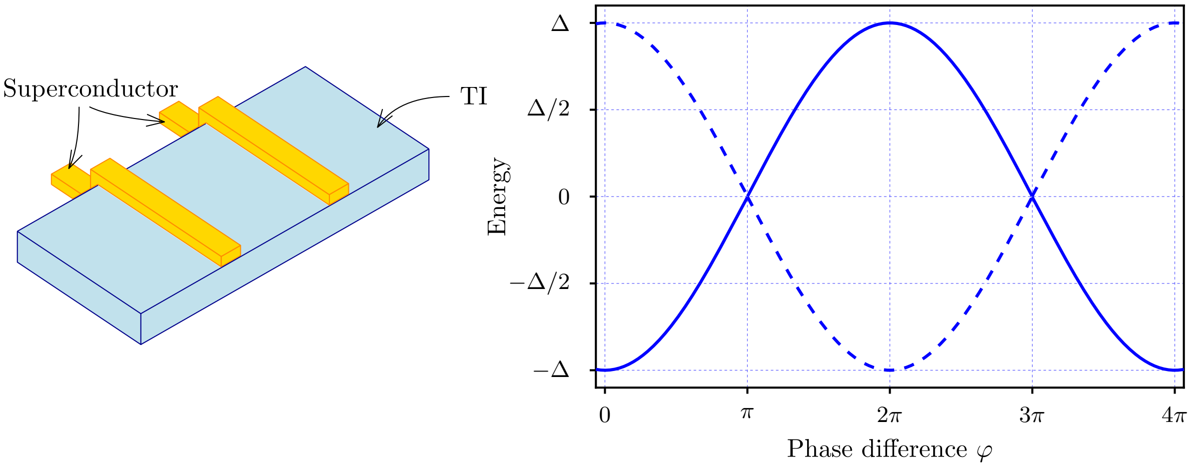

Figure 6.13.: Sketch of a TI-based Josephson junction and corresponding spectrum.

the voltage difference between two Shapiro steps, another consequence of the $4\pi-$periodicity of the spectrum. They were performed using HgTe as the TI and Niobium as the conventional superconductor.

The Josephson spectrometer is quite adapted to measure the ABS spectrum of a TI-based Josephson junction and get more insight on this $4\pi-$periodicity of the spectrum.

Design of the device

In collaboration with the university of Würzburg, we are planning to measure the ABS spectrum of TI-based Josephson junctions on the samples they used to measure the anomalous Shapiro steps [127, 128]. The difficulty here resides in the fact that the HgTe layers are quite fragile and cannot be heated at too high temperature, which is incompatible with the techniques used to fabricate the Josephson spectrometer.

The solution we choose is to use the inductive coupling scheme and fabricate the Josephson spectrometer on a different chip. It will then be brought as close as possible to the TI-based Josephson junction fabricated by the group of Würzburg. Using sapphire as a substrate for the spectrometer allows for a good alignment between the two chips. To favor good coupling, the TI-based junction is put in a superconducting loop, forming a RF-SQUID, the spectrum of which should be $2\Phi_0-$periodic in the flux threading the RF-SQUID loop.

In practice, due to unavoidable dust, the two loops will be separated by distance of the order of 50 µm. Simulations made with the 3D-MLSI simulator (described in Section 2.3.3) show that the coupling coefficient k stays quite high as long as the distance between the two loops is of the order of their radii. The spectrometer SQUID and the loop with the topological junction can be fabricated with a radius of order 30 µm, allowing for a relatively good coupling constant between them, of the order of 0.1. The resulting inductances l for the SQUID loop and l_c for the loop of the weak link are then of the order of 50 pH. The induced gap is of the order of 90 µeV [128], such that the constraint $1/(2\pi\sqrt{lC_s}) > 2\Delta/h$ to ensure the parasitic resonance away from the frequency range of interest corresponds to $C_s < 250\,\text{fF}$ for the series combination of the capacitances of the SQUID. This makes a condition on the critical current

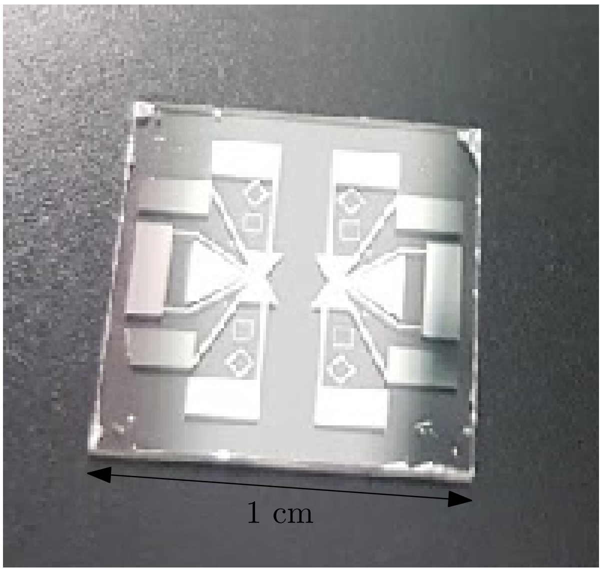

Figure 6.14.: Photography of a Josephson spectrometer fabricated on a sapphire substrate.

of the SQUID I_0 assuming a plasma frequency of 15 GHz, $I_0 < 3\,\mu\text{A}$. For a weak link of transmission 0.9, the Andreev peak measured with the spectrometer has a height of the order of 2 nA at phase difference π. Such a current is easily measurable with our setup.

Figure 6.14 shows a photography of a preliminary design of a Josephson spectrometer fabricated on a sapphire substrate.

6.2. Topological quantum circuits

6.2.1. Topology and quantized properties

Topology is a domain of mathematics which focuses on global properties of a given space rather than local ones. Two different geometric objects can share the same topological properties, such as the number of holes in a closed surface. Often in quantum physics, quantized properties can be linked to topological invariants. For instance, in the quantum Hall effect [129], the Hall conductance is quantized. This quantized conductance has later been restated in terms of a topological invariant (the Chern number over the magnetic Brillouin zone) of the band structure [130, 131]. Such topological invariants only depend on the global properties of the system and are thus robust against local perturbations. Finding a system exhibiting topologically quantized properties is therefore a much-pursued goal.

In order to deeper understand these topological invariants, in particular the Chern number, we follow the work of M. Berry [132] and a more recent review of it by A. Garg [133], as well as their introduction of the Berry phase and curvature, useful to compute Chern numbers.

6.2.2. The Berry curvature and the Chern number of a quantum system

These concepts intervene in the case of a quantum system, the Hamiltonian of which can be tuned by n external parameters $(X_1, \dots, X_n) = \boldsymbol{R}$. The eigenstates $|\Psi_i(\boldsymbol{R})\rangle$ and the eigenergies $E_i(\boldsymbol{R})$ of the system depend on the parameters. If the system is originally in eigenstate $|\Psi_j(\boldsymbol{R}(0))\rangle$ and the parameters $\boldsymbol{R}(t)$ are changed slowly, the system will follow the eigenstate $|\Psi_j(\boldsymbol{R}(t))\rangle$ as long as there is no degeneracy between the eigenstates. If, in a time T, the parameters are brought back to their original values: $\boldsymbol{R}(T) = \boldsymbol{R}(0)$, the wavefunction of the system can *a priori* have a different phase as the original eigenstate. Berry [132] showed that this phase factor consists of two terms:

- A dynamical phase, accounting for the change of energy:

$$\phi_j(T) = -\frac{1}{\hbar}\int_0^T E_j(\boldsymbol{R}(t))\, dt.$$

- A geometrical phase, called the Berry phase:

$$\gamma_j(T) = i\int_0^T \left\langle \Psi_j(\boldsymbol{R}(t)) \,\middle|\, \frac{d}{dt} \,\middle|\, \Psi_j(\boldsymbol{R}(t)) \right\rangle dt.$$

This phase γ_j is qualified of geometrical because it does not depend on the rate $\dot{\boldsymbol{R}}$ at which the parameters are varied. To show this propriety, we write the time derivative in γ_j as

$$\frac{d}{dt}|\Psi_j(\boldsymbol{R}(t))\rangle = \dot{\boldsymbol{R}}(t)\frac{d}{d\boldsymbol{R}}|\Psi_j(\boldsymbol{R}(t))\rangle.$$

It is more convenient to write the derivative with respect to $\boldsymbol{R}$ with a gradient symbol $\boldsymbol{\nabla}$, even if the parameter space is not the usual three-dimensional space. With this, the integral in γ_j can be expressed as an integral over the parameter $\boldsymbol{R}$:

$$\gamma_j = i\oint_{\mathcal{C}} \langle \Psi_j(\boldsymbol{R}) \,|\, \boldsymbol{\nabla}\Psi_j(\boldsymbol{R})\rangle \, d\boldsymbol{R}.$$

The contour $\mathcal{C}$ is the path followed by $\boldsymbol{R}$ in the parameter space. With this expression for the Berry phase, it is clear that it depends only on the path in the parameter space and not on the rate at which they are changed. This expression also shows that this phase is gauge-invariant. Adding a phase $\alpha(\boldsymbol{R})$ to $|\Psi_j(\boldsymbol{R})\rangle$ adds an $i\boldsymbol{\nabla}\alpha(\boldsymbol{R})$ term to the integral, which integrates to 0 over the closed contour $\mathcal{C}$.

The integrand is often called the Berry connection and is written $\boldsymbol{A}_j(\boldsymbol{R})$. The Berry curvature $\boldsymbol{B}_j(\boldsymbol{R})$ (mentioned earlier) is the curl of this connection. With this notation, the Berry phase appears as the integral of the Berry curvature over a surface $\mathcal{S}$ spanning $\mathcal{C}$, using Stokes theorem:

$$\gamma_j = \iint_{\mathcal{S}} \boldsymbol{B}_j(\boldsymbol{R}) \cdot d\boldsymbol{S}.$$

After a little algebra, the Berry curvature of the eigenstate Ψ_j can be expressed in terms of derivatives of Ψ_j:

$$\boldsymbol{B}_j\left(\boldsymbol{R}\right) = -\Im\left(\langle\boldsymbol{\nabla}\Psi_j\left(\boldsymbol{R}\right)| \times |\boldsymbol{\nabla}\Psi_j\left(\boldsymbol{R}\right)\rangle\right). \tag{6.11}$$

This expression for the Berry curvatures helps to understand its curvature name. It appears here as the cross product of the derivative of the eigenstates. In the usual three-dimensional Euclidean space, the Gaussian curvature K of an oriented surface can be expressed, close to a point where the normal is the $\boldsymbol{z}$ axis, as the cross product between the derivatives of the normal to the surface $\boldsymbol{n}$ [133]:

$$\frac{d\boldsymbol{n}}{dx} \times \frac{d\boldsymbol{n}}{dy} = K\boldsymbol{z}.$$

Equation (6.11) is similar to this expression for the Gaussian curvature K, in a more complex space. However, this expression is not practical to be computed. Expressing $\boldsymbol{\nabla}\Psi_j\left(\boldsymbol{R}\right)$ in the $\left(\Psi_i\left(\boldsymbol{R}\right)\right)_i$ basis and using the Schrödinger equation allows expressing the Berry curvature as

$$\boldsymbol{B}_j\left(\boldsymbol{R}\right) = -\Im\left(\sum_{i\neq j} \frac{\langle\Psi_j\,|\,\boldsymbol{\nabla}\mathcal{H}\,|\,\Psi_i\rangle \times \langle\Psi_i\,|\,\boldsymbol{\nabla}\mathcal{H}\,|\,\Psi_j\rangle}{\left(E_i - E_j\right)^2}\right). \tag{6.12}$$

This expression shows that degeneracies play an important role for the Berry curvature and the Berry phase. At a degeneracy point in parameter space, the Berry curvature is singular and decreases away from the degeneracies. For this reason, it is often compared to a magnetic field and the degeneracy to monopoles of this field. A recent review [133] emphasizes the relations between degeneracies in the spectrum of a quantum system and the Berry curvature and topological invariants. To better understand the implications of this in real systems, we consider a simple example.

6.2.3. A simple Hamiltonian with a degeneracy

The simplest system with a degeneracy is a two-level system with an energy crossing in the parameter space. The Hamiltonian of such a two-level system can be expressed as a 2×2 matrix. Because the Hamiltonian is Hermitian, this matrix can be written as a linear combination with real coefficients of the Pauli matrices (σ_x, σ_y, σ_z and $\sigma_0 = \mathrm{Id}$), defined as:

$$\sigma_x = \begin{pmatrix} 0 & 1 \\ 1 & 0 \end{pmatrix}, \quad \sigma_y = \begin{pmatrix} 0 & -i \\ i & 0 \end{pmatrix}, \quad \sigma_z = \begin{pmatrix} 1 & 0 \\ 0 & -1 \end{pmatrix}, \quad \sigma_0 = \begin{pmatrix} 1 & 0 \\ 0 & 1 \end{pmatrix}.$$

Such a Hamiltonian writes

$$\mathcal{H} = \alpha\sigma_x + \beta\sigma_y + \gamma\sigma_z + \delta\sigma_0,$$

where α, β, γ and δ are real coefficients depending on n parameters $\boldsymbol{R} = \left(X_1, \ldots, X_n\right)$. The $\delta\sigma_0$ term only shifts all the energy levels by the same value δ. δ can be thus taken as 0 without losing any generality. $\mathcal{H}$ can therefore be written

$$\mathcal{H} = \begin{pmatrix} \gamma & \alpha - i\beta \\ \alpha + i\beta & -\gamma \end{pmatrix}.$$

It is easy to calculate the spectrum of such a Hamiltonian. There are two eigenenergies E_+ and E_-, corresponding to eigenstates $|+(\boldsymbol{R})\rangle$ and $|-(\boldsymbol{R})\rangle$, such that

$$E_\pm = \pm\sqrt{\alpha^2+\beta^2+\gamma^2}.$$

These two levels can only be degenerate if α, β and γ are 0 at the same time. The smallest number of needed parameters to cancel these 3 coefficients at the same time is 3. This classical argument was first stated by von Neumann and Wigner [134], as well as Teller [135]. If we call these parameters X, Y and Z, it is always possible to write, up to a rotation and scalings,

$$\mathcal{H} = \frac{1}{2}\begin{pmatrix} Z & X-iY \\ X+iY & -Z \end{pmatrix}.$$

It is interesting to note that this Hamiltonian is that of a spin 1/2 in a magnetic field of direction $\boldsymbol{R} = (X, Y, Z)$. This system is often called the diabolo because the shape of the spectrum in a $X = 0$, $Y = 0$ or $Z = 0$ plane is a double cone.

The degeneracy is located at the $(0, 0, 0)$ point, called a Weyl point because of the similarity of the spectrum with a Weyl semi-metal.

The Berry curvature for the diabolo can easily be computed. Because $\mathcal{H} = X\sigma_x + Y\sigma_y + Z\sigma_z$, its gradient is just

$$\boldsymbol{\nabla}\mathcal{H} = \frac{1}{2}\begin{pmatrix}\sigma_x \\ \sigma_y \\ \sigma_z\end{pmatrix}.$$

For $\boldsymbol{R} \neq 0$, the Berry curvature for the $|+\rangle$ state can be calculated using expression (6.12):

$$\boldsymbol{B}_+(\boldsymbol{R}) = -\Im\left(\frac{\langle +(\boldsymbol{R})|\boldsymbol{\nabla}\mathcal{H}(0)|-(\boldsymbol{R})\rangle \times \langle -(\boldsymbol{R})|\boldsymbol{\nabla}\mathcal{H}(0)|+(\boldsymbol{R})\rangle}{\left(E_+(\boldsymbol{R})-E_-(\boldsymbol{R})\right)^2}\right).$$

The scalar products can easily be calculated if we take advantage of the isotropy of the spin and rotate the axis such that the Z axis is aligned with $\boldsymbol{R}$. In this rotated basis,

$$|\pm(\boldsymbol{R})\rangle = \begin{pmatrix}\pm 1 \\ 0\end{pmatrix}.$$

This gives

$$\boldsymbol{B}_+(\boldsymbol{R}) = -\frac{1}{2R^2}\begin{pmatrix}0\\0\\1\end{pmatrix}.$$

For the $|-\rangle$ state, the Berry curvature is simply the opposite.

In the unrotated basis,

$$\boldsymbol{B}_\pm(\boldsymbol{R}) = \mp\frac{\boldsymbol{R}}{2R^3}.$$

We now calculate the Berry phase of this system for a closed trajectory $\mathcal{C}$ in parameter space represented in blue in Figure 6.15. At $t = 0$, the system is prepared at the blue dot $(0, 0, R)$. The parameters evolve, following the blue circle in the $X = 0$ plane. At time $t = T$, the system is back at the blue dot. The accumulated Berry phase is given by

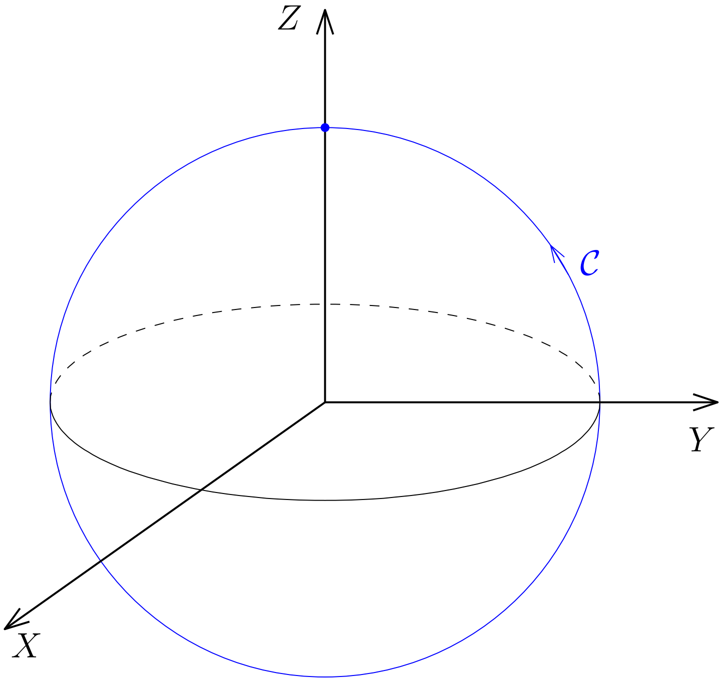

Figure 6.15.: Trajectory in parameter space.

$$\gamma_{\pm} = \iint_{\mathcal{S}} \boldsymbol{B}_{\pm}\left(\boldsymbol{R}\right) \cdot d\boldsymbol{S}.$$

An adequate surface $\mathcal{S}$ is the $X > 0$ hemisphere spanning $\mathcal{C}$.

$$\begin{aligned}\gamma_{\pm} &= \int_{\varphi=0}^{2\pi} \int_{\theta=0}^{\frac{\pi}{2}} \mp \frac{1}{2R^2} R^2 \sin\theta \, d\theta d\varphi, \\ \gamma_{\pm} &= \mp\pi.\end{aligned}$$

The system acquires a phase π when performing a rotation around the X axis.

Recalling that Hamiltonian $\mathcal{H}$ is that of a spin 1/2 in a magnetic field of direction $\boldsymbol{R}$, the path $\mathcal{C}$ consists of applying a rotating magnetic field in the $X = 0$ plane to the spin. The acquired Berry phase is $\mp\pi$. If the spin was prepared in the $|+z\rangle = \begin{pmatrix} 1 \\ 0 \end{pmatrix}$ state, it is in the $\begin{pmatrix} -1 \\ 0 \end{pmatrix} = |-z\rangle$ after one rotation around the X axis. This usual spin rotation is here explained as originating from the degeneracy in the spectrum of the spin.

The topological invariant linked to this Berry phase is the so-called Chern number, defined as the flux of the Berry curvature over a closed surface $\mathcal{S}$:

$$C_j = \frac{1}{2\pi} \oiint_{\mathcal{S}} \boldsymbol{B}_j\left(\boldsymbol{R}\right) \cdot d\boldsymbol{S}.$$

An important topological result is that the Chern number is always an integer. The demonstration of this result uses the same arguments as Dirac when describing magnetic monopoles [136].

It is 0 when the surface $\mathcal{S}$ encloses no degeneracy. If one degeneracy is enclosed, the Chern number quantifies the strength of this monopole of Berry curvature.

For the diabolo, this integral is twice the one calculated above, such that

$$C_{\pm} = \mp 1.$$

The sum of these two numbers is equal to 0. More generally, it can be proven [133] that the sum of the Chern numbers of all states involved in a degeneracy is always 0.

6.2.4. Engineering Weyl points: the biSQUID

Recently, devices were proposed [137, 138] in which crossings between Andreev Bound States occur, resulting in non-zero Chern numbers. They consist of n superconducting electrodes connected to the same normal metal region acting as a scattering element. If this region is smaller or of the order of the superconducting coherence length ($\xi \sim 100\,\mathrm{nm}$ for aluminum) and $n \geq 4$, there can be Weyl points in the Andreev Bound States spectrum. The integer Chern numbers of such degeneracies lead to quantized transconductance (in units of $4e^2/h$) between the superconducting leads [138, 139]. If there are too many conducting channels in the scattering region, there are also a lot of Weyl points and it is hard to distinguish between them. Thus, low density materials have to be used, such as 2D electron gases, graphene or nanowires.

This situation seems promising, as it is possible to fabricate devices with simple materials only. Another asset of this device is that the parameter space is accessible experimentally. It is indeed spanned by magnetic fluxes which can be individually tuned by using local flux lines. However, it is hard to control the number of Weyl singularities. It depends on the scattering properties of the central region, which are not fully accessible experimentally. One solution to design a Hamiltonian (and thus its spectrum) is to make a quantum electromagnetic circuit with capacitors, inductors and Josephson junctions, as reviewed in Ref. [46]. For instance, the plasma energy of a symmetric SQUID is exactly zero when the SQUID is flux biased at half a flux quantum, showing a degeneracy in the spectrum. However, it is impossible in practice to fabricate a perfectly symmetric SQUID, but it is possible to replace one of the junctions of the SQUID by a SQUID, in order to equate the Josephson energy of the SQUID to the third junction. From now on, we call this circuit (depicted in Figure 6.16) the biSQUID, and we will show that its spectrum has indeed Weyl points.

The biSQUID consists of three parallel Josephson junctions (of Josephson energies E_{J1}, E_{J2} and E_{J3}) separating a superconducting island (in blue) from the ground. It is possible to change the charge on the island by applying a gate voltage V_g on a capacitance C. This capacitance accounts for the capacitance between the gate and the superconducting island, as well as the intrinsic capacitance of the three junctions. The spacing between the junctions allow for magnetic field to thread through, creating fluxes Φ_L and Φ_R in the left and right loops. The three control parameters of the device are highlighted in red in the figure and are the magnetic flux Φ_L, the magnetic flux Φ_R and the gate voltage V_g.

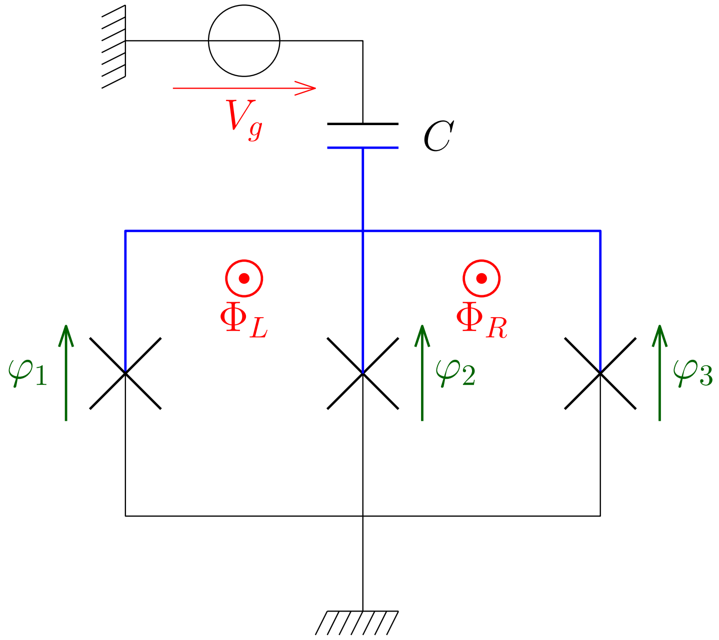

Figure 6.16.: Electrical schematic of the biSQUID.

6.2.5. Hamiltonian and spectrum of the biSQUID

In order to derive a Hamiltonian for this circuit, we need to know how many independent quantum variables are present in this circuit. The phase differences φ_1, φ_2 and φ_3 and their conjugates are all the variables here. But the two loops are linking them by

$$\begin{cases} \varphi_1 = \Phi_L/\varphi_0 + \varphi_2, \\ \varphi_2 = \Phi_R/\varphi_0 + \varphi_3. \end{cases}$$

These two equations imply that there is only one independent variable in the circuit. We choose φ_2 and call it φ. According to the calculations of Section 1.1.4, it is conjugate to the charge $Q = CV = C\varphi_0\dot{\varphi}$.

The potential energy of the circuit consists of the Josephson potential of the three junctions:

$$U(\varphi) = -E_{J1}\cos(\varphi + \varphi_L) - E_{J2}\cos\varphi - E_{J3}\cos(\varphi - \varphi_R).$$

φ_L and φ_R are the reduced fluxes: $\varphi_{L,R} = \Phi_{L,R}/\varphi_0$. The capacitive (kinetic) energy can be written as

$$K(\dot{\varphi}) = C(V - V_g)^2/2 = C(\varphi_0\dot{\varphi} - V_g)^2/2.$$

Introducing the number of Cooper pairs on the island $N = Q/(2e)$, the number of Cooper pairs brought by the gate voltage $n_g = CV_g/(2e)$ and the capacitive energy $E_C = 2e^2/C$, the kinetic energy can be expressed as

$$K(N) = E_C(N - n_g)^2.$$

This gives an expression for the Hamiltonian

$$\boxed{\mathcal{H}\left(\varphi,N\right)=-E_{J1}\cos\left(\varphi+\varphi_L\right)-E_{J2}\cos\varphi-E_{J3}\cos\left(\varphi-\varphi_R\right)+E_C\left(N-n_g\right)^2}, \tag{6.13}$$

where the quantum variables φ and N satisfy the canonical commutation relation:

$$[\varphi,N]=i.$$

In order to calculate the spectrum of this circuit, we write Hamiltonian (6.13) in the N basis. Because $[\varphi,N]=i$, it is possible to express $\mathrm{e}^{\pm i\varphi}$ in the $\left(\left|M\right\rangle\left\langle N\right|\right)_{(M,N)}$ basis:

$$\mathrm{e}^{\pm i\varphi}=\sum_{N=-\infty}^{+\infty}\left|N\pm1\right\rangle\left\langle N\right|.$$

As $\cos\left(\varphi+\delta\right)=\left(e^{i(\varphi+\delta)}+e^{-i(\varphi+\delta)}\right)/2$, every term in the Hamiltonian can be written in the $\left(\left|M\right\rangle\left\langle N\right|\right)_{(M,N)}$ basis. The resulting matrix has a tridiagonal shape:

$$\mathcal{H}=\begin{pmatrix}\ddots & \ddots & & & \\ \ddots & E_C\left(N-1-n_g\right)^2 & \alpha & & \\ & \alpha^* & E_C\left(N-n_g\right)^2 & \alpha & \\ & & \alpha^* & E_C\left(N+1-n_g\right)^2 & \ddots \\ & & & \ddots & \ddots\end{pmatrix} \tag{6.14}$$

where $\alpha=-\left(E_{J1}\mathrm{e}^{i\varphi_L}+E_{J2}+E_{J3}\mathrm{e}^{-i\varphi_R}\right)/2$ and α^* is the complex conjugate of α.

If two consecutive terms N and $N+1$ on the diagonal are equal and $\alpha=0$, states $\left|N\right\rangle$ and $\left|N+1\right\rangle$ are degenerate. In the $\left(\left|N\right\rangle,\left|N+1\right\rangle\right)$ basis, the corresponding matrix is indeed

$$\begin{pmatrix}E & 0\\ 0 & E\end{pmatrix}.$$

Two conditions on the control parameters n_g, φ_L and φ_R have to be fulfilled to have such a degeneracy:

- $E_C\left(N-n_g\right)^2=E_C\left(N+1-n_g\right)^2$,
- $E_{J1}\mathrm{e}^{i\varphi_L}+E_{J2}+E_{J3}\mathrm{e}^{-i\varphi_R}=0$.

The first condition is equivalent to

$$n_g=N+\frac{1}{2}. \tag{6.15}$$

Provided that it is possible to tune n_g as precisely as wanted, this condition can always be fulfilled.

The second condition can be interpreted geometrically. Solving the equality $E_{J1}\mathrm{e}^{i\varphi_L}+E_{J2}+E_{J3}\mathrm{e}^{-i\varphi_R}=0$ is equivalent to finding two angles φ_L and φ_R to form a triangle of sides E_{J1}, E_{J2} and E_{J3} as shown in Figure 6.17. It is only possible to find such angles as long as the following triangle inequalities are respected:

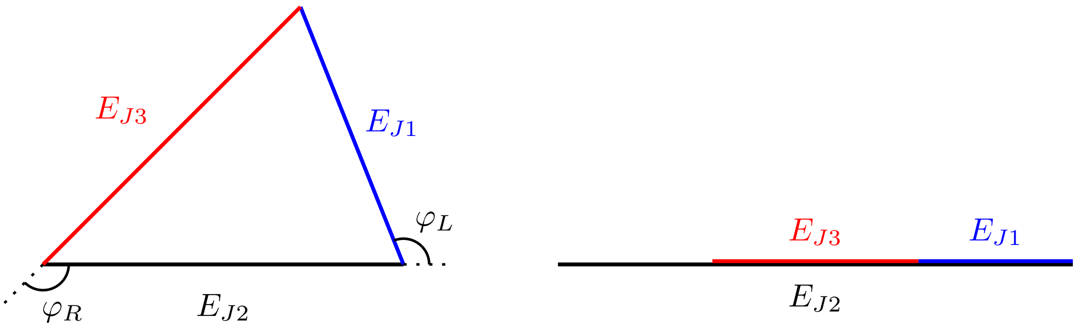

(a) (6.4) is satisfied

(b) $E_{J2} > E_{J1} + E_{J3}$

Figure 6.17.: The triangle inequality.

$$\begin{cases} E_{J1} \leq E_{J2} + E_{J3}, \\ E_{J2} \leq E_{J3} + E_{J1}, \\ E_{J3} \leq E_{J1} + E_{J2}. \end{cases} \tag{6.16}$$

If the inequalities are strict, there are two couples of solutions $(\varphi_L, \varphi_R) = \left(\phi_{1,2}, \tilde{\phi}_{1,2}\right)$ with the symmetry $\left(\phi_1, \tilde{\phi}_1\right) = \left(2\pi - \phi_2, 2\pi - \tilde{\phi}_2\right)$.

It is also possible to have a degeneracy between states $|N-1\rangle$ and $|N+1\rangle$ if the two following conditions are met.

- $E_C\left(N-1-n_g\right)^2 = E_C\left(N+1-n_g\right)^2$,
- $E_{J1}\mathrm{e}^{i\varphi_L} + E_{J2} + E_{J3}\mathrm{e}^{-i\varphi_R} = 0$.

The first one can be rewritten $n_g = N$ and the second one is the same as for the degeneracy between two consecutive states.

Figure 6.18 shows the first energy levels of the biSQUID for different sets of junctions parameters. The plasma frequency ω_p in the energy axis is that of the three parallel Josephson junctions with capacitance C: $\hbar\omega_p = \sqrt{2E_C\left(E_{J1} + E_{J2} + E_{J3}\right)}$. These spectra were calculated using an open-source package for Python: QuTiP [140]. This package allows simulating the dynamics of open quantum systems.

The left-hand side column (graphs (a), (c) and (e)) corresponds to a situation where $E_{J1} = E_{J2} = E_{J3} = E_C$, which satisfies the triangle inequalities (6.16).

Graph (a) shows the dependence on n_g of the spectrum (with $\varphi_L = \varphi_R = 2\pi/3$). As expected, the gap between the two first levels closes when $n_g = 1/2 + n$. For these values of n_g, there are other gap closings between two following levels. For integer values of n_g, the spectrum also has levels crossings, not between the two first levels, but between the second and the third.

Graph (c) has $n_g = 1/2$ and both reduced fluxes φ_L and φ_R vary between 0 and 2π. The gap between the two first levels (in blue and green) closes twice, when $\varphi_L = \varphi_R = 2\pi/3$ and when $\varphi_L = \varphi_R = 4\pi/3$, according to the complex equality $E_{J1}\mathrm{e}^{i\varphi_L} + E_{J2} + E_{J3}\mathrm{e}^{-i\varphi_R} = 0$.

In graph (e), $n_g = 0$, there are also gap closings at the same values of φ_L and φ_R. This time, the crossings occur between the second and third levels. Another difference with (c) is the shape of the spectrum around this gap closings. In (c), both levels look linear, while in (e), they look parabolic.

The right-hand side column shows the same spectra in the situation where one of the triangle inequalities is not satisfied. Here $E_{J2}/3 = E_{J1} = E_{J3} = E_C$. This results in no gap closing in (b), (d) and (f).

Figure 6.19 shows the dependence on the reduced fluxes (taken equal) and n_g of the first excitation (a), as well as the energy difference between the second and third energy levels (b).

The difference between half-integer and integers value of n_g can be understood by looking at the Berry curvature around these degeneracies.

6.2.6. Berry curvature and Chern number of the degeneracies

Half-integer number of Cooper pairs

When $n_g = 1/2$ (or any half-integer value), the degeneracy occurs between the two states with the lowest energy. To understand the shape of the levels crossings in Figure 6.18, we consider only states $|0\rangle$ and $|1\rangle$ around the degeneracy point. The Hamiltonian in the basis spanned by these states is

$$\mathcal{H} = \begin{pmatrix} E_C n_g^2 & \alpha \\ \alpha^* & E_C\left(1-n_g\right)^2 \end{pmatrix}, \tag{6.17}$$

with $\alpha = -\left(E_{J1}\mathrm{e}^{i\varphi_L} + E_{J2} + E_{J3}\mathrm{e}^{-i\varphi_R}\right)/2$. If we call (ϕ_L, ϕ_R) one degeneracy point (in the (φ_L, φ_R) parameter space), it is possible to expand the Hamiltonian around $(\phi_L, \phi_R, 1/2)$. We write $(\varphi_L, \varphi_R, n_g) = (\phi_L, \phi_R, 1/2) + (\delta\varphi_L, \delta\varphi_R, \delta n_g)$. With these notations,

$$\begin{aligned} E_C n_g^2 &\sim E_C\left(\frac{1}{4} + \frac{\delta n_g}{2}\right), \\ E_C\left(1-n_g\right)^2 &\sim E_C\left(\frac{1}{4} - \frac{\delta n_g}{2}\right), \\ \alpha &\sim -\frac{i}{2}\left(E_{J1}\mathrm{e}^{i\phi_L}\delta\varphi_L - E_{J3}\mathrm{e}^{-i\phi_R}\delta\varphi_R\right). \end{aligned}$$

With these expressions, matrix (6.17) can easily be written as a function of the Pauli matrices,

$$\mathcal{H} = \begin{cases} \left(\frac{E_{J1}\sin\phi_L}{2}\delta\varphi_L + \frac{E_{J3}\sin\phi_R}{2}\delta\varphi_R\right)\sigma_x \\ +\left(-\frac{E_{J1}\cos\phi_L}{2}\delta\varphi_L + \frac{E_{J3}\cos\phi_R}{2}\delta\varphi_R\right)\sigma_y \\ +\frac{E_C}{2}\delta n_g\sigma_z \\ +\frac{E_C}{4}\sigma_0. \end{cases}$$

If we subtract the term in σ_0 (only shifting the origin of energy), this Hamiltonian can be written in the form

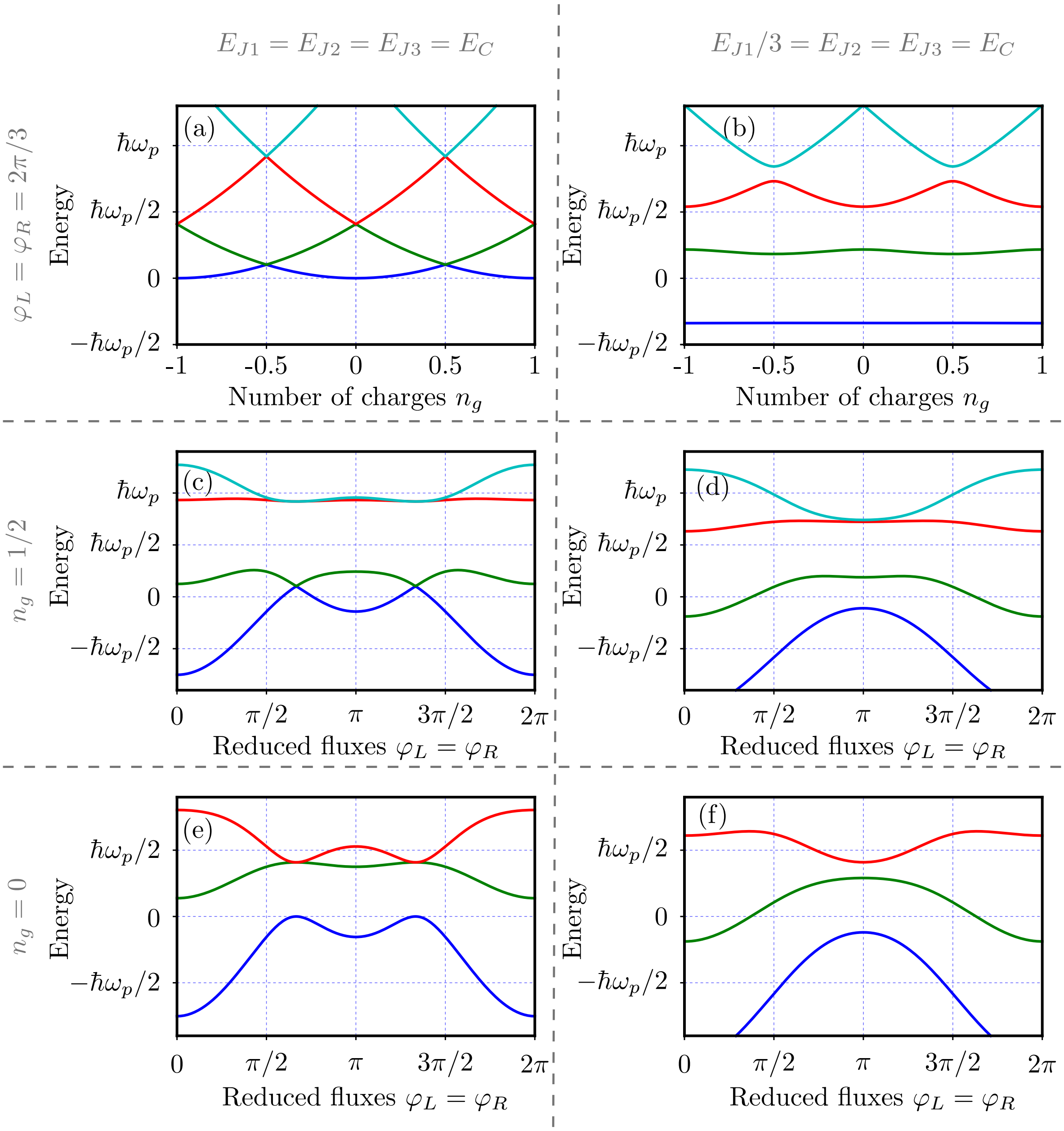

Figure 6.18.: Spectrum of the biSQUID.

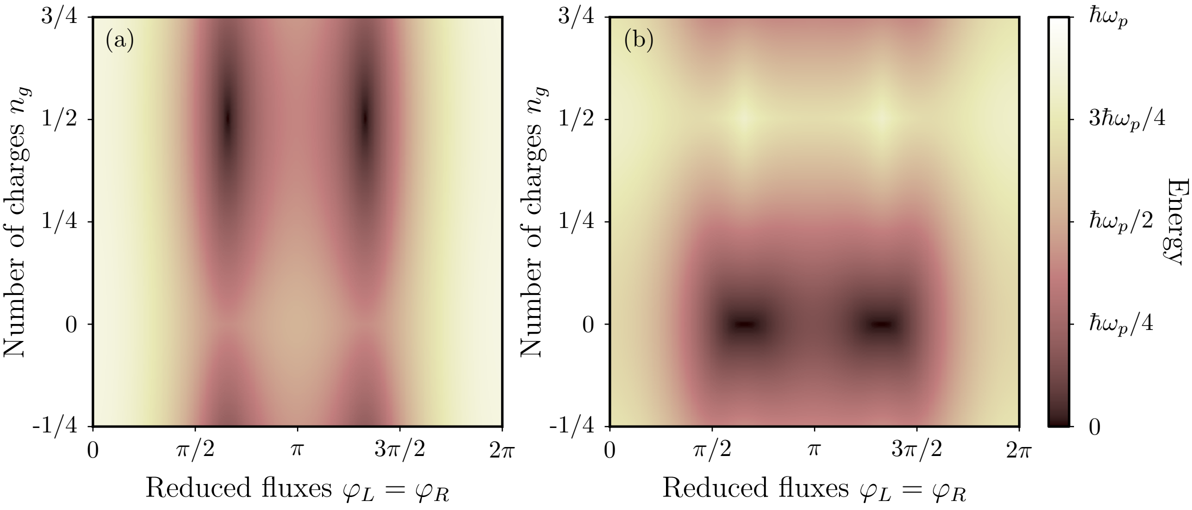

Figure 6.19.: First energy levels of the biSQUID for $\varphi_L = \varphi_R$: (a) First excitation ; (b) Difference between second and third energy level.

$$\mathcal{H} = \frac{1}{2} \begin{pmatrix} \sigma_x & \sigma_y & \sigma_z \end{pmatrix} M \begin{pmatrix} \delta\varphi_L \\ \delta\varphi_R \\ \delta n_g \end{pmatrix},$$

where the matrix M is the rotation and scaling matrix mentioned in Section 6.2.3.

$$M = \begin{pmatrix} E_{J1}\sin\phi_L & E_{J3}\sin\phi_R & 0 \\ -E_{J1}\cos\phi_L & E_{J3}\cos\phi_R & 0 \\ 0 & 0 & E_C \end{pmatrix}.$$

With these notations, Hamiltonian $\mathcal{H}$ is that of the diabolo of Section 6.2.3, deformed via the matrix M.

The Chern number of these degeneracies is thus ±1. For the lowest energy level, the sign of the Chern number is given by the sign of the determinant of the matrix M [138] and the opposite for the other state. Here it is the sign of $\sin(\phi_L + \phi_R)$.

For the case considered above ($E_{J1} = E_{J2} = E_{J3} = E_C$), the degeneracy at $(2\pi/3, 2\pi/3)$ has a Chern number of -1, while the degeneracy at $(4\pi/3, 4\pi/3)$ has a Chern number of 1.

Integer number of Cooper pairs

When $n_g = 0$ (or any integer value), the degeneracy occurs between states $|-1\rangle$ and $|1\rangle$. Only considering these states is not enough, as they are also coupled via $|0\rangle$. In the basis spanned by $|1\rangle$, $|0\rangle$ and $|-1\rangle$, the Hamiltonian is

$$\mathcal{H} = \begin{pmatrix} E_C(1+n_g)^2 & \alpha & 0 \\ \alpha^* & E_C n_g^2 & \alpha \\ 0 & \alpha^* & E_C(1-n_g)^2 \end{pmatrix}. \tag{6.18}$$

Around $(\phi_L, \phi_R, 0)$, this Hamiltonian can be expanded at first order in

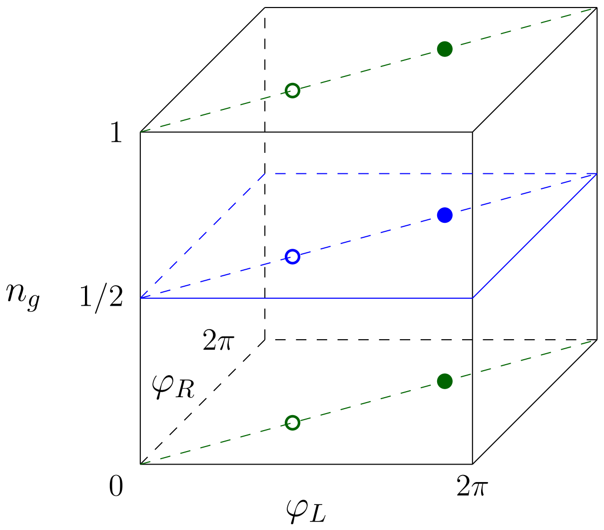

Figure 6.20.: Localization and Chern number of the degeneracy points in parameter space.

$$\mathcal{H} = \begin{pmatrix} E_C(1+2n_g) & \alpha & 0 \\ \alpha^* & 0 & \alpha \\ 0 & \alpha^* & E_C\left(1-2n_g\right) \end{pmatrix},$$

with $\alpha \sim -i\left(E_{J1}\mathrm{e}^{i\phi_L}\delta\varphi_L - E_{J3}\mathrm{e}^{-i\phi_R}\delta\varphi_R\right)/2$. $\tilde{\mathcal{H}} = E_C\mathrm{Id} - \mathcal{H}$ is similar to the Hamiltonian given in example in Ref. [133]. The Berry curvature of this Hamiltonian can be calculated using perturbation theory to yield a Chern number of 0 for state $|0\rangle$, -2 for $|-1\rangle$ and 2 for $|1\rangle$ (for the degeneracy at $(2\pi/3, 2\pi/3)$).

Figure 6.20 shows the localization and the Chern number of these degeneracy points in parameter space for the symmetric ($E_{J1} = E_{J2} = E_{J3} = E_C$) situation. The blue marks correspond to the degeneracies with linear crossings (± 1 Chern numbers). The green marks correspond to ± 2 Chern numbers. Empty circles are for negative values of Chern numbers and full circles for positive values.

6.2.7. An electron pump

As stated in the introduction of this section, topological invariants often lead to quantized properties which can experimentally be measured. In the case of the biSQUID, a slightly different circuit has to be considered to find such quantities. The adequate circuit is presented in Figure 6.21. The difference with the previous circuit resides in that the left loop was opened and a voltage source V_L was added. The phase difference of the left-hand side junction is now controlled via this voltage source. Applying a voltage V_L to the junction results in a linearly increasing phase difference: $\varphi_1 = \varphi_1^{(0)} + V_L t/\varphi_0$.

The current I_n flowing through the left-hand side junction due to state $|n\rangle$ can be expressed as a function of the Berry curvature of the Hamiltonian as derived in Appendix L,

$$I_n(t) = \frac{1}{\varphi_0}\frac{\partial E_n}{\partial \varphi_1} + 2e\left(-B_n^{(\varphi_R)}\dot{n}_g + B_n^{(n_g)}\dot{\varphi}_R\right).$$

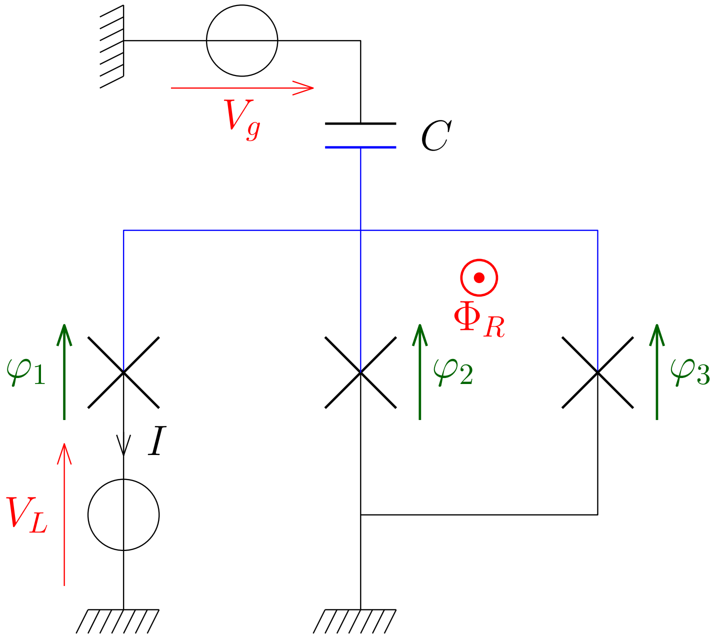

Figure 6.21.: Electrical schematic of the open version of the biSQUID.

If φ_R is kept constant and n_g increases with a constant rate $\dot{n}_g$, the current is given by

$$I_n(t) = \frac{1}{\varphi_0}\frac{\partial E_n}{\partial \varphi_1} - 2eB_n^{(\varphi_R)}\dot{n}_g.$$

When time evolves, φ_L and n_g run through $[0, 2\pi]$ and $[0, 1]$, taking values all over $[0, 2\pi] \times [0, 1]$ (as long as $\dot{\varphi}_L/(2\pi)$ and $\dot{n}_g$ are incommensurate). If the averaged current is measured, the first term in the expression averages to 0 and the second term becomes the integral of the Berry curvature over the surface $\mathcal{S} = [0, 2\pi] \times [0, 1]$,

$$\langle I_n \rangle = -\frac{e\dot{n}_g}{\pi}\iint_{\mathcal{S}} B_n^{(\varphi_R)}\left(\varphi_L, \varphi_R, n_g\right) d\varphi_L dn_g.$$

The surface $\mathcal{S}$ (shown in red in the left panel of Figure 6.22 for $\varphi_R = \pi$) is not a closed surface. It is possible to close it by adding the $\varphi_R = 0$ plane (on which the integral of $B_n^{(\varphi_R)}$ is zero). Due to the $2\pi-$periodicity in φ_L and the $1-$periodicity in n_g of the Berry curvature, the $\varphi_L = 0$ surface is the same as the $\varphi_L = 2\pi$ surface and the $n_g = 0$ surface is the same as the $n_g = 1$ surface. The resulting surface $\tilde{\mathcal{S}}$ is now a closed surface, and

$$\iint_{\mathcal{S}} B_n^{(\varphi_R)}\left(\varphi_L, \varphi_R, n_g\right) d\varphi_L dn_g = \oiint_{\tilde{\mathcal{S}}} \boldsymbol{B}_n \cdot \boldsymbol{dS}.$$

This integral is the Chern number of state $|n\rangle$ (up to a 2π factor), such that

$$\langle I_n \rangle = -2e\dot{n}_g C_n\left(\varphi_R\right).$$

If the system is kept away from the degeneracies, it will remain in the ground state of the Hamiltonian (as long as the sweeping rates of n_g and φ_L are slow enough to avoid Landau-

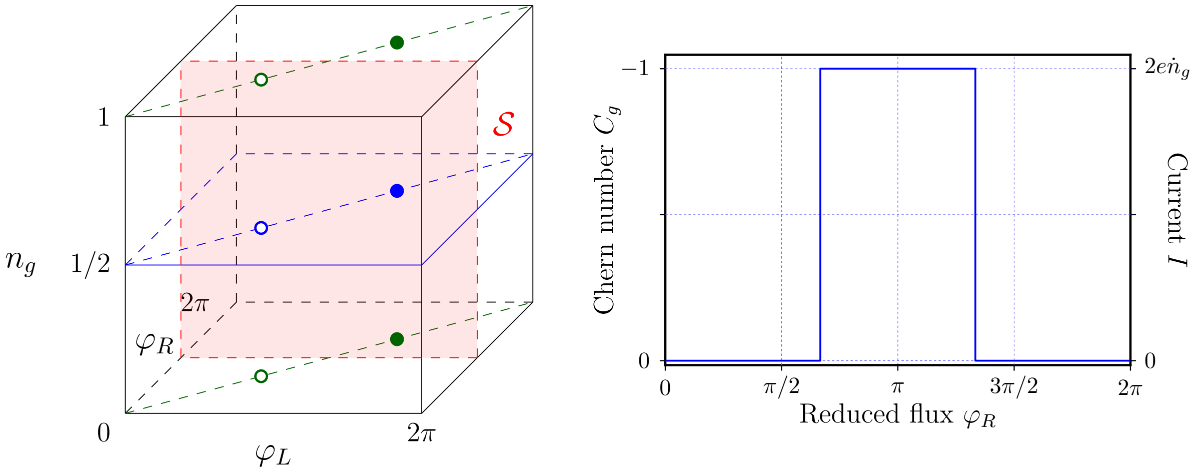

Figure 6.22.: Surface $\mathcal{S}$ in parameter space for $\varphi_R = \pi$ and quantization of the current.

Zener transitions). Only the Chern number C_g of the ground state is thus relevant. According to the calculations of Section 6.2.6, the Chern number C_g is zero outside of the two Weyl points and -1 between them. The current that should be measured in the open biSQUID is plotted in the right panel of Figure 6.22 for three identical junctions.

Realizing topological quantum circuits like the biSQUID is also one of the objectives of the Φ_0 group. Probing the spectrum of the biSQUID with the Josephson spectrometer to observe the Weyl points is the first step towards the measurement of a quantized current as the one shown in Figure 6.22.

6.2.8. Towards the Josephson spectroscopy of the biSQUID

To perform the spectroscopy of the biSQUID, there are two main prerequisites: being able to control the fluxes in the loops and the charge on the superconducting island. The independent control of two fluxes has already been demonstrated in this work with the spectroscopy of the RF-SQUID in Section 5.4. Concerning the control of the charge, the first concern is the amplitude of the charge noise on the superconducting island. This can be estimated by considering the voltage noise across the capacitance C to the ground. Its integrated value is $V_{rms} = \sqrt{k_B T/C}$, as derived in Section 2.4.3. As charge and voltage are proportional in a capacitance, the integrated charge noise is thus $Q_{rms} = \sqrt{C k_B T}$. In order to have a good control of the charge on the superconducting island, this noise has to be much smaller than $2e$. For instance, $Q_{rms} < e/10$ at 100 mK corresponds to a capacitance smaller than 180 aF. Because there are three junctions in parallel in the device, each junction capacitance has to be smaller than 60 aF. With the same oxidation parameters as the one used throughout this thesis, this corresponds to a surface area of 7200 nm^2 per junction which is manageable with an electron-beam lithography.

We propose using a Josephson spectrometer to perform the spectroscopy of the biSQUID. Among the three coupling schemes presented in Chapter 2, only the capacitive one is possible.

If a Josephson spectrometer is galvanically connected between the superconducting island and the ground, as represented in Figure 6.23, the capacitance of the spectrometer is added in

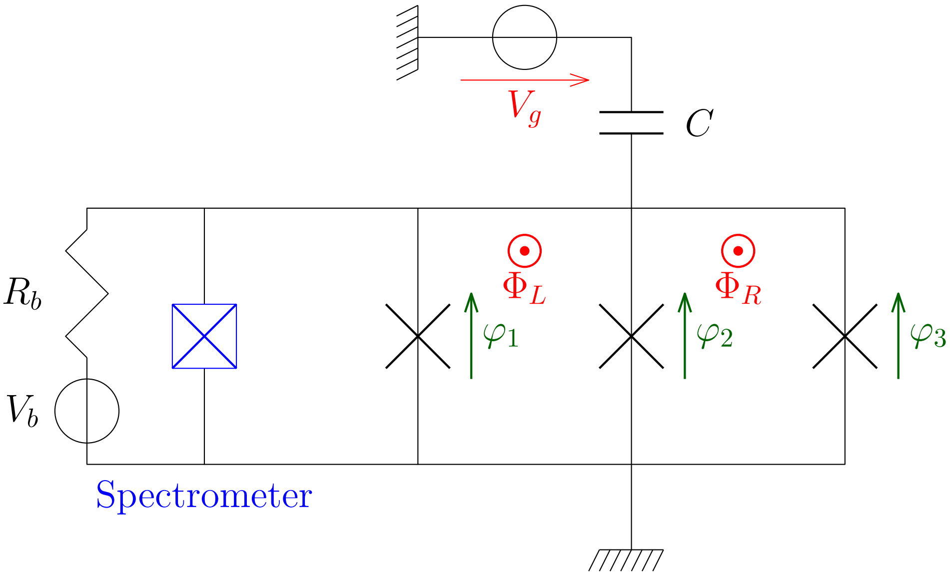

Figure 6.23.: Electrical schematic of a biSQUID galvanically coupled to a Josephson spectrometer.

parallel to the capacitance to the ground which increases the charge noise. The surface area of the Josephson junction used in the spectrometer thus also has to be of the order of 7200 nm^2, equivalent to a critical current of 500 pA. The peaks that would occur in the spectrum would then have a quite small height and hardly be measurable. Furthermore, the voltage applied on the spectrometer is also applied on the three junctions of the biSQUID, bringing them out of equilibrium and considerably changing their Hamiltonian.

The inductive coupling scheme is also not possible because there is no inductance in the biSQUID. Adding one in parallel of the three junctions changes greatly the Hamiltonian of the biSQUID because it shunts the Josephson inductance L_J of the three junctions. If the added inductance l_c is much larger than L_J, this effect is less visible. For each junction, the inductance is of the order of 600 nH, such that the total L_J is of the order of 200 nH. It is quite hard to fabricate an on-chip inductor with such a large inductance.

When considering capacitive coupling, as sketched in Figure 6.24, a first requirement is that the coupling capacitance C_c has to be smaller than the capacitance C to the ground, such that the charge noise is not increased. In that limit, the resonance frequency ω_m is given by

$$\Im\left(\frac{1}{Z_b + \frac{1}{iC_c\omega_m}}\right) = -C_J\omega_m, \tag{6.19}$$

where Z_b is the impedance of the biSQUID and C_J the capacitance of the spectrometer. To estimate Z_b, we model the three tunnel junctions of the biSQUID as inductances. This model is only valid for the first excitation of the spectrum since the next excitations have different energy due to the non-linear character of Josephson junctions. Writing L_1, L_2 and L_3 the Josephson inductances at zero phase difference of junctions 1, 2 and 3, the admittance of the

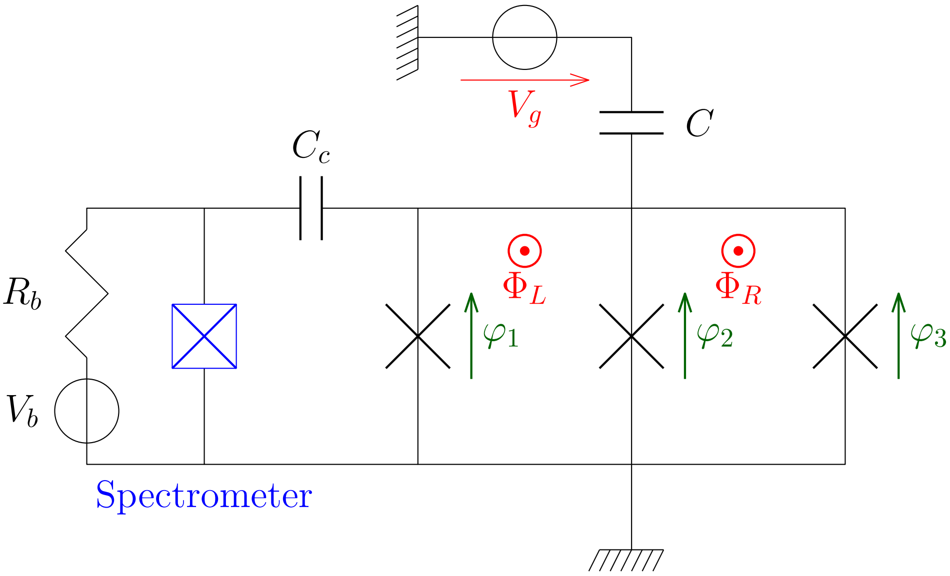

Figure 6.24.: Electrical schematic of a biSQUID capacitively coupled to a Josephson spectrometer.

biSQUID is

$$Y_b = \frac{\cos\varphi_1}{iL_1\omega} + \frac{\cos\varphi_2}{iL_2\omega} + \frac{\cos\varphi_3}{iL_3\omega} + iC\omega.$$

The resonant frequency of the bare biSQUID in this model is the frequency ω_0 such that $Y_b(\omega_0) = 0$,

$$\omega_0^2 = \frac{1}{C}\left(\frac{\cos\varphi_1}{L_1} + \frac{\cos\varphi_2}{L_2} + \frac{\cos\varphi_3}{L_3}\right).$$

Introducing $E_C = 2e^2/C$ and $E_{Jn} = \varphi_0^2/L_n$, this frequency can be written

$$(\hbar\omega_0)^2 = 2E_C\left(E_{J1}\cos\varphi_1 + E_{J2}\cos\varphi_2 + E_{J3}\cos\varphi_3\right).$$

This frequency describes quite well the actual plasma frequency of the biSQUID at $n_g = 1/2$. If E_{J1}, E_{J2} and E_{J3} satisfy the triangle inequalities (Equation (6.16)), $\omega_0 = 0$ at certain combinations of phase differences, as calculated above. To simplify the notations in the following calculations we write L_J the parallel combination of the three inductances, such that $Y_b = 1/(iL_J\omega) + iC\omega$. The resonance condition of Equation (6.19) can thus be written

$$\left(\frac{1}{C_c\omega_m} - \frac{L_J\omega_m}{1 - L_JC\omega_m^2}\right)^{-1} = -C_J\omega_m.$$

The evaluation of this expression yields

$$\omega_m = \omega_0\frac{1}{\sqrt{1 + \frac{1}{C}\frac{C_cC_J}{C_c+C_J}}}.$$

As stated above, having $C_c \ll C$ helps keeping the charge noise low. If we also impose $C_J \gg C$, the measured frequency is $\omega_m = \omega_0$. The condition $C_J \gg C$ is easy to satisfy in practice since C is quite small (of the order of 200 aF) to ensure a large charge energy for the biSQUID.

If we want to evaluate the dissipation at resonance, we can model it by a resistance R in parallel with the biSQUID accounting for losses in the dielectric. A typical value for the junctions we fabricate is 10 MΩ. At resonance, the impedance of the biSQUID is thus R, such that the impedance Z_e seen by the spectrometer is

$$Z_e = \left(\frac{1}{R_b + \frac{1}{iC_c\omega_0}} + iC_J\omega_0 \right)^{-1}.$$

In the limit where $C_J \gg C_c$, the real part of Z_e can be expressed as

$$R_e = \frac{C_c}{C_J} \frac{R}{1 + (RC_c\omega_0)^2}.$$

For $C_c \sim 10\,\mathrm{aF}$ and $C_J \sim 150\,\mathrm{fF}$ (corresponding to a critical current of 500 nA), this gives $R_e \sim 7\,\Omega$ if ω_0 is of the order of $2\pi \times 15\,\mathrm{GHz}$. This corresponds to a peak of height 30 nA, easily detectable with our setup. As the measured signal is proportional to R_e times the square of the critical current of the junction of the spectrometer and R_e is inversely proportional to its capacitance and thus to its critical current, the measured signal is proportional to the critical current. Larger junctions are thus favorable, both to increase the signal and to make sure that the measured frequency is actually the plasma frequency of the biSQUID.

Conclusion

Starting from an experimental realization of a spectrometer based on the Josephson effect [32], we have understood its imperfections and implemented a new design (presented in Figure (iii).1) to palliate them. The two main drawbacks of the first generation of spectrometer were the presence of several spurious resonant modes due to the electromagnetic environment of the junction and a non-uniform coupling to the system of interest.

Using a symmetrical SQUID (colored in blue in the SEM picture of Figure (iii).1) biased at half a flux quantum allows significantly decoupling the junctions from the environmental modes. The electromagnetic environment of the spectrometer is also carefully designed in order to suppress all remaining modes. The high impedance of inductors (in red) placed close to the junctions contributes to a good decoupling. A considerable part of the emitted microwaves, as well as incoming noise, is shunted by two large capacitors (in orange) at the other end of the inductors. The remaining resonant modes are then damped by large on-chip resistors (in green).

Coupling to the system of interest can be made using the inductance of the loop of the SQUID instead of a capacitor. This guarantees uniform phase excitation across the inductance, as opposed to a $1/\omega^2$ dependence for capacitive coupling.

All these improvements allow measuring an almost flat spectrum when the spectrometer is not coupled to any system of interest. The right-hand side of Figure (iii).1 shows such current-voltage characteristics. The top color map represents the evolution of the IV characteristics with respect to the flux Φ_e in the SQUID loop and the bottom curves are cuts along the red and dashed lines at $\Phi_e = 0$ and $\Phi_0/2$ in a logarithmic scale. The remaining background current at $\Phi_e = \Phi_0/2$ is of the order of 200 pA for junctions with a critical current of 100 nA. This corresponds to an intrinsic noise equivalent power of 10^{-17} W/$\sqrt{\text{Hz}}$ over a bandwidth of 180 GHz. The few residual undesired features at 150 and 275 µV have now been identified as due to the large shield planes visible in pale-yellow in the microscope picture. They can therefore be shifted out of the bandwidth of the spectrometer in the next version.

Spectra of four test systems were measured over a wide frequency range: an LC resonator mode at 150 GHz, the excitation of quasiparticles in a superconductor above 90 GHz, the plasma frequency of a Josephson junction at 15 GHz and the plasma frequency of a RF-SQUID at 80 GHz. The measured spectra agree quite well with the theory and allow proving that the spectrometer can be used in various situations. The spectroscopy of the RF-SQUID was made via a mutual inductance to the spectrometer which proved the possibility of using such a coupling scheme. As coupling to the loop mode was too weak in this case, future SQUID spectrometers will have the device under test directly inside the loop.

Finally, several systems particularly adapted to be probed by the Josephson spectrometer were presented, including hybridized ABS in close junctions, modified ABS due to spin-orbit coupling in InAs nanowires and HgTe-based weak links, as well as topological superconducting quantum circuits where the plasma energy levels can exhibit non-avoided energy crossings.

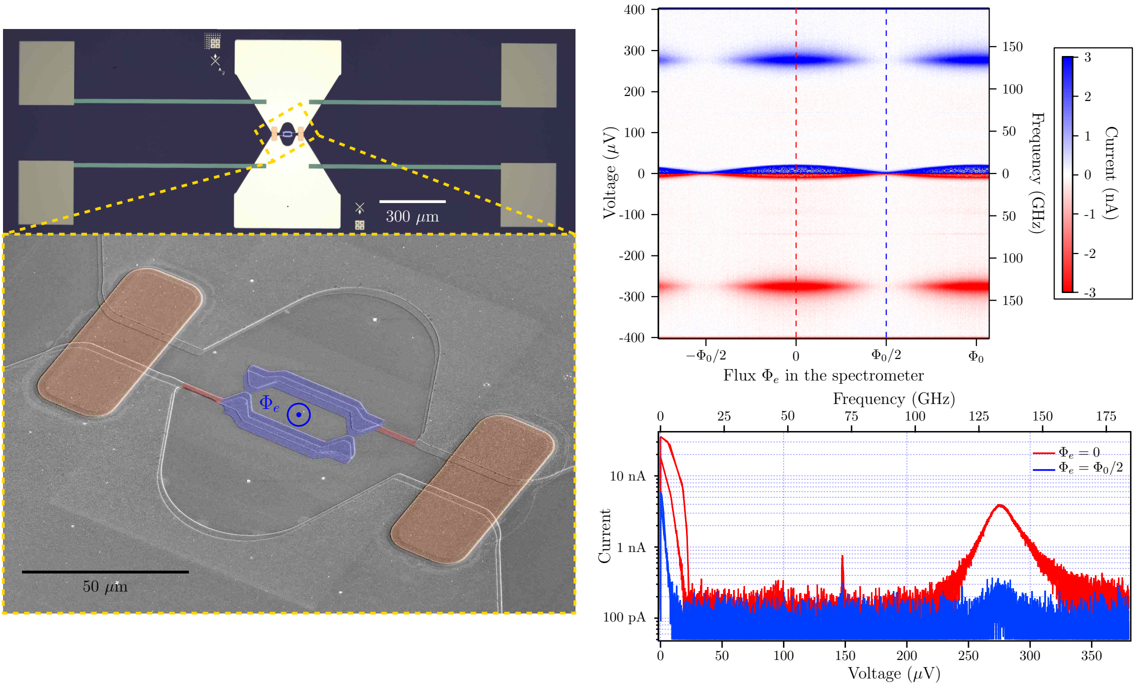

Figure (iii).1.: Microscope and SEM (Scanning Electron Microscope) pictures and current-voltage characteristic of the latest version of the spectrometer.

Perspectives

The resulting device can further be improved. Possible directions include fabricating it on a transparent sapphire chip as suggested in the previous chapter in the case of the envisaged coupling to a TI-based junction. With such a chip-spectrometer it will be possible to probe any system of interest, just by bringing it close enough and without fabrication process on it. This is convenient for fragile systems. With a SQUID loop of radius 50 µm, the coupling stays acceptable up to a distance of $\sim$ 100 µm easily achievable with simple alignment techniques. The group is currently working on a new setup in which the chip to probe can be moved with micro-metric screws and therefore carefully aligned with the spectrometer. The first alignment attempt resulted in a vertical distance of 10 µm between the two chips and a horizontal error of the order of 20 µm. Fabrication and characterization of spectrometers on a sapphire substrate have also already begun and show current-voltage characteristic comparable to the ones obtained on silicon substrates.

Another possible improvement consists of using a superconducting material with a higher gap to operate at higher frequencies: possibly up to 1.4 THz with niobium-based junctions. In that case, the fabrication is less simple as with aluminum because, in order to have a good oxide, one needs to form a Nb/Al/AlOx/Al/Nb sandwich which requires a sputtering system instead of an electron beam evaporator due to the refractory nature of niobium. However, experiments are in progress to test electron-beam evaporated Nb tunnel junctions. Al/AlOx/Al/Nb junctions have already been realized, with a measured gap larger than that of aluminum but still smaller than that of niobium. The voltage at which the quasiparticle branch starts is of the order of

800 µV, corresponding to a frequency of 400 GHz.

The Φ_0 group is also currently working on another device able to deliver a voltage stable to better than one part-per-billion using the stability of the Shapiro steps in presence of microwave irradiation. Combining this precise tunable voltage source with the spectrometer theoretically allows for an extremely narrow linewidth (of the order of the kHz or even smaller).

One of the main drawbacks of the developed spectrometer is that the measured signal relies on dissipation in the device under test. Being able to measure the amplitude and the phase of the microwave signal reflected to the junction would allow probing less dissipative systems and would thus increase the sensitivity of the spectrometer. The possibility of phase locking Josephson junctions to a coherent microwave source may lead to the development of such an on-chip broadband vector network analyzer.

Appendices

A. Spectrum of the Andreev Bound States

For a given energy E, there are four possible wavevectors in the Andreev approximation

$$k_{\alpha,\beta} = \alpha k_F + \beta i\kappa(E),$$

where $\alpha = \pm 1$ and $\beta = \pm 1$. In the left-hand side region ($x < 0$), only k with $\beta = -1$ are not diverging and in the right-hand side region, $\beta = 1$. The spinor $\Psi(x)$ describing the bound states can thus be written

$$\Psi(x) = \begin{cases} A \begin{pmatrix} a_A \\ b_A \end{pmatrix} \mathrm{e}^{-ik_F x+\kappa(E)x} + B \begin{pmatrix} a_B \\ b_B \end{pmatrix} \mathrm{e}^{ik_F x+\kappa(E)x} & \text{if} x < 0, \\ C \begin{pmatrix} a_C \\ b_C \end{pmatrix} \mathrm{e}^{-ik_F x-\kappa(E)x} + D \begin{pmatrix} a_D \\ b_D \end{pmatrix} \mathrm{e}^{ik_F x-\kappa(E)x} & \text{if} x > 0. \end{cases}$$

The A, B, C and D coefficients are to be determined with the wavefunction continuity equations at $x = 0$. The a_X and b_X are given by the u_k and v_k coefficients of Equation (1.13). Calling

$$\begin{cases} u = \sqrt{\dfrac{1}{2}\left(1 + \dfrac{\xi_{k_{1,1}}}{E}\right)}, \\ v = \sqrt{\dfrac{1}{2}\left(1 - \dfrac{\xi_{k_{1,1}}}{E}\right)}, \end{cases}$$

gives

$$\Psi(x) = \begin{cases} A \begin{pmatrix} u \\ v\mathrm{e}^{-i\varphi_L} \end{pmatrix} \mathrm{e}^{-ik_F x+\kappa(E)x} + B \begin{pmatrix} v \\ u\mathrm{e}^{-i\varphi_L} \end{pmatrix} \mathrm{e}^{ik_F x+\kappa(E)x} & \text{if} x < 0, \\ C \begin{pmatrix} v \\ u\mathrm{e}^{-i\varphi_R} \end{pmatrix} \mathrm{e}^{-ik_F x-\kappa(E)x} + D \begin{pmatrix} u \\ v\mathrm{e}^{-i\varphi_R} \end{pmatrix} \mathrm{e}^{ik_F x-\kappa(E)x} & \text{if} x > 0. \end{cases}$$

At $x = 0$, the wavefunction is continuous, so

$$A \begin{pmatrix} u \\ v\mathrm{e}^{-i\varphi_L} \end{pmatrix} + B \begin{pmatrix} v \\ u\mathrm{e}^{-i\varphi_L} \end{pmatrix} = C \begin{pmatrix} v \\ u\mathrm{e}^{-i\varphi_R} \end{pmatrix} + D \begin{pmatrix} u \\ v\mathrm{e}^{-i\varphi_R} \end{pmatrix}. \tag{A.1}$$

The derivative of the wavefunction follows

$$-\frac{\hbar^2}{2m}\frac{d\Psi}{dx}(x = 0^-) = -\frac{\hbar^2}{2m}\frac{d\Psi}{dx}(x = 0^+) + V_0\Psi(x = 0).$$

This can be rewritten as

$$\begin{aligned} &A\left(-ik_F+\kappa(E)\right)\begin{pmatrix} u \\ v\mathrm{e}^{-i\varphi_L}\end{pmatrix}+B\left(ik_F+\kappa(E)\right)\begin{pmatrix} v \\ u\mathrm{e}^{-i\varphi_L}\end{pmatrix}= \\ C\left(-ik_F-\kappa(E)-2\eta k_F\right)&\begin{pmatrix} v \\ u\mathrm{e}^{-i\varphi_R}\end{pmatrix}+D\left(ik_F-\kappa(E)-2\eta k_F\right)\begin{pmatrix} u \\ v\mathrm{e}^{-i\varphi_R}\end{pmatrix}, \end{aligned} \tag{A.2}$$

where $\eta = mV_0/(\hbar^2 k_F)$. In the zeroth order Andreev approximation, $\kappa(E)$ can be completely neglected with respect to k_F. Combining Equations (A.1) and (A.2) together gives a matrix equation linking A, B, C and D:

$$\begin{pmatrix} u & v & -v & -u \\ v\mathrm{e}^{-i\varphi_L} & u\mathrm{e}^{-i\varphi_L} & -u\mathrm{e}^{-i\varphi_R} & -v\mathrm{e}^{-i\varphi_R} \\ u & -v & \left(-1+2i\eta\right)v & \left(1+2i\eta\right)u \\ v\mathrm{e}^{-i\varphi_L} & -u\mathrm{e}^{-i\varphi_L} & \left(-1+2i\eta\right)u\mathrm{e}^{-i\varphi_R} & \left(1+2i\eta\right)v\mathrm{e}^{-i\varphi_R} \end{pmatrix}\begin{pmatrix} A \\ B \\ C \\ D \end{pmatrix}=0.$$

This equation has non-zero solutions only if the determinant of the matrix is zero. This condition can be written

$$\left(u^4+v^4\right)\left(1+\eta^2\right)=2u^2v^2\left(\eta^2+\cos\varphi\right),$$

which has two solutions

$$E_\pm = \pm\Delta\sqrt{1-\tau\sin^2\frac{\varphi}{2}}, \tag{A.3}$$

where τ is the transmission of the channel given by Equation (1.10).

B. Derivation of the current carried by an Andreev bound state

The current carried by an Andreev bound state is the derivative of the charge,

$$I = -2e\frac{d\langle\hat{n}\rangle}{dt}.$$

Ehrenfest theorem gives for the observable $\hat{n}$,

$$\frac{d\langle\hat{n}\rangle}{dt} = \frac{1}{i\hbar}\left\langle\left[\hat{n},\hat{\mathcal{H}}\right]\right\rangle.$$

Because phase φ and charge number n are conjugate, $\hat{n} = \frac{1}{i}\frac{\partial}{\partial\varphi}$. This gives for a state $|\Psi\rangle$,

$$\begin{aligned}\frac{d\langle\hat{n}\rangle}{dt} &= \frac{1}{i\hbar}\left\langle\Psi\left|\frac{1}{i}\frac{\partial}{\partial\varphi}\hat{\mathcal{H}}\right|\Psi\right\rangle - \frac{1}{i\hbar}\left\langle\Psi\left|\hat{\mathcal{H}}\frac{1}{i}\frac{\partial}{\partial\varphi}\right|\Psi\right\rangle,\\ &= -\frac{1}{\hbar}\left\langle\Psi\left|\frac{\partial\hat{\mathcal{H}}}{\partial\varphi}\right|\Psi\right\rangle,\\ &= -\frac{1}{\hbar}\left\langle\frac{\partial\hat{\mathcal{H}}}{\partial\varphi}\right\rangle.\end{aligned}$$

Consider an Andreev bound state $|\pm\rangle$ of energy $E_\pm$. The expectation value in the last equation is

$$\left\langle\frac{\partial\hat{\mathcal{H}}}{\partial\varphi}\right\rangle = \left\langle\pm\left|\frac{\partial\hat{\mathcal{H}}}{\partial\varphi}\right|\pm\right\rangle. \tag{B.1}$$

For $|\pm\rangle$, the Schrödinger equation gives $\hat{\mathcal{H}}|\pm\rangle = E_\pm|\pm\rangle$. Differentiating it with respect to φ gives

$$\frac{\partial\hat{\mathcal{H}}}{\partial\varphi}|\pm\rangle + \hat{\mathcal{H}}\frac{\partial|\pm\rangle}{\partial\varphi} = \frac{\partial E_\pm}{\partial\varphi}|\pm\rangle + E_\pm\frac{\partial|\pm\rangle}{\partial\varphi}.$$

Substituting this in Equation (B.1) yields

$$\left\langle\frac{\partial\hat{\mathcal{H}}}{\partial\varphi}\right\rangle = \langle\pm|\left(\frac{\partial E_\pm}{\partial\varphi}|\pm\rangle + E_\pm\frac{\partial|\pm\rangle}{\partial\varphi} - \hat{\mathcal{H}}\frac{\partial|\pm\rangle}{\partial\varphi}\right). \tag{B.2}$$

$\hat{\mathcal{H}}$ being Hermitian, the Schrödinger equation can also be written $\langle\pm|\hat{\mathcal{H}} = E_\pm\langle\pm|$. Combining this with Equation (B.2) gives

$$\begin{aligned}\left\langle \frac{\partial \hat{\mathcal{H}}}{\partial \varphi} \right\rangle &= \left\langle \pm \left| \frac{\partial E_\pm}{\partial \varphi} \right| \pm \right\rangle \\ &= \frac{\partial E_\pm}{\partial \varphi}.\end{aligned}$$

Therefore the current carried by an Andreev bound state $I_\pm$ can be expressed as

$$I_\pm = \frac{1}{\varphi_0} \frac{\partial E_\pm}{\partial \varphi}. \tag{B.3}$$

C. Resolution of the differential equation governing the dynamics of a Josephson junction in series with a resistance

The differential Equation (1.47) governing the dynamics of a Josephson junction in series with a resistance can be rewritten as

$$d\tilde{t} = \frac{d\varphi}{v - \sin\varphi}.$$

Integrating from time 0 at which the phase is 0 to time $\tilde{t}$ when the phase is φ gives

$$\tilde{t} = \int_0^{\varphi} \frac{d\phi}{v - \sin\phi}.$$

Using the substitution $u = \tan\phi/2$, for which $d\phi = 2du/(1+u^2)$, transforms the integral in

$$\begin{aligned}
\tilde{t} &= \int_0^{\tan\varphi/2} \frac{1}{v - \frac{2u}{1+u^2}} \frac{2du}{1+u^2},\\
\tilde{t} &= \int_0^{\tan\varphi/2} \frac{2du}{v(1+u^2) - 2u},\\
\tilde{t} &= \frac{2}{v}\int_0^{\tan\varphi/2} \frac{du}{1+u^2-2\frac{u}{v}},\\
\tilde{t} &= \frac{2}{v}\int_0^{\tan\varphi/2} \frac{du}{\left(u-\frac{1}{v}\right)^2 + 1 - \frac{1}{v^2}}.
\end{aligned}$$

For a bias voltage larger than RI_0, $v > 1$ and this integral can be rewritten as

$$\tilde{t} = \frac{2}{v}\frac{1}{1-\frac{1}{v^2}}\int_0^{\tan\varphi/2} \frac{du}{\left(\frac{u-\frac{1}{v}}{\sqrt{1-\frac{1}{v^2}}}\right)^2 + 1}.$$

A second substitution $w = \frac{u-\frac{1}{v}}{\sqrt{1-\frac{1}{v^2}}}$ leads to

$$\tilde{t} = \frac{2}{\sqrt{v^2-1}}\int_\alpha^\beta \frac{du}{w^2+1}, \tag{C.1}$$

where the integral limits α and β are

$$\begin{cases} \alpha = \dfrac{-1}{\sqrt{v^2-1}}, \\ \beta = \dfrac{v\tan\frac{\varphi}{2}-1}{\sqrt{v^2-1}}. \end{cases}$$

The integral in Equation (C.1) is simply the arctan function, such that

$$\tilde{t} = \frac{2}{\sqrt{v^2-1}}\left(\arctan\left(\frac{v\tan\frac{\varphi}{2}-1}{\sqrt{v^2-1}}\right) + \arctan\left(\frac{1}{\sqrt{v^2-1}}\right)\right).$$

This equation can be inverted to give the phase difference across the junction as a function of time,

$$\varphi = 2\arctan\left(\sqrt{1-\frac{1}{v^2}}\tan\left(\frac{\sqrt{v^2-1}}{2}\tilde{t} - \arctan\left(\frac{1}{\sqrt{v^2-1}}\right)\right) + \frac{1}{v}\right) + 2n\pi,$$

where

$$n = \left\lfloor \frac{\frac{\sqrt{v^2-1}}{2}\tilde{t} - \arctan\left(\frac{1}{\sqrt{v^2-1}}\right) + \frac{\pi}{2}}{\pi} \right\rfloor.$$

D. Mutual inductance and coupling constant

To estimate the mutual inductance M and thus the coupling coefficient k between two loops A and B, we have to calculate the flux Φ_{AB} of the magnetic field $\vec{B}_A$ generated by the current I_A flowing in loop A through loop B:

$$\Phi_{AB} = \iint_{S_B} \vec{B}_A \cdot d\vec{S}$$

. Introducing the vector potential $\vec{A}_A$ and using Stokes theorem, this expression is

$$\Phi_{AB} = \iint_{S_B} \left(\vec{\nabla} \times \vec{A}_A\right) \cdot d\vec{S} = \oint_{\mathcal{C}_B} \vec{A}_A \cdot \vec{dl}_B.$$

The potential vector $\vec{A}_A$ generated by loop A at a distance r is

$$\vec{A}_A = \frac{\mu_0}{4\pi} \oint_{\mathcal{C}_A} \frac{I_A}{r} \vec{dl}_A.$$

So the flux Φ_{AB} is

$$\Phi_{AB} = \frac{\mu_0}{4\pi} I_A \oint_{\mathcal{C}_A} \oint_{\mathcal{C}_B} \frac{\vec{dl}_A \cdot \vec{dl}_B}{r}.$$

The proportionality constant between Φ_{AB} and I_A is the mutual inductance $M = k\sqrt{L_A L_B}$, so we get the Neumann formula:

$$\boxed{M = \frac{\mu_0}{4\pi} \oint_{\mathcal{C}_A} \oint_{\mathcal{C}_B} \frac{\vec{dl}_A \cdot \vec{dl}_B}{r}}.$$

E. Mutual inductance between two concentric circular loops

It is possible to get an analytic expression for the mutual inductance between two concentric circular loops (represented in Figure 2.24) of radii r_A and r_B, using the Neumann formula:

$$M = \frac{\mu_0}{4\pi} \oint_{\mathcal{C}_A} \oint_{\mathcal{C}_B} \frac{\vec{dl}_A \cdot \vec{dl}_B}{r}.$$

If we parameterize the A loop with angle ϕ and the B loop with angle θ and if we call d the distance between the two loops centers,

$$\begin{aligned}
\vec{dl}_A &= r_A \left(-\sin\phi \vec{a}_x + \cos\phi \vec{a}_y\right) d\phi, \\
\vec{dl}_B &= r_B \left(-\sin\theta \vec{a}_x + \cos\theta \vec{a}_y\right) d\theta, \\
\vec{dl}_A \cdot \vec{dl}_B &= r_A r_B \cos\left(\phi - \theta\right) d\phi d\theta, \\
r &= \sqrt{r_A^2 + r_B^2 + d^2 - 2 r_A r_B \cos\left(\phi - \theta\right)}.
\end{aligned}$$

Substituting these expressions in the double integral gives

$$M = \frac{\mu_0}{4\pi} \int_0^{2\pi} \int_0^{2\pi} \frac{r_A r_B \cos\left(\phi - \theta\right)}{\sqrt{r_A^2 + r_B^2 + d^2 - 2 r_A r_B \cos\left(\phi - \theta\right)}} d\phi d\theta.$$

Using the rotation symmetry of the loops, it is possible to reduce this double integral to a simple integral: the integral over ϕ is the same independently of the value of the angle θ. Mathematically, this is equivalent to the substitution:

$$\begin{cases} \gamma = \phi - \theta, \\ \theta = \theta. \end{cases}$$

This gives

$$M = \frac{\mu_0}{2} \int_0^{2\pi} \frac{r_A r_B \cos\gamma}{\sqrt{r_A^2 + r_B^2 + d^2 - 2 r_A r_B \cos\gamma}} d\gamma.$$

Using the fact that

$$\int_0^{2\pi} \frac{\cos\gamma}{\sqrt{a - b\cos\gamma}} d\gamma = \frac{4\sqrt{a+b}}{b} \left(\frac{a}{a+b} K\left(\beta\right) - E\left(\beta\right) \right),$$

where K and E are complete elliptic integrals of the first and second kind as already defined in Section 1.2.3. The argument β is

$$\beta = \sqrt{\frac{2b}{a+b}}$$

. This gives an expression for M:

$$\begin{aligned} M &= \mu_0\sqrt{\left(r_A+r_B\right)^2+d^2}\left(\frac{r_A^2+r_B^2+d^2}{\left(r_A+r_B\right)^2+d^2}K\left(\beta\right)-E\left(\beta\right)\right), \\ \text{with } \beta &= 2\sqrt{\frac{r_Ar_B}{\left(r_A+r_B\right)^2+d^2}}. \end{aligned} \tag{E.1}$$

The inductances of loops A and B: L_A and L_B are in first order [104]

$$\begin{cases} L_A = \mu_0 r_A\left(\ln\dfrac{8r_A}{a}-2\right), \\ L_B = \mu_0 r_B\left(\ln\dfrac{8r_B}{a}-2\right), \end{cases} \tag{E.2}$$

where a is the width of the wires. In practical, the r_A/a and r_B/a ratios are close enough, so that the factor in parentheses in the expressions for L_A and L_B can be taken equal to the same value γ of order $1-2$. This gives for k:

$$k = \frac{1}{\gamma}\sqrt{\frac{\left(r_A+r_B\right)^2+d^2}{r_Ar_B}}\left(\frac{r_A^2+r_B^2+d^2}{\left(r_A+r_B\right)^2+d^2}K\left(\beta\right)-E\left(\beta\right)\right).$$

F. Flux focusing

When a magnetic field of magnitude B_e is applied to a Josephson junction, currents flow in the superconductor to prevent the magnetic field from penetrating. These currents create a magnetic field opposed to the applied field, such that the magnetic field is zero inside the superconductor. Figure F.1 shows the resulting magnetic field in a plane perpendicular to a Josephson junction. Here, the applied magnetic field $\vec{B}_e$ is along the vertical axis as represented in the figure. The two black rectangles in the center of the figure are the two superconducting electrodes forming the Josephson junction where they overlap. They have an extension L in the direction perpendicular to the plane of the figure. The plotted magnetic field was calculated using the 3D-MLSI simulator [73]. The magnetic field is not exactly zero everywhere in the superconductor because it can penetrate on a thickness of the order of the London length before being damped. In the junction, the amplitude of the field is larger than B_e: most of the field lines in the green region of width W are deviated through the junction. This results in a flux threading the junction of the order B_eLW, in general much larger than B_eLt (where t is the thickness of the barrier and thus the junction). There is no simple formula for W but it is easy to get an approximation with a simple physical argument:

If the length L was infinite, there would only be three possible paths for the magnetic field lines to cross the superconductors: getting around them by the left-hand side or by the right-hand side or crossing the junction. This results in three different regions in space, the size of which should be equal. Thus, $L \sim D/3$, where D is the total width of the superconductors.

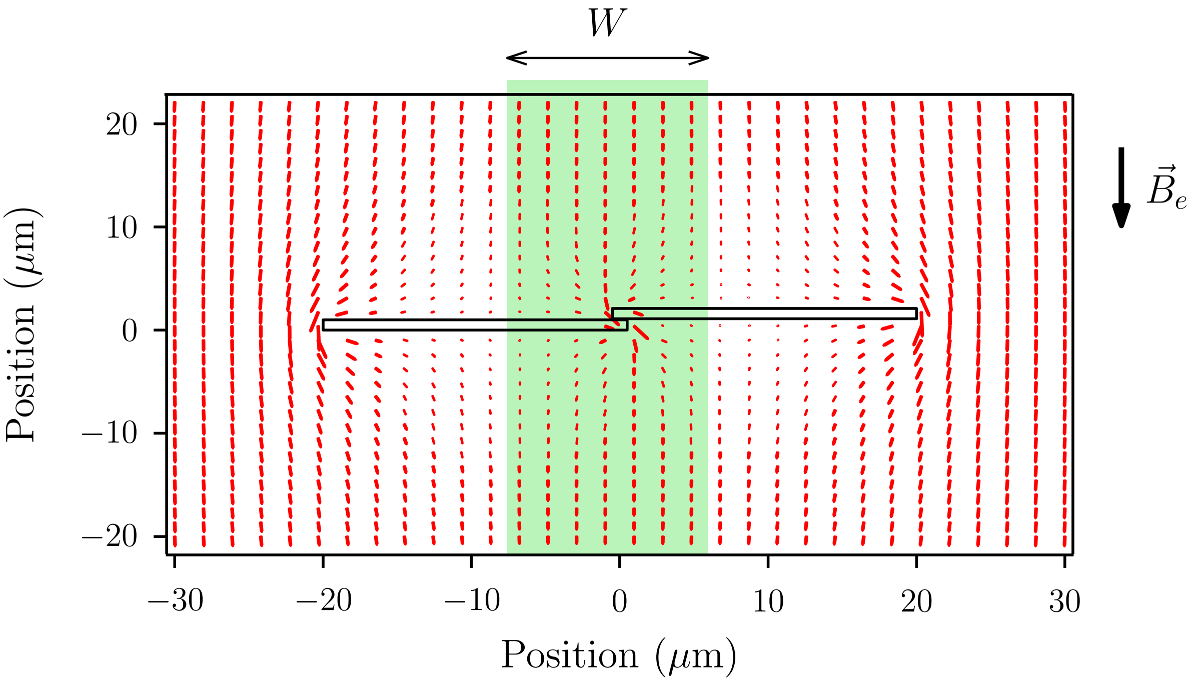

Figure F.1.: Flux focusing.

G. Quasiparticle current

The current through the junction is

$$I_N(V) = e\left(\overrightarrow{\Gamma}(V) - \overleftarrow{\Gamma}(V)\right),$$
$$I_N(V) = e\left(\overrightarrow{\Gamma}(V) - \overrightarrow{\Gamma}(-V)\right).$$

Using the calculated expression for $\overrightarrow{\Gamma}(V)$, this gives

$$I_N(V) = \frac{1}{eR_N}\left(\iint_{-\infty}^{+\infty} \frac{n_S(E)\, n_S(E'+eV)}{n_N^2} f(E)\left(1 - f\left(E'+eV\right)\right) P(E-E')dEdE' \right.$$
$$\left. - \iint_{-\infty}^{+\infty} \frac{n_S(E)\, n_S(E'-eV)}{n_N^2} f(E)\left(1 - f\left(E'-eV\right)\right) P(E-E')dEdE' \right).$$

The substitutions $\tilde{E} = E' + eV$ in the first integral and $\tilde{E} = E' - eV$ in the second integral give

$$I_N(V) = \frac{1}{eR_N}\left(\iint_{-\infty}^{+\infty} \frac{n_S(E)n_S(\tilde{E})}{n_N^2} f(E)\left(1 - f(\tilde{E})\right) P(E-\tilde{E}+eV)dEd\tilde{E} \right.$$
$$\left. - \iint_{-\infty}^{+\infty} \frac{n_S(E)n_S(\tilde{E})}{n_N^2} f(E)\left(1 - f(\tilde{E})\right) P(E-\tilde{E}-eV)dEd\tilde{E} \right).$$

Inverting the role of E and $\tilde{E}$ in the second integral gives

$$I_N(V) = \frac{1}{eR_N}\left(\iint_{-\infty}^{+\infty} \frac{n_S(E)n_S(\tilde{E})}{n_N^2} f(E)\left(1 - f(\tilde{E})\right) P(E-\tilde{E}+eV)dEd\tilde{E} \right.$$
$$\left. - \iint_{-\infty}^{+\infty} \frac{n_S(E)n_S(\tilde{E})}{n_N^2} f(\tilde{E})\left(1 - f(E)\right) P(\tilde{E}-E-eV)dEd\tilde{E} \right).$$

The detailed balance relation [66]: $P(-E) = \mathrm{e}^{-\beta E}P(E)$ allows writing the current as

$$I_N(V) = \frac{1}{eR_N}\left(\iint_{-\infty}^{+\infty} \frac{n_S(E)n_S(\tilde{E})}{n_N^2} f(E)\left(1 - f(\tilde{E})\right) P(E-\tilde{E}+eV)dEd\tilde{E} \right.$$
$$\left. - \iint_{-\infty}^{+\infty} \frac{n_S(E)n_S(\tilde{E})}{n_N^2} f(\tilde{E})\left(1 - f(E)\right) P(E-\tilde{E}+eV)\mathrm{e}^{-\beta(E-\tilde{E}+eV)}dEd\tilde{E} \right).$$

Regrouping the two integrals together yields

$$
\begin{aligned}
I_N(V) = \frac{1}{eR_N} \iint_{-\infty}^{+\infty} & \frac{n_S(E) n_S(\tilde{E})}{n_N^2} P(E - \tilde{E} + eV) \\
& \left(f(E) \left(1 - f(\tilde{E})\right) - f(\tilde{E}) \left(1 - f(E)\right) \mathrm{e}^{-\beta(E - \tilde{E} + eV)} \right) dE d\tilde{E}.
\end{aligned}
$$

Calling $E' = \tilde{E} - E$ transforms this integral to

$$
\begin{aligned}
I_N(V) = \frac{1}{eR_N} \iint_{-\infty}^{+\infty} & \frac{n_S(E) n_S(E + E')}{n_N^2} P(eV - E') \\
& \left(f(E) \left(1 - f(E + E')\right) - f(E + E') \left(1 - f(E)\right) \mathrm{e}^{-\beta(eV - E')} \right) dE dE'.
\end{aligned}
$$

Noticing that

$$
f(E) \left(1 - f(E + E')\right) = \frac{f(E) - f(E + E')}{1 - \mathrm{e}^{-\beta E'}},
$$

it is possible to express the current as

$$
\begin{aligned}
I_N(V) = \frac{1}{eR_N} \iint_{-\infty}^{+\infty} & \frac{n_S(E) n_S(E + E')}{n_N^2} \left(f(E) - f(E + E') \right) \\
& P(eV - E') \left(\frac{1}{1 - \mathrm{e}^{-\beta E'}} + \frac{\mathrm{e}^{-\beta(eV - E')}}{1 - \mathrm{e}^{\beta E'}} \right) dE dE'.
\end{aligned}
$$

The first line of this expression is Equation (3.8) for the quasiparticle current without environment. This gives the following expression for the current in presence of an environment.

$$
I_N(V) = \int_{-\infty}^{+\infty} I_{N,0} \left(\frac{E'}{e} \right) P(eV - E') \frac{1 - \mathrm{e}^{-\beta eV}}{1 - \mathrm{e}^{\beta E'}} dE'.
$$

H. Fabrication processes

This appendix describes the fabrication processes used to make devices SSQ05, SSQ14 and HS04, presented in Section 4.3.1, 4.3.2 and 4.3.3, as well as the spectrometers used in Chapter 5 based on the design of HS04. They include several lithography and evaporation steps. Sample SSQ05 has the simplest recipe and was realized in one lithography and one three-angle evaporation step. Sample SSQ14 needed two evaporation steps. One for the junctions and a second to add the shunt capacitors. Sample HS04 is the most complex design and required three evaporation steps. It is based on the recipe for SSQ14 with an additional evaporation for the resistive leads. This is summarized in Table H.1.

H.1. Optical lithography

All lithography steps used in the recipes for samples SSQ05, SSQ14 and HS04 are similar. They were performed with the Laserwriter LW405B allowing for patterning with an ultra-violet laser ray of diameter $\sim 800\,\mathrm{nm}$. The laser source is a GaN diode laser emitting at 405 nm. The stage on which the wafer sits can move along three perpendicular axes: a first vertical one to allow for a good focusing of the laser on the substrate and the two others to pattern the desired design.

Prior to exposure, MicroChem resist LOR5B is poured on a silicon wafer and spun at 1000 rpm during 60 s, resulting in a layer of $\sim 850\,\mathrm{nm}$. The substrate is subsequently baked at 200 °C for 5 min. When it is cooled down, Shipley resist S1813 is poured, spun at 3000 rpm for 45 s and baked at 115 °C for 1 min. The resulting layer is 1.5 µm thick. Only the top S1813 layer is photosensitive (to ultra-violet light). The bottom LOR5B layer develops as soon as it is in contact with the developer solution.

The prepared wafer is then loaded in the optical lithography setup and exposed at an energy

SSQ05	**SSQ14**	**HS04**
Optical lithography 1	Optical lithography 1	Optical lithography 1
Evaporation of the junctions	Evaporation of the junctions	Evaporation of the junctions
	Optical lithography 2	Optical lithography 2
	Evaporation of the shunt capacitors	Evaporation of the shunt capacitors
		Optical lithography 3
		Evaporation of the resistive leads

Table H.1.: Summary of the fabrication of samples SSQ05, SSQ14 and HS04.

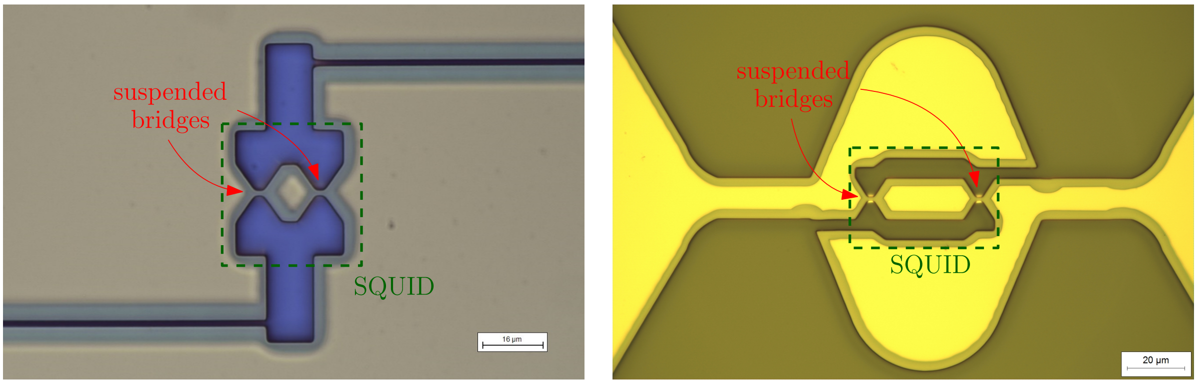

Sample SSQ05

Sample HS04

Figure H.1.: Samples after the first optical lithography step.

close to 200 mJ cm^{-2} following the designed pattern. It is then developed in a MF319 solution during 30 s and rinsed with water to stop development.

Figure H.1 shows samples SSQ05 and HS04 after the development following the first lithography step. The purple zones are the regions where both LOR5B and S1813 are removed. In the brightest regions, both resists are still present. In the zones between both colors, only the top layer is present, such that the regions indicated by red arrows consist of suspended bridges of S1813. These are the places where the junctions will be located. The loop of the SQUIDs will be formed of the material evaporated in the developed zones in the dashed green rectangles. The main difference between SSQ05 and HS04 resides in the width of the horizontal lines leaving the SQUIDs. For SSQ05, they were made as thin as possible, close to 1 µm, whereas for HS04 they are designed to be 6 µm wide.

H.2. Material evaporation

Deposition of metals and aluminum oxide is performed in a Plassys electron gun evaporator. The pressure in the chamber where the wafer sits is of the order of $10^{-7} - 10^{-6}$ mbar. It is in the 10^{-8} mbar range in a second chamber (~ 50 cm below) where the materials are sublimated by an electron beam.

After each evaporation, the samples are placed in a hot NMP bath at 80 °C during at least 1 h and then rinsed with isopropanol.

H.2.1. Sample SSQ05

In sample SSQ05, inductive leads are wanted between the SQUID and the bonding pads. To fabricate them, we use a three-angle evaporation technique allowing for thin leads connected to the SQUID without breaking the vacuum of the chamber. Figure H.2 explains this method for two typical patterns: a Josephson junction (on the left-hand side of the picture) and a single wire (on the right-hand side).

(a) 100 nm of titanium is evaporated vertically (in green) at a rate of 0.5 nm s^{-1}.

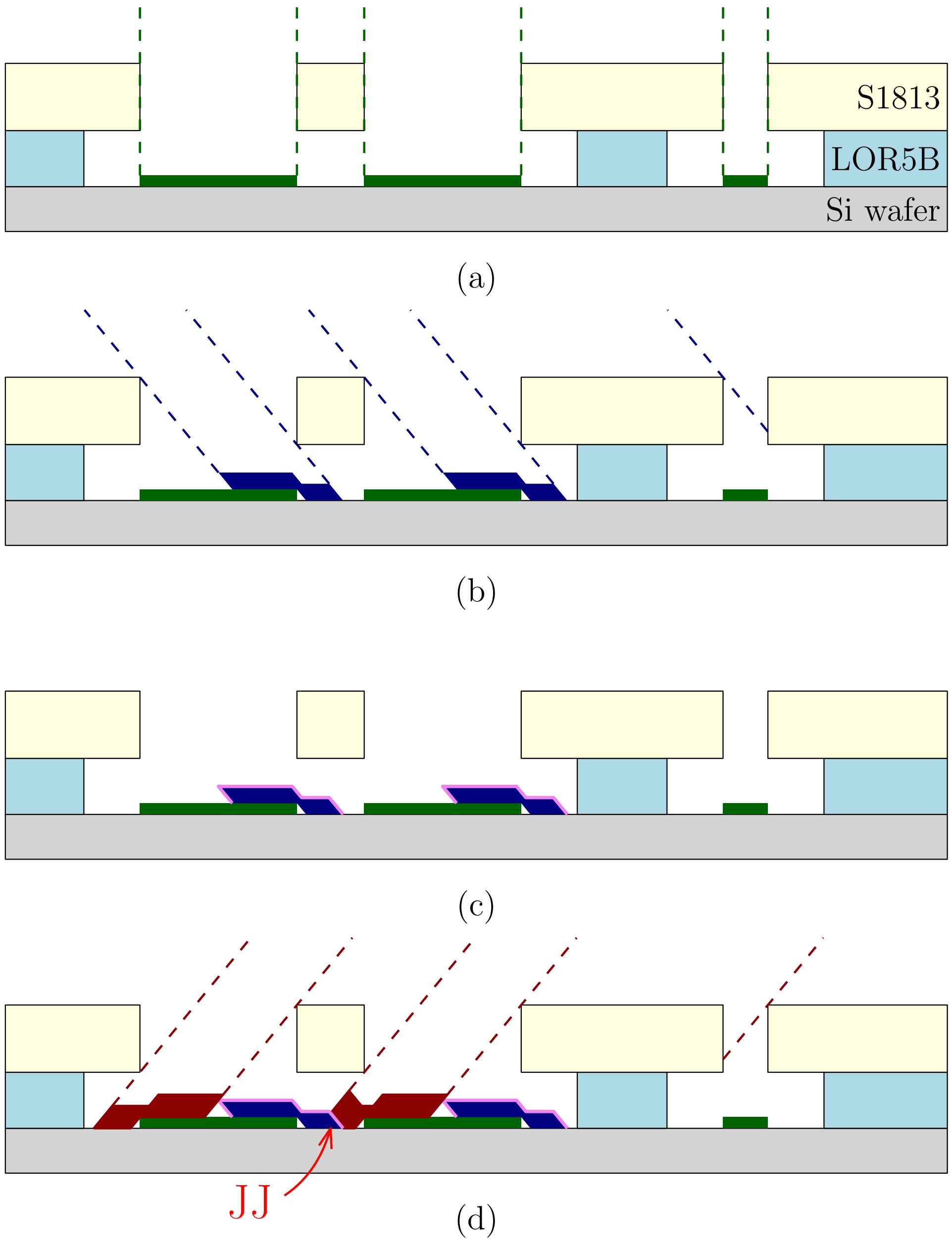

(a)

(b)

(c)

(d)

Figure H.2.: Three angle evaporation technique.

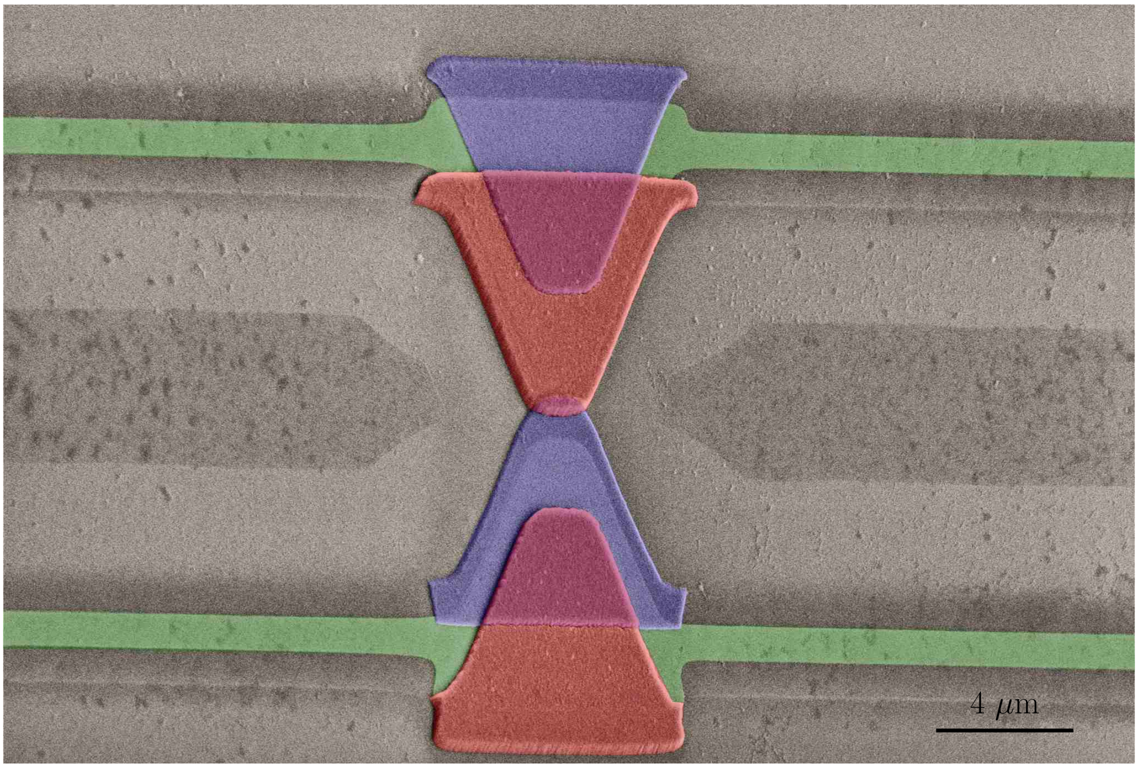

Figure H.3.: False colors SEM picture of a Josephson junction with titanium leads.

(b) A first layer of 150 nm of aluminum (in blue) is evaporated at a rate of $1\,\mathrm{nm\,s^{-1}}$ with an angle of $\sim 45°$ with respect to the vertical axis. In the design for the wire, all aluminum is evaporated onto the upper layer of resist.

(c) Oxygen is allowed in the chamber at a pressure of 200 mbar for 10 min, oxidizing the top of the aluminum layer. Alumina is depicted in violet.

(d) A second layer of 200 nm of aluminum (in red) is evaporated at a rate of $1\,\mathrm{nm\,s^{-1}}$ with the opposite angle with respect to the vertical axis. If the angle is chosen correctly, a Josephson junction (JJ) is formed under the bridge (indicated with a red arrow).

Figure H.3 shows a SEM (Scanning Electron Microscope) picture of a Josephson junction of area slightly smaller than $2\,\mathrm{\mu m^2}$ obtained with the three-angle evaporation technique. The blue and red zones are the two superconducting electrodes connected to the junction and the purple zones are the overlaps between the two electrodes. The junction is the small overlap in the center of the picture, and the green wires are highly-inductive titanium wires.

H.2.2. Samples SSQ14 and HS04

Evaporation of the junctions

For these samples, the inductance out of the loop of the SQUID is made smaller. To do so, the lines are designed wider, as shown in Figure H.1, and the leads are made in aluminum.

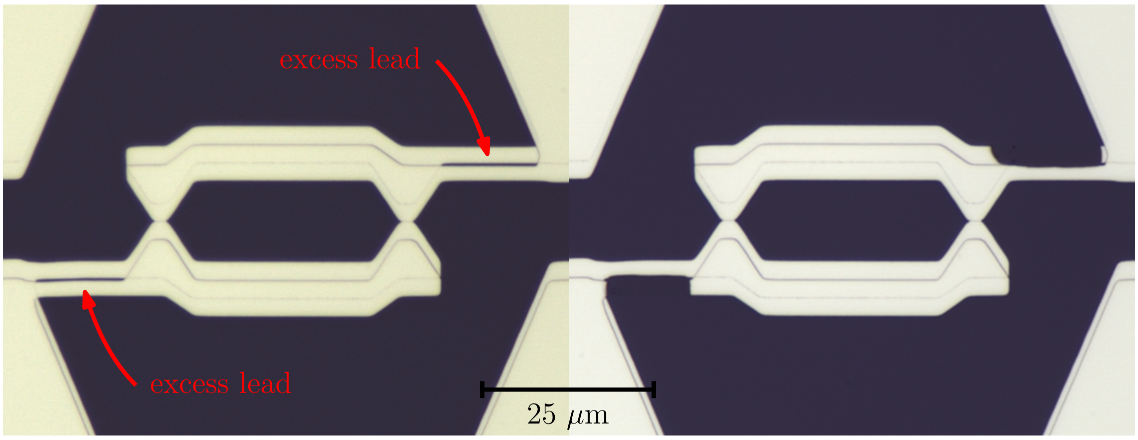

(a) Before etching (b) After etching

Figure H.4.: Microscope picture of a SQUID before and after etching the excess leads.

The first angle of the three-angle method used for sample SSQ05 is skipped. The result of this evaporation is shown in the left-hand side picture of Figure H.4 for sample HS04. It is not exactly the expected design as each lead is evaporated twice. In this design, each excess lead forms a loop with the desired lead closed by a large Josephson junction. This forms a RF-SQUID which has a resonance frequency possibly in the bandwidth of the spectrometer as shown in Appendix I. The excess leads have thus to be removed. To do so, a wet etching process is used:

- a thin layer of photosensitive resist is spun on the sample,
- a window is patterned in the resist on the unwanted lead,
- the sample is immersed in the developer for 5 more minutes than for a standard development to etch aluminum in the window.

The result of this process is shown in the right-hand side picture of Figure H.4.

Evaporation of the shunt capacitors

For samples SSQ14 and HS04, capacitors are patterned in another optical lithography process. After development and when the sample is put in the chamber, it is first etched with argon ions to remove the oxide layer which can contain impurities due to contact to air. The etching is performed with a current of 20 mA and a beam voltage of 500 V for 90 s with a tilt angle of 45° while the planetary is rotating at 5 rpm.

After this step, pure oxygen is allowed in the chamber up to a pressure of 200 mbar during 2 min to oxidize the top layer of aluminum with a good stoichiometry. After that, 125 nm of aluminum oxide is evaporated with a tilt angle of 45° at a rate of 0.2 nm s^{-1} while the planetary is rotating at 5 rpm. The rotation of the planetary and the tilt angle allow the aluminum easily climbing on top of the previously evaporated aluminum layers. Pure oxygen is again allowed in the chamber at the end of the alumina evaporation to make sure that the top of the oxide is of good quality. 150 nm of aluminum is finally evaporated vertically at a rate of 1 nm s^{-1}.

Evaporation of the resistive leads

For sample HS04, resistive leads are fabricated directly on the substrate. To guarantee a good electrical contact between them and the layer of aluminum below, when the sample is in the evaporator chamber, it is first etched with argon ions (with the same parameters as above) to remove the layer of aluminum oxide which formed when the sample was in the air. The evaporated leads are made of a first layer of 25 nm of palladium evaporated vertically at a rate of $0.2\,\mathrm{nm\,s^{-1}}$, on top of which is stacked a second layer of 45 nm of hafnium evaporated vertically at a rate of $0.2\,\mathrm{nm\,s^{-1}}$.

H.3. Comments on the shape of the junctions

The trapezoidal shape of the aluminum electrodes allows making sure that no spurious junction is added. Figure H.5 shows a sketch of evaporated junctions viewed from the top. The blue and red polygons are aluminum planes and the violet region is the Josephson junction.

If the two electrodes have rectangular shapes, as shown in panel (a), the current I represented in the figure has to cross the two regions (1) and (2) circled in black. If the blue layer is evaporated first, the current stays in the blue layer in region (1). But in region (2), the red layer is deposited above the blue one. If it is slightly shifted leftwards (due for instance to a misalignment with respect to the rotation axis for the evaporation) or thinner than the first layer, the wire through which the current I exits the device can be discontinuous because of the step due to the first layer. The current has to cross two additional Josephson junctions. Using a trapezoidal shape prevents this situation as can be seen in panel (b).

The biasing and measurement wires are also always connected on the sides of the junction to avoid parasitic junctions. (c) shows a situation with wires leaving the junction vertically. In that case, the current I arriving in the bottom blue lead crosses first the violet Josephson junction and has then to cross a large junction (the hatched violet area) between the red and blue layers before leaving in the top blue lead.

The design used in the following is that of panel (b).

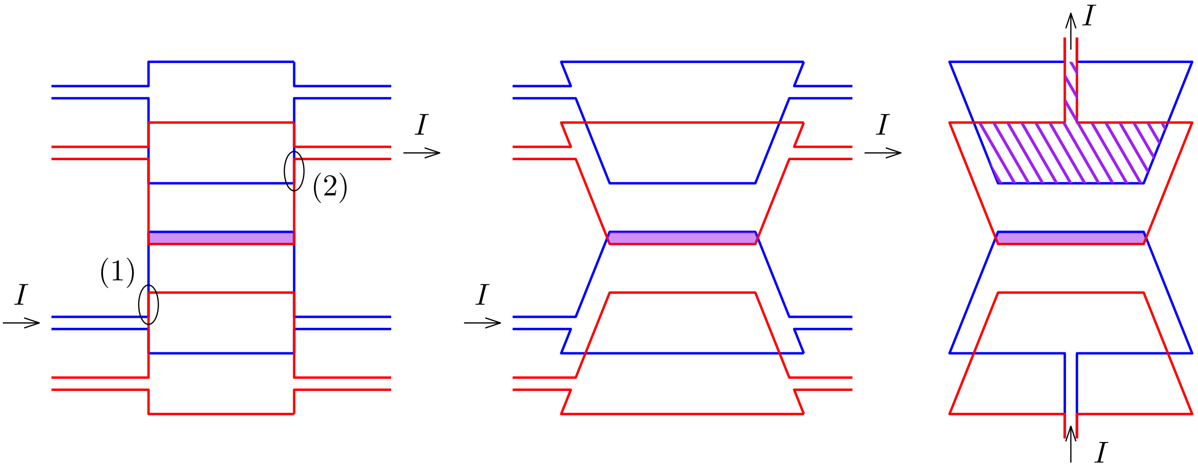

(a) (b) (c)

Figure H.5.: Three envisaged geometries for a junction.

I. Parasitic modes introduced by excess leads

Figure I.1 shows the microscope picture of a SQUID with two extra leads, labeled (α) and (β) in the figure. Each of these leads forms a RF-SQUID with the other lead. The Josephson junctions of these two RF-SQUIDs are shown in green. The equivalent electrical schematic is shown in Figure I.2, where the central SQUID is shown in blue. The two green Josephson junctions have critical current I_α and I_β.

The current-voltage characteristic of this device is shown in Figure I.3. In (a), the sample is flux-biased at $\varphi_e = 0$ and π. There are some visible peaks due to resonances in the large aluminum planes and other off-loop modes. At $\varphi_e = \pi$, all these peaks disappear. As shown in (b), the first of these peaks moves when magnetic field is applied and this displacement is not 2π periodic. (c) shows how this peak moves for applied flux from values smaller than $-3\Phi_0$ to larger than $2\Phi_0$. The measured pattern is not easy to decipher, but resembles two interlacing patterns with different periodicity which could come from the two RF-SQUIDs visible in Figures I.1 and I.2.

Lead (α) was etched using the method described in Section H.2.2 in order to verify this hypothesis. The measured spectrum is shown in (d). The pattern is now much simpler and is consistent with the expected plasma resonance for a RF-SQUID plotted in red on top of the spectrum. This red line was calculated, assuming not only the modulation of the plasma resonance of the RF-SQUID, but also the possibility for the large Josephson junction of the RF-SQUID to be threaded by magnetic field.

According to the calculations of Section 2.4.2, the supercurrent I_C of a Josephson junction threaded by a magnetic field is modulated via:

$$I_C = I_0 \left| \mathrm{sinc} \frac{\Phi_{JJ}}{2\varphi_0} \right|$$

Where Φ_{JJ} is the flux through the Josephson junction (and not in the loop of the RF-SQUID).

The plasma frequency of a RF-SQUID is derived in Chapter 5. It is

$$\omega_p = \omega_{p0} \sqrt{\frac{1}{\beta_L} + \cos\varphi_m}$$

Where ω_{p0} is the plasma frequency of the Josephson junction, $\beta_L = LI_C/\varphi_0$ is the ratio of the loop inductance to the Josephson inductance and φ_m is solution of

$$\varphi_m + \beta_L \sin\varphi_m = \frac{\Phi_x}{\varphi_0}$$

Φ_x is the flux threading the loop of the RF-SQUID. In our case, not only φ_m depends on the magnetic field, but also ω_{p0} and β_L. However, the dependence is softer for ω_{p0} and β_L, as $\omega_{p0} \propto \sqrt{I_C}$ and $\beta_L \propto I_C$.

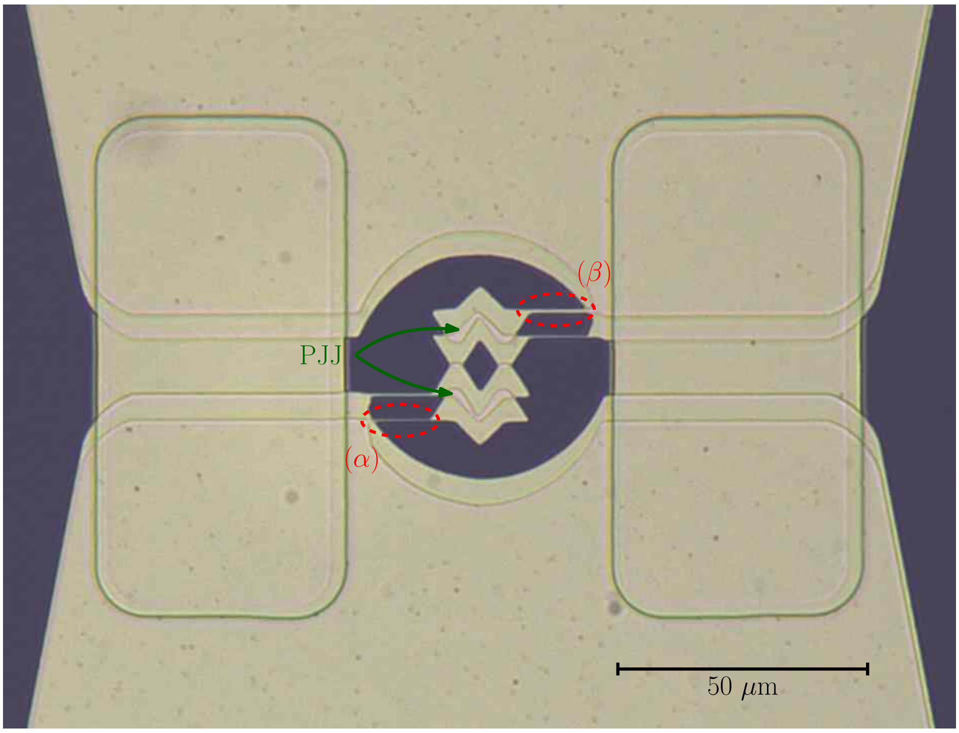

Figure I.1.: Microscope picture of a SQUID with two extra leads.

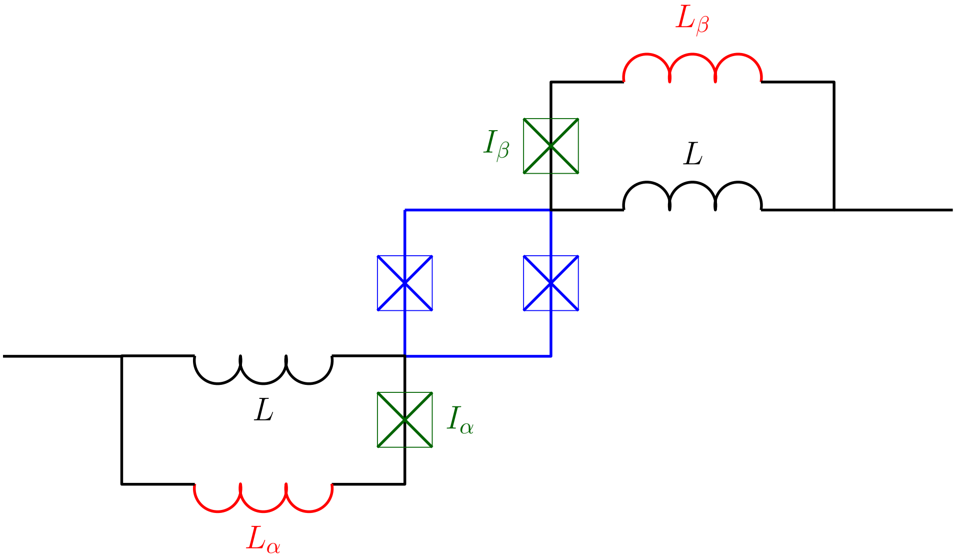

Figure I.2.: Electrical schematic of the SQUID with the two extra leads.

The fluxes Φ_x and Φ_{JJ} are both related to the applied magnetic field B via

$$\begin{cases} \Phi_x = BS_{RF} \\ \Phi_{JJ} = BS_{JJ} \end{cases}$$

S_{RF} and S_{JJ} are the surfaces of the loop of the RF SQUID and the large Josephson junction.

The red line in the figure was plotted with $\beta_L = 0.45$ and a ratio $S_{RF}/S_{JJ} = 9.8$. This ratio is quite far from the actual ratio between the surfaces of the loop $\mathcal{A}_{RF} = 52\,\mu\mathrm{m}^2$ and $\mathcal{A}_{JJ} \sim 2\,\mathrm{nm} \times 10\,\mu\mathrm{m} = 0.02\,\mu\mathrm{m}^2$. This is due to the magnetic field focusing by the superconductors: if a magnetic field is applied to the sample along an axis perpendicular to the plane of Figure I.1, it cannot penetrate the aluminum planes which are superconducting. The field lines are thus deviated and take the shortest way to reach the other side of the superconductors. The area to take to calculate the flux threading the Josephson junction is thus much larger than $\mathcal{A}_{JJ}$.

Finally, spectrum (e) of Figure I.3, was taken after that the second lead (β) was etched, leaving no resonance modulating with the magnetic field.

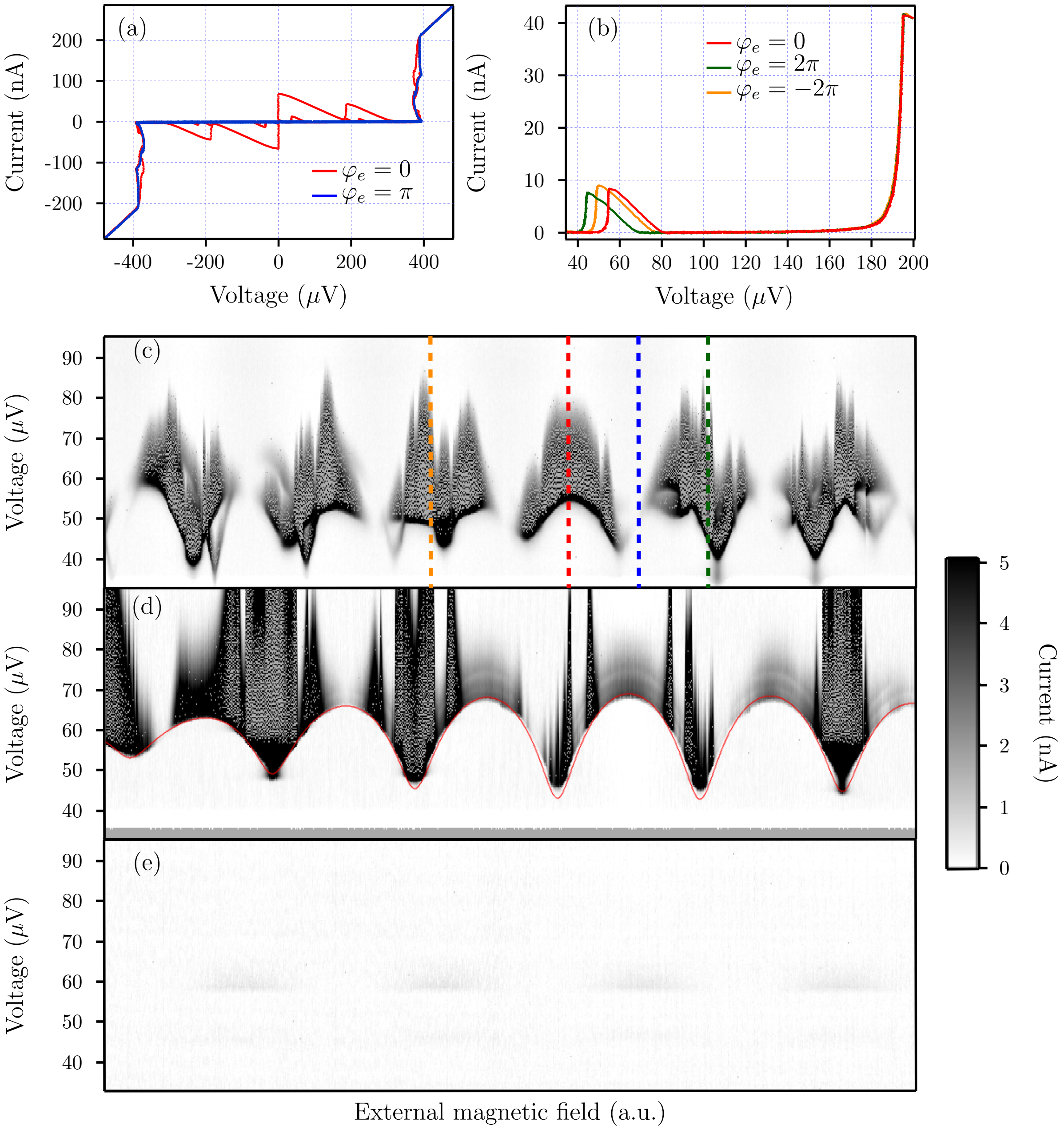

Figure I.3.: (a) Current-voltage characteristic at $\varphi_e = 0$ and π of the device of Figure I.1; (b) Zoom on the two first peaks at different applied flux ; (c) Map of IV characteristics for the same device ; (d) Map of IV characteristics without lead (α) ; (e) Map of IV characteristics without leads (α) and (β).

J. Derivation of an expression for the kinetic inductance

To derive the kinetic inductance of a superconductor, let's focus on its complex conductivity $\sigma(\omega) = \sigma_1(\omega) - i\sigma_2(\omega)$.

At zero temperature, the real part of the conductivity is 0 for frequencies below $2\Delta/\hbar$ because there only exists a non-dissipative current of Cooper pairs at these frequencies.

Tinkham [41] gives an expression for the imaginary part at zero temperature and low frequencies ($\hbar\omega \ll 2\Delta$):

$$\frac{\sigma_2(\omega)}{\sigma_n} = \frac{\pi\Delta}{\hbar\omega},$$

where σ_n is the conductivity in the normal state.

The complex impedance of a piece of superconductor of length l and section S is

$$Z(\omega) = \frac{l}{S\sigma(\omega)}.$$

At low frequencies, it is thus

$$Z(\omega) = i\frac{l}{S\sigma_2(\omega)},$$

$$Z(\omega) = i\frac{l}{S\sigma_n}\frac{\hbar\omega}{\pi\Delta}.$$

The resistance R_0 of the same piece of metal in the normal state is $R_0 = l/(S\sigma_n)$. This yields

$$Z(\omega) = i\frac{\hbar R_0}{\pi\Delta}\omega.$$

This expression is the impedance of an inductance L_K, called the kinetic inductance, such that

$$L_K = \frac{\hbar}{\pi\Delta}R_0.$$

K. Microwave simulation using Sonnet

The devices presented in Chapter 4 were simulated using Sonnet, a high frequency electromagnetic software. This software allows simulating planar metallic layers separated by dielectrics. It includes the possibility to simulate superconductors by taking into account their kinetic inductance. Sonnet encloses this stack of materials in a box with perfectly conducting metallic walls. This can unfortunately generate resonance modes due to the finite size of the box[1]. Sonnet then uses a finite element method to calculate the impedance and scattering matrices at each port in a specified frequency range.

As the two Josephson junctions of the SQUID act as microwave sources, they are designed in the Sonnet simulations as internal ports. It is possible to simulate the behavior of the SQUID at $\varphi_e = 0$ and π, by giving a different phase to the two ports. At $\varphi_e = 0$, the two junctions have the same phase difference, so they both generate microwaves at the same phase. On the contrary, at $\varphi_e = \pi$, both junctions have opposite phase differences, which is equivalent to adding a π phase difference between the ports in Sonnet. In addition, a capacitance is added in parallel of each port to account for the intrinsic capacitance C_J of the junctions.

K.1. Sample SSQ14

Figure K.1 shows the result of the simulation of sample SSQ14 with Sonnet. Panel (a) shows the real part of the impedance seen by the junction and panel (b) shows the z parameter introduced in Chapter 2,

$$z = \frac{\Re(Z)\, I_0}{V}.$$

For sample SSQ14, the critical current is $I_0 = 250\,\mathrm{nA}$. This corresponds to a minimal detectable z of $z_{min} = 5 \times 10^{-7}$. This simulation shows a high and narrow peak at 24 GHz, a smaller peak at 7 GHz and a wider and less intense peak around 70 GHz. To identify them, the current density was also simulated, as shown in Figure K.1, simulated at 24 GHz. Panels (a) and (b) show the amplitude of the current density in the x and y directions. Panel (c) and (d) show the phase of these currents. They circulate around the central region and correspond to a dipole-like mode.

The peaks at 7 GHz and 70 GHz are resonant modes due to the finite size of the box. This was observed by changing the size of the simulation box. When it was made smaller, the resonant frequencies moved to higher values.

---

[1] In the following simulations, these modes are damped by adding an extra layer of a material with high permeability and magnetic losses. This extra layer is present in the experimental setup. It is the material introduced in Section 4.4.

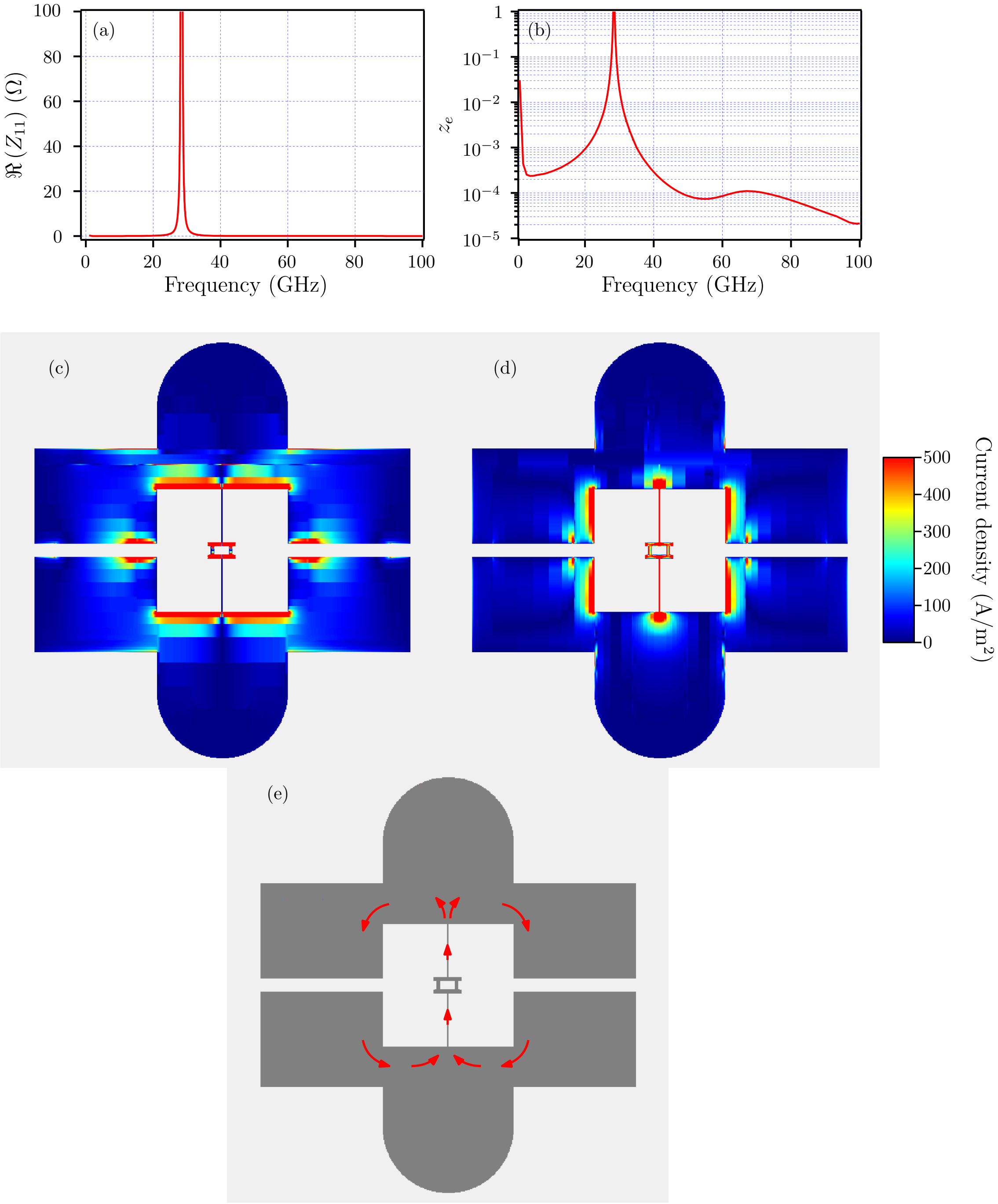

Figure K.1.: Simulation of sample SSQ14 with Sonnet. (a) Real part of the impedance seen by the junction ; (b) Corresponding z parameter ; Distribution of the current density at 24 GHz: (c) Current density in the x direction ; (d) Current density in the y direction ; (e) Schematic direction of the currents.

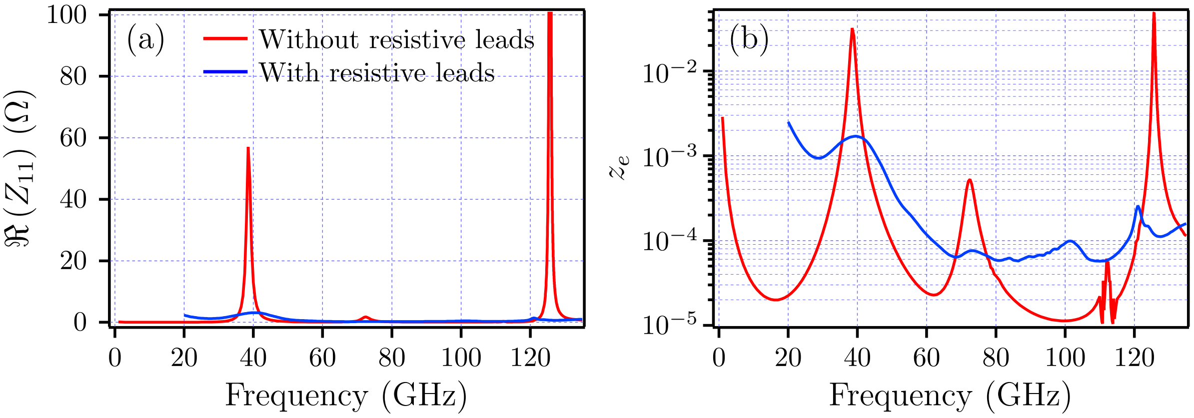

Figure K.2.: Simulation of sample HS04 using Sonnet with and without resistive leads.

K.2. Sample HS04

Figure K.2 shows the results of the simulation of sample HS04 with (blue) or without (red) resistive leads. Without leads, there are four main peaks, at 38.5 GHz, 72.5 GHz, 112 GHz and 126 GHz. The first peak is the same as observed for SSQ14 at 24 GHz. It is at smaller frequency because the size of the sample is larger, in particular the size of the loop around the central SQUID. The current distributions for the modes at 72.5 and 126 GHz are shown in Figure K.3. These modes correspond to “drumhead” like modes with currents circulating in the large aluminum regions above and below the central region. The mode at 112 GHz has a similar current distribution. The small peaks in its vicinity in Figure K.2 are due to box resonances at frequencies close to 112 GHz.

Adding resistive leads damps all these modes as visible in panel (b) of Figure K.2 and also lowers the two highest resonant frequencies.

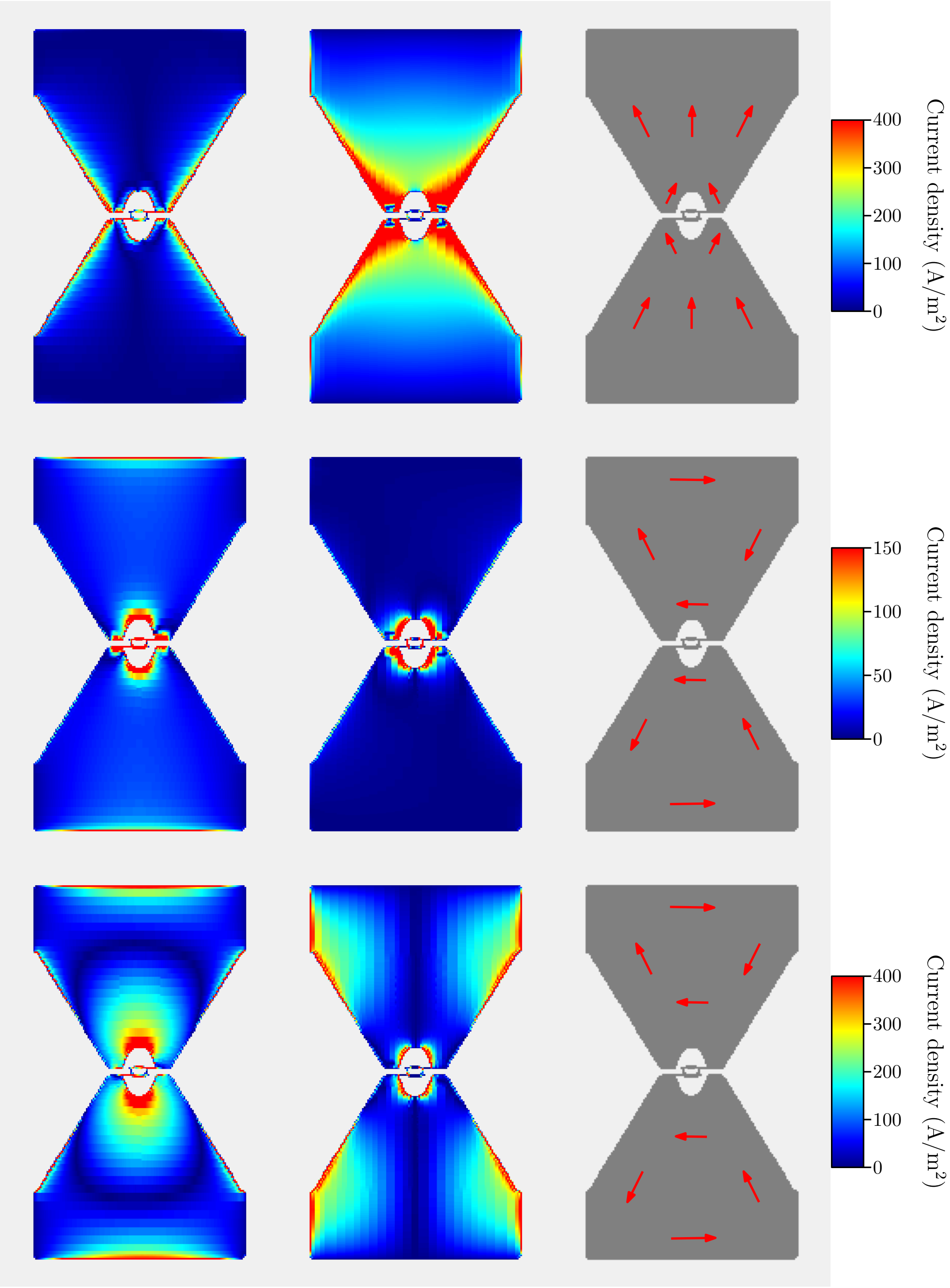

(a) 38.5 GHz

(b) 72.5 GHz

(c) 126 GHz

Figure K.3.: Current distribution in HS04 at 38.5, 72.5 and 126 GHz in the x direction (left-hand side column) and in the y direction (center column) and schematic direction of the currents (right-hand side column).

K.3. Spectroscopy of the RF-SQUID

The spectrometer presented in Section 5.4.2 was simulated using Sonnet. The simulation is close to the one described in Appendix K.2. Compared to this simulation, the gradiometric flux line was added, as well as the probed RF-SQUID. The Josephson junction of the RF-SQUID was modeled by a capacitance in parallel with an inductance. The capacitance represents the intrinsic capacitance of the Josephson junction, here of order 80 fF, while the inductance represents the Josephson inductance $L_J = \varphi_0/I_0 \sim 1\,\mathrm{nH}$ of the junction. When a magnetic flux is applied to the RF-SQUID, the phase difference across the Josephson junction is modified, resulting in a different Josephson inductance. This is how the effect of the magnetic field is implemented in the simulation. With this method, it is only possible to simulate values of the phase difference φ_x across the junction of the SQUID between $-\pi/2$ and $\pi/2$. For $\varphi_x > \pi/2$, the effective inductance is negative, which cannot be simulated in Sonnet.

Figure K.4 shows the spectrum simulated with Sonnet in green at $L_J = 1\,\mathrm{nH}$ (in full lines) and $L_J = 100\,\mathrm{nH}$ (in dashed lines), as well as the experimental data in red at $\varphi_x = 0$ (in full lines) and π (in dashed lines). For the simulated data, $L_J = 1\,\mathrm{nH}$ corresponds to $\varphi_x = 0$ and $L_J = 100\,\mathrm{nH}$ to $\varphi_x \to \pi/2$. The current I in the simulated data was obtained by

$$I = \frac{Z_{\mathrm{in}} I_0^2}{2\varphi_0 \omega},$$

where Z_{in} is the input impedance seen by the spectrometer, I_0 the critical current of the spectrometer ($I_0 = 45\,\mathrm{nA}$) and ω the frequency. This expression corresponds to the low coupling limit of Section 2.1.1. The simulated data exhibits a first peak before 20 GHz which is not observed experimentally. This mode is due to a microwave current flowing in the bias leads and is thus largely damped. The second peak close to 40 GHz with the large tail on the right-hand side is close to the one observed experimentally at 40 GHz. It corresponds to the mode already seen in samples SSQ14 and HS04 due to currents circulating in the shield planes around the central hole as represented in the first line of Figure K.3 for sample HS04. Close to 60 GHz, we observe experimentally two peaks. In the Sonnet simulation however, only one small peak at 60 GHz is present corresponding to a microwave current circulating in the gradiometric flux line. The presence of two peaks in the experimental data can originate from the fact that the two gradiometric lines are not perfectly identical as they are in the Sonnet simulation. The next peak at 70 GHz agrees well with the one seen in the experimental data. This mode was already present in sample HS04 and corresponds to current circulating in the shield plane as shown in the second line of Figure K.3 for sample HS04. The last peak, just before 80 GHz is the most interesting one. It is the mode of the RF-SQUID observed in the experiment and is moved when the inductance of the junction of the RF-SQUID is changed.

The simulated data shown here was multiplied by a factor of 4. The discrepancy between the simulated and measured currents is believed to originate from two different reasons. The first one is that the losses in the dielectrics (both the silicon substrate and the alumina layer) are difficult to estimate. In the simulations, loss tangents of the order of 10^{-4} were taken. In practice these values can greatly vary, especially at high frequencies where they are usually larger. The second reason is that the currents measured in the spectroscopy of the RF-SQUID can be underestimated (or overestimated). The bias resistance R_b of the sample consists of the two resistive HfPd leads, the resistance of which was not directly measured. A HfPd line of

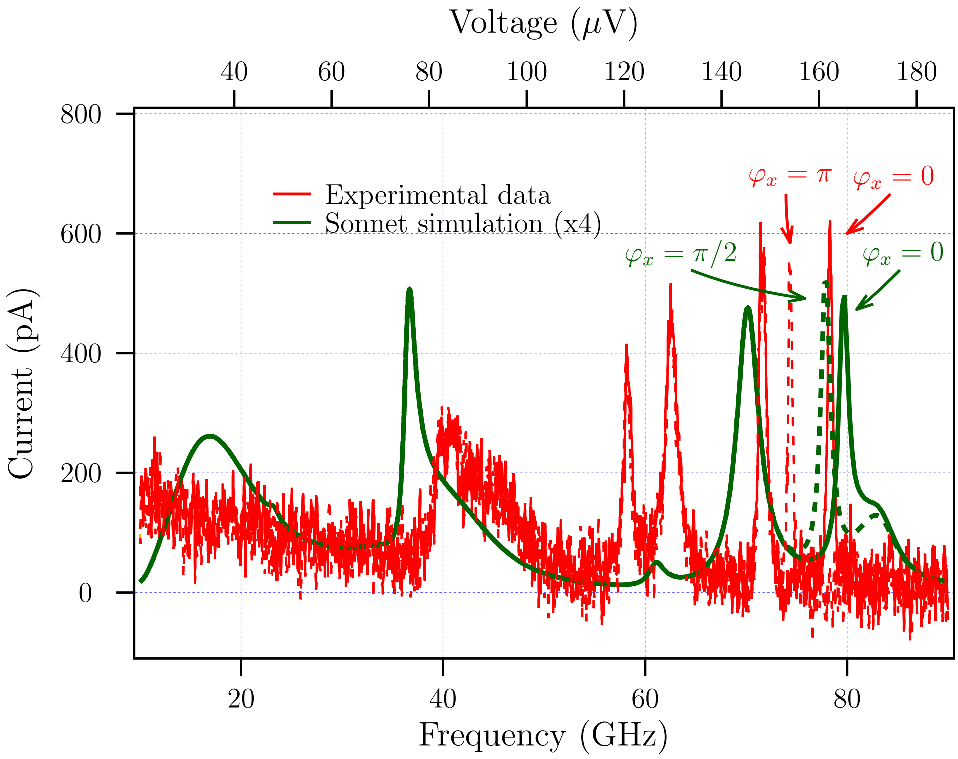

Figure K.4.: Red curve: experimental data at $\varphi_e = 0$ with $\varphi_x = 0$ (full line) and π (dashed line). Green curve: spectrum simulated with Sonnet at $\varphi_e = 0$ with Josephson inductances $L_J = 1\,\mathrm{nH}$ (full line) and $L_J = 100\,\mathrm{nH}$ (dashed line).

the same dimension with resistance $R'_b \sim R_b$ was measured in place of the actual leads. There can be a small discrepancy between the two resistance values, resulting in a scaling by a factor R'_b/R_b for the experimental data and a scaling by a factor $(R'_b/R_b)^2$ for the simulated data.

L. Expression of the current in terms of the Berry curvature

As charge and phase are conjugated, the current operator $\hat{I}$ is given by:

$$\hat{I} = \frac{1}{\varphi_0} \frac{\partial \mathcal{H}}{\partial \varphi_1}$$

For a quantum state $|\Psi\rangle$, the expected value of the current is thus:

$$I(t) = \frac{1}{\varphi_0} \left\langle \Psi \left| \frac{\partial \mathcal{H}}{\partial \varphi_1} \right| \Psi \right\rangle \tag{L.1}$$

The quantum state $|\Psi\rangle$ can be decomposed in the eigenstate basis of $\mathcal{H}$. So we need only calculate the scalar product (L.1) for the eigenstates of $\mathcal{H}$. For $|n\rangle$, this gives

$$\begin{aligned} I_n(t) &= \frac{1}{\varphi_0} \left\langle n \left| \frac{\partial \mathcal{H}}{\partial \varphi_1} \right| n \right\rangle \\ I_n(t) &= \frac{1}{\varphi_0} \langle n| \left(\frac{\partial}{\partial \varphi_1} \left(\mathcal{H} |n\rangle \right) - \mathcal{H} \frac{\partial |n\rangle}{\partial \varphi_1} \right) \end{aligned}$$

The time-dependent Schrödinger equation for state $|n\rangle$ can be written

$$\mathcal{H} |n\rangle = i\hbar \frac{\partial |n\rangle}{\partial t}$$

Injecting these expressions in the expression for the current gives

$$\begin{aligned} I_n(t) &= \frac{1}{\varphi_0} \langle n| \frac{\partial}{\partial \varphi_1} \left(i\hbar \frac{\partial |n\rangle}{\partial t} \right) + \frac{i\hbar}{\varphi_0} \frac{\partial \langle n|}{\partial t} \frac{\partial |n\rangle}{\partial \varphi_1} \\ I_n(t) &= \frac{i\hbar}{\varphi_0} \frac{\partial}{\partial \varphi_1} \left(\langle n| \frac{\partial |n\rangle}{\partial t} \right) - \frac{i\hbar}{\varphi_0} \frac{\partial \langle n|}{\partial \varphi_1} \frac{\partial |n\rangle}{\partial t} + \frac{i\hbar}{\varphi_0} \frac{\partial \langle n|}{\partial t} \frac{\partial |n\rangle}{\partial \varphi_1} \end{aligned}$$

At any time t, the state $|n\rangle$ also obeys the time-independent Schrödinger equation:

$$\mathcal{H} |n\rangle = E_n |n\rangle$$

This gives an expression for the current:

$$I_n(t) = \frac{1}{\varphi_0} \frac{\partial E_n}{\partial \varphi_1} - 4ie \frac{\partial \langle n|}{\partial \varphi_1} \frac{\partial |n\rangle}{\partial t}$$

The time derivative of $|n\rangle$ can be expressed as a function of derivatives of $|n\rangle$ with respect to all the parameters:

$$\frac{\partial \left| n \right\rangle}{\partial t} = \sum_{i=1}^{3} \frac{\partial \left| n \right\rangle}{\partial X_i} \dot{X}_i$$

Where $(X_i)_{i=(1,2,3)} = (\varphi_L, \varphi_R, n_g)$

$$I_n(t) = \frac{1}{\varphi_0} \frac{\partial E_n}{\partial \varphi_1} - 4e \sum_{i=1}^{3} i \frac{\partial \left\langle n \right|}{\partial \varphi_1} \frac{\partial \left| n \right\rangle}{\partial X_i} \dot{X}_i$$

Recalling expression (6.11) for the Berry curvature:

$$\boldsymbol{B}_n = -\Im \left\langle \boldsymbol{\nabla} n \right| \times \left| \boldsymbol{\nabla} n \right\rangle = \begin{pmatrix} B_n^{(\varphi_L)} \\ B_n^{(\varphi_R)} \\ B_n^{(n_g)} \end{pmatrix}$$

It appears that the current can be expressed in terms of the Berry curvature:

$$I_n(t) = \frac{1}{\varphi_0} \frac{\partial E_n}{\partial \varphi_1} + 2e \left(-B_n^{(\varphi_R)} \dot{n}_g + B_n^{(n_g)} \dot{\varphi}_R \right)$$

List of Symbols

Fundamental constants

$k_B = 1.381 \times 10^{-23}\ \mathrm{J\,K^{-1}}$	Boltzmann constant
$h = 6.626 \times 10^{-34}\ \mathrm{J\,s}$	Planck's constant
$e = 1.602 \times 10^{-19}\ \mathrm{C}$	Elementary charge
$\Phi_0 = h/(2e) = 2.068 \times 10^{-15}\ \mathrm{Wb}$	Magnetic flux quantum
$\varphi_0 = \Phi_0/(2\pi)$	Reduced magnetic flux quantum
$G_0 = 4e^2/h = 155\,\mu\mathrm{S}$	Superconducting quantum of conductance

Physical properties of a Josephson junction

Δ	Superconducting gap
τ	Transmission of a conduction channel
L_K	Kinetic inductance of a superconductor
φ	Phase difference across the junction
I_0	Supercurrent of the junction
C or C_J	Capacitance of the junction
R_N	Normal state resistance
$\omega_J = \lvert V \rvert / \varphi_0$	Josephson frequency, when the junction is biased at voltage V
$L_J = \varphi_0 / I_0$	Josephson inductance
$E_J = \varphi_0 I_0$	Josephson energy
$E_C = 2e^2/C_J$	Charging energy
$\omega_p = \sqrt{\dfrac{I_0}{\varphi_0 C_J}} = \dfrac{\sqrt{2E_C E_J}}{\hbar}$	Plasma frequency
$Z_J = \sqrt{\dfrac{L_J}{C_J}} = \dfrac{1}{\pi G_0}\sqrt{\dfrac{E_C}{2E_J}}$	Josephson impedance
$\beta_C = \dfrac{R^2 I_0 C}{\varphi_0} = \left(\dfrac{R}{Z_J}\right)^2$	Stewart-McCumber parameter of a Josephson junction shunted by a resistance R

Parameters of a SQUID

L	Inductance of the loop
$\beta_L = LI_0/\varphi_0 = L/L_J$	Ratio of loop inductance to the Josephson inductance
I_C	Supercurrent of the larger junction of the SQUID
I_0	Total supercurrent of the SQUID
Φ_e	Magnetic flux threading the SQUID
$\varphi_e = \Phi_e/\varphi_0$	Reduced flux in the SQUID
α	Ratio of the supercurrents of the two junctions ($\alpha \leq 1$)
ω_s	Resonance frequency of the LC mode of the SQUID

Spectrometer coupled to an external resonator

Z_e (resp. Y_e)	Impedance (resp. admittance) of the resonator
L_e	Inductance of the resonator
C_e	Capacitance of the resonator
R	Resistance of the resonator
$\omega_e = 1/\sqrt{L_e C_e}$	Resonance frequency of the resonator
Q_e	Quality factor of the resonator
$z = \dfrac{I_0}{\varphi_0 \omega_e \Re\left(Y_e\left(\omega_e\right)\right)}$	Coupling parameter of the spectrometer to the resonator
ω_0	Resonance frequency measured by the spectrometer
k	Coupling constant for two inductive loops

Mathematical functions

$K(x), E(x)$	Complete elliptic integral of the first and second kind of argument x
$J_n(x)$	n-th order Bessel function of the first kind of argument x

Bibliography

[1] Brian David Josephson. Possible new effects in superconductive tunnelling. *Physics letters*, 1(7):251–253, 1962. *Cited pages xi, 1, 11, and 41*

[2] P. W. Anderson and J. M. Rowell. Probable Observation of the Josephson Superconducting Tunneling Effect. *Physical Review Letters*, 10(6):230–232, March 1963. *Cited pages xi, 1, and 11*

[3] J Clarke and A.I. Braginski. *The SQUID Handbook*. WILEY-VCH Verlag GmbH & Co. KGaA, Weinheim, January 2005. *Cited pages xi, 1, and 40*

[4] Gian Luca Romani, Samuel J. Williamson, and Lloyd Kaufman. Biomagnetic instrumentation. *Review of Scientific Instruments*, 53(12):1815–1845, December 1982. *Cited pages xi, 1, and 40*

[5] Karsten Sternickel and Alex I. Braginski. Biomagnetism using SQUIDs: status and perspectives. *Superconductor Science and Technology*, 19(3):S160, 2006. *Cited pages xi, 1, and 40*

[6] Clark A. Hamilton. Josephson voltage standards. *Review of Scientific Instruments*, 71(10):3611–3623, September 2000. *Cited pages xi, 1, 41, and 42*

[7] N. Bergeal, F. Schackert, M. Metcalfe, R. Vijay, V. E. Manucharyan, L. Frunzio, D. E. Prober, R. J. Schoelkopf, S. M. Girvin, and M. H. Devoret. Phase-preserving amplification near the quantum limit with a Josephson ring modulator. *Nature*, 465(7294):64–68, May 2010. *Cited pages xi, 1, and 43*

[8] J.-D. Pillet, E. Flurin, F. Mallet, and B. Huard. A compact design for the Josephson mixer: The lumped element circuit. *Applied Physics Letters*, 106(22):222603, June 2015. *Cited pages xi, 1, and 43*

[9] M. H. Devoret and R. J. Schoelkopf. Superconducting Circuits for Quantum Information: An Outlook. *Science*, 339(6124):1169–1174, March 2013. *Cited pages xi, 1, and 42*

[10] J. H. Plantenberg, P. C. de Groot, C. J. P. M. Harmans, and J. E. Mooij. Demonstration of controlled-NOT quantum gates on a pair of superconducting quantum bits. *Nature*, 447(7146):836–839, June 2007. *Cited pages xi, 1, and 42*

[11] John M. Martinis, Michel H. Devoret, and John Clarke. Energy-Level Quantization in the Zero-Voltage State of a Current-Biased Josephson Junction. *Physical Review Letters*, 55(15):1543–1546, October 1985. *Cited pages xi, 1, and 42*

[12] Y. Nakamura, Yu A. Pashkin, and J. S. Tsai. Coherent control of macroscopic quantum states in a single-Cooper-pair box. *Nature*, 398(6730):786–788, April 1999. *Cited pages xi, 1, and 43*

[13] D. Vion, A. Aassime, A. Cottet, P. Joyez, H. Pothier, C. Urbina, D. Esteve, and M. H. Devoret. Manipulating the Quantum State of an Electrical Circuit. *Science*, 296(5569):886–889, May 2002. *Cited pages xi, 1, and 43*

[14] I. Chiorescu, Y. Nakamura, C. J. P. M. Harmans, and J. E. Mooij. Coherent Quantum Dynamics of a Superconducting Flux Qubit. *Science*, 299(5614):1869–1871, March 2003. *Cited pages xi, 1, and 43*

[15] Jens Koch, Terri M. Yu, Jay Gambetta, A. A. Houck, D. I. Schuster, J. Majer, Alexandre Blais, M. H. Devoret, S. M. Girvin, and R. J. Schoelkopf. Charge-insensitive qubit design derived from the Cooper pair box. *Physical Review A*, 76(4):042319, October 2007. *Cited pages xi, 1, and 43*

[16] Vladimir E. Manucharyan, Jens Koch, Leonid I. Glazman, and Michel H. Devoret. Fluxonium: Single Cooper-Pair Circuit Free of Charge Offsets. *Science*, 326(5949):113–116, October 2009. *Cited pages xi, 1, and 43*

[17] M. J. Wengler. Submillimeter-wave detection with superconducting tunnel diodes. *Proceedings of the IEEE*, 80(11):1810–1826, November 1992. *Cited pages xi, 1, and 40*

[18] J. Zmuidzinas and P. L. Richards. Superconducting detectors and mixers for millimeter and submillimeter astrophysics. *Proceedings of the IEEE*, 92(10):1597–1616, October 2004. *Cited pages xi, 1, and 40*

[19] I.K. Yanson, V.M. Svistunov, and I.M. Dmitrenko. Experimental Observation of Cooper Pair Tunneling Between Thin Layers of Superconducting Tin. *Zhurnal Eksp. Yheoret. Physics*, 20(6):1404, 1965. *Cited pages xi and 1*

[20] C. C. Grimes, P. L. Richards, and S. Shapiro. Far Infrared Response of Point-Contact Josephson Junctions. *Physical Review Letters*, 17(8):431–433, August 1966. *Cited pages xi and 1*

[21] A. H. Silver and J. E. Zimmerman. Multiple quantum resonance spectroscopy through weakly connected superconductors. *Applied Physics Letters*, 10(5):142–145, March 1967. *Cited pages xi, 1, 63, and 169*

[22] H. H. Zappe and B. S. Landman. Experimental investigation of resonances in low-Q Josephson interferometer devices. *Journal of Applied Physics*, 49(7):4149–4154, July 1978. *Cited pages xi, 1, and 63*

[23] David B. Tuckerman and J. H. Magerlein. Resonances in symmetric Josephson interferometers. *Applied Physics Letters*, 37(2):241–243, July 1980. *Cited pages xi, 1, 55, 63, and 71*

[24] S. M. Faris and E. A. Valsamakis. Resonances in superconducting quantum interference devices—SQUID's. *Journal of Applied Physics*, 52(2):915–920, February 1981. *Cited pages xi, 1, and 63*

[25] G. Paternò, A. M. Cucolo, and G. Modestino. Resonant modes in Nb baselayer interferometers with two Josephson junctions. *Journal of Applied Physics*, 57(5):1680–1685, March 1985. *Cited pages xi, 1, and 63*

[26] T. Holst, D. Esteve, C. Urbina, and M. H. Devoret. Effect of a Transmission Line Resonator on a Small Capacitance Tunnel Junction. *Physical Review Letters*, 73(25):3455–3458, December 1994. *Cited pages xi, 1, and 63*

[27] M. Hofheinz, F. Portier, Q. Baudouin, P. Joyez, D. Vion, P. Bertet, P. Roche, and D. Esteve. Bright Side of the Coulomb Blockade. *Physical Review Letters*, 106(21), May 2011. *Cited pages xi, 1, and 63*

[28] J. Basset, H. Bouchiat, and R. Deblock. High-frequency quantum admittance and noise measurement with an on-chip resonant circuit. *Physical Review B*, 85(8):085435, February 2012. *Cited pages xi, 1, and 63*

[29] A. W. Kleinsasser, M. W. Johnson, and K. A. Delin. Direct measurement of the Josephson plasma resonance frequency from I-V Characteristics. *IEEE Transactions on Applied Superconductivity*, 15(2):86–89, June 2005. *Cited pages xi, 1, and 63*

[30] René Lindell, Jari Penttilä, Mika Sillanpää, and Pertti Hakonen. Quantum states of a mesoscopic SQUID measured using a small Josephson junction. *Physical Review B*, 68(5):052506, August 2003. *Cited pages xi, 1, and 63*

[31] P.-M. Billangeon, F. Pierre, H. Bouchiat, and R. Deblock. Very High Frequency Spectroscopy and Tuning of a Single-Cooper-Pair Transistor with an On-Chip Generator. *Physical Review Letters*, 98(12):126802, March 2007. *Cited pages xi, 1, and 63*

[32] L. Bretheau, Ç Ö Girit, H. Pothier, D. Esteve, and C. Urbina. Exciting Andreev pairs in a superconducting atomic contact. *Nature*, 499(7458):312–315, July 2013. *Cited pages xii, xvi, xx, 1, 2, 5, 6, 47, 63, 64, 65, 77, 181, 193, and 219*

[33] L. Bretheau, Ç. Ö. Girit, M. Houzet, H. Pothier, D. Esteve, and C. Urbina. Theory of microwave spectroscopy of Andreev bound states with a Josephson junction. *Physical Review B*, 90(13):134506, October 2014. *Cited pages xii, xvi, 1, 5, 6, 47, 63, 77, and 181*

[34] K. K. Likharev. Superconducting weak links. *Reviews of Modern Physics*, 51(1):101–159, January 1979. *Cited pages xiii and 2*

[35] Akira Furusaki and Masaru Tsukada. Dc Josephson effect and Andreev reflection. *Solid State Communications*, 78(4):299–302, April 1991. *Cited pages xiii and 3*

[36] J.-D. Pillet, V. Benzoni, J. Griesmar, J.-L. Smirr, and Ç Ö Girit. Non-local Josephson effect in Andreev molecules. *arXiv:1809.11011 [cond-mat]*, September 2018. arXiv: 1809.11011. *Cited pages xix, 9, 190, 191, and 192*

[37] Jukka I. Väyrynen, Gianluca Rastelli, Wolfgang Belzig, and Leonid I. Glazman. Microwave signatures of Majorana states in a topological Josephson junction. *Physical Review B*, 92(13):134508, October 2015. *Cited pages xix, 9, and 193*

[38] A. Murani, A. Chepelianskii, S. Guéron, and H. Bouchiat. Andreev spectrum with high spin-orbit interactions: Revealing spin splitting and topologically protected crossings. *Physical Review B*, 96(16):165415, October 2017. *Cited pages xix, 9, and 193*

[39] Liang Fu and C. L. Kane. Josephson current and noise at a superconductor/quantum-spin-Hall-insulator/superconductor junction. *Physical Review B*, 79(16):161408, April 2009. *Cited pages xix, 9, and 198*

[40] V. Ginzburg and L. Landau. Toward the superconductivity theory. *Zhurnal Eksp. Yheoret. Physics*, 29:1064, 1950. *Cited page 11*

[41] Michael Tinkham. *Introduction to superconductivity.* Dover Publications, 2004. *Cited pages 11, 132, 161, and 251*

[42] R. Landauer. Spatial Variation of Currents and Fields Due to Localized Scatterers in Metallic Conduction. *IBM Journal of Research and Development*, 1(3):223–231, July 1957. *Cited pages 13 and 17*

[43] C. W. J. Beenakker. Universal limit of critical-current fluctuations in mesoscopic Josephson junctions. *Physical Review Letters*, 67(27):3836–3839, December 1991. *Cited page 13*

[44] Pierre-Gilles de Gennes. *Superconductivity of metals and alloys.* W.A. Benjamin, New York, 1966. OCLC: 654404058. *Cited page 14*

[45] Vinay Ambegaokar and Alexis Baratoff. Tunneling Between Superconductors. *Physical Review Letters*, 10(11):486–489, June 1963. *Cited page 17*

[46] Uri Vool and Michel H. Devoret. Introduction to Quantum Electromagnetic Circuits. *arXiv:1610.03438 [cond-mat, physics:quant-ph]*, October 2016. arXiv: 1610.03438. *Cited pages 20 and 205*

[47] Émile Mathieu. Mémoire sur le mouvement vibratoire d'une membrane de forme elliptique. *Journal de Mathématiques Pures et Appliquées*, 13:137–203, 1868. *Cited pages 21 and 23*

[48] W. C. Stewart. Current-voltage characteristics of josephson junctions. *Applied Physics Letters*, 12(8):277–280, April 1968. *Cited page 27*

[49] D. E. McCumber. Effect of ac Impedance on dc Voltage-Current Characteristics of Superconductor Weak-Link Junctions. *Journal of Applied Physics*, 39(7):3113–3118, June 1968. *Cited page 27*

[50] Richard E. Harris. Cosine and other terms in the Josephson tunneling current. *Phys. Rev. B*, 10(1):84–94, July 1974. *Cited page 32*

[51] T. A. Fulton, L. N. Dunkleberger, and R. C. Dynes. Quantum Interference Properties of Double Josephson Junctions. *Physical Review B*, 6(3):855–875, August 1972. *Cited page 36*

[52] Won-Tien Tsang and T. Van Duzer. dc analysis of parallel arrays of two and three Josephson junctions. *Journal of Applied Physics*, 46(10):4573, 1975. *Cited page 36*

[53] H. Weinstock, editor. *SQUID Sensors: Fundamentals, Fabrication and Applications.* Nato Science Series E:. Springer Netherlands, 1996. *Cited page 40*

[54] David Cohen, Edgar A. Edelsack, and James E. Zimmerman. Magnetocardiograms taken inside a shielded room with a superconducting point-contact magnetometer. *Applied Physics Letters*, 16(7):278–280, April 1970. *Cited page 40*

[55] Fernando Lopes da Silva. EEG and MEG: Relevance to Neuroscience. *Neuron*, 80(5):1112–1128, December 2013. *Cited page 40*

[56] D. J. Fixsen. The Temperature of the Cosmic Microwave Background. *The Astrophysical Journal*, 707(2):916, 2009. *Cited page 41*

[57] Sidney Shapiro. Josephson Currents in Superconducting Tunneling: The Effect of Microwaves and Other Observations. *Physical Review Letters*, 11(2):80–82, July 1963. *Cited pages 41 and 112*

[58] Jaw-Shen Tsai, A. K. Jain, and J. E. Lukens. High-Precision Test of the Universality of the Josephson Voltage-Frequency Relation. *Physical Review Letters*, 51(4):316–319, July 1983. *Cited page 41*

[59] B. Yurke, L. R. Corruccini, P. G. Kaminsky, L. W. Rupp, A. D. Smith, A. H. Silver, R. W. Simon, and E. A. Whittaker. Observation of parametric amplification and deamplification in a Josephson parametric amplifier. *Physical Review A*, 39(5):2519–2533, March 1989. *Cited page 43*

[60] I. Siddiqi, R. Vijay, F. Pierre, C. M. Wilson, M. Metcalfe, C. Rigetti, L. Frunzio, and M. H. Devoret. RF-Driven Josephson Bifurcation Amplifier for Quantum Measurement. *Physical Review Letters*, 93(20):207002, November 2004. *Cited page 43*

[61] Carlton M. Caves. Quantum limits on noise in linear amplifiers. *Physical Review D*, 26(8):1817–1839, October 1982. *Cited page 43*

[62] Steven H. Strogatz. *Nonlinear Dynamics And Chaos: With Applications To Physics, Biology, Chemistry, And Engineering.* CRC Press, Cambridge, Mass, 1 edition edition, December 2000. *Cited page 44*

[63] C. B. Whan and C. J. Lobb. Complex dynamical behavior in RCL-shunted Josephson tunnel junctions. *Physical Review E*, 53(1):405–413, January 1996. *Cited pages 45 and 46*

[64] A. B. Cawthorne, C. B. Whan, and C. J. Lobb. Complex dynamics of resistively and inductively shunted Josephson junctions. *Journal of Applied Physics*, 84(2):1126–1132, June 1998. *Cited page 45*

[65] D. V. Averin, Yu. V. Nazarov, and A. A. Odintsov. Incoherent tunneling of the cooper pairs and magnetic flux quanta in ultrasmall Josephson junctions. *Physica B: Condensed Matter*, 165-166:945–946, August 1990. *Cited page 48*

[66] Hermann Grabert and Michel Devoret. *Single Charge Tunneling.* Plenum Press, 1992. *Cited pages 48, 122, and 237*

[67] Milton Abramowitz and Irene A. Stegun, editors. *Handbook of Mathematical Functions: with Formulas, Graphs, and Mathematical Tables.* Dover Publications, New York, NY, 0009-revised edition edition, June 1965. *Cited page 50*

[68] David M. Pozar. *Microwave Engineering.* John Wiley & Sons, Hoboken, NJ, 4th edition edition, December 2011. *Cited pages 51, 78, 134, 140, and 146*

[69] Konstantin Likharev. *Dynamics of Josephson Junctions and Circuits.* Gordon and Breach Publishers, 1986. *Cited pages 55, 57, 98, and 101*

[70] AUTO, `http://indy.cs.concordia.ca/auto/`. *Cited page 59*

[71] F. Kos, S. E. Nigg, and L. I. Glazman. Frequency-dependent admittance of a short superconducting weak link. *Physical Review B*, 87(17):174521, May 2013. *Cited pages 63 and 182*

[72] D. N. Langenberg, D. J. Scalapino, and B. N. Taylor. Josephson-type superconducting tunnel junctions as generators of microwave and submillimeter wave radiation. *Proceedings of the IEEE*, 54(4):560–575, April 1966. *Cited page 63*

[73] M. M. Khapaev. Inductance extraction of multilayer finite-thickness superconductor circuits. *IEEE Transactions on Microwave Theory and Techniques*, 49(1):217–220, January 2001. *Cited pages 84, 174, and 235*

[74] Q. Dong, Y. X. Liang, D. Ferry, A. Cavanna, U. Gennser, L. Couraud, and Y. Jin. Ultra-low noise high electron mobility transistors for high-impedance and low-frequency deep cryogenic readout electronics. *Applied Physics Letters*, 105(1):013504, July 2014. *Cited page 92*

[75] H. W. Hubers, M. F. Kimmitt, N. Hiromoto, and E. Brundermann. Terahertz Spectroscopy: System and Sensitivity Considerations. *IEEE Transactions on Terahertz Science and Technology*, 1(1):321–331, September 2011. *Cited page 92*

[76] M. Büttiker, E. P. Harris, and R. Landauer. Thermal activation in extremely underdamped Josephson-junction circuits. *Physical Review B*, 28(3):1268–1275, August 1983. *Cited page 96*

[77] Michel H. Devoret, Daniel Esteve, John M. Martinis, Andrew Cleland, and John Clarke. Resonant activation of a Brownian particle out of a potential well: Microwave-enhanced escape from the zero-voltage state of a Josephson junction. *Physical Review B*, 36(1):58–73, July 1987. *Cited pages 96 and 97*

[78] James A. Blackburn, Matteo Cirillo, and Niels Grønbech-Jensen. Classical statistical model for distributions of escape events in swept-bias Josephson junctions. *Physical Review B*, 85(10):104501, March 2012. *Cited page 97*

[79] H. A. Kramers. Brownian motion in a field of force and the diffusion model of chemical reactions. *Physica*, 7(4):284–304, April 1940. *Cited page 97*

[80] L. Bretheau, Ç. Ö. Girit, C. Urbina, D. Esteve, and H. Pothier. Supercurrent Spectroscopy of Andreev States. *Physical Review X*, 3(4):041034, December 2013. *Cited page 98*

[81] Richard F. Voss and Richard A. Webb. Macroscopic Quantum Tunneling in 1-μm Nb Josephson Junctions. *Physical Review Letters*, 47(4):265–268, July 1981. *Cited page 101*

[82] Michel H. Devoret, John M. Martinis, and John Clarke. Measurements of Macroscopic Quantum Tunneling out of the Zero-Voltage State of a Current-Biased Josephson Junction. *Physical Review Letters*, 55(18):1908–1911, October 1985. *Cited page 101*

[83] Yu M. Ivanchenko and L. A. Zil'berman. The Josephson Effect in Small Tunnel Contacts. *Zhurnal Eksp. Yheoret. Physics*, 55(6):2395, 1969. *Cited page 102*

[84] John M. Martinis. Classical phase diffusion in small hysteretic Josephson junctions. *Physical Review Letters*, 63(14):1507–1510, 1989. *Cited page 103*

[85] R. L. Kautz and John M. Martinis. Noise-affected I-V curves in small hysteretic Josephson junctions. *Physical Review B*, 42(16):9903–9937, December 1990. *Cited page 103*

[86] H. H. Zappe. Minimum current and related topics in Josephson tunnel junction devices. *Journal of Applied Physics*, 44(3):1371–1377, March 1973. *Cited page 104*

[87] Y. C. Chen, Matthew P. A. Fisher, and A. J. Leggett. The return of a hysteretic Josephson junction to the zero-voltage state: I-V characteristic and quantum retrapping. *Journal of Applied Physics*, 64(6):3119–3142, September 1988. *Cited page 104*

[88] F. L. Vernon and R. J. Pedersen. Relaxation Oscillations in Josephson Junctions. *Journal of Applied Physics*, 39(6):2661–2664, May 1968. *Cited page 107*

[89] P. K. Tien and J. P. Gordon. Multiphoton Process Observed in the Interaction of Microwave Fields with the Tunneling between Superconductor Films. *Physical Review*, 129(2):647–651, January 1963. *Cited page 114*

[90] Lev Davidovich Landau. A theory of energy transfer II. *Phys. Z. Sowjetunion*, 2:46–51, 1932. *Cited page 115*

[91] Clarence Zener. Non-adiabatic crossing of energy levels. *Proc. R. Soc. Lond. A*, 137(833):696–702, September 1932. *Cited page 115*

[92] Landry Bretheau. *Localized excitations in superconducting atomic contacts: Probing the Andreev doublet.* PhD thesis, Ecole Polytechnique X, 2013. *Cited pages 115 and 191*

[93] G. E. Blonder, M. Tinkham, and T. M. Klapwijk. Transition from metallic to tunneling regimes in superconducting microconstrictions: Excess current, charge imbalance, and supercurrent conversion. *Physical Review B*, 25(7):4515–4532, April 1982. *Cited page 117*

[94] D. Averin and A. Bardas. ac Josephson Effect in a Single Quantum Channel. *Physical Review Letters*, 75(9):1831–1834, August 1995. *Cited page 117*

[95] E. N. Bratus', V. S. Shumeiko, and G. Wendin. Theory of Subharmonic Gap Structure in Superconducting Mesoscopic Tunnel Contacts. *Physical Review Letters*, 74(11):2110–2113, March 1995. *Cited page 117*

[96] J. J. Riquelme, L. de la Vega, A. Levy Yeyati, N. Agraït, A. Martin-Rodero, and G. Rubio-Bollinger. Distribution of conduction channels in nanoscale contacts: Evolution towards the diffusive limit. *Europhysics Letters*, 70(5):663–669, June 2005. *Cited page 119*

[97] Gerald B. Arnold. Superconducting tunneling without the tunneling Hamiltonian. II. Subgap harmonic structure. *Journal of Low Temperature Physics*, 68(1-2):1–27, July 1987. *Cited page 119*

[98] Julien Basset. *High frequency quantum noise of mesoscopic systems and current-phase relation of hybrid junctions.* PhD thesis, Universite Paris Sud, 2011. *Cited page 122*

[99] J. R. Schrieffer and D. M. Ginsberg. Calculation of the Quasiparticle Recombination Time in a Superconductor. *Physical Review Letters*, 8(5):207–208, March 1962. *Cited page 123*

[100] Allen Rothwarf and Michael Cohen. Rate of Capture of Electrons Injected into Superconducting Lead. *Physical Review*, 130(4):1401–1405, May 1963. *Cited page 123*

[101] C. S. Owen and D. J. Scalapino. Superconducting State under the Influence of External Dynamic Pair Breaking. *Physical Review Letters*, 28(24):1559–1561, June 1972. *Cited page 123*

[102] K. E. Gray and H. W. Willemsen. Inhomogeneous state of superconductors by intense tunnel injection of quasiparticles. *Journal of Low Temperature Physics*, 31(5-6):911–925, June 1978. *Cited page 123*

[103] J. Halbritter. On the oxidation and on the superconductivity of niobium. *Applied Physics A*, 43(1):1–28, May 1987. *Cited page 127*

[104] E. B. Rosa. The self and mutual-inductances of linear conductors. *Bulletin of the Bureau of Standards*, 4(2):301, January 1908. *Cited pages 130, 131, 157, 174, and 234*

[105] James C. Swihart. Field Solution for a Thin-Film Superconducting Strip Transmission Line. *Journal of Applied Physics*, 32(3):461–469, March 1961. *Cited pages 134 and 141*

[106] V. Belitsky, C. Risacher, M. Pantaleev, and V. Vassilev. Superconducting microstrip line model studies at millimeter and sub-millimeter waves. *International Journal of Infrared and Millimeter Waves*, 27(6):809–834, June 2006. *Cited page 135*

[107] F. C. Wellstood, C. Urbina, and John Clarke. Hot-electron effects in metals. *Physical Review B*, 49(9):5942, 1994. *Cited page 145*

[108] D. C. Mattis and J. Bardeen. Theory of the Anomalous Skin Effect in Normal and Superconducting Metals. *Physical Review*, 111(2):412–417, July 1958. *Cited page 161*

[109] Emisoftware, `https://www.emisoftware.com/calculator/coplanar-capacitance/`. *Cited page 179*

[110] C. Janvier, L. Tosi, L. Bretheau, Ç Ö Girit, M. Stern, P. Bertet, P. Joyez, D. Vion, D. Esteve, M. F. Goffman, H. Pothier, and C. Urbina. Coherent manipulation of Andreev states in superconducting atomic contacts. *Science*, 349(6253):1199–1202, September 2015. *Cited pages 184 and 193*

[111] Axel Freyn, Benoit Douçot, Denis Feinberg, and Régis Mélin. Production of Nonlocal Quartets and Phase-Sensitive Entanglement in a Superconducting Beam Splitter. *Physical Review Letters*, 106(25):257005, June 2011. *Cited page 191*

[112] Denis Feinberg, Thibaut Jonckheere, Jérôme Rech, Thierry Martin, Benoît Douçot, and Régis Mélin. Quartets and the current-phase structure of a double quantum dot superconducting bijunction at equilibrium. *The European Physical Journal B*, 88(4):99, April 2015. *Cited page 191*

[113] Zhaoen Su, Alexandre B. Tacla, Moïra Hocevar, Diana Car, Sébastien R. Plissard, Erik P. A. M. Bakkers, Andrew J. Daley, David Pekker, and Sergey M. Frolov. Andreev molecules in semiconductor nanowire double quantum dots. *Nature Communications*, 8(1):585, September 2017. *Cited page 191*

[114] Eduardo J. H. Lee, Xiaocheng Jiang, Manuel Houzet, Ramón Aguado, Charles M. Lieber, and Silvano De Franceschi. Spin-resolved Andreev levels and parity crossings in hybrid superconductor–semiconductor nanostructures. *Nature Nanotechnology*, 9(1):79–84, January 2014. *Cited page 193*

[115] David J. van Woerkom, Alex Proutski, Bernard van Heck, Daniël Bouman, Jukka I. Väyrynen, Leonid I. Glazman, Peter Krogstrup, Jesper Nygård, Leo P. Kouwenhoven, and Attila Geresdi. Microwave spectroscopy of spinful Andreev bound states in ballistic semiconductor Josephson junctions. *Nature Physics*, 13(9):876–881, September 2017. *Cited page 193*

[116] M. Hays, G. de Lange, K. Serniak, D. J. van Woerkom, D. Bouman, P. Krogstrup, J. Nygård, A. Geresdi, and M. H. Devoret. Direct Microwave Measurement of Andreev-Bound-State Dynamics in a Semiconductor-Nanowire Josephson Junction. *Physical Review Letters*, 121(4):047001, July 2018. *Cited page 193*

[117] B. van Heck, J. I. Väyrynen, and L. I. Glazman. Zeeman and spin-orbit effects in the Andreev spectra of nanowire junctions. *Physical Review B*, 96(7):075404, August 2017. *Cited page 193*

[118] L. Tosi, C. Metzger, M. F. Goffman, C. Urbina, H. Pothier, Sunghun Park, A. Levy Yeyati, J. Nygård, and P. Krogstrup. Spin-orbit splitting of Andreev states revealed by microwave spectroscopy. *arXiv:1810.02591 [cond-mat]*, October 2018. arXiv: 1810.02591. *Cited pages 194, 195, and 196*

[119] M. Zgirski, L. Bretheau, Q. Le Masne, H. Pothier, D. Esteve, and C. Urbina. Evidence for Long-Lived Quasiparticles Trapped in Superconducting Point Contacts. *Physical Review Letters*, 106(25):257003, June 2011. *Cited page 195*

[120] P. Krogstrup, N. L. B. Ziino, W. Chang, S. M. Albrecht, M. H. Madsen, E. Johnson, J. Nygård, C. M. Marcus, and T. S. Jespersen. Epitaxy of semiconductor–superconductor nanowires. *Nature Materials*, 14(4):400–406, April 2015. *Cited page 195*

[121] W. Chang, S. M. Albrecht, T. S. Jespersen, F. Kuemmeth, P. Krogstrup, J. Nygård, and C. M. Marcus. Hard gap in epitaxial semiconductor–superconductor nanowires. *Nature Nanotechnology*, 10(3):232–236, March 2015. *Cited page 195*

[122] M. F. Goffman, C. Urbina, H. Pothier, J. Nygård, C. M. Marcus, and P. Krogstrup. Conduction channels of an InAs-Al nanowire Josephson weak link. *New Journal of Physics*, 19(9):092002, 2017. *Cited page 195*

[123] Liang Fu and C. L. Kane. Topological insulators with inversion symmetry. *Physical Review B*, 76(4):045302, July 2007. *Cited page 198*

[124] Liang Fu and C. L. Kane. Superconducting Proximity Effect and Majorana Fermions at the Surface of a Topological Insulator. *Physical Review Letters*, 100(9):096407, March 2008. *Cited page 198*

[125] Jason Alicea. New directions in the pursuit of Majorana fermions in solid state systems. *Reports on Progress in Physics*, 75(7):076501, July 2012. *Cited page 198*

[126] C.W.J. Beenakker. Search for Majorana Fermions in Superconductors. *Annual Review of Condensed Matter Physics*, 4(1):113–136, 2013. *Cited page 198*

[127] J. Wiedenmann, E. Bocquillon, R. S. Deacon, S. Hartinger, O. Herrmann, T. M. Klapwijk, L. Maier, C. Ames, C. Brüne, C. Gould, A. Oiwa, K. Ishibashi, S. Tarucha, H. Buhmann, and L. W. Molenkamp. 4π-periodic Josephson supercurrent in HgTe-based topological Josephson junctions. *Nature Communications*, 7:10303, January 2016. *Cited pages 198 and 199*

[128] Erwann Bocquillon, Russell S. Deacon, Jonas Wiedenmann, Philipp Leubner, Teunis M. Klapwijk, Christoph Brüne, Koji Ishibashi, Hartmut Buhmann, and Laurens W. Molenkamp. Gapless Andreev bound states in the quantum spin Hall insulator HgTe. *Nature Nanotechnology*, 12(2):137–143, February 2017. *Cited pages 198 and 199*

[129] K. v. Klitzing, G. Dorda, and M. Pepper. New Method for High-Accuracy Determination of the Fine-Structure Constant Based on Quantized Hall Resistance. *Physical Review Letters*, 45(6):494–497, August 1980. *Cited page 200*

[130] D. J. Thouless, M. Kohmoto, M. P. Nightingale, and M. den Nijs. Quantized Hall Conductance in a Two-Dimensional Periodic Potential. *Physical Review Letters*, 49(6):405–408, August 1982. *Cited page 200*

[131] Mahito Kohmoto. Topological invariant and the quantization of the Hall conductance. *Annals of Physics*, 160:343–354, April 1985. *Cited page 200*

[132] M. V. Berry. Quantal Phase Factors Accompanying Adiabatic Changes. *Proceedings of the Royal Society of London A: Mathematical, Physical and Engineering Sciences*, 392(1802):45–57, March 1984. *Cited pages 200 and 201*

[133] Anupam Garg. Berry phases near degeneracies: Beyond the simplest case. *American Journal of Physics*, 78(7):661–670, July 2010. *Cited pages 200, 202, 205, and 212*

[134] J. von Neuman and E. Wigner. Uber merkwürdige diskrete Eigenwerte. *Physikalische Zeitschrift*, 30:467–470, 1929. *Cited page 203*

[135] E. Teller. The Crossing of Potential Surfaces. *The Journal of Physical Chemistry*, 41(1):109–116, January 1937. *Cited page 203*

[136] Paul A. M. Dirac. Quantized Singularities in the Electromagnetic Field. *Proc.Roy.Soc.Lond.*, A133:60–72, 1931. *Cited page 204*

[137] B. van Heck, S. Mi, and A. R. Akhmerov. Single fermion manipulation via superconducting phase differences in multiterminal Josephson junctions. *Physical Review B*, 90(15):155450, October 2014. *Cited page 205*

[138] Roman-Pascal Riwar, Manuel Houzet, Julia S. Meyer, and Yuli V. Nazarov. Multiterminal Josephson junctions as topological matter. *Nature Communications*, 7:11167, April 2016. *Cited pages 205 and 211*

[139] Erik Eriksson, Roman-Pascal Riwar, Manuel Houzet, Julia S. Meyer, and Yuli V. Nazarov. Topological transconductance quantization in a four-terminal Josephson junction. *Physical Review B*, 95(7):075417, 2017. *Cited page 205*

[140] J. R. Johansson, P. D. Nation, and Franco Nori. QuTiP: An open-source Python framework for the dynamics of open quantum systems. *Computer Physics Communications*, 183(8):1760–1772, August 2012. *Cited page 208*

Résumé

Cette thèse décrit la réalisation d’un nouveau dispositif pour la physique mésoscopique : le spectromètre Josephson. Il est composé de deux jonctions Josephson et repose sur l’effet Josephson pour convertir une tension continue en oscillations micro-ondes de fréquence pouvant atteindre 180 GHz. L’absorption de ces photons est directement mesurée sur la caractéristique courant-tension du spectromètre.

Le spectromètre est soigneusement dessiné pour éviter qu’il n’excite des modes électromagnétiques parasites et pour optimiser le couplage au système d’intérêt.

Le spectromètre Josephson est utilisé pour mesurer le spectre de quatre systèmes simples dans une large gamme de fréquences : un mode de résonateur LC autour de 150 GHz, l’excitation de quasiparticules dans un supraconducteur au-dessus de 90 GHz, la fréquence plasma d’une jonction Josephson autour de 15 GHz et la fréquence plasma d’un RF-SQUID autour de 80 GHz.

Finalement, quelques systèmes plus complexes et stimulants pouvant être sondés avec le spectromètre sont présentés, ainsi que quelques améliorations à apporter à la version actuelle du spectromètre.

Mots Clés

Physique mésoscopique, jonction Josephson, supraconducteur, topologie, circuits quantiques

Abstract

This thesis discusses the realization of a new device for mesoscopic physics: the Josephson spectrometer. It consists of two Josephson junctions and relies on the Josephson effect to convert a DC voltage to microwave oscillations at frequencies up to 180 GHz. Absorption of the emitted photons is directly measured in the current-voltage characteristic of the spectrometer.

The spectrometer is carefully designed in order to avoid exciting parasitic electromagnetic modes and to optimize the coupling to the device under test.

The Josephson spectrometer is used to measure the spectra of four simple systems over a wide frequency range: a LC resonator mode around 150 GHz, the excitation of quasiparticles in a superconductor above 90 GHz, the plasma frequency of a Josephson junction around 15 GHz and the plasma frequency of a RF-SQUID around 80 GHz.

Finally, some more complex and challenging targets for the spectrometer are presented, as well as improvements to be implemented to the current version of the device.

Keywords

Mesoscopic physics, Josephson junction, superconductor, topology, quantum circuits